HAL
open science

Réalisation expérimentale de l'effet Hong-Ou-Mandel atomique

Raphael Lopes

To cite this version:

Raphael Lopes. Réalisation expérimentale de l'effet Hong-Ou-Mandel atomique. Optics [physics.optics]. Institut d'Optique Graduate School, 2015. English. NNT : 2015IOTA0001 . tel-01199886

HAL Id: tel-01199886

https://pastel.hal.science/tel-01199886v1

Submitted on 16 Sep 2015

HAL is a multi-disciplinary open access archive for the deposit and dissemination of scientific research documents, whether they are published or not. The documents may come from teaching and research institutions in France or abroad, or from public or private research centers.

L'archive ouverte pluridisciplinaire **HAL**, est destinée au dépôt et à la diffusion de documents scientifiques de niveau recherche, publiés ou non, émanant des établissements d'enseignement et de recherche français ou étrangers, des laboratoires publics ou privés.

INSTITUT D'OPTIQUE GRADUATE SCHOOL

ÉCOLE DOCTORALE ONDES ET MATIERE

DISCIPLINE Physique

THÈSE

pour l'obtention du grade de Docteur en science de l'Institut d'Optique Graduate School

préparée au Laboratoire Charles Fabry

soutenue le 29/04/2015

par

Raphael LOPES

An atomic Hong–Ou–Mandel experiment

Directeur de thèse :	Denis Boiron	–	Institut d'Optique (LCFIO - Palaiseau)

Composition du jury :

Directeur de thèse :	Denis Boiron	–	Institut d'Optique (LCFIO - Palaiseau)
Président du jury :	Philippe Bouyer	–	Institut d'Optique (LP2N - Bordeaux)
Rapporteurs :	John Rarity	–	University of Bristol
	Frédéric Chevy	–	École Normale Supérieure (LKB - Paris)
Examinateurs :	Rosa Tualle-Brouri	–	Institut d'Optique (LCFIO - Palaiseau)
Membres invités :	Alain Aspect	–	Institut d'Optique (LCFIO - Palaiseau)

Declaration

I declare that this thesis is a presentation of my original research work unless otherwise stated with due reference to the literature and acknowledgement of collaborative research and discussions.

Mar salgado

" Ó mar salgado, quanto do teu sal
São lágrimas de Portugal!
Por te cruzarmos, quantas mães choraram,
Quantos filhos em vão rezaram!
Quantas noivas ficaram por casar
Para que fosses nosso, ó mar!
Valeu a pena? Tudo vale a pena
Se a alma não é pequena.
Quem quer passar além do Bojador
Tem que passar além da dor.
Deus ao mar o perigo e o abismo deu,
Mas nele é que espelhou o céu"

Fernando Pessoa

Abstract

In this thesis, we report the first realisation of the Hong–Ou–Mandel experiment with massive particles in momentum space. This milestone experiment was originally performed in quantum optics: two photons arriving simultaneously at the input ports of a 50:50 beam-splitter always emerge together in one of the output ports. The effect leads to a reduction of coincidence counts which translates into a dip when particles are indistinguishable.

We performed the experiment with metastable helium atoms where the specificities of the Micro-Channel-Plate detector allows one to recover the momentum vector of each individual atom. After listing the necessary tools to perform this experiment with atoms, the experimental sequence is discussed and the results are presented. In particular we measured a coincidence count reduction that cannot be explained through any simple classical model. This corresponds to the signature of a two-particle interference, and confirms that our atomic pair source produces beams which have highly correlated populations and are well mode matched. This opens the prospect of testing Bell's inequalities involving mechanical observables of massive particles, such as momentum, using methods inspired by quantum optics. It also demonstrates a new way to produce and benchmark twin-atom pairs that may be of interest for quantum information processing.

Keywords: Quantum atom optics — Bose–Einstein condensate — Four-wave mixing — Atomic pairs — Optical lattices — Correlations — Single-Atom detector — Metastable helium

Résumé

Cette thèse décrit l'observation expérimentale de l'effet Hong-Ou-Mandel avec une source atomique ultra-froide. L'expérience originale réalisée en 1987 par C. K. Hong, Z. Y. Ou et L. Mandel illustre de façon simple une interférence à deux particules explicable uniquement par la mécanique quantique : deux particules bosoniques et indiscernables, arrivant chacune sur une face d'entrée différente d'une lame semi-réfléchissante ressortent ensemble. Cet effet se traduit par une réduction du taux de détection en coïncidence entre les deux voies de sortie quand les particules arrivent simultanément sur la lame. Cette expérience fut originalement réalisée avec des photons et nous rapportons ici la première mise en oeuvre expérimentale avec des particules massives se propageant dans l'espace libre.

Après présentation des différentes techniques nécessaires à sa réalisation, nous décrivons cette expérience et analysons les résultats obtenus. En particulier, la réduction du taux de coïncidence est suffisamment forte pour exclure toute interprétation classique ; l'observation de cet effet constitue une brique fondamentale dans le domaine de l'information quantique atomique.

Mots-clé : Optique quantique atomique — Condensat de Bose–Einstein — Mélange à quatre ondes — Paires atomiques — Réseau optique — Corrélations — Détecteur à atome unique — Hélium métastable

Acknowledgements

I would like to express my very great appreciation to my advisor Denis Boiron, who has been a huge support over my PhD thesis. I learned so much from him and his good humour was very important to face all the difficulties that we had on the experiment. I would also like to thank him for all his advices and opinions that are very important for me. My special thanks are extended to my group members: Alain Aspect who so often asks so called "naive question" that so often shift things around and allows us to face a problem from a different approach; Chris Westbrook with whom I had the pleasure to have very interesting and productive discussions about future projects on the experiment; and Marc Cheneau with whom I had the opportunity, or better said, the privilege to work with daily. I appreciated his rigour and dedication and I am sure that his future experiment will be very successful. Most importantly I would like to express my most sincere gratitute to all four for giving me the *keys* of the experiment and letting me carry it. It was an unique opportunity that I will never forget.

I would like to thank all the atom optic group permanents and in special Isabelle Bouchoule and David Clément for all the support and conversations (that were very often continued in the Bus 91 and RER). I would also like to thank the support from the quantum optic group both permanents and students that very often helped us in very different situations going from signal generator loan (very long loan I have to say) to a car battery charge. In special I would like to thank Antoine Browaeys. Not only his thesis was one of the most valuable references during my entire thesis but also for his advices and remarks.

I obviously want to thank the PhD students with who I worked. J.C. Jaskula, M.Bonneau and J.Ruaudel that welcomed me at the beginning of my thesis. Particularly, I would like to thank Josselin who teached me most of the things I know about the metastable helium experiment and with who I particularly enjoyed working with. I wish him all the best for his future. I would also like to express my gratitude to Almaz Imanaleiev and Pierre Dussarrat for having participated in the results here discussed and helping me in the most stressful moments of the thesis. I think that the two together will be able to tackle all the difficulties and I have no doubt that the experiment is in good hands. I would also like to thank the PhD students/postdoc: Vincent, Asling, Cécile, Cécile, Lauriane, Guilhem, Quentin, Rockson, Steven, Jérémie, Valentin, Giuseppe, Lorenzo and others that have either already left or have just joined the group. From those who have already left, I would like to specially thank Guillaume Salomon, Bess Fang, Ralf Kohlhaas and Kilian Muller for all the discussions about physics or life in general. Ralf, the Gryffindor room was definitely the best by the way. Ah, and Lauriane I have to say that I am definitely going to miss your cakes (for real).

I would also like to thank all those people, colleagues, family and friends, who have contributed to this thesis directly or indirectly and in special to: Sofia for all those weekends and late nights when I was simply not there; Marco for opening the RAG library door every weekend so that I could continue my work; Guido for sending me the most stupid/incredible comments/links/photos at any hour (seriously time zones are very confusing); and Luis for all the poker nights and *clássicos* (dude you seriously have to change club and learn how to play poker).

This thesis was supported by the PhD grant SFRH/BD/62377/2009 from FCT, co–financed by FSE, POPH/QREN and EU.

Contents

Introduction **3**
Manuscript organisation 5

1 Basic concepts of the Hong–Ou–Mandel experiment **13**
1.1 HOM effect: basic explanation 14
1.1.1 Generalisation of the HOM effect 17
1.1.2 Generalisation for any input state 20
1.1.3 Classical threshold 22
1.2 HOM-dip visibility and Cauchy-Schwarz inequality 23
1.3 HOM experiment with atoms: necessary tools 27

2 Experimental requisites towards the HOM experiment: BEC-stability **33**
2.1 Status of the experiment in the beginning of the project 34
2.1.1 Metastable helium 34
2.1.2 The Micro-Channel-Plate: He* detector 35
2.1.3 Cooling protocol 39
2.1.4 Vertical dipole trap 40
2.1.5 The 1D optical lattice 42
2.1.6 Summary 43
2.2 Bose–Einstein condensate of metastable Helium 44
2.2.1 Arrival time instability of the condensate 44
2.2.2 Anisotropy of the BEC: phase fluctuation issues 47
2.2.3 Quasi-BEC or BEC? 47
2.2.4 Crossed dipole trap: solution to both issues 50
2.2.5 Condensate: determination of the chemical potential and size 54
2.3 Conclusion 59

3 Experimental requisites towards the HOM experiment: atomic pair production **65**
3.1 Theory of shallow optical periodic potentials 66
3.1.1 Formation of a periodic potential 66
3.1.2 Energy band structure in the presence of a lattice 67
3.1.3 Adiabatic loading 68
3.1.4 Spontaneous emission 71
3.1.5 Instabilities in the presence of a lattice 71
3.2 Dynamical instability: pair creation 72
3.2.1 Determination of the phase-matching conditions 74
3.2.2 Atomic beam shape prediction 80
3.3 Pair creation: experimental realisation 81
3.3.1 Geometrical alignment 83
3.3.2 Loading procedure of the 1D lattice 83
3.3.3 Atomic pair production 85

3.3.4 Evolution of the pairs in the trapping potential . . . 86
3.4 Correlated pairs of atoms: analysis . . . 91
3.4.1 Cross-correlation and autocorrelation . . . 91
3.4.2 Non-classical correlations . . . 95
3.5 Conclusions . . . 98

4 Experimental requisites towards the HOM experiment: atomic beam-splitter 105
4.1 Bragg diffraction . . . 106
4.2 Beam-splitter calibration with the BEC . . . 110
4.2.1 Geometrical alignment of the beam-splitter . . . 111
4.2.2 Alignment via Bragg diffraction . . . 112
4.2.3 Resonance condition in free space . . . 114
4.2.4 50:50 beam-splitter and mirror stability . . . 115
4.3 Beam-splitter used on the atomic pairs . . . 116
4.4 Noise induced by the beam-splitter on the atomic beams . . . 118
4.5 Phase stability of the beam-splitter . . . 119
4.6 Autocorrelation measurement via a 50:50 beam-splitter . . . 123
4.7 Conclusion . . . 125

5 Atomic Hong–Ou–Mandel experiment 129
5.1 HOM effect: how to measure? . . . 130
5.1.1 How to tune distinguishability? . . . 130
5.1.2 Filtering method: 3D detection and noiseless beam-splitter . . . 133
5.2 HOM: experimental sequence . . . 136
5.3 Analysis and measurement of the HOM effect . . . 137
5.3.1 Analysis: momentum selection . . . 138
5.3.2 Analysis: optimisation of the integration volume . . . 140
5.3.3 Analysis: population stability . . . 142
5.4 Dip visibility: theoretical estimation . . . 144
5.4.1 Pair population . . . 146
5.4.2 Evolution of the signal to noise ratio of the HOM-dip visibility with $\langle n \rangle$. 148
5.5 HOM-dip width: some explanation . . . 151
5.5.1 Prediction of the width . . . 152
5.5.2 Comparison with the experimental results . . . 154
5.6 Coalescence effect . . . 157
5.6.1 Autocorrelation measurement . . . 157
5.6.2 Conditional probability . . . 160
5.7 Others way to measure the destructive interference: variance of the population difference . . . 161
5.8 Role of the interactions . . . 163
5.9 Conclusion . . . 164

Conclusion and perspectives 167
Perspectives - Bell's inequalities . . . 168

A Speed of sound expression in the case of a quasi-1D Bose–Einstein condensate 173

B Characterisation of the crossed dipole trap 175
B.1 Crossed dipole trap potential . . . 178

C Raman transfer set-up for a metastable Helium experiment 183

D Detailed calculations for the HOM experiment 185

D.1 Beam-splitter scattering matrix 185
D.1.1 50:50 beam-splitter 186
D.1.2 Mirror 187
D.2 Field operator evolution 187
D.3 Cross-correlation and HOM-dip 189
D.3.1 Visibility without assumption of the incoming state 189
D.3.2 Indistinguishable and distinguishable cases 190
D.3.3 HOM-dip width 191
D.4 Autocorrelation and coalescence effect 192
D.4.1 Width of the autocorrelation measurement 194
D.5 Variance of the population difference 194
D.6 Effect of the beam-splitter transmittance 195

E Detailed calculations for test of Bell's inequality **199**

Complete Bibliography **205**

List of publications **217**

Introduction

Quantum mechanics often sounds abstract or inaccessible when theoretically discussed. Concepts such as entanglement and non-locality have for very long seemed out of reach. However, continuous technical advances open the way to probe this theory in its more deep details and to constantly put its validity to the test. The realisation of benchmark experiments allowed to truly understand the theory behind it and to realise how vast and rich is its field of applications.

Entanglement is probably one of the most intriguing feature of quantum mechanics, described by Albert Einstein as a "spooky action at a distance". The physical object is affected without being physically touched, contrarily to the contact description of interactions supported by early classical mechanical theories. Entanglement, in its most basic formulation, corresponds to two particles generated or interacting as a pair in such way that the quantum state description of each particle cannot be done individually, instead, it describes the pair. This means, for instance, that if the two particles are travelling away from each other, any measurement performed on one of the two will immediately affect the other one. This led Einstein, Podolsky and Rosen to question the completeness of quantum mechanics in their famous 1935's paper [1] against the Copenhagen interpretation [2]. Since no information can travel faster then the speed of light, than how can a particle immediately feel the effect of the other? Are there *hidden variables* shared by both particles which guarantee that the two "combine" their answer at the beginning of the experiment? These questions raised a spirited discussion in the scientific community with Bohr [3] and Schrödinger [4, 5] defending the completeness of quantum theory contrary to the predictions of Einstein. These questions, which stayed for a long time in the epistemological domain, were converted to an algebraic form by Bell in the early 60's, leading to the famous Bell's inequalities tests [6]. Therefore all local theories of natural phenomena formulated within the framework of local-realism may be tested using a single experimental arrangement whose result differs from the prediction of a complete quantum theory description [7, 8], where the two particles are inseparable and their description is non-local. Since both descriptions do not lead to the same results, an experimental violation of one of the tests, corresponding in most cases to an algebraic inequality, proves that local-realism cannot describe the result and that quantum mechanics is complete.

With the advent of the first laser in the 60's and the development of single photon pairs, optics entered deeply in the realm of quantum mechanics. It began to be possible, via a pumped radiative atomic cascade [9–11] or spontaneous parametric down-conversion in a non-linear crystals [12, 13], to produce correlated single pairs of photons. The first experimental protocols for tests of non-locality were formulated in the 70's using polarisation detection [9, 14, 15] and the first experiments performed just a few years later [8, 10, 16, 17] proving that quantum mechanics is intrinsically non-local. Since then, tests of Bell's inequalities are getting closer to the original paradox with tests on momentum and phase measurements [18], with increasing space-like separation of the two observers [19] and higher detection efficiency [20, 21].

This action "at distance" is at the heart of several recent developments in the topic of quantum cryptography [22, 23], quantum information [24–26] or even quantum teleportation [27, 28].

The flexibility of the experimental realisations and the increasing distances between the particles [29–32] make us believe that this topic of research will revolutionise our future.

Almost 40 years after the first laser, another technological jump led to the observation of the first Bose–Einstein condensate (BEC) [33]. This macroscopic state of matter described by a single wave-function opened the door to an incredible vast field of research and applications. One of the most interesting feature of cold atoms experiments is the ability to simulate many different Hamiltonian. Allowing us, from very general assumptions, to follow the evolution of a system with the advantage of controlling its different parameters. This allows one to simulate the behaviour of solid state physics, getting deeper in the understanding of superconductivity [34–36], to realise analogues of cosmological objects [37–39], to study the low energy structure of matter such as the Higgs amplitude mode [40, 41], to perform inertial precision measurements [42, 43] or to generate entangled states in analogy to what is done in quantum optics [44–46], the last being the main interest of our work.

Since the Bose–Einstein condensate is a macroscopic coherent source of matter-waves, as a laser is in quantum optics for photons, it did not take long until the first atomic pairs experiments were performed. From the very strong non-linearity of the condensate, due to the atom-atom interactions, it has been possible to create atomic pairs via condensate collisions [47, 48] or through dissociation of weakly bound molecules near a magnetic-field Feshbach resonance [49]. The domain of both atomic spin and atomic pairs in momentum space have, in the last years, showed promising results with the measurement of squeezing in momentum space and spin domain [50–52] and entanglement [53].

One of the milestone experiments in quantum optics is the one performed by Hong, Ou and Mandel [54] in 1987. It corresponds to a simple conceptual experiment at the origin of very pure entangled state production. The experiment consists of two photons entering a 50:50 beam-splitter, one in each input port. When both photons are identical, their probabilities of exiting in different output ports cancelled out due to destructive interference effect. Consequently, one will always detect both photons emerging together in one of the two output ports. The resulting output state is a maximally entangled state which is widely used in quantum optics [55, 56]. On the other hand, if photons become distinguishable the destructive interference effect vanishes and the output state is no longer entangled. With this experiment, one can measure accurately the correlation strength of the pair, the source bandwidth, path lengths and arrival time of the two photons on the beam-splitter. It is also widely used for logical operations leading, for instance to the realisation of a C-NOT gate [57, 58]. Outside quantum optics, this experiment has been recently realised in the microwave frequency domain [56], with levitons [59], electrons [60] and surface plasmons [61, 62]. Similar effects have also been observed with independently prepared single atom sources in individual optical tweezers [63].

In this manuscript, we discuss the realisation of a Hong–Ou–Mandel experiment with atomic pairs in momentum space, in close analogy to the original quantum optics experiment [54]. Atoms with different momenta are recombined on a 50:50 atomic beam-splitter performed by Bragg diffraction [43]. Via the correlation reduction at the output ports, we identify the quantum destructive interference effect between identical paths.

Manuscript organisation

The manuscript is organised as follows:

- **Chapter 1**

  A brief introduction to the Hong–Ou–Mandel effect, its description and a link to the Cauchy–Schwarz inequality will be given. This will allow us to understand the fundamental interest lying behind this experiment and how can one use it to describe the pair source. From this discussion, the most essential tools in order to adapt the photonic experiment to matter-waves sources will be listed;

- **Chapter 2**

  An overview of the apparatus, before this work started, is given, pointing out the deficiencies that were present. The solutions adopted in order to suppress those weak points and how this played an important role in the experimental realisation of the atomic Hong-Ou-Mandel effect will be discussed. Among the improvements made, we will give special attention to the new crossed dipole trap designed for the experiment;

- **Chapter 3**

  We divide our discussion on the role of the different lattices at play in our experiment in two chapters. In this chapter, we start by introducing the most basic concepts of the effect of a periodic potential on the atoms. Since the pairs are produced via dynamical instabilities of a BEC placed in a moving lattice, we will then discuss the theory behind it and the experimental realisation of atomic pairs in momentum space;

- **Chapter 4**

  The basic tools to manipulate the atoms will be presented in this chapter. We will focus our discussion in how to perform an atomic 50:50 beam-splitter and mirror. Another lattice will be presented and discussed in detail, the beam-splitter lattice. In this chapter, we will give particular attention to the theory of Bragg diffraction at the heart of the atomic mirror and beam-splitter;

- **Chapter 5**

  Finally, the main result of this manuscript will be presented, namely the Hong–Ou–Mandel experiment with matter waves. We will show that it is possible with the atomic source to realise a two-particle interference and that no simple classical theory can explain our result. The analysis will give deep insights on the atomic source properties and how it can be used for non-classical interferometric studies, opening the way to more complex tests of quantum non-locality via tests of Bell's inequalities;

- **Appendix A**

  This appendix corresponds to the derivation of the speed of sound in a condensate following the method described in Ref. [64]. This is useful for systems lying in the intermediate quasi-condensate regime.

- **Appendix B**

  A more detailed calibration of the crossed-dipole trap is given with emphasis on the experimental determination of the trapping beams waists;

- **Appendix C**

  A brief description of stimulated two-photon Raman scattering is given. The most important numbers, specifically, the detuning used, the angle between the two beams and the transfer efficiency are specified;

- **Appendix D**

  This appendix is a complement to Chapter 5. We will describe the steps towards the expressions used for the HOM-dip visibility and width. A special attention is also given to the mirror or 50:50 beam-splitter imperfections where we will show that these imperfections do not have a strong impact on the HOM-dip visibility;

- **Appendix E**

  In the conclusion of this manuscript, a brief introduction to a possible scheme to perform the test of Bell's inequalities in momentum space will be discussed. The derivation of the main results shown in the Perspectives are here summarised.

As a side note, although in this manuscript only the work performed to the realisation of the Hong–Ou–Mandel is discussed, I would like to point out that I also participated in other projects during my PhD whose related publications are added at the end of this manuscript. In particular, I strongly participated in two projects:

The acoustic analog to the dynamical Casimir effect in a Bose-Einstein condensate [39]. *In this project, we modulated the condensate density via the modulation of the optical trap stiffness, in which the condensate is obtained. This modulation is performed with velocities above and below the speed of sound of the condensate. This is equivalent to modulating the index of refraction of an optical cavity close to the speed of light, leading to the pairwise creation of photons [65, 66]. This phenomenon has recently been observed in Ref. [67] where pairs of photons in the micro-wave domain were produced and two-mode squeezing observed in the emitted radiation.*

In our experiment, we observed the production of two atomic clouds with opposite momenta and proved, through the measurement of the correlation between the two clouds, that the process is pairwise. We also studied the response of the system to the modulation frequency. Via Bragg spectroscopy, we were able to show that the energy given to the system was split between the two clouds forming the pair in analogy to parametric down-conversion for quantum optics. Therefore, we were able to prove pairwise creation of particles with momenta ranging from the phononic branch to the particle branch of the Bogoliubov dispersion relation.

The study of 2nd order coherence of Superradiance from a Bose–Einstein condensate [68]. *In an anisotropic source, a collective emission builds up more efficiently in the directions of highest optical thickness. For that reason, in an elongated BEC, we excite atoms such that an allowed emission dipole can radiate along the elongated BEC axis. Superradiance is, therefore, expected to occur along this axis, in the so called "endfire" modes [69, 70]. Just after been released from the crossed dipole trap, the atoms are excited through the application of a very intense and close to resonance (600 MHz detuned) laser beam. The atoms initially in the $m_j = 1$ state are equally scattered into $m_j = \pm 1$ and $m_j = 0$.*

We focused our study in the atoms scattered to the two endfire mode of the $m_j = 0$ state corresponding to Raman superradiance [71]. We observed that the second order auto-correlation function reaches a value close to 2. This shows clearly that, despite strong amplified emission in the endfire modes, the atoms undergoing a superradiant process have statistics comparable to that of a thermal sample. These large fluctuations can be simply understood by modelling the superradiant emission as a four-wave mixing process; they arise from the fact that the emission is triggered by spontaneous emission. In order to confirm this explanation, we performed a coherent transfer of population from the state $m_j = 1$ to $m_j = 0$ via stimulated Raman scattering. In this case, vacuum fluctuations do not initiate the scattering process and the resulting mode occupation is not thermal but coherent which translates into the measurement of a very-nearly flat second order normalised auto-correlation function equal to 1.

Bibliography

[1] A. Einstein, B. Podolsky, and N. Rosen, "Can Quantum-Mechanical Description of Physical Reality Be Considered Complete?", Phys. Rev. **47**, 777–780 (1935) (cit. on pp. 3, 168).

[2] J. G. Cramer, "The transactional interpretation of quantum mechanics", Rev. Mod. Phys. **58**, 647–687 (1986) (cit. on pp. 3, 168).

[3] N. Bohr, "Can Quantum-Mechanical Description of Physical Reality be Considered Complete?", Phys. Rev. **48**, 696–702 (1935) (cit. on p. 3).

[4] E. Schrödinger, "Discussion of Probability Relations between Separated Systems", Mathematical Proceedings of the Cambridge Philosophical Society **31**, 555–563 (1935) (cit. on p. 3).

[5] E. Schrödinger, "Probability relations between separated systems", Mathematical Proceedings of the Cambridge Philosophical Society **32**, 446–452 (1936) (cit. on p. 3).

[6] J. S. Bell, "On the Einstein-Podolsky-Rosen paradox", Physics **1**, 195–200 (1964) (cit. on pp. 3, 169).

[7] J. F. Clauser, M. A. Horne, A. Shimony, and R. A. Holt, "Proposed Experiment to Test Local Hidden-Variable Theories", Phys. Rev. Lett. **23**, 880–884 (1969) (cit. on pp. 3, 169, 200).

[8] J. F. Clauser and A. Shimony, "Bell's theorem. Experimental tests and implications", Reports on Progress in Physics **41**, 1881 (1978) (cit. on p. 3).

[9] S. J. Freedman and J. F. Clauser, "Experimental Test of Local Hidden-Variable Theories", Phys. Rev. Lett. **28**, 938–941 (1972) (cit. on pp. 3, 168, 169).

[10] E. S. Fry and R. C. Thompson, "Experimental Test of Local Hidden-Variable Theories", Phys. Rev. Lett. **37**, 465–468 (1976) (cit. on p. 3).

[11] A. Aspect, P. Grangier, and G. Roger, "Experimental Tests of Realistic Local Theories via Bell's Theorem", Phys. Rev. Lett. **47**, 460–463 (1981) (cit. on p. 3).

[12] D. C. Burnham and D. L. Weinberg, "Observation of Simultaneity in Parametric Production of Optical Photon Pairs", Phys. Rev. Lett. **25**, 84–87 (1970) (cit. on pp. 3, 94).

[13] L.-A. Wu, H. J. Kimble, J. L. Hall, and H. Wu, "Generation of Squeezed States by Parametric Down Conversion", Phys. Rev. Lett. **57**, 2520–2523 (1986) (cit. on pp. 3, 14, 21, 72, 91).

[14] A. Aspect, "Proposed experiment to test the nonseparability of quantum mechanics", Phys. Rev. D **14**, 1944–1951 (1976) (cit. on p. 3).

[15] M. Lamehi-Rachti and W. Mittig, "Quantum mechanics and hidden variables: A test of Bell's inequality by the measurement of the spin correlation in low-energy proton-proton scattering", Phys. Rev. D **14**, 2543–2555 (1976) (cit. on p. 3).

[16] A. Aspect, P. Grangier, and G. Roger, "Experimental Realization of Einstein-Podolsky-Rosen-Bohm *Gedankenexperiment* : A New Violation of Bell's Inequalities", Phys. Rev. Lett. **49**, 91–94 (1982) (cit. on pp. 3, 168, 169).

[17] A. Aspect, J. Dalibard, and G. Roger, "Experimental Test of Bell's Inequalities Using Time-Varying Analyzers", Phys. Rev. Lett. **49**, 1804–1807 (1982) (cit. on pp. 3, 168, 169).

[18] J. G. Rarity and P. R. Tapster, "Experimental violation of Bell's inequality based on phase and momentum", Phys. Rev. Lett. **64**, 2495–2498 (1990) (cit. on pp. 3, 168, 169).

[19]G. Weihs, T. Jennewein, C. Simon, H. Weinfurter, and A. Zeilinger, "Violation of Bell's Inequality under Strict Einstein Locality Conditions", Phys. Rev. Lett. **81**, 5039–5043 (1998) (cit. on p. 3).
[20]M. A. Rowe, D. Kielpinski, V. Meyer, C. A. Sackett, W. M. Itano, C. Monroe, and D. J. Wineland, "Experimental violation of a Bell's inequality with efficient detection", Nature **409**, 791–794 (2001) (cit. on p. 3).
[21]M. Giustina, A. Mech, S. Ramelow, B. Wittmann, J. Kofler, J. Beyer, A. Lita, B. Calkins, T. Gerrits, S. W. Nam, R. Ursin, and A. Zeilinger, "Bell violation using entangled photons without the fair-sampling assumption", Nature **497**, 227–230 (2013) (cit. on p. 3).
[22]A. K. Ekert, "Quantum cryptography based on Bell's theorem", Phys. Rev. Lett. **67**, 661–663 (1991) (cit. on p. 3).
[23]J. L. Duligall, M. S. Godfrey, K. A. Harrison, W. J. Munro, and J. G. Rarity, "Low cost and compact quantum key distribution", New Journal of Physics **8**, 249 (2006) (cit. on p. 3).
[24]E. Knill, R. Laflamme, and G. J. Milburn, "A scheme for efficient quantum computation with linear optics", Nature **409**, 46–52 (2001) (cit. on pp. 3, 16).
[25]J. M. Raimond, M. Brune, and S. Haroche, "Manipulating quantum entanglement with atoms and photons in a cavity", Rev. Mod. Phys. **73**, 565–582 (2001) (cit. on p. 3).
[26]H. J. Kimble, "The quantum internet", Nature **453**, 1023–1030 (2008) (cit. on p. 3).
[27]C. H. Bennett, G. Brassard, C. Crépeau, R. Jozsa, A. Peres, and W. K. Wootters, "Teleporting an unknown quantum state via dual classical and Einstein-Podolsky-Rosen channels", Phys. Rev. Lett. **70**, 1895–1899 (1993) (cit. on p. 3).
[28]D. Bouwmeester, J.-W. Pan, K. Mattle, M. Eibl, H. Weinfurter, and A. Zeilinger, "Experimental quantum teleportation", Nature **390**, 575–579 (1997) (cit. on p. 3).
[29]R. Ursin, F. Tiefenbacher, T. Schmitt-Manderbach, H. Weier, T. Scheidl, M. Lindenthal, B. Blauensteiner, T. Jennewein, J. Perdigues, P. Trojek, B. Omer, M. Furst, M. Meyenburg, J. Rarity, Z. Sodnik, et al., "Entanglement-based quantum communication over 144[thinsp]km", Nat Phys **3**, 481–486 (2007) (cit. on p. 4).
[30]T. Scheidl, R. Ursin, A. Fedrizzi, S. Ramelow, X.-S. Ma, T. Herbst, R. Prevedel, L. Ratschbacher, J. Kofler, T. Jennewein, and A. Zeilinger, "Feasibility of 300 km quantum key distribution with entangled states", New. J. Phys. **11**, 085002 (2009) (cit. on p. 4).
[31]X.-S. Ma, T. Herbst, T. Scheidl, D. Wang, S. Kropatschek, W. Naylor, B. Wittmann, A. Mech, J. Kofler, E. Anisimova, V. Makarov, T. Jennewein, R. Ursin, and A. Zeilinger, "Quantum teleportation over 143 kilometres using active feed-forward", Nature **489**, 269–273 (2012) (cit. on pp. 4, 25).
[32]A. Rubenok, J. A. Slater, P. Chan, I. Lucio-Martinez, and W. Tittel, "Real-World Two-Photon Interference and Proof-of-Principle Quantum Key Distribution Immune to Detector Attacks", Phys. Rev. Lett. **111**, 130501 (2013) (cit. on pp. 4, 25).
[33]M. H. Anderson, J. R. Ensher, M. R. Matthews, C. E. Wieman, and E. A. Cornell, "Observation of Bose-Einstein Condensation in a Dilute Atomic Vapor", Science **269**, 198–201 (1995) (cit. on p. 4).
[34]M. Greiner, C. A. Regal, and D. S. Jin, "Emergence of a molecular Bose-Einstein condensate from a Fermi gas", Nature **426**, 537–540 (2003) (cit. on p. 4).
[35]W. S. Bakr, A. Peng, M. E. Tai, R. Ma, J. Simon, J. I. Gillen, S. Fölling, L. Pollet, and M. Greiner, "Probing the Superfluid–to–Mott Insulator Transition at the Single-Atom Level", Science **329**, 547–550 (2010) (cit. on p. 4).
[36]"A Quantum Gas Microscope for Fermionic Atoms", arXiv [1503.02648] (cit. on pp. 4, 27).
[37]J. Steinhauer, "Observation of self-amplifying Hawking radiation in an analogue black-hole laser", Nat Phys **10**, 864–869 (2014) (cit. on p. 4).
[38]O. Lahav, A. Itah, A. Blumkin, C. Gordon, S. Rinott, A. Zayats, and J. Steinhauer, "Realization of a Sonic Black Hole Analog in a Bose-Einstein Condensate", Phys. Rev. Lett. **105**, 240401 (2010) (cit. on p. 4).

[39]J.-C. Jaskula, G. Partridge, M. Bonneau, R. Lopes, J. Ruaudel, D. Boiron, and C. Westbrook, "Acoustic Analog to the Dynamical Casimir Effect in a Bose-Einstein Condensate", Phys. Rev. Lett. **109**, 220401 (2012) (cit. on pp. 4, 7, 34, 44, 46, 167, 217).

[40]M. Endres, T. Fukuhara, D. Pekker, M. Cheneau, P. Schau[bgr], C. Gross, E. Demler, S. Kuhr, and I. Bloch, "The /'Higgs/' amplitude mode at the two-dimensional superfluid/Mott insulator transition", Nature **487**, 454–458 (2012) (cit. on p. 4).

[41]L. Pollet and N. Prokof'ev, "Higgs Mode in a Two-Dimensional Superfluid", Phys. Rev. Lett. **109**, 010401 (2012) (cit. on p. 4).

[42]C. Salomon, N. Dimarcq, M. Abgrall, A. Clairon, P. Laurent, P. Lemonde, G. Santarelli, P. Uhrich, L. Bernier, G. Busca, A. Jornod, P. Thomann, E. Samain, P. Wolf, F. Gonzalez, et al., "Cold atoms in space and atomic clocks:" Comptes Rendus de l'Académie des Sciences - Series {IV} - Physics **2**, 1313–1330 (2001) (cit. on p. 4).

[43]A. D. Cronin, J. Schmiedmayer, and D. E. Pritchard, "Optics and interferometry with atoms and molecules", Rev. Mod. Phys. **81**, 1051–1129 (2009) (cit. on pp. 4, 108).

[44]M. Riebe, H. Haffner, C. F. Roos, W. Hansel, J. Benhelm, G. P. T. Lancaster, T. W. Korber, C. Becher, F. Schmidt-Kaler, D. F. V. James, and R. Blatt, "Deterministic quantum teleportation with atoms", Nature **429**, 734–737 (2004) (cit. on p. 4).

[45]R. Blatt and D. Wineland, "Entangled states of trapped atomic ions", Nature **453**, 1008–1015 (2008) (cit. on p. 4).

[46]C. Gross, H. Strobel, E. Nicklas, T. Zibold, N. Bar-Gill, G. Kurizki, and M. K. Oberthaler, "Atomic homodyne detection of continuous-variable entangled twin-atom states", Nature **480**, 219–223 (2011) (cit. on p. 4).

[47]J. M. Vogels, K. Xu, and W. Ketterle, "Generation of Macroscopic Pair-Correlated Atomic Beams by Four-Wave Mixing in Bose-Einstein Condensates", Phys. Rev. Lett. **89**, 020401 (2002) (cit. on pp. 4, 27).

[48]A. Perrin, H. Chang, V. Krachmalnicoff, M. Schellekens, D. Boiron, A. Aspect, and C. I. Westbrook, "Observation of Atom Pairs in Spontaneous Four-Wave Mixing of Two Colliding Bose-Einstein Condensates", Phys. Rev. Lett. **99**, 150405 (2007) (cit. on pp. 4, 27, 34, 167).

[49]M. Greiner, C. A. Regal, J. T. Stewart, and D. S. Jin, "Probing Pair-Correlated Fermionic Atoms through Correlations in Atom Shot Noise", Phys. Rev. Lett. **94**, 110401 (2005) (cit. on p. 4).

[50]J. Esteve, C. Gross, A. Weller, S. Giovanazzi, and M. K. Oberthaler, "Squeezing and entanglement in a Bose-Einstein condensate", Nature **455**, 1216–1219 (2008) (cit. on p. 4).

[51]J.-C. Jaskula, M. Bonneau, G. B. Partridge, V. Krachmalnicoff, P. Deuar, K. V. Kheruntsyan, A. Aspect, D. Boiron, and C. I. Westbrook, "Sub-Poissonian Number Differences in Four-Wave Mixing of Matter Waves", Phys. Rev. Lett. **105**, 190402 (2010) (cit. on pp. 4, 34, 39, 167).

[52]R. Bucker, J. Grond, S. Manz, T. Berrada, T. Betz, C. Koller, U. Hohenester, T. Schumm, A. Perrin, and J. Schmiedmayer, "Twin-atom beams", Nat Phys **7**, 608–611 (2011) (cit. on pp. 4, 27).

[53]H. Strobel, W. Muessel, D. Linnemann, T. Zibold, D. B. Hume, L. Pezzè, A. Smerzi, and M. K. Oberthaler, "Fisher information and entanglement of non-Gaussian spin states", Science **345**, 424–427 (2014) (cit. on pp. 4, 27, 162, 163).

[54]C. K. Hong, Z. Y. Ou, and L. Mandel, "Measurement of subpicosecond time intervals between two photons by interference", Phys. Rev. Lett. **59**, 2044–2046 (1987) (cit. on pp. 4, 13, 14, 16, 17, 130–132, 134, 143, 152).

[55]M. R. Ray and S. J. van Enk, "Verifying entanglement in the Hong-Ou-Mandel dip", Phys. Rev. A **83**, 042318 (2011) (cit. on p. 4).

[56]C. Lang, C. Eichler, L. Steffen, J. M. Fink, M. J. Woolley, A. Blais, and A. Wallraff, "Correlations, indistinguishability and entanglement in Hong-Ou-Mandel experiments at microwave frequencies", Nat Phys **9**, 345–348 (2013) (cit. on pp. 4, 25).

[57] J. Chen, J. B. Altepeter, M. Medic, K. F. Lee, B. Gokden, R. H. Hadfield, S. W. Nam, and P. Kumar, "Demonstration of a Quantum Controlled-NOT Gate in the Telecommunications Band", Phys. Rev. Lett. **100**, 133603 (2008) (cit. on p. 4).
[58] A. Crespi, R. Ramponi, R. Osellame, L. Sansoni, I. Bongioanni, F. Sciarrino, G. Vallone, and P. Mataloni, "Integrated photonic quantum gates for polarization qubits", Nat Commun **2**, 566 (2011) (cit. on p. 4).
[59] J. Dubois, T. Jullien, F. Portier, P. Roche, A. Cavanna, Y. Jin, W. Wegscheider, P. Roulleau, and D. C. Glattli, "Minimal-excitation states for electron quantum optics using levitons", Nature **502**, 659–663 (2013) (cit. on p. 4).
[60] E. Bocquillon, V. Freulon, J.-M. Berroir, P. Degiovanni, B. Plaçais, A. Cavanna, Y. Jin, and G. Fève, "Coherence and Indistinguishability of Single Electrons Emitted by Independent Sources", Science **339**, 1054–1057 (2013) (cit. on p. 4).
[61] J. S. Fakonas, H. Lee, Y. A. Kelaita, and H. A. Atwater, "Two-plasmon quantum interference", Nat Photon **8**, 317–320 (2014) (cit. on p. 4).
[62] G. Di Martino, Y. Sonnefraud, M. S. Tame, S. Ké na-Cohen, F. Dieleman, S. K. Ozdemir, M. S. Kim, and S. A. Maier, "Observation of Quantum Interference in the Plasmonic Hong-Ou-Mandel Effect", Phys. Rev. Applied **1**, 034004 (2014) (cit. on p. 4).
[63] A. M. Kaufman, B. J. Lester, C. M. Reynolds, M. L. Wall, M. Foss-Feig, K. R. A. Hazzard, A. M. Rey, and C. A. Regal, "Two-particle quantum interference in tunnel-coupled optical tweezers", Science **345**, 306–309 (2014) (cit. on pp. 4, 27).
[64] F. Gerbier, "Quasi-1D Bose-Einstein condensates in the dimensional crossover regime", EPL (Europhysics Letters) **66**, 771 (2004) (cit. on pp. 6, 48, 59, 78, 173, 174).
[65] V. V. Dodonov, "Dynamical Casimir effect: Some theoretical aspects", Journal of Physics: Conference Series **161**, 012027 (2009) (cit. on p. 7).
[66] F. X. Dezael and A. Lambrecht, "Analogue Casimir radiation using an optical parametric oscillator", EPL (Europhysics Letters) **89**, 14001 (2010) (cit. on p. 7).
[67] C. M. Wilson, G. Johansson, A. Pourkabirian, M. Simoen, J. R. Johansson, T. Duty, F. Nori, and P. Delsing, "Observation of the dynamical Casimir effect in a superconducting circuit", Nature **479**, 376–379 (2011) (cit. on p. 7).
[68] R. Lopes, A. Imanaliev, M. Bonneau, J. Ruaudel, M. Cheneau, D. Boiron, and C. I. Westbrook, "Second-order coherence of superradiance from a Bose-Einstein condensate", Phys. Rev. A **90**, 013615 (2014) (cit. on pp. 7, 34, 37, 53, 217).
[69] S. Inouye, A. P. Chikkatur, D. M. Stamper-Kurn, J. Stenger, D. E. Pritchard, and W. Ketterle, "Superradiant Rayleigh Scattering from a Bose-Einstein Condensate", Science **285**, 571–574 (1999) (cit. on p. 7).
[70] M. G. Moore and P. Meystre, "Theory of Superradiant Scattering of Laser Light from Bose-Einstein Condensates", Phys. Rev. Lett. **83**, 5202–5205 (1999) (cit. on p. 7).
[71] D. Schneble, G. K. Campbell, E. W. Streed, M. Boyd, D. E. Pritchard, and W. Ketterle, "Raman amplification of matter waves", Phys. Rev. A **69**, 041601 (2004) (cit. on p. 7).

Chapter 1

Basic concepts of the Hong–Ou–Mandel experiment

Contents

1.1 HOM effect: basic explanation 14
1.1.1 Generalisation of the HOM effect 17
1.1.2 Generalisation for any input state 20
1.1.3 Classical threshold 22
1.2 HOM-dip visibility and Cauchy-Schwarz inequality 23
1.3 HOM experiment with atoms: necessary tools 27

All photons are equal but some photons are more equal than others

Title of Ref. [72] probably inspired by George Orwell's book "Animal Farm".

The experiment of C. K. Hong, Z. Y. Ou, and L. Mandel performed in 1987 [54] and widely known as the Hong–Ou–Mandel (HOM) experiment is one of the most important demonstration of quantum mechanics. In this experiment, two photons produced via parametric down-conversion are recombined on a beam-splitter. Two photodiodes placed at the output ports of the beam-splitter register the output signal. A synchronisation is then performed to compare the signal of both detectors and recover the coincidence counts, meaning the probability for detecting a photon in one of the two detectors at time interval $t + dt$ knowing that the other photon had been detected at time t on the other detector.

According to Newtonian particle theory, for the case of non-interacting particles, one would expect to detect a coincidence count for half of the realisations since the four cases illustrated in Fig. 1.1 are equally probable. However, for classical indistinguishable waves an interference pattern appears. In the case considered here, the relative phase is kept undetermined, such that after averaging over N realisations, the interference washes out. By looking at the coincidence count, one would find that for indistinguishable waves the coincidence count is reduced by a factor two compared to the case of distinguishable waves. By indistinguishable classical waves one means that they have the same polarisation, spatial mode, etc... For single indistinguishable photons, however, the same result does not apply. The 1987's experiment showed that in this case the coincidence count goes to zero although the relative phase of the two photons is

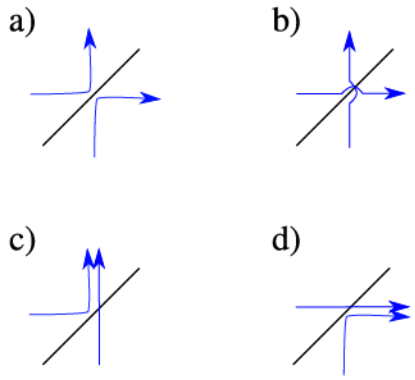

Figure 1.1: ***Classical scenarios for two incoming particles.*** *Schematic representation of all four cases corresponding to the different possibles arrangements of two particles arriving on a 50:50 beam-splitter. The blue arrows represent the arriving particles. Case: a) both particles are reflected; b) both transmitted; c) and d) one reflected and the other one transmitted.*

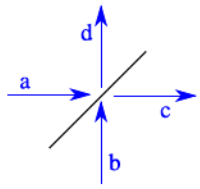

Figure 1.2: ***Beam-splitter input and output ports convention.*** *The 50:50 beam-splitter is schematically represented. Two photons arrive at the beam-splitter through ports a and b represented by incident blue arrows. The output ports are designed by c and d.*

completely random. This means that one will never detect at the same time one photon per output port and that the two photons always emerge together. This two-photon destructive interference effect is known as the HOM effect [54].

This chapter is organised as follow. In Section 1.1, the basic understanding of the HOM effect will be summarised. One will also discussed the quantumness of the effect and the necessary conditions that the input state must fulfil. In Section 1.2, the connection between the HOM-dip visibility and the violation of the Cauchy-Schwarz inequality will be presented and explored in order to generalise the interpretation of this effect to an arbitrary state. Finally, in Section 1.3, the analogy with atomic pairs will be discussed, introducing the major difficulties and challenges associated with this experiment and the required tools to perform it.

1.1 HOM effect: basic explanation

The HOM experiment can hardly be seen as an interferometer since it does not correspond to a situation where a wave is split and recombined on a 50:50 beam-splitter, but to a situation where two particles, here photons, arrive on the input ports of a 50:50 beam-splitter. The easiest experimental way to have two photons arriving simultaneously on a beam-splitter is to create them simultaneously and at equal distance from the beam-splitter. This is commonly performed in quantum optics via generation of photon pairs when an intense laser beam, called pump beam, passes through a non-linear medium [13]. Another method consists in using spontaneous emission of photons from trapped atoms such that a finite probability of having two atoms emitting at the same time exists [73].

The HOM effect appears via a reduction of the coincidence count. Which translates in the reduction of the correlator $\langle \hat{c}^\dagger \hat{d}^\dagger \hat{c}\, \hat{d} \rangle$, where $\langle\rangle$ accounts for the quantum average. The operators $\hat{a}$, $\hat{b}$ correspond to the incoming field operators of the beam-splitter and $\hat{c}$, $\hat{d}$ to the outgoing

field operators (see Fig. 1.2). The simplest way to calculate such a correlator is to transform the operators and the state vector back in the input space before the beam-splitter and to use the Heisenberg picture. The transformation matrix between the operators $\hat{c}$, $\hat{d}$ and $\hat{a}$, $\hat{b}$ can be worked out from first principles,

$$\begin{pmatrix} \hat{c} \\ \hat{d} \end{pmatrix} = \hat{S} \begin{pmatrix} \hat{a} \\ \hat{b} \end{pmatrix}.$$

The scattering matrix $\hat{S}$ represents the 50:50 beam-splitter operator and can be written as

$$\hat{S} = \frac{1}{\sqrt{2}} \begin{pmatrix} 1 & ie^{-i\phi_S} \\ ie^{i\phi_S} & 1 \end{pmatrix},$$

with ϕ_S a phase associated to the beam-splitter. [1] It is then possible to rewrite the operators such that

$$\hat{c} = \frac{1}{\sqrt{2}} \left(\hat{a} + ie^{-i\phi_S} \hat{b} \right),$$
$$\hat{d} = \frac{1}{\sqrt{2}} \left(\hat{b} + ie^{i\phi_S} \hat{a} \right).$$

Considering first the ideal case of an input state with exactly one photon in each channel, $|1_a, 1_b\rangle$, one obtains

$$|1_a,\, 1_b\rangle = \hat{a}^\dagger \hat{b}^\dagger |0,\, 0\rangle \rightarrow \frac{1}{2} \left(\hat{c}^\dagger \hat{d}^\dagger |0,0\rangle + i \left(\hat{d}^\dagger \hat{d}^\dagger e^{i\phi_S} + \hat{c}^\dagger \hat{c}^\dagger e^{-i\phi_S} \right) |0,0\rangle - \hat{d}^\dagger \hat{c}^\dagger |0,0\rangle \right). \tag{1.1}$$

One immediately sees that $\hat{d}^\dagger \hat{c}^\dagger |0,0\rangle$ and $\hat{c}^\dagger \hat{d}^\dagger |0,0\rangle$ are identical but associated with opposite phases, such that the sum of their amplitudes vanishes. This corresponds to a destructive interference effect, leading to a suppression of coincidence counts between the output ports of the 50:50 beam-splitter. This suppression is the marking feature of the HOM experiment. Please note that this result is only true for identical photons.

Let us consider the case of two photons arriving to a beam-splitter but with perpendicular polarizations, for example photon a with horizontal polarization, a_H, and b with vertical polarization, b_V, where the subscript index stands for the polarization. Consequently, after the 50:50 beam-splitter one retrieves

$$|1_{a,H},\, 1_{b,V}\rangle = \hat{a}_H^\dagger \hat{b}_V^\dagger |0,\, 0\rangle \rightarrow \frac{1}{2} \left(\hat{c}_H^\dagger \hat{d}_V^\dagger |0,0\rangle + i \left(\hat{d}_H^\dagger \hat{d}_V^\dagger e^{i\phi_S} + \hat{c}_H^\dagger \hat{c}_V^\dagger e^{-i\phi_S} \right) |0,0\rangle - \hat{d}_H^\dagger \hat{c}_V^\dagger |0,0\rangle \right). \tag{1.2}$$

and since the output states $\hat{d}_H^\dagger \hat{c}_V^\dagger |0,0\rangle$ and $\hat{c}_H^\dagger \hat{d}_V^\dagger |0,0\rangle$ are different their amplitude does not sum, and no destructive interference effect is observed. This means that for distinguishable photons, one will not measure a reduction of the cross-correlation or coincidence count.

The output state, for the case of indistinguishable particles, can be written via Eq. (1.1) as

$$|\psi\rangle_{\text{out}} = \frac{1}{\sqrt{2}} \left(ie^{-i\phi_S} |2_c, 0_d\rangle + ie^{i\phi_S} |0_c, 2_d\rangle \right), \tag{1.3}$$

[1] This notation can seem rather unusual for photons, but as we will see later in Chapter 4 and in Appendix D it is well suited for describing the effect of the atomic beam-splitter. The atomic beam-splitter corresponds then to a $\pi/2$ Rabi oscillation with ϕ_S corresponding to the relative phase between the laser beams forming the optical lattice.

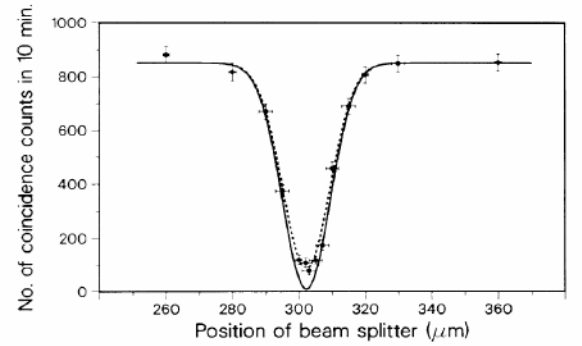

Figure 1.3: **1987 Hong–Ou–Mandel dip.** *Measurement of the coincidence count reduction as function of the beam-splitter displacement. The minimum value corresponds to the case of perfect indistinguishable particles. The solid line corresponds to the theoretical predicted curve while the dashed line corresponds to an attenuation of 0.9 of the first curve. Figure copied from Ref. [54].*

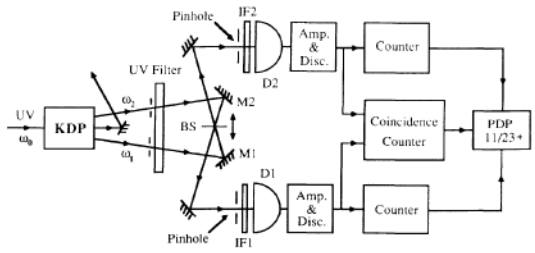

Figure 1.4: ***Schematic representation of the 1987's Hong–Ou–Mandel experiment.*** *Two photons produced via parametric down-conversion are plugged into a 50:50 beam-splitter, after passing through a frequency and spatial filter. Two photodiodes register the number of detected photons on both output ports. A coincidence count is then performed afterwards. Figure copied from Ref. [54].*

which is a maximally entangled two-photon state [24]. The coalescence effect, which translates the tendency of photons to always exit together, is a feature of the symmetry of the wave function associated to bosons [74]. For fermions, one would obtain the output state $|\psi\rangle_{out} = \hat{c}^\dagger \hat{d}^\dagger |0,0\rangle$, corresponding to a maximum coincidence count [75].

The HOM effect translates thus to a vanishing coincidence count when particles are made indistinguishable [76]. This means that the cross-correlator $G^{(2)}_{cd}$, defined by

$$G^{(2)}_{cd} = \langle \hat{c}^\dagger \hat{d}^\dagger \hat{c} \hat{d} \rangle \,, \tag{1.4}$$

tends to zero. On the other hand, since we are considering a 50:50 beam-splitter, the average output populations are the same, $\langle \hat{n}_d \rangle = \langle \hat{n}_c \rangle$ with $\langle \hat{n}_c \rangle = \langle \hat{c}^\dagger \hat{c} \rangle$ the number of photons in the output port c and $\langle \hat{n}_d \rangle = \langle \hat{d}^\dagger \hat{d} \rangle$ the number of photons in the output port d.

As we have seen two scenarios are then possible. Either the photons are indistinguishable, meaning that it is impossible to identify which photon has been reflected or transmitted, or they are distinguishable, meaning that one can know, via some quantity, which particle has been reflected or transmitted. The crossover between these two scenarios is responsible for the HOM-dip represented in Fig. 1.3. Going from distinguishable to indistinguishable particles was originally performed by changing the optical path, that is, by changing the position of the beam-splitter, as it can been seen in the schematic representation of the original experiment shown in Fig. 1.4. When the change in the optical path is such that the two photons do not overlap on the beam-splitter, the particles are distinguishable. On the other hand, when the two particles overlap on the beam-splitter their paths are indistinguishable and one retrieves the zero coincidence count [2] as shown in Fig. 1.3. Other strategies can be exploited in order to control the distinguishability between the two particles [72]. For example, in Refs. [74, 77, 78], the polarization of the two produced photons was used in order to tune their distinguishability.

It is important to note that originally, the HOM experiment had for goal to determine the wavepacket size of the photons with a resolution of a few hundreds of femtoseconds. The size was determined through the width of the dip which is directly linked to the correlation length of the particles [54]. We will see in Chapter 5, however, that the width of the HOM-dip can also be due to the contribution of the spectral and spatial filtering procedure.

[2] In fact, the cross-correlation does not reach zero. According to the authors the difference is due to a non perfect spatial overlap.

1.1.1 Generalisation of the HOM effect

In contrast to the previous situation, input states containing more than one photon per channel lead to partial destructive interference and, consequently, to a non vanishing coincidence count. Consider the following situation where instead of having one photon per input port one considers the input state $|2_a, 2_b\rangle$

$$|\psi\rangle_{\text{in}} = |2_a, 2_b\rangle = \frac{\hat{a}^{\dagger 2}\hat{b}^{\dagger 2}}{2}|0, 0\rangle.$$

Applying the same transformation as before, one finds

$$|\psi\rangle_{\text{out}} = -\frac{1}{8}\left[e^{-2i\phi_S}\hat{d}^\dagger\hat{d}^\dagger\hat{d}^\dagger\hat{d}^\dagger + e^{2i\phi_S}\hat{c}^\dagger\hat{c}^\dagger\hat{c}^\dagger\hat{c}^\dagger + 2\hat{c}^\dagger\hat{c}^\dagger\hat{d}^\dagger\hat{d}^\dagger\right]|0, 0\rangle\,. \tag{1.5}$$

One sees that the probability of detecting two photons coincidently does not vanish and the destructive interference is only partial. This means that, although one will never detect at the same time one particle per output port, one may detect two particles at the same time in both output ports. Consequently, the coincidence count does not go to zero but presents a finite value. This effect was discussed in detail in Refs. [79, 80].

The same calculation can be performed for a twin-Fock state with N particles

$$|N_a, N_b\rangle$$

leading to a multi-particle-interference effect. The state can be rewritten as

$$|\psi\rangle_{\text{out}} = \frac{i^N}{2^N N!}\left(e^{i\phi_S}\hat{d}^{\dagger 2} + e^{-i\phi_S}\hat{c}^{\dagger 2}\right)^N|0, 0\rangle\,.$$

The probability of detecting n particles, n being an even number, at one of the two output ports, as a function of the total number of particles $2N$ is equal to

$$P(n, \text{even}) = \frac{1}{2^N}\binom{n}{n/2}\binom{(N-n)}{(N-n)/2}, \tag{1.6}$$

while the probability to detect an odd number in one of the two output ports is always zero, $P(n, \text{odd}) = 0$.

Fig. 1.5 summarises the different distributions for $2N = 2$, $2N = 4$ and $2N = 10$. The situation with $2N = 2$ corresponds to the discussed two photon interference [54, 81]. With increasing number of particles, $2N = 10$ for example, one retrieves the characteristic U-shape discussed in Ref. [82]. This shape indicates that for indistinguishable particles, when the total number of particles at the input ports increases, the probability of detecting all particles in one of the output ports increases although the coincidence count does not strictly vanishes. In the case of distinguishable particles, the probability of detecting n between $2N$ particles follows the binomial distribution, see Fig. 1.6a). One has an increased probability of detecting the averaged value of N due to 50 % transmission of the beam-splitter. These distributions have been recently studied both theoretically and experimentally with photons [82, 83].

In conclusion, in the case of indistinguishable particles, the variance of the distributions increases when compared to the distinguishable case, see Fig. 1.6b).

The U-shape, however, corresponds only to the particular case of a perfect detection, any losses would translate into a non-vanishing probability to detect odd number of photons. It is also essential to be able to detect single photons in order to differentiate the even from

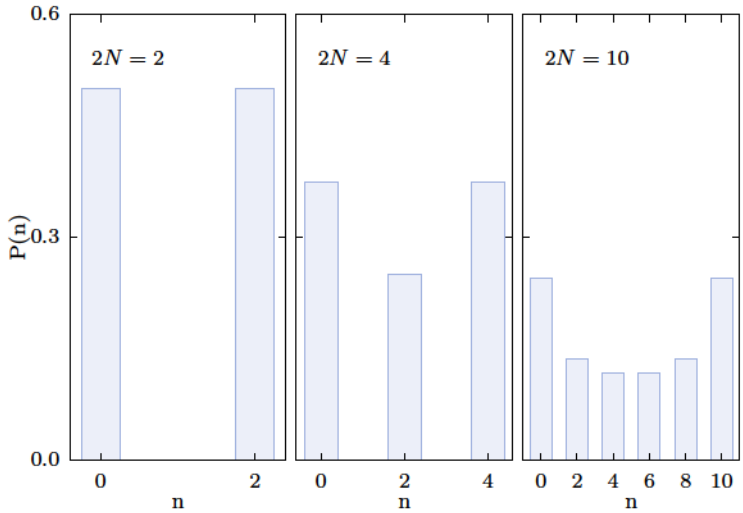

Figure 1.5: **U-shape of the HOM effect with increasing number of particles per input ports.** *Each canvas represents the probability to detect n particles (P(n)) on one of the two outcome ports for N incoming particles per port. From left to right, the total number of incoming particles 2N increases from 2 to 10. For the case of N = 2, one retrieves the expected annihilation of coincidence counts which translates in a null probability to detect one particle per output port. When the total number of particles increases, although for odd number one still has a null probability, one starts to detect even numbers of particles different from the extreme cases 0 or 2N which means that the coincidence count has a certain finite value.*

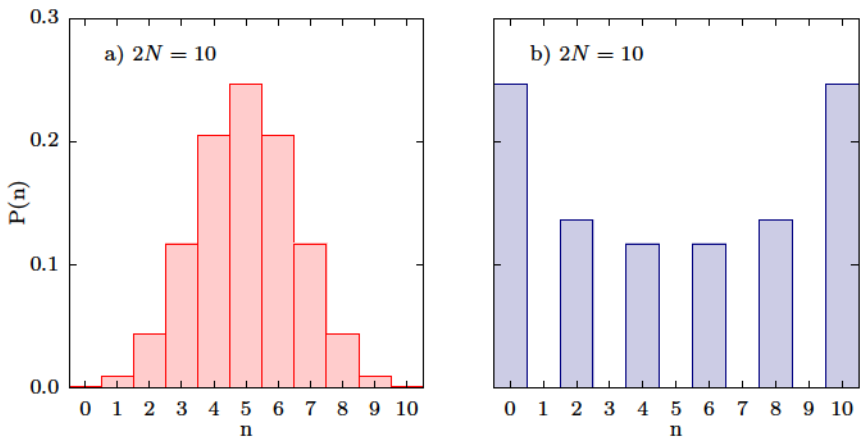

Figure 1.6: **Distribution of the number of particles at one of the two output ports for both distinguishable and indistinguishable 2N = 10 particles.** *Red histogram corresponds to the binomial distribution that one would obtain without interference effect. This corresponds to the case of distinguishable particles. In blue, the indistinguishable particle interference distribution for 2N = 10 particles. One can see that the probability of detecting even numbers in one of the output ports follow a U-shape distribution.*

the odd number. Furthermore, in the case of a multimode source, the U-shape also tends to vanish as discussed in Ref. [82–84]. In Ref. [83], a twin-beam produced via parametric down-conversion is used. Although the total photon number in each beam can fluctuate, the relative population is ideally very well defined, indicating photon-number correlations between the beams. The number of photons per beam N is set to 5×10^{10} photons. The two beams are then filtered both spatially (performed by the presence of a pinhole on the incoming beams) and spectrally (via a Fabry–Perot interferometer), being afterwards recombined on a 50:50 beam-splitter. Measurements with different numbers of modes show that the U-shape becomes less visible as the number of modes increases. This is represented in Fig. 1.7 for a selection of 1.2 modes, see Fig. 1.7a), where the U-shape is visible. For higher mode number, however, the shape tends to disappear as shown in Fig. 1.7b). It is also important to note that the filtering

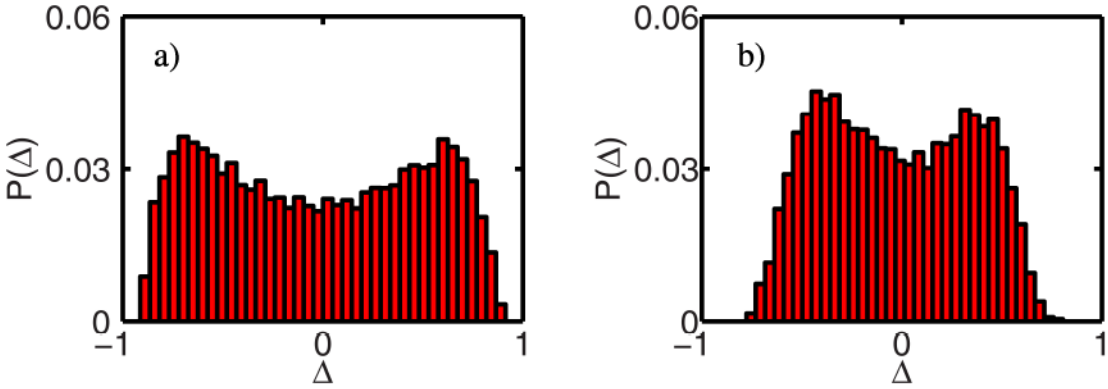

Figure 1.7: **Effect of the number of modes in the output port number of atoms distribution.** *Probability distributions $P(\Delta)$ obtained for the effective numbers of modes $m = 1.2$ (a)) and $m = 3.4$ (b)). One sees that when the effective number of modes increases the U-shape tends to disappear. Figure copied from Ref. [83].*

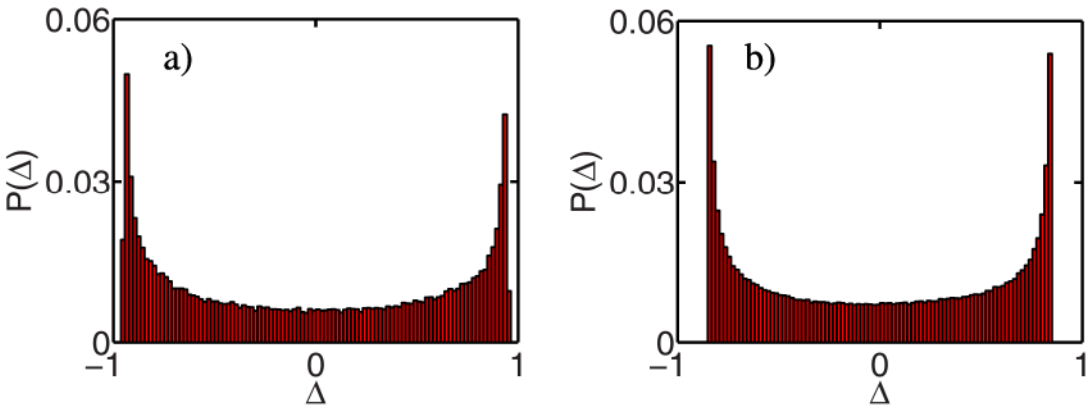

Figure 1.8: **U-shape obtained with classical states.** *U-shape observed for classical beams with the fluctuations in the relative phase increased artificially. The probability distribution $P(\Delta)$ for: a) the thermal state and b) the coherent state with artificially randomised phase. Figure copied from Ref. [83].*

procedure lowers the efficiency of detection, since photons are lost in the process. Consequently, the probability of detecting odd numbers increases and the effect is less marked.

In the same article, the authors show that in this situation, with high number of photons, multimode source and imperfect detection efficiency, classical states with random relative phases can reproduce the behaviour of a strongly correlated state, $|N,N\rangle$ for example. The random phase between the two input waves allows to replicate the enhanced relative phase uncertainty of the state $|N_a,N_b\rangle$.

The interferometric result for classical states is shown in Fig. 1.8. Both the situation of a thermal state (a) and a coherent state (b), with relative random-phases, simulate the discussed U-shape. One concludes that in the case of macroscopic populations with imperfect detection efficiency one can not distinguish the result obtained for a classical state from a quantum state. Consequently, this raises the question of whether the HOM effect, with a number of input particles close to one, can also be replicated for a classical state.

1.1.2 Generalisation for any input state

As seen previously, increasing the number of particles at the input port of a 50:50 beam-splitter tends to weaken the destructive interference effect. Although the previous calculations were based on twin Fock states, one can generalise the result without any assumption on the incoming state.

The cross-correlation between ports c and d for the case of indistinguishable photons or distinguishable ones can then be written, respectively, as (see the detailed demonstrations in Appendix D)

$$G^{(2)}_{cd,\,\text{Ind.}} = \frac{1}{4}\left(G^{(2)}_{aa} + G^{(2)}_{bb}\right), \tag{1.7a}$$

$$G^{(2)}_{cd,\,\text{Dis.}} = \frac{1}{4}\left(G^{(2)}_{aa} + G^{(2)}_{bb}\right) + \frac{1}{2}G^{(2)}_{ab}, \tag{1.7b}$$

where $G^{(2)}_{ii} = \langle \hat{i}^\dagger \hat{i}^\dagger \hat{i}\,\hat{i}\rangle$ stands for the autocorrelation of the input ports $i = a, b$ and $G^{(2)}_{ab} = \langle \hat{a}^\dagger \hat{b}^\dagger \hat{a}\,\hat{b}\rangle$ for the cross-correlation between the input ports a and b. In the case of the input state $|1_a, 1_b\rangle$,

$$G^{(2)}_{aa} = G^{(2)}_{bb} = 0\,,$$
$$G^{(2)}_{ab} = 1\,,$$

and, consequently,

$$G^{(2)}_{cd,\,\text{Ind.}} = 0\,,$$
$$G^{(2)}_{cd,\,\text{Dis.}} = \frac{1}{2}\,,$$

leading to the complete annihilation of coincidence counts when the particles are indistinguishable. This formalism is however applicable to any input state as will be discussed in Section 5.3.

For the discussed input state $|2_a, 2_b\rangle$, one immediately sees that

$$G^{(2)}_{aa} = G^{(2)}_{bb} = 2\,,$$
$$G^{(2)}_{ab} = 4$$

so,

$$G^{(2)}_{cd,\,\text{Ind.}} = 1\,,$$
$$G^{(2)}_{cd,\,\text{Dis.}} = 3$$

and, therefore, the indistinguishable case does not correspond to a fully vanishing coincidence count. This effect is related to the visibility [85] defined as

$$\bar{V} = 1 - \frac{G^{(2)}_{cd,\,\text{Ind.}}}{G^{(2)}_{cd,\,\text{Dis.}}} \tag{1.9}$$

which for a state $|2_a, 2_b\rangle$ is equal to $\bar{V} = 0.66$ instead of $\bar{V} = 1$ for the two particle case $|1_a, 1_b\rangle$. Experimentally, the visibility corresponds to the contrast of the dip present on the coincidence count as a function of τ as shown in Fig. 1.3. For a coincidence count evolving from a finite background value to zero, the visibility reaches the maximum value of 1. For non-vanishing minimum values of the coincidence count the visibility decreases.

Parametric down-conversion

Consider the output state of a 2-mode parametric down-conversion process [86] which is often used in quantum optics [13]

$$|\psi\rangle_{in} = \sum_{n=0}^{N} \frac{\tanh^n(\lambda)}{\cosh(\lambda)} |n, n\rangle$$

where λ is related to the average number of particles via the relation $\langle n\rangle = \sinh^2(\lambda)$. The autocorrelation and cross-correlation are then equal to [87]

$$G^{(2)}_{aa} = G^{(2)}_{bb} = 2\langle n\rangle^2 , \tag{1.10a}$$

$$G^{(2)}_{ab} = \langle n\rangle (1 + 2\langle n\rangle) , \tag{1.10b}$$

which gives the following result for the cross-correlation measured on the output ports

$$G^{(2)}_{cd,\text{Ind.}} = \langle n\rangle^2 , \tag{1.11a}$$

$$G^{(2)}_{cd,\text{Dis.}} = \langle n\rangle^2 \left(2 + \frac{1}{2\langle n\rangle}\right) , \tag{1.11b}$$

in the case of indistinguishable and distinguishable particles, respectively. This leads to a visibility $\bar{V}$ defined by Eq. (1.9) of

$$\bar{V} = 1 - \frac{1}{2 + \frac{1}{2\langle n\rangle}}, \tag{1.12}$$

that tends to 1 when $\langle n\rangle \to 0$ and to 0.5 when $\langle n\rangle \to \infty$. The first case, when $\langle n\rangle \to 0$, corresponds to the situation for which it is very unlikely to have more than one particle per input port, that is, to the case of the input state $|1_a, 1_b\rangle$. When $\langle n\rangle$ increases, the probability of having more than one particle per input port is no longer negligible and the visibility decreases towards the asymptotic value of 0.5.

Fig. 1.9a) shows the evolution of the visibility $\bar{V}$ as a function of the averaged number of particles at the input ports $\langle n\rangle$ varying between 0.0 and 4.0. One sees that as the average number increases towards $\langle n\rangle = 1$ the visibility reduces rapidly. At low population ($\langle n\rangle < 0.4$), as shown in the inset the visibility goes from 1.0 for $\langle n\rangle = 0$ to 0.75 for $\langle n\rangle = 0.2$. This is due to the fact that the probability of having more than one particle per input port increases rapidly as represented in Fig. 1.9b) where the probability of detecting n particles for an average population $\langle n\rangle$

$$P(\langle n\rangle, n) = \left| \frac{\tanh^n\left[\sinh^{-1}\left(\sqrt{\langle n\rangle}\right)\right]}{\cosh\left[\sinh^{-1}\left(\sqrt{\langle n\rangle}\right)\right]} \right|^2 \tag{1.13}$$

is represented as a function of $\langle n\rangle$. As $\langle n\rangle$ increases the probability of detecting more than one particle is no longer negligible when compared to the one of detecting one particle. This is rapidly the case, as shown in Fig. 1.9b) where for an average population of $\langle n\rangle = 0.2$ the probability of detecting two particles is only a factor four weaker than the probability of detecting one particle.

It is now clear that increasing the number of particles per input port has as consequence a reduction of the HOM-dip visibility towards a finite value of 0.5. This means that for the case of two correlated macroscopic beams of indistinguishable particles, the cross-correlation after passing through a 50:50 beam-splitter is twice smaller than for the case of distinguishable particles.

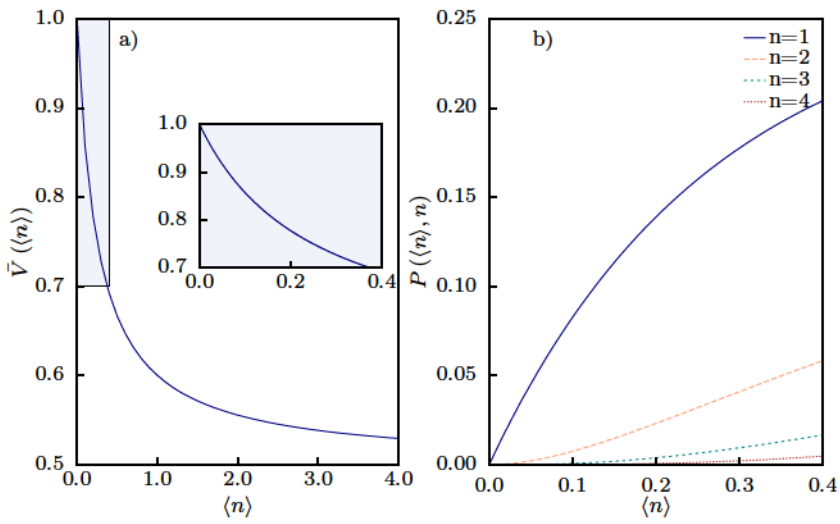

Figure 1.9: **Evolution of the HOM-dip visibility as a function of the averaged population $\langle n\rangle$.** *a) HOM-dip visibility $\bar{V}$ as a function of the averaged population per input port $\langle n\rangle$. b) Evolution of the probability to find n particles (P(n)) in one of the input port as a function of the averaged population $\langle n\rangle$. The distribution corresponds to the parametric down-conversion state.*

1.1.3 Classical threshold

Although the HOM effect has been presented and described so far as a pure quantum effect, a natural question to ask is whether it is possible or not to re-interpret this experiment through classical wave arguments. The answer to this question is yes and no. Yes, because it is possible to predict a reduction of the cross-correlation when the paths of our two particles become indistinguishable. And no, because, the contrast in this situation is bound to 0.5. For classical waves with random phases it is impossible to measure a visibility above 0.5. This means that a classical description gives a threshold value for the visibility above which no simple classical explanation can predict the result as we will see.

Consider two incoming electromagnetic waves $\mathcal{E}_a$ and $\mathcal{E}_b$ of same amplitude $\mathcal{E}_0$ but different phases

$$\mathcal{E}_a = \mathcal{E}_0 e^{i\phi_a} ,$$
$$\mathcal{E}_b = \mathcal{E}_0 e^{i\phi_b} ,$$

on a 50:50 beam-splitter. The two outcoming waves can be written as

$$\mathcal{E}_c = \frac{1}{\sqrt{2}}\left(\mathcal{E}_a + ie^{-i\phi_S}\mathcal{E}_b\right) ,$$
$$\mathcal{E}_d = \frac{1}{\sqrt{2}}\left(\mathcal{E}_b + ie^{i\phi_S}\mathcal{E}_a\right) .$$

The intensity at the two output ports I_c and I_d becomes then

$$I_c = 2I_0 \sin^2\left(\frac{\phi_b - \phi_a + \phi_S}{2}\right) ,$$
$$I_d = 2I_0 \cos^2\left(\frac{\phi_b - \phi_a + \phi_S}{2}\right) ,$$

and, consequently, the product intensity $I_c I_d$ is equal to

$$I_c I_d = 4I_0^2 \cos^2\left(\frac{\phi_b - \phi_a}{2}\right)\sin^2\left(\frac{\phi_b - \phi_a}{2}\right) = I_0^2 \sin^2\left(\phi_b - \phi_a + \phi_S\right) .$$

The question is then to know if it is possible, via classical arguments to retrieve a vanishing coincidence count. Since classical waves interfere, it is indeed possible to select an area where the intensity is always zero. Then, if the detector is at this position the coincidence count would go to zero when the waves interfere (indistinguishable waves) and finite when the waves are distinguishable (orthogonal polarisations for example). If now one changes randomly the phase between the two incoming waves in each realisation, the interferometric pattern will move randomly and, wherever the detector is placed, once averaged over all realisations, the coincidence count will never be equal to zero. For a twin Fock state, however, it is well known that the relative phase between the two photons is completely undefined since it is the Heisenberg conjugate of the particle number difference whose uncertainty is zero [88–90]. Consequently, choosing randomly the relative phase between the two incoming particles does not change a thing. In this situation, classical waves would never present a zero coincidence count while a quantum state, as a twin Fock state, would.

Averaging the classical wave interference over the phase difference $\phi_b - \phi_a$ ($\langle\rangle_\phi$) leads to

$$\langle I_d\rangle_\phi = \langle I_c\rangle_\phi = I_0 \tag{1.14a}$$

$$\langle I_d I_c\rangle_\phi = I_0^2/2\,, \tag{1.14b}$$

and to the visibility

$$\begin{aligned}\bar{V} &= 1 - \frac{\langle I_d I_c\rangle_\phi}{\langle I_d\rangle_\phi\langle I_c\rangle_\phi}\\ &= 0.5.\end{aligned}$$

In order to randomise the phase, one can also vary from realisation to realisation the phase of the 50:50 beam-splitter, ϕ_S. In fact, this is what we performed experimentally as will be discussed in Chapter 5. Thus, the visibility cannot exceed the threshold value of 0.5 meaning that, via classical arguments, one can never measure $\bar{V} > 0.5$. In fact, this threshold of 0.5 corresponds, to the best possible situation for classical waves since population imbalance at the entrance of the beam-splitter or losses at the beam-splitter would always lead to a reduction of the interference contrast and, consequently, of $\bar{V}$.

It is important to keep in mind that, via simple classical arguments, the maximum prediction for the HOM-dip visibility can not exceed the value of $\bar{V}_{\text{thres}} = 0.5$. Any result above this limit leads to the confirmation that quantum destructive interference are at play and that the input state is not a classical state.

1.2 HOM-dip visibility and Cauchy-Schwarz inequality

As seen previously, in order to quantify the destructive interference the visibility of the HOM-dip can be expressed as

$$\bar{V} = 1 - \frac{G^{(2)}_{cd,\,\text{Ind.}}}{G^{(2)}_{cd,\,\text{Dis.}}}$$

which combined with Eq. (1.7) leads to the expression

$$\bar{V} = \frac{2G^{(2)}_{ab}}{\left(G^{(2)}_{aa} + G^{(2)}_{bb}\right) + 2G^{(2)}_{ab}}. \tag{1.15}$$

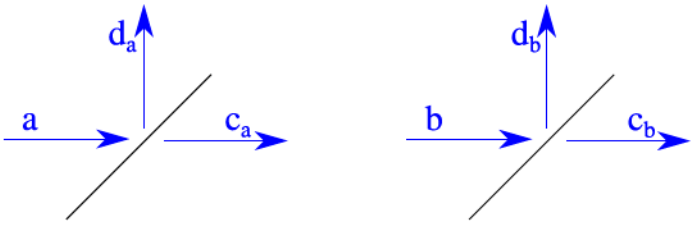

Figure 1.10: **Beam a and b split by a beam-splitter, schematic representation.** *Splitting of the incoming beams a and b in order to determine their autocorrelation. Beam a (blue incoming arrow) is split on a 50:50 beam-splitter (black trace) into two outcoming beams c_a and d_a. The same scheme is represented for beam b.*

From this expression, one directly sees that if the cross-correlation between the input particles a and b becomes much stronger than their respective autocorrelation then the visibility increases to 1. On the other hand, for a source with a finite autocorrelation value, meaning that the number of photons per beam is higher than one, the visibility of the HOM-dip decreases. This comparison between cross-correlation and autocorrelation is linked to the Cauchy-Schwarz (CS) inequality [91–93].

The CS inequality is ubiquitous in mathematics and physics [94]. Its utility ranges from proofs of basic theorems in linear algebra to the derivation of the Heisenberg uncertainty principle. In its basic form, the CS inequality simply states that the absolute value of the inner product of two vectors cannot be larger than the product of their lengths. In the present situation, the interest of the CS inequality is related to the detected intensity fields of the two incoming photons. Considering the two photons as classical electromagnetic waves the inequality writes as

$$\langle I_a I_b \rangle \leq \sqrt{\langle I_a^2 \rangle \cdot \langle I_b^2 \rangle}, \tag{1.16}$$

where I_a and I_b corresponds to the intensity of the beams a and b. In order to measure $\langle I_a^2 \rangle$, one cannot just measure $\langle I_a \rangle$ and take the value to the square. Since no detector directly measures the square of the intensity field, one needs to be ingenious. The solution is then to place a 50:50 beam-splitter in the path of each beam as represented in Fig. 1.10. The electromagnetic field is then split into two output ports c and d. For the case of beam a one has

$$I_a = \left(I_{c_a} + I_{d_a}\right)$$

and for beam b

$$I_b = \left(I_{c_b} + I_{d_b}\right).$$

Let us focus on the case of beam a (the calculations for beam b are identical). By measuring the cross-correlation at the output ports $\langle I_{c_a} I_{d_a} \rangle$, which for a perfect 50:50 beam-splitter corresponds to

$$\langle I_{c_a} I_{d_a} \rangle = \frac{1}{4} \langle I_a^2 \rangle,$$

one recovers the value of $\langle I_a^2 \rangle$ and $\langle I_b^2 \rangle$. Eq. (1.16) can then be written as

$$\langle I_a I_b \rangle \leq 16 \langle I_{c,a} I_{d,a} \rangle \langle I_{c,b} I_{d,b} \rangle. \tag{1.17}$$

In quantum mechanics, however, the expression of the CS inequality changes slightly. The

beam-splitter, as described in Section 1.1, leads to the following expressions

$$\hat{c}_a^\dagger = \frac{1}{\sqrt{2}}\left(\hat{a}^\dagger + ie^{-i\phi_S}\hat{O}^\dagger\right), \tag{1.18a}$$

$$\hat{d}_a^\dagger = \frac{1}{\sqrt{2}}\left(ie^{i\phi_S}\hat{a}^\dagger + \hat{O}^\dagger\right), \tag{1.18b}$$

with $\hat{O}^\dagger$ the Heisenberg operator for vacuum. As before, looking at the quantity $\langle \hat{n}_{c_a}\hat{n}_{d_a}\rangle$ with $\langle \hat{n}_i\rangle = \langle \hat{i}^\dagger\hat{i}\rangle$, where the number of atoms is the equivalent of the intensity, we obtain

$$\langle \hat{n}_{c,a}\hat{n}_{d,a}\rangle = \frac{1}{4}\langle \hat{a}^\dagger\hat{a}^\dagger\hat{a}\,\hat{a}\rangle = \frac{1}{4}\langle \hat{n}_a(\hat{n}_a - 1)\rangle = \frac{1}{4}\langle :\hat{n}_a^2:\rangle \tag{1.19a}$$

$$\langle \hat{n}_{c,b}\hat{n}_{d,b}\rangle = \frac{1}{4}\langle \hat{b}^\dagger\hat{b}^\dagger\hat{b}\,\hat{b}\rangle = \frac{1}{4}\langle \hat{n}_b(\hat{n}_b - 1)\rangle = \frac{1}{4}\langle :\hat{n}_b^2:\rangle \tag{1.19b}$$

with $\langle : :\rangle$ standing for the normal ordering average [95]. This non-intuitive ordering average can easily be seen as a consequence of the total number of particles conservation after a beam-splitter. In this sense, if one measures 1 particle of a total number of N particles, one has to detect $N-1$ particles on the other port. Thus, the CS inequality can now be written as

$$\langle \hat{n}_a\hat{n}_b\rangle^2 \leq \langle :\hat{n}_a^2:\rangle\langle :\hat{n}_b^2:\rangle. \tag{1.20}$$

Please note the importance of the normal ordering in this new expression of the CS inequality. Let us consider the case of the state seen earlier, $|1_a, 1_b\rangle$. For this particular, case one has $\langle :\hat{n}_a^2:\rangle = \langle :\hat{n}_b^2:\rangle = 0$ while $\langle \hat{n}_a\hat{n}_b\rangle^2 = 1$. The inequality does not hold any more and one violates the CS inequality [96]. This results shows that for the case of stronger-than-classical correlations the CS inequality is violated. In fact, it is important to note that for distinguishable particles a violation of such inequality does hold information on the correlation strength [97]. In the case of indistinguishable particles, however, the inequality violation is only possible for non-classical states.

The experimental production of such states is widely used for tests of quantum mechanics [56, 98, 99], quantum networking [100, 101] and quantum information [31, 32, 102] for example. The connection between the CS inequality violation and the properties of indistinguishability for entanglement is discussed in Ref. [103]. It states that the violation of the CS inequality can lead to a proof of entanglement in the case of indistinguishable particles.

The CS inequality can thus be written as

$$G_{ab}^{(2)} \leq \sqrt{G_{aa}^{(2)}G_{bb}^{(2)}}. \tag{1.21}$$

In order to easily express the violation of this inequality, the parameter C

$$C = \frac{G_{ab}^{(2)}}{\sqrt{G_{aa}^{(2)}G_{bb}^{(2)}}} \tag{1.22}$$

corresponding to a correlation coefficient is introduced. This parameter is smaller than unity classically, but can be larger than unity for states with stronger-than-classical correlations. In order words, $C > 1$ indicates a violation of the CS inequality. The idea is now to connect this correlation coefficient C to the HOM-dip visibility $\bar{V}$. Starting from Eq. (1.15) one can express $\bar{V}$ by the general expression

$$\bar{V} = \frac{1}{1 + (\delta/C)} \tag{1.23}$$

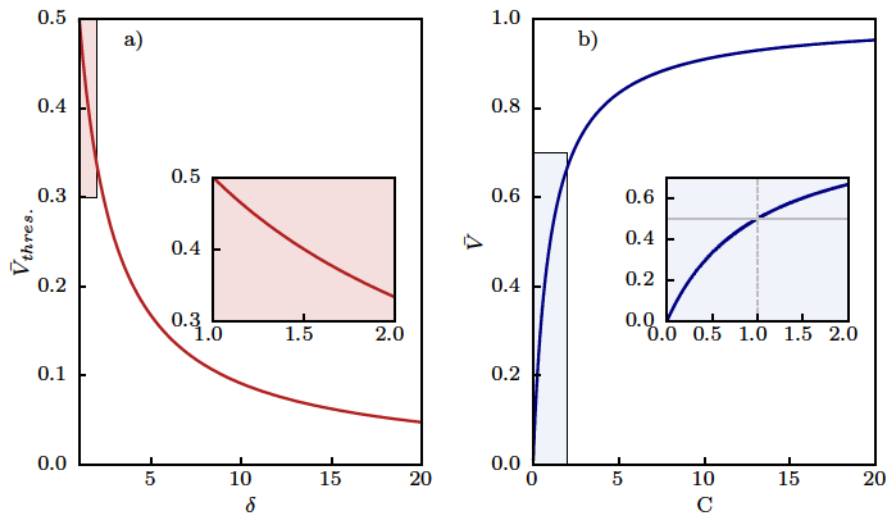

Figure 1.11: **HOM-visibility and visibility threshold as a function of δ and C.** *a) HOM-dip visibility threshold $\bar{V}_{thres}$ as a function of the imbalance parameter δ. One can see that the maximum value is set to 0.5 since $\delta \geq 1$. The inset shows the threshold inside a range close to the one measured experimentally in our system. b) HOM-dip visibility as a function of C for $\delta = 1$. One sees that the visibility threshold goes above 0.5 when $C > 1$ and saturates at 1 for $C \to \infty$. The inset shows the value of $\bar{V}$ for the correlation coefficient C in the range of the experimental values of C (see Section 3.4.2). The gray line indicates the threshold value of 0.5 while the dashed gray lines indicates $C = 1$.*

where $\delta = \left(G^{(2)}_{aa} + G^{(2)}_{bb}\right) / 2\sqrt{G^{(2)}_{aa} G^{(2)}_{bb}}$.

For $C = 1$, which corresponds to the maximum reachable value for a classical state, one gets the threshold limit for the visibility

$$\bar{V}_{\text{thres}} = \frac{1}{1+\delta}, \tag{1.24}$$

with $\delta \geq 1$ since all the correlators $G^{(2)}$ have positive values. The value of $\bar{V}_{\text{thres}}$ is represented in Fig. 1.11a) as a function of δ. It is shown that the maximum value of $\bar{V}_{\text{thres}}$ is equal to $\bar{V}_{\text{thres}} = 0.5$, obtained for $\delta = 1$. For $\delta > 1$ the value of $\bar{V}_{\text{thres}}$ decreases and corresponds to situations where the two beams have different autocorrelation values which can be explained from imbalanced populations, background noise, different production processes, etc. .

For $\delta = 1$ the visibility becomes

$$\bar{V} = \frac{1}{1+1/C}.$$

As one can see in Fig. 1.11b), when C is higher than 1 the visibility $\bar{V}$ goes over 0.5 and reaches unity when $C \to \infty$, corresponding to a situation where the autocorrelation value is zero. This means that the probability to find more than one photon per beam vanishes. Such state corresponds to $|\psi\rangle = |1_a, 1_b\rangle$ discussed at the beginning of this chapter.

We have seen so far that the HOM effect corresponds to a destructive interference which translates to a reduction of the coincidence count depending on the properties of the input state. This interference allows to quantify the number of particles present per input port as well as the correlation between the particles arriving at the beam-splitter. The HOM-dip visibility

$$\bar{V} = 1 - \frac{G^{(2)}_{cd,\,\mathrm{Ind.}}}{G^{(2)}_{cd,\,\mathrm{Dis.}}}$$

can reach the maximum value of 1 and cannot be explained through classical wave interference if $\bar{V} > \bar{V}_{\mathrm{thres}}$ with $\bar{V}_{\mathrm{thres}}$ being at most equal to 0.5. Thus, we conclude that despite the fundamental interest of performing the HOM experiment, which is an essential proof of the validity of quantum mechanics, this experiment is also a fundamental tool to determine certain properties of the source as the averaged population, stronger-than-classical correlations and indistinguishability.

The objective of the work done during this project was, based on the wide experience accumulated in the domain of quantum optics, to adapt the photonic HOM effect to cold atom experiments and to perform the same kind of experiments but with a source of correlated atomic pairs. For this purpose, in the next section the required tools and expected difficulties to probe this effect with atoms are summarised.

1.3 HOM experiment with atoms: necessary tools

The most difficult part to implement the HOM experiment with cold atoms is the production and control of atomic pairs. Although the cold atom community is obtaining promising results for atomic pair creation in both spin domain [53, 104] and momentum space domain [47, 48, 52, 105], the ability to produce and detect single pairs of matter waves that can be easily manipulated is still not common. The known examples include the case of trapped ions [101] and atoms [63, 106, 107]. However, in these cases, particles are not travelling apart from each other and the input/output ports of the 50:50 beam-splitter are the same contrary to the case of the HOM experiment.

The difficulty with atomic pairs in momentum space lies in the fact that particles are distinguished by their momenta which are continuous external degrees of freedom. Small modifications of the initial conditions translates into the production of different pairs. In other words, contrary to spin squeezing where the particle is either ↑ or ↓, in the case of momentum pair creation there are no boundaries. In this sense, the experimental realisation is very demanding in terms of control and stability. We will discuss in Chapter 3 the achieved atomic pair production in our experiment based on dynamical instabilities [105, 108].

Another question that naturally raises from interference phenomenon with matter-waves is the role played by interactions [109]. In contrast to what happens with photons, particles can interact via collisions or induced dipole forces. However, when the number of particles at play is low, as the HOM experiments requires, the role played by interactions is negligible [109] (see Section 5.8).

Also the detection of atoms can be an issue. Along this chapter, the discussion was always based on the ability to detect single particles. In that sense, the domain of cold atoms have done great improvements with single-atom-resolved fluorescence of atoms trapped in a lattice [36, 110–112] or via fluorescent resonant light sheet lying under the cloud [113]. Another technique relies on the unique properties of metastable helium atoms used in our experiment. This very

stable excited state lies 20 eV above the ground state. When in contact with a metallic surface, the internal energy of the atom is sufficient to produce an electronic burst which is later amplified and recorded as explained in Subsection 2.1.2. This single atom detection technique is at the heart of correlation measurement in our experiment from the Hanbury Brown and Twiss effect with matter waves [114, 115] to the violation of CS inequality on atomic pairs resulting from Bose–Einstein condensate collisions [96].

Finally, the last difference when compared to the original HOM experiment stands from the selection of both frequency and spatial modes via pinholes or spectral filters and on the atomic beam-splitter. Regarding the atom beam-splitter this is a well known domain with a vast literature [116–118]. The filtering procedure, however, has no direct analogue. Nevertheless, one will see in Chapter 5 that in our experiment, via the 3D-resolution of the detector, we are able to filter the contribution of the different modes.

In conclusion, in order to efficiently observe the HOM effect with matter-waves four main tools need to be at our disposal:

- a single atom detector;
- a source of atomic pairs with stronger-than-classical correlations ($C > 1$);
- a coherent atomic 50:50 beam-splitter;
- a filtering procedure in order to guarantee indistinguishability between particles.

In the next chapters, we will discuss in details these key tools.

Bibliography

[13]L.-A. Wu, H. J. Kimble, J. L. Hall, and H. Wu, "Generation of Squeezed States by Parametric Down Conversion", Phys. Rev. Lett. **57**, 2520–2523 (1986) (cit. on pp. 3, 14, 21, 72, 91).

[24]E. Knill, R. Laflamme, and G. J. Milburn, "A scheme for efficient quantum computation with linear optics", Nature **409**, 46–52 (2001) (cit. on pp. 3, 16).

[31]X.-S. Ma, T. Herbst, T. Scheidl, D. Wang, S. Kropatschek, W. Naylor, B. Wittmann, A. Mech, J. Kofler, E. Anisimova, V. Makarov, T. Jennewein, R. Ursin, and A. Zeilinger, "Quantum teleportation over 143 kilometres using active feed-forward", Nature **489**, 269–273 (2012) (cit. on pp. 4, 25).

[32]A. Rubenok, J. A. Slater, P. Chan, I. Lucio-Martinez, and W. Tittel, "Real-World Two-Photon Interference and Proof-of-Principle Quantum Key Distribution Immune to Detector Attacks", Phys. Rev. Lett. **111**, 130501 (2013) (cit. on pp. 4, 25).

[36]"A Quantum Gas Microscope for Fermionic Atoms", arXiv [1503.02648] (cit. on pp. 4, 27).

[47]J. M. Vogels, K. Xu, and W. Ketterle, "Generation of Macroscopic Pair-Correlated Atomic Beams by Four-Wave Mixing in Bose-Einstein Condensates", Phys. Rev. Lett. **89**, 020401 (2002) (cit. on pp. 4, 27).

[48]A. Perrin, H. Chang, V. Krachmalnicoff, M. Schellekens, D. Boiron, A. Aspect, and C. I. Westbrook, "Observation of Atom Pairs in Spontaneous Four-Wave Mixing of Two Colliding Bose-Einstein Condensates", Phys. Rev. Lett. **99**, 150405 (2007) (cit. on pp. 4, 27, 34, 167).

[52]R. Bucker, J. Grond, S. Manz, T. Berrada, T. Betz, C. Koller, U. Hohenester, T. Schumm, A. Perrin, and J. Schmiedmayer, "Twin-atom beams", Nat Phys **7**, 608–611 (2011) (cit. on pp. 4, 27).

[53]H. Strobel, W. Muessel, D. Linnemann, T. Zibold, D. B. Hume, L. Pezzè, A. Smerzi, and M. K. Oberthaler, "Fisher information and entanglement of non-Gaussian spin states", Science **345**, 424–427 (2014) (cit. on pp. 4, 27, 162, 163).

[54]C. K. Hong, Z. Y. Ou, and L. Mandel, "Measurement of subpicosecond time intervals between two photons by interference", Phys. Rev. Lett. **59**, 2044–2046 (1987) (cit. on pp. 4, 13, 14, 16, 17, 130–132, 134, 143, 152).

[56]C. Lang, C. Eichler, L. Steffen, J. M. Fink, M. J. Woolley, A. Blais, and A. Wallraff, "Correlations, indistinguishability and entanglement in Hong-Ou-Mandel experiments at microwave frequencies", Nat Phys **9**, 345–348 (2013) (cit. on pp. 4, 25).

[63]A. M. Kaufman, B. J. Lester, C. M. Reynolds, M. L. Wall, M. Foss-Feig, K. R. A. Hazzard, A. M. Rey, and C. A. Regal, "Two-particle quantum interference in tunnel-coupled optical tweezers", Science **345**, 306–309 (2014) (cit. on pp. 4, 27).

[72]F. T. ppel, A. Aiello, and G. Leuchs, "All photons are equal but some photons are more equal than others", New. J. Phys. **14**, 093051 (2012) (cit. on pp. 13, 16).

[73]J. Beugnon, M. P. A. Jones, J. Dingjan, B. Darquié, G. Messin, A. Browaeys, and P. Grangier, "Quantum interference between two single photons emitted by independently trapped atoms", Nature **440**, 779–782 (2006) (cit. on p. 14).

[74]S. P. Walborn, A. N. de Oliveira, S. Pádua, and C. H. Monken, "Multimode Hong-Ou-Mandel Interference", Phys. Rev. Lett. **90**, 143601 (2003) (cit. on p. 16).

[75]Y. L. Lim and A. Beige, "Generalized Hong–Ou–Mandel experiments with bosons and fermions", New. J. Phys. **7**, 155–155 (2005) (cit. on p. 16).
[76]Z. Y. Ou, *Multi-Photon Quantum Interference* (Springer, 2007) (cit. on pp. 16, 153).
[77]T. B. Pittman, D. V. Strekalov, A. Migdall, M. H. Rubin, A. V. Sergienko, and Y. H. Shih, "Can Two-Photon Interference be Considered the Interference of Two Photons?", Phys. Rev. Lett. **77**, 1917–1920 (1996) (cit. on pp. 16, 130).
[78]Y. J. Lu, R. L. Campbell, and Z. Y. Ou, "Mode-Locked Two-Photon States", Phys. Rev. Lett. **91**, 163602 (2003) (cit. on p. 16).
[79]Z. Y. Ou, J.-K. Rhee, and L. J. Wang, "Observation of Four-Photon Interference with a Beam Splitter by Pulsed Parametric Down-Conversion", Phys. Rev. Lett. **83**, 959–962 (1999) (cit. on pp. 17, 130, 158).
[80]B. H. Liu, F. W. Sun, Y. X. Gong, Y. F. Huang, G. C. Guo, and Z. Y. Ou, "Four-photon interference with asymmetric beam splitters", Opt. Lett. **32**, 1320–1322 (2007) (cit. on p. 17).
[81]L. Mandel, "Photon interference and correlation effects produced by independent quantum sources", Phys. Rev. A **28**, 929–943 (1983) (cit. on p. 17).
[82]T. S. Iskhakov, K. Y. Spasibko, M. V. Chekhova, and G. Leuchs, "Macroscopic Hong–Ou–Mandel interference", New. J. Phys. **15**, 093036 (2013) (cit. on pp. 17, 18, 162).
[83]K. Y. Spasibko, F. Töppel, T. S. Iskhakov, M. Stobińska, M. V. Chekhova, and G. Leuchs, "Interference of macroscopic beams on a beam splitter: phase uncertainty converted into photon-number uncertainty", New. J. Phys. **16**, 013025 (2014) (cit. on pp. 17–19).
[84]R. Campos, B. Saleh, and M. Teich, "Quantum-mechanical lossless beam splitter: SU(2) symmetry and photon statistics", Physical Review A **40**, 1371–1384 (1989) (cit. on p. 18).
[85]R. J. Lewis-Swan and K. V. Kheruntsyan, "Proposal for demonstrating the Hong–Ou–Mandel effect with matter waves", Nat Commun **5** (2014) (cit. on pp. 20, 135).
[86]W. H. Louisell, A. Yariv, and A. E. Siegman, "Quantum Fluctuations and Noise in Parametric Processes. I.", Phys. Rev. **124**, 1646–1654 (1961) (cit. on pp. 21, 72).
[87]C. M. Savage, P. E. Schwenn, and K. V. Kheruntsyan, "First-principles quantum simulations of dissociation of molecular condensates: Atom correlations in momentum space", Phys. Rev. A **74**, 033620 (2006) (cit. on pp. 21, 202).
[88]G. Grynberg, A. Aspect, and C. Fabre, *Introduction aux lasers et à l'optique quantique* (Ecole polytechnique, Département de physique Paris, Palaiseau, 1997) (cit. on p. 23).
[89]G. Agarwal, *Quantum Optics*, Quantum Optics (Cambridge University Press, 2012) (cit. on p. 23).
[90]H.-A. Bachor and T. C. Ralph, *A Guide to Experiments in Quantum Optics, 2nd, Revised and Enlarged Edition* (Mar. 2004) (cit. on p. 23).
[91]P. Edwards, X. Huang, and Y. Li, "Novel Macroscopic Violation of a Cauchy Schwarz Inequality Using Bunched and Unbunched Twin Beams", in *Coherence and quantum optics vii*, edited by J. Eberly, L. Mandel, and E. Wolf (Springer US, 1996), pp. 713–714 (cit. on p. 24).
[92]H. J. Kimble, M. Dagenais, and L. Mandel, "Photon Antibunching in Resonance Fluorescence", Phys. Rev. Lett. **39**, 691–695 (1977) (cit. on p. 24).
[93]A. M. Marino, V. Boyer, and P. D. Lett, "Violation of the Cauchy-Schwarz Inequality in the Macroscopic Regime", Phys. Rev. Lett. **100**, 233601 (2008) (cit. on p. 24).
[94]J. M. Steele, *The Cauchy-Schwarz Master Class: An Introduction to the Art of Mathematical Inequalities* (Cambridge University Press, Cambridge, 2004) (cit. on p. 24).
[95]R. Glauber, "The Quantum Theory of Optical Coherence", Phys. Rev. **130**, 2529–2539 (1963) (cit. on pp. 25, 123).
[96]K. V. Kheruntsyan, J.-C. Jaskula, P. Deuar, M. Bonneau, G. B. Partridge, J. Ruaudel, R. Lopes, D. Boiron, and C. I. Westbrook, "Violation of the Cauchy-Schwarz Inequality with Matter Waves", Phys. Rev. Lett. **108**, 260401 (2012) (cit. on pp. 25, 28, 97, 98, 167, 217).
[97]T. Wasak, P. Sza ńkowski, P. Zi ń, M. Trippenbach, and J. Chwede ńczuk, "Cauchy-Schwarz inequality and particle entanglement", Phys. Rev. A **90**, 033616 (2014) (cit. on pp. 25, 98).

[98] P. G. Kwiat, K. Mattle, H. Weinfurter, A. Zeilinger, A. V. Sergienko, and Y. Shih, "New High-Intensity Source of Polarization-Entangled Photon Pairs", Phys. Rev. Lett. **75**, 4337–4341 (1995) (cit. on p. 25).

[99] C. Santori, D. Fattal, J. Vuckovic, G. S. Solomon, and Y. Yamamoto, "Indistinguishable photons from a single-photon device", Nature **419**, 594–597 (2002) (cit. on p. 25).

[100] A. Kuhn, M. Hennrich, and G. Rempe, "Deterministic Single-Photon Source for Distributed Quantum Networking", Phys. Rev. Lett. **89**, 067901 (2002) (cit. on p. 25).

[101] L.-M. Duan and C. Monroe, "*COLLOQUIUM* : QUANTUM NETWORKS WITH TRAPPED IONS", Rev. Mod. Phys. **82**, 1209–1224 (2010) (cit. on pp. 25, 27).

[102] P. Michler, A. Kiraz, C. Becher, W. V. Schoenfeld, P. M. Petroff, L. Zhang, E. Hu, and A. Imamoglu, "A Quantum Dot Single-Photon Turnstile Device", Science **290**, 2282–2285 (2000) (cit. on p. 25).

[103] T. Wasak, P. Sza ńkowski, P. Zi ń, M. Trippenbach, and J. Chwede ńczuk, "Cauchy-Schwarz inequality and particle entanglement", Phys. Rev. A **90**, 033616 (2014) (cit. on p. 25).

[104] B. Lücke, J. Peise, G. Vitagliano, J. Arlt, L. Santos, G. Tóth, and C. Klempt, "Detecting Multiparticle Entanglement of Dicke States", Phys. Rev. Lett. **112**, 155304 (2014) (cit. on p. 27).

[105] G. K. Campbell, J. Mun, M. Boyd, E. W. Streed, W. Ketterle, and D. E. Pritchard, "Parametric Amplification of Scattered Atom Pairs", Phys. Rev. Lett. **96**, 020406 (2006) (cit. on pp. 27, 45, 71, 86).

[106] T. Wilk, A. Gaëtan, C. Evellin, J. Wolters, Y. Miroshnychenko, P. Grangier, and A. Browaeys, "Entanglement of Two Individual Neutral Atoms Using Rydberg Blockade", Phys. Rev. Lett. **104**, 010502 (2010) (cit. on p. 27).

[107] A. G. Manning, R. Khakimov, R. G. Dall, and A. G. Truscott, "Single-Atom Source in the Picokelvin Regime", Phys. Rev. Lett. **113**, 130403 (2014) (cit. on p. 27).

[108] M. Bonneau, J. Ruaudel, R. Lopes, J.-C. Jaskula, A. Aspect, D. Boiron, and C. I. Westbrook, "Tunable source of correlated atom beams", Phys. Rev. A **87**, 061603 (2013) (cit. on pp. 27, 34, 44–46, 83, 91, 167, 217).

[109] E. Andersson, M. T. Fontenelle, and S. Stenholm, "Quantum statistics of atoms in microstructures", Phys. Rev. A **59**, 3841–3850 (1999) (cit. on pp. 27, 163, 164).

[110] W. S. Bakr, J. I. Gillen, A. Peng, S. Folling, and M. Greiner, "A quantum gas microscope for detecting single atoms in a Hubbard-regime optical lattice", Nature **462**, 74–77 (2009) (cit. on p. 27).

[111] J. F. Sherson, C. Weitenberg, M. Endres, M. Cheneau, I. Bloch, and S. Kuhr, "Single-atom-resolved fluorescence imaging of an atomic Mott insulator", Nature **467**, 68–72 (2010) (cit. on p. 27).

[112] E. Haller, J. Hudson, A. Kelly, D. Cotta, B. Peaudecerf, G. Bruce, and S. Kuhr, "Single-atom imaging of fermions in a quantum-gas microscope", arXiv [1503.02005v2] (cit. on p. 27).

[113] R. Bücker, A. Perrin, S. Manz, T. Betz, C. Koller, T. Plisson, J. Rottmann, T. Schumm, and J. Schmiedmayer, "Single-particle-sensitive imaging of freely propagating ultracold atoms", New. J. Phys. **11**, 103039 (2009) (cit. on p. 27).

[114] M. Schellekens, R. Hoppeler, A. Perrin, J. V. Gomes, D. Boiron, A. Aspect, and C. I. Westbrook, "Hanbury Brown Twiss Effect for Ultracold Quantum Gases", Science **310**, 648–651 (2005) (cit. on pp. 28, 34).

[115] J. V. Gomes, A. Perrin, M. Schellekens, D. Boiron, C. I. Westbrook, and M. Belsley, "Theory for a Hanbury Brown Twiss experiment with a ballistically expanding cloud of cold atoms", Phys. Rev. A **74**, 053607 (2006) (cit. on pp. 28, 120).

[116] D. M. Giltner, R. W. McGowan, and S. A. Lee, "Atom Interferometer Based on Bragg Scattering from Standing Light Waves", Phys. Rev. Lett. **75**, 2638–2641 (1995) (cit. on pp. 28, 106).

[117] E. M. Rasel, M. K. Oberthaler, H. Batelaan, J. Schmiedmayer, and A. Zeilinger, "Atom Wave Interferometry with Diffraction Gratings of Light", Phys. Rev. Lett. **75**, 2633–2637 (1995) (cit. on p. 28).

[118] M. Kozuma, L. Deng, E. W. Hagley, J. Wen, R. Lutwak, K. Helmerson, S. L. Rolston, and W. D. Phillips, "Coherent Splitting of Bose-Einstein Condensed Atoms with Optically Induced Bragg Diffraction", Phys. Rev. Lett. **82**, 871–875 (1999) (cit. on p. 28).

Chapter 2

Experimental requisites towards the HOM experiment: BEC-stability

Contents

2.1 Status of the experiment in the beginning of the project . . . 34
2.1.1 Metastable helium . . . 34
2.1.2 The Micro-Channel-Plate: He* detector . . . 35
2.1.3 Cooling protocol . . . 39
2.1.4 Vertical dipole trap . . . 40
2.1.5 The 1D optical lattice . . . 42
2.1.6 Summary . . . 43
2.2 Bose–Einstein condensate of metastable Helium . . . 44
2.2.1 Arrival time instability of the condensate . . . 44
2.2.2 Anisotropy of the BEC: phase fluctuation issues . . . 47
2.2.3 Quasi-BEC or BEC? . . . 47
2.2.4 Crossed dipole trap: solution to both issues . . . 50
2.2.5 Condensate: determination of the chemical potential and size . . . 54
2.3 Conclusion . . . 59

"-T'as vu les atomes de la mélasse?
- heuuu... je crois pas. Mais j'ai peut-être fermé l'oeil au mauvais moment."

JR and RL in the lab...

In Chapter 1, four fundamental blocks were listed in order to experimentally accomplish the HOM experiment with atoms. Each block will be discussed in more detail in the next chapters. In this chapter, we will give an outline of the experimental apparatus, pointing out its deficiencies at the beginning of this project and how we solved them.

The chapter is organised as follow. In Section 2.1, we start by reviewing some of the most fundamental protocols of the experiment. A brief overview of the status of the apparatus when this work started is given, indicating the points that were missing or not adapted to the realisation of the atomic HOM experiment. In Section 2.2, the experimental realisation of a metastable helium BEC, with higher focus on the new dipole trap configuration implemented

during this thesis, is presented and the actual BEC conditions are summarised, pointing out the improvements made and their significance for present and future experiments.

2.1 Status of the experiment in the beginning of the project

The metastable helium experiment at the Institut d'Optique is one of the oldest cold atoms experiments where the first BEC of metastable helium 4 was obtained in 2001 by A. Robert *et al.* [119]. This set-up is at the origin of many different important results in the domain of quantum atom optics such as the Hanbury Brown and Twiss effect with atoms [114, 120, 121], atomic pairs sources in momentum space [48, 51, 108], superradiance [68], dynamical Casimir effect with matter waves [39], and more recently the atomic HOM effect [122].

This manuscript is focused on the work carried between the years 2011 and 2014. During this time the atomic HOM experiment and the atomic analogue to the dynamical Casimir effect, alongside with the study of superradiance, were performed. The results presented in this thesis are a consequence not only of new improvements done on the existing set-up but also all the work done by previous researchers since 1996. The goal of this section is to summarise the main characteristics of the apparatus, at the beginning of this thesis, and its operating procedure.

2.1.1 Metastable helium

The reason for helium 4 not being cooled in its fundamental state lies in the fact that the internal state can not be magnetically trapped since it has no global spin and that the closest excited state is 19.8 eV above it (see Fig. 2.1). This huge difference of energy corresponds to a wavelength of 50 nm that is difficult to address experimentally. Since most cold atom techniques are based on light-matter interactions [123, 124] it is then a bad candidate to be cooled.

On the other hand, the 2^3S_1 metastable state has a spin induced magnetic dipole moment that allows one to trap it magnetically and presents accessible optical transitions at 1.08 μm and 389 nm as represented in Fig. 2.1. For these reasons, the metastable state 2^3S_1 is a good candidate to be trapped and cooled, making Helium one of the few non-alkali atoms to have been condensed [119, 125–132]. In Table 2.1 the most important values of the metastable helium 4 are summarised.

One of the particularities of this metastable atom is its internal energy. Each trapped atom has an internal energy of 19.8 eV which is large compared to the energy scale of such systems (the recoil energy being equal to $E_{\text{rec}} = 10^{-11}$ eV). This is the most important reason why we are working with this atom. When it hits a metallic plate its energy is sufficient to release an electron since the electron binding energy of most metals (work function) is equal to a few eV. This electron can be amplified leading to a macroscopic electronic signal. Experimentally this is performed by letting the atoms fall towards a micro-channel-plate at the end of the experimental sequence which allows us to detect each atom individually.

Another important characteristic of helium atom is its low mass. This implies that the recoil velocity allows one to resolve efficiently the momentum distribution of scattered atoms. This will be an important feature to distinguish the atomic pairs from the initial BEC source and we will come back to this point later.

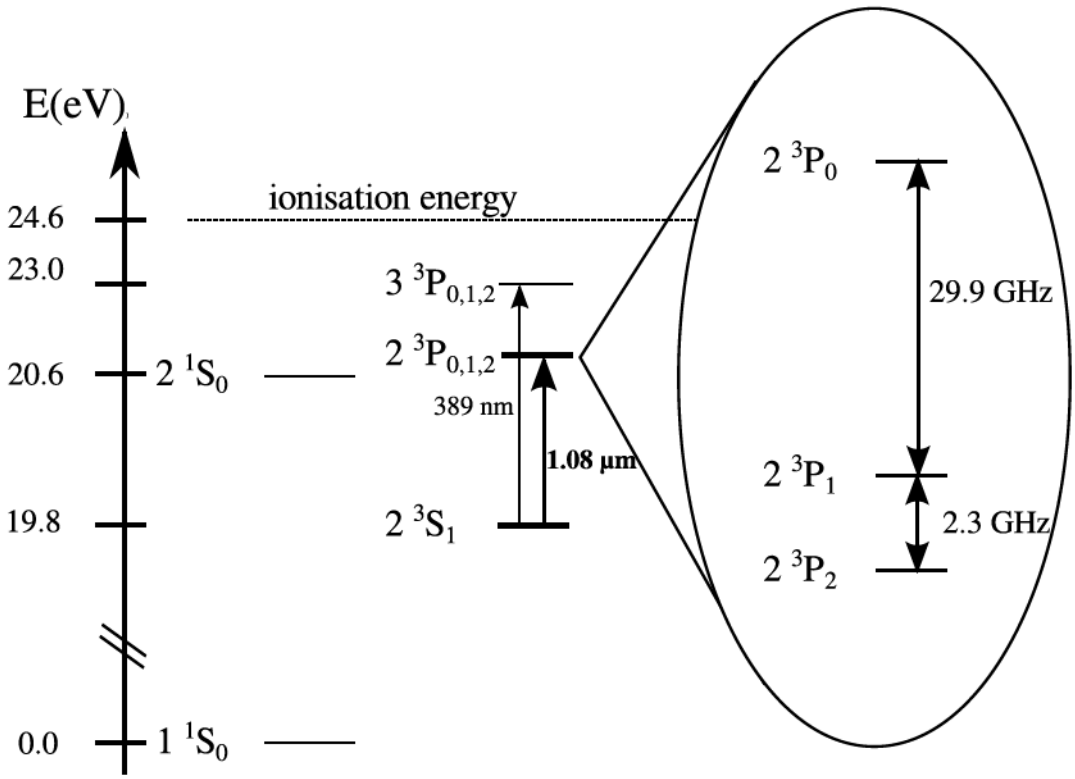

Figure 2.1: Helium 4 atomic structure. Energy level representation of the first excited states of helium atom. The metastable state 2^3S_1 is represented 19.8 eV above the fundamental level and the optical transitions with the excited state $2^3P_{0,1,2}$ used for cooling and manipulate the metastable state are represented.

Optical transitions

Two optical transitions have to be considered (see Fig. 2.1),

- the P_2 line, corresponding to the transition between $2^3S_1 \rightarrow 2^3P_2$, which is used for all cooling mechanisms, namely for the magneto-optical-trap (MOT), optical molasses, Zeeman slower, re-pumping and 1D Doppler cooling (see Subsection 2.1.3);
- and the P_0 line, corresponding to $2^3S_1 \rightarrow 2^3P_0$ transition, through which the beam-splitter and the Raman transfer are performed (see Chapter 4 and Appendix C for more details).

To address these two transitions two DBR laser diodes [136] are used on the experiment, one locked, by saturation absorption, on the P_2 transition and another one locked on the P_0 transition.

2.1.2 The Micro-Channel-Plate: He* detector

More details on the Micro-Channel-Plate detector can be found in the thesis of Lynn Hoendervanger Ref. [137] and Ref. [138].

The Micro-Channel-Plate (MCP), shown in Fig. 2.2, corresponds to the best suited metastable helium detector for cold atoms experiments. It operates in the same way as a photomultiplier does for photons: when a metastable helium atom hits the metallic plate, its internal energy is sufficient to extract at least one electron from the plate which is later amplified through the channel (see scheme of Fig. 2.2a)). In order to increase the electronic signal, two plates are placed one behind the other which allows us to multiply the flux by a factor 10^7. Since the pressure in the science chamber is very low ($P \leq 10^{-10}$ mbar) the probability of detecting anything else

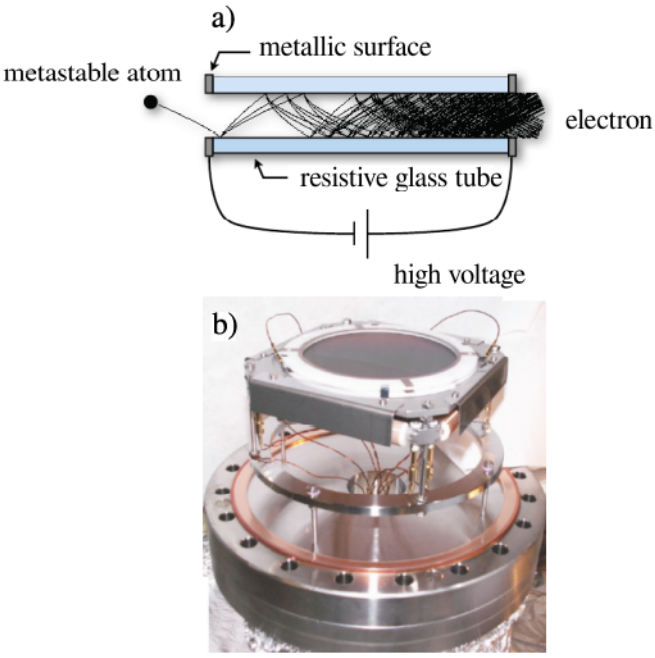

Figure 2.2: Representation of the Micro-Channel-Plate. a) Schematic representation of the mechanism of the channel plate detector. The atom hits the channel and releases a few electrons. Due to a high voltage difference between the edges of the metallic tube, the electron signal is amplified and corresponds at the end of the tube to a macroscopic electron burst easily detectable. b) The plate is shown in its mount with the delay lines laying beneath the MCP. The MCP corresponds to hundreds of tubes as the one described in a) with a separation between each of 5 μm. *The tubes draw an angle of* 7 ° *along the vertical direction and have an effective diameter of* 25 μm. *This angle is responsible for the vertical resolution. Two atoms arriving at the same time but separated by less than* 25 μm *produce two identical electron burst and cannot be distinguish. This leads to a vertical resolution of* 150μm, *full width at half-maximum*

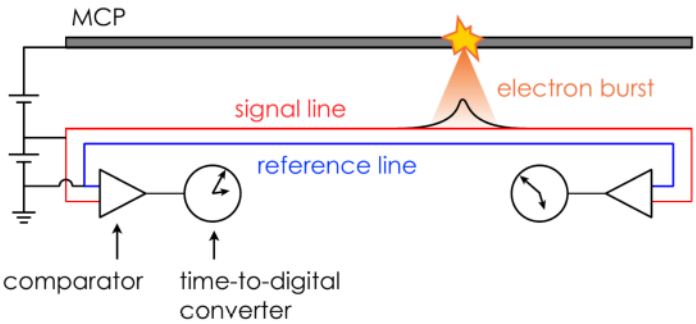

Figure 2.3: Delay line schematic representation. The electron burst coming from the MCP falls to the delay line. The electric signal propagates then along the line in both directions. Two detectors at the ends of the lines register the arrivals time of both signals. A comparison is performed between the recorded times of the two detectors. Knowing the length of the line and the propagation velocity along it, one infers the position of the electron burst and, as a consequence, of the atoms on the MCP. The precision on the position of the atom is limited by the finite width of the electronic signal. This is responsible for the transverse resolution of our detector of 400μm, *full width at half-maximum. Two perpendicular delay lines are then placed below the MCP, in order to determine both components on the horizontal plane. The delay lines do several loops in order to completely map the area beneath the MCP. This allows, with the arrival time, to reconstruct the position of the atom in all three directions of space.*

Quantity	Symbol	Value
Lifetime of the 2^3S_1 metastable state [133]		7870 (510) seconds
Mass	m_{He}	6.65×10^{-27} kg
Wavelength of the transition ($2^3\,S_1 \rightarrow 2^3P_2$)	λ_{rec}	1083 nm
Radiative decay rate	Γ	$2\pi \times 1.62$ MHz
Saturation intensity	I_{sat}	1.6 W/m^2
Scattering length for the s-wave (see Ref. [134, 135])	a_{11}	7.512×10^{-9} m
Recoil momentum	$k_{rec} = \frac{2\pi}{\lambda_{rec}}$	5.8×10^6 m^{-1}
Recoil velocity	$v_{rec} = \frac{\hbar v_{rec}}{m_{He}}$	9.2 cm/s
Recoil energy	$E_{rec} = \frac{\hbar^2 k_{rec}^2}{2m_{He}}$	2.8×10^{-29} J
Recoil temperature	$T_{rec} = \frac{E_{rec}}{k_B}$	2.06 μK

***Table 2.1:** Main values of metastable helium 4. Summary of the most important values associated to the metastable helium 4 atom.*

than single metastable atoms is negligible [139]. This technique allows us to detect independent single atoms and avoids any double counting. Indeed, once the internal energy of the atom has been transferred into an electron burst the probability for the same atom to produce another electron burst is negligible. However, the detection efficiency of this process is quite reduced since not all atoms succeed in extracting an electron. From our most recent experimental results, we estimate the detection efficiency to be at least equal to 25 (5) % [68, 122] (see Section 3.4.2).

Since the electron propagation time is reduced, shorter than a nanosecond, the arrival time measurement of the electron burst reflects directly the arrival time of the atom. In our experiment, the detector lays 46 cm below the atomic cloud and so we are essentially sensitive to the initial speed of the atom or, as in the case of a condensate, to the velocity of the atoms after the conversion of the interaction potential into kinetic energy has been done.

For the case of a very elongated condensate with long axis along the vertical z direction, which was the case for a condensate obtained in the vertical trap alone, however, this is untrue. The time-of-flight is not sufficiently long to neglect the initial size of the condensate. Consequently, the arrival time of each atom is given by its initial speed and position along the condensate [140]. This anisotropy of the cloud has, since then, changed with the addition of an horizontal trap (see Section 2.2). The time difference due to the finite size of the cloud is now currently around 34 μs and lies below the vertical resolution of the detector as we will see later on. For the case of the atomic pairs, as we will see, the arrival time reflects only their initial speed (see Section 3.3).

By measuring the arrival time of the atoms, one recovers the initial velocity of each detected atom along the vertical $z-$axis. For the other two transverse components of the velocity vector, it is impossible, from the MCP signal alone, to determine their components. In order to fully describe the velocity vector, it is then necessary to add two delay lines.

Delay lines

A delay line corresponds to a metallic, transmission line with a well defined length. It is placed under the MCP and its functionality is the following. The electron burst produced by the atom comes out of the channel and falls on the metallic line which lays below the MCP. The electrons propagate along the line on both directions at a speed $v \approx c/3$, with c the speed of light. By measuring the arrival time of both pulses on each end of the line one can, knowing the total length of the line, recover the position of the atom along this direction (see Fig. 2.3 for a schematic representation of the process). If now one places two of those lines perpendicular to each other, it becomes possible to get the coordinates of each atom on the horizontal plan. Combined with the arrival time measurement, one is able to fully reconstruct the velocity vector of each detected individual atom. The pulses are converted into digital (binary) output through a Time to Digital Converter (TDC) to be later analysed (see Ref. [139] for more details).

Detector resolution

The resolution of the detector is mainly determined by geometrical and electronic features. Transversely the resolution is limited by the spread of the electron burst which is approximatively equal to 400 μm, while vertically the dominant limitation is due to the inclination (7-8°) of the channels and leads to a detector resolution of 150 μm (for a detailed description see Ref. [141]).

Converted into speed, this corresponds to a resolution of 1.3×10^{-3} m/s or 1.4×10^{-2} v_{rec} along the transverse direction and of 4.6×10^{-4} m/s or 5×10^{-3} v_{rec} longitudinally.

Detector saturation

When the flux of incident atoms is high, as for the case of a BEC, a local saturation of the detector is noticeable.[1] An asymmetric arrival time distribution is then visible (see Fig. 2.7 for instance). This asymmetry can be due to [142]:

- Local saturation

  The saturation corresponds to a massive extraction of electrons from the walls of the channels that have a certain loading time. If many atoms arrive at the same time then the first ones are normally detected while the latest are more likely missed. This kind of phenomenon translates to an asymmetric shape of the arrival time distribution. This usually happens for a local flux of 10^5 atom/cm^2/s.

- Electronic saturation

  The consecutive signal treatment induces a dead time of approximatively 20 ns. If two atoms arrive with a time difference shorter than this value, they cannot produce two distinguishable electron burst and, consequently, one of the two is missed. This corresponds then to a maximum temporal flux of 1/20 ns = 5×10^7 atoms/s. However, this value is also limited by the maximum flux of the electronics which saturates at 5×10^6 atoms/s.

- Reconstruction saturation

  During the reconstruction algorithms used to transform the four electronic signals, corresponding to the four outputs of the two delay lines, into a 3D coordinate of one single

[1] Consequently, no information can be sorted out from the density profile of the BEC. This will be discussed in Section 2.2.

atom a selection is performed. If the atom flux increases strongly then it becomes difficult to differentiate the four since each electron burst has a finite width. It is then impossible to reconstruct each atom individually [139]. This translates into a dip centred at the maximum intensity of the cloud.

Detection efficiency

With the pair production system, discussed along this manuscript, a sub-shot noise variance has been measured. Considering that the produced pairs are maximally correlated and that the variance goes to zero (see Section 3.4.2 and Ref. [51] for more details) we estimate the detection efficiency to be higher than 25 (5) %. However, no upper bound has been estimated yet.

2.1.3 Cooling protocol

Helium source

The first step in order to create a BEC of metastable helium is to transfer some helium atoms to the 2^3S_1 excited state. As shown in Fig. 2.1, the metastable state has an internal energy of 19.8 eV corresponding to a wavelength of approximatively 50 nm. Although one can not address this transition optically, it is possible to excite atoms in a very easy and *dirty* way by letting the atoms pass through a high electric potential difference. A plasma is then created with all kind of excited states and ionised particles [143, 144]. A very weak fraction ($\leq 10^{-2}$%) of atoms are transferred to the 2^3S_1 metastable state which can be addressed optically using laser beams with wavelength of 1083 nm [124]. After this electric discharge, the atoms move fast on all three axis.

One would then like to collimate the produced metastable atoms in order to direct them into a trap where they could be effectively cooled down. For this purpose, four laser beams create the equivalent of a lens for atoms via transverse molasses and collimate the atomic beam [136, 145]. This technique allows us not only to capture the atoms but to keep only the ones lying on the metastable state. The longitudinal velocity is limited by cooling the discharge structure, represented in Fig. 2.4 by (b), with liquid nitrogen down to 77 K. However, after this procedure the atoms are still moving with a speed of 1500 m/s along the axis of propagation. In order to load the magnetic-optical-trap, one still needs to strongly reduce their speed.

Zeeman slower

A 3 m long Zeeman slower is used [124, 136]. The length of the Zeeman slower, which is a characteristic of all metastable Helium experiments, is due to the very long lifetime of the excited state 2^3P_2 which corresponds to $\tau = 1/\Gamma = 0.1\,\mu$s. Since the recoil velocity, given by the absorption of a photon, is approximatively equal to 0.1 m/s and knowing that the initial speed is equal to 1500 m/s then, it is necessary for each atom to perform 15000 cycles of absorption-emission to slow down to zero. The typical time is 1.5 ms which corresponds to a distance travelled of approximatively 3 m. The laser beam responsible for the cycling process is detuned 400 MHz to the red of the transition and a spatially varying magnetic field compensates the Doppler shift along the distance [124].

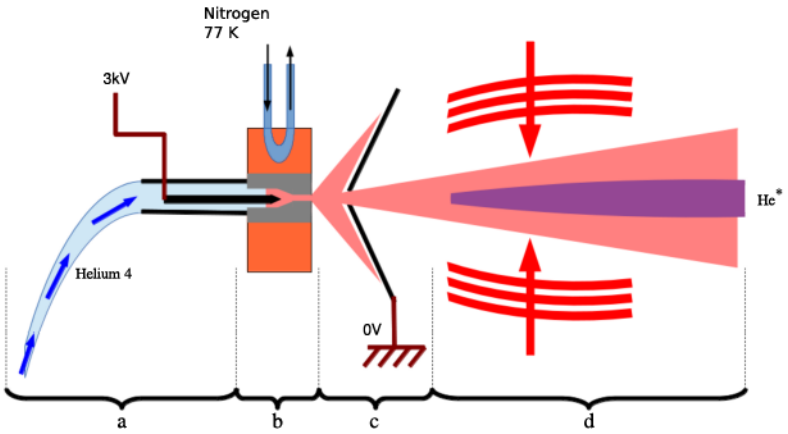

Figure 2.4: Source of metastable helium atoms. A constant flux of helium atoms is sent towards a metallic needle connected to a 3 kV power supply. A plasma takes place between the needle and the cone in front of it connected to the ground. The container represented in (b) is cooled down by liquid nitrogen during this phase in order to reduce the atomic longitudinal speed. A transverse molasses is then applied in order to reduce the transversal spreading of the metastable helium atoms allowing to effectively load a MOT located at the end of a 3 m long Zeeman slower.

Magnetic trap

The Zeeman slower loads directly a magneto-optical trap (MOT) with a flux of $10^8 - 10^9$ at/s which saturates after 2 s. The MOT beams correspond to a set of three pairs of laser beams with polarization σ^+, for two of the pairs, and σ^- for the other pair. The six beams are detuned by 56 MHz to the red of the transition.

Up to 10^8 metastable Helium 4 atoms with an approximate temperature of 300 μK are then loaded in a Ioffre-Pritchard like magnetic trap where an optical pumping phase is performed [136]. A 1D Doppler cooling stage is also performed in the magnetic trap where a close-to-resonance low-intensity laser beam is applied on the atoms for 6 s [146]. The cloud temperature is then equal to 150 μK. The magnetic trap is afterwards compressed in order to increase the cloud density and the atoms are cooled via evaporative cooling by radio frequency (RF) coupling [147]. The RF is ramped between 30 to 6.2 MHz in 6 s, knowing that the bias field lies at 5.5 MHz. At the end of this stage, up to 5×10^6 metastable helium atoms are trapped and cooled at a temperature of approximatively 15 μK. The evaporation can be continued until condensation is reached, which was the procedure that allowed the first observation of metastable helium condensate in 2001 [119]. Nevertheless, due to the presence of magnetic instabilities, the bias field fluctuates between successive experimental cycles. This leads to an instability on the evaporation process and, as a consequence, on the total number of atoms present in the BEC [148]. In order to avoid these instabilities the atoms are now transferred to a vertical dipole trap since the year 2010 [149, 150].

2.1.4 Vertical dipole trap

In order to create an attractive or repulsive potential via light-matter interaction one can take advantage of the induced dipole of the electromagnetic field [151] (see Appendix B for more details). The optical vertical dipole trap, whose optical bench is represented in Fig. 2.5, is formed from a single far-detuned 1.5-μm-wavelength laser, from IPG company. The vertical dipole trap corresponds to a laser beam focused to a waist $w_0 = 43$ μm. The induced dipole

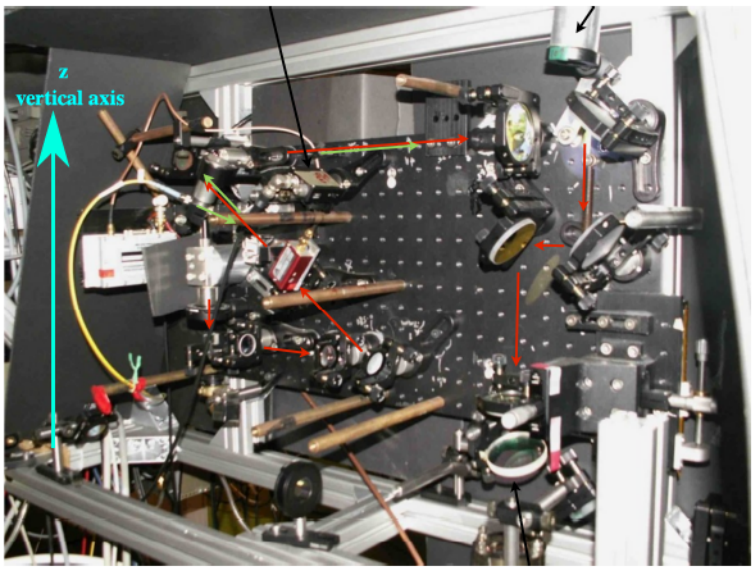

Figure 2.5: Picture of the optical bench of the vertical dipole trap. This optical bench is suspended in the vertical position above the science chamber. Figure copied from Ref. [150].

potential plus gravity can then be written as

$$V_{\text{opt.}}(x,y,z) = V_{\text{vert}} \frac{\text{Exp}\left[-\frac{2(x^2+y^2)}{w_{\text{vert}}^2\left(\left(\frac{z-z_0}{z_{\text{vert}}}\right)^2+1\right)}\right]}{\left(\frac{z-z_0}{z_{\text{vert}}}\right)^2+1} - mgz\,, \tag{2.1}$$

where

$$V_{\text{vert}} = -\frac{3\pi c^2}{2\omega_0^3}\frac{2P_{\text{vert}}}{\pi w_{\text{vert}}^2}\left(\frac{\Gamma}{\omega_0-\omega_{\text{dip}}}+\frac{\Gamma}{\omega_0+\omega_{\text{dip}}}\right),$$

with $\Gamma = 2\pi \times 1.6\,\text{MHz}$ corresponding to the radiative decay rate of the transition $2^3\text{S}_1 \rightarrow 2^3\text{P}_2$, ω_0 the frequency of the transition, ω_{dip} the frequency of the electromagnetic field, w_{vert} the waist of the vertical beam, $z_{\text{vert}} = \left(\pi w_{\text{vert}}^2\right)/\lambda_{\text{dip}}$ the vertical beam Rayleigh length and $z_0 = 2.3$ mm the central position of the vertical waist.

The intensity is ramped up to a full power of $P \approx 1.5$W in approximately 1 s. The magnetic trap is then switched off in a time scale on the order of 100 μs and a bias magnetic field $\text{B}_0 = 3\,\text{G}$ is applied in the horizontal direction in order to maintain the polarisation of the atoms. At full power, the trap provides a potential depth of 50 μK. However, since the beam propagates along the vertical direction (z–axis) due to gravity an effective lip is formed at the bottom of the vertical potential [149]. The height of the lip defines the effective depth of the potential and depends strongly on the optical power. Typically up to $1-3\times10^5$ atoms are transferred in this potential with a temperature, after thermalisation of the cloud, of 3 μK. The typical lifetime of atoms in the sub-level state $m_j = +1$ is then of 22 s. At full power, the typical trapping frequencies are $\omega_\perp = 2\pi \times 2.4\,\text{kHz}$ and $\omega_z = 2\pi \times 15\,\text{Hz}$. Further cooling is achieved by evaporation as the trap laser intensity I is decreasing from its maximum value, I_0 , to a constant nonzero value, I_F , in an exponential way over approximatively 4 s as

$$I(t) = (I_0 - I_F)e^{(-t/\tau_{ev})} + I_F\,,$$

where the time constant $\tau_{ev} = 1\,\text{s}$. After evaporation, a condensate with up to 3×10^4 atoms is obtained with a remaining thermal fraction on the order of 5% at a temperature $T_{\text{therm}} =$

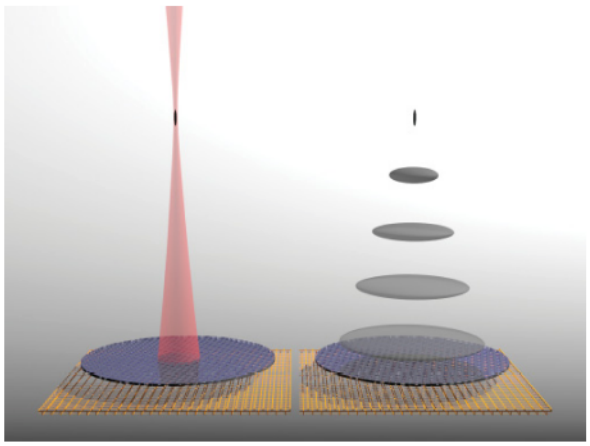

Figure 2.6: Schematic representation of a vertical trap BEC time-of-flight. The expansion of the condensate obtained in a vertical dipole trap is schematically represented. Figure copied from Ref. [150].

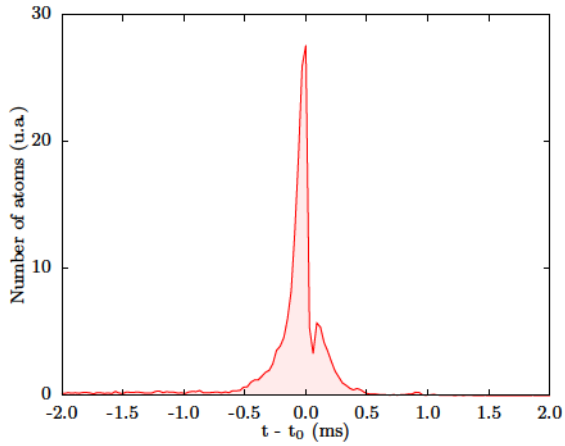

Figure 2.7: Typical arrival time distribution of a condensante obtained in the vertical dipole trap. The condensate arrival time distribution presents a half-width at half-maximum of 0.08 ms *and a residual thermal cloud at temperature of* 200 μK. *The central dip in the density profile is due to saturation of the detector (see Subsection 2.1.2 for more information). t_0 corresponds to the central arrival time and is equal to* 308 ms.

300 nK. The condensate has then a very elongated shape with a vertical Thomas-Fermi radius of $L = 400\,\mu$m and a transverse radius of $R = 4\,\mu$m, see Subsection 2.2.2. The typical trapping frequencies are then, at the end of the evaporation, equal to $\omega_\perp = 2\pi\times1.3$ kHz and $\omega_z = 2\pi\times7$ Hz. The typical critical temperature is around 600 nK. Once the trapping beams are switched off, the atoms fall to the MCP detector, located 46 cm below the trapping region. The expansion of the cloud is schematically represented in Fig. 2.6. The detection corresponds to a very long time-of-flight (308 ms) allowing us to reconstruct the initial speed of the atoms. A typical time-of-flight density distribution profile, along the vertical axis, is represented in Fig. 2.7. The hole in the distribution and the anisotropic shape are due to the saturation of the detector.

The vertical dipole trap allowed the experiment to gain stability over density and temperature. However, an arrival time fluctuation of the BEC obtained in the vertical dipole trap is noticeable and attributed to the vertical optical bench stability. In order to improve the experimental stability a horizontal dipole trap was added to the set-up. This is widely discussed on Section 2.2 and corresponds to one of the additions to the experimental apparatus during this thesis.

2.1.5 The 1D optical lattice

The existing lattice, at the beginning of this work, was formed by two counter-propagating laser beams with wavelength of $\lambda_{\text{lat}} = 1064$ nm (detuned 19 nm from resonance) coming from a Mephisto laser split in two independent optical paths. Both beams were focused to a $1/e^2$ Gaussian beam waist radius of 200 μm. The two beams were counter propagating and forming an angle of 7° with respect to the vertical axis. This angle is due to the restricted optical axis of our science chamber and determined by the position of the four windows represented by the letters $W_{1,2,3,4}$ in Fig. 2.8. The usual optical power is 13 mW corresponding to a lattice depth of 0.8 E_{lat} with E_{lat} defined by

$$E_{\text{lat}} = \frac{\hbar^2 k_{\text{lat}}^2}{2m_{He}}$$

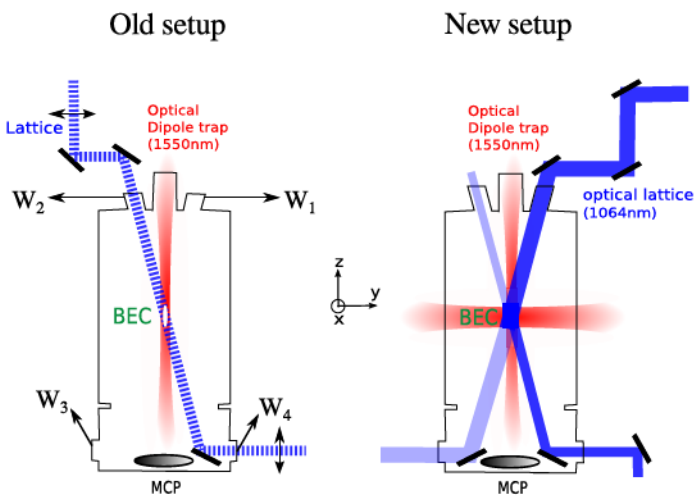

Figure 2.8: Lattice alignment geometry. Before and after this project. The lattice is now aligned with the vertical axis and superposed with the vertical dipole trap defining the long axis of the condensate.

and

$$k_{\text{lat}} = \frac{2\pi}{\lambda_{\text{lat}}}.$$

The lattice depth can, however, be tuned up to a maximum value of $4\,E_{\text{lat}}$. As we will see later on, we are interested in working with very shallow lattices for the pair creation process.

Since the two beams are independent, one can change their respective frequency and, as a consequence, change the lattice speed. This is used to give a certain velocity to the lattice and to create atom pairs via dynamical instabilities.

One particular change that has been done during this project is the geometrical alignment of the lattice. Since both beams made an angle of 7° with respect to the vertical z−axis, the lattice was also making an angle of 7° with respect to the vertical direction, see Fig. 2.8 left side. This small angle had a noticeable effect on the pair creation process as we will see in Section 3.3. The lattice beams are now forming an angle of 7^0 and -7^0 which leads to a 1D optical lattice aligned along the z−axis, see Fig. 2.8 right panel.

2.1.6 Summary

The characteristic values discussed so far are summarise in Tables 2.2 and 2.3.

We have shown that several different tools were at disposal at the beginning of this project. However, there were still some issues to address, namely:

- the vertical dipole trap stability
- and the geometrical alignment of the 1D optical lattice.

The beam-splitter, essential for the HOM experiment, was not built. In this sense, a lot of experimental work was needed before hopping to achieve the atomic HOM experiment. The following sections describe in details all this changes and their impacts on the physics at play.

Step	Temperature (μK)	Number of atoms
MOT + Molasses	300	10^8
Magnetic trap + optical pumping + 1D Doppler cooling	150	$1-5\times10^7$
RF evaporative cooling	15	5×10^6
Dipole trap (loading)	3	1×10^5
BEC (vertical trap)		$3-6\times10^4$
Residual thermal cloud	0.3	10^3

Table 2.2: Characteristic temperature and atom number along the current experimental cycle. Summary of the temperature and number of atoms along the different steps of the typical cycling procedure.

Geometrical Details	**Waist** (μm)	**Maximum Power** (mW)	**Axis of propagation**	**Wavelength** (nm)
	43	2000	vertical z−axis	1550
BEC	$\omega_\perp(2\pi\times$ Hz)	$\omega_z(2\pi\times$ Hz)	**Number of Atoms**	**Anisotropy** (L/R)
	1550	7	$3-6\times10^4$	100

Table 2.3: Typical values of the BEC in the vertical dipole trap. We summarise in this table the most important information about the vertical dipole trap and the obtained BEC.

2.2 Bose–Einstein condensate of metastable Helium

A Bose–Einstein condensate is a state of matter of a dilute Bose gas obtained when a large fraction of bosons occupy the lowest energetic quantum state [147, 152]. Such a state is reached by cooling down the gas as well as increasing its density leading to an increase of its phase-space density. For a 3D gas, when $n\lambda_{dB}^3 > 2.6$, where n and λ_{dB} correspond to the density and the thermal de Broglie wavelength respectively, a BEC is obtained [153]. The condensation leads to the extinction of phase fluctuations and density fluctuations over the length of the cloud.

For the experiment reported in this thesis the interest of using a BEC is twofold. First, it is a source of high density and allows one to easily probe non linear effects such as superradiance or spontaneous parametric down-conversion. Second, the source has a very small spread in momentum space which allows us to easily distinguish the BEC from the produced atomic pairs after time-of-flight. For these reasons our starting point will always correspond to a BEC of metastable helium 4.

2.2.1 Arrival time instability of the condensate

As discussed in Refs. [39, 108, 141, 142] and in Subsection 2.1.4, we noticed that the central arrival time of the condensate, obtained in the vertical dipole trap (alone), was fluctuating from shot to shot realisations. The fluctuations presented a RMS width of 0.1 ms determined from 2100 repetitions of the same experimental cycle. This has to be compared to a single event

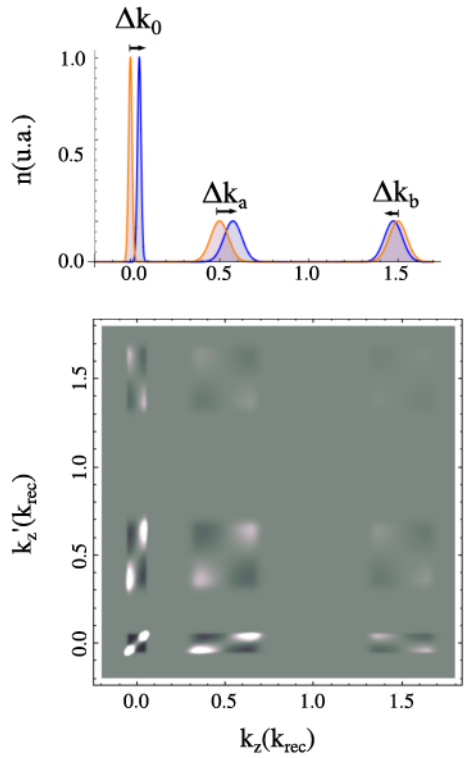

Figure 2.9: Jitter effect on the two-body correlation function. The fluctuation of the condensate induces fluctuations of the atomic pairs velocities via conservation of momentum (upper panel). These fluctuations, once computed, translate into the appearance of artificial structures on the normalised two-body correlation function. Figures copied from Ref. [141].

arrival time distribution, which has a RMS width of approximatively 0.08 ms. The arrival time fluctuation is then comparable to a single arrival time distribution and can not be neglected.

Since the atoms are detected after a very long time-of-flight, the fluctuation corresponds mainly to an initial speed fluctuation [142]. This initial instability is prejudicial to our pair production as we will see in Section 3.2. Indeed, the physical process at the origin of the pair production (dynamical instability, see Refs. [105, 108, 154, 155]) depends on the initial BEC speed. If the speed is not well defined, neither are the velocities of the pairs produced and, consequently, the same initial experimental conditions are not maintained in between realisations.

Consequences of this instability

One specific consequence of these instabilities was reported in Ref. [142] page 128, where artificial two-body correlations appear due to arrival time fluctuations of the atomic pairs. Since the initial velocity of the condensate fluctuates the phase-matching conditions lead to fluctuations of the pair velocities (see Section 3.2 for more informations). In Fig. 2.9, we schematically represent the two atomic beams a and b (corresponding to our atom pairs) with initial speed fluctuations (Δk_a and Δk_b, respectively, see Fig. 2.9) due to fluctuations of the BEC (Δk_0 see Fig. 2.9). The expected two-body correlation function between atoms with momenta k_z and k_z' is represented in the bottom panel. One can see that artificial structures appear, centred on the three clouds, when they should not (see Ref. [141, 142] for more informations).

This means that in order to accurately measure the correlations between the two beams, for instance, one needs to select from N realisations the $M < N$ events corresponding to similar initial speed in order to avoid the artificial contribution from BEC fluctuations. This, however,

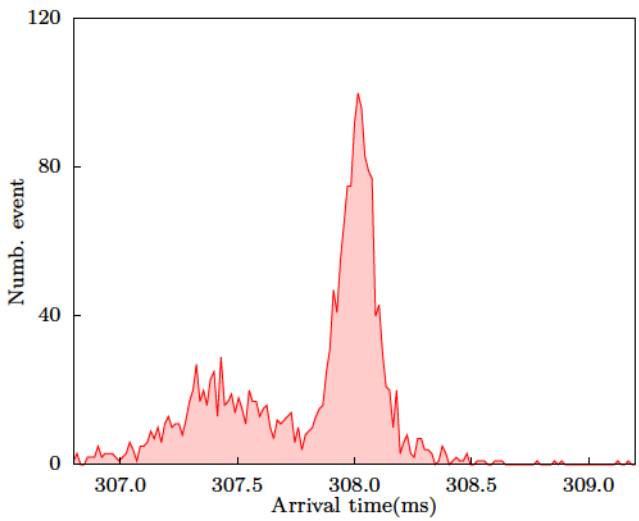

Figure 2.10: ***Arrival time fluctuation of the BEC.*** *Fluctuations of the arrival time distribution of the BEC produced in the vertical trap alone. Each detected condensate density profile is fitted and the center of its distribution correspond to one entry of the represented histogram. The represented distribution correspond to the addition of the different central arrival time of 2100 condensate realisations.*

strongly reduces the total number of events under consideration and is an issue in terms of signal-to-noise ratio.

Another possibility consists in refocusing each condensate arrival time distribution and, consequently, correct the fluctuations after detection. This does not allow us to safely correct the shift in the atom pairs reconstruction since the atoms travel with different velocities, see Fig. 2.9. One can then fit each cloud forming the pair and refocusing it [39, 108]. However, this becomes impossible to perform when one wants to work with very low population, as in the case of the HOM experiment. The solution is then to use more sophisticated analysis protocols such as the Principal Component Analysis.

Whatever one might choose to do, the most general consequence is that some events have to be selected from the total sample of realisations. This leads unequivocally to a diminution of the signal-to-noise ratio and to an effective slower experimental cycle, since it is necessary to repeat the experiment more times to retrieve the same number of useful events.

Quantitative measurement of the fluctuations

In order to quantitatively discuss this effect, let us look at the arrival time distribution of the condensate (see Fig. 2.7 for instance) on the MCP after the time-of-flight of 308 ms. We fit the arrival time distribution of one BEC retrieving its central arrival time. From one experimental realisation to the other this central value fluctuates. We thus obtain a distribution of central arrival times as represented in Fig. 2.10. The figure corresponds to 2100 identical experimental sequences. One can identify two distinct groups in the distribution shown in Fig. 2.10. The first one is centred at approximatively 308 ms with a RMS width of 0.1 ms. The second group corresponds to condensates arriving sooner, around 307.3 ms and with an RMS fluctuation of 0.2 ms. Once more, by comparing those fluctuations to a single arrival time, with width equal to 0.08 ms, one immediately see that the fluctuations are not negligible. Indeed, a fluctuation of $0.1-0.2$ ms translates into an initial speed fluctuation of $1-2\times10^{-2}v_{\mathrm{rec}}$ which, as we will see in Chapter 3, change the velocity of the produced atomic pairs by approximatively $1-5\times10^{-2}\,\mathrm{v_{rec}}$. Knowing that the typical autocorrelation width is equal to $1\text{–}2\times10^{-2}\,\mathrm{v_{rec}}$ along the vertical axis (we will show this result in Section 3.4), it is important to suppress these fluctuations.

2.2.2 Anisotropy of the BEC: phase fluctuation issues

Another issue that comes with the vertical trap is that the resulting BEC is very elongated since the transverse frequency of the trap $\omega_\perp = 2\pi \times 1275\,\text{kHz}$ is much larger than the longitudinal frequency $\omega_z = 2\pi \times 7\,\text{Hz}$.

For such strongly anisotropic condensate the well know *Thomas–Fermi approximation* does no longer hold [156, 157].[2] This approximation consists, in the regime where the atomic interactions are dominant ($\mu \gg \omega_i, k_B T$), in neglecting the kinetic energy term of the Gross-Pitaevskii equation

$$\mu\psi(z) = \left[-\frac{\hbar^2}{2m}\frac{\partial^2}{\partial z^2} + V(z) + g\left|\psi(z)\right|^2\right]\psi(z)\,,$$

where m corresponds to the atomic mass, $\psi(z)$ the wave-function in real space, μ the chemical potential, $V(z)$ the trapping potential along the longitudinal axis and $g = \frac{4\pi\hbar^2 a}{m}$, with a the scattering length. The cloud corresponds then to an inverted parabola with radii R, along the transverse direction, and L, along the vertical axis, given by the equations

$$R = \sqrt{\frac{2\,\mu}{m\,\omega_\perp^2}}\,, \tag{2.2a}$$

$$L = \sqrt{\frac{2\,\mu}{m\,\omega_z^2}}\,, \tag{2.2b}$$

with the chemical potential determined through normalisation of the wave function

$$\mu = \frac{\hbar\,\bar{\omega}}{2}\left(15N_{at}\,a\,\sqrt{\frac{m\bar{\omega}}{\hbar}}\right)^{2/5} \tag{2.3}$$

where $\bar{\omega} = \left(\omega_z\omega_\perp^2\right)^{1/3}$ and N_{at} the total number of atoms.

2.2.3 Quasi-BEC or BEC?

In some cases, such as in atom-chip experiments [158] or 2D lattice potentials [159] or even anisotropic dipole traps [160], the transverse confinement can become so strong compared to the chemical potential that the system is "frozen" in the transverse direction and behaves as a real unidimensional system. In this 1D case, the transverse profile of the cloud corresponds to the fundamental solution of the harmonic oscillator, which is a Gaussian of width $\sqrt{\hbar/2m\omega_\perp}$, and the longitudinal profile to a parabola defined by the 1D chemical potential $\mu_{1D} = \hbar\omega_\perp\sqrt{1 + 4\,a\,n_{1D}}$, with $n_{1D} = N_{at}/(2L)$ the one-1D density, such that [161]

$$L = \sqrt{\frac{2\left(\hbar\omega_\perp - \mu_{1D}\right)}{m\,\omega_z^2}}\,. \tag{2.4}$$

In our case the transverse trapping frequency $\omega_\perp$ is much higher than the longitudinal one, as seen so far. This leads to a stronger transverse confinement than longitudinal and the question is then to know how truly 1D this system is .

[2] Nevertheless, as we will see in Subsection 2.2.4 it is now possible to tune the anisotropy of our condensate and to verify the Thomas–Fermi approximation. For this purpose, we remind here the most important results.

The 3D and 1D regimes can be differentiated through the parameter [161]

$$\chi = N\frac{\omega_z a}{\omega_\perp a_\perp}$$

where $a_{\perp,z} = \sqrt{\frac{\hbar}{m\omega_{\perp,z}}}$. When $\chi \gg 1$, the 3D Thomas-Fermi approximation is valid while for $\chi \ll 1$ the system is unidimensional.

For a condensate obtained in the vertical dipole trap $\omega_z = 2\pi \times 7\,\text{Hz}$, $\omega_\perp = 2\pi \times 1275\,\text{Hz}$ and $N_{at} = 3\times10^4$ atoms, one finds a value $\chi = 0.88$ which lies in between the two scenarios. For such trapping potential, the system is neither fully 1D nor 3D but corresponds to an intermediate regime which is explored in Ref. [64].

BEC length and chemical potential for both 3D and quasi-1D regime

In Ref. [64][3], the author shows that for the intermediate case where $\chi \approx 1$ it is possible to find an approximate solution which can be applied to both 3D and 1D situations. The method used in the article consists, via a local density approximation, to assume a Gaussian shape for the radial component of the wave function, $f_\perp(\rho)$, whose width ($w_\perp$) is a variational parameter that verifies

$$\mu_{l.e.} = -\frac{\hbar^2}{2m}\frac{\Delta_\perp f_\perp(\rho)}{|f_\perp(\rho)|} + \frac{1}{2}m\omega_\perp^2\rho^2 + \frac{4\pi\hbar^2 a}{m}n_{1D}(z)\,|f_\perp(\rho)|^2,$$

with $\mu_{l.e.}$ the local equilibrium chemical potential and $n_{1D}(z)$ corresponds to the 1D, integrated over radial degrees of freedom, density profile of the cloud. We consider a system where the longitudinal confinement is sufficiently weak to neglect the density derivatives of n_{1D} and $f_\perp$ as a function of z.

The following equalities are then obtained by developing $f_\perp(\rho)$ to the first order in $w_\perp$,

$$w_\perp\,[n_{1D}(z)] = a_\perp\,[1 + 4a\,n_{1D}(z)]^{1/4}$$

and

$$\mu_{l.e.} = \hbar\omega_\perp\sqrt{1 + 4an_{1D}(z)}$$

with the total chemical potential μ corresponding to

$$\mu = \mu_{l.e.}\,[n_{1D}(z)] + V(z) \tag{2.5}$$

where $V_z = \frac{1}{2}\,m\omega_z^2 z^2$ is the trapping potential along the longitudinal axis.

One can now determine the condensate lengths, its density profile along the longitudinal axis and the chemical potential. Let us consider the case of $z = L$ where the local density $n_{1D}(L) = 0$ and $\mu_{l.e.} = \hbar\omega_\perp$, which leads to

$$\mu = \hbar\omega_\perp + \frac{1}{2}m\omega_z^2 L^2, \tag{2.6}$$

and to the following expression of L

$$L = \frac{a_z^2}{a_\perp}\sqrt{\alpha}$$

[3]Typos are present in this paper. The results presented here correspond to a reviewed version of the article.

with $\alpha = 2(\mu/\hbar\omega_\perp - 1)$. Using both Eq. (2.5) and Eq. (2.6), one retrieves the longitudinal density profile

$$n_{1D}(z) = \left(1 - \tilde{z}^2\right)^2 \frac{\alpha^2}{16a} + \left(1 - \tilde{z}^2\right) \frac{\alpha}{4a},$$

with $\tilde{z} = z/L$. Since the total number of atoms corresponds to the integration of $n_{1D}(z)$

$$N_{at} = \int_{-L}^{L} n_{1D}(z)dz,$$

one obtains the following equality for the length of the condensate along the longitudinal axis

$$\frac{1}{15\gamma}\left[(LG)^5 + 5\,(LG)^3\right] = N_{at} \tag{2.7}$$

with $G = a_\perp/a_z^2$ and $\gamma = aa_\perp/a_\parallel^2$.

Knowing N_{at} and the trapping frequencies it is then possible to extract the value of L. From that one retrieves the value of the chemical potential μ, via Eq. (2.6) as well as the value of α. The Gaussian width of the condensate, for $z = 0$, corresponds then to

$$w_\perp(0) = a_\perp\,[1 + 4an_{1D}(0)]^{1/4} \tag{2.8}$$

where $n_{1D}(0)$

$$n_{1D}(0) = \left(\frac{a_\perp}{a_z^2}\right)^2 \times \frac{L^2}{4a}\left[\left(\frac{a_\perp}{a_z^2}\right)^2 \times \frac{L^2}{4a} + 1\right].$$

Quasi-condensate regime

For an elongated condensate with $T = 0$ K, the cloud exhibits a suppression of density fluctuations as well as phase fluctuations. However, as it was shown in Ref. [162], at finite temperatures T, below critical temperature $T_c \approx N^{1/3}\hbar\bar{\omega}$, excitations can still exist. The low energy excitations contribute to axial fluctuations of the phase. In Ref. [162] it is discussed that these excitations decrease with the temperature and for sufficiently low values compared to a critical phase fluctuation temperature given by

$$T_\phi = 15\,(\hbar\omega_z)^2\,\frac{N_{at}}{32\mu k_B}, \tag{2.9}$$

can be safely neglected. This means that for temperatures T above T_ϕ and below T_c ($T_c > T > T_\phi$) even if density fluctuations are suppressed, the phase can still fluctuate. In that sense, the system does not reach true BEC, since phase fluctuations are still present. The system is then in an intermediate situation often called quasi-condensate in contrast to the "real" condensate regime ($T_\phi, T_c > T$).

For the case of a BEC obtained in the vertical dipole trap alone ($\omega_z = 2\pi \times 7$ Hz, $\omega_\perp = 2\pi \times 1275$ Hz and $N_{at} = 3 \times 10^4$ atoms), the phase fluctuation temperature is equal to 14 nK which is well below the condensation temperature of $T_c \approx 600$ nK and below the estimated temperature of the residual thermal cloud of $T \approx 200$ nK. As a consequence, phase fluctuations are still present which translates after time-of-flight into density fluctuations. This leads to phase fluctuations during the atomic pair production and in a reducing coherence length of the condensate.

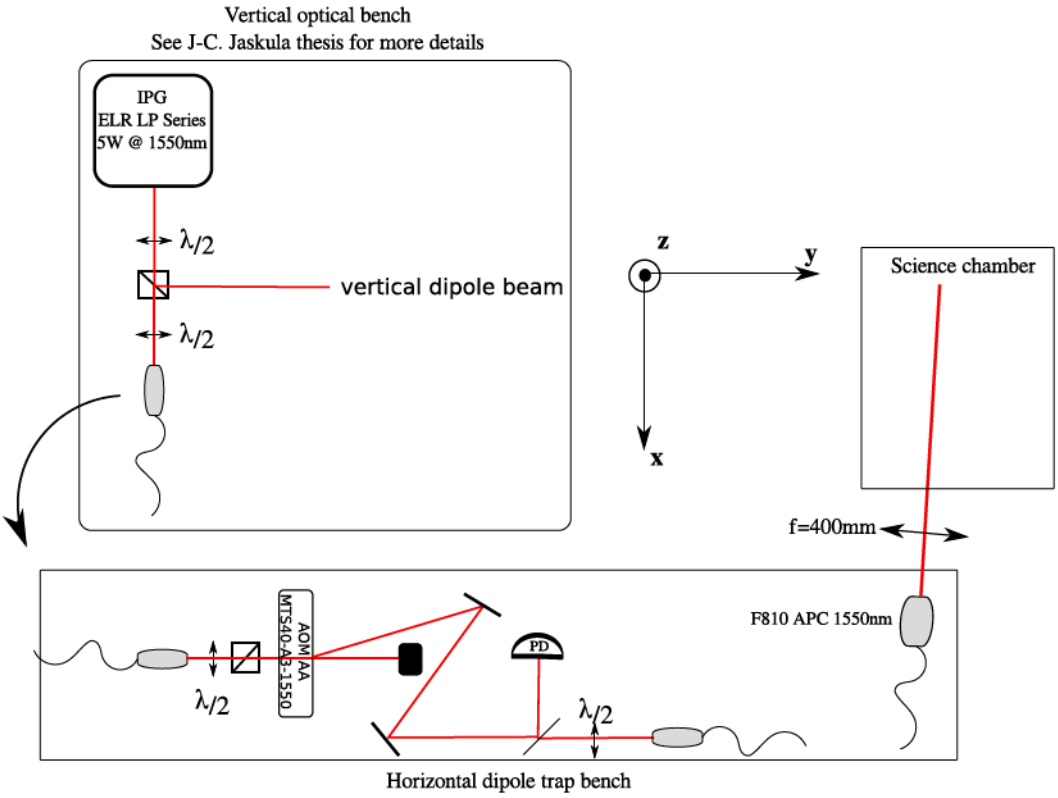

Figure 2.11: Schematic representation of the optical bench for the horizontal beam trap. The laser beam is split in two with one part used for the vertical dipole trap as described in Ref. [150] and the other injected into a polarisation-maintaining optical fiber sending the optical power to another optical bench. There, the beam goes through an acousto-optic modulator where it is diffracted to order +1 with an efficiency of 90%. The optical power is set by increasing the RF power at the acousto-optic modulator entrance. The beam is then split with 1% power sent to a photodiode in order to lock the horizontal beam intensity. The other part is again injected. The final output coupler corresponds to a F810APC from Thorlabs company leading to a diameter beam of 7 mm. *The beam is then focused by a focus lens of* $f = 400$ mm *leading to a waist on the atoms of* 82 μm.

2.2.4 Crossed dipole trap: solution to both issues

In order to solve both the arrival time fluctuation of the BEC and its phase fluctuation, we built a new dipole trap, a horizontal one, crossed with the original vertical trap on the atoms. The horizontal laser beam is obtained by splitting the original vertical one in two independent optical paths with independent acousto-optic modulators as represented in Fig. 2.11. The effective maximum power on the atoms is equal to 2 W. Almost 90% of the total power is used for the vertical dipole trap and around 10% to the horizontal trap. A relative frequency difference is set to 80 MHz between the two beams in order to avoid low frequency modulation of the trap intensity [4].

One beam propagates along the vertical $z-$axis corresponding to the "original" trap described in Ref. [150] and the second on the horizontal plane, forming an angle 8.6 ° respectively to the $x-$axis defined by the magnetic trap (see Fig. 2.11 and Fig. 2.12). The typical optical power at the end of the evaporation is 600 mW for the vertical trap and 30mW for the horizontal one.

With the new crossed dipole trap, the vertical confinement of the trapping potential does no longer depend on the vertical beam. The longitudinal trapping frequency is then essentially given by the intensity of the horizontal beam. The total trapping potential can then be written as

[4] If the modulation intensity is close to a trapping frequency, this induces parametric excitation of the cloud. Since the typical frequencies of our trap is on the order of the kHz, a detuning by 80 MHz between both trapping beams guarantee that we avoid the resonance.

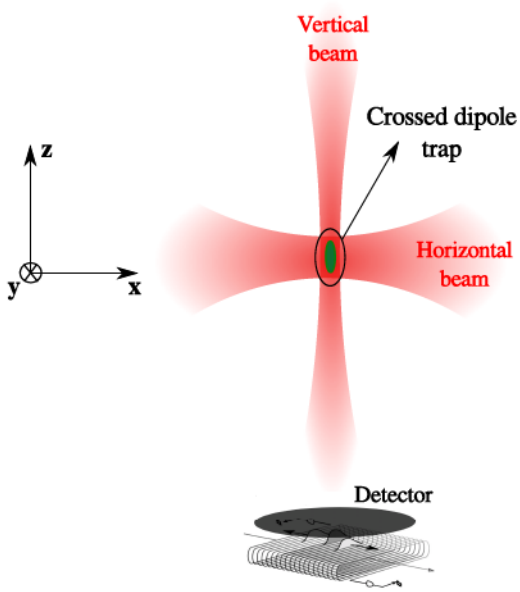

Figure 2.12: Schematic representation of the crossed dipole trap.

$$V_{\text{opt}}(x,y,z) = V_{\text{vert.}}(x,y,z) + V_{\text{hor}} \frac{\text{Exp}\left[-\frac{2(y^2+(z-z_0)^2)}{w_{\text{hor}}^2\left[\left(\frac{x}{x_{\text{hor}}}\right)^2+1\right]}\right]}{\left(\frac{x}{x_{\text{hor}}}\right)^2+1}, \tag{2.10}$$

where $V_{\text{vert.}}(x,y,z)$ is given by Eq. (2.1) and

$$V_{\text{hor}} = -\frac{3\pi c^2}{2\omega_0^3}\frac{2P_{\text{hor}}}{\pi w_{\text{hor}}^2}\left(\frac{\Gamma}{\omega_0-\omega_{\text{dip}}}+\frac{\Gamma}{\omega_0+\omega_{\text{dip}}}\right),$$

where $x_{\text{hor}} = \left(\pi w_{\text{hor}}^2\right)/\lambda_{\text{dip}}$ is the horizontal beam Rayleigh length and w_{hor} the horizontal beam radius waist at $1/e^2$ (see more information in Appendix B).

Arrival time fluctuations

In Fig. 2.13a) the arrival time fluctuations before adding the horizontal trap is represented, as discussed previously, while in Fig. 2.13b) the same analysis is performed for a condensate obtained in a crossed dipole trap.

One can see that, by adding the horizontal trap, the fluctuations were reduced to a RMS value of 0.04 ms which is very close to the temporal resolution of our detector. The addition of the horizontal trap has proved to reduce the arrival time fluctuations and, at the moment, the remaining fluctuations are, in practice, completely negligible. Indeed, the fluctuations are much smaller than the time-of-flight distribution of a condensate obtained in the crossed dipole trap (which trapping frequencies are different from the one of the vertical trap). A single condensate arrival time distribution corresponds to a typical RMS value of 0.5 ms. The residual fluctuations are then a tenth of the arrival time distribution width. For most of our analysis no selections, based on the arrival time-of-flight, are then necessary. This decreases significantly the acquisition time in order to retrieve a satisfactory signal-to-noise ratio.

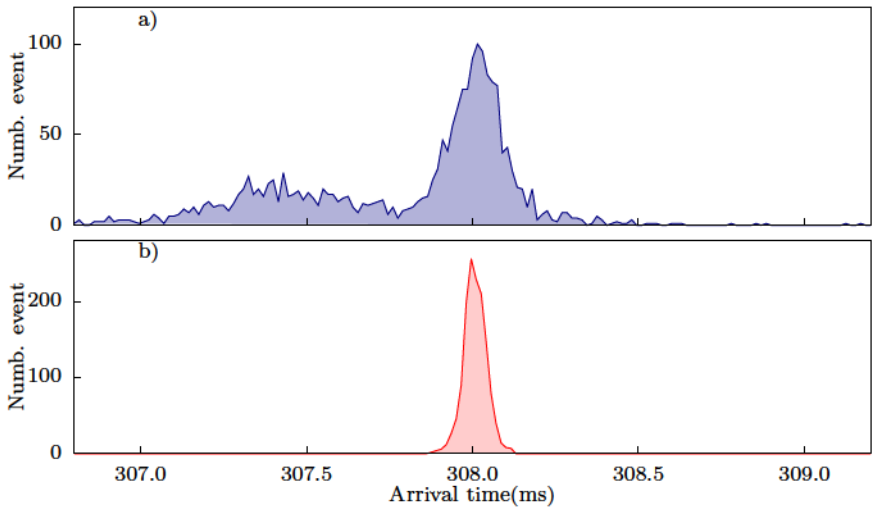

Figure 2.13: Crossed dipole trap effect on the arrival time fluctuation of the BEC. a) Fluctuations of the arrival time distribution for a BEC produced in the vertical trap alone. b) Fluctuations of the arrival time distribution for a BEC produced in the crossed dipole trap. The number of files for b) is approximatively equal to those in a). One can see, that the crossed dipole trap leads to a reduced arrival time fluctuations.

Obtained condensate: some numbers

With the two available trapping beams, it is now possible to easily tune the longitudinal frequency from 7 to 200 Hz keeping a constant transverse frequency of 1275 Hz (see Section B.1 for more details). The aspect ratio of the condensate can thus be tuned between 200 to 6 . This represents a strong improvement in terms of control and flexibility of our experiment.

In the following manuscript, most of the results correspond to a trapping potential with frequencies equal to $\omega_\perp \sim 2\pi \times 1.275\,\text{kHz}$, transversally, and $\omega_z \sim 2\pi \times 93\,\text{Hz}$, along the vertical direction. We obtain a condensate with $4-7\times10^4$ atoms in the $m_j = 1$ sub-level state, where the uncertainty on the atomic population comes from the detection efficiency of our MCP. In this case, as one can see in Table 2.4, χ is much larger than 1 indicating that one had reach the 3D condensation regime. As discussed before, for the vertical trap alone, corresponding to a vertical frequency equal to $\omega_z = 2\pi \times 7\,\text{Hz}$, the value of $\chi = 0.88$ and corresponds to an intermediate regime.

$\omega_\perp = 2\pi \times 1275\,\text{Hz}$			
	$\omega_z = 2\pi \times 7\,\text{Hz}$ $N_{at} = 3\times10^4$	$\omega_z = 2\pi \times 93\,\text{Hz}$ $N_{at} = 5\times10^4$	$\omega_z = 2\pi \times 170\,\text{Hz}$ $N_{at} = 7\times10^4$
χ	0.88	19.47	49.82

Table 2.4: Typical values of χ for different optical traps accessible in our experimental set-up. By changing the value of ω_z it is possible to go from the quasi-1D regime into deep 3D-regime.

Regardless of the phase fluctuations, one can now see in Table 2.5 the different regimes available with this new trapping potential. For $\omega_z = 2\pi \times 7\,\text{Hz}$ (case of the vertical trap alone) the situation corresponds to the quasi-condensate regime while for frequencies $\omega_z = 2\pi \times (93\,,\,170\,)$ Hz, obtained in the crossed dipole trap, we recover the real condensation regime with $T_\phi > T_c > T$.

	$\omega_\perp = 2\pi \times 1275\,\mathrm{Hz}$		
	$\omega_\parallel = 2\pi \times 7\,\mathrm{Hz}$ $N_{at} = 3 \times 10^4$	$\omega_\parallel = 2\pi \times 93\,\mathrm{Hz}$ $N_{at} = 5 \times 10^4$	$\omega_\parallel = 2\pi \times 170\,\mathrm{Hz}$ $N_{at} = 7 \times 10^4$
$T_\phi\,(\mu\mathrm{K})$	0.014	1.53	5.00
$T_c\,(\mu\mathrm{K}) \approx$	0.330	0.600	1.00
$T\,(\mu\mathrm{K}) \approx$	0.200		

Table 2.5: *Typical values of T_ϕ, T_c and T. Scaling of the phase fluctuation temperature T_ϕ for different trapping potential configurations and comparison with the respective condensation temperatures T_c and residual thermal cloud temperature T. For trapping frequencies of $\omega_z > 2\pi \times 93\,\mathrm{Hz}$, one does not expect any phase fluctuations along the condensate.*

The addition of the horizontal dipole trap allowed us to enter deeply in the real condensate regime and to avoid phase fluctuations in the condensate.

These fluctuations, if remaining, translate into density fluctuations after time-of-flight [163]. By measuring the two-body correlation function, one can then experimentally probe if they are still present in the system.

Density fluctuations and autocorrelation measurement

The local two-body correlation corresponds to the probability of detecting a particle at a time interval $t + \Delta t$ knowing that another particle has been detected at time t. For a condensate, the normalised second order correlation is flat and equal to 1 which indicates the suppression of density fluctuations. On the other hand, if the second order autocorrelation presents a value superior to 1 and structures [142], then one can identify density fluctuations and link this result to phase fluctuations, as seen in Ref. [164, 165] and discussed in Ref. [166].

The second-order autocorrelation function is obtained for the condensate as [68]

$$\begin{aligned} g^{(2)}(\Delta k_z) &= \int_{\Omega_1} d\Delta k_x\, d\Delta k_y \int_{\Omega_V} d^3\mathbf{k} \frac{\langle : \hat{n}(\mathbf{k})\hat{n}(\mathbf{k}+\Delta\mathbf{k}) : \rangle}{\langle \hat{n}(\mathbf{k})\rangle \langle \hat{n}(\mathbf{k}+\Delta\mathbf{k})\rangle}\,, \\ g^{(2)}(\Delta k_y) &= \int_{\Omega_2} d\Delta k_x\, d\Delta k_z \int_{\Omega_V} d^3\mathbf{k} \frac{\langle : \hat{n}(\mathbf{k})\hat{n}(\mathbf{k}+\Delta\mathbf{k}) : \rangle}{\langle \hat{n}(\mathbf{k})\rangle \langle \hat{n}(\mathbf{k}+\Delta\mathbf{k})\rangle}\,, \end{aligned} \tag{2.11}$$

where $\hat{n}$ is the number operator such that $N_{at}(\mathbf{k}) = \langle n(\mathbf{k})\rangle$. The volume Ω_1 is defined by the boundary conditions $|\Delta k_x| < 3 \times 10^{-2}\, k_{\mathrm{rec}}$, $|\Delta k_y| < 3 \times 10^{-2}\, k_{\mathrm{rec}}$ and Ω_2 by $|\Delta k_x| < 3 \times 10^{-2}\, k_{\mathrm{rec}}$, $|\Delta k_z| < 3 \times 10^{-3}\, k_{\mathrm{rec}}$. Ω_V is the volume centred on the cloud with a half-width at $1/\sqrt{e}$ along z equal to $0.1\, k_{\mathrm{rec}}$ and no constraint in the xy–plane.

It is fundamental to avoid detector saturation in order to not influence the detected number of atoms. We thus transfer a small fraction of the entire BEC population into a magnetic field insensitive sub-level state ($m_j = 0$) via two-photon Raman scattering (see Appendix C for more details). A strong magnetic gradient is afterwards applied in order to get rid of the non-transferred atoms.

In Fig. 2.14 we represent the second order correlation function as a function of $\Delta\mathbf{k}$, for the case of a trapping potential with vertical trapping frequency of $\omega_z = 2\pi \times 93\,\mathrm{Hz}$ and transverse frequency $\omega_\perp = 2\pi \times 1275\,\mathrm{Hz}$ [68], with a) corresponding to a cut along the z–axis and b) along the transverse y–axis. An almost flat dependence of $g^{(2)}(\mathbf{k})$ as a function of $\Delta\mathbf{k}$ is recovered. The increase of $g^{(2)}$ at $\Delta\mathbf{k} \to 0$ can either be accounted by small phase fluctuations induced by

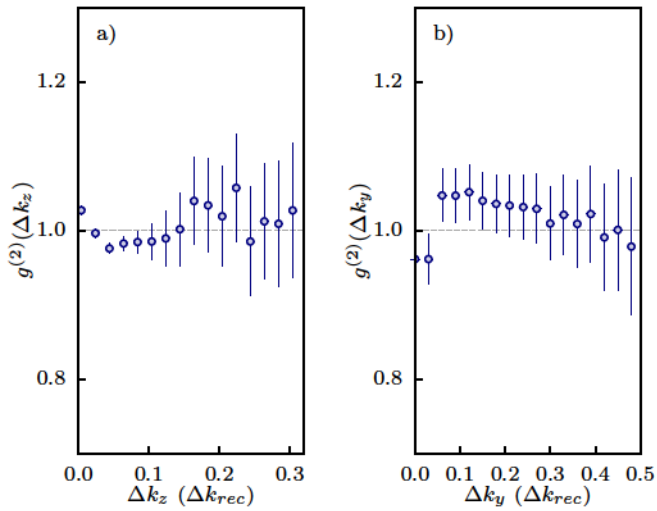

Figure 2.14: Autocorrelation function $g^{(2)}$ of the BEC. Condensate autocorrelation projection on the z and y–axis. An almost flat dependence of $g^{(2)}$ as a function of $\Delta\mathbf{k}$ is recovered.

the residual thermal fluctuations of the cloud or due to weak detector saturation. The observed correlation is, however, much flatter than the one observed in Ref. [142] and we believe that the phase fluctuations in the condensate are almost negligible.

2.2.5 Condensate: determination of the chemical potential and size

Once the trap is switched off the condensate expands [167]. The size of the cloud, in both transverse and longitudinal axis at a certain time t after released from the trap, is given by the following equations

$$R(t) = R(0)\sqrt{1+(\omega_\perp t)^2}, \tag{2.12a}$$

$$L(t) = L(0)\left(1+\epsilon^2\left[(\omega_z t)\arctan[\omega_z t] - \log\sqrt{1+(\omega_z t)^2}\right]\right), \tag{2.12b}$$

with $\epsilon = \frac{\omega_z(0)}{\omega_\perp(0)}$. For the trapping frequencies under consideration, *i.e.* $\omega_z = 2\pi \times 93\,\text{Hz}$ and $\omega_\perp = 2\pi \times 1275\,\text{Hz}$ one finds (through the Thomas-Fermi approximation) a condensate radius of $L(0) = 58\,\mu\text{m}$ along the vertical direction and $R(0) = 4.4\,\mu\text{m}$ transversally. One expects to detect, after 308 ms time-of-flight, a cloud with size equal to

$$L(tof) = 1.25\,\text{mm} \tag{2.13a}$$

and

$$R(tof) = 1.08\,\text{cm}. \tag{2.13b}$$

One could then predict the chemical potential of the condensate by measuring the arrival time distribution of the cloud after time-of-flight. However, this prediction is not directly applicable to our experimental situation. Two reasons are behind it:

- The first reason is that the condensate corresponds to a very high flux of atoms resulting in a saturation of the MCP. Consequently, both the real number of atoms and the size of

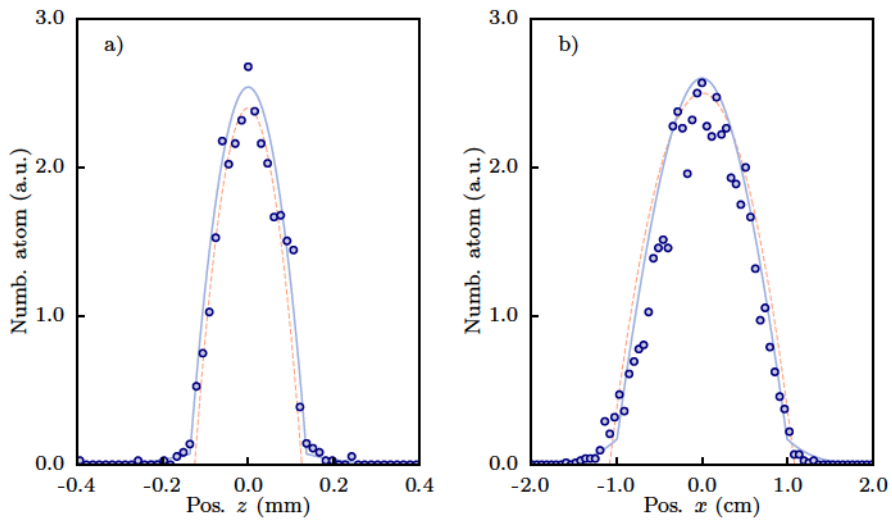

Figure 2.15: Time-of-flight density profile of a BEC. a) Cut of the density profile along the vertical z−axis. b) Cut of the density profile along the transverse x−axis. The density profiles correspond to an integration on the other two axis of $[0.14 \times 0.14]$ (cm^2) *for the vertical cut and of* $[0.14 \times 0.03]$ (cm^2) *for the transverse cut. The blue line indicates, in both panels, a fitting function corresponding to a parabola plus Gaussian function. The orange dashed line represents the estimated parabolic shape after time-of-flight obtained by Eq. (2.13).*

the cloud after time-of-flight are blurred. This, however, can be avoided by transferring a small fraction of the condensate into the insensitive sub-level state $m_j = 0$ via stimulated two-photon Raman scattering event (see Appendix C for more details) and to push the remaining atoms through a magnetic field gradient;

- The second reason is linked to the solution of the first one. If the cloud is transferred to the sub-level $m_j = 0$ after being released from the trap the scattering length changes between ≈ 7 to ≈ 5 nm. Since this is done just after releasing the cloud from the trapping potential, the change on the interaction potential is not negligible. The expansion of the cloud is thus modified in a non-trivial way and, as a consequence, the result from Ref. [167] can not be directly applied. The solution would then consist in transferring the atoms after a few hundreds of microseconds of expansion. At this time the interaction potential has reduced sufficiently to be negligible and a change on the scattering length will not change the BEC expansion. Nevertheless, this implies that during the initial expansion, with the atoms still in the $m_j = 1$ state and thus sensitive to any residual magnetic field, the expansion of the cloud can also be modified. At the moment this effect has not been yet calibrated experimentally.

Experimentally, we weakly transfer the BEC into the state $m_j = 0$ just after turning off the trapping potential to avoid detector saturation. Although the expansion evolution described by Eq. (2.12) does not strictly apply, one can compare roughly the experimental result to the theoretical predictions. For this purpose we perform cuts along both longitudinal and transverse density profile after time-of-flight as represented in Fig. 2.15a) and b), respectively.

The arrival time distribution is fitted on both directions by a parabolic function plus Gaussian, represented by the blue line in both panels, in order to account for the contribution of a residual thermal cloud. The experimental radius is extracted for both longitudinal, $L_{\text{exp}} = 1.3$ mm, and transverse directions, $R_{\text{exp}} = 0.97$ cm. Compared to the values of Eq. (2.13), one can see that the experimental result is in good agreement with the predictions. To have a more visual comparison, the density profile given by Eq. (2.12a) and Eq. (2.12b) are represented by an orange dashed line Fig. 2.15.

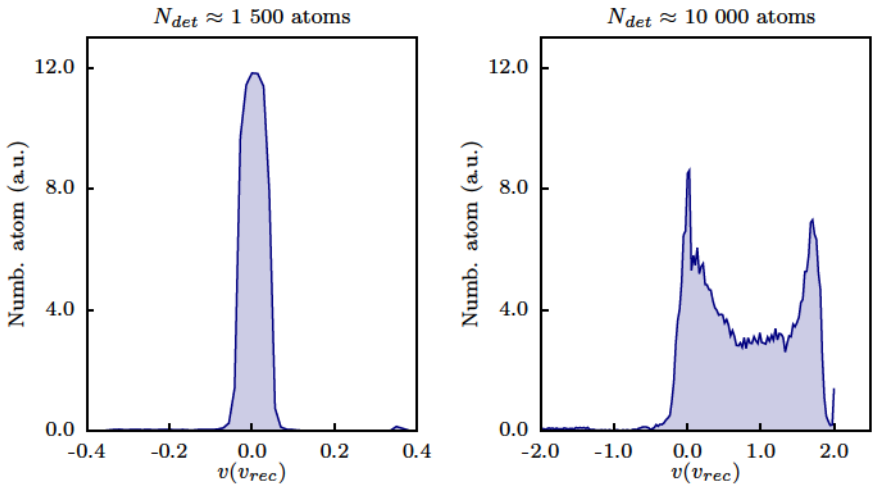

Figure 2.16: Determination of the number of atoms inside the BEC. a) Typical distribution along the vertical axis for the condensate obtained in the crossed-dipole trap. The total number of detected atoms is around 1500. b) Arrival time distribution of the condensate after application of a 1D vertical moving lattice with speed equal to 9.3 cm/s [5] and depth equals to $2\,E_{rec}$ applied for 200 µs inside the crossed dipole trap. The condensate is then widely enlarged along the vertical direction (the distribution goes from a width of approximatively $0.05\,v_{rec}$ in a) to $2\,v_{rec}$ in b)) although its transverse profile does not change much, guaranteeing that all the atoms fall on the detector. The number of detected atoms increases then almost by a factor 10 revealing the saturation effect.

We thus conclude that transferring the atoms in the state $m_j = 0$ immediately after releasing the BEC from the trap does not change significantly the expansion of the cloud. Nevertheless, this measurement is not sufficiently precise to quantitatively determine the initial BEC size and chemical potential. The solution is then to determine the real number of atoms inside the condensate, the trapping frequencies and apply the predictions given by Eq. (2.12a) and Eq. (2.12b).

Determination of the total number of atoms

To avoid saturation on the MCP and an erroneous determination of the number of atoms in the BEC, one solution consists in enlarging the arrival time distribution. By doing so, the arrival flux lowers and one can, taking into account the detection efficiency of the MCP, retrieve the total number of atoms. In order to do so, a deep moving optical lattice is applied to the condensate. The atoms are then diffracted into different classes of momenta (see Section 3.4). This is represented in Fig. 2.16 where the left panel corresponds to a saturated detection of the condensate and the right panel to the arrival time distribution after application of the lattice. The number of detected atoms is strongly enhanced going from $N_{det} \approx 1500$ atoms to $N_{det} \approx 10000$ atoms which illustrate the saturation effect.

From our detection efficiency estimation (at least 25 (5) %) we retrieve a total number of atoms around 5×10^4 atoms. However, the detection efficiency uncertainty leads to an uncertainty in the total number of atoms which is not negligible.

[4] The condensate is then at resonance with the Bragg diffraction condition, see Section 4.1.

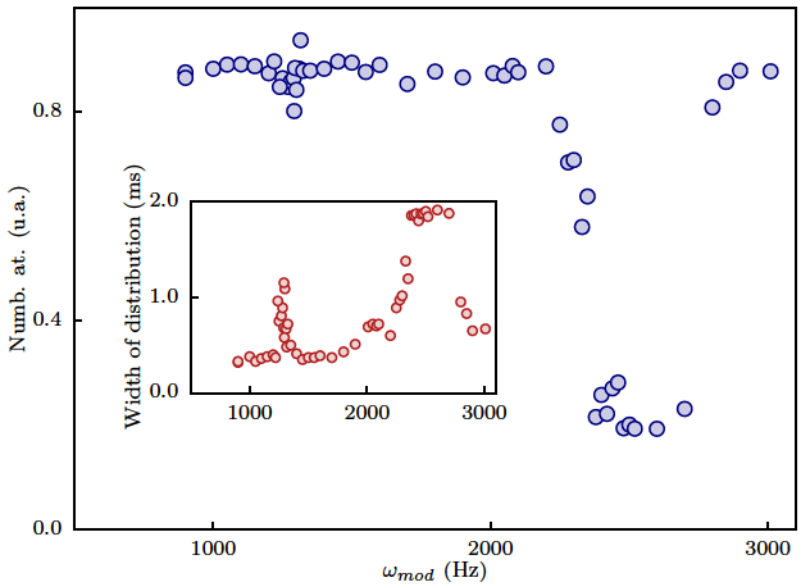

Figure 2.17: Experimental measurement of the transverse frequencies of the dipole trap. The optical intensity of the dipole trap beams is modulated between 1 kHz and 3 kHz. Two resonances are visible corresponding the dipole resonance of the trap at $\omega_\perp/2\pi$ and the quadrupole resonance at $2\times\omega_\perp/2\pi$. The value of $\omega_\perp/2\pi = 1275\,(8)$ Hz is in good agreement with the theoretical predictions of $\omega_\perp/2\pi = 1258$ Hz obtained for a vertical beam waist of 43 μm.

Trapping frequencies

In order to experimentally probe the trapping frequencies, one needs to decouple transverse and longitudinal directions. For the case of an ideal Bose gas without interactions the first quadrupole oscillation is expected to occur at twice the trapping frequency [168, 169]. In the case of a very elongated BEC however, the first resonances are expected at $\omega = \sqrt{5/2}\,\omega_z$ and $\omega = 2\omega_\perp$ [168].

Transverse direction

To probe the transverse frequency, the vertical beam intensity is modulated, at a tunable frequency ω_{mod}. When one modulates the trap at a frequency close to the resonance frequency, the cloud heats and eventually *explodes* depending of the amplitude of the modulation. When the modulation frequency is far from the resonance condition, one recovers after time-of-flight, an arrival time distribution very sharp corresponding to the unperturbed cold atomic cloud. When one gets closer to the resonance condition, the distribution gets larger and the number of detected atoms with arrival time close to t_0 lowers. By looking at both the central number of detected atoms and width of the distribution, one can identify the resonant frequency. The modulation frequency is tuned from 1 kHz to 3 kHz and the number of atoms detected in a small volume around t_0 given by

$$N_{at}(0) = \int_{-\infty}^{\infty}\int_{-\infty}^{\infty} \mathrm{dx\,dy} \int_{t_0-\sigma_t}^{t_0+\sigma_t} dt\; n\,(\mathrm{x,y,t})\,,$$

with n the atomic density of the detected cloud, is measured as a function of ω_{mod} as represented in Fig. 2.17. As a complementary measurement, the arrival time distribution width is extracted from a Gaussian fit and represented as a function of ω_{mod} in Fig. 2.17 (inset).

Two resonances, the first one at $\omega_{\text{mod}} = 2\pi\times 1275\,(8)$ Hz and the second at $\omega_{\text{mod}} = 2\pi\times 2542\,(15)$ Hz, are visible. While the second resonance is clearly noticeable for both quantities,

the first one is only discernible in the analysis of the width distribution. We attribute the second resonance to $2\omega_\perp$, which agrees with the theoretical prediction ($\omega_\perp = 2\pi \times 1258 Hz$) for an optical power equal to $P_{\text{hor}} = 30\,\text{mW}$, $P_{\text{vert}} = 585\,\text{mW}$ and waists of $43\,\mu\text{m}$ and $82\,\mu\text{m}$ for the vertical and horizontal beams respectively. The first resonance corresponds to residual heating due to dipole oscillations at $\omega_\perp$. The transverse resonance has also been checked for others power of the vertical beam. In all scenarios, the theoretical prediction is always close to the experimental result which confirms our estimation of the vertical waist.

Longitudinal direction

The addition of the horizontal beam is mainly going to affect the vertical trap confinement. In the crossed dipole trap, the frequency along the $z-$axis can easily be tuned from a few Hz to a few hundreds of Hz by changing the horizontal beam power. Although the same analysis, as for the transverse frequency, could be carried out, this would correspond to a very long modulation time in order to probe a few Hz of confinement. For this reason, we decided to determine the longitudinal frequency from direct observation of the cloud oscillation in the dipole trap.

This is performed by giving an initial velocity (via Bragg diffraction, see Subsection 4.1), along the vertical direction, to the condensate. The BEC is then kept inside the trap for a certain holding time, t_{hold}. For small enough velocities and deep traps, the trapping potential can be approximate by an harmonic potential.The BEC speed oscillates in time, with frequency equal to the longitudinal trapping frequency. This oscillation is recovered by switching off the trap at different holding times. After a very long time-of-flight, one has access to the initial speed of the condensate at the instant the trap has been switched off and can then reconstruct the oscillation.

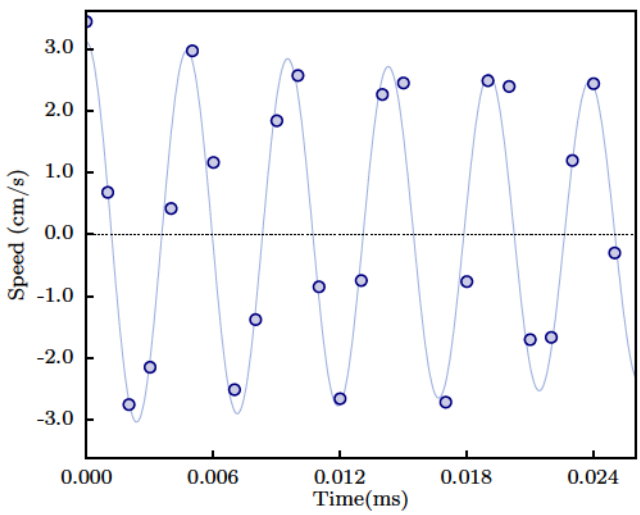

Figure 2.18: ***Vertical oscillation of the BEC in the crossed dipole trap.*** *Oscillation of the central arrival time, after time-of-flight, of a condensate as a function of the holding time in the crossed dipole trap. The arrival time oscillation corresponds to the velocity oscillation of the cloud inside the dipole trap. The frequency corresponds to the vertical trapping frequency.*

Fig. 2.18 shows this oscillation for the case of a horizontal beam power $P_{\text{hor}} = 110\,\text{mW}$. The trapping potential presents a frequency equal to $\omega_z = 2\pi \times 210\,(1)$ Hz along the longitudinal axis with a small attenuation due to atom losses. For a horizontal beam power of 30 mW, which is the typical value in most of our experiments, the frequency oscillation is then equal to $\omega_z = 2\pi \times 93\,(4)$ Hz.

Typical BEC-size determination

In Table 2.6 the different possible configurations of the experiment and the characteristic values of the condensate following both Ref. [64] (1D–3D intermediate regime) and the Thomas–Fermi approximation are summarised. In Table 2.6, L stands for the radius of the parabola along the longitudinal long axis of the condensate, R the transverse parabolic radius according to the Thomas–Fermi approximation and $w_\perp(0)$ to the central transverse radius according to Ref. [64].

		$\omega_\perp = 2\pi \times 1275\,\mathrm{Hz}$		
		$\omega_\parallel = 2\pi \times 7\,\mathrm{Hz}$	$\omega_\parallel = 2\pi \times 93\,\mathrm{Hz}$	$\omega_\parallel = 2\pi \times 170\,\mathrm{Hz}$
		$N_{at} = 3 \times 10^4$	$N_{at} = 5 \times 10^4$	$N_{at} = 7 \times 10^4$
Ref. [64] (1D-3D crossover description)	L (μm)	323	55.00	37.00
	$w_\perp(0)$ (μm)	2.28	3.45	3.86
	$\frac{\mu}{2\pi}$ (kHz)	2.29	6.36	9.12
Thomas-Fermi approximation	L (μm)	430	60.05	39.64
	R (μm)	2.36	4.40	5.30
	$\frac{\mu}{2\pi}$ (kHz)	1.79	6.18	8.99

Table 2.6: Typical values of μ, L, R and $w_\perp(0)$. Summary of the different accessible values of the chemical potential μ, vertical radius of the condensate L and transverse radius R according to the Thomas–Fermi approximation. Comparison of those values with the ones obtained following Ref. [64], with $w_\perp(0)$ corresponding to the Gaussian width of the condensate at $z = 0$.

2.3 Conclusion

We have shown that several experimental limitations have been solved with the construction of a crossed dipole trap. We had in mind with this modification to increase the stability of the experiment and to simplify the comprehension of our results. The arrival time fluctuation has been strongly reduced avoiding us to perform complex analysis. Namely, since no post-selection is needed this implies a more effective use of the data acquired. This translates, for the same signal-to-noise ratio, in a reduced acquisition time [6]. It was also shown that it is possible to tune our chemical potential and trapping frequencies such that one can easily choose the configuration of the obtained BEC.

[6] To give an order of magnitude almost half of the realisations were not used after post-selection due to arrival time fluctuations. Thus the arrival time fluctuations made the experimental cycle, in practise, twice longer.

Bibliography

[39] J.-C. Jaskula, G. Partridge, M. Bonneau, R. Lopes, J. Ruaudel, D. Boiron, and C. Westbrook, "Acoustic Analog to the Dynamical Casimir Effect in a Bose-Einstein Condensate", Phys. Rev. Lett. **109**, 220401 (2012) (cit. on pp. 4, 7, 34, 44, 46, 167, 217).

[48] A. Perrin, H. Chang, V. Krachmalnicoff, M. Schellekens, D. Boiron, A. Aspect, and C. I. Westbrook, "Observation of Atom Pairs in Spontaneous Four-Wave Mixing of Two Colliding Bose-Einstein Condensates", Phys. Rev. Lett. **99**, 150405 (2007) (cit. on pp. 4, 27, 34, 167).

[51] J.-C. Jaskula, M. Bonneau, G. B. Partridge, V. Krachmalnicoff, P. Deuar, K. V. Kheruntsyan, A. Aspect, D. Boiron, and C. I. Westbrook, "Sub-Poissonian Number Differences in Four-Wave Mixing of Matter Waves", Phys. Rev. Lett. **105**, 190402 (2010) (cit. on pp. 4, 34, 39, 167).

[64] F. Gerbier, "Quasi-1D Bose-Einstein condensates in the dimensional crossover regime", EPL (Europhysics Letters) **66**, 771 (2004) (cit. on pp. 6, 48, 59, 78, 173, 174).

[68] R. Lopes, A. Imanaliev, M. Bonneau, J. Ruaudel, M. Cheneau, D. Boiron, and C. I. Westbrook, "Second-order coherence of superradiance from a Bose-Einstein condensate", Phys. Rev. A **90**, 013615 (2014) (cit. on pp. 7, 34, 37, 53, 217).

[105] G. K. Campbell, J. Mun, M. Boyd, E. W. Streed, W. Ketterle, and D. E. Pritchard, "Parametric Amplification of Scattered Atom Pairs", Phys. Rev. Lett. **96**, 020406 (2006) (cit. on pp. 27, 45, 71, 86).

[108] M. Bonneau, J. Ruaudel, R. Lopes, J.-C. Jaskula, A. Aspect, D. Boiron, and C. I. Westbrook, "Tunable source of correlated atom beams", Phys. Rev. A **87**, 061603 (2013) (cit. on pp. 27, 34, 44–46, 83, 91, 167, 217).

[114] M. Schellekens, R. Hoppeler, A. Perrin, J. V. Gomes, D. Boiron, A. Aspect, and C. I. Westbrook, "Hanbury Brown Twiss Effect for Ultracold Quantum Gases", Science **310**, 648–651 (2005) (cit. on pp. 28, 34).

[119] A. Robert, O. Sirjean, A. Browaeys, J. Poupard, S. Nowak, D. Boiron, C. I. Westbrook, and A. Aspect, "A Bose-Einstein Condensate of Metastable Atoms", Science **292**, 461–464 (2001) (cit. on pp. 34, 40).

[120] R. Hanbury Brown and R. Q. Twiss, "Correlation between Photons in two Coherent Beams of Light", Nature **177**, 27–29 (1956) (cit. on p. 34).

[121] T. Jeltes, J. M. McNamara, W. Hogervorst, W. Vassen, V. Krachmalnicoff, M. Schellekens, A. Perrin, H. Chang, D. Boiron, A. Aspect, and C. I. Westbrook, "Comparison of the Hanbury Brown-Twiss effect for bosons and fermions.", Nature **445**, 402–5 (2007) (cit. on p. 34).

[122] R. Lopes, A. Imanaliev, A. Aspect, M. Cheneau, D. Boiron, and C. I. Westbrook, "Atomic Hong-Ou-Mandel experiment", Nature **520**, 66–68 (2015) (cit. on pp. 34, 37, 217).

[123] C. N. Cohen-Tannoudji, "Nobel Lecture: Manipulating atoms with photons", Rev. Mod. Phys. **70**, 707–719 (1998) (cit. on p. 34).

[124] W. D. Phillips, "Nobel Lecture: Laser cooling and trapping of neutral atoms", Rev. Mod. Phys. **70**, 721–741 (1998) (cit. on pp. 34, 39).

[125] F. Pereira Dos Santos, J. Léonard, J. Wang, C. J. Barrelet, F. Perales, E. Rasel, C. S. Unnikrishnan, M. Leduc, and C. Cohen-Tannoudji, "Bose-Einstein Condensation of Metastable Helium", Phys. Rev. Lett. **86**, 3459–3462 (2001) (cit. on p. 34).

[126]S. V. Nguyen, S. C. Doret, C. B. Connolly, R. A. Michniak, W. Ketterle, and J. M. Doyle, "Evaporative cooling of metastable helium in the multi-partial-wave regime", Phys. Rev. A **72**, 060703 (2005) (cit. on p. 34).
[127]A. S. Tychkov, T. Jeltes, J. M. McNamara, P. J. J. Tol, N. Herschbach, W. Hogervorst, and W. Vassen, "Metastable helium Bose-Einstein condensate with a large number of atoms", Phys. Rev. A **73**, 031603 (2006) (cit. on p. 34).
[128]R. Dall and A. Truscott, "Bose–Einstein condensation of metastable helium in a bi-planar quadrupole Ioffe configuration trap", Optics Communications **270**, 255–261 (2007) (cit. on p. 34).
[129]M. Keller, M. Kotyrba, F. Leupold, M. Singh, M. Ebner, and A. Zeilinger, "Bose-Einstein condensate of metastable helium for quantum correlation experiments", Phys. Rev. A **90**, 063607 (2014) (cit. on p. 34).
[130]Q. Bouton *et al.* (in preparation). (cit. on p. 34).
[131]W. Vassen, C. Cohen-Tannoudji, M. Leduc, D. Boiron, C. I. Westbrook, A. Truscott, K. Baldwin, G. Birkl, P. Cancio, and M. Trippenbach, "Cold and trapped metastable noble gases", Rev. Mod. Phys. **84**, 175–210 (2012) (cit. on p. 34).
[132]J. R. Anglin and W. Ketterle, "Bose-Einstein condensation of atomic gases", Nature **416**, 211–218 (2002) (cit. on p. 34).
[133]S. S. Hodgman, R. G. Dall, L. J. Byron, K. G. H. Baldwin, S. J. Buckman, and A. G. Truscott, "Metastable Helium: A New Determination of the Longest Atomic Excited-State Lifetime", Phys. Rev. Lett. **103**, 053002 (2009) (cit. on p. 37).
[134]S. Moal, M. Portier, J. Kim, J. Dugué, U. D. Rapol, M. Leduc, and C. Cohen-Tannoudji, "Accurate Determination of the Scattering Length of Metastable Helium Atoms Using Dark Resonances between Atoms and Exotic Molecules", Phys. Rev. Lett. **96**, 023203 (2006) (cit. on p. 37).
[135]M. Przybytek and B. Jeziorski, "Bounds for the scattering length of spin-polarized helium from high-accuracy electronic structure calculations", J. Chem. Phys. **123**, 134315 (2005) (cit. on p. 37).
[136]A. Browaeys, "Piégeage magnétique d'un gaz d'hélium métastable : vers la condensation de Bose-Einstein", Theses (Université Paris Sud - Paris XI, Nov. 2000) (cit. on pp. 35, 39, 40).
[137]H. Hoendervanger, Lynn, "A New Metastable Helium Machine : An Investigation into the Attributes of Trapping, Cooling and Detecting Metastable Helium", Theses (Institut d'Optique Graduate School, Oct. 2014) (cit. on p. 35).
[138]A. L. Hoendervanger, D. Clément, A. Aspect, C. I. Westbrook, D. Dowek, Y. J. Picard, and D. Boiron, "Influence of gold coating and interplate voltage on the performance of chevron micro-channel plates for temporally and spatially resolved single particle detection", Rev. Sci. Instrum. **84**, 023307, pages (2013) (cit. on p. 35).
[139]M. Schellekens, "The Hanbury Brown and Twiss Effet for Cold Atoms", Theses (Université Paris Sud - Paris XI, May 2007) (cit. on pp. 37–39).
[140]T. Wasak, J. Chwede ńczuk, P. Zi ń, and M. Trippenbach, "Raman scattering of atoms from a quasicondensate in a perturbative regime", Phys. Rev. A **86**, 043621 (2012) (cit. on p. 37).
[141]J. Ruaudel, "Creation and characterization of a tunable source of correlated atoms pairs", Theses (Institut d'Optique Graduate School, Dec. 2013) (cit. on pp. 38, 44, 45, 74, 77, 83, 86, 87).
[142]M. Bonneau, "Atomic four-wave mixing in an optical lattice", Theses (Université Paris Sud - Paris XI, Dec. 2011) (cit. on pp. 38, 44, 45, 53, 54, 71, 83, 181).
[143]A. J. Palmer, M. Baker, and R. T. Sang, "Quantitative comparison of rare-gas cold cathode discharge metastable atomic beam sources", Rev. Sci. Instrum. **75**, 5056–5058 (2004) (cit. on p. 39).
[144]W. Lu, M. D. Hoogerland, D. Milic, K. G. H. Baldwin, and S. J. Buckman, "A bright metastable atom source at 80 K", Rev. Sci. Instrum. **72**, 2558–2561 (2001) (cit. on p. 39).

[145] A. Aspect, N. Vansteenkiste, R. Kaiser, H. Haberland, and M. Karrais, "Preparation of a pure intense beam of metastable helium by laser cooling", Chemical Physics **145**, 307–315 (1990) (cit. on p. 39).

[146] P. O. Schmidt, S. Hensler, J. Werner, T. Binhammer, A. Görlitz, and T. Pfau, "Doppler cooling of an optically dense cloud of magnetically trapped atoms", J. Opt. Soc. Am. B **20**, 960–967 (2003) (cit. on p. 40).

[147] W. Ketterle, "Nobel lecture: When atoms behave as waves: Bose-Einstein condensation and the atom laser", Rev. Mod. Phys. **74**, 1131–1151 (2002) (cit. on pp. 40, 44).

[148] J. C. Viana Gomes, "THERMOMETRY AND COHERENCE PROPERTIES OF A ULTRA-COLD QUANTUM GAS OF METASTABLE HELIUM", Theses (Université Paris Sud - Paris XI, Feb. 2007) (cit. on p. 40).

[149] G. B. Partridge, J.-C. Jaskula, M. Bonneau, D. Boiron, and C. I. Westbrook, "Bose-Einstein condensation and spin mixtures of optically trapped metastable helium", Phys. Rev. A **81**, 053631 (2010) (cit. on pp. 40, 41).

[150] J.-C. Jaskula, "Creation and characterization of non-classical states for quantum atom optics", Theses (Université Paris Sud - Paris XI, Dec. 2010) (cit. on pp. 40–42, 50, 175, 176).

[151] R. Grimm, M. Weidemüller, and Y. B. Ovchinnikov, "Optical Dipole Traps for Neutral Atoms", in , Vol. 42, edited by B. Bederson and H. Walther, Adv. Atom. Mol. Opt. Phy. (Academic Press, 2000), pp. 95–170 (cit. on pp. 40, 66, 71, 178).

[152] W. Ketterle and N. J. van Druten, "Bose-Einstein condensation of a finite number of particles trapped in one or three dimensions", Phys. Rev. A **54**, 656–660 (1996) (cit. on p. 44).

[153] C. Pethick and H. Smith, *Bose-Einstein Condensation in Dilute Gases* (Cambridge University Press, 2002) (cit. on pp. 44, 75, 111).

[154] B. Wu and Q. Niu, "Landau and dynamical instabilities of the superflow of Bose-Einstein condensates in optical lattices", Phys. Rev. A **64**, 061603 (2001) (cit. on pp. 45, 71, 77–80).

[155] K. M. Hilligsøe and K. Mølmer, "Phase-matched four wave mixing and quantum beam splitting of matter waves in a periodic potential", Phys. Rev. A **71**, 041602 (2005) (cit. on pp. 45, 71).

[156] L. H. Thomas, "The calculation of atomic fields", P Camb. Philos. Soc. **23**, 542 (1927) (cit. on p. 47).

[157] E. Fermi, "Un metodo statistico per la determinazione di alcune proprietà dell'atomo.", Rend. Lincei **6**, 602–607 (1927) (cit. on p. 47).

[158] J. Esteve, J.-B. Trebbia, T. Schumm, A. Aspect, C. Westbrook, and I. Bouchoule, "Observations of Density Fluctuations in an Elongated Bose Gas: Ideal Gas and Quasicondensate Regimes", Phys. Rev. Lett. **96**, 130403 (2006) (cit. on p. 47).

[159] B. Paredes, A. Widera, V. Murg, O. Mandel, S. Folling, I. Cirac, G. V. Shlyapnikov, T. W. Hansch, and I. Bloch, "Tonks-Girardeau gas of ultracold atoms in an optical lattice", Nature **429**, 277–281 (2004) (cit. on p. 47).

[160] T. Kinoshita, T. Wenger, and D. S. Weiss, "Observation of a One-Dimensional Tonks-Girardeau Gas", Science **305**, 1125–1128 (2004) (cit. on p. 47).

[161] C. Menotti and S. Stringari, "Collective oscillations of a one-dimensional trapped Bose-Einstein gas", Phys. Rev. A **66**, 043610 (2002) (cit. on pp. 47, 48).

[162] D. S. Petrov, G. V. Shlyapnikov, and J. T. M. Walraven, "Phase-Fluctuating 3D Bose-Einstein Condensates in Elongated Traps", Phys. Rev. Lett. **87**, 050404 (2001) (cit. on p. 49).

[163] S. Dettmer, D. Hellweg, P. Ryytty, J. J. Arlt, W. Ertmer, K. Sengstock, D. S. Petrov, G. V. Shlyapnikov, H. Kreutzmann, L. Santos, and M. Lewenstein, "Observation of Phase Fluctuations in Elongated Bose-Einstein Condensates", Phys. Rev. Lett. **87**, 160406 (2001) (cit. on p. 53).

[164] S. Hofferberth, I. Lesanovsky, B. Fischer, T. Schumm, and J. Schmiedmayer, "Non-equilibrium coherence dynamics in one-dimensional Bose gases.", Nature **449**, 324–7 (2007) (cit. on p. 53).

[165]S. Manz, R. Bücker, T. Betz, C. Koller, S. Hofferberth, I. E. Mazets, A. Imambekov, E. Demler, A. Perrin, J. Schmiedmayer, and T. Schumm, "Two-point density correlations of quasicondensates in free expansion", Phys. Rev. A **81**, 031610 (2010) (cit. on p. 53).

[166]I. Bouchoule, M. Arzamasovs, K. V. Kheruntsyan, and D. M. Gangardt, "Two-body momentum correlations in a weakly interacting one-dimensional Bose gas", Phys. Rev. A **86**, 033626 (2012) (cit. on p. 53).

[167]Y. Castin and R. Dum, "Bose-Einstein Condensates in Time Dependent Traps", Phys. Rev. Lett. **77**, 5315–5319 (1996) (cit. on pp. 54, 55).

[168]M.-O. Mewes, M. R. Andrews, N. J. van Druten, D. M. Kurn, D. S. Durfee, C. G. Townsend, and W. Ketterle, "Collective Excitations of a Bose-Einstein Condensate in a Magnetic Trap", Phys. Rev. Lett. **77**, 988–991 (1996) (cit. on pp. 57, 175, 176).

[169]L. Landau and E. Lifshitz, *Mechanics, Course of Theoretical Physics, Volume 1*, Butterworth Heinemann (Butterworth-Heinemann, 1976), pp. 80–84 (cit. on p. 57).

Chapter 3

Experimental requisites towards the HOM experiment: atomic pair production

Contents

3.1 Theory of shallow optical periodic potentials **66**
3.1.1 Formation of a periodic potential 66
3.1.2 Energy band structure in the presence of a lattice 67
3.1.3 Adiabatic loading 68
3.1.4 Spontaneous emission 71
3.1.5 Instabilities in the presence of a lattice 71
3.2 Dynamical instability: pair creation **72**
3.2.1 Determination of the phase-matching conditions 74
3.2.2 Atomic beam shape prediction 80
3.3 Pair creation: experimental realisation **81**
3.3.1 Geometrical alignment 83
3.3.2 Loading procedure of the 1D lattice 83
3.3.3 Atomic pair production 85
3.3.4 Evolution of the pairs in the trapping potential 86
3.4 Correlated pairs of atoms: analysis **91**
3.4.1 Cross-correlation and autocorrelation 91
3.4.2 Non-classical correlations 95
3.5 Conclusions **98**

> To restrict quantum mechanics to be exclusively about piddling laboratory operations is to betray the great enterprise. A serious formulation will not exclude the big world outside the laboratory.
>
> J.S.Bell

The next experimental step required for the realisation of the atomic HOM experiment is the creation and manipulation of atomic pairs. This is achieved through the manipulation of optical periodic potentials created by the superposition of laser beams.

A brief theoretical description of weak periodic optical potential applied to cold atoms is performed in Section 3.1 with emphasis on the appearance of an energy band structure. In Section 3.2, based on the description of dynamical instabilities, the theory behind the atomic pair creation mechanism is discussed and is followed by the description of the experimental realisation in Section 3.3. The detailed analysis of the produced state is performed in Section 3.4 and a summary of the most important results given in Section 3.5.

3.1 Theory of shallow optical periodic potentials

In this section, the basic tools to understand the dynamics of atoms in the presence of an optical lattice are summarised following closely Refs. [170–172]. The theoretical background has mainly been developed in condensed matter where the electrons live in a periodic potential created by the crystalline structure of the atoms or molecules. For cold atoms, the analogy is almost directly applicable, since the light, with periodic spatial modulation, induces, via dipole interaction, a periodic potential seen by the atoms.

3.1.1 Formation of a periodic potential

The induced dipole produced by the electromagnetic field leads to the potential [172]

$$V_{\text{lat}}(\mathbf{r}) = \frac{\hbar\Gamma^2 I(\mathbf{r})}{8I_{\text{sat}}} \sum_{i\neq j} \frac{d_{ij}^2}{\Delta_{ij}} \tag{3.1}$$

where Δ_{ij} denotes the detuning between the laser frequency and the transition $i \rightarrow j$, Γ^{-1} the lifetime of the excited state, I_{sat} the saturation intensity and d_{ij} the specific line strength associated to the dipole matrix element between levels i and j

$$\mu_{ij} = \langle e_i|\hat{\mu}|g_j\rangle = d_{ij}\|\hat{\mu}\|,$$

with $\hat{\mu} = e \cdot \mathbf{r}$, representing the electric dipole operator. The rotating wave approximation has been applied in Eq. (3.1) since the laser wavelength for the lattice ($\lambda_{\text{lat}} = 1064\,\text{nm}$) is similar to the atomic transition wavelength ($\lambda_0 = 1083\,\text{nm}$) [151].

In order to create an effective optical lattice, that is, a periodic potential in space, it is necessary to perform a spatial modulation of the light intensity. This is done by the interference of two laser beams propagating with a relative angle 2θ, with same wave number $2\pi/\lambda_{\text{lat}}$ and polarisation, and with frequencies ω_1, ω_2 as represented in Fig. 3.1. The total electromagnetic field can be written as

$$\begin{aligned}\mathcal{E}_T(z) = \mathcal{E}_1 \exp\left(i\left[k_{lat}z + \arctan(\theta)k_{\text{lat}}x - \omega_1 t + \phi_1\right]\right)\\ + \mathcal{E}_2 \exp\left(i\left[-k_{lat}z + \arctan(\theta)k_{\text{lat}}x - \omega_2 t + \phi_2\right]\right)\end{aligned}$$

with $I_0 = |\mathcal{E}_0|^2$ and $k_{lat} = \sin(\theta)\, 2\pi/\lambda_{\text{lat}}$. For simplicity, the amplitude of the two electromagnetic fields are assumed equal $\mathcal{E}_1 = \mathcal{E}_2 = \mathcal{E}_0$ and the phase difference, $\Delta\phi = \phi_2 - \phi_1$, constant over time. The intensity profile corresponds to

$$I(z) = 4I_0 \sin^2\left(k_{lat}z + \frac{(\omega_2 - \omega_1)\, t}{2}\right) \tag{3.2}$$

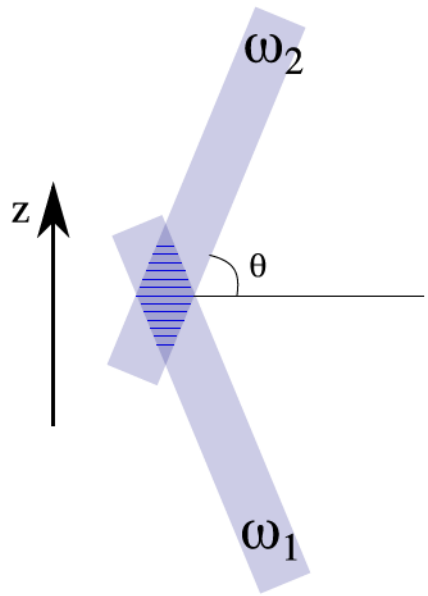

Figure 3.1: Schematic representation of the optical lattice. A laser beam, called 2, with frequency ω_2 and intensity I_2 coming from the top interferes with a laser beam, called 1, with frequency ω_1 and intensity I_1 giving raise to a periodic intensity modulation in the overlapping zone of the two laser beams.

and the lattice periodicity is equal to $a_{\text{lat}} = \lambda/(2\sin(\theta))$.

Two possible situations can occur, either $\omega_2 = \omega_1$ and the optical lattice is stationary, or $\omega_2 \neq \omega_1$ and the lattice moves with a velocity defined along the vertical direction (in the picture $z-$direction) by

$$v_{\text{lat}} = -\frac{(\omega_2 - \omega_1)}{2k_{\text{lat}}} = \frac{\delta_{\text{lat}}}{2k_{\text{lat}}}. \tag{3.3}$$

In both situations, the periodic potential, in the lattice frame of reference, corresponds to

$$V_{\text{lat}}(z) = V_0 \sin^2(k_{lat} z) \tag{3.4}$$

with

$$V_0 = -\frac{\hbar\Gamma^2 I_0}{(2I_{\text{sat}}\Delta_{\text{lat}})},$$

where $\Delta_{\text{lat}} = 2\pi c\left(\frac{1}{\lambda_0} - \frac{1}{\lambda_{\text{lat}}}\right)$.

In the laboratory frame of reference, the atoms are at rest and the lattice moves with a speed given by Eq. (3.3). Therefore, in the lattice frame of reference this corresponds to atoms moving with the same speed but in opposite direction.

3.1.2 Energy band structure in the presence of a lattice

The BEC corresponds to a very elongated cloud of atoms with long axis along the vertical direction. The optical lattice is also aligned along the vertical direction and thus the system in which the dynamics takes place is almost unidimensional. The 1D Schrödinger equation for an atom in such a system can be written as [1]

$$H\psi_{n,q}(z) = \left[-\frac{\hbar^2}{2m}\frac{\partial^2}{\partial z^2} + V_{\text{lat}}(z)\right]\psi_{n,q}(z) = E_{n,q}\psi_{n,q}(z) \tag{3.5}$$

[1]Since the atoms are weakly confined along the vertical direction, the optical dipole trap potential is not taken into account.

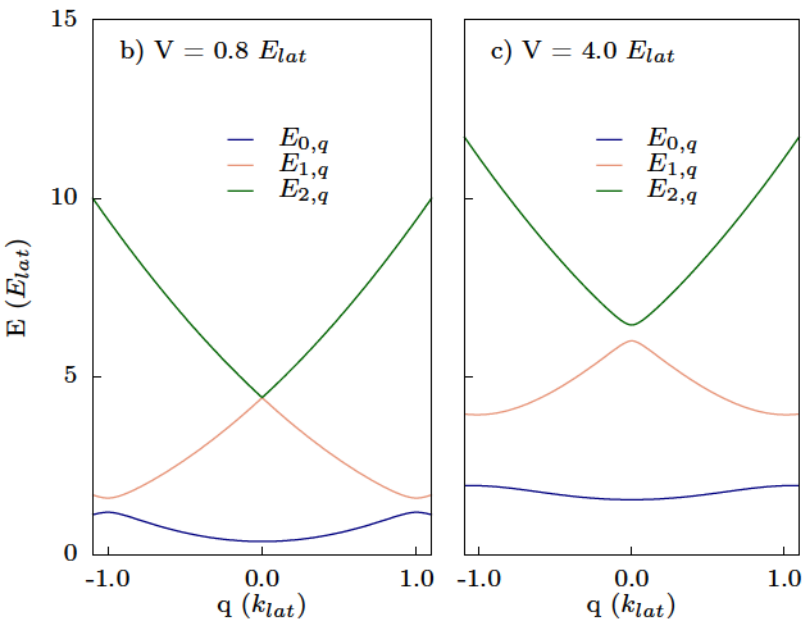

Figure 3.2: Energy bands as a function of the lattice depth V_0. Energy band structure for a) $V_0 = 0.8\,E_{lat}$ and b) $V_0 = 4.0\,E_{lat}$, where in blue we represent the lower energy band. Increasing the lattice depth increases the energy gap between the lower energy band and the second. The recoil energy of the lattice is equal to $E_{lat} = \frac{\hbar^2 k_{lat}^2}{2m}$.

whose solutions correspond to Bloch wave functions [170–172] that can be decomposed to plane waves of momenta $q + 2mk_{\text{lat}}$ [173],

$$|\psi_{n,q}\rangle = \sum_{m=-\infty}^{\infty} a_{n,m}(q)|\phi_{q+2mk_{\text{lat}}}\rangle\,, \tag{3.6}$$

where n stands for the band energy level, q for the quasi-momentum associated to the Bloch function and k_{lat} is the lattice periodicity in reciprocal space. The coefficients $a_{n,m}(q)$ correspond to the projection of the Bloch wave function of energy $E_{n,q}$ on the plane wave $|\phi_{q+2mk_{\text{lat}}}\rangle$.

Substituting Eq. (3.6) in Eq. (3.5), one finds

$$\left[\frac{\hbar^2\left(q+2mk_{\text{lat}}\right)^2}{2m} + \frac{V_0}{2}\right] a_{n,m}(q) - \frac{V_0}{4}\left(a_{n,m+1}(q) + a_{n,m-1}(q)\right) = E_{n,q}a_{n,m}(q)\,. \tag{3.7}$$

Due to the potential periodicity only the first neighbours components $m+1$ and $m-1$ contribute to the solution of the particle with quasi-momentum q. Solving these coupled equations is equivalent to the diagonalisation of a $m \times m$ matrix. The eigenvalues correspond to the energy bands $E_{n,q}$, represented in Fig. 3.2 in the first Brillouin zone with n equal to 0, 1 and 2.

The dispersion relation of an atom in a periodic potential is no longer quadratically dependent on the momentum k, as it is the case in free space, even for weak lattice depths.

3.1.3 Adiabatic loading

For atomic pair creation, it is necessary to avoid Bragg diffraction, see Chapter 4, or any secondary effect that could induce losses or noise in one of the two atomic beams forming the pair [174, 175]. For this purpose one has to adiabatically load the BEC in the lattice such that

the projection of the state in Bloch waves has only a non-vanishing weight in the lowest energy band. The adiabatic condition reads [176]

$$\left|\langle\psi_{n,q}|\frac{\partial H}{\partial t}|\psi_{0,q}\rangle\right| \ll \frac{\left|E_{n,q}(t) - E_{0,q}(t)\right|^2}{\hbar}, \tag{3.8}$$

where the left term is always smaller than $\frac{dV(t)}{dt}$ [173, 176, 177].

In a shallow lattice, where the band gap is small, the energy difference reduces to

$$\Delta E(q,t) = E_{1,q}(t) - E_{0,q}(t)\,.$$

As an example, let us look at the situation depicted in Fig. 3.3 corresponding to a linear ramp of the lattice depth between $V(t=0) = 0$ and $V(t=T) = V_0$. The inequality can then be rewritten as

$$\frac{\hbar V_0}{T\Delta E^2(q,t)} \ll 1\,. \tag{3.9}$$

The difference of energy between the two band levels for an atom with quasi-momentum q depends on the lattice depth. Since the lattice depth changes in time, it is then necessary to ensure that for the entire duration of the loading, the inequality Eq. (3.9) holds [178].

For the case of an atom at rest in the lattice frame of reference ($q = 0$), the energy difference, $\Delta E^2(0,t)$, is larger than $16E_{\text{lat}}^2$ [173, 177, 179] and Eq. (3.9) simplifies to

$$\frac{\hbar V_0}{T} \ll 16E_{lat}^2.$$

For Helium 4 atoms, due to the low atomic mass, this is easily verified since the recoil energy is very large.

Consider the case of the atomic pair creation where the lattice depth is typically equal to $V_0 = 0.8\,\text{E}_{\text{lat}}$. For an atom at rest in the lattice frame of reference, the adiabatic condition is then equal to

$$T \gg \frac{\hbar 0.8}{16E_{\text{lat}}} \gg 180ns.$$

The typical lattice rise time, for a sudden loading, is around 200 ns. Consequently an atom at rest, even in this situation, will not be diffracted.

However, to produce atomic pairs in the 1D optical lattice, the BEC needs to be loaded with a quasi-momentum higher than $0.5\,\text{k}_{\text{lat}}$ in the lattice frame of reference (this will be discussed in Section 3.2). The time necessary to verify adiabatic loading will then be different. For the experimental data shown in this manuscript, the BEC is loaded at -0.57 k_{lat}, in the lattice frame of reference, and one of the two clouds forming the pair has a quasi-momentum close to the 1st Brillouin zone boundary. For the BEC, the main interest is to avoid diffraction during the loading of the lattice as well as during its extinction. For the atomic pairs only what happens at the moment the lattice is turned off needs to be considered (before there are no pairs)[2].

The adiabatic threshold condition corresponds then to

$$\frac{\hbar V_0}{T\Delta E^2(q,t)} = 1. \tag{3.10}$$

[2]The presence of scattering processes during the extinction of the lattice would result in losses of atoms from the pairs. This gives us an idea why it is so important to verify the adiabatic criterion.

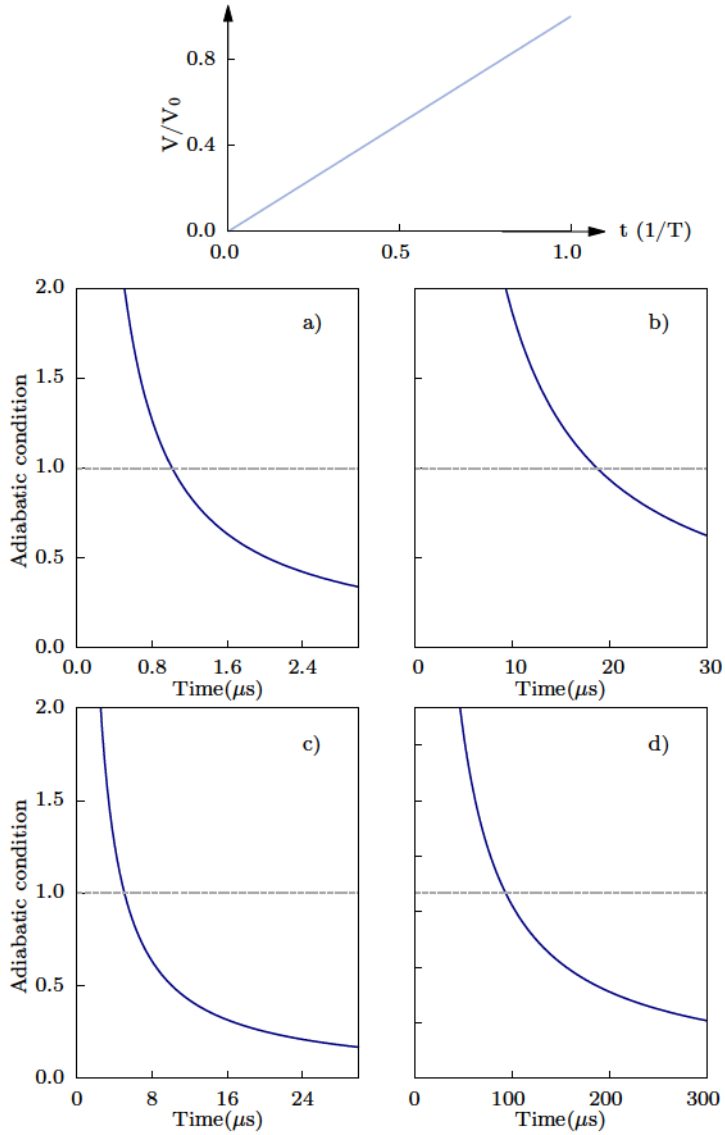

Figure 3.3: Adiabatic loading conditions for different lattice depths, V_0, and quasi-momenta, q_0. The lattice depth is ramped on linearly as represent in the top panel. Adiabatic threshold for different lattice depth V_0 ($V_0 = 0.8\,E_{lat}$ for a) and b) ; $V_0 = 4.0\,E_{lat}$ for c) and d)) and different quasi-momentum q_0 ($q_0 = -0.57\,k_{lat}$ for a) and c) ; $q_0 = -0.9\,k_{lat}$ for b) and d)). The loading criterion corresponds for: a) $T \gg 1.0\,\mu s$, b) $T \gg 20\,\mu s$, c) $T \gg 5\,\mu s$, d) $T \gg 100\,\mu s$.

In Fig. 3.3, we represent the adiabatic threshold condition given by Eq. (3.10) as a function of T at the beginning of the loading. For a linear ramp, this corresponds to the critical situation, since the gap between the two energy band is at its minimum. The result for two different maximum lattice depths ($V_0 = 0.8\,E_{lat}$, Fig. 3.3 a), b) and $V_0 = 4.0\,E_{lat}$, Fig. 3.3c), d)) and two quasi-momenta ($q_0 = 0.57\,k_{lat}$, Fig. 3.3a), c) and $q_0 = 0.9\,k_{lat}$, Fig. 3.3b), d)) are compared. The adiabatic criterion is represented with a dashed line. As expected, for deeper lattices the adiabatic criterion implies longer loading times. In the same way, when the atom reaches the border of the Brillouin zone, it has a higher probability transfer and, as a consequence, the adiabatic criterion is satisfied for slower loading functions.

In the case of a lattice depth equal to $V_0 = 0.8\,E_{lat}$, the loading of the condensate with quasi-momentum $q_0 = -0.57\,k_{lat}$ requires a linear ramp duration $T \gg 1.0\,\mu s$ in order to fulfil the adiabatic criterion. For an atom (one of the two atoms forming a pair for instance) with quasi-momentum $q = 0.9\,q_{lat}$, the loading/extinction criterion requires $T \gg 20\,\mu s$. Please note that for shallow lattice potentials, as in our case, the linear ramp is sufficient to easily satisfy the

adiabatic criterion and, as a consequence, was used in the experimental realisation. However, such a simple ramp does not correspond to the optimised loading procedure, where one would rather have a smoother increase of the lattice depth over time [3] [178, 180, 181].

3.1.4 Spontaneous emission

During the loading process, heating can also induce losses. It has been shown in Ref. [142] that heating, in our experimental set-up, is mostly due to the spontaneous emission rate induced by the lattice. For one beam, the spontaneous emission rate is given by [151, 182]

$$\Gamma_{sp.,1\text{beam}} = \frac{\Gamma}{2}\frac{s}{s+1+(2\Delta_{\text{lat}}/\Gamma)^2} \tag{3.11}$$

with $s = I_0/I_{sat}$. This can be simplified, for the case of shallow lattices ($s \ll 1$), into

$$\Gamma_{sp.,1\text{beam}} \approx \frac{\Gamma}{2\hbar\Delta_{\text{lat}}}V_0 = \frac{\Gamma^3 P_0}{\pi I_s w_{\text{lat}}^2 \Delta_{\text{lat}}^2} \tag{3.12}$$

where $\Gamma = 2\pi\times 1.62\,\text{MHz}$ corresponds to the radiative decay rate of the transition, $w_{\text{lat}} = 200\,\mu\text{m}$ corresponds to the waist of the lattice beam on the atoms and $\Delta_{\text{lat}} = 2\pi \times c\left(\frac{1}{\lambda_{\text{lat}}} - \frac{1}{\lambda_0}\right)$ to the detuning. For a power of 13 mW, corresponding to the case of $V_0 = 0.8\,\text{E}_{\text{lat}}$, we find $\Gamma_{sp.1\text{beam}} = 0.018\,\text{s}^{-1}$. This leads to a heating of [151, 183]

$$\frac{dE}{dt} = 2\times\Gamma_{sp.}\times E_{\text{rec}} = 72\,\text{nK}\cdot\text{s}^{-1}.$$

For our typical lattice duration, around 1 ms, this has a negligible effect and justifies the use of a laser wavelength $\lambda_{\text{lat}} = 1064\,\text{nm}$ with a detuning approximatively equal to $\Delta_{\text{lat}} \approx 2\pi\times 5\,\text{THz}$, sufficiently large to avoid spontaneous emission.

3.1.5 Instabilities in the presence of a lattice

Instabilities can arise even if the cloud is adiabatically loaded. These occur when the condensate is not at rest in the lattice frame of reference [184, 185]. We emphasise here two instabilities: the energetic instability and the dynamical instability.

- The energetic instability is a static instability, that is, the perturbation does not grow in time. It corresponds to a saddle point in the minimisation of the functional energy and it occurs when a BEC moves respectively to an impurity (a thermal atom for instance [186]) with a speed higher than the speed of sound in the condensate [187–190].
- The dynamical instability corresponds to the existence of an imaginary eigenvalue of the Hamiltonian at a given q, in the lattice frame of reference, implying that the population at q grows exponentially over time. This instability was widely studied in Refs. [154, 191, 192] and its applications were also treated in Refs. [105, 155] where it was pointed out that the mechanism behind it is pairwise, that is, the growth of population at q is linked to an increased population at $-q$. It is important to note that in the case of dynamical instabilities,

[3] In Ref. [178], the optimised expression for the lattice loading is given and corresponds to

$$V(t) = \frac{V_{max}}{1+\exp\left(-\alpha t/\tau_{ramp}\right)}$$

where α and τ_{ramp} are adjustable parameters.

atoms with quasi-momenta q and $-q$ (the atomic pairs) are present in the condensate. If the pairs have a speed higher than the speed of sound, energetic instabilities can also take place. Thus the system, which is initially dynamically unstable, also becomes energetically unstable leading to second order effects both on the distribution of the pairs and on the temperature of the BEC.

3.2 Dynamical instability: pair creation

The fundamental mechanism behind the atomic pair production in our experimental set-up is the dynamical instability [188, 193, 194]. This can be viewed as a four-wave mixing process, in the sense that, a pair of atoms is coherently transferred from an initial momentum state k_0, in the laboratory frame of reference, to two new momenta states k_a and k_b forming a pair.

Four-wave mixing

The mechanism is inspired from non-linear optics, where a coherent beam passing through a non-linear medium leads to the creation of a pair of photons verifying momentum and energy conservation.

The Hamiltonian describing this process is given by

$$\hat{H}_{FWM} = \sum_{j=p_1,p_2,s,i} h\nu_j \left(\hat{n}_j + 1\right) \; + \hbar\kappa \left(\hat{a}_{p_1}\hat{a}_{p_2}\hat{a}_s^\dagger\hat{a}_i^\dagger + h.c.\right), \tag{3.13}$$

where p_1, p_2 are the two photons pumps, that can be identical, and s, i are the signal and idler photons produced by the non-linear response of the non-linear medium and $\hat{n}_j$ the number operator. The conservation of energy and momentum implies that

$$\mathbf{k}_{p_1} + \mathbf{k}_{p_2} = \mathbf{k}_s + \mathbf{k}_i, \tag{3.14a}$$

$$\nu_{p_1} + \nu_{p_2} = \nu_s + \nu_i. \tag{3.14b}$$

When the pump is weakly depleted, the operators of the pump beams can be replaced by numbers, N_{p_1} and N_{p_2}, respectively, and Eq. (3.13) can be re-written as

$$\hat{H}_{FWM} = \hat{H}_0 + \hbar\kappa\sqrt{N_{p_1}}\sqrt{N_{p_2}}\left(\hat{a}_s^\dagger\hat{a}_i^\dagger + c.c.\right)$$

with $\hat{H}_0 = \sum_{j=p_1,p_2,s,i} h\nu_j\left(\hat{n}_j + 1\right)$. This corresponds to the parametric down-conversion Hamiltonian which is often used in quantum optics [13, 86]. However, since the phase-matching conditions can be verified by several sets $\{s_l, i_l\}$ of photon pairs, the Hamiltonian can be written more generally as

$$\hat{H}_{FWM} = \sum_l \hat{H}_{0,l} + \sum_l \hbar\kappa\sqrt{N_{p_1}}\sqrt{N_{p_2}}\left(\hat{a}_{s,l}^\dagger\hat{a}_{i,l}^\dagger + c.c.\right)$$

leading to the state

$$|\psi(t)\rangle = e^{-i\hat{H}_{FWM}t/\hbar}|0\rangle, \tag{3.15}$$

that corresponds to a superposition of twin-Fock states with $1, 2, 3, \ldots$ pairs in each distinct mode l. In quantum optics, it is usual to filter only two modes. The wave-function is then given by

$$|\psi\rangle = \sum_n \frac{\tanh(\lambda)^n}{\cosh(\lambda)} |n, n\rangle_{s,i}\,, \tag{3.16}$$

where $|n, n\rangle_{s,i}$ corresponds to a state with n particles in the signal and idler mode, and λ is related to the averaged population

$$\langle n\rangle = \sinh^2(\lambda)\,.$$

With atoms the same physics apply [195]. The non-linearities are then coming from the interaction between atoms and the Hamiltonian can be written as

$$\hat{H}_{FWM} = \int d\mathbf{r}\, \hat{\psi}(\mathbf{r},t)^\dagger \left[-\frac{\hbar^2\nabla}{2m} + V(\mathbf{r},t)\right] \hat{\psi}(\mathbf{r},t) + \frac{g}{2}\int d\mathbf{r}\, \hat{\psi}(\mathbf{r},t)^\dagger \hat{\psi}(\mathbf{r},t)^\dagger \hat{\psi}(\mathbf{r},t)\hat{\psi}(\mathbf{r},t), \tag{3.17}$$

with $g = \frac{4\pi\hbar^2 a}{m}$ and a the scattering length. The field operator $\hat{\psi}(\mathbf{r},t)$ is decomposed in three terms: the pump field p, the idler (i) and signal (s),

$$\hat{\psi}(\mathbf{r},t) = \Phi_p(\mathbf{r},t)\hat{a}_p \;+\; \Phi_s(\mathbf{r},t)\hat{a}_s \;+\; \Phi_i(\mathbf{r},t)\hat{a}_i.$$

This allows one to re-write the interacting component of the Hamiltonian as a sum of several terms. Most of them are non-resonant terms since they do not conserve energy and momentum. The resonant term that conserves both quantities can be written as

$$\hat{H}_{(int)FWM} = 2g \int d\mathbf{r}\, {\Phi_p}^2 \Phi_s^* \Phi_i^*\; \hat{a}_i^\dagger \hat{a}_s^\dagger \hat{a}_p^2 \;+ h.c.\,,$$

which is equivalent to the interaction term obtained in Eq. (3.13). This interaction Hamiltonian describes the coherent transfer of two atoms from the BEC to two new momenta. From now on, the term idler and signal will be replaced by a and b.

The conservation of both momentum vector and energy of the process leads to the following phase-matching conditions

$$2\mathbf{k}_0 = \mathbf{k}_a + \mathbf{k}_b \tag{3.18a}$$
$$2E_0 = E_a + E_b, \tag{3.18b}$$

where $\mathbf{k}_0$ and E_0 stand, respectively, for the momentum and energy of the condensate.

These conditions can not be fulfilled in free-space for any values of $\mathbf{k}_0$ since the dispersion relation is quadratic. When an optical lattice potential is added, the energy dispersion relation becomes periodic and the phase-matching conditions can be verified.

For simplicity, instead of talking about atomic pairs, since several pairs can be created at the same time, the term atomic beams will be often used. Two cloud of atoms are then generated. The one with momentum, in the laboratory frame of reference, closest to the BEC will be called beam a and the second, beam b.

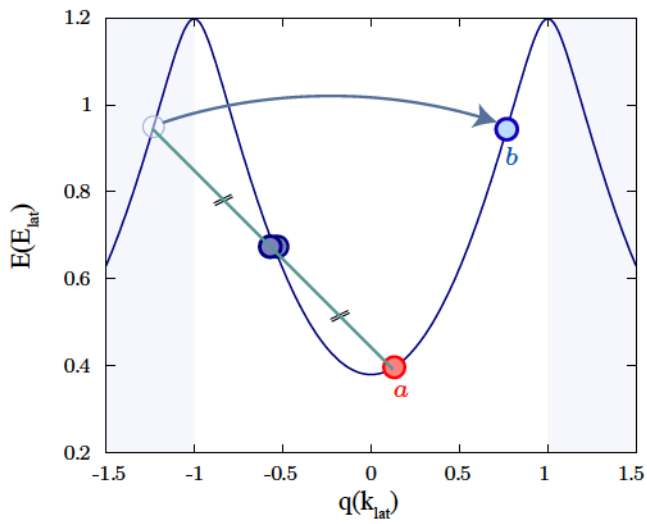

Figure 3.4: Schematic representation of phase-matching conditions for the pair creation process. Two atoms from the condensate q_0 (blue circles) are scattered into the quasi-momenta q_a (red circles) and $q_b + 2k_{lat}$ (light blue circles for q_b and $q_b + 2k_{lat}$) such that both energy and momentum conservation are fulfilled.

3.2.1 Determination of the phase-matching conditions

The atomic pair creation takes place in the dipole trap whose transverse frequencies are much larger than the longitudinal frequency and, as said previously, the system can be approximatively described as 1D. More information on this subject and the validity of this approximation can be found in Ref. [141], page 77.

Therefore, one can write the phase-matching conditions of the 1D system along the longitudinal $z-$axis as

$$2E(q_0) = E(q_a) + E(q_b), \tag{3.19a}$$

$$2q_{z,0} = q_{z,a} + q_{z,b}\,[2k_{\text{lat}}]^{4} \tag{3.19b}$$

where, since the atoms are evolving in an optical lattice, the momentum has been replaced by their respective quasi-momenta. The phase-matching conditions are represented in Fig. 3.4 where two atoms from the condensate with $q_{z\,0} = -0.57\,\text{k}_{\text{lat}}$ (dark blue circle) are transferred to $q_{z\,a} = 0.15$ (red circle) and $q_{z,b} = -1.3\,\text{k}_{\text{lat}} + 2\,\text{k}_{\text{lat}} = 0.7\,\text{k}_{\text{lat}}$ (blue circle). Since the process is 1D, the quasi-momentum will always refer to the vertical component and the index z will be, from now on, dropped.

Knowing the initial quasi-momentum of the condensate q_0, it is then possible to retrieve the values of the pairs quasi-momenta q_a and q_b from Eq. (3.19b) and their respective energies will be given by the dispersion relation $E_0(q_i)$[5].

Mean field correction: a simple approach

Since the four-wave mixing process is based on interactions, it is necessary to add the mean-field contribution (gn) to the phase-matching condition. Keeping in mind that we are interested in

[4]Where the notation $[2k_{\text{lat}}]$ corresponds to $\pm 2k_{\text{lat}}$ such that beam b is projected into the 1st Brillouin zone, see Fig. 3.4.

[5]$E_0(q)$ corresponds to the lowest energy band without interaction corrections.

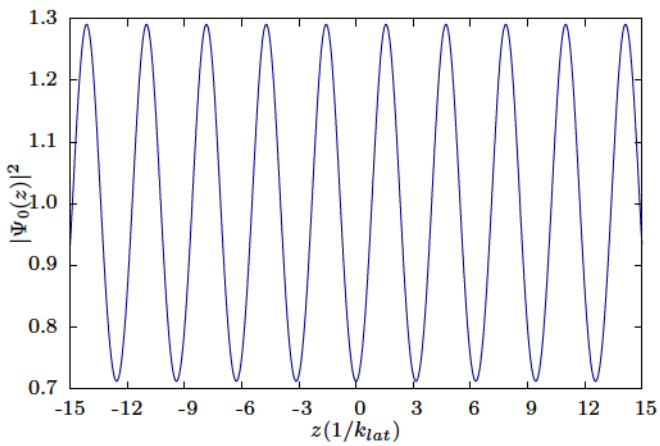

Figure 3.5: Modulation of the condensate wave-function by the optical lattice. Spacial modulation of the BEC wave function with initial quasi-momentum of $q_0 = -0.57\,\mathrm{q}_{lat}$ by a periodic optical lattice potential with depth $V_0 = 0.8\,\mathrm{E}_{lat}$.

producing pairs with low populations (necessary for the HOM effect), the mean field contribution due to the pairs is negligible. However, the same does not hold for the condensate mean field contribution. The energy conservation is then given by [6]

$$2\left[E(q_0) + gn_0\right] = E(q_a) + 2gn_0 + E(q_b) + 2gn_0\,,$$
$$2E(q_0) = E(q_a) + E(q_b) + 2gn_0\,,$$

where n_0 is the density of the BEC given by

$$n_0 = gN_0 \int d\mathbf{r}\left|\psi_0(\mathbf{r})\right|^2 .$$

As a consequence, the phase-matching conditions of Eq. (3.18) are shifted and broadened. Indeed, the wave-function of the BEC described by the Bloch wave

$$\psi_0(z) = \sum_{m=-\infty}^{\infty} a_{0,m}(q_0)e^{iq_0 z}\,, \tag{3.20}$$

corresponds to a modulated function in space. As an example in Fig. 3.5, $\left|\psi_0(z)\right|^2$ is represented for a lattice depth $V_0 = 0.8\,\mathrm{E}_{\mathrm{lat}}$ and BEC initial quasi momentum $q_0 = -0.57\,\mathrm{q}_{\mathrm{lat}}$. The energy conservation can then be written as

$$2q_0 = q_a + q_b\ [2q_{\mathrm{lat}}], \tag{3.21a}$$
$$E(q_a) + E(q_b) + 2g\left(n_0 - \delta n_0\right) \leq 2E(q_0) \leq E(q_a) + E(q_b) + 2g\left(n_0 + \delta n_0\right), \tag{3.21b}$$

where δn_0 corresponds to the modulation amplitude. The energy conservation condition does no longer correspond to a single solution, but to a range of solutions limited by the conditions

$$E(q_a) + E(q_b) = 2E(q_0) - 2g\left(n_0 + \delta n_0\right),$$
$$E(q_a) + E(q_b) = 2E(q_0) - 2g\left(n_0 - \delta n_0\right)\ .$$

One will then have a range of q_0 satisfying the phase-matching conditions. This is represented in Fig. 3.6 for the case of $V_0 = 0.8\,\mathrm{E}_{\mathrm{lat}}$, $q_0 = -0.57\,\mathrm{q}_{\mathrm{lat}}$ and $gn_0 = 0.067\,\mathrm{E}_{\mathrm{lat}}$. The sum of the atomic pair energies $(E(q_a) + E(q_b))$, with q_b verifying the conservation of momentum

$$q_b = q_a - 2q_0\ [2k_{\mathrm{lat}}]\ ,$$

[6] The term $2 \times 2gn_0$ in the right side comes from the fact that an atom from either beam a or b is distinguishable from the condensate. The mean-field contribution for one atom inside the condensate, on the contrary, is equal to gn_0 [153].

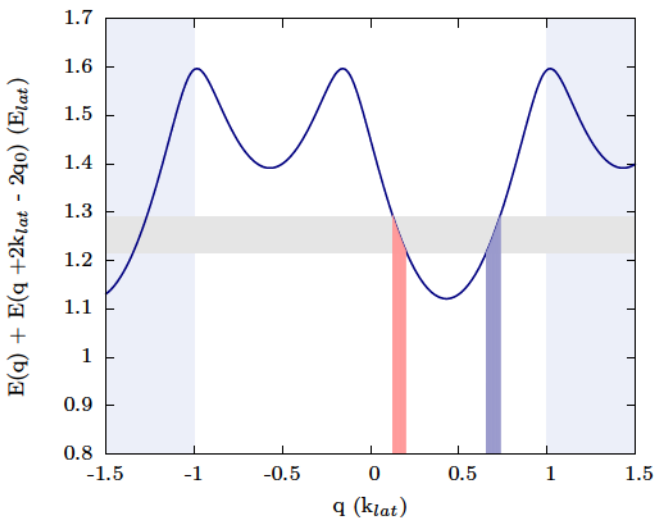

Figure 3.6: Determination of the phase-matching condition taking into account the mean-field contribution. Representation of the total energy of the atomic pairs $E(q) + E(q+2q_{lat} - 2q_0)$ for a fixed condensate quasi-momentum q_0 as a function of q (blue line). The gray shaded area corresponds to twice the energy of the two atoms from the condensate whose range is defined by Eq. (3.23). The intersection between the line and shaded area correspond to both pairs with a width given by the mean-field potential. The red shaded area indicates the atomic beam a and the light blue the atomic beam b.

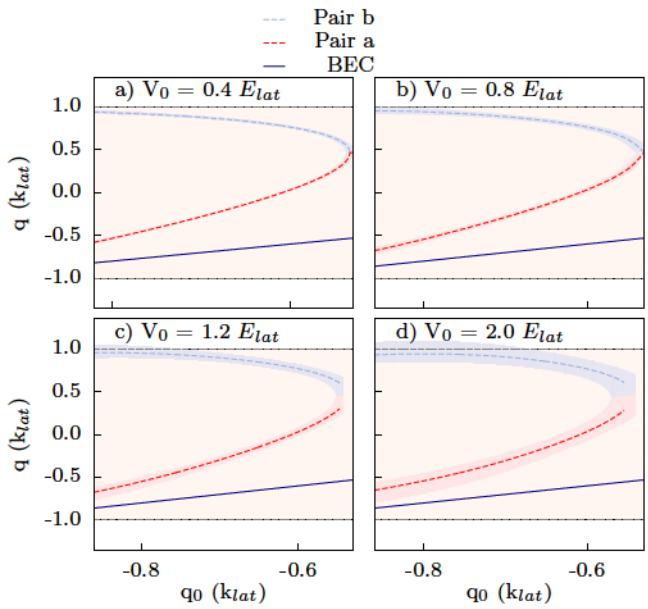

Figure 3.7: Determination of the phase-matching condition taking into account the mean-field potential for different condensate quasi-momentum q_0 and lattice depth V_0. Phase matching conditions for the atomic pair production as a function of the condensate quasi-momentum q_0 for a lattice depth V_0 of: a) $V_0 = 0.4\,E_{lat}$, b)$V_0 = 0.8\,E_{lat}$, c) $V_0 = 1.2\,E_{lat}$ and d) $V_0 = 2.0\,E_{lat}$. The red shaded area indicates the atomic beam a and the light blue the atomic beam b. The widths are fixed by the mean-field modulation. The dark blue line represents the condensate quasi-momentum.

is plotted as a function of q_a. When the total energy of the pair intersects the energy zone defined by the boundaries

$$2E(q_0) - 2g\,(n_0 + \delta n_0)\,, \tag{3.22}$$

$$2E(q_0) - 2g\,(n_0 - \delta n_0)\,, \tag{3.23}$$

represented in gray on the graph, the values of q_a (in red) and q_b (in blue) are found. These correspond to beam a and b, respectively.

By applying the same procedure for different values of the BEC quasi-momentum q_0, one

obtains the phase matching curve displayed in Fig. 3.7 for four different lattice depths. From these curves, it is possible to extract the expected quasi-momenta of atomic beams a and b (q_a, q_b) as a function of the condensate quasi-momentum q_0. One sees that the pair production starts for values of q_0 above a critical value $q_c > 0.5k_{\text{lat}}$ depending on the lattice depth. When q_0 is close to the value of q_c, the atomic pairs are not well separated in momentum space. For deeper lattices, the spread of the pairs and the threshold value tends to increase. These observations are in good agreement with the numerical results of Ref. [154].

Mean field correction: a numerical method

The previous procedure, although very intuitive, does not allow us to predict the atomic beam shape nor the atomic beams dynamics. In order to get this information we will, following Ref. [154], start by solving the stationary Gross-Pitaevskii equation

$$\mu\psi(z) = \left[-\frac{\hbar^2}{2m}\frac{\partial^2}{\partial z^2} + V(z) + g\left|\psi(z)\right|^2\right]\psi(z), \tag{3.24}$$

where $V(z)$ corresponds to the lattice potential [7]. The wave-function of the condensate, as in Eq. (3.20), corresponds then to a Bloch wave with initial quasi-momentum q_0.

This resolution is performed numerically by first finding the solutions of Eq. (3.24) without interactions, given by

$$\psi_0(z) = \sum_{m=-\infty}^{\infty} a_{0,m,0}(q_0)e^{iq_0 z}.$$

By solving the m coupled equations

$$\left[\frac{\hbar^2\left(q_0 + 2mq_{\text{lat}}\right)^2}{2m} + \frac{V_0}{2}\right]a_{0,m,0}(q_0) - \frac{V_0}{4}\left(a_{0,m+1,0}(q) + a_{0,m-1,0}(q_0)\right) = E_{0,q_0,0}a_{0,m,0}(q_0),$$

one finds the coefficients $a_{0,m,0}$ of the wave function $\psi_0(z)$. One can now add the contribution of the mean-field potential, such that the m coupled equations are now given by

$$\begin{aligned}&\left[\frac{\hbar^2\left(q_0 + 2mq_{\text{lat}}\right)^2}{2m} + \frac{V_0}{2}\right]a_{0,m,1}(q_0) - \frac{V_0}{4}\left(a_{0,m+1,1}(q_0) + a_{0,m-1,1}(q_0)\right)\\ &+ n_0 g\sum_{p,p'} a_{0,p,0}a^*_{0,p',0}a_{0,m+p,1} + n_0 g\left|a_{0,m,0}\right|^2 a_{0,m,1} = E_{0,q_0,1}a_{0,m,1}(q_0).\end{aligned}$$

The solution of these equations give us the value of the coefficients $a_{0,m,1}$ and allow us to recover the wave-function

$$\psi_1(z) = \sum_m a_{0,m,1}e^{iq_0 z}.$$

Doing the same procedure but replacing $a_{0,m,0}$ by $a_{0,m,1}$, the solution of $\psi_2(z)$ can be find. This self-consistent procedure is developed until both energy and wave-function correction of higher orders become negligible [141].

Once a solution of Eq. (3.24) is obtained, one needs to test the stability of the wave-function. In order to do so, we add a small perturbation to the condensate wave-function and study

[7] The dipole trap potential is neglected along the longitudinal axis.

its response [154]. This corresponds to adding to the wave-function of the condensate the perturbation

$$\delta\phi_{q_0}(z,q',t) = v_{q_0}(z,q',t)e^{iq'z} + w^*_{q_0}(z,q',t)e^{-iq'z},$$

where $v_{q_0}(z,q',t)$ and $w_{q_0}(z,q',t)$ are two functions with the same spatial periodicity of the lattice. These functions correspond to excitations with quasi-momentum q_0+q' and q_0-q', in the lattice frame of reference, and have weak amplitudes. By solving the time dependent Gross-Pitaevskii equation

$$i\hbar\frac{\partial\psi(z,t)}{\partial t} = -\frac{\hbar^2}{2m}\frac{\partial^2\psi(z,t)}{\partial z^2} + \frac{V_0}{2}\left(1-\cos\left(2zq_{\text{lat}}\right)\right) + gn_0\left|\psi(z,t)\right|^2\psi(z,t), \tag{3.25}$$

one gets, in first order approximation,

$$i\hbar\frac{\partial}{\partial t}\begin{pmatrix} v_{q_0}(z,q',t) \\ w_{q_0}(z,q',t)\end{pmatrix} = \mathcal{M}_{q_0}(z,q')\begin{pmatrix} v_{q_0}(z,q',t) \\ w_{q_0}(z,q',t)\end{pmatrix}, \tag{3.26}$$

where $\mathcal{M}_{q_0}(z,q')$ is equal to

$$\mathcal{M}_{q_0}(z,q') = \begin{pmatrix} \mathcal{L}(q_0+q') & gn_0\psi^2_{q_0} \\ -gn_0\psi^{2*}_{q_0} & -\mathcal{L}(-q_0+q')\end{pmatrix} \tag{3.27}$$

and

$$\mathcal{L}(q) = -\frac{\hbar^2}{2m}\left(\frac{\partial}{\partial z}+iq\right)^2 + \frac{V_0}{2}\sin^2(zk_{\text{lat}}) - \mu + 2gn_0\left|\psi_{q_0}\right|^2. \tag{3.28}$$

Through the diagonalisation of the matrix $\mathcal{M}$, one can determine the eigenvalues of the system. If one of the eigenvalues is complex, the system is not stable and the respective perturbation growths exponentially in time leading to a depletion of the condensate. This corresponds to the dynamical instability or, in other words, the atomic pair production.

These instabilities can be stimulated with the introduction of a seed — stimulated process — or can happen spontaneously due to vacuum fluctuations — spontaneous pair creation. Our main interest is in the latter.

The eigenvalues of $\mathcal{M}$ are computed by fixing the BEC quasi-momentum q_0 and scanning the perturbation quasi-momentum, q', in the 1st Brillouin zone. Each imaginary eigenvalue corresponds to a quasi-momentum q' verifying the phase-matching conditions of the atomic pairs. By identifying the values of q' for which the eigenvalue has an imaginary term and knowing q_0, one extracts the values of q_a and q_b. The complex part of the imaginary eigenvalue corresponds to the growth rate of the excitation. In Fig. 3.8, one can see that the rate increases with the lattice depth and with the absolute value of q_0. This means that for deeper lattices and larger BEC quasi-momenta the pair production rate increases. Consequently, in order to produce the same number of atomic pairs for different quasi-momenta or lattice depths, one has to adapt the lattice duration.

In Fig. 3.8, the quasi-momenta q_a and q_b are plotted for different q_0 ranging from $-0.9\,\text{k}_{\text{lat}}$ to $-0.5\,\text{k}_{\text{lat}}$, with different lattice depths: V_0 = a) $0.4\,\text{E}_{\text{lat}}$; b) $0.8\,\text{E}_{\text{lat}}$; c) $1.2\,\text{E}_{\text{lat}}$ and d) $2.0\,\text{E}_{\text{lat}}$. The density is kept constant and the mean-field term is equal to $gn_0 = 0.067\,\text{E}_{\text{lat}}$ [8]. One recovers similar features as for the method discussed previously just by adding the mean-field contribution. Namely, the phase matching conditions, the critical value q_c and width solutions for beam a and b are qualitatively the same.

[8] This value is extracted from the typical BEC numbers given in Chapter 2, Table 2.6, with $n_0 = \frac{N_{at}}{\frac{4}{3}\pi w_\perp^2(0)L}$ where $w_\perp(0)$ and L are obtained from Ref. [64].

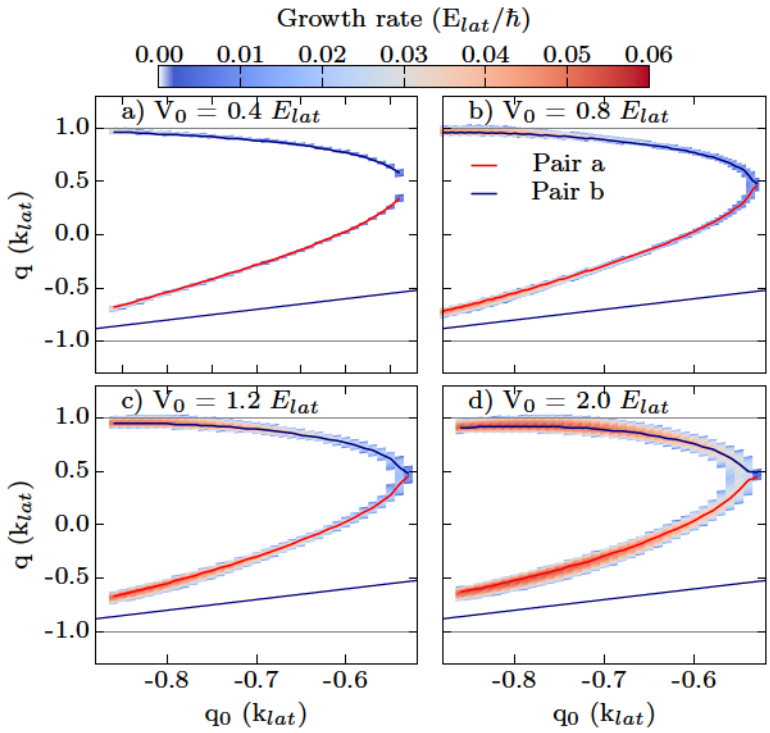

Figure 3.8: Phase matching conditions and growth rate of the pairs following Ref. [154]. Phase matching conditions as a function of the condensate quasi-momentum q_0 for different lattice depths V_0: a) $V_0 = 0.4\,E_{lat}$, b)$V_0 = 0.8\,E_{lat}$, c) $V_0 = 1.2\,E_{lat}$ and d) $V_0 = 2.0\,E_{lat}$. The red line indicates the quasi-momentum associated to beam a while the blue line indicates beam b. The dark blue line corresponds to the BEC quasi-momentum.

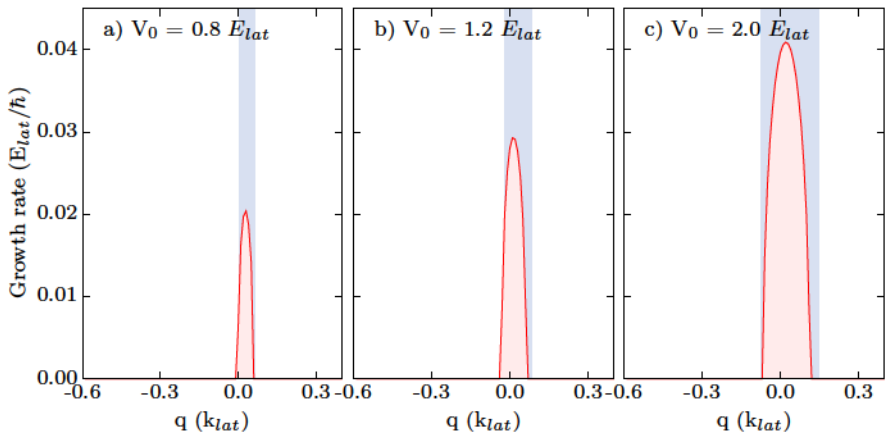

Figure 3.9: Comparison between the width of the atomic beam a for the case of an intuitive addition of the mean-field potential and for the resolution of the Gross-Pitaevskii equation following [154]. The different canvas correspond to lattice depth V_0 equal to: a) $0.8E_{lat}$, b) $1.2E_{lat}$ and c)$2E_{lat}$. The condensate quasi-momentum corresponds to $q_0 = -0.6\,q_{lat}$. One can see that the range of values of q_a that verify the phase-matching condition is equivalent between the two methods.

Comparison between the two methods

The resonance widths are compared in more detail in Fig. 3.9 where the result following the self-consistent solution (red area) is superimposed to the naive solution obtained by adding the mean-field contribution (blue shaded area). Despite a small shift in the upper q branch, both results agree in terms of central phase-matching condition, as well as in terms of the resonance width. The first treatment of the interactions cannot, however, predict the expected growth rate as a function of q_0 and, in this sense, can not explain the shape of the produced pairs.

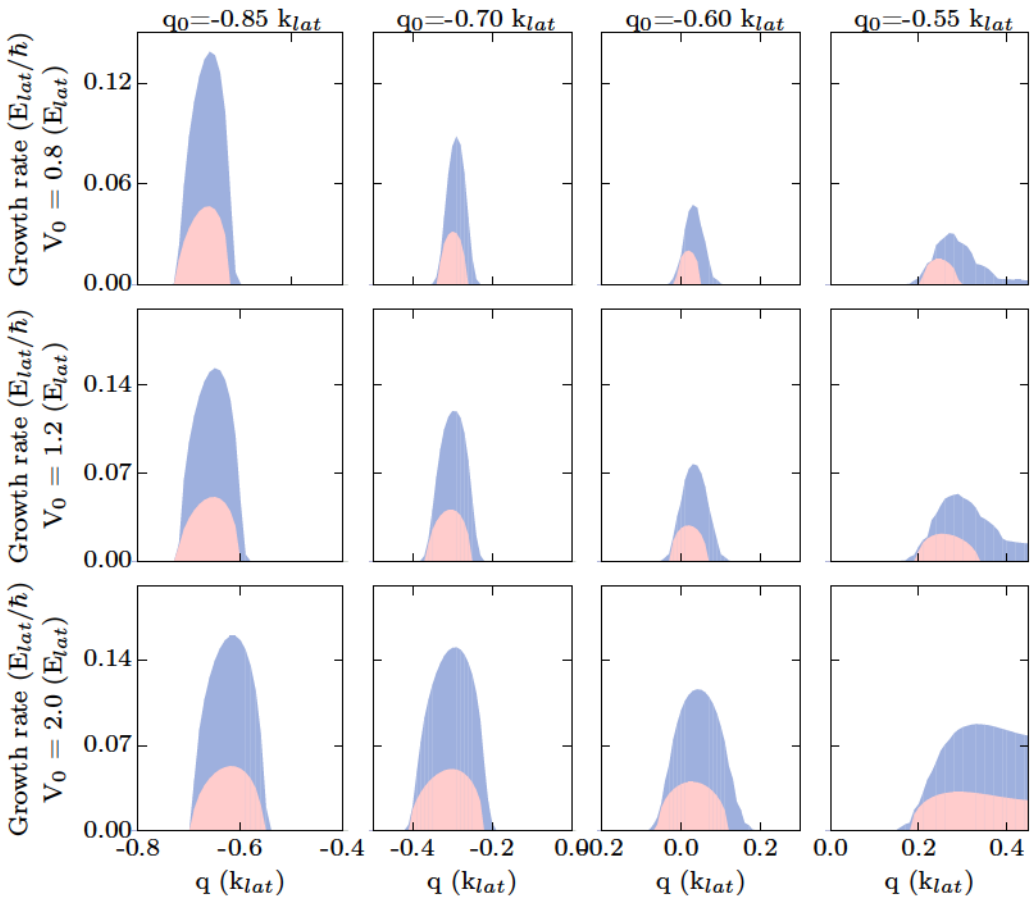

Figure 3.10: Growth rate of the atomic beam a as a function of q. In order to recover the shape of beam a, we assume that the BEC can be decomposed into several plane waves of different quasi-momenta centred around q_0. The result is represented in blue shaded area. This method is compared to the solution obtained for a single plane wave description of the condensate with quasi-momentum q_0, in red.

3.2.2 Atomic beam shape prediction

Following Ref. [154], it is now possible to estimate the shape of the atomic beams. For short lattice application time, such that the exponential growth of the pair is still close to a linear growth, the momentum distribution of the beam is a multiple of the growth rate value as a function of q' [9]. For a longer lattice application time, this is untrue since the process becomes to be seeded and the shape "shrinks" around the maximum eigenvalue. Nonetheless, we will always work in the weakly populated regime where the growth rate distribution gives us enough information about the beam shape.

It is important, however, to point out that since the condensate is represented by a plane wave of quasi-momentum q_0, the gain width does not take into account the initial momentum distribution of the *real* BEC. In order to be able to predict the correct shape of the atomic beams, one needs to take into account the initial momentum spread of the condensate.

The exact wave function of the condensate can be retrieved by solving the time dependent Gross-Pitaevskii equation in imaginary time. For our typical parameters, the density in momentum space can be approximated by a Gaussian of width $\sigma \approx 6 \times 10^{-3} k_{\text{lat}}$. We thus represent the distribution of the condensate as a coherent sum of plane waves convoluted by this Gaussian

[9] The growth rate corresponds to the complex part of the eigenvalue obtained through the solution of the GPE as described previously. The complex part is a function of the perturbation quasi-momentum q' and, consequently, the growth rate also depends on it.

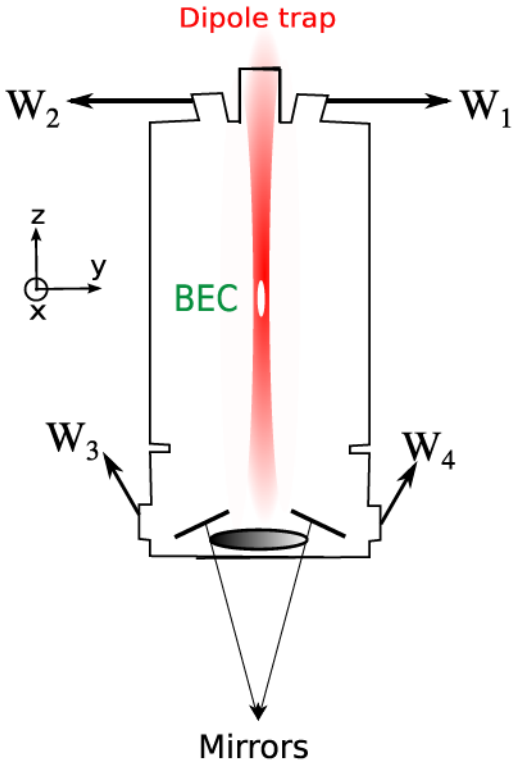

Figure 3.11: Schematic representation of the optical access to the science chamber. W_1, W_2, W_3 and W_4 correspond to the four windows through which the optical lattice can be aligned on the atoms. Two mirrors inside the science chamber guarantee that a laser beam centred on either W_1 or W_2 will exit through W_3 or W_4, respectively.

shape. The atomic beam width can then be estimated through a convolution between the gain at each q centred around q_0 and the width of the initial BEC distribution. As a consequence, one can see an enlargement of beam a as represented in Fig. 3.10 for several lattice depths (from 0.8 to $2\,E_{lat}$ from top to down) and different central BEC quasi-momenta q_0 (from 0.85 to $0.55\,k_{lat}$ from left to right) with, in blue, the realistic growth-rate prediction for the atomic beam a taking into account the BEC momentum distribution and, in red, the growth-rate for a plane wave of quasi-momentum q_0. One can see that for a shallow lattice and a small central quasi-momentum, q_0, the growth-rate of beam a is wider than the central (q_0) growth-rate. In this regime, the dominant contribution for the atomic beam shape comes from the condensate initial momentum distribution. This is precisely the situation in which the pair were obtained in order to achieve the atomic HOM experiment.

In this section, the phase-matching conditions have been discussed. By changing the detuning between the two laser beams, the quasi-momentum of the BEC in the lattice frame of reference is changed and the produced atomic pairs selected. The population of the atomic beams can also be controlled through the lattice application time. This method corresponds then to a very tunable way of producing atomic pairs in momentum space and represents a huge improvement over the control of the atomic pairs production in our experiment.

3.3 Pair creation: experimental realisation

After having briefly described the theoretical steps required to understand the pair creation mechanism, we will now focus on the experimental realisation and analysis of the atomic beams.

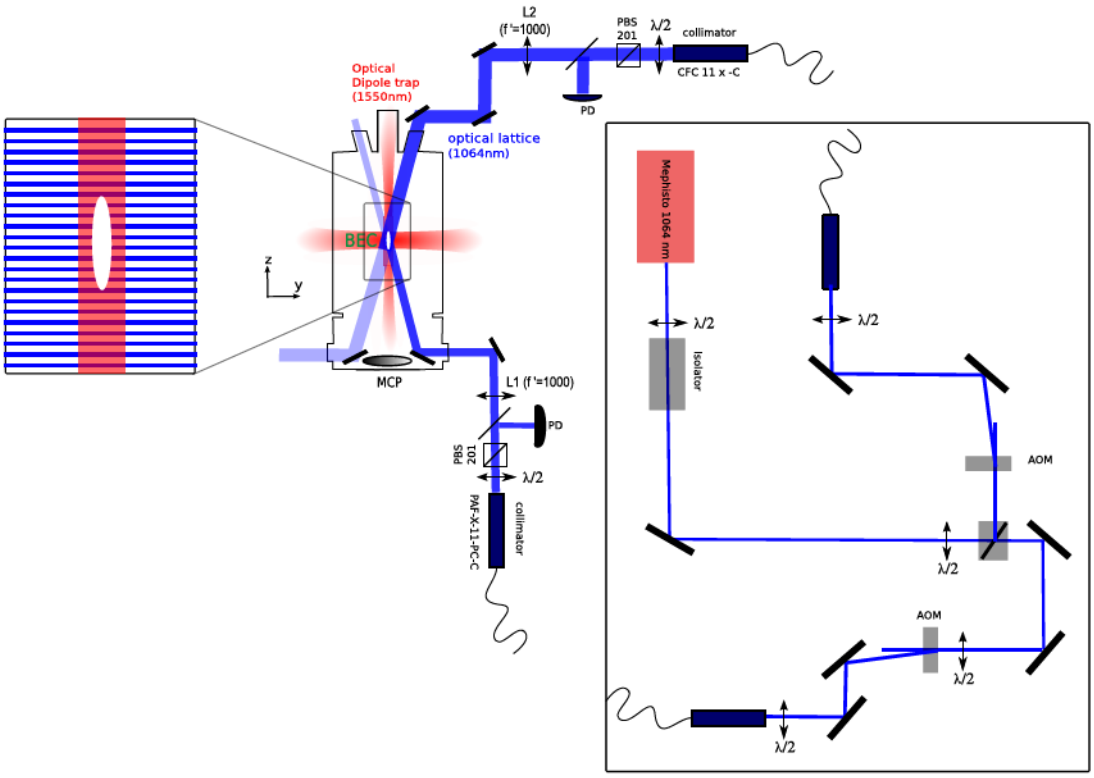

Figure 3.12: Schematics representation of the optical bench for the optical lattice.

The optical lattice consists in two laser beams with wavelength of 1064 nm, see Fig. 3.12. At the beginning of this work, the laser beams formed an angle of 7° degrees with respect to the vertical z−axis. The two beams were then going through the science chamber windows W_2 and W_4 (see Fig. 3.11). Instead, we now use the windows W_1 and W_4 (see Fig. 3.11) to align the lattice along the vertical z−axis. The relative angle between both beams correspond then to $\theta = 2\theta = 166\,°$ and the beam waist is equal to 200 μm for the upward beam and 400 μm for the downward one. [10]

As seen in Section 3.1, by changing the detuning between the two laser beams, δ_{lat}, one can control the speed of the condensate in the lattice frame of reference. For a value of $\delta_{\text{lat}} = 2\pi \times 100.5\,\text{kHz}$ the lattice speed is equal to $-0.57\,\text{v}_{\text{lat}}$ and one produces two atomic beams with momenta $k_a = 0.73\,\text{k}_{\text{lat}}$ and $k_b = 1.27\,\text{k}_{\text{lat}}$, in the laboratory frame of reference. This situation is interesting for performing the HOM experiment as we will explain in Chapter 4.

Effect of vertical alignment

In Fig. 3.13 and Fig. 3.14, the 2D atomic distributions are represented for $\delta_{\text{lat}} = 2\pi \times 100.5\,\text{kHz}$ and $P_{up} = 13\,\text{mW}$ ($V_0 = 0.8\,\text{E}_{\text{lat}}$) in the xz and yz−plane, for the new and old optical lattice alignment, respectively. The old configuration corresponds to an angle of 7° with respect to the vertical z−axis while the new configuration is aligned along the vertical axis. The lattice is kept for 300 μs at its maximum depth and, in both situations, the loading as well as the extinction of the lattice are performed adiabatically.

[10] At the time the new lattice alignment has been performed, no collimator was available to guarantee the same waist on the atoms for both beams. As a temporary solution, the waist of the downward beam was changed to 400 μm which is two times larger than the upward beam. In order to have the same intensity profile on the atoms, the downward beam has four times the power of the upward beam. Since the condensate size is much smaller that the lattice beam waists, the intensity profile is uniform over the condensate.

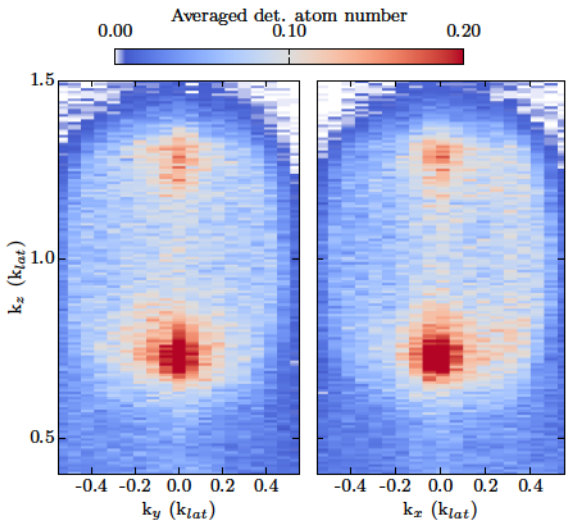

Figure 3.13: Two-dimensional momentum distribution of the atomic pairs obtained in the vertical optical lattice in the laboratory frame of reference. Representation of the $z-y$ momentum distribution of the atomic pairs produced in the optical lattice with the new alignment. Beam a corresponds to the cloud with central momentum $0.73k_{lat}$ and beam b with momentum $1.27k_{lat}$ produced in a moving lattice with velocity equal to $0.57\ v_{lat}$.

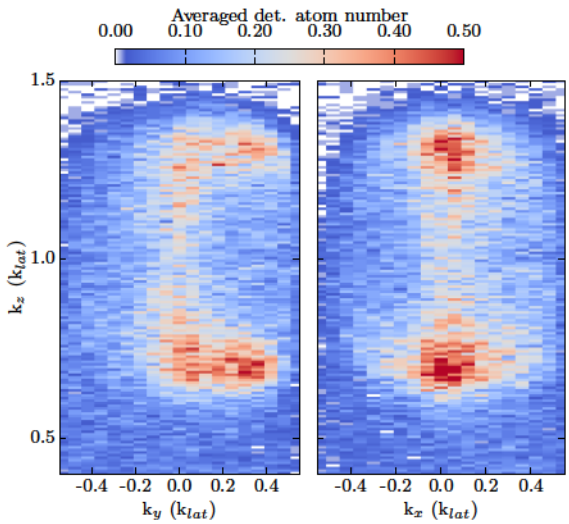

Figure 3.14: Two-dimensional momentum distribution of the atomic pairs obtained in the old optical lattice in the laboratory frame of reference. Pair creation in lattice aligned 7° with regard to the vertical $z-$axis. One can see that along the $y-$axis the shape of the pairs is no longer centred on zero and follow the inclination of the optical lattice.

In the case of the old geometry, as one can see in Fig. 3.14, the atomic beams are no-longer centred transversally around $\{x,\ y\} = \{0,\ 0\}$ but are asymmetric along the $y-$axis corresponding to the inclination of the lattice. With the new alignment this feature disappears [108, 141, 142]. This change is crucial in order to guarantee a good spatial overlap of the two atomic beams in the HOM experiment as it will be discussed in Chapter 5.

3.3.1 Geometrical alignment

The lattice alignment is based on the repulsive dipole potential of each lattice beam. One turns on each laser beam individually, for 100 μs, on the atoms after switching off the dipole trap. Since the lattice beams are blue detuned, the light induces a repulsive dipole force on the atoms that are now falling due to gravity. Since the lattice beams are almost aligned along the vertical axis, the atoms feel a strong repulsive potential lying beneath them and are, consequently, repelled transversally. After a long time-of-flight of 308 ms, the repulsive dipole force translates into a hole in the 2D $xy-$plane density distribution, see Fig. 3.15.

Fig. 3.15 shows the obtained results for the upward (Fig. 3.15 a)) and downward (Fig. 3.15 b)) lattice beams. The hole in the transverse distribution corresponds to the repulsive potential of the lattice beam which is centred on the atomic cloud. A good alignment would correspond to an almost symmetric ring as seen in the figure.

3.3.2 Loading procedure of the 1D lattice

In order to adiabatically load the BEC in the lattice, the intensity of the laser beams has to be ramped slowly over a time T. [11] The minimal value of T for atoms at different quasi-momenta

[11] We consider a linear ramp, although this is not the optimised situation as reported in Ref. [178].

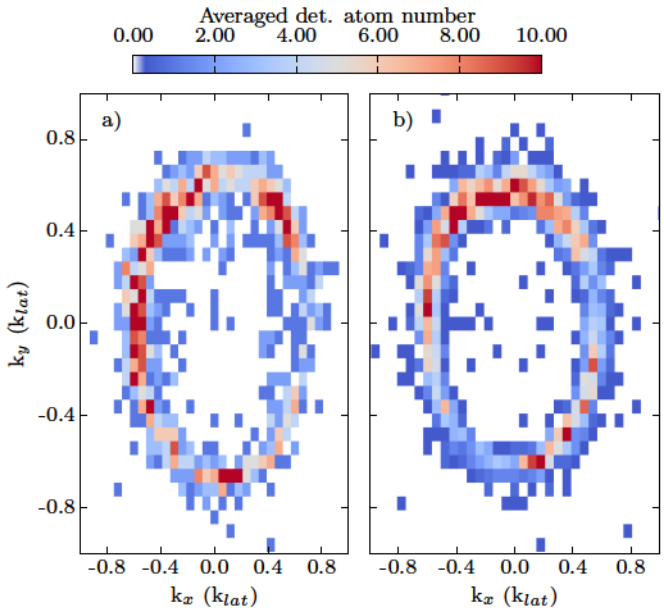

***Figure 3.15:** Alignment of the optical lattice beams on the condensate. Geometrical alignment of the lattice beams by applying each beam independently on the condensate. Since the laser is blue detuned, the light creates a repulsive potential. The atoms are then repelled at the intensity maximum giving raise to an halo after time-of-flight. Alignment effect for: a) the upward lattice beam, b) downward lattice beam.*

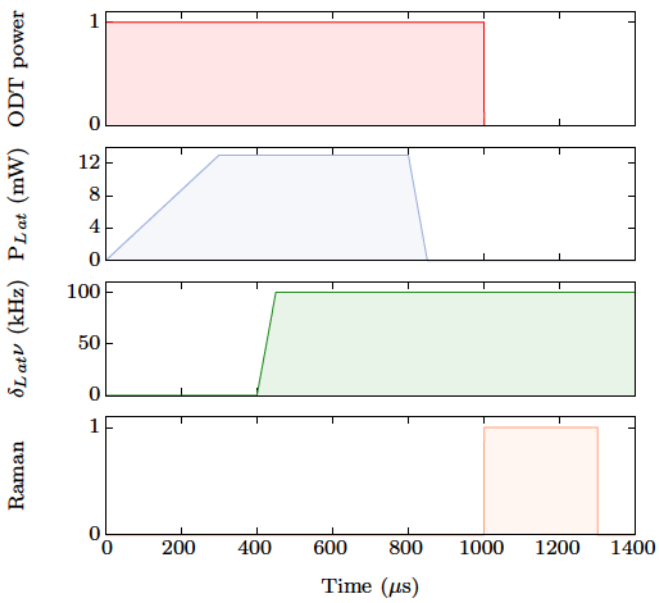

***Figure 3.16:** Loading procedure of the optical lattice. From top to bottom. In red, we represent the optical trap power as a function of time. In blue, the lattice depth is represented as a function of time. One can see the adiabatic loading performed in 300 μs and the adiabatic extinction in 50 μs. The two lattice beams detuning is then represented in green. One can see the adiabatic acceleration of the lattice once the lattice depth has reached its maximum value. Finally, in orange, the stimulated two-photon Raman scattering process is represented. This is performed in order to transfer the atoms from the state $m_j = 1$ to the insensitive magnetic field state $m_j = 0$.*

and lattice depth was discussed in Subsection 3.1.3. For a condensate with quasi-momentum $q = -0.57\,\mathrm{q_{lat}}$, which is the case considered here, the condition $T \gg 1\,\mu$s has to be verified.

The procedure is done, as represented in Fig. 3.16, by first ramping up the lattice depth from 0 to $V_0 = 0.8E_{\mathrm{lat}}$ in 300 μs. During this time, the lattice speed is kept at zero so that the BEC

is kept at rest inside the dipole trap. After reaching the maximum value of V_0, the lattice is accelerated from 0 to $0.57\,\mathrm{v_{lat}}$ in $50\,\mu$s. The condensate is afterwards modulated by the optical lattice potential for $350\,\mu$s and undergoes spontaneous pair production.

After this time the pair creation process starts to be slightly seeded by the first produced atoms. For the HOM experiment it is required that the averaged number of atoms remains as low as possible. It is then essential to stop the process as quickly as possible. This means, however, to extinct the lattice abruptly which can lead to diffraction. The adopted procedure is to lower the lattice depth with a linear ramp from the maximum value V_0 to 0 in $50\,\mu$s. This time is sufficient to guarantee that the atoms in beam b, that lie close to the boundary of the 1st Brillouin zone, do not undergo Bragg diffraction (for $q_b = 0.72\,\mathrm{k_{lat}}$, the condition $T \gg 4\,\mu$s is verified). On the other hand, the time is sufficiently short to guarantee that the averaged pair population does not growth during the adiabatic extinction of the lattice.

Experimentally, the adiabaticity of the loading process is checked by a band mapping technique [179]. The test consists in turning off the lattice in the same manner as it was turned on. If the atoms have been transferred to higher energy bands, than they will be projected to Brillouin zones once the lattice is turned off. This can be checked by looking at the populations at $k_0 \pm 2nk_{\mathrm{lat}}$. In our case, no diffraction is visible for the loading ramp. For the extinction ramp, less than 0.02 % of the initial BEC population is transferred to $k_0 + 2k_{\mathrm{lat}}$ and no visible diffraction of the pairs is recovered.

The pair production time can then be estimated as

$$T_{\mathrm{prod.}} = [\text{Time of the moving lattice at full power}] - [\text{acceleration time of the lattice}] = 350\mu\mathrm{s}.$$

This is sufficient to guarantee an average population of the pairs around $20-40$ in each beam. By taking into account the MCP detection efficiency of 25 % this leads to approximatively $5-10$ detected atoms on average.

3.3.3 Atomic pair production

As described in Section 3.2, it is possible to theoretically predict the distribution in momentum space of the atomic beams. The experimental density profile is then compared to the predicted one in Fig. 3.17 where we represent, in blue, the experimental density profile and, in red, the theoretical prediction with an adjusted growth time in order to fit the amplitude of the atomic beam a. The description of the atomic beam width due to the momentum distribution of the BEC agrees well with the experimental observation. However, two important discrepancies are noticed.

- First there is a background noise between the two atomic beams that is not fully described by the theoretical model. This background can eventually be explained by energetic instabilities, since the pairs are moving above the speed of sound of the condensate ($c = 0.24\,\mathrm{v_{lat}}$ with c the speed of sound, see Appendix A) [189, 193, 196]. This would lead to collisions between the pairs and the condensate and possibly explain this background population.

- Second, there is an anisotropy between the population of the clouds a and b. The theoretical model is based on a Hamiltonian closely related to parametric down-conversion process which gives raise to a symmetric population between the two beams, see Eq. (3.17). However, since beam b has a quasi-momentum above the threshold limit value (q_c) for dynamical instability it can lead to secondary four-wave mixing events. This effect should, in principle, be negligible since beam b is very dilute. However, four-wave mixing

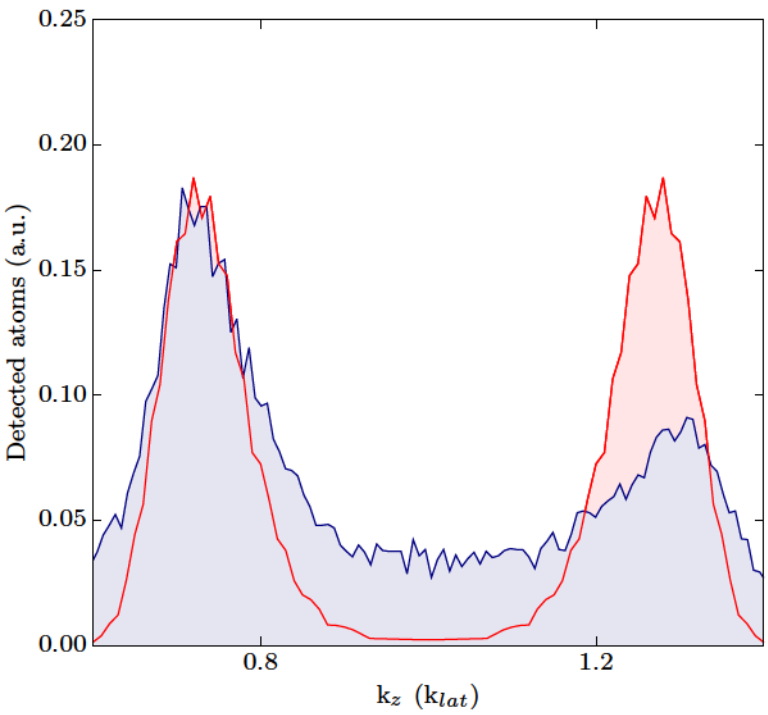

Figure 3.17: ***Density profile of beams a and b, experimental result and theoretical predictions.*** *The theoretical prediction for the atomic beams shape as a function of the momentum k in the laboratory frame of reference (red shaded area) is compared to the experimental density profile (blue shaded area). The lattice depth is $V_0 = 0.8E_{lat}$ and the lattice is moving at $-0.57v_{lat}$. The amplitude of the theoretical prediction is adjusted to the experimental profile corresponding then to a fitting parameter.*

processes triggered by an atom from the BEC and an atom from cloud b can happen. This would result in losses from beam b.

The population difference between the two atomic beams have also been reported in the experiment of W. Ketterle's group [105] and, in this sense, we believe that it must correspond to a physical process rather than an experimental artefact. Further tests are being performed in order to understand this discrepancy between the two beams. In particular we are interested in study the dependence of the atomic beam population difference as a function of the speed of sound in the BEC and as a function of beam b quasi-momentum.

In Fig. 3.18 are represented the density profiles along the longitudinal $z-$axis (left panel) of the condensate and the atomic pairs for the case of an initial quasi-momentum $q_0 = -0.57\,\mathrm{q_{lat}}$ and a lattice depth $V_0 = 0.8\,\mathrm{E_{lat}}$. Since the condensate saturates completely the MCP, no information can be extracted from its transverse profile. The transverse 2D distribution of both beams a and b is also shown. One can see that the two clouds present *shoulders* (right panel) which indicates that pairs are also created in excited transverse modes. Those are not dominant since their growth rate is much weaker than the fundamental mode as discussed in more detail in Ref. [141], page 81.

3.3.4 Evolution of the pairs in the trapping potential

The three clouds of different quasi-momenta (the BEC at q_0, beam a at q_a and beam b at q_b) evolve in a potential formed by the dipole trap and the lattice. Although the trapping potential has always been neglected in the 1D theoretical treatment presented so far, it plays an important role on the time evolution of the pairs. The BEC is, in the laboratory frame of reference, always

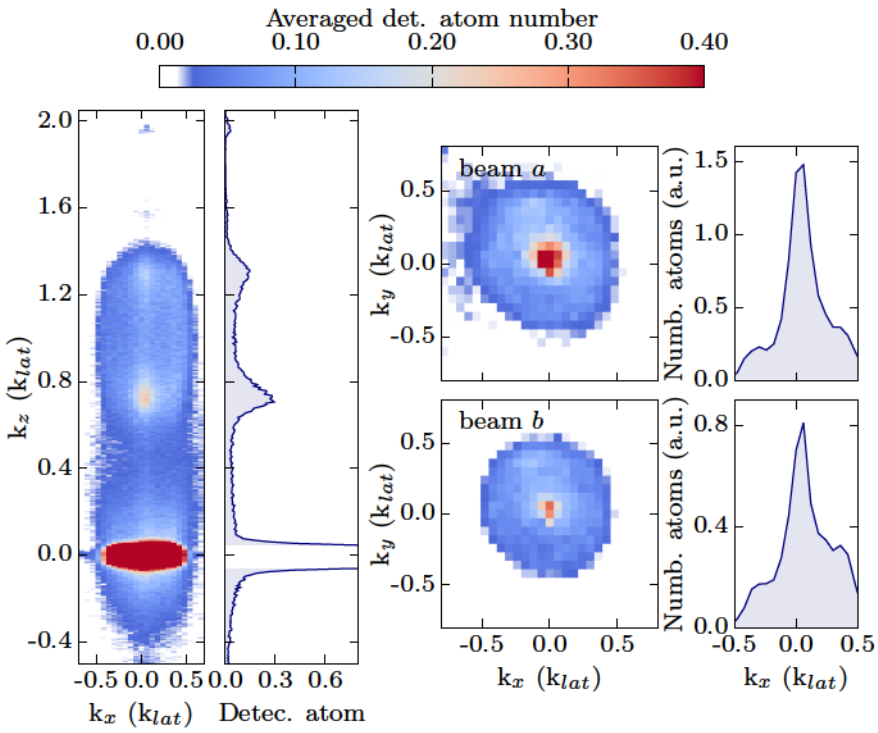

Figure 3.18: Density profiles of the atomic pairs in the case of the HOM-experimental realisation before application of the beam-splitter From left to right: 2D momentum distribution of the atoms in the xz−plane. The condensate saturates the detector and, as a consequence, its width along the x−axis has no physical meaning. The pairs appear with momenta $k_a = 0.73\,k_{lat}$ and $k_b = 1.27\,k_{lat}$. We also represent a 2D momentum distribution in the xy−plane for beam a (upper panel) and beam b (bottom panel). The integration length along the vertical z−axis is equal to $0.01\,k_{lat}$ and centred on $k_a = 0.73\,k_{lat}$ and on $k_b = 1.27\,k_{lat}$, respectively. Finally, we show the cut along the x−axis of the 2D momentum distribution on xy−plane for both beam a (upper panel) and beam b (bottom panel). The cut corresponds to an integration length along the y−axis equal to $0.05\,k_{lat}$.

at rest and does not explore spatially the trapping region, however, the same can not be said for the pairs.

The atomic beams have a finite speed in the laboratory frame of reference and thus can move. One important point is their position when the optical trap is switched off. If they did not leave the maximum density region of the BEC, their expansion, once the trap is switched off, can be strongly perturbed by the mean-field potential. Moreover, since the speed of the two atomic beams are different, the effect of the mean-field potential is going to affect them differently. This represents a huge experimental difficulty in order to achieve the HOM experiment since the particles have to be well mode matched when overlapped.

Experimental observation of the spatial shape deformation

The lattice is adiabatically switched on and kept at its maximum power for 400 μs. The experiment is performed for a lattice depth of $0.8\,E_{lat}$ and speed $v_{lat} = 0.77\,v_{lat}$ which leads to the production of cloud a with momentum, in the laboratory frame of reference, equal to $0.31\,k_{lat}$. After switching off the lattice, the cloud is kept in the dipole trap for a certain waiting time (τ_w), after which the dipole trap is switched off in less than a microsecond. The atoms expand and their longitudinal as well as transverse velocities components are recovered after time-of-flight. The momentum distribution of cloud a, in the xy−plane is shown in Fig. 3.19. It is possible to notice a *hole* in the transverse distribution for waiting times lower than 50 μs. For longer τ_w, the expected transverse Gaussian shape is recovered as discussed in Ref. [141].

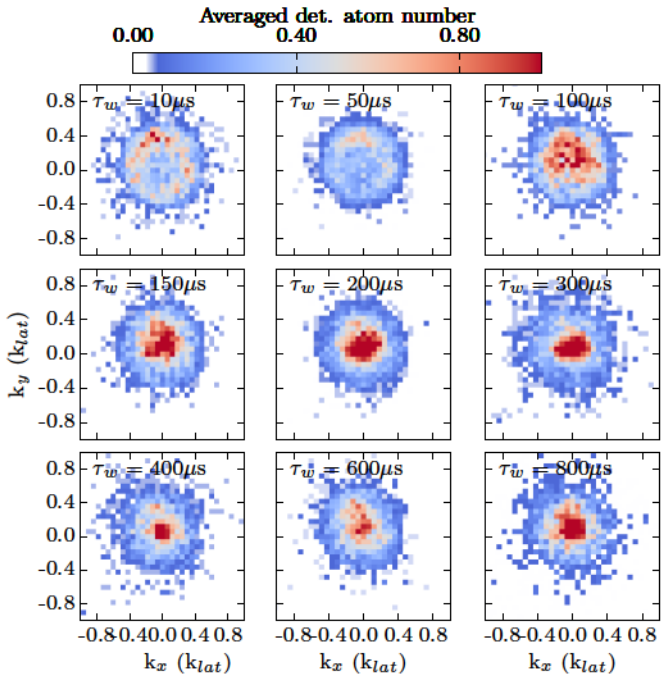

Figure 3.19: Transverse shape of the atomic beam a as a function of the holding time in the optical dipole trap. For the first panels, a hole appears in the transverse shape of beam a which tends to disappear for longer holding times τ_w.Each panel corresponds to a 2D momentum distribution in the xy−plane.

Mathematical description of the problem

One possible explanation for the spatial shape deformation, would be that if beam a is superposed to the condensate when the trap is switched off, then the cloud would feel a very strong repulsive potential beneath it. That would translate into a repulsive transverse force and, after time-of-flight, this would lead to the formation of a hole on the horizontal plane. In order to test this assumption, let us look at the atomic beams dynamics. Two distinct situation are to be considered.

First, one has to consider the atomic beam displacement in the optical potential formed by the dipole trap and the periodic optical lattice. This corresponds to the first instants after production of the first atomic pairs. The particle evolution equations are then given by [186]

$$\hbar \frac{d^2 q}{dt^2} = -\frac{\partial V(0,0,z)}{\partial z} \tag{3.29a}$$

$$\frac{dz}{dt} = \frac{1}{\hbar}\frac{\partial E(q)}{\partial q} - v_{\text{lat}}, \tag{3.29b}$$

where v_{lat} corresponds to the speed of the lattice and the dipole potential is taken at $\{x, y\} = \{0, 0\}$. It is important to note that the atom spatial evolution depends on the group velocity given by $\frac{1}{\hbar}\frac{\partial E}{\partial q}$.

Consider the case of a weak lattice and a BEC quasi-momentum equal to $-0.77\,\text{k}_{\text{lat}}$. This corresponds to the produced atomic beams represented in Fig. 3.19 where the hole has been identified, with beam $q_a = -0.46\,k_{\text{lat}}$ and $q_b = 0.92\,q_{\text{lat}}$, in the lattice frame of reference. Since beam a is moving slower than beam b with respect to the condensate, the effect of the interactions will be maximally felt on beam a. In order to determine the spatial displacement of the atomic beam, one needs to evaluate the time after which the first pairs have been produced. We experimentally estimated that the first produced pairs are generated, for the current value of

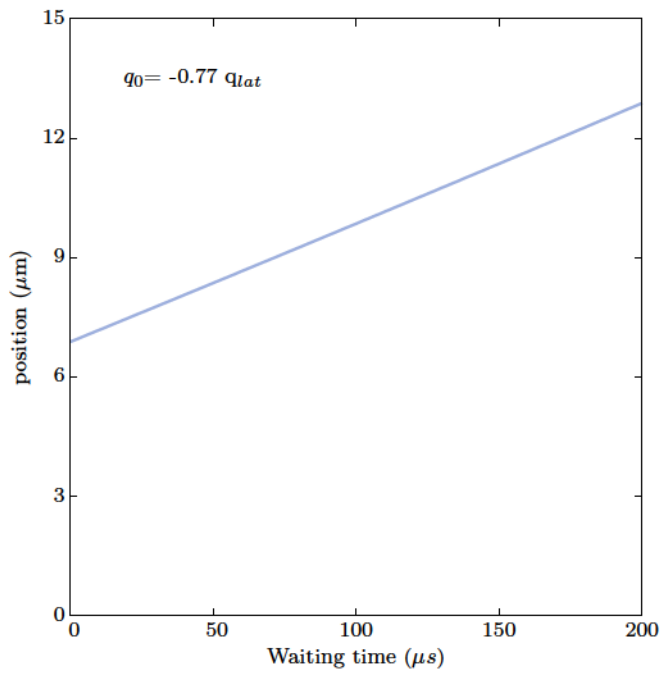

Figure 3.20: Central position of beam a as a function of the holding time τ_w . The experimental situation corresponds to a lattice depth $V_0 = 0.8\,E_{lat}$ and a condensate quasi-momentum, in the lattice frame of reference, equal to $q_0 = -0.77\,v_{lat}$. This is related to the observation made in Fig. 3.19

q_0, after approximatively 200 μs and, since the lattice application time is equal to 400 μs, this means that the pairs are travelling for 200 μs in an optical potential formed by both an optical lattice and a dipole trap. From Eq. (3.29b), we recover a spatial displacement for beam a equal to 7 μm. This means that at the time the lattice is switched off, beam a has already moved 7 μm.

The second situation corresponds to the evolution of the atomic cloud in the dipole trap alone. The equations of position and momentum correspond then to the evolution of a particle in a quasi-harmonic potential.

In Fig. 3.20, one shows the evolution of the central position of beam a, from the initial position of 7 μm, when the lattice has been extinct to the final position of the particle, after $\tau_w = 200\,\mu$s, equal to 13 μm. When compared to the Thomas-Fermi radius of the condensate, approximatively equal to 60 μm, one concludes that beam a is still deeply inside the condensate. This means that the observed behaviour as a function of the waiting time, τ_w, reported in Fig. 3.19 cannot be understand through a simple spatial argument.

Another experiment provides more insight in this observation. In this experimental sequence, after producing the pairs via dynamical instabilities, we change the lattice speed in order to, via Bragg diffraction (see Chapter 4), accelerate the beam a. The atoms with initial momentum k_a are transferred to a momentum $k_a + 2k_{\text{lat}}$. The dipole trap is then immediately switched off, such that the atoms did not have enough time to significantly move. We then compare the situation with and without Bragg diffraction as shown in Fig. 3.21 and Fig. 3.22, respectively. One can see that for the situation in which beam a is not diffracted, a hole is noticeable in the 2D atomic distribution and disappears when the beam is diffracted, showing that the speed of the cloud during the expansion plays an important role. We also notice a shrink in the transverse distribution of beam b.

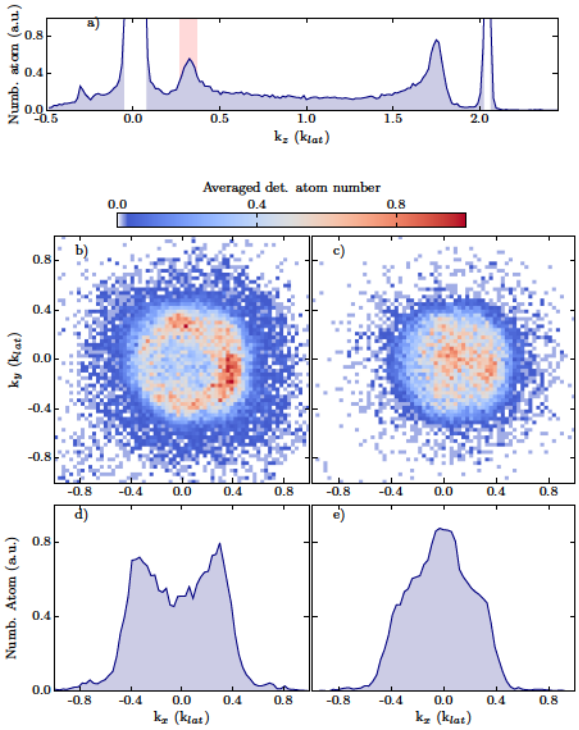

Figure 3.21: *Effect of the initial speed on the transverse shape of beam a. a) Vertical density representation with cloud a at $k_a = 0.31\,k_{lat}$ in the laboratory frame of reference and cloud b at $1.72\,k_{lat}$. Bragg diffraction from the condensate at $k = 2k_{lat}$ is visible due to the fact that the lattice is non-adiabatically switched off. b) Transverse profile of beam a. One can see that the cloud present a hole in the transverse plane. The cut along the x−axis represented in d) allow us to visualise more clearly the effect. c) Transverse profile of beam b. No structure similar to beam a is visible. This is, once more, easier to observe through the cut along the x−axis represented in e).*

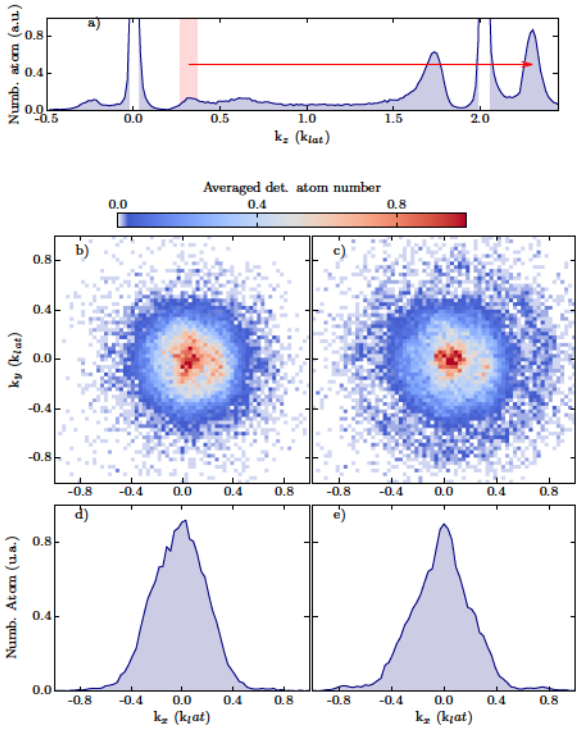

Figure 3.22: *Effect of the initial speed on the transverse shape of beam a after being Bragg diffracted. Beam a is diffracted just after being produced and the dipole trap is immediately switched off afterwards. a) Density profile of the clouds along the vertical direction. The initial momentum of beam a is represented by the red box. The arrow line indicates the diffraction performed. Beam a has now an initial momentum higher than beam b. Bragg diffraction from the condensate is also noticeable at $k = 2k_{lat}$. b) 2D density profile on the xy horizontal plane centred on cloud a. The hole in Fig. 3.21 is no longer present has it is possible to check via the cut along the x−axis represented in d). c) 2D density profile on the xy−plane centred on cloud b. The cloud gets thinner when compared to the situation of Fig. 3.21 but has still a similar shape.*

The formation of a hole in the transverse density profile of beam *a*, after time-of-flight, is still an open question that needs to be further investigated. The explanation based on the spatial overlap between beam *a* and the condensate cannot explain entirely our observation. From Fig. 3.21 and Fig. 3.22, we conclude that the initial speed of the atoms plays an important role, and that atoms with higher velocities will be less disturbed. Since the situation of interest for the HOM experiment corresponds to a beam *a* with higher vertical velocity than the one studied here, one can expect a negligible effect. Nevertheless, in order to avoid any possible distortion of the cloud, we will, for the HOM experimental sequence, wait for 200 μs before releasing the atoms from the optical dipole trap (see Chapter 5).

With these results in mind, one can now investigate the correlation properties of the pairs and their interest for the realisation of quantum atom experiments.

3.4 Correlated pairs of atoms: analysis

In order to use the atomic pairs for the HOM scheme, one needs to guarantee that the momentum difference between the two atomic beams is equal to the momentum transfer of the beam-splitter. As it will be explain in Chapter 4 due to the limiting optical access of our science chamber the beam-splitter momentum transfer corresponds to $\Delta k = 0.55 k_{\text{lat}}$. The pairs are then produced with a momentum difference equal to $0.55\,\text{k}_{\text{lat}}$ as represented in Fig. 3.18. This is achieved by loading the condensate in a moving lattice with speed $v_0 = 0.57\,\text{v}_{\text{lat}}$. The two atomic beams, a and b, are then centred around momenta $k_a = 0.73\,(1)\ \text{k}_{\text{lat}}$ and $k_b = 1.27\,(2)\ \text{k}_{\text{lat}}$, respectively.

3.4.1 Cross-correlation and autocorrelation

The main interest of a non-linear process as four-wave mixing is the ability to transform a classical state (a coherent state for instance) in a strongly, quantum, correlated state due to the non-linearities of the system. This non-classical characteristics can be quantified via non-local correlations, variance reduction below shot-noise and entanglement. Following the well known results for parametric down conversion [13], in this section, the study of correlation measurement is applied to our atomic pairs.

The parametric down-conversion Hamiltonian given by Eq. (3.13) leads to multimode state described by

$$|\psi(t)\rangle = e^{-i\hat{H}t/\hbar}|0\rangle\,,$$

with

$$\hat{H} = \sum_l \hat{H}_{0,l} + \sum_l \hbar\kappa\sqrt{N_{p_1}}\sqrt{N_{p_2}}\left(\hat{a}^\dagger_{s,l}\hat{a}^\dagger_{i,l} + c.c.\right).$$

In order to determine the mode size, we compare the two-body autocorrelation function to the density distribution [108].

Autocorrelation function: mode characterization

For a two mode state corresponding to

$$|\psi\rangle = \sum_n \frac{\tanh^n(\lambda)}{\cosh(\lambda)}|n,\,n\rangle_{a,b} \tag{3.30}$$

where λ is related to the averaged number of particles per mode, through the relation $\langle n\rangle = \sinh^2(\lambda)$, the autocorrelation can be written as

$$\begin{aligned} g^{(2)}_{aa} &= \frac{\langle\hat{a}^\dagger\hat{a}^\dagger\hat{a}\,\hat{a}\rangle}{\langle\hat{a}^\dagger\hat{a}\rangle\langle\hat{a}^\dagger\hat{a}\rangle} \\ &= \frac{1}{8\cosh^2(\lambda)\sinh^4(\lambda)}\left[8\sinh^2(\lambda)\cosh^2(\lambda)\left(2\sinh^2(\lambda)\right)\right] \\ &= 2. \end{aligned} \tag{3.31}$$

If the source is multimode, the autocorrelation function

$$g^{(2)}_{aa}(\mathbf{k}, \Delta\mathbf{k} + \mathbf{k})$$

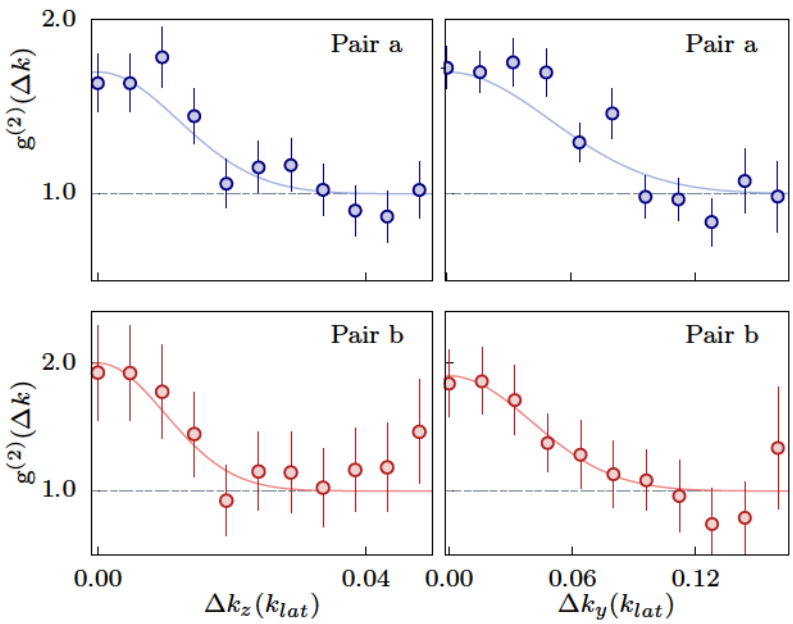

Figure 3.23: 2nd order autocorrelation function for both beams a and b. Left panels: Projection of the 2nd order autocorrelation function along the longitudinal z−axis for both atomic beams. The area of integration is equal to $\Omega_2 = \left[\mathcal{L}_x \times \mathcal{L}_y\right] = [2\times10^{-2}]^2\ \mathrm{k}_{lat}^2$. *Right panels: Projection of the 2nd order autocorrelation function along the transverse y−axis (the same shape is recovered along the x−axis) for both atomic beams. The integration area is equal to* $\Omega_1 = [\mathcal{L}_x \times \mathcal{L}_z] = [2\times10^{-2}\times1\times10^{-2}]\ \mathrm{k}_{lat}^2$.

is no longer flat but evolves with the momentum difference, Δk, where $\Delta\mathbf{k} = \mathbf{k}-\mathbf{k}'$ with $\mathbf{k}$ and $\mathbf{k}'$ corresponding to momenta vector of two atoms in the same atomic beam. The autocorrelation function will reach the maximum value of 2 in the central region and decreases to 1 when $\Delta\mathbf{k}$ is larger than the mode size.

Since several atoms with different momenta are produced, it is preferable, in order to maximise the signal to noise ratio of the autocorrelation function, to integrate over $\mathbf{k}$ in a volume Ω_V comparable to the atomic beam momentum spread. The 3D autocorrelation function corresponds then to

$$g_{aa}^{(2)}(\Delta k_x,\,\Delta k_y,\,\Delta k_z) = \int_{\Omega_V} d^3\mathbf{k}\,\frac{\langle :\hat{n}(\mathbf{k})\hat{n}(\mathbf{k}+\Delta\mathbf{k}):\rangle}{\langle\hat{n}(\mathbf{k})\rangle\,\langle\hat{n}(\mathbf{k}+\Delta\mathbf{k})\rangle}\,, \tag{3.32}$$

which is projected into the longitudinal axis (z) and one of the transverse axis (y) by integration over an area, Ω_1 and Ω_2 small when compared to the autocorrelation cross section area. The autocorrelation projections are then given by

$$\begin{aligned} g_{aa}^{(2)}(\Delta k_z) &= \int_{\Omega_1} d\Delta k_x d\Delta k_y \int_{\Omega_V} d^3\mathbf{k}\frac{\langle :\hat{n}(\mathbf{k})\hat{n}(\mathbf{k}+\Delta\mathbf{k}):\rangle}{\langle\hat{n}(\mathbf{k})\rangle\,\langle\hat{n}(\mathbf{k}+\Delta\mathbf{k})\rangle}\,,\\ g_{aa}^{(2)}(\Delta k_y) &= \int_{\Omega_2} d\Delta k_x d\Delta k_z \int_{\Omega_V} d^3\mathbf{k}\frac{\langle :\hat{n}(\mathbf{k})\hat{n}(\mathbf{k}+\Delta\mathbf{k}):\rangle}{\langle\hat{n}(\mathbf{k})\rangle\,\langle\hat{n}(\mathbf{k}+\Delta\mathbf{k})\rangle}\,, \end{aligned} \tag{3.33}$$

where $\langle : :\rangle$ corresponds to the normal ordering average and the integration surfaces are equal to

$$\begin{aligned} \Omega_1 &= \left[\mathcal{L}_x \times \mathcal{L}_y\right] = \left[2\times10^{-2}\right]^2\ \mathrm{k}_{\mathrm{lat}}^2\,,\\ \Omega_2 &= [\mathcal{L}_x \times \mathcal{L}_z] = \left[2\times10^{-2}\times1\times10^{-2}\right]\mathrm{k}_{\mathrm{lat}}^2\,. \end{aligned}$$

	Local	
	Cloud a	**Cloud** b
$\sigma_{z,l}$ (k_{lat})	0.012 (2)	0.010 (2)
$\sigma_{y,l}$ (k_{lat})	0.05 (1)	0.04 (2)
$A_{l,z}$	0.70 (5)	1.00 (5)
$A_{l,y}$	0.70 (5)	0.90 (5)

Table 3.1: *Autocorrelation fitting parameters for beams a and b. Summary of the fitting parameters of Eq. (3.35) applied to the projections of the 2nd order correlation function along the longitudinal z−axis and transverse x−axis represented in Fig. 3.23.*

The autocorrelation function for both clouds are computed and displayed in Fig. 3.23. The solid lines represent an empirical Gaussian fit given by

$$g^{(2)}_{aa}(\Delta k_z) = A_{lz} \exp\left(-\frac{z^2}{2\sigma^2_{z,l}}\right) + 1\,, \tag{3.34}$$

$$g^{(2)}_{aa}(\Delta k_y) = A_{ly} \exp\left(-\frac{y^2}{2\sigma^2_{y,l}}\right) + 1\,. \tag{3.35}$$

Those fits are used in order to determine both the maximum amplitude correlation and the correlation width defined as the half-width at $1/\sqrt{e}$. The resulting fitting parameters are summarised in Table 3.1. One can see that the amplitudes differ and are equal to 1.00 (5) , for beam b, and 0.70 (5) , for beam a. This difference is probably due to the background population which can affect differently the two clouds or to the losses associated to beam b.

The two atomic beams show the same autocorrelation width inside the confidence interval given by the standard deviation. The mode size, in both transverse and longitudinal axis, is attributed to the autocorrelation width and the number of modes is deduced from the ratio between the density width and the autocorrelation width.

Estimation of the number of modes

The widths of the atomic beams distributions are retrieved by fitting the density profile by an empirical Gaussian function. For the two clouds, the half-width at $1/\sqrt{e}$ corresponds to

$$\sigma_{n(k)z} = 0.06\,(1)\ k_{lat},$$
$$\sigma_{n(k)\perp} = 0.08\,(1)\ k_{lat}.$$

Performing the ratio between these values and those of the autocorrelation function, one can estimate the number of modes in each atomic beam to be

$$n_{\text{mode},z} = \frac{\sigma_{n(k)z}}{\sigma_{z,l}} = 4-8\,,$$
$$n_{\text{mode},\perp} = \frac{\sigma_{n(k)\perp}}{\sigma_{z,\perp}} = 1-2\,.$$

We thus conclude that each cloud has, roughly, between 4 to 32 modes. Furthermore, knowing that the total number of atoms in each atomic beam is estimated around $10-30$, one estimate that the number of atoms per mode is in between 0.3 and 8. Although this technique only gives a rough estimation of the number of modes it allows one to predict the order of magnitude for the mode occupation in our system.

Cross-correlation function: pair production

In the same way as we did for the autocorrelation function, one can define the cross-correlation function between atoms with momenta $\mathbf{k}_a$ and $\mathbf{k}_b+\Delta\mathbf{k}$ verifying phase-matching conditions [12]. For the case of a two-mode state produced through spontaneous parametric down-conversion the cross-correlation is given by

$$\begin{aligned} g^{(2)}_{ab} &= \frac{\langle \hat{a}^\dagger \hat{b}^\dagger \hat{a}\, \hat{b}\rangle}{\langle \hat{a}^\dagger \hat{a}\rangle \langle \hat{b}^\dagger\, \hat{b}\rangle} \\ &= \frac{1}{8\cosh^2(\lambda)\sinh^4(\lambda)}\left[8\sinh^2(\lambda)\cosh^2(\lambda)\left(1+2\sinh^2(\lambda)\right)\right] \\ &= 2+\frac{1}{\langle n\rangle}. \end{aligned} \tag{3.36}$$

When $\langle n\rangle \to \infty$, the cross-correlation amplitude tends to the autocorrelation amplitude of 2, and in contrast, when the mode occupation is reduced, $g^{(2)}_{ab}$ increases.

The cross-correlation function is then given by

$$g^{(2)}_{ab}(\Delta k_x,\, \Delta k_y,\, \Delta k_z) = \int_{\Omega_{V_a}} d^3\mathbf{k}_a \int_{\Omega_{V_b}} d^3\mathbf{k}_b \frac{\langle :\hat{n}(\mathbf{k}_a)\hat{n}(\mathbf{k}_b+\Delta\mathbf{k}):\rangle}{\langle \hat{n}(\mathbf{k}_a)\rangle\, \langle \hat{n}(\mathbf{k}_b+\Delta\mathbf{k})\rangle}\,, \tag{3.37}$$

which is projected into the longitudinal axis (z) and one of the transverse axis (y) by integration over the surface, $\Omega_{1'}$ and $\Omega_{2'}$, that are small when compared to the cross-correlation cross section. The projections are the written as

$$\begin{aligned} g^{(2)}_{ab}(\Delta k_z) &= \int_{\Omega'_1} d\Delta k_x d\Delta k_y \int_{\Omega_{V_a}} d^3\mathbf{k}_a \int_{\Omega_{V_b}} d^3\mathbf{k}_b \frac{\langle :\hat{n}(\mathbf{k}_a)\hat{n}(\mathbf{k}_b+\Delta\mathbf{k}):\rangle}{\langle \hat{n}(\mathbf{k}_a)\rangle\, \langle \hat{n}(\mathbf{k}_b+\Delta\mathbf{k})\rangle}\,, \\ g^{(2)}_{ab}(\Delta k_y) &= \int_{\Omega'_2} d\Delta k_x d\Delta k_z \int_{\Omega_{V_a}} d^3\mathbf{k}_a \int_{\Omega_{V_b}} d^3\mathbf{k}_b \frac{\langle :\hat{n}(\mathbf{k}_a)\hat{n}(\mathbf{k}_b+\Delta\mathbf{k}):\rangle}{\langle \hat{n}(\mathbf{k}_a)\rangle\, \langle \hat{n}(\mathbf{k}_b+\Delta\mathbf{k})\rangle}\,, \end{aligned} \tag{3.38}$$

with $\Omega_{1'} = \left[\mathcal{L}_x \times \mathcal{L}_y\right] = \left[2\times 10^{-2}\right]^2 \mathrm{k}^2_{\mathrm{lat}}$ and $\Omega_{2'} = [\mathcal{L}_x \times \mathcal{L}_z] = \left[2\times 10^{-2} \times 1\times 10^{-2}\right] \mathrm{k}^2_{\mathrm{lat}}$.

The data shown in Fig. 3.24 corresponds to the projection of the cross-correlation function along the longitudinal axis (z) and one of the transverse direction (y) (the same shape can be recovered for the other transverse direction). One can see an increase of the cross-correlation for $\Delta\mathbf{k} \to 0$, indicating that beam a and b are correlated and produced in pairs. The empirical Gaussian fit

$$g^{(2)}_{ab}(\Delta k_z) = A_{c,z}\exp\left(-\frac{z^2}{2\sigma^2_{z,c}}\right)+1\,, \tag{3.39}$$

$$g^{(2)}_{ab}(\Delta k_y) = A_{c,y}\exp\left(-\frac{y^2}{2\sigma^2_{y,c}}\right)+1 \tag{3.40}$$

is used in order to determine both the amplitude correlation and the correlation width defined as the half-width at $1/\sqrt{e}$. The obtained fitting parameters are summarised in Table 3.2. The

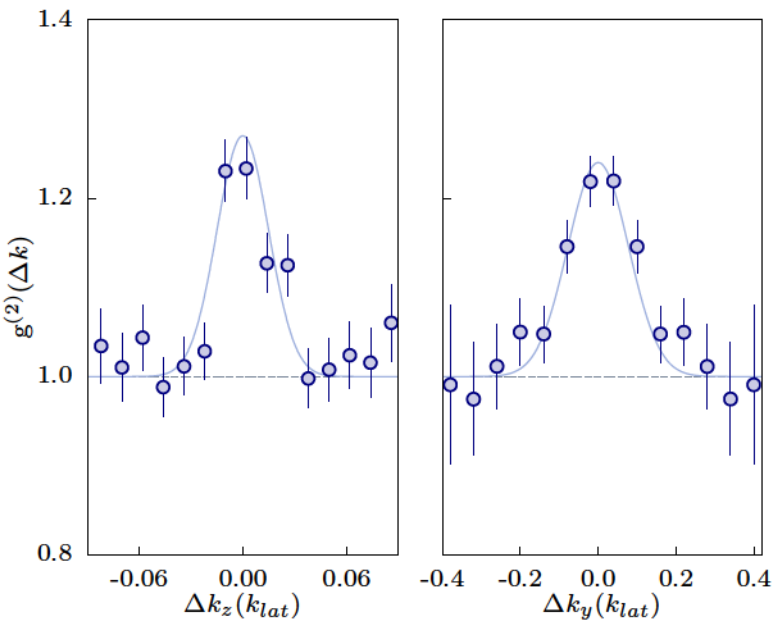

Figure 3.24: 2nd order cross-correlation as a function of the momentum difference between two atoms from beam a and b. Left panel: Projection of the 2nd order cross-correlation function along the longitudinal z−axis. The integration area in the transverse plane is equal to $\Omega_{2'} = \left[\mathcal{L}_x \times \mathcal{L}_y\right] = [2\times10^{-2}]^2\ \mathrm{k}_{lat}^2$. *Right panels: Projection of the 2nd order cross-correlation function along the transverse y−axis (the same shape is recovered along the x−axis). The integration area is equal to* $\Omega_{1'} = [\mathcal{L}_x \times \mathcal{L}_z] = [2\times10^{-2}\times1\times10^{-2}]\ \mathrm{k}_{lat}^2$.

Cross	
$\sigma_{c,z}$ ($\mathrm{k_{lat}}$)	0.025 (3)
$\sigma_{c,y}$ ($\mathrm{k_{lat}}$)	0.08 (1)
$A_{c,z}$	0.27 (3)
$A_{c,y}$	0.24 (3)

Table 3.2: Cross-correlation fitting parameters. Summary of the fitting parameters of Eq. (3.40) applied to the projections of the 2nd order cross-correlation function along the longitudinal z−axis and transverse y−axis represented in Fig. 3.24.

cross-correlation function is, for both directions, two times larger than the autocorrelation function. Since the averaged population is estimated to $N \approx 0.3$–8 one would expect from Eq. (3.36) a maximum correlation value of 2.1– 5.3. This value is in disagreement with our result of 1.3. This indicates that either the produced atomic beams cannot be trustily described through spontaneous parametric down-conversion or that subsequent losses are reducing the cross-correlation value.

3.4.2 Non-classical correlations

Correlations are present in day to day live. In most classical systems, two quantities can be associated such that the presence of one of the two implies an increased probability of finding the other. However, for a statistical classical experiment, relative number fluctuations can never correspond to a distribution with lower than Poissonian fluctuations. For instance, consider a system that produces $N/2$ classical pairs of bullets with opposite velocities. On average, one has $N/2$ bullets in each direction with a variance, following the Poisson law, equal to the expected

value $N/2$. The variance of the bullets difference corresponds then to the sum of the variance of both distributions and is equal to N. This intrinsic fluctuation is often called shot noise.

For a quantum state, it is possible to measure a variance lying below the classical shot noise limit. Such a state is often called squeezed state since it corresponds to a squeezed distribution of one variable describing the state. In the case of a parametric down-conversion state described by Eq. (3.16), the normalised variance of the population difference between beams a and b is given by

$$V = \frac{\langle \Delta N^2 \rangle - \langle \Delta N \rangle^2}{\langle N_a + N_b \rangle} \tag{3.41}$$

and is equal to 0, since $\langle \Delta N^2 \rangle = \langle \Delta N \rangle^2 = 0$, corresponding to a maximally squeezed state.

However, this result assumes a perfect detection efficiency. If most of the atoms are lost due to low detection efficiency, then the fluctuation increases and, since the loss is a classical process, the distribution evolves to a Poisson law. To quantify this effect, one can describe the detection efficiency as a beam-splitter with a coefficient of transmission $\sqrt{\eta}$, with η the detection efficiency. Consider the effect on the variance of the variable $\hat{n}_a = \hat{a}^\dagger \hat{a}$. The operator $\hat{a}$, due to the action of the beam-splitter, transforms into

$$\hat{a}'^\dagger = \sqrt{\eta}\hat{a}^\dagger + \sqrt{1-\eta}\hat{O}^\dagger,$$

where $\hat{O}^\dagger$ is the vacuum operator at the other input port of the beam-splitter. The averaged quantity can be written as

$$\langle \hat{n}'^2_a \rangle = \eta^2 \langle \hat{n}_a^2 \rangle + \eta(1-\eta)\langle \hat{n}_a \rangle,$$

while

$$\langle \hat{n}'_a \rangle^2 = \eta^2 \langle \hat{n}_a \rangle^2,$$

and $\langle \hat{n}'_a \rangle = \eta \langle \hat{n}_a \rangle$. The expression for the detected variance is then given by

$$V_{det} = \eta V + (1-\eta), \tag{3.42}$$

where V corresponds to the *real* normalised variance of the variable. It is then clear that even if the initial state has a zero variance, the detected variance can increase to the shot noise limit ($V = 1$) if $\eta \to 0$. On the other hand, if one assumes that the input state has an almost zero variance, then the measurement of sub shot noise fluctuation provides an estimation of the detection efficiency η.

The normalised variance of the population difference corresponding to Eq. (3.41) is recovered for our atomic beams. The atom number inside two different *boxes*, A, fixed on top of beam a, and B, moving from A towards beam b, are compared. The integration volumes (A and B) correspond to $\Omega_V = \left[\Delta k_\perp^2 \times \Delta k_z\right] = \left[0.26^2 \times 0.19\right] k_{rec}^3$. The value of the normalised variance is showed in Fig. 3.25 as a function of the analysis box, B. It is possible to see that when B is on top of A the variance goes artificially to zero and when B is centred on top of beam b (corresponding to the red shaded area) the variance falls below the shot-noise threshold, reaching a minimum value of 0.75 (5) .

This result means that beam a and b correspond to a pair and that their state has stronger-than-classical correlations. This is fundamental in order to perform quantum atom optics experiments.

Assuming that the variance is equal to zero, one can then recover the detection efficiency η. Since nothing can guarantee that $V = 0$, we can only argue that the detection efficiency cannot be lower than $\eta_{\text{min}} = 1 - V_{\text{det.}}$. In our experiment, this results in $\eta_{\text{min.}} = 25\,(5)$ %.

This allows us to give a lower bound of 25 (5) % to our detection efficiency.

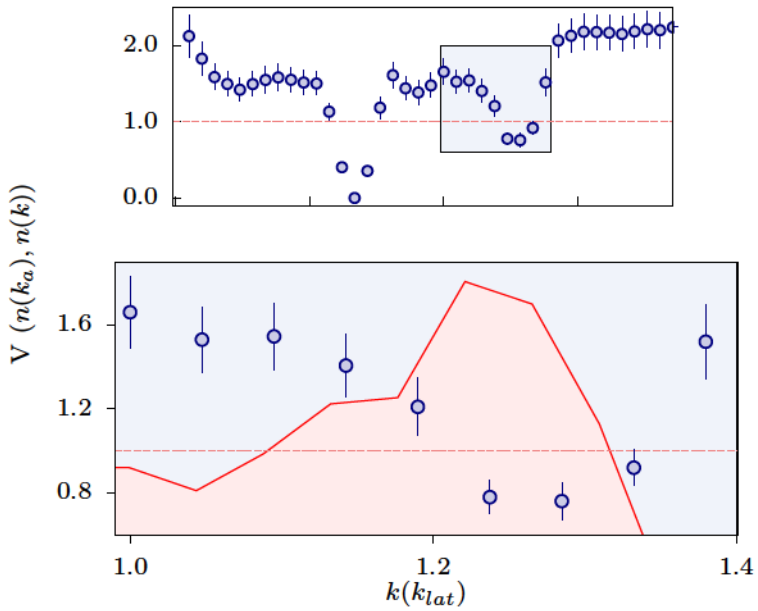

Figure 3.25: Variance of the difference of population as a function of the position of the analysed zones. The atom number inside two different boxes, A, fixed on top of beam a, and B, moving from A towards beam b, are compared. A reduction below shot-noise is clearly visible when the second zone, B, is centred on top of beam b (blue circles). The bottom canvas corresponds to a zoom performed on the upper one. Beam b is represented in red shaded colour for guidance.

Cauchy-Schwarz inequality

A complementary study is done using the Cauchy–Schwarz (CS) inequality. In Ref. [96], it is shown that the CS inequality can be adapted to integrated quantities. The violation of this inequality for the correlation functions indicates that the cross-correlation between the atomic beams cannot be classically described. This is then related to the measurement of the normalised variance described previously.

Let us consider the non-normalised correlation function described by

$$G^{(2)}_{ij} = \langle \hat{N}_i \hat{N}_j \rangle = \frac{(\eta)^2}{\Omega_{V_i}\Omega_{V_j}} \int_{\Omega_{V_i}} d^3\mathbf{k}_i \int_{\Omega_{V_j}} d^3\mathbf{k}_j \tilde{G}^{(2)}\left(\mathbf{k}_i, \mathbf{k}_j\right) , \tag{3.43}$$

where $\tilde{G}^{(2)}\left(\mathbf{k}_i, \mathbf{k}_j\right) = \langle \hat{n}(\mathbf{k}_i)\hat{n}(\mathbf{k}_j)\rangle$ corresponds to the second-order correlation function between the atom number densities $\hat{n}(\mathbf{k})$ at two points in momentum space. The volumes of integration $\Omega_{V_{i,j}}$ are defined as

$$\Omega_{V_{i,j}} = \left[\Delta k_\perp^2 \Delta k_z\right] k_{lat}^3,$$

with the integration lengths along the longitudinal, z–axis (Δk_z), and transverse axis, x– and y–axis ($\Delta k_\perp$).

For identical mode occupancy, that is $\langle n\rangle_a = \langle n\rangle_b$ and $G^{(2)}_{aa} = G^{(2)}_{bb}$, the normalised variance of the difference can then be written as

$$\begin{aligned} V &= 1 + \frac{G^{(2)}_{aa} - G^{(2)}_{ab}}{\langle n\rangle_a} \\ &= 1 + (1 - C)\frac{G^{(2)}_{aa}}{\langle n\rangle_a} , \end{aligned}$$

where the parameter C corresponds to the correlation coefficient

$$C = G^{(2)}_{ab} / G^{(2)}_{aa} ,$$

or in its more general form

$$C = G^{(2)}_{ab} / \sqrt{G^{(2)}_{aa} G^{(2)}_{bb}} . \tag{3.44}$$

One can see that for $C > 1$ it is possible to recover a sub-shot noise variance and corresponds to a violation of the Cauchy-Schwarz inequality

$$G^{(2)}_{ab} \leq \sqrt{G^{(2)}_{aa} G^{(2)}_{bb}} . \tag{3.45}$$

The correlation coefficient (C) is then smaller than one for a classical state and larger for states with stronger-than-classical correlations, in the case of indistinguishable particles [97], as discussed in Section 1.2.

In Fig. 3.26 the coefficient parameter C is measured from the experimental data as a function of the integration volumes Ω_{V_a} and Ω_{V_b} centred on the atomic beams a and b, respectively. The integration volume corresponds to a parallelepiped of size $\Omega_V = \left[\Delta k_\perp^2 \times \Delta k_z\right]\left(k^3_{\text{lat}}\right)$. In Fig. 3.26a) we represent the value of C for a fixed integration length along the transverse direction, $\Delta k_\perp = 0.048 k_{\text{lat}}$, as a function of the integration length along the vertical axis, Δk_z. In Fig. 3.26b), on the other hand, we represent C for a fixed $\Delta k_z = 0.028 k_{\text{lat}}$ as a function of a varying $\Delta k_\perp$. It is possible to see that, for small integration volumes, the violation of the CS inequality increases until it reaches a plateau. The optimised volume of integration is approximatively equal to the cross-correlation width as summarised in Table 3.1. This is coherent with the fact that C decreases when the volume of integration reaches the cross-correlation width (as discussed in supplementary material of Ref. [96]).

An optimised volume corresponding to

$$\Omega_{V_a} = \Omega_{V_b} = \left[\Delta k_\perp^2 \Delta k_z\right] = \left[0.048^2 \times 0.028\right] k^3_{\text{lat}}$$

is represented in Fig. 3.26a) and b) by a red circle.

We recover a value of $C = 1.75\,(20)$ which proves, once more, that the two atomic beams are strongly correlated.

3.5 Conclusions

We have showed that the atomic beams produced via dynamical instabilities in a moving 1D lattice constitute a pairwise system with stronger-than-classical correlation. This pair production mechanism allows us to precisely tune the momentum difference between the two atomic beams and their mode occupancy.

Certain details concerning the atomic pair creation and propagation are still open questions that will be addressed in the near future. However, the pair creation process is sufficiently under control to allows us to use it in interferometric scheme, as for example, the HOM experiment.

Table 3.3 summarises all the relevant measurements performed along this Chapter. The different widths measured for both the auto- and cross-correlation and the optimised volume of integration for CS inequality violation are given. The estimated number of modes along the longitudinal and transverse direction and the distribution width are also provided.

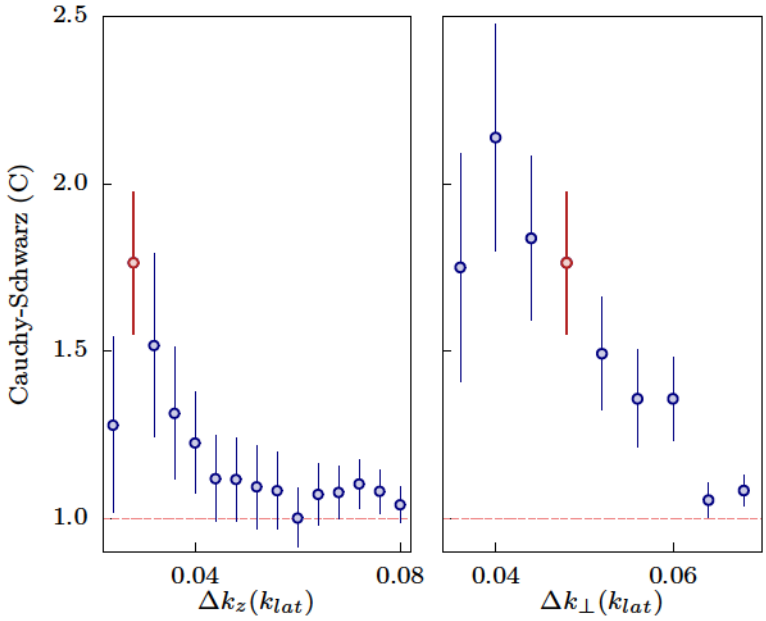

Figure 3.26: Correlation parameter C as a function of the integration volume. The correlation parameter C, indicating a violation of the CS inequality for $C > 1$, is represented as a function of the integration volume along the: a) longitudinal axis with integration length along both transverse directions fixed to $\Delta k_\perp = 0.05 k_{lat}$; b) transverse axis with integration length along the other transverse directions fixed to $\Delta k_\perp = 0.05 k_{lat}$ and along the longitudinal direction to $\Delta k_z = 0.028 k_{lat}$. The threshold limit between classical and quantum correlations ($C = 1$) is represented by the red dashed line.

	Local		**Cross**	**CS inequality**
	Cloud *a*	**Cloud** *b*		
σ_z (k_{lat})	0.012 (2)	0.010 (2)	0.025 (3)	
$\sigma_\perp$ (k_{lat})	0.05 (1)	0.04 (2)	0.08 (1)	
$\sigma_{n(k)z}$ (k_{lat})	0.06 (1)	0.06 (2)		
$\sigma_{n(k)\perp}$ (k_{lat})	0.08 (1)	0.08 (2)		
$N_{modes,z}$	5 (1)	6 (2)		
$N_{modes,\perp}$	1.5 (5)	1.5 (5)		
$\Delta k_{c,z}$ (k_{lat})				0.028
$\Delta k_{c,\perp}$ (k_{lat})				0.048

Table 3.3: Summary of the density profile widths and correlation functions for beams a and b.

Bibliography

[12]D. C. Burnham and D. L. Weinberg, "Observation of Simultaneity in Parametric Production of Optical Photon Pairs", Phys. Rev. Lett. **25**, 84–87 (1970) (cit. on pp. 3, 94).

[13]L.-A. Wu, H. J. Kimble, J. L. Hall, and H. Wu, "Generation of Squeezed States by Parametric Down Conversion", Phys. Rev. Lett. **57**, 2520–2523 (1986) (cit. on pp. 3, 14, 21, 72, 91).

[64]F. Gerbier, "Quasi-1D Bose-Einstein condensates in the dimensional crossover regime", EPL (Europhysics Letters) **66**, 771 (2004) (cit. on pp. 6, 48, 59, 78, 173, 174).

[86]W. H. Louisell, A. Yariv, and A. E. Siegman, "Quantum Fluctuations and Noise in Parametric Processes. I.", Phys. Rev. **124**, 1646–1654 (1961) (cit. on pp. 21, 72).

[96]K. V. Kheruntsyan, J.-C. Jaskula, P. Deuar, M. Bonneau, G. B. Partridge, J. Ruaudel, R. Lopes, D. Boiron, and C. I. Westbrook, "Violation of the Cauchy-Schwarz Inequality with Matter Waves", Phys. Rev. Lett. **108**, 260401 (2012) (cit. on pp. 25, 28, 97, 98, 167, 217).

[97]T. Wasak, P. Sza ńkowski, P. Zi ń, M. Trippenbach, and J. Chwede ńczuk, "Cauchy-Schwarz inequality and particle entanglement", Phys. Rev. A **90**, 033616 (2014) (cit. on pp. 25, 98).

[105]G. K. Campbell, J. Mun, M. Boyd, E. W. Streed, W. Ketterle, and D. E. Pritchard, "Parametric Amplification of Scattered Atom Pairs", Phys. Rev. Lett. **96**, 020406 (2006) (cit. on pp. 27, 45, 71, 86).

[108]M. Bonneau, J. Ruaudel, R. Lopes, J.-C. Jaskula, A. Aspect, D. Boiron, and C. I. Westbrook, "Tunable source of correlated atom beams", Phys. Rev. A **87**, 061603 (2013) (cit. on pp. 27, 34, 44–46, 83, 91, 167, 217).

[141]J. Ruaudel, "Creation and characterization of a tunable source of correlated atoms pairs", Theses (Institut d'Optique Graduate School, Dec. 2013) (cit. on pp. 38, 44, 45, 74, 77, 83, 86, 87).

[142]M. Bonneau, "Atomic four-wave mixing in an optical lattice", Theses (Université Paris Sud - Paris XI, Dec. 2011) (cit. on pp. 38, 44, 45, 53, 54, 71, 83, 181).

[151]R. Grimm, M. Weidemüller, and Y. B. Ovchinnikov, "Optical Dipole Traps for Neutral Atoms", in , Vol. 42, edited by B. Bederson and H. Walther, Adv. Atom. Mol. Opt. Phy. (Academic Press, 2000), pp. 95–170 (cit. on pp. 40, 66, 71, 178).

[153]C. Pethick and H. Smith, *Bose-Einstein Condensation in Dilute Gases* (Cambridge University Press, 2002) (cit. on pp. 44, 75, 111).

[154]B. Wu and Q. Niu, "Landau and dynamical instabilities of the superflow of Bose-Einstein condensates in optical lattices", Phys. Rev. A **64**, 061603 (2001) (cit. on pp. 45, 71, 77–80).

[155]K. M. Hilligsøe and K. Mølmer, "Phase-matched four wave mixing and quantum beam splitting of matter waves in a periodic potential", Phys. Rev. A **71**, 041602 (2005) (cit. on pp. 45, 71).

[170]N. Ashcroft and N. Mermin, *Solid State Physics* (Saunders College, Philadelphia, 1976) (cit. on pp. 66, 68).

[171]C. Kittel, *Introduction to Solid State Physics*, 6th (John Wiley & Sons, Inc., New York, 1986) (cit. on pp. 66, 68).

[172]M. Greiner, "Ultracold quantum gases in three-dimensional optical lattice", PhD thesis (Ludwig-Maximilians-Universität München, 2003) (cit. on pp. 66, 68).

[173]J. H. Denschlag, J. E. Simsarian, H. Häffner, C. McKenzie, A. Browaeys, D. Cho, K. Helmerson, S. L. Rolston, and W. D. Phillips, "A Bose-Einstein condensate in an optical lattice", J. Phys. B-At. Mol. Opt. **35**, 3095 (2002) (cit. on pp. 68, 69, 106).
[174]A. Ferris, M. Davis, R. Geursen, P. Blakie, and A. Wilson, "Dynamical instabilities of Bose-Einstein condensates at the band edge in one-dimensional optical lattices", Phys. Rev. A **77**, 012712 (2008) (cit. on p. 68).
[175]N. Katz, E. Rowen, R. Ozeri, and N. Davidson, "Collisional Decay of a Strongly Driven Bose-Einstein Condensate", Phys. Rev. Lett. **95**, 220403 (2005) (cit. on p. 68).
[176]A. Messiah, *Quantum mechanics*, Quantum Mechanics vol. 1 (North-Holland, 1965) (cit. on p. 69).
[177]J. Dalibard, *Cours du collège de France* (2014) (cit. on pp. 69, 107).
[178]T. Gericke, F. Gerbier, A. Widera, S. Fölling, O. Mandel, and I. Bloch, "Adiabatic loading of a Bose–Einstein condensate in a 3D optical lattice", J. Mod. Optic **54**, 735–743 (2007) (cit. on pp. 69, 71, 83).
[179]M. Greiner, I. Bloch, O. Mandel, T. Hänsch, and T. Esslinger, "Exploring Phase Coherence in a 2D Lattice of Bose-Einstein Condensates", Phys. Rev. Lett. **87**, 160405 (2001) (cit. on pp. 69, 85, 106).
[180]M. Greiner, O. Mandel, T. Esslinger, T. W. Hansch, and I. Bloch, "Quantum phase transition from a superfluid to a Mott insulator in a gas of ultracold atoms", Nature **415**, 39–44 (2002) (cit. on p. 71).
[181]S. R. Clark and D. Jaksch, "Dynamics of the superfluid to Mott-insulator transition in one dimension", Phys. Rev. A **70**, 043612 (2004) (cit. on p. 71).
[182]H. Metcalf and P. Van der Straten, *Laser Cooling and Trapping*, Graduate texts in contemporary physics (Springer, 1999) (cit. on p. 71).
[183]F. Gerbier and Y. Castin, "Heating rates for an atom in a far-detuned optical lattice", Phys. Rev. A **82**, 013615 (2010) (cit. on p. 71).
[184]M. Modugno, C. Tozzo, and F. Dalfovo, "Role of transverse excitations in the instability of Bose-Einstein condensates moving in optical lattices", Phys. Rev. A **70**, 043625 (2004) (cit. on p. 71).
[185]O. Morsch and M. Oberthaler, "Dynamics of Bose-Einstein condensates in optical lattices", Rev. Mod. Phys. **78**, 179–215 (2006) (cit. on p. 71).
[186]L. Fallani, "Bose-Einstein condensates in optical lattices", Theses (Universitá degli Studi di Firenze Facoltà di Scienze Matematiche Fisiche e Naturali) (cit. on pp. 71, 88).
[187]K. Berg-Sørensen and K. Mølmer, "Bose-Einstein condensates in spatially periodic potentials", Phys. Rev. A **58**, 1480–1484 (1998) (cit. on p. 71).
[188]B. Wu and Q. Niu, "Superfluidity of Bose–Einstein condensate in an optical lattice: Landau–Zener tunnelling and dynamical instability", New. J. Phys. **5**, 104 (2003) (cit. on pp. 71, 72).
[189]L. De Sarlo, L. Fallani, J. Lye, M. Modugno, R. Saers, C. Fort, and M. Inguscio, "Unstable regimes for a Bose-Einstein condensate in an optical lattice", Phys. Rev. A **72**, 013603 (2005) (cit. on pp. 71, 85).
[190]N. Fabbri, D. Clément, L. Fallani, C. Fort, M. Modugno, K. van der Stam, and M. Inguscio, "Excitations of Bose-Einstein condensates in a one-dimensional periodic potential", Phys. Rev. A **79**, 043623 (2009) (cit. on p. 71).
[191]L. Fallani, L. De Sarlo, J. Lye, M. Modugno, R. Saers, C. Fort, and M. Inguscio, "Observation of Dynamical Instability for a Bose-Einstein Condensate in a Moving 1D Optical Lattice", Phys. Rev. Lett. **93**, 140406 (2004) (cit. on p. 71).
[192]J. Ruostekoski and L. Isella, "Dissipative Quantum Dynamics of Bosonic Atoms in a Shallow 1D Optical Lattice", Phys. Rev. Lett. **95**, 110403 (2005) (cit. on p. 71).

[193]M. Machholm, C. Pethick, and H. Smith, "Band structure, elementary excitations, and stability of a Bose-Einstein condensate in a periodic potential", Phys. Rev. A **67**, 053613 (2003) (cit. on pp. 72, 85).
[194]S. Burger, F. S. Cataliotti, C. Fort, P. Maddaloni, F. Minardi, and M. Inguscio, "Quasi-2D Bose-Einstein condensation in an optical lattice", EPL (Europhysics Letters) **57**, 1 (2002) (cit. on p. 72).
[195]L. Deng, E. W. Hagley, J. Wen, M. Trippenbach, Y. Band, P. S. Julienne, J. E. Simsarian, K. Helmerson, S. L. Rolston, and W. D. Phillips, "Four-wave mixing with matter waves", Nature **398**, 218–220 (1999) (cit. on p. 73).
[196]J. Ruostekoski and Z. Dutton, "Dynamical and energetic instabilities in multicomponent Bose-Einstein condensates in optical lattices", Phys. Rev. A **76**, 063607 (2007) (cit. on p. 85).

Chapter 4

Experimental requisites towards the HOM experiment: atomic beam-splitter

Contents

4.1 Bragg diffraction 106
4.2 Beam-splitter calibration with the BEC 110
4.2.1 Geometrical alignment of the beam-splitter 111
4.2.2 Alignment via Bragg diffraction 112
4.2.3 Resonance condition in free space 114
4.2.4 50:50 beam-splitter and mirror stability 115
4.3 Beam-splitter used on the atomic pairs 116
4.4 Noise induced by the beam-splitter on the atomic beams 118
4.5 Phase stability of the beam-splitter 119
4.6 Autocorrelation measurement via a 50:50 beam-splitter 123
4.7 Conclusion 125

> This is your work, envious one! And I hardly think the future generations will bless you for it...
>
> Stanisław Lem in Cyberiad

In this chapter, we will discuss the realisation of an atomic 50:50 beam-splitter and mirror. With the goal of this project being the realisation of a *two-atom interferometer*, one needs to be able to coherently manipulate the atomic pairs. To do so, we will show in this chapter how one can use Bragg diffraction to perform an atomic mirror and 50:50 beam-splitter in momentum space. The basic theoretical description is briefly reviewed in Section 4.1 and the calibration on the BEC performed in Section 4.2 and on the atomic pairs in Section 4.3, respectively. The noise added by the beam-spitter and its phase stability are described in Section 4.4 and Section 4.5. In Section 4.6, the autocorrelation of beam b is recovered after splitting the beam via a 50:50 beam-splitter, in very close analogy to what is performed in quantum optics.

4.1 Bragg diffraction

Bragg diffraction consists in an elastic multiphoton deflection process by which the atomic de Broglie wave is coherently diffracted by a periodic dipole potential [116]. This translates to a population transfer of an atom with momentum k to another momentum k'.

Focussing on the temporal evolution of a BEC in a periodic potential, let us consider the condensate as a plane wave with quasi-momentum q_0

$$\phi_{q_0}(z) = \frac{1}{\sqrt{L_z}} e^{iq_0 z},$$

and study its temporal evolution in a periodic potential as a function of the lattice duration. This will show us how to perform an atomic mirror as well as a 50:50 beam-splitter.

At time $t = 0$, an optical lattice is turned on. The wave function of the BEC is then projected to Bloch waves described by

$$|\Phi(t=0)\rangle = \sum_{n=0}^{\infty} |\psi_{n,q_0}\rangle\langle\psi_{n,q_0}|\phi_{q_0}\rangle \tag{4.1}$$

where $\langle\psi_{n,q_0}|\phi_{q_0}\rangle = a^*_{n,m=0}(q)$ as described in Chapter 3. The system evolves and, at any given time t, the state is described by

$$|\Phi(t)\rangle = \sum_{n=0}^{\infty} a^*_{n,0}(q_0) e^{-iE_{n,q_0}t/\hbar} |\psi_{n,q_0}\rangle, \tag{4.2}$$

with E_{n,q_0} the energy for the quasi-momentum q_0 in the energy band n and

$$|\psi_{n,q_0}\rangle = \sum_{m=-\infty}^{\infty} a_{n,m}(q_0)|\phi_{q_0+2mk_{\text{lat}}}\rangle$$

the associated Bloch wave, where $|\phi_{q_0+2mk_{\text{lat}}}\rangle$ corresponds to a plane wave of quasi-momentum $q_0 + 2mk_{\text{lat}}$ and k_{lat} represents the periodicity of the considered lattice in momentum space. For a shallow lattice, for instance $V_0 = 0.8E_{\text{lat}}$ (as used in most of our experiments), only the two first coefficients $a_{0,0}$, $a_{1,0}$ are non negligible since only those have non vanishing values in the 1st Brillouin zone as shown in Fig. 4.1. Therefore the wave-function at a time t, considering only first neighbours coefficients ($m = \pm 1$), which is a good approximation for shallow lattices, can then be re-written as

$$\begin{aligned}|\Phi(t)\rangle &= a^*_{0,0}(q_0)e^{-iE_{0,q_0}t/\hbar}|\psi_{0,q_0}\rangle + a^*_{1,0}(q_0)e^{-iE_{1,q_0}t/\hbar}|\psi_{1,q_0}\rangle \\ &= \sum_{m=-1}^{m=1}\left[a^*_{0,0}(q_0)a_{0,m}(q_0)e^{-iE_{0,q_0}t/\hbar} + a^*_{1,0}a_{1,m}e^{-iE_{1,q_0}t/\hbar}\right]|\phi_{q_0+2mk_{\text{lat}}}\rangle.\end{aligned}$$

For $t = \tau$, the lattice is suddenly switched off and the state is projected to the plane wave basis that corresponds to the measurement basis. The amplitude of probability b_0 associated to the diffracted quasi-momentum q_0 and $b_{\pm 1}$ associated to $q_0 \pm 2k_{\text{lat}}$ is then given by [173, 179]

$$b_0(q_0, \tau) = \left|a_{0,0}(q_0)\right|^2 e^{-iE_{0,q_0}\tau/\hbar} + \left|a_{1,0}(q_0)\right|^2 e^{-iE_{1,q_0}\tau/\hbar}, \tag{4.3a}$$

$$b_{\pm 1}(q_0, \tau) = a^*_{0,0}(q_0)a_{0,\pm 1}(q_0)e^{-iE_{0,q_0}\tau/\hbar} + a^*_{1,0}(q_0)a_{1,\pm 1}(q_0)e^{-iE_{1,q_0}\tau/\hbar}. \tag{4.3b}$$

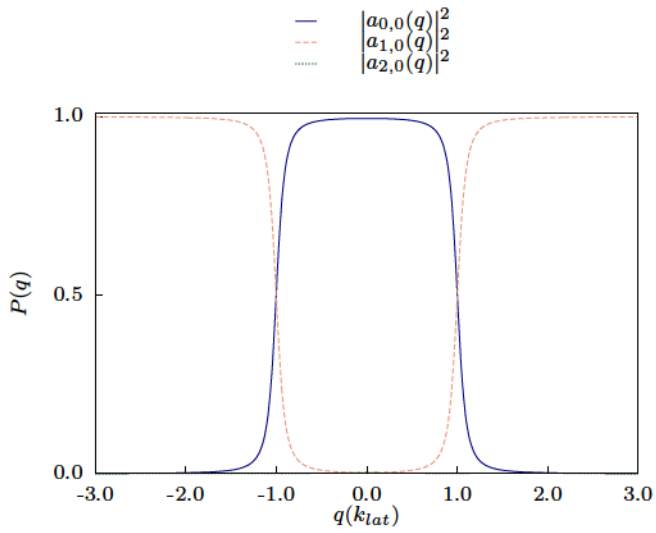

Figure 4.1: *Coefficients values of the decomposition into Bloch waves for a plane wave function with quasi-momentum q_0 loaded suddenly in a lattice of depth equal to $0.8\,E_{lat}$.*

Let us consider the simplest case, often used for the atomic beam-splitter, of $q_0 = -k_{\text{lat}}$. For this initial quasi-momentum $|a_{0,0}|^2 = |a_{1,0}|^2 = 0.5$ (see Fig. 4.1) and $a^*_{0,0}a_{0,1} = -0.5$, $a^*_{1,0}a_{1,1} = 0.5$, $a^*_{0,0}a_{0,-1} = a^*_{1,0}a_{1,-1} = 0$ (see in Fig. 4.2).

The wave function at time τ, in the measurement basis, is then described by

$$|\Phi(\tau)\rangle = e^{-i\left(E_{1,-k_{\text{lat}}}+E_{0,-k_{\text{lat}}}\right)\tau/\hbar}\left[\cos\left(\frac{\Delta E}{\hbar}\tau/2\right)|\phi_{-k_{\text{lat}}}\rangle + e^{i\varphi}\sin\left(\frac{\Delta E}{\hbar}\tau/2\right)|\phi_{-k_{\text{lat}}+2k_{\text{lat}}}\rangle\right]$$

with φ a phase accumulated during the Bragg diffraction process [1] and ΔE equal to [177]

$$\Delta E = E_{1,-k_{\text{lat}}} - E_{0,-k_{\text{lat}}} = \hbar\Omega_R = E_{\text{lat}} + \frac{3V_0}{4} - \left(E_{\text{lat}} + \frac{V_0}{4}\right) = \frac{V_0}{2}\,,$$

where Ω_R corresponds to the two-photon Rabi frequency and E_{lat} to the recoil energy given by the lattice. The wave function as a function of τ can then be written as

$$|\Phi(\tau)\rangle = e^{i\theta}\left[\cos\left(\Omega_R\tau/2\right)|\phi_{-k_{\text{lat}}}\rangle + e^{i\varphi}\sin\left(\Omega_R\tau/2\right)|\phi_{-k_{\text{lat}}+2k_{\text{lat}}}\rangle\right]\,,$$

and the probability to find an atom in either $q = -k_{\text{lat}}$ or $q = -k_{\text{lat}} + 2k_{\text{lat}} = k_{\text{lat}}$ after a certain time τ is equal to

$$P_{-k_{\text{lat}}}(\tau) = \cos^2\left(\Omega_R\tau/2\right)\,, \tag{4.4a}$$

$$P_{k_{\text{lat}}}(\tau) = \sin^2\left(\Omega_R\tau/2\right)\,. \tag{4.4b}$$

The population between $-k_{\text{lat}}$ and k_{lat} oscillates over time as it is represented in Fig. 4.3 for the case of a lattice depth equal to $0.8E_{\text{lat}}$. This oscillation corresponds to a Rabi oscillation [177].

The value of τ allows one to coherently exchange the population between the two momenta, with a certain probability. The two important cases are

- $\Omega_R\tau = \pi$ that corresponds to a total inversion of populations — an atomic mirror;
- $\Omega_R\tau = \pi/2$ that corresponds to a 50:50 exchange of populations — 50:50 beam-splitter.

[1] This phase can correspond to the phase difference between the two laser beams forming the lattice.

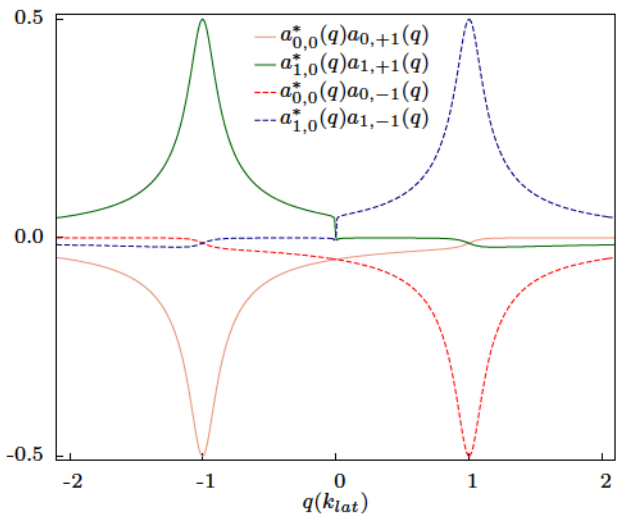

Figure 4.2: Crossed coefficients values of $a^*_{0,0}a_{0,1}$, $a^*_{1,0}a_{1,1}$, $a^*_{0,-1}a_{0,-1}$ and $a^*_{1,0}a_{1,-1}$ as a function of the quasi-momentum q. The coefficients product $a^*_{0,0}a_{0,1}$ (in orange), $a^*_{1,0}a_{1,1}$ (in green), $a^*_{0,-1}a_{0,-1}$ (in dashed red) and $a^*_{1,0}a_{1,-1}$ (in dashed blue) are represented as a function of q for $V_0 = 0.8E_{lat}$. For the example given in the text of $q = -1k_{lat}$ one sees that non-zero terms correspond to $a^*_{0,0}a_{0,1}$ and $a^*_{1,0}a_{1,1}$ corresponding to a diffraction of population into $q = +1k_{lat}$.

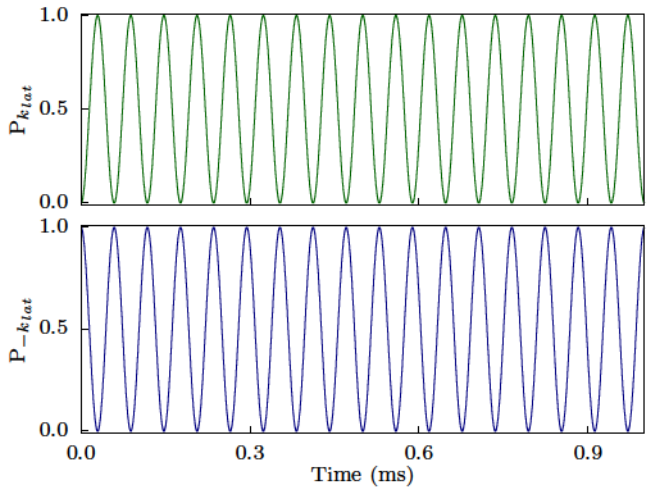

Figure 4.3: Example of a Rabi oscillation. Rabi oscillation of the population between the quasi-momenta $+k_{lat}$ and $-k_{lat}$ for a lattice depth of $V_0 = 0.8\,E_{lat}$. The initial quasi-momentum q_0 is equal to $-1k_{lat}$ such that the probability to diffract to $q_0 + 2k_{lat} = k_{lat}$ is maximum.

These two cases are very often used as atomic mirror and beam-splitter in momentum space [43]. For the 50:50 beam-splitter, essential for the HOM experiment, the wave function corresponds then to

$$|\Phi(\tau = \frac{\pi}{2\Omega_R})\rangle = \frac{1}{\sqrt{2}}\left(|\phi_{-k_{\text{lat}}}\rangle + e^{i\varphi}|\phi_{k_{\text{lat}}}\rangle\right)$$

and one recovers the scattering matrix notation for the 50:50 beam-splitter used in Chapter 1.

Resonance condition

In the case of a non-resonant initial quasi-momentum, meaning that q is close to $-k_{\text{lat}}$ but not equal, the equations are more complicated. One can see from Fig. 4.1 and Fig. 4.2 that the

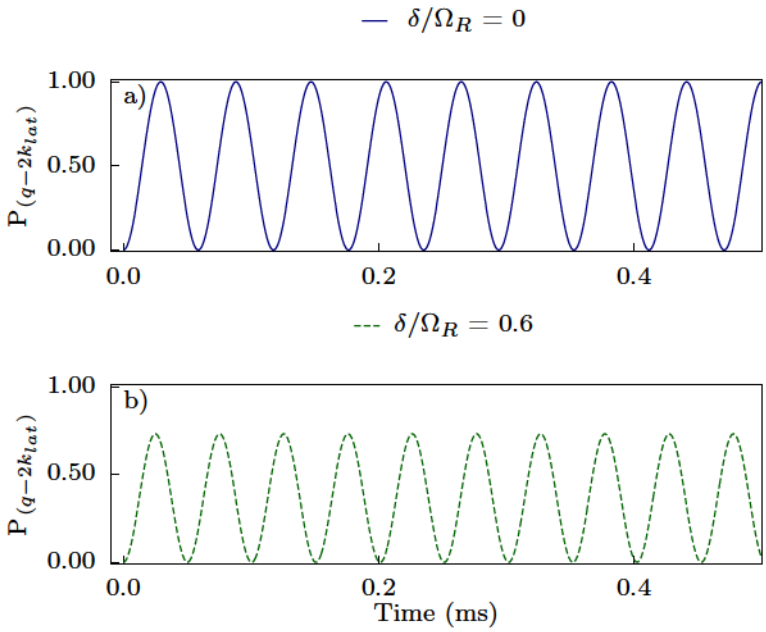

Figure 4.4: *Comparison between a Rabi oscillation at resonance and out of resonance. a) Rabi oscillation at resonance ($\delta = 0$), b) Rabi oscillation out of resonance ($\delta/\Omega_R = 0.6$).*

probability amplitudes are different when compared to the resonant case and that the transfer probability lowers. Besides this effect also the oscillation frequency changes. The effective frequency is now equal to

$$\Omega_{\text{eff}} = \frac{\Delta E}{\hbar} = \frac{1}{\hbar}\sqrt{\frac{V_0^2}{4} + \left(\frac{\hbar^2}{2m}\right)^2 \left(q_0^2 - (q_0 + 2k_{\text{lat}})^2\right)^2} \tag{4.5}$$

$$= \sqrt{\Omega_R^2 + \delta^2}\,, \tag{4.6}$$

where $\delta = \frac{\hbar}{2m}\left(q_0^2 - (q_0 + 2k_{\text{lat}})^2\right)$ corresponds to the frequency shift towards resonance. The transfer probability can then be written as

$$P_{(q_0+2k_{\text{lat}})} = \frac{\Omega_R^2}{\Omega_R^2 + \delta^2} \times \sin^2\left(\sqrt{\Omega_R^2 + \delta^2}\;\tau/2\right). \tag{4.7}$$

As shown in Fig. 4.4, for $\delta = 0$ the population in k_{lat} and $-k_{\text{lat}}$ oscillate with frequency Ω_R from zero to unity with opposite phase. When $\delta \neq 0$, the population transfer does not reach unity and the oscillation frequency increases as described in Eq. (4.6).

In order to effectively exchange the populations between the two momenta, it is then crucial to verify the resonance condition, that corresponds to $q_0 = -k_{\text{lat}}$. Consider the case of an atom at rest in the laboratory frame of reference. In the lattice frame of reference, the atom has a velocity equal to the velocity of the lattice but in the opposite direction. The atomic velocity is then given by

$$v_{\text{BEC}} = -v_{\text{lat}} = -\frac{\hbar k_{\text{lat}}}{m}\,,$$

with v_{BEC} the speed of the atom. The atom speed corresponds then to the inverse velocity of the optical lattice which is given by the frequency difference, $\omega_2 - \omega_1$, of the two laser beams responsible for the lattice. One can thus write the resonance condition as

$$\delta_0 = \omega_2 - \omega_1 = -4E_{\text{lat}}/\hbar, \tag{4.8}$$

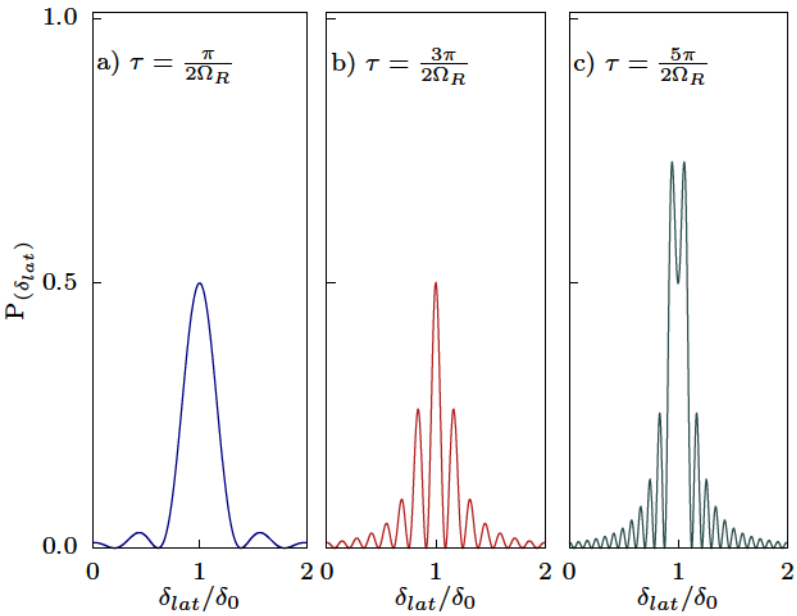

Figure 4.5: Resonance condition for Bragg diffraction. Bragg diffraction probability as a function of the resonance detuning δ for a lattice duration of a) $\tau = \pi/2\Omega_R$, b) $\tau = 3\pi/\Omega_R$ and c) $\tau = 5\pi/2\Omega_R$.

with δ_0 the frequency difference between the two laser beams such that $q_0 = -k_{\text{lat}}$.

If the atom is not at rest in the laboratory frame of reference, the resonance is shifted by δ defined as

$$\delta = -2\mathbf{v}_{\text{init.}} \cdot \frac{\mathbf{v}_{\text{lat}}}{|\mathbf{v}_{\text{lat}}|} k_{\text{lat}}/\hbar\,, \tag{4.9}$$

with v_{init} the atom velocity in the laboratory frame of reference.

Experimentally, one can find the resonance condition by keeping τ constant and varying the value of $\delta_{\text{lat}} = \omega_2 - \omega_1$. The resonance corresponds then to the value of $\delta_{\text{lat}} = \delta_0$ for which the transfer efficiency reaches its maximum value. However, the value of τ has to be chosen carefully. The transfer of population as a function of $\delta_{\text{lat}}/\delta_0$ is compared in Fig. 4.5 for different duration τ. One can see that for $\tau = \frac{5\pi}{2\Omega_R}$, the most efficient transfer is reached for a value of $\delta_{\text{lat}} \neq \delta_0$. Meaning that one will tend, in order to increase the transfer efficiency at fixed value of τ, to get out of resonance. In order to avoid this misalignment, the resonance calibration has to be performed at $\tau \approx \frac{3\pi}{2\Omega_R}$ where the transfer efficiency is always maximum for $\delta_{\text{lat}} = \delta_0$ and the resonance is thinner than in the case $\tau = \frac{\pi}{2\Omega_R}$.

4.2 Beam-splitter calibration with the BEC

In this Section, the characterisation of the *beam-splitter lattice*, responsible for both atomic mirror and 50:50 beam-splitter, is described. The calibration is first performed on the condensate. This allows us to calibrate the beam-splitter on a coherent source with a small momentum spread and to later apply our results to the atomic pairs.

The beam-splitter lattice is formed by two laser beams with a flat intensity profile of radius 1.0 mm, wavelength equal to $\lambda_0 = 1083$ nm and relative angle between the two beams $\theta = 32.5\,°$. The periodicity in momentum space of the lattice is equal to $k_{\text{bms}}/2 = \sin(\theta/2)\,\frac{2\pi}{\lambda_0}$ [2]. The two-

[2] k_{bms} corresponds to the momentum given to the atoms after diffraction.

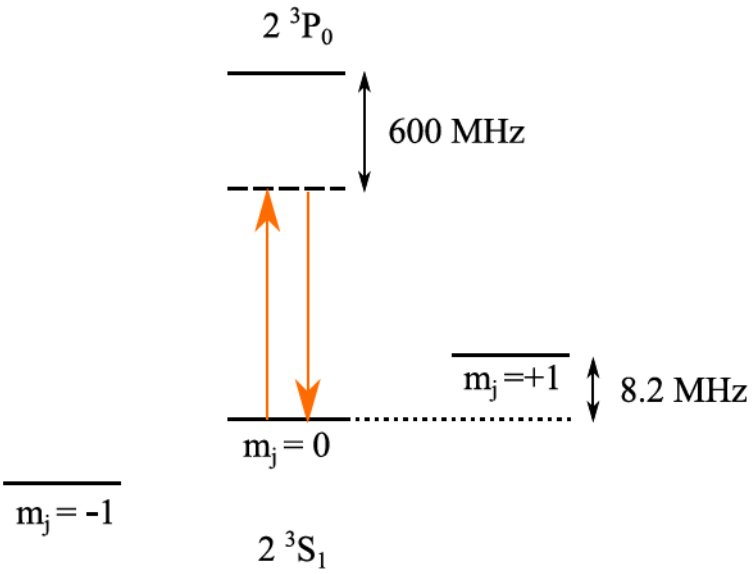

Figure 4.6: Representation of the atomic transition $2^3S_1 \rightarrow 2^3P_0$ used for the atomic beam-splitter. The energetic difference between the sublevels $m_j = \pm 1$ is due to a magnetic bias field of 3 G. This corresponds to an energy difference of $\hbar \times 2\pi \times 8.2$ MHz.

photon Rabi frequency is equal to [153]

$$\Omega_R = \frac{V_0}{2} = \frac{\Gamma^2 I_0 d_{0,0}^2}{4 I_{sat} \Delta},$$

where the detuning Δ is equal to $2\pi \times 600$ MHz and $d_{0,0} = \frac{1}{\sqrt{3}}$ corresponds to the dipole matrix element associated to the transition $2^3S_1 \rightarrow 2^3P_0$ represented in Fig. 4.6.

For the 600 MHz detuning, the effective spontaneous rate $\Gamma_{sp.}$ is equal to 0.17 ms^{-1}. For the application time of the mirror (100 μs) the heating due to spontaneous emission corresponds to

$$T_{\text{mirror}} = 64\,\text{nK}$$

and for the case of the 50-50 beam-splitter duration (50 μs) to

$$T_{\text{bms}} = 32\,\text{nK}.$$

The resonance condition, according to Eq. (4.9), corresponds then to

$$\delta_0 = -\frac{\hbar k_{\text{bms}}^2}{2m} = -2\pi \times 13\,\text{kHz},$$

for an atom at rest in the laboratory frame of reference.

4.2.1 Geometrical alignment of the beam-splitter

Since the pair creation is performed along the vertical axis, it is important to guarantee that the beam-splitter lattice is also vertical. The alignment is performed by diffracting the condensate to several diffraction orders via the application of a very strong lattice for a very short time, corresponding to the Kapitza-Dirac regime [197]. If the lattice is purely aligned along the vertical axis, the momentum difference vector between the different orders of diffraction will only have a non-zero component along the vertical z−axis. This corresponds to several atomic

clouds separated in momentum space by the quantity k_{bms} along the $z-$axis and with zero transverse components. However, if the alignment is not perfect, this means that the lattice has a small angle with respect to the vertical direction, each diffracted cloud will have a non-zero momentum component along the $x-$ and/or $y-$ axis. The key advantage of the Kapitza-Dirac regime is that, since the cloud is diffracted several times, we have access to a high multiple of the momentum vector given to each atom. Even if one vector components is small, since it is multiplied several times, we will be able to measure it.

This is represented in the two left panels of Fig. 4.7. We show a 2D momentum distribution on the xz and $yz-$plane after strong diffraction of the condensate in the beam-splitter lattice. It is possible to see five diffracted clouds corresponding to the diffraction orders from -2 to $+3$. To avoid saturation of the detector, the Raman transfer efficiency is lowered such that only a small fraction of the BEC is detected (see more about our Raman transfer in Appendix C). Fig. 4.7a) and c) correspond to a 2D distribution on the $xy-$plane of the diffracted peak at $+3k_{\text{bms}}$ and $-2k_{\text{bms}}$, respectively. Although it is not possible, within our transverse resolution, to identify any modification along the transverse $y-$axis, a small shift is visible along the $x-$axis. To quantify this shift, a cut along the $x-$axis is shown in canvas b) and d). By fitting the distribution with a Gaussian, we find that the diffracted cloud at $+3k_{\text{bms}}$ is centred at $3\times10^{-2}\,(1)\ \text{k}_{\text{lat}}$ while the diffracted cloud at $-2k_{\text{bms}}$ is at $-4\times10^{-2}\,(1)\ \text{k}_{\text{lat}}$. This corresponds to a shift along the $x-$axis of $7\times10^{-2}\,(2)\ \text{k}_{\text{lat}}$ accumulated over 5 diffraction orders. We thus measure an acquired momentum along the $x-$axis of $1.4\times10^{-2}\,(3)\ \text{k}_{\text{lat}}$ per order of diffraction. This is related to an angle along the $x-$axis between the two laser beams forming the lattice

$$\theta_x = 2\sin^{-1}\left(1.4\times10^{-2}/2\right)\times\frac{1083}{1064}\,1/\sin(166°/2) = 0.82\,°.$$

Both the mirror and the 50:50 beam-splitter correspond to 1st order diffraction and the angle along the $x-$axis will have a negligible effect since the accumulate momentum is of the same order as the resolution of the detector. In this sense, the beam-splitter lattice can be, under first order diffraction, considered as a 1D vertical lattice.

Since the cloud is diffracted several times, for the case of the Kapitza-Dirac regime, along the vertical direction and each peak of Fig. 4.7e) corresponds to an integer of k_{bms}, it is possible to measure, very precisely, the value of k_{bms}. By fitting the five diffracted peaks along the vertical direction we find a value of $k_{\text{bms}} = 0.550\,(5)\ \text{k}_{\text{lat}}$.

4.2.2 Alignment via Bragg diffraction

As for the case of the pair production lattice, one has to guarantee that the laser beams forming the beam-splitter lattice overlap on the atomic cloud. Since the wavelength of both beams is close to the atomic transition, one cannot use the repulsive dipole force, as performed in Chapter 3 and the alignment is performed through Rabi oscillation measurement. As before, the Rabi oscillation is obtained by comparing the number of atoms at $+k_{\text{bms}}$ with the ones staying at 0 with a transfer efficiency given by

$$\text{eff} = \frac{N(k_{\text{bms}})}{N(k_{\text{bms}}) + N(0)}, \tag{4.10}$$

where $N(k)$ stands for the number of atoms with momentum k. The oscillation is displayed in Fig. 4.8 where a maximum transfer of 0.94 (3) is obtained for a two-photon Rabi frequency equal to 6.0 (1) kHz. This experimental value agrees well with the expected theoretical value of

$$\Omega_R = \frac{\Gamma^2 I_0 d_{0,0}^2}{4 I_{sat}\Delta} = 2\pi\times 7\,\text{kHz},$$

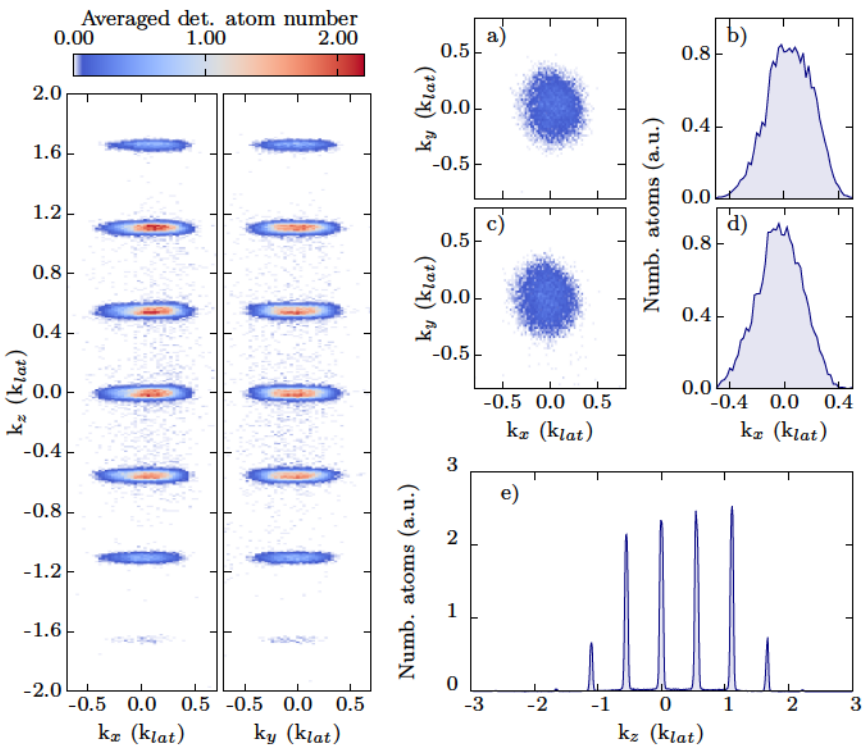

Figure 4.7: Kapitza-Dirac diffraction of the condensate via the beam-splitter optical lattice. Each image corresponds to an average over 30 identical experimental realisations. Left panels: 2D momentum distribution on the xz and yz−planes of the atoms after diffraction on the beam-splitter optical lattice. Diffraction of the condensate by the beam-splitter lattice: alignment along the vertical axis. Right panels: a) 2D momentum distribution on the xy−plane of the diffraction order +3 corresponding to a momentum along the vertical z−axis of $3\,k_{bms}$. *b) Cut along the x−axis of the 2D momentum distribution of panel a). The center of the cloud is determined by a Gaussian fit and equals to* 3×10^{-2} (1) k_{lat}. *c) 2D momentum distribution on the xy−plane of the diffraction order −2 corresponding to a momentum along the vertical z−axis of* $-2\,k_{bms}$. *d) Cut along the x−axis of the 2D momentum distribution of panel c). The center of the cloud is determined by a Gaussian fit and equals to* -4×10^{-2} (1) k_{lat}. *e) Cut along the z−axis of the diffraction pattern. The transverse integration area is equal to* $[0.05\times10^{-2}]^2$ (k_{lat}^2).

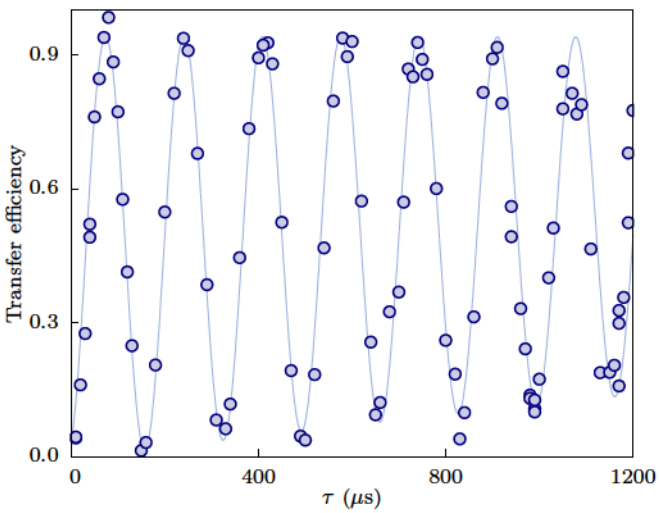

Figure 4.8: Optimised two-photon Rabi oscillation of the condensate on the beam-splitter optical lattice. The lattice is shinned on the atoms and kept for a certain duration τ. *By comparing the populations between the diffracted peak and the initial cloud as described by Eq. (4.10), we retrieve the following oscillation curve corresponding to a Rabi oscillation. We used a frequency sweep for one of the laser beams equal to* 4.7 kHz/ms *in order to compensate the gravity acceleration (blue circles). The oscillation is fitted by Eq. (4.7) with free parameters* Ω_R *and the amplitude transfer probability.*

obtained for a beam intensity of $10\,\mu\mathrm{W/mm}^2$. We thus conclude that the lattice is well aligned on the atoms.

The curve of 4.8 gives us two informations. First, that one can coherently transfer the population between the external states $|\phi_{k=0}\rangle$ and $|\phi_{k=k_{\mathrm{bms}}}\rangle$ for more than 1 ms after which decoherence, mainly coming from spontaneous emission ($\Gamma_{sp} = 0.17\,\mathrm{ms}^{-1}$), lowers the transfer efficiency. And second, it allows us to determine the duration, τ, in order to perform either a 50:50 beam-splitter or a mirror.

4.2.3 Resonance condition in free space

Both the 50:50 beam-splitter and mirror are applied after releasing the atoms from the trapping potential. In order to stay at resonance with the atoms, one has to place the lattice in an accelerating frame of reference in order to compensate the shift induced by the gravitational acceleration. For this purpose a frequency sweep is applied to one of the laser beams. Another frequency shift comes from the fact that the atoms are immediately transferred, via two-photon Raman scattering, to the insensitive magnetic field $m_j = 0$. Due to the geometry of the two lasers beams responsible for the Raman transition a small momentum, $k_{\mathrm{Raman}} = +0.2\,\mathrm{k_{lat}}$, along the vertical direction is given to the atom (see Appendix C for more details).

These two effects lead to a shift in the Bragg diffraction resonance that needs to be compensated. The condition of resonance can then be written as

$$\delta_{\mathrm{lat}} = \omega_2 - \omega_1 = \delta_0 = -\frac{\hbar k_{\mathrm{bms}}^2}{2m} + k_{\mathrm{bms}} g t - \frac{\hbar k_{\mathrm{Raman}} k_{\mathrm{bms}}}{m}, \tag{4.11}$$

with $k_{\mathrm{bms}} g = 2\pi \times 5.07\,\mathrm{kHz/ms}$. This means that if the lattice is not placed in the free fall frame of reference, after 1 ms, the resonance has shifted $2\pi \times 5.07\,\mathrm{kHz}$. Knowing that for the typical intensity of the beam-splitter lattice the resonance width at $t = 3\pi/2\Omega_R$ is approximatively equal to $2\pi \times 5\,\mathrm{kHz}$, see Fig. 4.9 for instance, one can immediately understand that if the shift is not compensate one gets, very rapidly, out of resonance.

To experimentally get the temporal evolution of the resonance condition, we probe the resonant frequency difference δ_0 as a function of the time delay, T, between the end of the Raman transfer and the beam-splitter lattice application (see Fig. 4.10 top panel, red circles). We find, from the linear fit, that the frequency difference evolves at 4.7 (5) kHz/ms, compatible with the theoretical prediction of 5.07 kHz/ms. We then test several compensation rates at 3.9 (3) , 4.7 (3) and 6.6 (3) kHz/ms. For a frequency sweep rate of 4.7 (3) kHz/ms, the resonance is almost constant over T, this means that one has compensate the shift induced by the gravitational acceleration [3]. The effect of the optimised compensation is visible in the Rabi oscillation as shown in Fig. 4.10 (bottom panel). When the compensation rate is equal to 4.7 kHz/ms, the oscillation is maintained over $t > 1\,\mathrm{ms}$ (red circles), while without any compensation, the oscillation vanishes after $200\,\mu\mathrm{s}$ (blue circles).

The value of the detuning at time $T = 0$ corresponds to the quantity

$$\delta_0 = -\frac{\hbar k_{\mathrm{bms}}^2}{2m} - \frac{\hbar k_{\mathrm{Raman}} k_{\mathrm{bms}}}{m} = -2\pi \times 23.6\,(3)\ \mathrm{kHz}\,,$$

in agreement with the expected result of $-2\pi \times 22.7\,\mathrm{kHz}$.

[3] The difference with respect to the theoretical prediction comes from the fact that, at the time this measurement was done, we did not have in our experiment a spectrum analyser able to demodulate the frequency ramp. More recently, this alignment has been repeated and a optimised frequency compensation was obtained for 5.0 kHz/ms in agreement with the theoretical prediction.

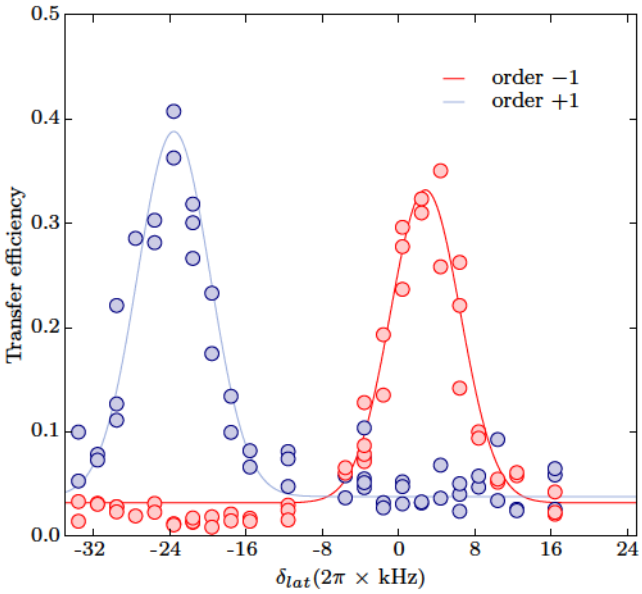

Figure 4.9: Determination of the resonance diffraction condition for the beam-splitter optical lattice. Resonance condition for the beam-splitter diffraction order +1 (corresponding to $q_0 = -k_{lat}$ and thus to a diffracted cloud at $q_0 + k_{lat}$), in blue circles, and −1 ($q_0 = +k_{lat}$), in red circles. The experimental data is fitted by a parabolic function which retrieves the correct behaviour of the theoretical sinus cardinal function, see Eq. (4.7). The resonance frequency is equal to $2\pi \times 2.8$ kHz for the order −1 and of $-2\pi \times 23.6$ kHz for the +1 order.

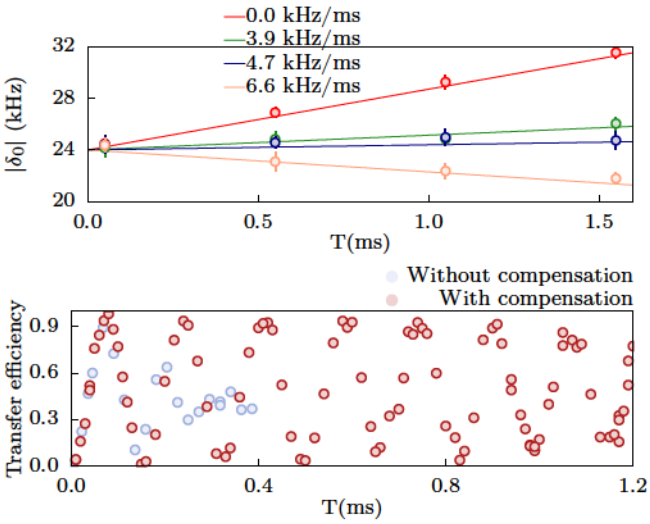

Figure 4.10: Gravity acceleration compensation for the Bragg diffraction resonance. Upper panel: Displacement of the resonance for a compensation rate of 0 (red curve), 3.9 (green line), 4.7 (blue line) and 6.6 kHz/ms (orange line). The theoretical optimal gravity compensation rate is equal to 5.07 kHz/ms in good agreement with our measurement. Bottom panel: Two-photon Rabi oscillation for the case of an optimised gravity compensation (red circles) and without gravity compensation (blue circles).

4.2.4 50:50 beam-splitter and mirror stability

The atomic HOM experiment consists in several repetitions of the same experimental procedure where two atoms are recombined on a 50:50 beam-splitter. One important aspect to ensure is the stability of the 50:50 beam-splitter as well as the one of the mirror.

For this purpose, a test is done with a BEC weakly transferred to the state $m_j = 0$ to avoid detection saturation. We then perform a mirror and 50:50 beam-splitter over 30 different realisations. The transmission efficiency and reflectance for both situations are estimated and the

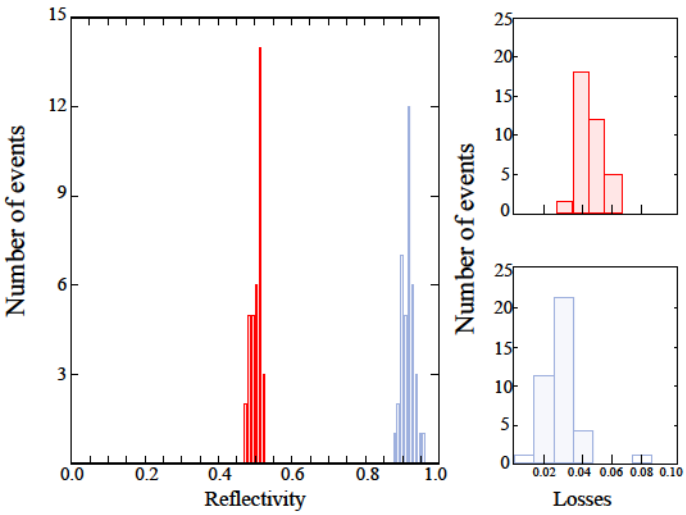

Figure 4.11: Calibration of the beam-splitter transmittance and losses for both mirror and beam-splitter applications. Left panel: Reproducibility of the 50:50 beam-splitter operation (red histogram) and mirror (blue histogram). Right top panel: Losses induced by the 50:50 beam-splitter. Right bottom panel: Losses induced by the mirror.

reflectance of each realisation is shown in Fig. 4.11 where each bin corresponds to a reflectance of one percent,

- For a 50:50 beam-splitter – $\Omega_R\tau = \pi/2 = 50\,\mu$s –, the distribution is centred around a reflectance of 0.51 and has a standard deviation of 0.02 (red histograms);
- For the mirror – $\Omega_R\tau = \pi = 100\,\mu$s – the reflectivity is centred on 0.93 and the distribution presents a standard deviation of 0.02 (blue histograms).

We also observe a weak population transfer to higher diffraction orders. These high orders diffractions represent losses in our beam-splitter operations. To quantitatively measure them, the populations present in non-resonant diffraction orders are compared to the ones present in the 0 and +1. The losses correspond to

$$\text{Losses} = \frac{N(|k| > 2k_{\text{bms}})}{N(0) + N(2k_{\text{bms}}) + N(|k| > 2k_{\text{bms}})}$$

and are plotted in the two right panels of Fig. 4.11. The losses associated with the mirror have an average value of 0.03 and the distribution over 30 realisations presents a standard deviation of 0.01. For the beam-splitter the losses have an average value of 0.05 and a standard deviation of 0.01. However, as shown in detail in Appendix D, these small imperfections have negligible impact on the HOM result.

4.3 Beam-splitter used on the atomic pairs

With the first calibrations of the beam-splitter done so far on the condensate, let us now adjust them to the atomic beams.

Resonance condition for the atomic pairs

Since the pairs are moving in the laboratory frame of reference, the frequency difference between the two laser beams forming the beam-splitter lattice has to be adjusted to the momentum

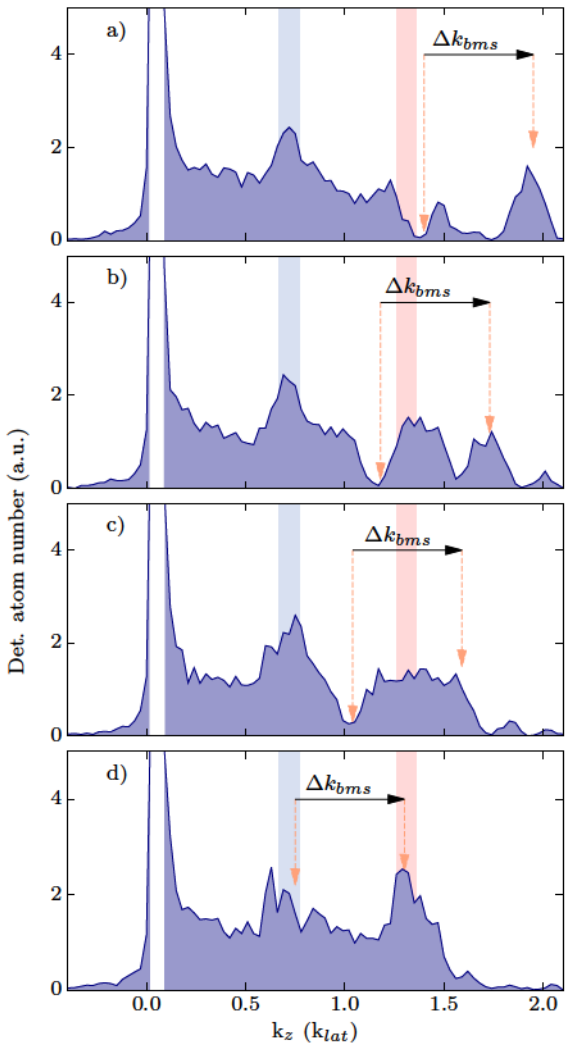

Figure 4.12: Calibration of the beam-splitter resonance on the atomic pairs. From top to bottom the frequency difference corresponds to: a) $\delta_{lat} = 2\pi \times 85$ kHz, b) 74 kHz, c) 66 kHz, d) 57 kHz. The blue and red boxes represent the initial positions of beam a and b. The arrows in orange indicate the diffracted classes of momenta. The difference between the two is always equal to $\Delta k_{bms} = 0.55\,k_{lat}$ and corresponds to the momentum periodicity of the beam-splitter lattice. The diffraction always occurs from lower to higher momentum as indicated by the direction of the black arrow.

difference of atomic beams a and b. Since the beam-splitter exchanges the two atomic beams, the condition of resonance for beam a, with momentum k_a, to be transferred into $k_a + k_{\text{bms}}$ is the same than the one of transferring beam b, with momentum k_b, into $k_b - k_{\text{bms}}$. From Eq. (4.11) and knowing that beam a has an initial momentum $k_a = 0.73\,(1)\ k_{\text{lat}}$ along the vertical direction (beam b corresponds to $k_b = 1.27\,(2)\ k_{\text{lat}} = k_a + k_{\text{bms}}$), we find that beam a is at resonance for a frequency different equal to $\delta_0 = 2\pi \times 58$ kHz.

Contrary to what happens with the condensate, where the diffracted population is easily measurable, for the atomic pairs the situation is more complicated since the diffraction of beam a is going to superimpose with beam b. Thus, by measuring the transfer efficiency, one can never reach zero nor one, since both external states have non-zero population at the beginning of the interaction.

The solution is to take advantage of the background population between beams a and b seen in Section 3.3. One can then look at the population transfer to the order +1 for atoms with momentum equal or lower than k_b but higher than k_a, such that they diffract to classes of momenta where the populations are zero before application of the beam-splitter.

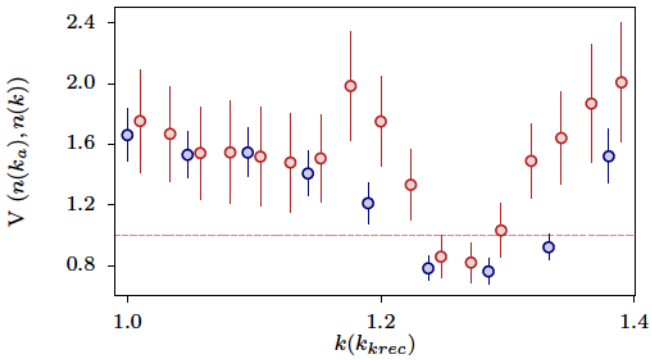

Figure 4.13: *Effect of the beam-splitter application on the variance of the difference between the atomic pairs. Variance as a function of the analysed zone for the atomic pairs after application of a mirror (red curve) or directly after producing the pairs (blue curve). The application of the mirror leads to a small increase of the fluctuations.*

This is shown in Fig. 4.12 where the effect of the beam-splitter lattice, calibrated such that it acts as a mirror, on the atomic distribution is represented as a function of the laser detuning δ_{lat}. The blue and red shaded area indicate the initial central position of beam a and b, respectively. The orange arrows show the diffracted population, with the arrow on the left indicating the atoms at resonance and the right one the transferred population.

Fig. 4.12a) corresponds to the situation for which the lattice has a frequency difference of $2\pi \times 84\,\text{kHz}$, almost at resonance with beam b. As expected for the case of a π pulse, the atomic beam b has a central hole and a diffracted cloud is visible at $k_b + k_{\text{bms}}$. The half-width of the diffracted peak at $1/\sqrt{e}$, as a function of k, is equal to $0.06\,\text{k}_{\text{lat}}$ and corresponds to the resonance width of the mirror in momentum space. Canvas b) corresponds to $\delta_0 = 2\pi \times 74\,\text{kHz}$ which, theoretically, is resonant with $k = 1.066\,\text{k}_{\text{lat}}$ and a hole is visible around this value. The third canvas corresponds to $\delta_0 = 2\pi \times 66\,\text{kHz}$, the diffracted cloud is no longer distinguishable from beam b, since the transferred atoms are expected at $1.45\,\text{k}_{\text{lat}}$ and overlap with those of beam b. For the same reason, the transfer efficiency does not reach a value of 1, since the two momenta have a non-vanishing initial population. Finally, the last canvas corresponds to $\delta_0 = 2\pi \times 57\,\text{kHz}$. There are neither hole nor diffracted cloud meaning that beam a and b are exchanged. This is in good agreement with the expected result of $0.58\,\text{k}_{\text{lat}}$.

4.4 Noise induced by the beam-splitter on the atomic beams

In this section, we would like to see if the beam-splitter lattice adds noise to the population difference between the atomic beams a and b. One can, for example, compare the variance of the population difference without mirror to the situation in which the atomic beams are exchanged via the application of an atomic mirror.

First we create pairs of atoms in momentum space then, the atoms are transferred to the $m_j = 0$ state via two-photon Raman scattering done in $300\,\mu\text{s}$ after switching off the dipole trap. The atomic mirror is then immediately applied, and the populations between beam a and b are exchanged with an efficiency of 93%. The variance of the difference is then measured as described in Subsection 3.4.2. The normalised variance V presents a minimum when both zones are centred on top of the atomic beams as seen in Fig. 4.13. Both the obtained results with (red points) or without the mirror (blue points) are plotted in the same figure.

The measured normalised variance of the difference after exchanging the two atomic beams is equal to $0.80\,(5)$, while the minimum registered without mirror is equal to $0.75\,(5)$. This

difference is negligible but can be partially explained by the value of the mirror reflectivity of 93 %. This corresponds to a reduction of the detection efficiency that can be written as

$$\sqrt{\tilde{\eta}} = \sqrt{\eta} \times \sqrt{R}.$$

Assuming that the *real* variance of the difference is zero [4] the detected variance is then given by $V_{\text{det.}} = 1 - \tilde{\eta} = 0.77$ (see Subsection 3.4.2) and allows one to partially understand the measured difference.

The beam-splitter lattice appears to be rather noiseless and can be safely used to coherently manipulate the atomic pairs.

4.5 Phase stability of the beam-splitter

Although for the HOM experiment the phase induced by the 50:50 beam-splitter on the atoms does not modify the experimental result (see Chapter 1), it is interesting to look at its stability for possible future applications. The first tests were performed by applying twice the beam-splitter on the BEC in order to produce two clouds of equal momenta. Those clouds are then overlapping on the detector after time-of-flight due to their expansion. This leads to an interference pattern whose central position depends on the relative phase of the two beam-splitter pulses [198].

After releasing the BEC from the optical trap, the beam-splitter is shinned once and two diffracted clouds with momenta $0.55\,\mathrm{k_{lat}}$ and $1.10\,\mathrm{k_{lat}}$ are produced corresponding to first and second order Bragg diffraction. One millisecond later, the beam-splitter is again applied on the atomic beams but this time only first order diffraction from the peak at $0.55\,\mathrm{k_{lat}}$ occurs. After the second pulse, two clouds of atoms with identical velocities propagate in space. This is schematically represented in Fig. 4.14a) and b), where the blue line corresponds to the trajectory of the cloud with momentum $1.10\,\mathrm{k_{lat}}$ and the red one corresponds to the trajectory of the other cloud that had been first diffracted at $0.55\,\mathrm{k_{lat}}$ and afterwards into $1.10\,\mathrm{k_{lat}}$. For simplicity, let us call the blue cloud 1 and the red one 2.

In order to observe interferences, the two clouds need to overlap after time-of-flight. Their spatial separation after the application of the last beam-splitter pulse corresponds to

$$z_1(t) = z_0 + 2v_{\text{bms}}t - \frac{1}{2}gt^2\,,$$

and

$$z_2(t) = z_0 + 2v_{\text{bms}}t - v_{\text{bms}}\tau - \frac{1}{2}gt^2\,,$$

with τ the time difference between the two beam-splitter pulses.

The two clouds fall on the MCP and their respective arrival time leads to the equality [5]

$$\frac{1}{2}g\left(t_1^2 - t_2^2\right) + 2v_{\text{bms}}\left(t_2 - t_1\right) = v_{\text{bms}}\tau\,.$$

Consider the solution in which $t_2 = t_1 + \Delta t$ with Δt corresponding to a small time difference when compared to the time-of-flight of t_1. This leads to the expression

$$-gt_1\Delta t + 2v_{\text{bms}}\Delta t = v_{\text{bms}}\tau\,,$$

[4] The detection efficiency η has been estimated to 25% through the variance of the difference equal to 0.75 (5) assuming that the real variance is equal to zero.

[5] It is important to note that we are only looking at the arrival time of the distribution center. Both clouds have a certain spread in momentum space which is going to be translated in an arrival time width.

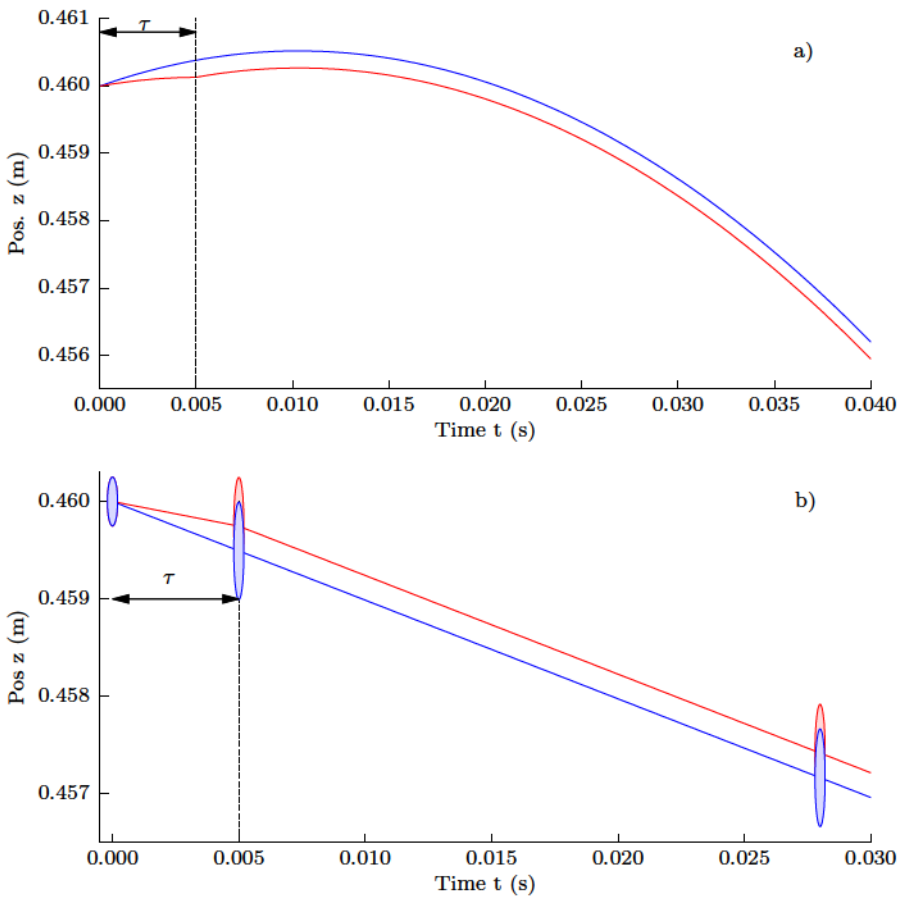

Figure 4.14: *Representation of the interference between two condensates. a) At scale representation of the trajectories of the two atomic clouds for a time interval between the two Bragg pulses of* 5 ms *in the laboratory frame of reference. b) Schematic representation of the overlap of the two clouds during the time-of-flight. The size of the condensate is not at scale. The two clouds are represented in red and blue. Their overlap corresponds to the interference zone.*

where since $gt_1 \gg 2v_{\text{bms}}$ and $\tau = 1$ ms

$$\Delta t = -\frac{v_{\text{bms}}\tau}{gt_1} = -17\mu s\,.$$

Knowing that the arrival time of the condensate corresponds to a distribution with half-width at $1/\sqrt{e}$ approximatively equal to 400 μs, one can conclude that for $\tau = 1$ ms the two clouds are still well overlapped. It would be necessary to wait between the two beam-splitter pulses for more than $\tau = 27$ ms in order to substantially reduce their spatial overlap.

Since the two clouds are overlapping after time-of-flight, one can now determine the relative phase between both clouds accumulated during these trajectories in order to estimate the interference pattern. In the free-fall frame of reference, the relative phase difference is then obtained through the propagation operator in free space [115] and by adding the phases imprinted by the beam-splitter lattice on the atoms, φ_1 and φ_2 (see Appendix D for more details). The phase difference is then equal to

$$\begin{aligned}\Delta\phi &= \frac{mz_1^2}{2\hbar t} - \frac{mz_2^2}{2\hbar t} + \varphi_1 - \varphi_2 \\ &= \frac{m}{2\hbar t}\left(z_1^2 - z_2^2\right) + \varphi_1 - \varphi_2\end{aligned}$$

with $z_2 = z_1 - v_{\text{bms}}\tau$ and $v_{\text{bms}}\tau \ll z_1$,

$$\Delta\phi = \frac{m v_{\text{bms}}\tau}{2\hbar t} z_1 + \Delta\varphi\,,$$

where $\Delta\varphi = \varphi_1 - \varphi_2$.

After time-of-flight, cloud 1 corresponds to a distribution of atoms centred on $t_0 = 321$ ms and with an half-width of 400 μs. An atom with arrival time difference Δt, respectively to the center of the distribution, is then, in the laboratory frame of reference, described by

$$z_1(t_0 + \Delta t) = z_0 + 2v_{\text{bms}}(t_0 + \Delta t) - \frac{1}{2} g\,(t_0 + \Delta t)^2\ .$$

In first order in Δt, one can write

$$z_1(t_0 + \Delta t) = \text{const.} + \left(\frac{g\Delta t}{\hbar} m v_{\text{bms}}\tau\right),$$

with the constant term corresponding to $\frac{m v_{\text{bms}}\tau}{\hbar t_0} + \frac{2v_{\text{bms}}t_0 - 1/2 g t_0^2}{2\hbar t_0} m v_{\text{bms}}\tau$.

The phase difference can thus finally be written as

$$\Delta\phi = \Delta\varphi + \text{const.} - \frac{g\Delta t m v_{\text{bms}}\tau}{\hbar}\,,$$

which for $\tau = 1$ ms corresponds to a fringe spacing $t_{\text{fringe}} = \frac{1}{k_{\text{bms}} g\tau} = 200\ \mu$s.

Suppose that both atomic wave-packets are described by two Gaussian functions, with same half-width at $1/\sqrt{e}$ equal to σ such that

$$f_1(\Delta t) = \exp\frac{-(t_0 - \Delta t)^2}{2\sigma^2}\,,$$
$$f_2(\Delta t) = \exp\frac{-(t_0 - dT - \Delta t)^2}{2\sigma^2}\,,$$

where $dT = -\frac{v_{\text{bms}}\tau}{g t_0}$ accounts for the arriving time difference between the two clouds. Then after time-of-flight, if the two clouds overlap on the detector inside their correlation length, [6] their amplitudes sum and one recover the total intensity. The phase difference accumulated by the two different clouds induces a periodic distribution of the number of atoms (atomic intensity) on the arrival time distribution described by

$$\begin{aligned} N_{at}(\Delta t) &= \left|f_1(\Delta t) + f_2(\Delta t)\right|^2 \\ &= 2\cos\left(\Delta\phi\right) f_1(\Delta t) \times f_2(\Delta t) + \left|f_1(\Delta t)\right|^2 + \left|f_2(\Delta t)\right|^2 \\ &= 2\cos\left(\Delta\phi\right)\exp\left(-\frac{(t_0 - \Delta t)^2}{2\sigma^2} - \frac{(t_0 - dT - \Delta t)^2}{2\sigma^2}\right) \\ &+ \exp\left(-\frac{(t_0 - \Delta t)^2}{\sigma^2}\right) + \exp\left(-\frac{(t_0 - dT - \Delta t)^2}{\sigma^2}\right) \end{aligned} \tag{4.12}$$

[6] For a pure condensate, the correlation length is equivalent to the size of the cloud. However, during the expansion of the cloud interactions play a very important role and the density is not the same along the entire cloud and so, the phase coherence along the cloud can change. Here, the number of atoms in each cloud is reduced in order to avoid the effect of interactions as well as the saturation of the detector.

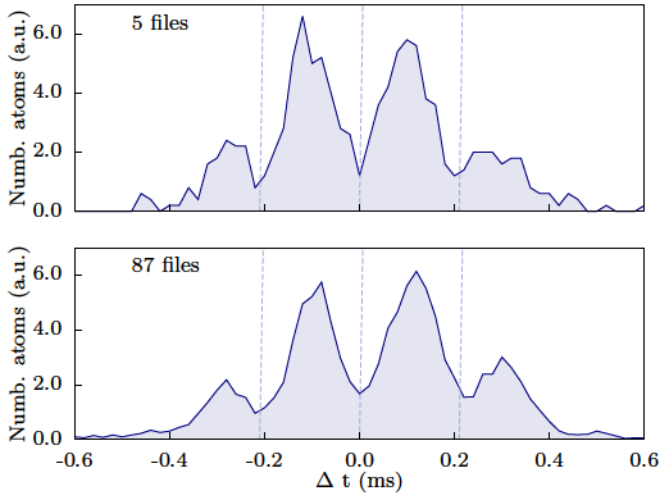

Figure 4.15: ***Interference between two clouds from the condensate.*** *Two clouds of atoms are extracted from the condensate with momentum of* $k = 1.01k_{bms}$*. After time-of-flight, they recombine on the MCP and interfere leading to the following patterns. a) Corresponds to an average over 5 identical experimental realisations and b) corresponds to an average over 87 realisations. Since the interference pattern is still visible after averaging over 87 repetitions, one can conclude that the phase fluctuation is small.*

with periodicity $k_{\mathrm{bms}}g\tau$.

The interference pattern position is then going to depend on the phase difference between the two imprinted terms φ_1 and φ_2. If from one experimental realisation to another $\Delta\varphi$ fluctuates, the central position of the interference moves, and, after averaging over several realisations, the interference pattern washes out.

Experimentally, we detect density fringes on the arrival time distribution with a periodicity of 200 μs as expected. This can be seen in Fig. 4.15. In Fig. 4.15a), an average over 5 realisations is performed, while in Fig. 4.15b) the distribution corresponds to 87 realisations. One can see that the fringes never reach a contrast of one which we attribute to an imbalanced populations between the two atomic clouds. However, the fact that after 87 realisations, the same contrast is recovered indicates that the relative phase of the interferometric scheme does not fluctuate much. This is a proof of a relatively stable phase difference between the two laser beams forming the beam-splitter lattice.

One can also estimate how sensitive is the contrast of the interference pattern on the fluctuation of the imprinted phase difference $\Delta\varphi$. For this purpose, we consider the theoretical prediction of two equally populated clouds produced with 1ms difference and detected 321 ms later, represented in Fig. 4.16. If the phase is perfectly stable, Fig. 4.15a), the interference signal has a contrast of 1 and periodicity of 200 μs as expected. Fig. 4.15b) corresponds to an integration over the phase difference $\Delta\varphi$ performed between $-\pi/4$ to $\pi/4$, which accounts for imprinted phase difference fluctuations between $-\pi/4$ to $\pi/4$. The contrast lowers slightly, meaning, that even if the relative phase between the two beam-splitter pulses vary over $\pi/4$, the interference contrast is almost unaffected. To modify it significantly, the fluctuations need to vary over $\pm 3\pi/4$ for which the interference pattern washes out as shown in Fig. 4.16c).

With these experimental tests, one can guarantee that the phase difference fluctuation is smaller than $3\pi/4$. This test is only a first qualitative estimation of the phase fluctuations in our system. Other tests are currently being carried on in order to get a more quantitative estimation of those fluctuations.

It is also important to note that the current study is only sensitive to the phase difference

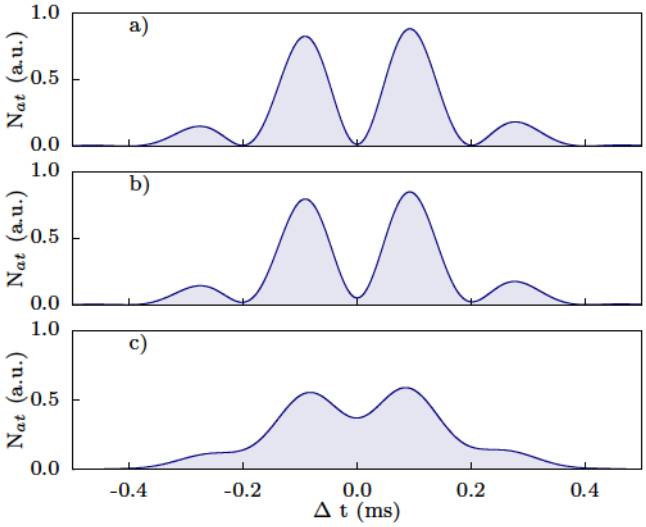

Figure 4.16: Effect of phase fluctuations on condensate interference. Predicted interference pattern between two cloud of atoms from the condensate with equals population and with relative phase fluctuations of a) $\pm\pi/8$; b) $\pm\pi/4$, c) $\pm 3\pi/4$.

between the two pulses and does not give any information about the absolute phase stability of the beam-splitter. For EPR-like experiment, for example, the absolute phase stability can be necessary as proposed in Ref. [199].

4.6 Autocorrelation measurement via a 50:50 beam-splitter

As said previously, our detection mechanism is very similar to a photo-multiplier where each atom is converted into an electronic signal and, as so, the same quantum detection theory [95, 200, 201], can be applied. The main advantage of our detector is that its dead time, estimated around 20 ns, as well as its temporal resolution, 300 ns, are smaller than the typical arriving time difference between two atoms from the same mode, that is usually on the order of 1 μs. This implies that one can, without splitting the incoming beam, do an autocorrelation measurement as shown in Section 3.4.1.

However in optics, the arrival time difference between two photons from the same source lays below the time resolution of the photo-diodes and it is impossible to directly measure the autocorrelation function. The solution is then to split the incoming beam in two through a 50:50 beam-splitter. Then, by detecting the number of photons on the two output ports of the 50:50 beam-splitter and performing a comparison between the two signals one can recover the normalised autocorrelation function. Since we also have an atomic beam-splitter, we can compare our *direct* measurement of the autocorrelation function, to the usual method used in quantum optics.

The normalised autocorrelation is given by

$$g^{(2)}_{bb} = \frac{\langle \hat{b}^\dagger \hat{b}^\dagger \hat{b}\hat{b} \rangle}{\langle \hat{b}^\dagger \hat{b} \rangle \cdot \langle \hat{b}^\dagger \hat{b} \rangle}$$

where $\langle \hat{b}^\dagger \hat{b}^\dagger \hat{b}\hat{b} \rangle = \langle \hat{n}_b (\hat{n}_b - 1) \rangle$. This normal ordering average comes naturally from the fact that when n particles are at play, if one detects 1 particle on one side of the 50:50 beam-splitter, $n-1$ particles are detected on the other side [202]. As in Chapter 1, the output ports field operators

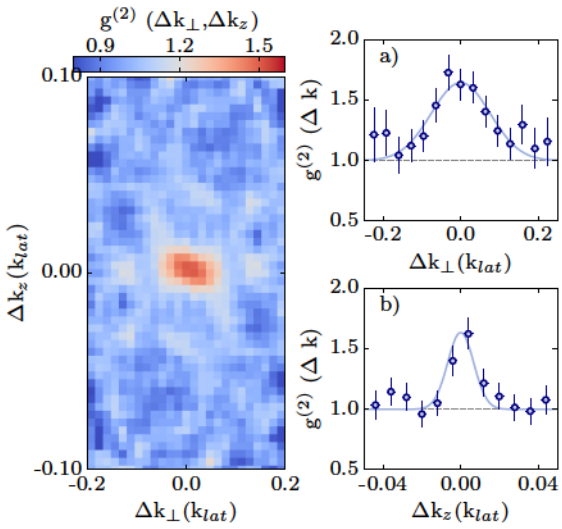

Figure 4.17: *Autocorrelation measurement on beam b via application of a 50:50 beam-splitter. The autocorrelation is obtained after splitting beam b in two via a 50:50 beam-splitter application. Left panel: 2D autocorrelation function representation as a function of the momenta difference between beam k_b and the diffracted beam $k_b + k_{bms}$, on longitudinal z−axis Δk_z and transverse direction $\Delta k_\perp$. Right panels: a) Projection of the autocorrelation function on the transverse direction x (the same behaviour is recovered for the y−axis.). The blue line represents a Gaussian fit from which the amplitude and width are extracted. The integration along the other two axis correspond to an integration area of $[\mathcal{L}_x \times \mathcal{L}_z] = [2\times10^{-2} \times 1\times10^{-2}]\ \mathrm{k}_{lat}^2$. b) Projection of the autocorrelation function on the vertical z−axis. The blue line represents a Gaussian fit from which the amplitude and width are extracted. The integration along the two others axis correspond to $\left[\mathcal{L}_x \times \mathcal{L}_y\right] = [2\times10^{-2}]^2\ \mathrm{k}_{lat}^2$*

(c and d) can be written as

$$\hat{c} = \frac{1}{\sqrt{2}}(\hat{b} + \hat{O})$$
$$\hat{d} = \frac{1}{\sqrt{2}}(\hat{b} - \hat{O})$$

with $\hat{O}$ the vacuum operator and, consequently, the correlation between ports corresponds to

$$\frac{\langle \hat{c}^\dagger \hat{d}^\dagger \hat{c}\hat{d}\rangle}{\langle \hat{c}^\dagger \hat{c}\rangle \cdot \langle \hat{d}^\dagger \hat{d}\rangle} = \frac{\langle \hat{b}^\dagger \hat{b}^\dagger \hat{b}\hat{b}\rangle}{\langle \hat{b}^\dagger \hat{b}\rangle \cdot \langle \hat{b}^\dagger \hat{b}\rangle}.$$

In order to compare these two methods, we experimentally perform a 50:50 atomic mirror on beam b. The cross-correlation between the number of atoms present in $N(k_b)$ with the ones at $N(k_b + k_{\mathrm{bms}})$ is computed, by the same method as in Section 3.4.1. Fig. 4.17 shows the obtained correlation function on the yz−plane as well as the integrated projections on the x and z−axis.

By fitting the curves with an empirical Gaussian function, we retrieve the half-width at $1/\sqrt{e}$ of the obtained autocorrelation $\sigma_z = 8.2\times10^{-3}\,(1)\ \mathrm{k_{lat}}$ along the vertical z−axis and $\sigma_\perp = 6\times10^{-2}\,(1)\ \mathrm{k_{lat}}$ along the transverse directions. The amplitude of the correlation is equal to $1.6\,(1)\ \mathrm{k_{lat}}$ below the measured autocorrelation value of beam b in Section 3.4, that was equal to $2.00\,(5)$. The reason for this difference is still unclear at the moment.

The width of the correlation is, in very good agreement with the direct measurement, allowing us to conclude that the beam-splitter momentum periodicity is very well defined. This means that an atom with momentum k is diffracted into $k + k_{\mathrm{bms}} \pm \Delta k_{\mathrm{bms}}$ with Δk_{bms} much smaller than the autocorrelation function width, $\sigma_z = 8.2\times10^{-}3\,(1)\ \mathrm{k_{lat}}$.

4.7 Conclusion

In this Chapter, the atomic beam-splitter based on Bragg diffraction has been intensively discussed. The geometrical alignment and calibration of the beam-splitter, as well as the stability of both reflectance and transmittance were discussed. Preliminary calibrations of the phase stability of the beam-splitter via BEC interference has been presented opening the way to promising future experiments.

Perspectives, the adiabatic passage

The actual calibration of the beam-splitter shows that it can be directly used for the realisation of the HOM experiment. However, some limitations are still present. Since we are interested in dealing with the entire atomic beam, this implies a broad resonance condition. A direct consequence, when a square pulse is used, is a non-vanishing probability to diffract the cloud to higher diffraction orders. This translates into losses for both the 50:50 beam-splitter and mirror, as discussed in Section 4.2, that have been estimated to be of a few percent and, in this sense, are completely negligible (see discussion in Appendix D).

However, the use of a square pulse can also lead to a non-uniform value of the reflectivity over the entire momentum spread of the cloud as seen in Section 4.1. One possible solution for this problem would be to use adiabatic pulses in analogy with the technology developed in RMN (see for instance Ref. [203] and Ref. [204] for more details). The idea is then, through a combination of specific intensities, frequencies and phases, to transfer the population of the atomic beams with equal efficiency inside a tunable momentum width, see Ref. [205] for instance. This project is currently being developed in our team.

Along the past three chapters, we reported the different improvements to the existing metastable helium experiment in order to accomplish the HOM experiment. The three fundamental blocks that have been discussed at this point of the manuscript correspond to

- a single atom detector;
- a source of atomic pairs;
- a coherent atomic 50:50 beam-splitter and mirror.

We have shown that this three blocks are well under control in our experiment and we are now ready to finally discuss the atomic Hong–Ou–Mandel experiment.

Bibliography

[43] A. D. Cronin, J. Schmiedmayer, and D. E. Pritchard, "Optics and interferometry with atoms and molecules", Rev. Mod. Phys. **81**, 1051–1129 (2009) (cit. on pp. 4, 108).

[95] R. Glauber, "The Quantum Theory of Optical Coherence", Phys. Rev. **130**, 2529–2539 (1963) (cit. on pp. 25, 123).

[115] J. V. Gomes, A. Perrin, M. Schellekens, D. Boiron, C. I. Westbrook, and M. Belsley, "Theory for a Hanbury Brown Twiss experiment with a ballistically expanding cloud of cold atoms", Phys. Rev. A **74**, 053607 (2006) (cit. on pp. 28, 120).

[116] D. M. Giltner, R. W. McGowan, and S. A. Lee, "Atom Interferometer Based on Bragg Scattering from Standing Light Waves", Phys. Rev. Lett. **75**, 2638–2641 (1995) (cit. on pp. 28, 106).

[153] C. Pethick and H. Smith, *Bose-Einstein Condensation in Dilute Gases* (Cambridge University Press, 2002) (cit. on pp. 44, 75, 111).

[173] J. H. Denschlag, J. E. Simsarian, H. Häffner, C. McKenzie, A. Browaeys, D. Cho, K. Helmerson, S. L. Rolston, and W. D. Phillips, "A Bose-Einstein condensate in an optical lattice", J. Phys. B-At. Mol. Opt. **35**, 3095 (2002) (cit. on pp. 68, 69, 106).

[177] J. Dalibard, *Cours du collège de France* (2014) (cit. on pp. 69, 107).

[179] M. Greiner, I. Bloch, O. Mandel, T. Hänsch, and T. Esslinger, "Exploring Phase Coherence in a 2D Lattice of Bose-Einstein Condensates", Phys. Rev. Lett. **87**, 160405 (2001) (cit. on pp. 69, 85, 106).

[197] P. L. Kapitza and P. A. M. Dirac, "The reflection of electrons from standing light waves", Math. Proc. Cambridge **29**, 297–300 (1933) (cit. on p. 111).

[198] M. R. Andrews, C. G. Townsend, H.-J. Miesner, D. S. Durfee, D. M. Kurn, and W. Ketterle, "Observation of Interference Between Two Bose Condensates", Science **275**, 637–641 (1997) (cit. on p. 119).

[199] A. J. Ferris, M. K. Olsen, and M. J. Davis, "Atomic entanglement generation and detection via degenerate four-wave mixing of a Bose-Einstein condensate in an optical lattice", Phys. Rev. A **79**, 043634 (2009) (cit. on p. 123).

[200] C. Cohen-Tannoudji, J. Dupont-Roc, and G. Grynberg, *Photons et atomes : introduction à l'électrodynamique quantique*, Savoirs actuels, Précédemment publié en co-édition par InterÉditions et CNRS Éditions (Paris, 1987), dans la collection Savoirs actuels, ISSN 0989-3334, avec un avant-propos différent (EDP sciences Paris, Les Ulis, 2001) (cit. on p. 123).

[201] R. Glauber, "Coherent and Incoherent States of the Radiation Field", Phys. Rev. **131**, 2766–2788 (1963) (cit. on p. 123).

[202] R. Glauber, "The Quantum Theory of Optical Coherence", Physical Review **130**, 2529–2539 (1963) (cit. on p. 123).

[203] M. A. Bernstein, K. F. King, and X. J. Zhou, *Handbook of MRI Pulse Sequences*, 1st ed. (Academic Press, Sept. 21, 2004) (cit. on p. 125).

[204] A. Tannús and M. Garwood, "Adiabatic pulses", NMR in Biomedicine **10**, 423–434 (1997) (cit. on p. 125).

[205] T. Esslinger, F. Sander, M. Weidemüller, A. Hemmerich, and T. Hänsch, "Subrecoil Laser Cooling with Adiabatic Transfer", Phys. Rev. Lett. **76**, 2432–2435 (1996) (cit. on p. 125).

Chapter 5

Atomic Hong–Ou–Mandel experiment

Contents

5.1 HOM effect: how to measure? . . . 130
5.1.1 How to tune distinguishability? . . . 130
5.1.2 Filtering method: 3D detection and noiseless beam-splitter . . . 133
5.2 HOM: experimental sequence . . . 136
5.3 Analysis and measurement of the HOM effect . . . 137
5.3.1 Analysis: momentum selection . . . 138
5.3.2 Analysis: optimisation of the integration volume . . . 140
5.3.3 Analysis: population stability . . . 142
5.4 Dip visibility: theoretical estimation . . . 144
5.4.1 Pair population . . . 146
5.4.2 Evolution of the signal to noise ratio of the HOM-dip visibility with $\langle n \rangle$ 148
5.5 HOM-dip width: some explanation . . . 151
5.5.1 Prediction of the width . . . 152
5.5.2 Comparison with the experimental results . . . 154
5.6 Coalescence effect . . . 157
5.6.1 Autocorrelation measurement . . . 157
5.6.2 Conditional probability . . . 160
5.7 Others way to measure the destructive interference: variance of the population difference . . . 161
5.8 Role of the interactions . . . 163
5.9 Conclusion . . . 164

> The whole is greater than the sum of its parts.
>
> Aristotle

As discussed in Chapter 1, in order to attain the HOM experiment, four fundamental experimental blocks are necessary:

- a single atom detector — the MCP detector briefly discussed in Subsection 2.1.2. This is the atomic equivalent of a photomultiplier in optics. It allows us to extract both second order auto- and cross- correlation;

- a source of atomic pairs — the pairs are produced via dynamical instabilities from a condensate placed on a moving lattice, as described in Section 3.2 and Section 3.3. The pairs show stronger-than-classical correlations, as demonstrated in Section 3.4. The averaged number of atoms also needs to be lower than 1, as discussed in Section 1.2;
- a coherent atomic 50:50 beam-splitter and mirror — performed via Bragg diffraction on a lattice designated *beam-splitter* lattice as discussed in Chapter 4;
- and a filtering procedure in order to guarantee the indistinguishability between particles — performed by filtering the atom source after the beam-splitter via the 3D reconstruction in momentum space of our detector. For a lossless beam-splitter it is the equivalent of an atomic pinhole. This will be developed in Section 5.1.

This chapter is organised as follow. In Section 5.1 the filtering method adopted in the experiment will be discussed and the procedure to detect the HOM effect pointed out. The experimental protocol to accomplish the two-particle interferometer will be presented in Section 5.2. The analysis of the interferometric effect will be discussed in Section 5.3, where we identify a decrease of the cross-correlation between two output ports as a function of the overlap between the two atomic beams. The obtained result allows us to conclude that the dip cannot be explained classically. The comparison with the theoretical expected visibility will be developed in Section 5.4 and the expected dip width in Section 5.5. In Section 5.6, the coalescence effect, corresponding to the increased probability of detecting two particles in one of the two output ports, is discussed and compared to the destructive interference result. Linked to both quantities is the variance of the difference of population that can also be used in order to probe the interference behaviour, as shown in Section 5.7. Finally, the role of particle interactions will be briefly discussed in Section 5.8 closing the analysis of the two-particle interference effect.

5.1 HOM effect: how to measure?

The HOM effect corresponds to a situation where two photons, with undefined relative phases, are plugged at the input ports of a 50:50 beam-splitter. If the two photons are indistinguishable the coincidence count between the two output ports of the beam-splitter vanishes, unlike what one would expect for classical particles or waves. One can measure this result in two different ways, either by focusing on the coalescence effect of the out-coming state [79]

$$|\psi\rangle_{\text{out}} = |0_c,\, 2_d\rangle + |2_c,\, 0_d\rangle,$$

that is, the increased probability of detecting two particles in one of the two output ports, or by looking at the reduction of the coincidence counts between the two output ports. In quantum optics experiments, the HOM effect is often probed via the reduction of coincidence counts. In this situation, two photodiodes at the output ports of the 50:50 beam-splitter, c and d, detect the out coming photons and a coincidence count is performed between the two. The coincidence count corresponds to the probability of detecting one photon on a time interval $t + \Delta t$ in one of the output ports knowing that another photon has been detected at time t at the other. When the photons are indistinguishable this coincidence count reaches zero but, on the other hand, if the photons are distinguishable, the coincidence count has a finite, non-zero, value.

5.1.1 How to tune distinguishability?

Distinguishability between particles can either be experimentally achieved with a change in the optical paths [54, 206] or phase difference [77]. In the 1987 experiment of Hong, Ou and Mandel,

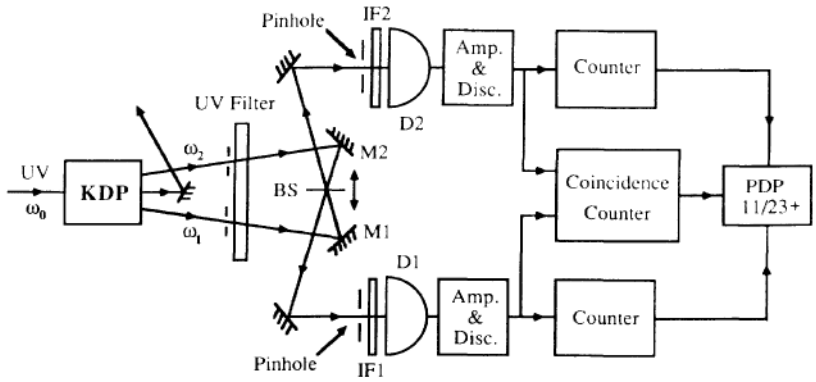

Figure 5.1: ***Schematic representation of the 1987's HOM experiment.*** *Two photons produced via parametric down-conversion are plugged into a 50:50 beam-splitter, after passing through a frequency and spatial filter. Two photodiodes register the number of detected photons on both output ports. A coincidence count is performed afterwards. Figure copied from Ref. [54].*

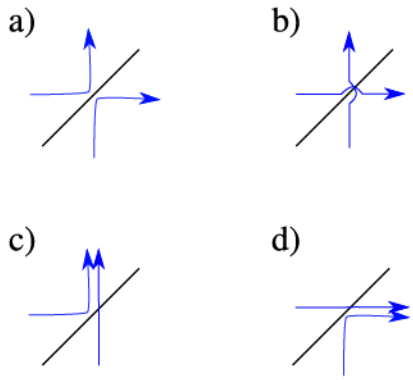

Figure 5.2: **Classical scenarios for two incoming particles.** *Schematic representation of the four possible cases.The blue arrows represent the arriving particles beams on a 50:50 beam-splitter. Case: a) both particles are reflected; b) both transmitted; c) and d) one particle is reflected and the other one transmitted.*

the optical path was tuned by changing the position of the beam-splitter. If the paths of the photons are different, they do not overlap on the beam-splitter and it is possible to distinguish them. On the other hand, if the photons overlap, below the coherence length of the photon wavepacket, the particle's paths are indistinguishable and the coincidence count decreases to zero. The original experimental set-up is schematically represented in Fig. 5.1 [54]. The source corresponds to a pair of photons produced via parametric down-conversion. Since this is a multimode source, a filter is applied in order to select both the spatial and temporal modes. The two photons travel apart from each other until they reach the mirrors M1, M2 that recombine the beams on a 50:50 beam-splitter. The photons are then either transmitted or reflected as schematically represented in Fig. 5.2. Two photodiodes placed at each exit of the beam-splitter record the number of photons per port. When two photons exit coincidently the beam-splitter through different ports, a coincidence count is recovered. By changing the position of the beam-splitter and counting the number of coincidences, one retrieves the celebrated HOM-dip where the minimum corresponds to the case of indistinguishable paths and the background to distinguishable paths as shown in Fig. 5.3.

Adaptation to the case of atoms

The beam-splitter, in our case, acts on momentum space. By changing the application time of the beam-splitter, we can tune the distinguishability of the two atomic beams. The indistinguishable

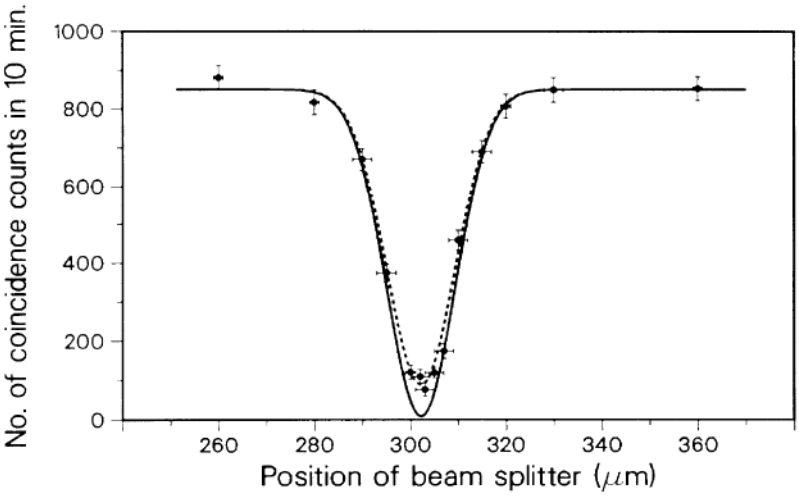

Figure 5.3: 1987 HOM-dip. It is possible to see that the coincidence count goes to zero when the position of the beam-splitter is such that the two photons are indistinguishable. Since their speed is equal to the speed of light, the spatial width of the dip gives an indirect information on the temporal correlation length of the photons. Figure copied from Ref. [54].

case corresponds to the situation in which the two atoms overlap on the 50:50 beam-splitter and one cannot say which one has been transmitted or reflected, as represented in Fig. 5.4a). In the case of a bad temporal overlap between the two beams, due to an application time of the beam-splitter such that the atoms do not overlap, see Fig. 5.4b), one gets the distinguishable case. The output ports c and d correspond to the two atomic beams after the 50:50 beam-splitter. Their momenta is equal to k_c and k_d, with $k_c = k_a$ and $k_d = k_b$, which leads to different arrival times on the detector. With the temporal resolution of the detector being shorter than the time difference between the two correlated atoms, one can directly measure their cross-correlations and extract the coincidence count. The HOM experiment consists then to measure the cross-correlation between the two clouds c and d as a function of the 50:50 beam-splitter application time, t_s.

Knowing the initial speed of the two clouds and the time at which the atomic mirror has been applied (t_m), one can determine the application time of the 50:50 beam-splitter, t_s, corresponding to the indistinguishable situation. Consider that beam a has an initial speed v_a and beam b a speed v_b along the vertical direction. In the laboratory frame of reference, the position of the two clouds corresponds to

$$z_a = z_0 + v_a t - \frac{1}{2} g t^2 ,$$
$$z_b = z_0 + v_b t - \frac{1}{2} g t^2 .$$

After a time t_m, the position difference between both clouds along z is equal to $\Delta z = (v_a - v_b)t_m$. At this moment the mirror is applied and the velocities are exchanged. The position difference between the two clouds is then equal to

$$\Delta z = (v_a - v_b)t_m - (v_a - v_b)(t - t_m).$$

If the 50:50 beam-splitter is applied at $t_s = 2t_m$, then $\Delta z = 0$ and the two atomic beams overlap. This corresponds to $\tau = t_s - t_m = t_m - t_0$ where, for simplicity, we will consider $t_0 = 0$. On the other hand, if the atoms do not overlap at the moment when the beam-splitter is shinned ($t_s \neq 2t_m$), then the reflection of beam a is different than the transmission of beam b and the paths are made distinguishable, see Fig. 5.4.

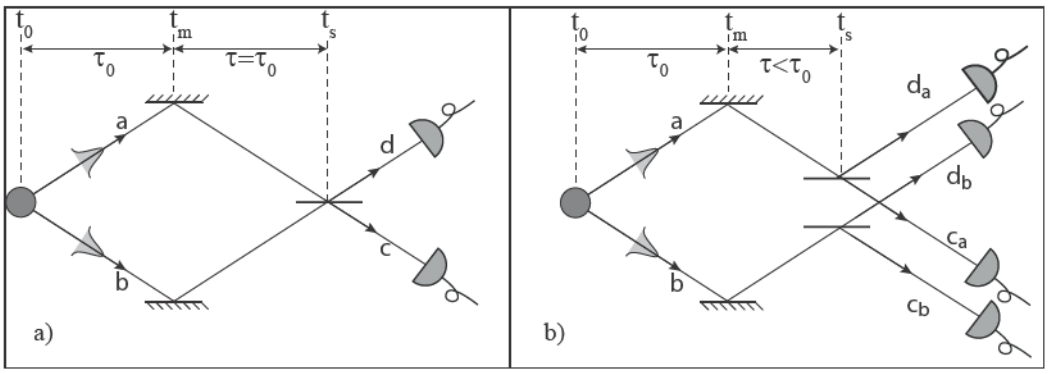

Figure 5.4: Schematic representation of two-particles interference. a) Beam-splitter application in the case of indistinguishable particles. b) Beam-splitter application in the case of distinguishable particles.

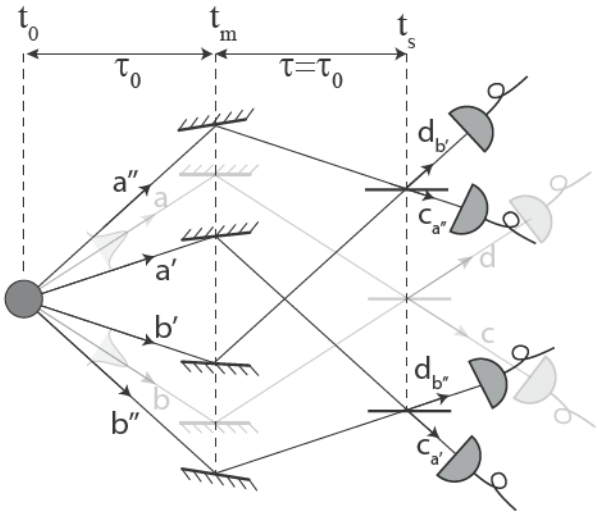

Figure 5.5: Schematic representation of multimode two-particles interference. Several modes are outcoming from the initial source, mode a correlated with b, a′ with b′ and a″ with b″. The mirror and beam-splitter are calibrated such that a and b overlap on the beam-splitter. This implies that mode a′ overlap with mode b″ and a″ with b′.

In contrast to the experiment of Hong, Ou and Mandel in which the beam-splitter position defines the distinguishability of the particles, in our case, since the atomic beam-splitter is performed in momentum space, it is the application time of the 50:50 beam-splitter that defines it.

5.1.2 Filtering method: 3D detection and noiseless beam-splitter

Similar to the photonic case, our atomic source is not single mode but multimode, as discussed in Section 3.4. This means that each atomic beam corresponds to several modes, each one correlated to its symmetric in the other beam. Due to phase-matching conditions, the two modes have to verify the momentum condition $k_a + k_b = 2k_{\text{lat}} + 2k_0$ as discussed in Section 3.2. At time t_s, the two atomic beams are swapped. This means that an atom with initial momentum k_a has a probability of 50% to be diffracted into $k_a + k_{\text{bms}}$. This is also valid for beam b with momentum given by $k_b - k_{\text{bms}}$ after the 50:50 beam-splitter. In order to exchange a pair of correlated atoms one has to verify both

$$|k_b - k_a - k_{\text{bms}}| < \delta k \tag{5.1a}$$

and

$$|k_a + k_b - 2k_{\text{lat}} - 2k_0| < \delta k\,, \tag{5.1b}$$

where δk accounts for the mode size in momentum space. Only the atoms with momenta such that both conditions are verified will correspond to a perfect indistinguishable case. Those that are exchanged with atoms from another mode will always be distinguishable.

This is schematically shown in Fig. 5.5 where two atomic pairs corresponding to particles $\{a', b'\}$ and $\{a'', b''\}$ are produced, with

$$k_{b'} - k_{a'} = k_{\text{bms}} - \delta k$$

and

$$k_{b''} - k_{a''} = k_{\text{bms}} + \delta k\,,$$

where

$$k_{\text{bms}} = k_b - k_a.$$

In this scenario, a' and b' are correlated as well as a'' and b'', but no correlation exists between a'' and b' or a' and b''. This corresponds to atoms with momenta vector difference

$$(k_{b''} - k_{a''}) - (k_{b'} - k_{a'}) = 2\delta k \geq \sigma_c$$

where σ_c represents the cross-correlation function width. In our experimental realisation, both mirror and 50:50 beam-splitter have resonances sufficiently wide in order to effectively swap the entire beams. Thus, the situation discussed above needs to be considered.

In order to obtain a maximum HOM-dip visibility, it is necessary to filter out the distinguishable cases. In Fig. 5.5 this corresponds to neglect the contribution of a', b'' and a'', b'. In optics, this is easily done by placing narrow-band interference filters just before the detectors and pinholes in the optical paths [54, 206]. With atoms this is more demanding. One could imagine an equivalent process via selective Bragg diffraction. However, this technique can only perform selections along the axis of the beam-splitter lattice (z–axis) and no selection would be performed transversally. The solution, for our experiment, relies on our 3D detector resolution.

Since we are able to reconstruct the velocity vector in all three directions of each atom, one can select those that are recombined with their partner. Experimentally, this is simply performed by reducing the integration volume around the two momenta of interest $k_c = k_a$ and $k_d = k_b$. By reducing the bandwidth of the selection, one can recover a two-mode configuration. It is, however, very important to select the right momenta k_c and k_d. For this purpose we adjust the atomic beam production in order to match, as close as possible, the beam-splitter lattice periodicity k_{bms}. In this sense, we guarantee that the population maxima correspond to a recombined pair as schematically represented in Fig. 5.6. It is important to note that this filtering technique is only possible if the beam-splitter transfer is very well defined in momentum space, which we have proved to be true in Chapter 4, otherwise each atom is arbitrarily recombined with another. If the uncertainty is greater than the correlation length, no *post-filtering* can be performed since several different *modes* would have been mixed.

Our filtering method consists then to reduce the volume of integration, around the central zones of analysis, until a maximum visibility is obtained as schematically shown in Fig. 5.7. This is similar to the detection mode techniques used in quantum optics [207–209].

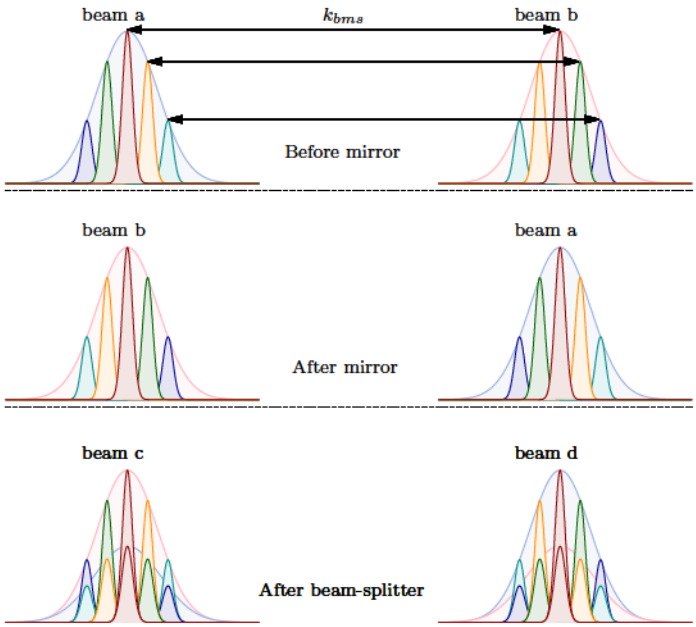

Figure 5.6: Schematic representation of the HOM experiment with mode representation. Description from top to bottom. The atomic beams are formed of several modes. Each mode is represented by a different color and the correlated mode in the other beam is represented with the same colour. The mirror, corresponding to a Bragg diffraction process, leads to a translation of each atomic beam. Thus, beam a replaces beam b and vice-versa. After the 50:50 beam-splitter, the correlated modes are mixed as shown at the bottom of this figure. We can see that only the central mode, in red, is overlapping with its peer. This is due to the fact that the momentum given by the Bragg pulse is equal to the momentum difference of the atomic beams central distribution. The other modes will then, never, be overlapped with their peers. This means, here, that only the center of the distribution will correspond to a perfect indistinguishable situation.

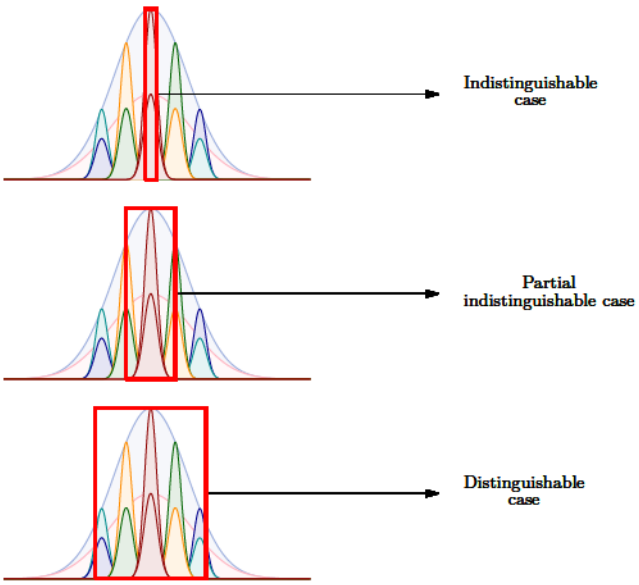

Figure 5.7: Schematic representation of the mode selection performed in our experiment. As explained in Fig. 5.6 only the center of the distribution corresponds to an overlap between identical modes. By performing a selection in momentum space, corresponding to the volume of our integration, one can then evolve from a perfect indistinguishable situation (only one mode inside the integration volume) or mixed situation between indistinguishable and distinguishable cases.

A different approach is, however, suggested in Ref. [85]. In this article, instead of varying the application time t_s, the momenta under analysis $\{k_c, k_d\}$ are tuned. This allows one to pass from a distinguishable case, for example in Fig. 5.5 $\{k'_a, k''_b\}$, to an indistinguishable scenario when looking at $\{k_a, k_b\}$. However, this analysis can only be performed in a situation where τ is such that an indistinguishable case exists. In order words, one will inevitably have to scan τ in order to find the overlap between the two atomic beams. Moreover, the populations between the distinguishable and indistinguishable cases can be different since they correspond to different classes of momenta in the atomic distribution. This leads to a modification of the HOM-dip shape if the cross-correlation is not normalised. For all these reasons, we have decided to not use this method of analysis for our HOM experiment.

The distinguishability of our atomic beams is done by changing the application time of the beam-splitter, t_s. A selection in k is performed through the MCP resolution in order to filter the modes in momentum space and to maximise the visibility of the HOM-dip.

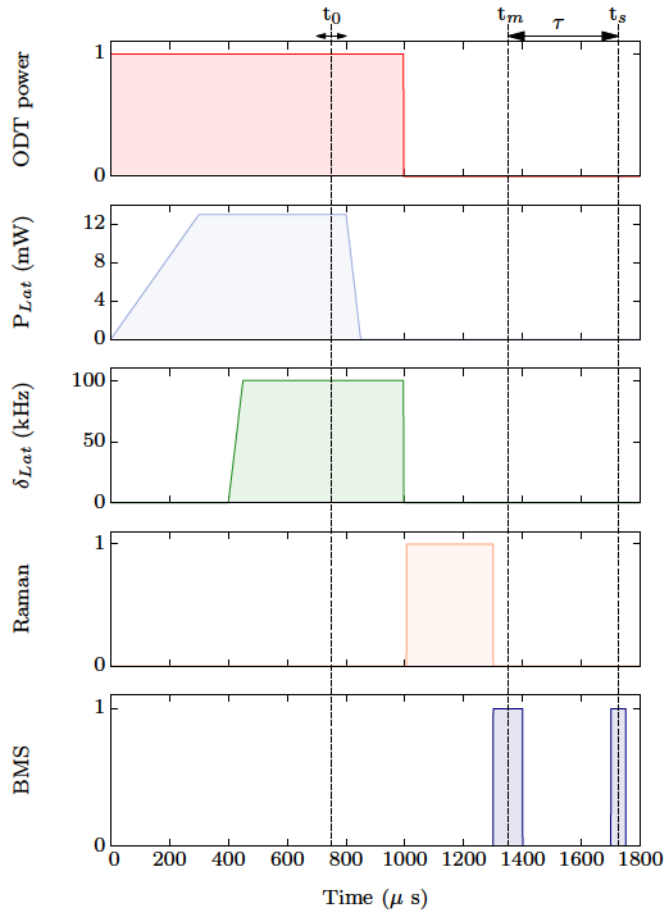

Figure 5.8: Experimental sequence for the HOM experiment. Inside the dipole trap (power indicated in red), the lattice is adiabatically switched on, by ramping both its depth (blue sky shaded area) and detuning (green shaded area) in 350 μs. The BEC is then, in the lattice frame of reference, moving at a speed $v_0 = -0.57\,\mathrm{v}_{lat}$ and start to produce atomic pairs due to dynamical instabilities. At time t_0, the first atoms forming the pairs start to be produced 50 μs before the lattice is adiabatically switched off. The atoms are then kept in the dipole trap for 200 μs. At this point the optical dipole trap (ODT) is switched off and atoms are released. They are then transferred to the insensitive sub-level $m_{j=0}$ in 300 μs via stimulated two-photon Raman transfer. The atomic mirror is then shinned on the atoms via a Bragg pulse of 100 μs length (dark blue shaded area) at time t_m. A second pulse is performed after a time $\tau = t_s - t_m$ corresponding to the application of the 50:50 beam-splitter.

5.2 HOM: experimental sequence

The experimental sequence in order to achieve the atomic HOM experiment is represented in Fig. 5.8. With the atoms still trapped in the optical dipole trap, the lattice is adiabatically turned on, in two steps (power and frequency), as explained in Subsection 3.3.2. The lattice speed is set to $-0.57\,\mathrm{v}_{\mathrm{lat}}$ and the lattice is kept on for 350 μs. [1]. The lattice is then switched off adiabatically and the atoms are kept in the dipole trap for 200 μs in order to avoid distortion of the transverse profile during the expansion, see Subsection 3.3.4. The optical trap is afterwards rapidly switched off and the atoms immediately transferred to the insensitive magnetic field state $m_j = 0$ via stimulated two-photon Raman scattering in 300 μs (see more details in Appendix C). At this moment, the atoms have already been travelling away from each other for at least 500 μs and the distance between the two atomic beams, along the vertical direction, is equal to 25 μm.

The mirror is then applied (corresponds to t_m in Fig. 5.8) in order to invert the velocities of beam a and b, via Bragg diffraction with an efficiency of 93 (2) %. The indistinguishable case corresponds then to a time t_s such that $t_s - t_m = t_m - t_0$ estimated at $t_s - t_m \approx 550\,\mu$s. The

[1] $v_{\mathrm{lat}} = 9.3$ cm/s as defined in Section 3.3. We estimate that the first atoms are produced approximatively 300 μs (corresponding to t_0, see Fig. 5.8) after switching on the lattice.

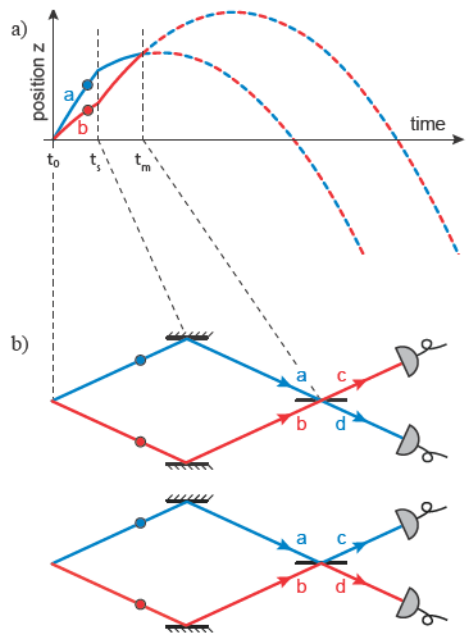

Figure 5.9: **Schematic representation of the atomic HOM experiment.** *a) The time diagram shows the evolution of the atomic pairs along the vertical axis (blue and red lines). Between t_0 and t_m, t_m and t_s, and after t_s, the atoms move under the influence of gravity (drawing not to scale). At t_m, the twin atom velocities are swapped using Bragg diffraction on an optical lattice. At time t_s, when the atomic trajectories cross again, the same lattice is applied for half the amount of time in order to realise a beam-splitter. b) In the centre-of-mass frame of reference, the trajectories of the atoms resemble those of the photons in the HOM experiment. A joint detection arises either when both atoms are transmitted through the beam-slitter (upper panel) or when both are reflected (lower panel). If the two particles are indistinguishable, these processes end in the same final quantum state and the probability of coincidence detection results from the addition of their amplitudes. For bosons these amplitudes have same modulus but opposite signs, thus their sum vanishes and so also the probability of coincidence detection.*

difficulty of determining the exact value of t_s comes essentially from the uncertainty associated to the instant at which the first pairs are produced, t_0. Since the population of beam a and b are rather small, we estimate that the first pairs are produced at the end of the lattice application. Furthermore, both mirror and 50:50 beam-splitter have durations that are not negligible with respect to $t_m - t_0$. This increases the uncertainty associated to the instant t_s for which particles are made indistinguishable.

After time-of-flight, the atoms hit the MCP and their arrival time is recorded. The velocity vector of each atom after application of the 50:50 beam-splitter is recovered as discussed in Subsection 2.1.2. The analysis is then performed by extracting the cross-correlation between the two atomic beams c and d, where, $k_c = k_a$ and $k_d = k_b$. The interferometer scheme corresponds to the one represented in Fig. 5.9a) where gravity induces parabolic trajectories on the particles. In the beam-splitter frame of reference, one retrieves the well known massless interferometric scheme represented in Fig. 5.9b).

We roughly estimate the 50:50 beam-splitter time application corresponding to indistinguishable paths to $t_s - t_m = \tau = 550\,(100)\ \mu$s.

5.3 Analysis and measurement of the HOM effect

Atoms fall on the detector and the cross-correlation between beam c and d given by

$$G^{(2)}_{cd}(\tau) = \eta^2 \langle \hat{N}_c(\tau)\hat{N}_d(\tau)\rangle = \frac{\eta^2}{\Omega_{V_c}\Omega_{V_d}} \int_{\Omega_{V_c}} d^3\mathbf{k}_c \int_{\Omega_{V_d}} d^3\mathbf{k}_d \langle \hat{n}(\mathbf{k}_c,\,\tau)\hat{n}(\mathbf{k}_d,\,\tau)\rangle\ , \tag{5.2}$$

is obtained for different values of τ, with $\Omega_{V_c} = \Omega_{V_d} = \left[\mathcal{L}_\perp^2 \mathcal{L}_z\right]\left(k_{\text{lat}}^3\right)$ corresponding to the volume of integration and η the detection efficiency. We chose not to normalise the cross-correlation for ease of comparison with the original HOM realisation. The result shown in Fig. 5.10 corresponds to the optimised integration volume of $\Omega_V = \left[0.048^2 \times 0.028\right](k_{\text{lat}}^3)$. The cross-correlation function $G_{cd}^{(2)}$ decreases from 0.060 (8) to 0.019 (4) at $\tau = \tau_0 = 550\,\mu$s. The value of τ_0 is coherent with the expected overlap between the two clouds, $t_s = 2t_m \approx 550\,\mu$s.

In order to quantify the visibility of the HOM-dip, the following definition

$$\bar{V} = 1 - \frac{G^{(2)}(\tau_0)}{G_{\text{bg.}}^{(2)}} \tag{5.3}$$

$$= 1 - \frac{G_{\text{Ind.}}^{(2)}}{G_{\text{Dis.}}^{(2)}}, \tag{5.4}$$

is used, where if $\bar{V} > 0.5$ the effect cannot be explained classically (see Chapter 1). This threshold is represented by the red shaded area and corresponds to the maximum interference contrast obtained for two classical waves with random phases at the input ports. From the values of $G_{cd}^{(2)}(\tau_0)$ and $G_{bg.}^{(2)}$, we recover a value of $\bar{V} = 0.65\,(7)$, two standard deviations above the classical limit [2].

This effect can only correspond to a quantum two-particle destructive interference and shows that the atomic pairs have more-than-classical correlations and that one can coherently manipulate the input state.

Along this Section we will discuss in detail the analysis lying beneath this result.

5.3.1 Analysis: momentum selection

In order to optimise the destructive interference effect, one looks at the correlation between atoms with momenta k_c and k_d as discussed previously. By fixing the initial condensate quasi-momentum at $-0.57\,\text{q}_{\text{lat}}$, we generate two atomic beams a and b with distributions centred at $0.73\,(1)\,\text{k}_{\text{lat}}$ and $1.27\,(1)\,\text{k}_{\text{lat}}$ in the laboratory frame of reference. This corresponds to a momentum difference equal to $0.54\,(2)\,\text{k}_{\text{lat}}$ consistent with the beam-splitter periodicity $k_{\text{bms}} = 0.55\,\text{k}_{\text{lat}}$. This mismatch comes from our difficulty in measuring the central distribution of beam b and is due to the losses associated to beam b that tend to distort its profile along the vertical z−axis. In Section 5.5 we will see that this mismatching may partially explain the obtained HOM-dip width.

The value of k_c and k_d used for the analysis are determined in the following way. As we have seen in Section 3.3, the two atomic beams, a and b, have different populations. After application of the 50:50 beam-splitter, however, their population are mixed and should be equal after averaging over several realisations. Consequently, the analysis is performed between the central distributions of beams c and d for which the maximum population is detected. The issue that one can face is that the central distributions do not correspond to the two correlated modes. For this purpose, we allow ourselves to displace slightly the two boxes of analysis in order to maximise the HOM-dip visibility. This displacement has always to be smaller than the cross-correlation length in order to verify Eq. (5.1). In practise, the centers of the analysis

[2] It is important to note that, for our experiment, from realisation to realisation, the phase of the beam-splitter was randomly chosen. This allows us to directly compare the recovered dip in the cross-correlation as a function of τ to the expected classical threshold. We will show in Section 5.4, however, that this threshold value is in fact overvalued and that one can estimate the real threshold knowing the auto and cross-correlations of beams a and b.

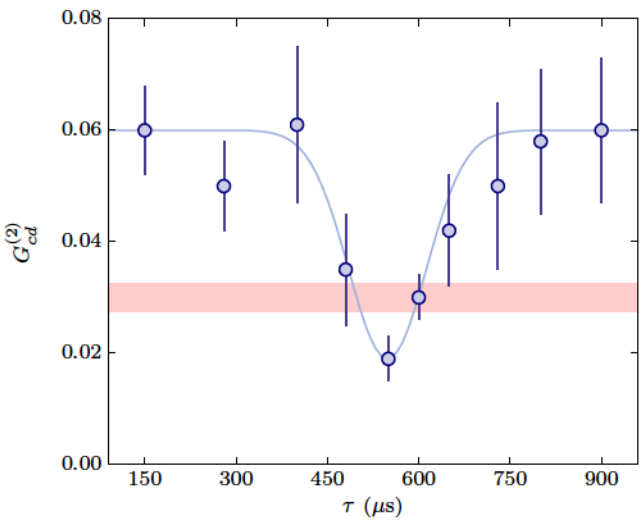

Figure 5.10: **Atomic HOM-dip in the cross-correlation function.** *The correlation $G^{(2)}_{cd}$ between the output ports of the beam-splitter, defined in Eq. (5.2), was measured as a function of the propagation duration $\tau = t_s - t_m$ between the mirror and the beam-splitter. The HOM-dip is directly visible as a marked reduction of the correlation when τ equals the duration of propagation $t_m - t_0 \simeq 500\,\mu$s between the source and the mirror, corresponding to symmetric paths between the source and the beam-splitter. A Gaussian fit (blue line) precisely locates the dip at $\tau = 550\,(50)\ \mu$s, with a half-width at half-maximum of $70\,(40)\ \mu$s, where the uncertainty corresponds to the 68 % confidence interval. The measured visibility is $V = 0.65\,(7)$. It is two standard deviations beyond the classical-to-quantum threshold represented by the red shaded area, which takes into account the experimental uncertainty over the background correlation value. Each data point was obtained from an averaged over about 500 to 1000 repetitions of the experiment. Error bars denote the standard deviation of the statistical ensemble. The mean detected atom number was constant over the range of values of τ displayed here.*

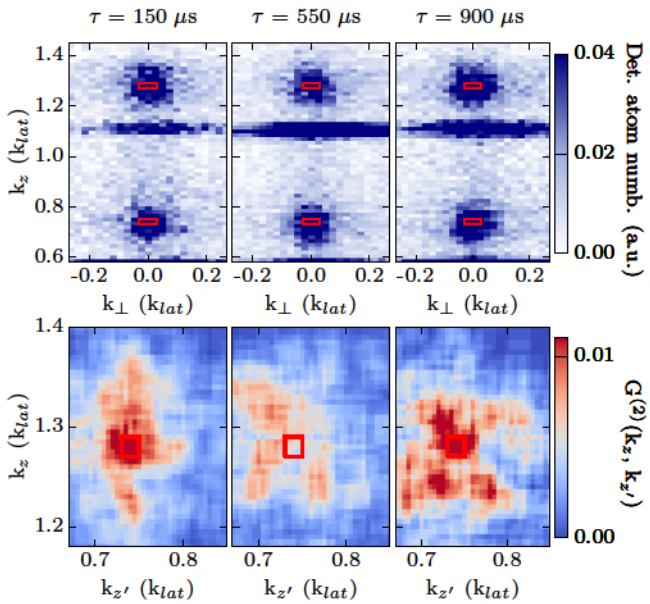

Figure 5.11: *2D determination of the optimised centred analysis $\{k_a, k_b\}$. Upper panels, from left to right, 2D momenta distribution for the detected atom number on the yz−plane, integrated over a length of $0.048\,k_{lat}$ along the x−axis, for $\tau = 150, 550, 900\ \mu$s. Bottom panels, from left to right: 2D cross-correlation between momentum k_z, $k_{z'}$ for an integration volume of $\Omega_V = [0.048^2 \times 0.028]\,(k_{lat}{}^3)$ for $\tau = 150, 550, 900\ \mu$s. The red shaded square correspond to the integration length on the longitudinal z−axis. The bin size is of $0.014\,k_{lat}$ on both axis.*

volume correspond to $k_c = 0.740\,k_{\rm lat}$ and $k_d = 1.275\,k_{\rm lat}$, as represented in Fig. 5.7. In order to avoid the contribution of several modes, we are also selective on the integration volume, as discussed earlier. The idea is to guarantee that only two modes are selected.

In Fig. 5.11, top panels, the 2D momentum distribution on the $yz-$plane for both distinguishable case (left and right panels) and indistinguishable case (center panel) are represented. In all three cases, it is possible to distinguish the two atomic beams c and d as well as diffracted atoms from the condensate by the beam-splitter along the $z-$axis. The diffraction probability is very weak but, since the population of the BEC is much larger than the number of produced pairs, the diffracted fraction is still clearly visible. However, since the BEC diffracted atoms are well separated from the pairs in momentum space they do not tarnish the analysis on the pairs.

No noticeable pair population difference is visible on the 2D distribution in accordance with the fact that on averaged both distinguishable and indistinguishable situations have the same density distributions. The 2D cross-correlation function (bottom canvas), defined by Eq. (5.2), is estimated for a fixed volume of integration corresponding to $\Omega_{c',d'} = \left[\mathcal{L}_z \times \mathcal{L}_\perp^2\right] = \left[0.028 \times 0.048^2\right] (k_{\text{lat}}^3)$ and centred on $\mathbf{C}_c = (0,\, 0,\, k_{z'})\,(k_{\text{lat}})$ and $\mathbf{C}_d = (0,\, 0,\, k_z)\,(k_{\text{lat}})$. One can immediately see that, for most sets of $\{k_{c'};\, k_{d'}\}$, the cross-correlation is weaker when $\tau = 550\,\mu$s in accordance to the expected time $t_m - t_0 \approx 550\,\mu$s. The minimum value of $G^{(2)}_{cd}$, inside the atomic beams, occurs when $k_c = 0.740\,\text{k}_{\text{lat}}$ and $k_d = 1.275\,\text{k}_{\text{lat}}$, corresponding to the values of k_c and k_d with maximum averaged populations.

The central positions, $k_c = 0.740\,\text{k}_{\text{lat}}$ and $k_d = 1.275\,\text{k}_{\text{lat}}$ optimise the HOM-dip visibility and hereafter we will always place the center of our analysis volume on $\mathbf{C}_c = (0,\, 0,\, 0.740)\,(k_{\text{lat}})$ and $\mathbf{C}_d = (0,\, 0,\, 1.275)\,(k_{\text{lat}})$.

5.3.2 Analysis: optimisation of the integration volume

With the value of k_c and k_d fixed, one can now try to optimise the signal by changing the volume of integration. This corresponds to adapt the pinhole size to our mode size as often performed in quantum optics [206].

Since the correlation varies with time τ, one can estimate the contrast by fitting the cross-correlation as a function of τ with the empirical Gaussian function

$$G^{(2)}(\tau) = G^{(2)}_{\text{bg.}}\left(1 - \bar{V} e^{-\frac{(\tau-\tau_0)^2}{2\sigma^2}}\right) \tag{5.5}$$

where $G^{(2)}_{\text{bg.}}$ corresponds to the background correlation obtained for distinguishable particles and $\bar{V}$ to the visibility of the HOM-dip. In Fig. 5.12, left panel, the visibility is represented as a function of the integration volume Ω_V. For each $(\mathcal{L}_\perp;\, \mathcal{L}_z)$ set, corresponding to a volume $\Omega_V = \left[\mathcal{L}_\perp^2 \mathcal{L}_z\right]$, one gets the related visibility. One can see that for smaller integration volumes the visibility increases until reaching saturation. For large volumes, the visibility decreases as a consequence of the multimode source contribution (as discussed in detail in Subsection 5.1.2).

The visibility of the HOM-dip can be compared to the situation in which two coherent beams with undetermined relative phase are recombined on a 50:50 beam-splitter. The obtained reduction of the cross-correlation in this situation, see Chapter 1, corresponds to the classical-to-quantum threshold and can be written as

$$V_{\text{thres.}} = \frac{1}{1+\delta}, \tag{5.6}$$

with δ corresponding to

$$\delta = \frac{G^{(2)}_{aa} + G^{(2)}_{bb}}{2\sqrt{G^{(2)}_{aa} G^{(2)}_{bb}}}, \tag{5.7}$$

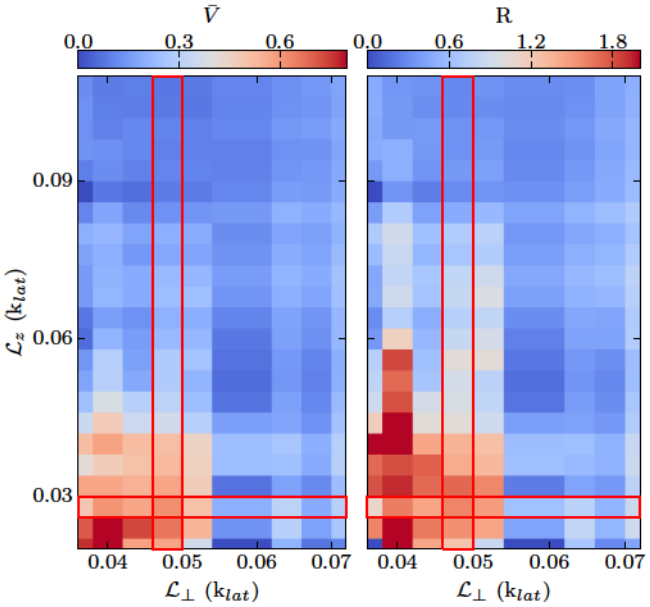

Figure 5.12: 2D representation of the visibility $\bar{V}$ and ratio to the classical threshold R for different integration volumes. Left panel, 2D representation of $\bar{V}$ as a function of the integration volume $\Omega_V = [\mathcal{L}_\perp^2 \times \mathcal{L}_z]\,(k_{lat}^3)$. For smaller volumes one observe an increased visibility until it saturates while for larger volumes the visibility decreases to zero. The bin size corresponds to 0.004 k_{lat} in both directions. Right panel, 2D representation of R as a function of the integration volume $\Omega_V = [\mathcal{L}_\perp^2 \times \mathcal{L}_z]\,(k_{lat}^3)$. For smaller integration volumes the ratio increases to its maximum value of 1.5. The red boxes indicate the values of $\mathcal{L}_z$ and $\mathcal{L}_\perp$ corresponding to the cuts shown in Fig. 5.13.

see Appendix D for complementary information. If the incoming pairs have the same autocorrelation value, then $\delta = 1$. This is usually true for particles produced in pairs and one recovers the threshold value of $\bar{V}_{\text{thres.}} = 0.5$. In our system, beam b has a lower population than beam a and, consequently, $\delta \neq 1$. This changes the value of δ and, as a consequence, the classical threshold is no longer 0.5. The threshold value $\bar{V}_{\text{thres}}$ is obtained as a function of Ω_V and the ratio R between the obtained HOM-dip visibility and the visibility threshold

$$R = \frac{\bar{V}}{\bar{V}_{\text{thres}}}, \tag{5.8}$$

is represented in Fig. 5.12 (right panel). One sees that for small volumes of integration the HOM-dip visibility is almost twice as large than the threshold value and tends to zero for increasing volumes.

In order to quantitatively identify the optimised zone the 2D plots of Fig. 5.12 are projected along the vertical $z-$ and transverse $y-$axis as represented in Fig. 5.13. Canvas a) and c) correspond to a situation for which the integration length on the $z-$axis is kept constant at $\mathcal{L}_z = 0.028\,\text{k}_{\text{lat}}$ and the integration length on the transverse direction, $\mathcal{L}_\perp$, is varied (the cut corresponds to the horizontal red boxes of Fig. 5.12). One finds an optimum value at $\mathcal{L}_\perp = 0.048\,\text{k}_{\text{lat}}$ for which we obtain an optimised visibility, respectively to the signal-to-noise ratio, of $\bar{V} = 0.65\,(7)$ and a ratio $R = 1.44\,(20)$. Canvas b) and d) correspond to the inverse situation, for which $\mathcal{L}_\perp = 0.048$, is kept constant, and $\mathcal{L}_z$ is varied (corresponds to the vertical red boxes of Fig. 5.12). We thus obtain the optimised value of $\bar{V} = 0.65\,(7)$ for $\mathcal{L}_z = 0.028\,\text{k}_{\text{lat}}$. The optimised volume of integration is obtained by performing the same method for all different fixed values of $\mathcal{L}_z$ and $\mathcal{L}_\perp$.

The optimised result corresponds to the one represented here for which we obtain $\bar{V} = 0.65\,(7)$ and a threshold value equal to $\bar{V}_{\text{thres}} = 0.45(4)$. The ratio between the HOM-dip visibility and the threshold result corresponds to $R = 1.44\,(20)$. These results are obtained for

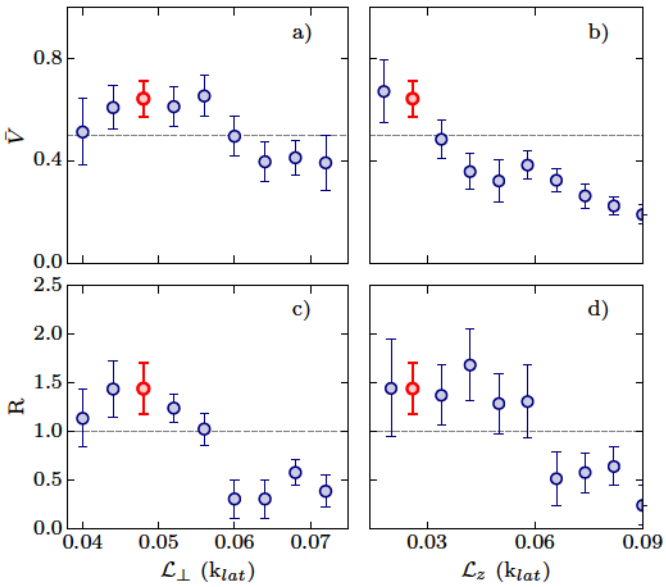

Figure 5.13: Evolution of both the visibility and the visibility / threshold ratio as a function of the integration volume $\Omega_V = [\mathcal{L}_\perp^2 \times \mathcal{L}_z]\,(k_{lat}^3)$. a) and c) The integration length on the z–axis is kept constant at $\mathcal{L}_z = 0.028\,k_{lat}$. The visibility $\bar{V}$ and the ratio R given by Eq. (5.8) are respectively shown as a function of the integration length on the transverse direction, $\mathcal{L}_\perp$. b) and d) The integration length on the perpendicular directions x and y is kept constant at $\mathcal{L}_\perp = 0.048\,k_{lat}$. $\bar{V}$ and R are respectively plotted as a function of the integration length on the longitudinal z–axis, $\mathcal{L}_z$.

a volume of integration Ω_V equal to $\Omega_V = \left[0.028 \times 0.048^2\right]\left(k_{\text{lat}}^3\right)$. We represent in Fig. 5.14, the correlation dip as a function of τ with the adapted threshold value of 0.45 (4) in green.

To see more directly the effect of the integration volume, we show in Fig. 5.15 the evolution of $G_{cd}^{(2)}(\tau)$ for two different integration volumes. Fig. 5.15a) corresponds to the optimised volume discussed so far, $\Omega_V = \left[0.028 \times 0.048^2\right]\left(k_{\text{lat}}^3\right)$, while Fig. 5.15b) corresponds to a larger volume of integration $\Omega_V = \left[0.048^3\right](k_{\text{lat}}^3)$. It is possible to see that for an increased integration volume the HOM-dip width decreases. The dip width passes from 70 (30) μs to 40 (20) μs. Also the background correlation increases with the volume of integration which is expected since the number of detected atoms also increases. The visibility, on the other hand, decreases from 0.65 (7) to 0.39 (7) .

The optimised volume of integration gives complementary information about the mode size of our source [207–209]. Along the vertical direction the length of integration $\mathcal{L}_z = 0.028\,k_{\text{lat}}$ is slightly larger than the correlation function width obtained in Section 3.4. Transversally, however, the integration length is comparable to the mode size recovered from the auto-correlation function.

The HOM-dip visibility has been optimised as a function of the integration volume. The volume for which the signal-to-noise ratio is maximal corresponds to $\Omega_V = \left[0.028 \times 0.048^2\right]\left(k_{\text{lat}}^3\right)$.

5.3.3 Analysis: population stability

When comparing the non-normalised cross-correlation as a function of τ, an important point is to guarantee that the populations in beam c and d are stable over the entire experimental realisation.

In contrast to quantum optics experiments, the cycle rate of cold atoms experiments is much longer. Each data point of Fig. 5.10 corresponds to an acquisition time of approximatively

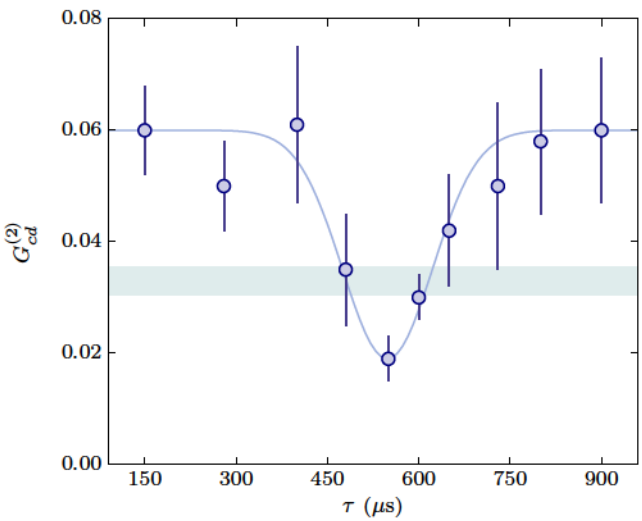

Figure 5.14: **Cross-correlation between beams c and d as a function of τ with the adapted threshold value.** *Representation of the cross-correlation as a function of τ with the respective classical-to-quantum threshold value deduced from Eq. (5.6) in green. One can see that the minimum value of $G^{(2)}_{cd}(\tau)$ is three standard deviations below this threshold.*

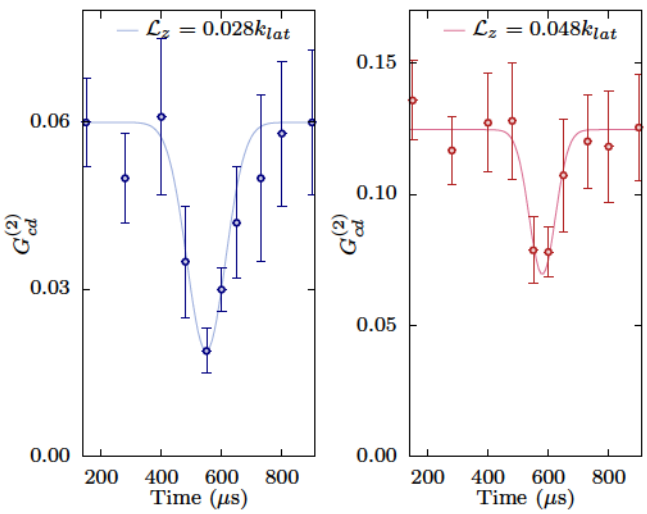

Figure 5.15: *Experimental observation of the destructive interference effect for two different integration volumes. Reduction of the cross-correlation between ports c and d as a function of τ. For $\tau \approx 550\,\mu s \approx \tau_0$, one retrieves the minimum cross-correlation value corresponding to the indistinguishable paths scenario. a) Evolution of $G^{(2)}_{cd}$ as a function of τ for a volume of integration $\Omega_V = [0.048^2 \times 0.028]\,(k^3_{lat})$. b) Evolution of $G^{(2)}_{cd}$ as a function of τ for a volume of integration $\Omega_V = [0.048^3]\,(k^3_{lat})$.*

12 hours. To give an idea, for the original HOM experiment each data point corresponds to an acquisition time of 10 min. [54]. This means, in our case, that over the entire realisation of the experimental curve, which took approximatively two and half weeks, the number of produced atoms in beams a and b needed to be constant.

In Fig. 5.16a) and b), the number of detected atoms in both output ports c and d is represented as a function of τ. One can see that the population in both beams is rather stable with an averaged number of atoms in beam c equal to 0.18 (1) , and 0.19 (1) in beam d. Furthermore, we compare the stability of the mean averaged product

$$\langle n_c \rangle \cdot \langle n_d \rangle = \frac{\eta^2}{\Omega_{V_c}\Omega_{V_d}} \int_{\Omega_{V_c}} \int_{\Omega_{V_d}} d^3\mathbf{k}_c d^3\mathbf{k}_d \langle n_{\mathbf{k}_c} \rangle \cdot \langle n_{\mathbf{k}_d} \rangle$$

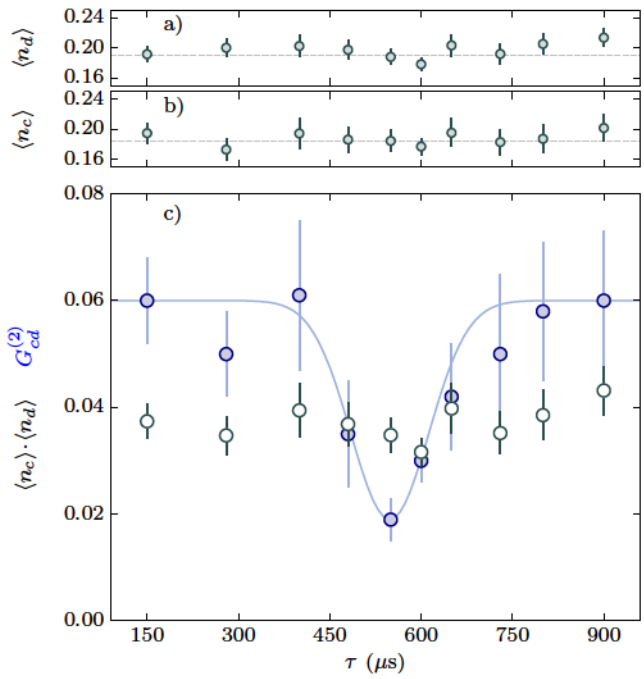

Figure 5.16: **Stability of the output population over propagation duration.** *a) Averaged atom number detected in $\mathcal{V}_c$ as a function of the propagation time τ. The mean value of n_c is 0.19 with a standard deviation of 0.01. b) Averaged atom number detected in $\mathcal{V}_d$ as a function of the propagation time τ. The mean value of n_d is 0.18 with a standard deviation of 0.01. c) The cross-correlation between the output ports c and d (solid blue circles), corresponding to the HOM-dip, is compared to the product of the averaged density populations $\langle n_c \rangle \cdot \langle n_d \rangle$ (open gray circles). The product of the averaged population is constant while the cross-correlation exhibits a dip around $\tau = 550\,\mu$s.*

with the integrated cross-correlation

$$G^{(2)}_{cd} = \frac{\eta^2}{\Omega_{V_c}\Omega_{V_d}} \int_{\Omega_{V_c}} \int_{\Omega_{V_d}} d^3\mathbf{k_c} d^3\mathbf{k_d} \langle n_{\mathbf{k}_c} n_{\mathbf{k}_d} \rangle \, .$$

If the HOM-dip was due to a population reduction as a function of τ, then the curve $\langle n_c \rangle \cdot \langle n_d \rangle$ would present the same dip as the cross-correlation $G^{(2)}_{cd}$. This is, however, clearly not the case as one can see in Fig. 5.16c).

One can also represent the normalised cross-correlation as a function of τ. This is shown in Fig. 5.17 where it is possible to see that the reduction of coincidence counts is still present and that the minimum correlation value lies below the classical threshold value of $G^{(2)}_{\text{thres}} = 0.81\,(7)$.

In conclusion, although the data corresponds to a very long acquisition period, the averaged atom number is rather stable over τ and the HOM-dip cannot be classically interpreted by a variation of the population.

The visibility gives us information about the input state, in particular, if the incoming atoms are strongly correlated. Experimentally, we observed an optimised visibility of 0.65 (7) which allows us to exclude any possible simple classical explanation of our result [3]. The most important results of the analysis until now are summarised in Table 5.1.

5.4 Dip visibility: theoretical estimation

For an incoming state corresponding to a two-mode Fock state with one atom per mode, $|1, 1\rangle$, it is expected that the cross-correlation function reaches the minimum value of zero as function

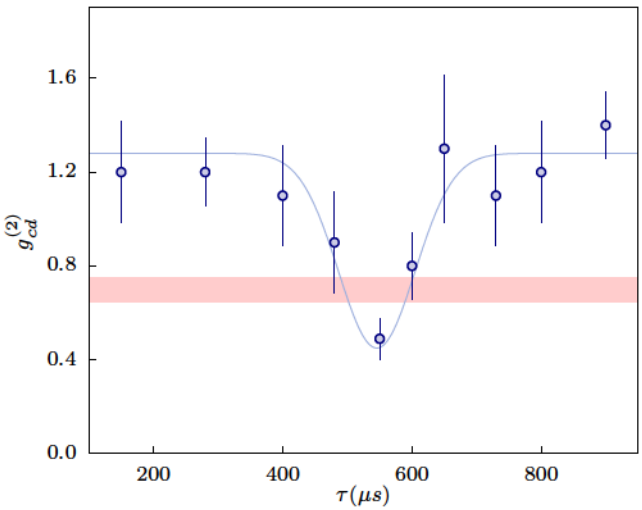

Figure 5.17: Normalized cross-correlation function as a function of τ. The dip is still present although the cross-correlation is now averaged by the population product of beam c and d.

Optimised integration volume	
Integration length along the vertical axis $\mathcal{L}_z(k_{\text{lat}})$	0.028
Integration length along the transverse axis $\mathcal{L}_\perp(k_{\text{lat}})$	0.048
Maximum visibility $\bar{V}$	0.65 (7)
Threshold visibility $\bar{V}_{\text{thres}}$	0.45 (4)
Ratio between observed visibility and threshold R	1.44 (20)
δ defined by Eq. (5.7)	1.15 (5)

Table 5.1: HOM-dip result for the optimised volume of integration.

of τ. It is clear from Fig. 5.10 that this does not happen here. Two factors may be responsible for this effect, either the detected particles are not fully indistinguishable or the number of atoms contained in the integration volume exceed unity for each beam.

It is possible, for perfectly indistinguishable particles, to determine the expected visibility. For this, one only needs to measure the auto and cross-correlations before application of the 50:50 beam-splitter. In our experiment, this consists in performing the same experimental procedure as for the HOM experiment but without application of the mirror or the beam-splitter. The visibility $\bar{V}$ corresponds then, as seen in Chapter 1, to

$$\bar{V} = \frac{2G^{(2)}_{ab}}{G^{(2)}_{aa} + G^{(2)}_{bb} + 2G^{(2)}_{ab}} = \frac{1}{1 + (\delta/C)}, \tag{5.9}$$

with $\delta = \frac{G^{(2)}_{aa}+G^{(2)}_{bb}}{2\sqrt{G^{(2)}_{aa}G^{(2)}_{bb}}}$ and $C = \frac{G^{(2)}_{ab}}{\sqrt{G^{(2)}_{aa}G^{(2)}_{bb}}}$ (demonstrations can be found in Appendix D). In Section 3.4, see Fig. 3.26, one saw that for $\mathcal{L}_z = 0.028$ and $\mathcal{L}_\perp = 0.048$, C reaches the value 1.75 (2) and, for the same volume of integration, $\delta = 1.15\,(5)$. The expected visibility for perfectly

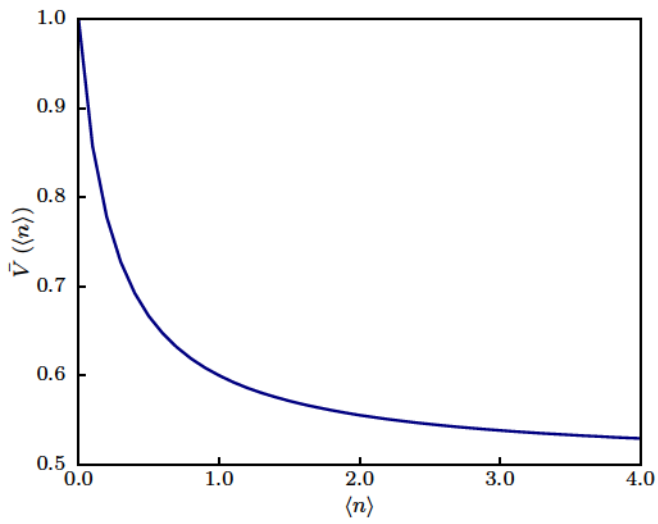

Figure 5.18: Evolution of the HOM-visibility $\bar{V}$ as a function of the averaged population $\langle n \rangle$. For $\langle n \rangle \to 0$, the maximum dip-visibility of 1 is obtained for the case of a state obtained through spontaneous parametric down-conversion. For $\langle n \rangle \to \infty$, the visibility decreases to the classical threshold of 0.5. In the graphic representation, we stop at $\langle n \rangle = 4$ for which the visibility has already decreased to $\bar{V} = 0.53$.

indistinguishable atoms is then equal to

$$\begin{aligned}\bar{V}_{\text{expect.}} &= (1 + 1.15\,(5)\ /1.75\,(2)\ )^{-1} \\ &= 0.60\,(1)\ .\end{aligned}$$

This value agrees with the measured visibility $\bar{V} = 0.65\,(7)$.

The finite value of $G^{(2)}_{cd}$ at the center of the dip is not due to a weak indistinguishability. Therefore, the observed result must be explained by the population of the two incoming beams.

5.4.1 Pair population

As discussed in Chapter 1, for a simple model where the produced atomic state corresponds to a twin-Fock state obtained through parametric down-conversion, the dip visibility can be related to the averaged population via the relation

$$\bar{V} = 1 - \frac{1}{2 + \frac{1}{2\langle n \rangle}}. \tag{5.10}$$

For averaged populations higher than one, $\langle n \rangle > 1$, the visibility is strongly reduced, as it is shown in Fig. 5.18, and tends to the asymptotic value of 0.5 for $\langle n \rangle \to \infty$.

From Eq. (5.10), it is then possible to extract the expected visibility at a given value of $\langle n \rangle$. This can be used in order to understand our experimental result. Nonetheless, it is important to keep in mind that this comparison is only qualitative, since, as seen in Section 3.4, the produced atomic pairs have different populations and their correlations do not correspond to those of a state generated by parametric down-conversion.

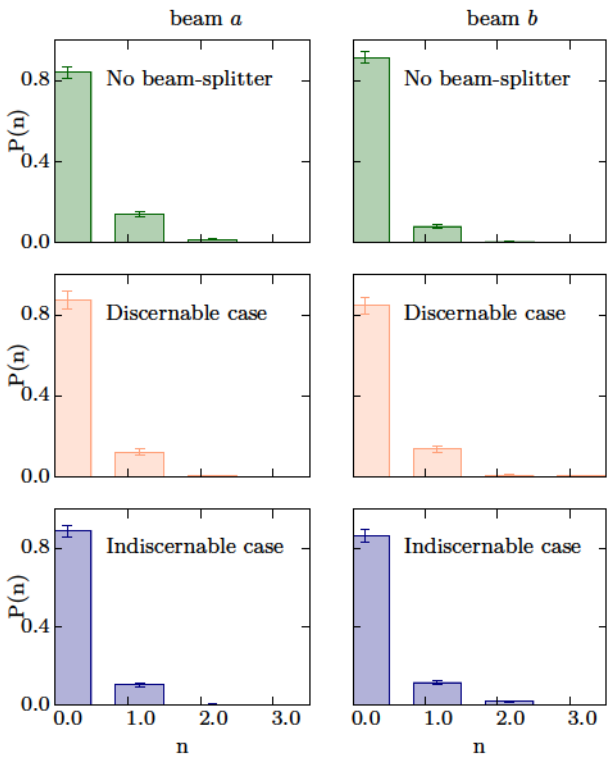

Figure 5.19: Probability of the detected atom number before application of the beam-splitter and after the beam-splitter in the distinguishable and indistinguishable case. Probability of detecting n atoms in either beams a (left panels) or b (right panels) before the beam-splitter (upper canvas), after the beam-splitter in the case of distinguishable particles (mid canvas) and for the case of indistinguishable particles (bottom canvas). The probability is obtained for an ensemble of 1000 experimental realisations. In all three cases, the probability of detecting zero particles is dominant (between 80 to 90%) and the probability of detecting two particles is at most a factor four weaker than the probability of detecting one particle. Before the beam-splitter, one can see that the probabilities are not the same between beam a and b due population imbalance between the two beams.

Determination of the averaged population in beam a and b.

Let us assume an initial Poisson law distribution such that the probability of having n atoms in either ports a or b corresponds to

$$P(n) = \frac{N^n}{n!} e^{-N}$$

with N the averaged number of atoms $\langle n \rangle = N$. The probability of detecting p atoms among N, knowing that the efficiency of detection is η can be written as

$$P_{\text{det}}(p) = \sum_{n=0}^{N} \frac{N^n}{n!} e^{-N} \eta^p (1-\eta)^{n-p} \binom{n}{p}. \tag{5.11}$$

Knowing the value of the detection efficiency, it is possible to retrieve the *real* averaged population. The value of η has been probed through the measurement of sub-shot noise variance and estimated to be equal or higher than $\eta = 0.25\,(5)$, as discussed in Section 3.4.2. The real averaged population is then obtained by fitting the probabilities of detecting p atoms, over 1700 identical realisations, via Eq. (5.11) with N as free parameter. The experimental probabilities of detecting 0, 1, 2 or 3 atoms, inside volume $\Omega_V = \left[0.048^2 \times 0.028\right] (k_{\text{lat}}^3)$, are shown in Fig. 5.19 for beam a and b. One can see, for instance, that the probability of detecting zero atoms is higher in beam b than in beam a. This reflects the population asymmetry between the beams. By fitting those distributions, the averaged populations of beam a and b are recovered.

	Pop. Det. Beam a			**Pop. Det. Beam** b				
	P(0)	P(1)	P(2)	P(0)	P(1)	P(2)		
Exp.	0.82 (3)	0.16 (1)	0.021 (4)	0.90 (3)	0.090 (9)	0.005 (6)		
	Theor. Pop. Det. Beam a			**Theor. Pop. Det. Beam** b				
η	P(0)	P(1)	P(2)	P(0)	P(1)	P(2)	N_a	N_b
0.15	0.82 (3)	0.16 (2)	0.016 (5)	0.90 (2)	0.094 (6)	0.005 (2)	1.3 (2)	0.7 (1)
0.25	0.82 (2)	0.16 (2)	0.016 (3)	0.90 (2)	0.090 (11)	0.005 (2)	0.8 (1)	0.5 (1)
0.35	0.81 (3)	0.17 (2)	0.018 (5)	0.90 (4)	0.094 (10)	0.005 (3)	0.6 (1)	0.3 (1)

Table 5.2: *Average population per atomic beam. The upper part of the table shows the experimental probabilities of detecting* 0, 1 *and* 2 *particles for both atomic beam a and b. These probabilities are extracted from the number of atoms detected over* 1700 *identical experimental realisations. In order to retrieve the real population distribution, we assume that the statistical distribution follow a Poisson law where the free parameter is the averaged population* N_a *for beam a and* N_b *for beam b. Since the value of the detection efficiency* η *plays a crucial role in the real population determination, we repeat this analysis for different values of* η *from* 0.15, 0.25 *and* 0.35. *This is shown in the lower part of the table where we adjust the population averaged of both beam a and b in order to fit the values of* P(0, 1, 2). *For each value of* η, *we extract the values of* $N_a = \langle n_a \rangle$ *and* $N_b = \langle n_b \rangle$ *corresponding to the real populations which best fit the experimental results.*

The values of $N = \langle n \rangle$ are summarised in Table 5.2 for different values of the detection efficiency $\eta = 0.15, 0.25$ and 0.35. We extract a value of $\langle n_a \rangle = 0.8\,(3)$ and $\langle n_b \rangle = 0.5\,(3)$ where the uncertainties are essentially due to the uncertainty on the detection efficiency η. This corresponds, using Eq. (5.10), to an expected visibility $\bar{V} = 0.65\,(8)$ with uncertainty coming essentially from population differences between the two beams. Since Eq. (5.10) is based on the fact that the incoming modes have symmetric populations our comparison corresponds to a very rough estimation. Nonetheless, this simple interpretation seems to agree with our results.

5.4.2 Evolution of the signal to noise ratio of the HOM-dip visibility with $\langle n \rangle$

As we have seen so far, the visibility of the HOM-dip depends on the averaged population $\langle n \rangle$ as described by Eq. (5.10). However a smaller population translates into a higher probability of having zero particles at the input port. An interferometer with zero particles per input port is useless in terms of statistical uncertainty and, consequently, the error associated to the visibility increases when one reduces $\langle n \rangle$. For an infinite number of realisations this would not be an issue since one would always detect an event after $M \to \infty$ repetitions. The problem is that, in the real world, one cannot perform an infinite number of repetitions. The question is then to know if an optimal situation, in term of signal-to-noise ratio, exists.

Consider that the experiment is performed a finite number of times M and that the pairs correspond to the result of a spontaneous parametric down-conversion process. The incoming pairs are then described by the state

$$|\psi\rangle = \sum_n \frac{\tanh^n(\lambda)}{\cosh(\lambda)} |n, n\rangle ,$$

and the visibility can then be written, as showed in Chapter 1, as

$$\bar{V} = 1 - \frac{1}{2 + \frac{1}{2\langle n \rangle}}$$

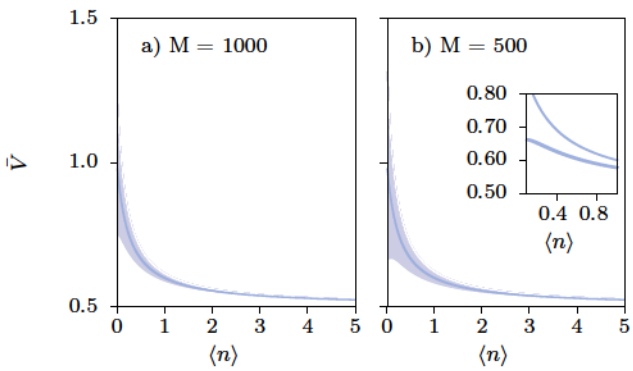

Figure 5.20: Optimisation of the signal-to-noise ratio for the HOM-visibility as a function of the averaged population $\langle n \rangle$. Representation of the visibility as a function of the averaged pair population $\langle n \rangle$ in the case of a parametric down-conversion state. The blue area corresponds to the expected standard deviation for M repetitions of the same experiment. a) $M = 1000$ repetitions, b) $M = 500$ repetitions. One can see an optimised value of α for $\langle n \rangle = 0.2 - 0.6$ atoms per mode.

with the associated uncertainty

$$\delta\bar{V} = \frac{\partial \bar{V}}{\partial \langle n \rangle} \delta\langle n \rangle.$$

This uncertainty depends on the averaged population uncertainty, $\delta\langle n \rangle$, defined by

$$\delta\langle n \rangle = \frac{\sqrt{\langle n \rangle (\langle n \rangle + 1)}}{\sqrt{M}}, \tag{5.12}$$

where the uncertainty corresponds to the square root of the variance for a distribution corresponding to a spontaneous two-mode state obtained via parametric down-conversion. The uncertainty $\delta\bar{V}$ is then given by

$$\delta\bar{V} = \frac{\sqrt{\langle n \rangle (\langle n \rangle + 1)}}{\sqrt{M}} \frac{2}{(4\langle n \rangle + 1)^2}. \tag{5.13}$$

In the extreme situation $\langle n \rangle \to 0$, the uncertainty $\delta\bar{V}$ tends to zero which is totally against what one would intuitively expect.

To take into account the reduction of effective realisations, $M_{\text{eff.}}$, we subtract to M the number of events where the detected particles is equal to 0. The effective number of realisations is then equal to

$$M_{\text{eff.}} = M\left(1 - P_{\text{det.}}(0)\right),$$

where $P_{\text{det.}}(0)$ corresponds to the probability of detecting zero particles either one of the two ports, and is equal to

$$P_{\text{det.}}(0) = \sum_{p}^{\infty} (1-\eta)^p \left| \frac{\tanh^p(\lambda)}{\cosh(\lambda)} \right|^2$$

The value of $\delta\bar{V}$ is then given by

$$\delta\bar{V} = \frac{\sqrt{\langle n \rangle (\langle n \rangle + 1)}}{\sqrt{M\left(1 - P_{\text{det.}}(0)\right)}} \frac{2}{(4\langle n \rangle + 1)^2}. \tag{5.14}$$

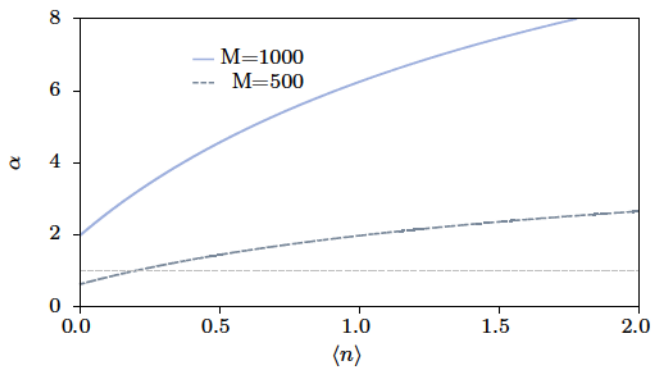

Figure 5.21: *Signal-to-noise ratio of the HOM-dip above threshold of* 0.5. *We represent the signal-to-noise ratio of the HOM-dip as a function of the averaged population* $\langle n \rangle$ *in the case of 1000 identical experimental realisations. The gray line at 1.0 indicates that the visibility is at one standard deviation from the threshold value.*

In Fig. 5.20, the evolution of $\bar{V}$, with uncertainty $\delta\bar{V}$, represented by the blue area, is represented as a function of $\langle n \rangle$, for the case of $M = 1000$, Fig. 5.20a), and $M = 500$, Fig. 5.20b). One can see that if M is sufficiently large, the optimised value of $\bar{V}$ is recovered for the lowest possible values of $\langle n \rangle$. This guarantees that the probability of having more than one particle per input channel is as weak as possible. For the case of our experiment, $\langle n \rangle = 0.5 - 0.8 \approx 0.65$ and one recovers, from this model, a visibility of $\bar{V} = 0.635\,(35)$ with the uncertainty given by Eq. (5.14). Compared to the experimental value of $\bar{V} = 0.65\,(7)$, we see that the value of $\bar{V}$ agrees, however, the uncertainty seems to be underestimate in our calculation. For higher values of $\langle n \rangle$ the visibility decreases to the asymptotic value of one half and the error bars get smaller. In a real experiment, however, one is more interested in guaranteeing the optimised signal-to-noise ratio.

In Fig. 5.21, we represent the signal-to-noise ratio determined by

$$\alpha = \frac{\bar{V} - 0.5}{\delta\bar{V}},$$

If $\alpha = 1$, the visibility is one standard deviation above the classical threshold of 0.5. One can then see for increasing values of $\langle n \rangle$ that the signal-to-noise ratio increases to an asymptotic value depending on M. This means that for a fixed number of repetitions the signal-to-noise ratio tends to increase when $\langle n \rangle$ gets larger. This seems contra-intuitive to the basic explanation of the HOM-experiment. For the average population used in our experimental realisation, $\langle n \rangle \approx 0.65$, and knowing that the number of realisations varies between 500 to 1000, one would expect a signal-to-noise ratio equal to 4.3 which is two times larger than the one measured experimentally and equal to 2. This difference might be explained from the fact that our input state does not correspond exactly to a spontaneous parametric down-conversion state or, due to fluctuations of the BEC density that would lead to average population fluctuations.

In real experiments with acquisition time constraints, the signal-to-noise ratio of the HOM-dip visibility increases with the average population. Our choice of $\langle n \rangle \approx 0.5$–$0.8 \approx 0.65$ seems appropriate to investigate the HOM visibility. This intermediate regime guarantees a good signal-to-noise ratio and, on the other hand, allows us to measure a visibility well above the 0.5 threshold value.

Increasing the number of atoms per atomic beams, however, might increases secondary four-wave mixing processes that translate into losses in our system. This would tend to weaken the HOM effect.

In Table 5.3, we summarise some quantities that have been extracted from our experimental results and that are going to be useful in the next section, namely, the density width of beams

	Cloud a	**Cloud** b	**Cloud** c	**Cloud** d
Density center (k_{lat})	0.73 (1)	1.27 (2)	0.735 (7)	1.272 (8)
Density width at $1/\sqrt{e}$ (k_{lat})				
$\hat{z}$	0.06 (1)	0.06 (1)	0.08 (2)	0.08 (2)
$\hat{x}$	0.08 (2)	0.08 (2)	0.10 (3)	0.012 (3)
$\hat{y}$	0.08 (2)	0.08 (2)	0.10 (3)	0.012 (3)
Cauchy integration volume Ω_V (k_{lat}^3)				
$\mathcal{L}_x$	0.048	0.048		
$\mathcal{L}_y$	0.048	0.048		
$\mathcal{L}_z$	0.028	0.028		
Correlation coefficient C	1.75 (20)			
δ from Eq. (5.9)	1.15 (5)			
HOM-dip visibility $\bar{V}$ from Eq. (5.9)	0.6 (1)			
HOM integration volume Ω_V (k_{lat}^3)				
$\mathcal{L}_x$			0.048	0.048
$\mathcal{L}_y$			0.048	0.048
$\mathcal{L}_z$			0.028	0.028
HOM-integration center (k_{lat})			0.740	1.275
HOM-dip visibility $\bar{V}$			0.65 (7)	
Average number of atoms detected inside Ω_V	0.21	0.13	0.19	0.18
Averaged population	0.84	0.52	0.76	0.72
HOM-dip $\bar{V}$ from Eq. (5.10) with $\langle n \rangle = 0.5 - 0.8$			0.64 (8)	
HOM-dip $\bar{V}$ from Eq. (5.10) for $\langle n \rangle = 0.65$ and uncertainty given by Eq. (5.14)			0.64 (2)	

Table 5.3: *Summary of the HOM analysis.*

before and after the interferometric scheme, the integration volume in order to optimise the HOM-dip visibility, the averaged population and the HOM-dip visibility among others.

5.5 HOM-dip width: some explanation

From the HOM-dip, one can determine how different is the input state from a twin-Fock state with one atom per mode. However, this is not the only information that can be recovered from this experiment. For example, the main interest of the original HOM experiment was to

determine the size of the photon wavepacket [54]. Through the measurement of the dip width, the wavepacket size was recovered with a precision of 1 fs. In this Section, the HOM-dip width in our experiment is discussed. We will show that as for the original experiment of 1987, the HOM-dip width is mostly determined by the filtering methods.

5.5.1 Prediction of the width

The general expression of $G^{(2)}(\tau)$ assuming a 50:50 beam-splitter and perfect mirror can be written as (see Appendix D for more details on this calculation)

$$\begin{aligned} G^{(2)}_{cd}(\tau) = \frac{1}{4}[&\langle \hat{a}^\dagger_{k_a+k_{\text{bms}}} \hat{a}^\dagger_{k_b-k_{\text{bms}}} \hat{a}_{k_a+k_{\text{bms}}} \hat{a}_{k_b-k_{\text{bms}}} \rangle - \langle \hat{e}^{i(\phi_1-\phi_1'+\phi_2-\phi_2')} a^\dagger_{k_a} \hat{a}^\dagger_{k_b} \hat{a}_{k_a+k_{\text{bms}}} \hat{a}_{k_b-k_{\text{bms}}} \rangle \\ &- \langle \hat{e}^{-i(\phi_1-\phi_1'+\phi_2-\phi_2')} a^\dagger_{k_a+k_{\text{bms}}} \hat{a}^\dagger_{k_b-k_{\text{bms}}} \hat{a}_{k_a} \hat{a}_{k_b} \rangle + \langle \hat{a}^\dagger_{k_a} \hat{a}^\dagger_{k_b} \hat{a}_{k_a} \hat{a}_{k_b} \rangle] \\ &+ \frac{1}{4}[\langle \hat{a}^\dagger_{k_a} \hat{a}^\dagger_{k_b-k_{\text{bms}}} \hat{a}_{k_a} \hat{a}_{k_b-k_{\text{bms}}} \rangle + \langle \hat{a}^\dagger_{k_b} \hat{a}^\dagger_{k_a+k_{\text{bms}}} \hat{a}_{k_b} \hat{a}_{k_a+k_{\text{bms}}} \rangle] \end{aligned} \tag{5.15}$$

with

$$\phi_1 = -(\phi_S - \phi_M) - \frac{\hbar t_s}{2m}(k_a + k_{\text{bms}})^2 - \frac{\hbar t_m}{2m}(k_a^2 - (k_a + k_{\text{bms}})^2), \tag{5.16a}$$

$$\phi_1' = -\phi_M - \frac{\hbar t_s}{2m}k_a^2 + \frac{\hbar t_m}{2m}(k_a^2 - (k_a + k_{\text{bms}})^2), \tag{5.16b}$$

$$\phi_2 = (\phi_S - \phi_M) - \frac{\hbar t_s}{2m}(k_b - k_{\text{bms}})^2 - \frac{\hbar t_m}{2m}(k_b^2 - (k_b - k_{\text{bms}})^2), \tag{5.16c}$$

$$\phi_2' = \phi_M - \frac{\hbar t_s}{2m}k_b^2 + \frac{\hbar t_m}{2m}(k_b^2 - (k_b - k_{\text{bms}})^2). \tag{5.16d}$$

This means that the indistinguishable case, corresponding to the application time $t_{s,0}$, leads to a value of $\tau_0 = t_{s,0} - t_m = t_m$.

The extreme cases

From Eq. (5.15), one can identify the autocorrelation contribution $G^{(2)}_{aa} = \langle \hat{a}^\dagger_{k_a} \hat{a}^\dagger_{k_b-k_{\text{bms}}} \hat{a}_{k_a} \hat{a}_{k_b-k_{\text{bms}}} \rangle$ and $G^{(2)}_{bb} = \langle \hat{a}^\dagger_{k_b} \hat{a}^\dagger_{k_a+k_{\text{bms}}} \hat{a}_{k_b} \hat{a}_{k_a+k_{\text{bms}}} \rangle$ as well as the cross-correlations

$$G^{(2)}_{ab} = \langle \hat{a}^\dagger_{k_a} \hat{a}^\dagger_{k_b} \hat{a}_{k_a} \hat{a}_{k_b} \rangle = \langle \hat{a}^\dagger_{k_b-k_{\text{bms}}} \hat{a}^\dagger_{k_a+k_{\text{bms}}} \hat{a}_{k_b-k_{\text{bms}}} \hat{a}_{k_a+k_{\text{bms}}} \rangle$$

and

$$G^{(2)}_{ab} = \langle \hat{a}^\dagger_{k_a} \hat{a}^\dagger_{k_b} \hat{a}_{k_b-k_{\text{bms}}} \hat{a}_{k_a+k_{\text{bms}}} \rangle = \langle \hat{a}^\dagger_{k_a+k_{\text{bms}}} \hat{a}^\dagger_{k_b-k_{\text{bms}}} \hat{a}_{k_b} \hat{a}_{k_a} \rangle,$$

where $k_b = k_a + k_{\text{bms}}$. The cross-correlation between the output ports of the beam-splitter can then be rewritten as

$$G^{(2)}_{cd}(\tau) = \frac{1}{4}\left[G^{(2)}_{aa} + G^{(2)}_{bb}\right] + \frac{1}{2}G^{(2)}_{ab}\left[1 - \cos(\theta)\right] \tag{5.17}$$

with $\theta = \phi_1 + \phi_2 - \phi_1' - \phi_2' = \frac{\hbar}{m}\left[k_{\text{bms}}(k_a + k_{\text{bms}} - k_b)\right](\tau - t_m)$ and $\tau = t_s - t_m$. For the indistinguishable case, τ is equal to t_m, thus $\cos(\theta) = 1$, and the minimum value of the cross-correlation function is reached corresponding to

$$G^{(2)}_{cd}(\tau_0) = \frac{1}{4}\left(G^{(2)}_{aa} + G^{(2)}_{bb}\right).$$

On the other hand, if $\tau \to \infty$, the cosine term averages to zero in the volume of integration and one extracts the distinguishable value of $G^{(2)}_{cd}$, given by

$$G^{(2)}_{cd}(\infty) = \frac{1}{4}\left(G^{(2)}_{aa} + G^{(2)}_{bb}\right) + \frac{1}{2}G^{(2)}_{ab}.$$

Multimode scenario

From the single mode picture, one can not define a width since the wavepacket is infinitely long [76]. Mathematically, this means that the oscillating term

$$\cos(\theta) = \cos\left(\frac{\hbar}{m}\left(k_{\text{bms}}(k_a + k_{\text{bms}} - k_b)\right)(\tau - t_m)\right),$$

is always equals to 1, since $k_a + k_{\text{bms}} - k_b = 0$.

For a multimode source, however, the cross-correlation depends on $(k_a + k_{\text{bms}} - k_b)(\tau - t_m)$, and, after integration over k, will evolve with τ. Along the transverse direction, we will assume that the integration length is sufficiently small so that all the functions at play are uniform and, as a consequence, only integration along the vertical z−axis is going to determine the width of the HOM-dip. This reduces the problem to a 1D treatment that is easier to treat.

From Eq. (5.17), one can identify five fundamental quantities that can provide insights on the dip width (see Table 5.3 and Table 5.4), in particular:

- the autocorrelation widths associated to $G^{(2)}_{aa}$ and $G^{(2)}_{bb}$ ($\sigma_{l,a}$ and $\sigma_{l,b}$, respectively), although they are not directly linked to the oscillation term and have a negligible influence;
- the cross-correlation width associated to $G^{(2)}_{ab}$ (σ_c);
- the density width, since the cloud has a finite size in momentum space (σ_{n_a} and σ_{n_b});
- the stability of the beam-splitter which relates to a width in momentum space of the diffraction momentum k_{bms}. This width has been probed in Chapter 4 to be smaller than the autocorrelation width;
- and the lengths of integration $\mathcal{L}_a$, for beam k_a, and $\mathcal{L}_b$, for beam k_b, along the z−axis that are identical and equal to $\mathcal{L}_z/2$.

The integrated cross-correlation function between ports c and d can then be written, assuming a Gaussian description for the correlations and density, as

$$\begin{aligned}
G^{(2)}_{cd,\text{Meas.}}(\tau, k_{aC}, k_{bC}) = \left(\frac{\eta}{\mathcal{L}_z}\right)^2 \mathcal{N}_a\mathcal{N}_b \int_{k_{\text{bms},c}-\mathcal{L}_z/2}^{k_{\text{bms},c}+\mathcal{L}_z/2} \frac{dk_{\text{bms}}}{\mathcal{L}_z} \int_{k_{aC}-\mathcal{L}_a}^{k_{aC}+\mathcal{L}_a} dk_a \int_{k_{bC}-\mathcal{L}_b}^{k_{bC}+\mathcal{L}_b} dk_b \\
\times \exp\left(-\frac{(k_a - \bar{k}_a)^2}{2\sigma^2_{n_a}}\right)\exp\left(-\frac{(k_b - \bar{k}_b)^2}{2\sigma^2_{n_b}}\right)\exp\left(-\frac{(k_{\text{bms}} - k_{\text{bms},c})^2}{2\sigma^2_{\text{bms}}}\right) \\
\times\left\{\frac{1}{4}\left[g^{(2)}_{aa}(0)\exp\left(-\frac{(k_a - k_{aC})^2}{2\sigma^2_{la}}\right) + g^{(2)}_{bb}(0)\exp\left(-\frac{(k_b - k_{bC})^2}{2\sigma^2_{lb}}\right)\right]\right. \\
\left. + \frac{1}{2}\left[g^{(2)}_{ab}(0)\exp\left(-\frac{((k_a + k_b)/2 - 1)^2}{2\sigma^2_c}\right)(1 - \cos\theta)\right]\right\}, \qquad (5.18)
\end{aligned}$$

with $\bar{k}_a$ and $\bar{k}_b$ the central positions for the two atomic beams, k_{aC} and k_{bC} the central position around which the integration is performed and $g^{(2)}_{aa}$, $g^{(2)}_{bb}$ and $g^{(2)}_{ab}$ the normalised correlation functions given by the analysis performed before the beam-splitter.

	Local		Cross
	Cloud k_a	Cloud k_b	
Correlation : σ_z (k_{lat})	0.012 (2)	0.010 (2)	0.025 (3)
Density: $\sigma_{n(k)z}$ (k_{lat})	0.06 (1)	0.06 (2)	

Table 5.4: Width at $1/\sqrt{e}$ for the density and correlation functions.

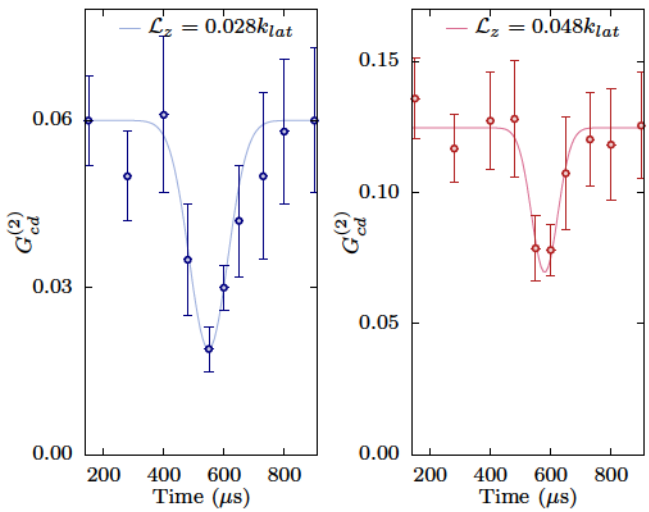

Figure 5.22: Experimental observation of the destructive interference effect for two different integration volumes. Reduction of the cross-correlation between ports c and d as a function of τ. For $\tau \approx 550\,\mu s \approx \tau_0$, one retrieves the minimum cross-correlation value corresponding to the indistinguishable paths scenario. a) Evolution of $G^{(2)}_{cd}$ as a function of τ for a volume of integration $\Omega_V = [0.048^2 \times 0.028]\,(k^3_{lat})$. b) Evolution of $G^{(2)}_{cd}$ as a function of τ for a volume of integration $\Omega_V = [0.048^3]\,(k^3_{lat})$.

5.5.2 Comparison with the experimental results

Consider the situation of our experimental analysis discussed in Section 5.3.1. In this case, the beam-splitter corresponds to a diffraction in momentum space equal to $k_{bms,c} = 0.55\,k_{lat}$ with an estimated uncertainty equal to $\sigma_{BMS} = 1 \times 10^{-2}\,k_{lat}$ (see Chapter 4). The centers of the two volumes of analysis $k_{aC} = 0.740\,k_{lat}$ and $k_{bC} = 1.275\,k_{lat}$ correspond to the ones used in the HOM-analysis discussed in Subsection 5.3.1. The values of the half-widths are given in Table 5.3 and Table 5.4 (see Subsection 3.5 for more details). The only free parameter is then the integration volume which is defined by our analysis.

Consider the two cases discussed earlier and represented in Fig. 5.22, where the left panel corresponds to $\mathcal{L}_z = 2\mathcal{L}_a = 2\mathcal{L}_b = 0.028\,k_{lat}$ and the right panel to the integration length $\mathcal{L}_z = 0.048\,k_{lat}$. A Gaussian fit gives, for the second case, a width smaller than for the first case ($\sigma_{HOM,\mathcal{L}_z=0.028} \approx 70\,(30)\ \mu s$ and $\sigma_{HOM,\mathcal{L}_z=0.048} \approx 45\,(10)\ \mu s$). The visibility is also smaller since the situation corresponds to a sum of distinguishable and indistinguishable paths, even when $\tau = \tau_0$, as schematically represented in Fig. 5.7

One can then try to estimate the theoretical width of the HOM-dip from Eq. (5.18) assuming $2\mathcal{L}_{a,b} = 0.028\,k_{lat}$ and $2\mathcal{L}_{a,b} = 0.048\,k_{lat}$. The result is represented in Fig. 5.23a) and b) where for both cases the dip is centred around $\tau_0 = 550\,\mu s$. In the first case, $\mathcal{L}_z = 0.028\,k_{lat}$, the theoretical HOM-dip prediction, $122\,\mu s$, is wider than the one measured, $70\,(30)\ \mu s$. For the second situation, $\mathcal{L}_z = 0.048\,k_{lat}$ one expects a width of $100\,\mu s$ still far away from the measured

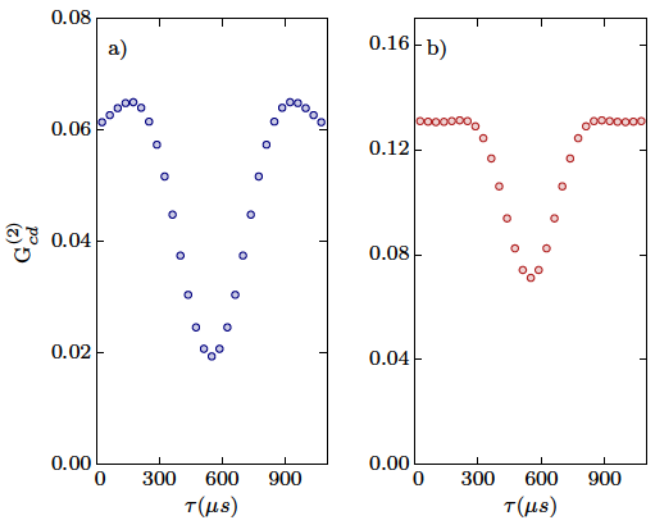

Figure 5.23: ***Theoretical prediction for the HOM-dip width.*** *a) Evolution of $G^{(2)}$ as a function of τ for a volume of integration of $\Omega_V = [0.048^2 \times 0.028]\,(k_{lat}^3)$ obtained by Eq. (5.18). b) Evolution of $G^{(2)}$ as a function of τ for a volume of integration of $\Omega_V = [0.048^3]\,(k_{lat}^3)$. These two curves are the theoretical predictions of the experimental situation represented in Fig. 5.22a) and b) respectively with the center of integration zones defined by $\mathbf{C}_c = (0,\ 0,\ 0.74)\,(k_{lat})$ and $\mathbf{C}_d = (0,\ 0,\ 1.275)\,(k_{lat})$.*

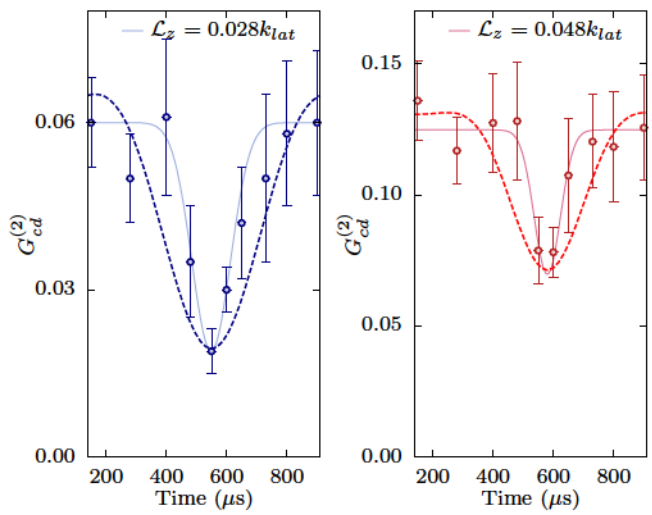

Figure 5.24: **Direct comparison between the experimental HOM-dip and the theoretical prediction.** *We compare the obtained result for the HOM-dip via integration of Eq. (5.18) for $k_{aC} = 0.74\,\mathrm{k}_{lat}$ and $k_{bC} = 1.275\,\mathrm{k}_{lat}$ with the HOM-dip obtained experimentally. Two situations are considered: a) with $\mathcal{L}_z = 0.028\,\mathrm{k}_{lat}$ and b) with $\mathcal{L}_z = 0.048\,\mathrm{k}_{lat}$.*

value of 45 (10) μs.

Two observations can be made. The first is that in both cases the dip is wider than the one observed experimentally. This difference might come from the uni-dimensionality of our analysis. Indeed, we assumed that the transverse overlap was perfect and that integration along the transverse axis had no influence on the width. As shown in Chapter 4 the beam-splitter lattice is slightly tilted on the $x-$axis, thus the overlap is not perfect. This would irremediably translate into a thinner dip. Also, the fact that both mirror and 50:50 beam-splitter are pulses of duration length equal to 100 μs and 50 μs, respectively, lead to a floating averaged over $G^{(2)}(\tau)$ which is not taken into account by our model.

Second, the volume of integration seems to determine the HOM-dip width. For a broader volume of integration, we find that not only the background value $G^{(2)}_{cd}(\infty)$ increases as expected

	$\mathcal{L}_z = 0.028\,\mathrm{k_{lat}}$	$\mathcal{L}_z = 0.048\,\mathrm{k_{lat}}$
$\sigma_{\text{theo.}}$ ($\mathrm{k_{lat}}$)	122 (4)	100 (3)
$\sigma_{\text{exp.}}$ ($\mathrm{k_{lat}}$)	70 (30)	45 (10)
	Ratio between width for $\mathcal{L}_z = 0.028$ and $\mathcal{L}_z = 0.048$	
$\sigma_{\text{theo.}}$ ($\mathrm{k_{lat}}$)	1.22 (5)	
$\sigma_{\text{exp.}}$ ($\mathrm{k_{lat}}$)	1.56 (75)	

Table 5.5: ***Comparison between the experimental HOM-dip width and the theoretically predicted one.***

since the number of atoms under analysis increases, but also the dip gets thinner and smaller in concordance to the experimental results shown in Fig. 5.22. One explanation is that that for larger volumes, one averages over paths that are both distinguishable and indistinguishable, even for $\tau = \tau_0$, which tends to squeeze the curve of $G^{(2)}(\tau)$. For the case of a vanishing local correlation and broad cross-correlations function, one can assume that the only varying term corresponds to $(1 - \cos\theta)$. Then $G^{(2)}_{cd}(\tau)$ simplifies to

$$G^{(2)}_{cd}(\tau) = \eta^2 N_a N_b \{1 - \alpha \mathrm{sinc}^2(\mathcal{L}_z k_{\mathrm{bms}} \frac{\hbar}{2m}[\tau - t_m])\} \tag{5.19}$$

with $\tau = t_s - t_m$ and α a coefficient proportional to k_{bms}, k_{aC} and k_{bC}. The cross-correlation corresponds then to a sinus cardinal function whose width at $1/\sqrt{e}$ is inversely proportional to the integration length. For smaller integration volumes, the dip get larger as observed both experimentally, (Fig. 5.22) and theoretically (Fig. 5.23).

From this analysis, one is able to recover the qualitative behaviour of the HOM-dip. Namely, we have seen that for larger integration volumes the dip gets thinner and weaker which agrees with the experimental observations. The widths of the observed HOM-dip do not match exactly the expected values as shown in Table 5.5. Nevertheless, one can see that our description follows correctly the evolution of the width as a function of the integration length. This is shown by the agreement between the widths ratio of $\mathcal{L}_z = 0.028$ and $0.048\,\mathrm{k_{lat}}$ from both theoretical and experimental results.

Different effects on $G^{(2)}(\tau)$

One can now study the dependence of the HOM-dip width as a function of the different quantities at play, meaning, the correlations functions, density and matching conditions between $k_a + k_{\mathrm{bms}}$ and k_b.

Let us consider the effect of both the cross- and local correlation widths. Fig. 5.25a) corresponds to the situation in which the integration length is equal to $\mathcal{L}_z = 0.028\,\mathrm{k_{lat}}$, $\sigma_c = 0.025\,\mathrm{k_{lat}}$, $\sigma_{la} = 0.010\,\mathrm{k_{lat}}$, $\sigma_{lb} = 0.010\,\mathrm{k_{lat}}$, $\sigma_{\mathrm{bms}} = 0.010\,\mathrm{k_{lat}}$ and the central positions of the volume of analysis are $k_{aC} = 0.740\,\mathrm{k_{lat}}$ and $k_{bC} = 1.275\,\mathrm{k_{lat}}$. This corresponds to the analysis performed in the Subsection 5.3.1 and Subsection 5.5.2.

The theoretical HOM-dip presents a contrast of 0.65 and a half-width at $1/\sqrt{e}$ equal to 122 μs. We compare this situation to Fig. 5.25b) where k_{aC} is now equal to $0.8\,\mathrm{k_{lat}}$. Since the two *clouds* under analysis belong to different modes and, in this sense, are not indistinguishable, one expects a flat dependence of $G^{(2)}_{cd}$ with τ. Although there is a slight oscillation around $\tau - t_m = 0$

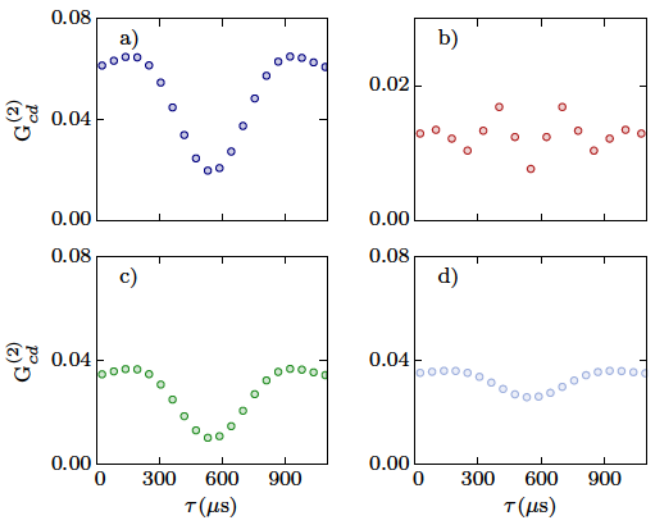

Figure 5.25: Theoretical HOM-dip estimations for different initial parameters. a) Same parameters as the ones used in Fig. 5.23a). b) Same as a) but with $k_{aC} = 0.8\,k_{lat}$ instead of $0.74\,k_{lat}$. c) Same as a) but for $\sigma_{la} = \sigma_{lb} = 0.050\,k_{lat}$ instead of $\sigma_{la} = 0.010\,k_{lat}$. d) Same as a) but for $\sigma_c = 0.050\,k_{lat}$ instead of $\sigma_c = 0.025\,k_{lat}$.

which is completely negligible, the result shows no significant reduction of $G^{(2)}$ as a function of τ.

Fig. 5.25c) and d) are similar to the case a), but this time for an autocorrelation width $\sigma_{la} = \sigma_{lb} = 0.050\,k_{lat}$ (canvas c)) and $\sigma_c = 0.050\,k_{lat}$ (canvas d)). For the case of a larger autocorrelation function, the only effect is a reduction of the background correlation $G^{(2)}_{bg.}$ due to the fact that the integrated value of the autocorrelation functions decreases. Case d), however, leads to both a reduction of the background correlation value as well as a reduction of the visibility. This is due to the fact that the integrated cross-correlation decreases and, as a consequence

$$C = G^{(2)}_{ab} / \sqrt{G^{(2)}_{aa} G^{(2)}_{bb}}\,,$$

gets smaller, leading to a weaker visibility as discussed in Section 1.2.

The HOM-dip width is, for our experimental conditions, defined by the integration volume and the central positions of the analysis, $\{k_{aC}; k_{bC}\}$. The fundamental properties of the pairs, such as the auto- and cross-correlations contribute poorly.

5.6 Coalescence effect

The HOM effect can also be viewed as a coalescence effect, in the sense that two photons will always emerge together at one of the two output ports. This translates into the creation of a maximally entangled state

$$|\psi\rangle_{out} = \frac{1}{\sqrt{2}} \left(|0_c, 2_d\rangle + |2_c, 0_d\rangle\right).$$

5.6.1 Autocorrelation measurement

In order to detect this coalescence effect, one has to perform an auto-correlation measurement at one of the two output ports. In quantum optics, one cannot directly measure this quantity

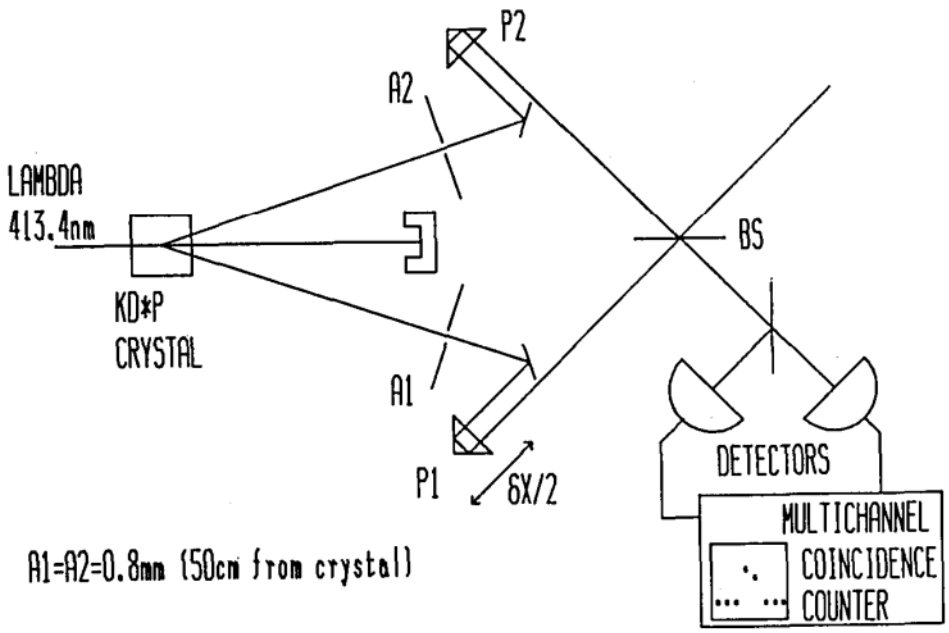

Figure 5.26: Schematic representation of the experiment described in Ref. [206]. The experiment allows one to determine the autocorrelation of the output ports c and d. Another beam-splitter is placed on the path of the output port c and through the cross-correlation measurement between the output ports of the new beam-splitter the autocorrelation of c is recovered. Figure copied from Ref. [206]

since the dead time of one photodiode is larger than the time difference between two photons. In order to get rid of this problem, it is usual in quantum optics to place in one of the two output ports another beam-splitter and to look at the joint probability between the two new output ports [79, 206]. This is represented in Fig. 5.26, where a 50:50 beam-splitter is placed at the exit port c.

The autocorrelation of one of the output ports (let us consider only the case of port c) evolves between the distinguishable case and the indistinguishable case as follow (see more informations in Section D.4)

$$G^{(2)}_{cc,\,\mathrm{Dis}} = \frac{1}{2} G^{(2)}_{ab}\,, \tag{5.20a}$$

$$G^{(2)}_{cc,\,\mathrm{Ind}} = G^{(2)}_{ab}\,, \tag{5.20b}$$

and corresponds to an increase of $G^{(2)}_{cc}(\tau)$ when $\tau = \tau_0$. In the case of the photonic experiment, it is difficult to perform both measurements, that is the cross-correlation between ports c and d and the autocorrelation of each port, at the same time. On the contrary, in our experiment, the MCP detector has a dead time much smaller than the arrival time difference between the two atoms. Thus, one can directly compare the cross-correlation between ports c and d, to the autocorrelation at each output port.

In Fig. 5.27, we represent the normalised cross-correlation (blue circles) as well as the normalised autocorrelation at the output port c and d [4] (green circles) as a function of τ. It is possible to identify an increase on the autocorrelation function with maximum slightly displaced when compared to the cross-correlation dip and amplitude. The blue line indicates the empirical Gaussian fit from which the visibility is obtained. One can now try to predict the expected width of the autocorrelation function. The autocorrelation for the output port c can be written

[4] We averaged the autocorrelation functions of port c and d.

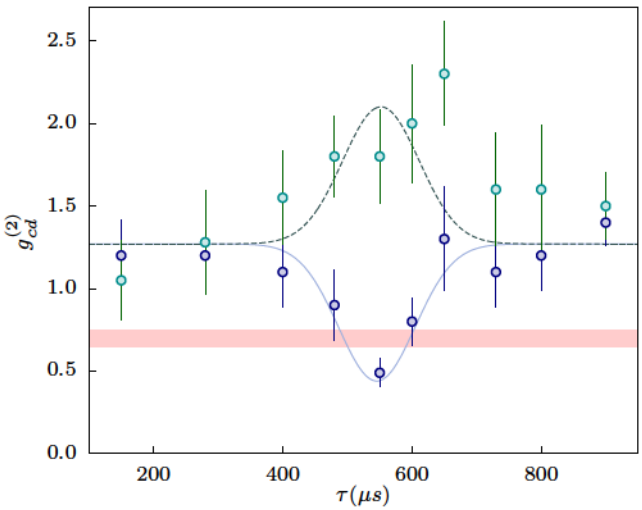

Figure 5.27: Cross and autocorrelation for output ports of the beam-splitter. Comparison between the normalized cross-correlation as a function of τ between ports c and d (blue circles) and the normalised averaged value of the autocorrelation of port c and d as a function of τ (green circles). The blue line corresponds to the a Gaussian fit applied to the cross-correlation function. The dashed green line corresponds to the symmetric fit which should correspond to the expected result for the autocorrelation function as a function of τ.

as

$$G^{(2)}_{cc} = \frac{1}{4}\left(G^{(2)}_{aa} + G^{(2)}_{bb}\right) + \frac{1}{2}G^{(2)}_{ab}\left(1 + \cos\left(\frac{\hbar k_{\text{bms}}}{m}(k_a - k'_a)(\tau - t_m)\right)\right). \tag{5.21}$$

The autocorrelation at the output port c, $G^{(2)}_{cc}$ measured over the volume Ω_V, with integration length $\mathcal{L}_a$ along the vertical z–axis, is then equal to (the same calculation holds for $G^{(2)}_{dd}$)

$$\begin{aligned} G^{(2)}_{cc}(\tau, k_{aC}) = &\left(\frac{\eta}{\mathcal{L}_z}\right)^2 \mathcal{N}_a\mathcal{N}_b \int_{k_{\text{bms},c}-\mathcal{L}_z/2}^{k_{\text{bms},c}+\mathcal{L}_z/2} \frac{dk_{\text{bms}}}{\mathcal{L}_z} \int_{k_{aC}-\mathcal{L}_a}^{k_{aC}+\mathcal{L}_a} dk_a \int_{k_{bC}-\mathcal{L}_b}^{k_{bC}+\mathcal{L}_b} dk_b \\ &\times \exp\left(-\frac{(k_a - k_{aC})^2}{2\sigma^2_{n_a}}\right)\exp\left(-\frac{(k_b - k_{bC})^2}{2\sigma^2_{n_b}}\right)\exp\left(-\frac{(k_{\text{bms}} - k_{\text{bms},c})^2}{2\sigma^2_{\text{bms}}}\right) \\ &\times \left\{\frac{1}{4}\left(g^{(2)}_{aa}(0)\exp\left(-\frac{(k_a - k_{aC})^2}{2\sigma^2_{la}}\right) + g^{(2)}_{bb}(0)\exp\left(-\frac{(k_b - k_{bC})^2}{2\sigma^2_{lb}}\right)\right)\right. \\ &\left. + \frac{1}{2}\left(g^{(2)}_{ab}(0)\exp\left(-\frac{(k_a + k_b/2 - 1)^2}{2\sigma^2_c}\right)[1 + \cos\vartheta]\right)\right\} \end{aligned} \tag{5.22}$$

where $\vartheta = \frac{k_{\text{bms}}\hbar}{m}(k_a - k'_a)(\tau - t_m)$. If one assumes that the integration length $\mathcal{L}_z$ is small when compared to the typical width of the functions at play, then $G^{(2)}_{cc}$ rewrites simply in terms of

$$G^{(2)}_{cc} = \left(\frac{\eta}{\mathcal{L}_z}\right)^2 \mathcal{N}_a\mathcal{N}_b \int_{k_{bms,c}-\mathcal{L}_z/2}^{k_{bms,c}+\mathcal{L}_z/2} \frac{dk_{\text{bms}}}{\mathcal{L}_z} \int_{k_{aC}-\mathcal{L}_a}^{k_{aC}+\mathcal{L}_a} dk_a \int_{k_{bC}-\mathcal{L}_b}^{k_{bC}+\mathcal{L}_b} dk_b\,(1 + \cos\vartheta) \tag{5.23}$$

which leads to $G^{(2)}_{cc} = \eta^2\mathcal{N}_a\mathcal{N}_b\left(1 + \alpha\text{sinc}^2(\frac{\hbar}{2m}\mathcal{L}_z(\tau - t_m))\right)$ and, in this sense, the evolution of $G^{(2)}_{cc}$ is the symmetric function of the cross-correlation described by Eq. (5.19). Thus, the width and the amplitude of the *bump* must be equal to those of the dip. However, this is not the observed result as one can see in Fig. 5.27, where the green dashed line indicates the expected result for the autocorrelation as a function of τ. The center of the bump is shifted respectively to the cross-correlation dip which is unexpected. This discrepancy will be further studied in the future.

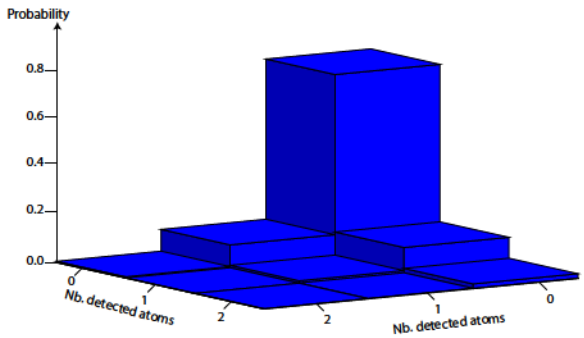

Figure 5.28: Conditional probability detection $P(n|m)$ between ports c and d for the indistinguishable case.

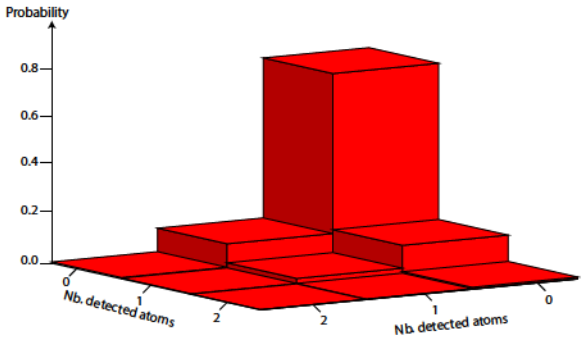

Figure 5.29: Conditional probability detection $P(n|m)$ between ports c and d for the distinguishable case.

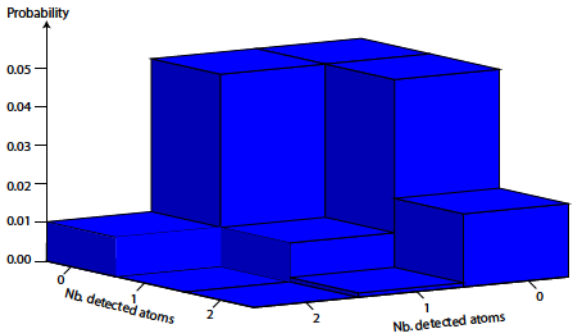

Figure 5.30: Conditional probability detection $P(n|m)$ between ports c and d for the indistinguishable case zoomed on the terms $P(0|2)$, $P(2|0)$ and $P(1|1)$.

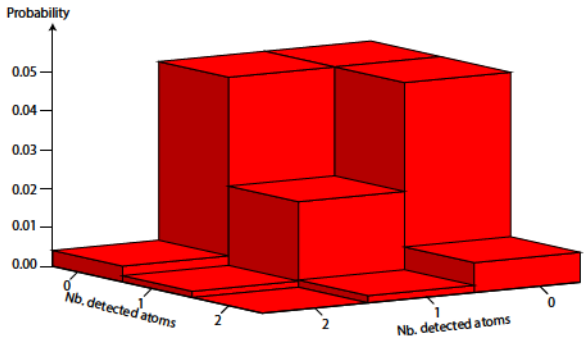

Figure 5.31: Conditional probability detection $P(n|m)$ between ports c and d for the distinguishable case zoomed on the terms $P(0|2)$, $P(2|0)$ and $P(1|1)$.

5.6.2 Conditional probability

Another proof of the coalescence effect can come from the direct measurement of the conditional probability of detecting n atoms in port c having detected m atoms in port d. This probability $P(n|m)$ is represented for both the indistinguishable situation (blue histogram) $\tau = 150\,\mu$s (see Fig. 5.28) and for the distinguishable situation (red histogram) $\tau = 550\,\mu$s (see Fig. 5.29). Since the averaged population is rather small, for most of the realisations no atomic count is registered in neither one of the two output ports. For this reason, we zoom on the joint probability $P(2|0)$, $P(0|2)$ and $P(1|1)$ for the indistinguishable case (see Fig. 5.31) as well as for the distinguishable one (see Fig. 5.30).

We note that for indistinguishable paths, the conditional probability $P(1|1)$ reduces, while the probability of having two atoms in one of the output ports and zero on the other one increases. This reduction of the coincidence probability corresponds to the HOM effect. The asymmetry between $P(0|2)$ and $P(2|0)$ may come from the fact that we did not averaged over sufficient realisations to recover a symmetric situation (for the distinguishable case it corresponds to an average over 500 realisations and for the indistinguishable case over 1000 realisations.)

However, one has to keep in mind that these probabilities are obtained for detected atoms and do not correspond to the real distributions. Since it is difficult to recover the initial conditional probabilities, this result is only useful as a qualitative estimation of the coalescence at play in this experiment.

5.7 Others way to measure the destructive interference: variance of the population difference

Although originally centred on the reduction of the cross-correlation between ports c and d, the HOM effect can also be studied through other quantities as for example the normalised variance of the difference between the two clouds c and d. This will be discussed in this section and constitutes a complementary measurement to the cross-correlation analysis.

The variance of the difference between the two output ports c and d corresponds to (see Section 3.4.2 and Appendix D.5 for more details)

$$V_{cd} = \frac{\left\langle \left(a^\dagger_{k_c} a_{k_c} - a^\dagger_{k_d} a_{k_d}\right)^2 \right\rangle - \langle a^\dagger_{k_c} a_{k_c} - a^\dagger_{k_d} a_{k_d}\rangle^2}{\langle a^\dagger_{k_c} a_{k_c}\rangle + \langle a^\dagger_{k_d} a_{k_d}\rangle}, \tag{5.24}$$

and can be re-written for the case of identical populations between c and d, $\langle a^\dagger_{k_c} a_{k_c}\rangle = \langle a^\dagger_{k_d} a_{k_d}\rangle = \langle n\rangle$ as

$$V_{cd} = \frac{G^{(2)}_{cc} + G^{(2)}_{dd} - 2G^{(2)}_{cd}}{2\langle n\rangle} + 1\,.$$

In the case of distinguishable particles, $G^{(2)}_{cd}(\infty) = G^{(2)}_{cc}(\infty) = G^{(2)}_{dd}(\infty)$, and one finds a normalised variance equal to

$$V_{\text{Dis.}} = 1. \tag{5.25}$$

While for the case of indistinguishable particles, we have

$$G^{(2)}_{cc}(\tau_0) = G^{(2)}_{dd}(\tau_0) = \frac{1}{4}\left(G^{(2)}_{aa} + G^{(2)}_{bb}\right) + G^{(2)}_{ab}\,,$$
$$G^{(2)}_{cd}(\tau_0) = \frac{1}{4}\left(G^{(2)}_{aa} + G^{(2)}_{bb}\right)\,,$$

and

$$V_{\text{Ind.}} = 1 + \frac{1}{\langle n\rangle} G^{(2)}_{ab}. \tag{5.26}$$

One can see that this normalised variance of the difference increases for the case of indistinguishable particles. As a function of τ, it is then expected to measure a *bump* around $\tau = \tau_0$.

The visibility of the variance $\bar{V}_V$ corresponding to

$$\bar{V}_V = \frac{V_{\text{Ind.}}}{V_{\text{Dis.}}} - 1, \tag{5.27}$$

is then equal, for the case of particles generated through spontaneous parametric down-conversion, to

$$\bar{V}_V = \frac{1}{\langle n\rangle} G^{(2)}_{ab} = \frac{1}{\langle n\rangle}\langle n\rangle \cdot (1 + 2\langle n\rangle)\,, \tag{5.28}$$

and it scales linearly with $\langle n\rangle$.

For a finite detection efficiency η, the detected value of the variance is equal to (see Section 3.4.2)

$$V_{det.} = \eta V + (1 - \eta)\,,$$

leading to the expressions

$$V_{\text{Ind., det.}} = \left(\frac{G^{(2)}_{ab}}{\langle n\rangle}\eta\right) + 1\,, \tag{5.29a}$$

$$V_{\text{Dis., det.}} = 1\,. \tag{5.29b}$$

The visibility of the *bump* is then equal to

$$\bar{V}_V = \frac{G^{(2)}_{ab}}{\langle n\rangle}\eta = \eta\,(1 + 2\langle n\rangle)\,. \tag{5.30}$$

When compared to the cross-correlation visibility

$$\bar{V} = 1 - \frac{1}{2 + \frac{1}{2\langle n\rangle}},$$

one immediately sees that both quantities are preferably applied to distinct situations:

- Large populations: $\langle n\rangle \to \infty$, $\bar{V} \to 0.5$ while $\bar{V}_V$ grows linearly with $\eta\langle n\rangle$. In this situation, it is advantageous to measure the visibility of the variance rather than the visibility of the cross-correlation;
- Small populations: $\langle n\rangle \to 0$, $\bar{V}$ tends to the maximum value of 1 while $\bar{V}_V$ reaches its minimum value of η. Then for a lower number of particles, it is preferable to look at the cross-correlation.

It is important to note that the situation in which $\langle n\rangle \to \infty$ is rather distinct from the original HOM experiment. The coincidence count will no longer go to zero as it is reported in Ref. [82] and discussed in Subsection 1.1.1. These situations are closer to the squeezed experiments performed in the domain of spin states as for example in Refs. [53, 210].

The variance of the population difference, V, as a function of τ has also been experimentally probed in our experimental set-up. Since it is preferable to have more than a particle per input port, the pair production rate was increased, by increasing the lattice duration. The obtained average population was then equal to $\langle n\rangle \approx 2$. From Eq. (5.30) one would expect to obtain a visibility of $\eta\,(1 + 2\langle n\rangle)$ approximatively equal to 1.

For this experimental sequence, contrary to the description made in Section 5.2, the Raman transfer from sub-level $m_j = 1$ to the sub-level $m_j = 0$ was performed after the interferometric scheme. As a consequence, the time between the pair production and the application of the mirror was on the order of $t_m - t_0 \approx 250\,(50)$ μs. By varying the time delay τ between the mirror and the 50:50 beam-splitter, one observes the evolution of V as shown in Fig. 5.32c). One sees that when the atoms are made indistinguishable, that is $\tau \approx 250\,\mu$s, the variance increases for $k_d = 1.275$ (and $k_c = 0.74$) (see Fig. 5.32a)). The value of the visibility $\bar{V}_V$ is equal to $1.0\,(2)$ which agrees with the expected result of Eq. (5.30). The width of the *bump*, on the other hand, is two times larger than the width of the cross-correlation between ports c and d as a function of τ. This can be understood by looking at the evolution of V over τ, without integration over $k_{a,b}$ (see Appendix D.5 for the demonstration), which is equal to

$$V(\tau) = 1 + \frac{\alpha}{2}G^{(2)}_{ab}\left[1 + \cos\left(\frac{2\hbar k_{\text{bms}}}{m}(\tau - t_m)(k_a + k_{\text{bms}} - k_b)\right)\right]. \tag{5.31}$$

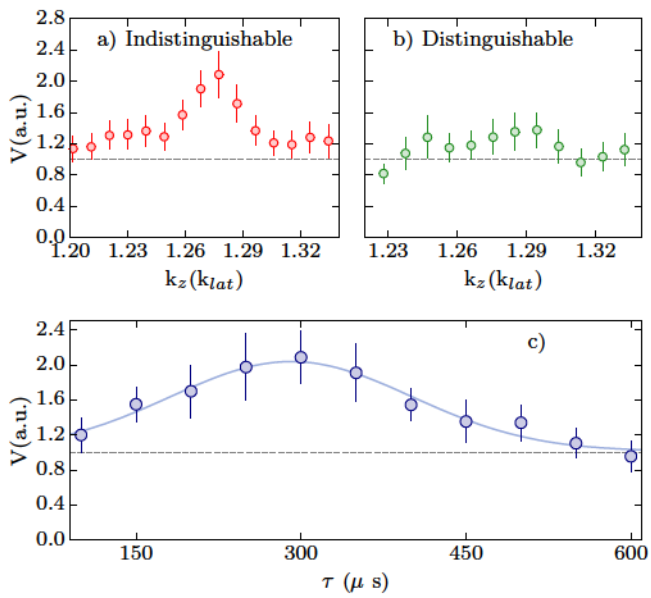

Figure 5.32: Variance as a function of τ. a) Evolution of the variance as a function of the momentum vector component along the vertical axis k for indistinguishable paths. b) Evolution of the variance as a function of the momentum vector component along the vertical axis k for distinguishable paths. c) Evolution of the variance V as a function of τ. An increase of the variance appears clearly when the paths are indistinguishable. The contrast of approximatively 1 is coherent with the averaged number of atoms $\langle n \rangle = 2$ and the detection efficiency $\eta = 0.25$.

One notices that the oscillating term has now a periodicity two times larger than the cross-correlation (see Eq. (5.17)), leading to a broader width after integration.

The visibility of the variance gives insight on the macroscopic (high number of particles) particle-interference. This study deviates from the original HOM experiment and approach the thematic of atomic interferometry in momentum space. This domain is very well developed in the topic of spin squeezing [53, 210–212] or with trapped atoms [213–215] and has applications in metrology [216, 217]. However, in our case, particles are moving in real space which can, in the future, open the way to inertial measurements interferometry with non-classical states.

5.8 Role of the interactions

Finally, in contrast to photons, atoms interact with each other. Let us consider the role of interactions in the HOM effect. In Ref. [109], the effect of interactions on the dip-visibility was studied in detail. It was shown that the interactions are responsible for an effective Coulomb potential and that the visibility decreases rapidly when the interaction potential is large when compared to the frequency of the two photon Rabi oscillation.

In the experiment discussed so far, the frequency Ω_R is equal to 6 kHz while the chemical potential of the pairs is almost negligible since the pairs are weakly populated — the total number of atoms in both clouds does not exceed thirty atoms. Assuming that the cloud has a size comparable to the one of the condensate [5], the chemical potential is then equal to 400 Hz and we obtain a ratio of

$$\frac{\mu}{2\hbar\Omega_R} = 0.033\,. \tag{5.32}$$

[5]The expansion effect is not considered, but it will only lower the effect of interactions

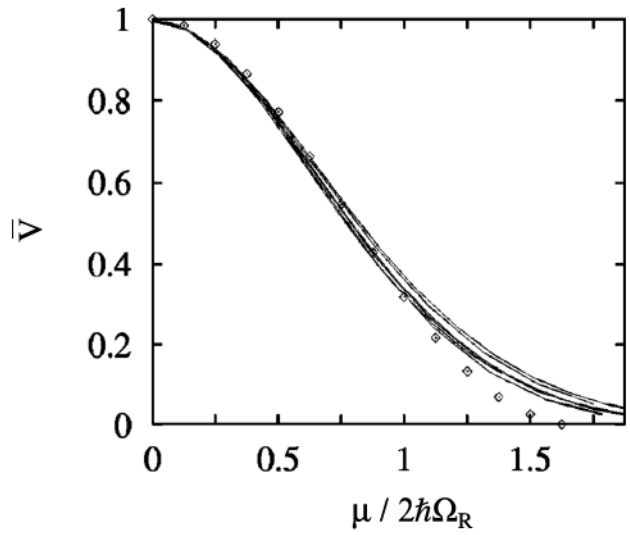

Figure 5.33: HOM-visibility as a function of the interactions. *Evolution of the HOM-visibility V as a function of the ratio between the chemical potential and the 2-photon Rabi frequency. Figure copied from [109].*

As it can be seen in Fig. 5.33, for a ratio of 0.033 , the interactions will not induce changes on the expected visibility. We can then safely neglect the influence of the interactions on the observed HOM signal.

5.9 Conclusion

Along this chapter the atomic realisation of the HOM experiment has been discussed. We have shown how to combine the different blocks discussed in Chapter 2, Chapter 3 and Chapter 4 in order to perform the analogue experiment with atoms.

The visibility of the HOM-dip 0.65 (7) presented in Section 5.3 was compared to the classical visibility threshold of 0.45 (4) above which the result cannot be explained through simple classical models. Hereupon, our experimental visibility can only be explained via quantum mechanics and demonstrates the ability of producing pairs of atoms with stronger-than-classical correlations in momentum space and to manipulate them coherently. The value of the obtained visibility has been compared to theoretical models assuming that the incoming state was obtained through parametric down-conversion (see Section 5.4). The agreement between this ideal model and our results is rather good, showing that simple theoretical arguments can qualitatively describe our experiment. However, the HOM-dip width has proved to be harder to fully understand. The qualitative model presented in Section 5.5 gives some intuition to the experimental result but does not fully describe our observations.

Furthermore, we have shown, that our experiment allows us to observe directly both the reduction on the cross-correlation between the two output ports c and d as well as the autocorrelation of each port, although the later behaves unexpectedly when compared to the cross-correlation value as a function of τ.

Finally, we pointed out the fact that through the measurement of the variance of the difference of population, information about many particles-interference effect can be retrieved. This kind of measurements could be useful for future tests of inertial measurements using pairs of atoms in momentum space.

Bibliography

[53]H. Strobel, W. Muessel, D. Linnemann, T. Zibold, D. B. Hume, L. Pezzè, A. Smerzi, and M. K. Oberthaler, "Fisher information and entanglement of non-Gaussian spin states", Science **345**, 424–427 (2014) (cit. on pp. 4, 27, 162, 163).

[54]C. K. Hong, Z. Y. Ou, and L. Mandel, "Measurement of subpicosecond time intervals between two photons by interference", Phys. Rev. Lett. **59**, 2044–2046 (1987) (cit. on pp. 4, 13, 14, 16, 17, 130–132, 134, 143, 152).

[76]Z. Y. Ou, *Multi-Photon Quantum Interference* (Springer, 2007) (cit. on pp. 16, 153).

[77]T. B. Pittman, D. V. Strekalov, A. Migdall, M. H. Rubin, A. V. Sergienko, and Y. H. Shih, "Can Two-Photon Interference be Considered the Interference of Two Photons?", Phys. Rev. Lett. **77**, 1917–1920 (1996) (cit. on pp. 16, 130).

[79]Z. Y. Ou, J.-K. Rhee, and L. J. Wang, "Observation of Four-Photon Interference with a Beam Splitter by Pulsed Parametric Down-Conversion", Phys. Rev. Lett. **83**, 959–962 (1999) (cit. on pp. 17, 130, 158).

[82]T. S. Iskhakov, K. Y. Spasibko, M. V. Chekhova, and G. Leuchs, "Macroscopic Hong–Ou–Mandel interference", New. J. Phys. **15**, 093036 (2013) (cit. on pp. 17, 18, 162).

[85]R. J. Lewis-Swan and K. V. Kheruntsyan, "Proposal for demonstrating the Hong–Ou–Mandel effect with matter waves", Nat Commun **5** (2014) (cit. on pp. 20, 135).

[109]E. Andersson, M. T. Fontenelle, and S. Stenholm, "Quantum statistics of atoms in microstructures", Phys. Rev. A **59**, 3841–3850 (1999) (cit. on pp. 27, 163, 164).

[206]J. G. Rarity and P. R. Tapster, "Fourth-order interference in parametric downconversion", J. Opt. Soc. Am. B **6**, 1221–1226 (1989) (cit. on pp. 130, 134, 140, 158).

[207]J.-F. Morizur, S. Armstrong, N. Treps, J. Janousek, and H.-A. Bachor, "Spatial reshaping of a squeezed state of light", The European Physical Journal D **61**, 237–239 (2011) (cit. on pp. 134, 142).

[208]N. Treps, V. Delaubert, A. Maître, J. M. Courty, and C. Fabre, "Quantum noise in multipixel image processing", Phys. Rev. A **71**, 013820 (2005) (cit. on pp. 134, 142).

[209]M. Martinelli, N. Treps, S. Ducci, S. Gigan, A. Maître, and C. Fabre, "Experimental study of the spatial distribution of quantum correlations in a confocal optical parametric oscillator", Phys. Rev. A **67**, 023808 (2003) (cit. on pp. 134, 142).

[210]B. Lucke, M. Scherer, J. Kruse, L. Pezze, F. Deuretzbacher, P. Hyllus, O. Topic, J. Peise, W. Ertmer, J. Arlt, L. Santos, A. Smerzi, and C. Klempt, "Twin Matter Waves for Interferometry Beyond the Classical Limit", Science **334**, 773–6 (2011) (cit. on pp. 162, 163).

[211]L. Gil, R. Mukherjee, E. Bridge, M. Jones, and T. Pohl, "Spin Squeezing in a Rydberg Lattice Clock", Phys. Rev. Lett. **112**, 103601 (2014) (cit. on p. 163).

[212]N. Behbood, F. Martin Ciurana, G. Colangelo, M. Napolitano, G. z. Tó th, R. J. Sewell, and M. W. Mitchell, "Generation of Macroscopic Singlet States in a Cold Atomic Ensemble", Phys. Rev. Lett. **113**, 093601 (2014) (cit. on p. 163).

[213]M. F. Riedel, P. Böhi, Y. Li, T. W. Hänsch, A. Sinatra, and P. Treutlein, "Atom-chip-based generation of entanglement for quantum metrology", Nature **464**, 1170–1173 (2010) (cit. on p. 163).

[214]C. Gross, T. Zibold, E. Nicklas, J. Estève, and M. K. Oberthaler, "Nonlinear atom interferometer surpasses classical precision limit", Nature **464**, 1165–1169 (2010) (cit. on p. 163).
[215]T. Berrada, S. van Frank, R. Bücker, T. Schumm, J.-F. Schaff, and J. Schmiedmayer, "Integrated Mach–Zehnder interferometer for Bose–Einstein condensates", Nat Commun **4** (2013) (cit. on p. 163).
[216]C. F. Ockeloen, R. Schmied, M. F. Riedel, and P. Treutlein, "Quantum Metrology with a Scanning Probe Atom Interferometer", Phys. Rev. Lett. **111**, 143001 (2013) (cit. on p. 163).
[217]W. Muessel, H. Strobel, D. Linnemann, D. B. Hume, and M. K. Oberthaler, "Scalable Spin Squeezing for Quantum-Enhanced Magnetometry with Bose-Einstein Condensates", Phys. Rev. Lett. **113**, 103004 (2014) (cit. on p. 163).

Conclusion and perspectives

> We develop all those long-winded ideas which can just interpret the reality of our lives in different ways, without really extending our body of worthwhile knowledge about the big things.
>
> Irvine Welsh, Trainspotting

For the past years, the metastable helium experiment of the laboratory Charles–Fabry has been at the forefront of development in the domain of atomic pair source in momentum space. Atomic pairs were first produced by collision between two condensates in 2007 [48]. From this experiment it has been shown that the pairs are correlated in a non classical way via measurement of sub-shot noise variance [51] and later through Cauchy–Schwarz inequality violation [96]. Other pair production mechanism has been developed via matter wave analogue to the dynamical Casimir effect in 2012 [39] and pair creation in momentum space via dynamical instabilities in 2013 [108]. The last technique allowed us to produce a stable and tunable source of atomic pairs in momentum space with non-classical correlations. The goal of these years of investigation has been the accomplishment of milestone experiments of quantum optics with matter-waves. In this manuscript, we report the first realisation of the atomic HOM experiment using the atomic pairs developed in Ref. [108].

In this thesis, we have described the different steps towards the realisation of the atomic HOM experiment. In Chapter 1, the basic theoretical background for the HOM experiment for both photons and atoms are explained. From the knowledge of quantum optics, we identified the necessary points to address and predicted the difficulties towards its experimental realisation with an atomic source. Despite the conceptual interest of the HOM experiment, we shown that this experiment can also be used to probe the purity of our atomic source and how far it stands from a two-mode squeezed state with one particle per mode. The HOM experiment is also the first evidence of the mode matching of our non-classical atomic pairs.

In Chapter 2, a brief description of the experimental status at the beginning of this work was performed showing the imperfections that were necessary to address. In order to improve the stability of the condensate, a horizontal trap was added as discussed in Section 2.2. This addition provided us a more stable and tunable initial source of atoms.

The pair production mechanism obtained via dynamical instabilities of a condensate placed on a moving lattice is discussed in Chapter 3. The geometrical alignment of the lattice has been changed in order to decouple the vertical axis from the transverse directions allowing us to retrieve an experimental situation closer to the 1D description of the system. In Section 3.3, we have provided the theoretical and experimental steps behind the pair creation process, such as phase-matching conditions, momentum spread and relative population of the atomic pairs.

In Chapter 4, the experimental realisation and characterisation of the atomic beam-splitter

has been explained in great detail. Particular attention was given to the resonance conditions and how to perform the calibration on the atomic pairs. We have also showed that the beam-splitter does not add noise to the initial state formed by the atomic pairs. Besides, we have shown how to use the atomic 50:50 beam-splitter in order to perform autocorrelation measurements in analogy to quantum optics. This confirmed previous experimental results where the autocorrelation was directly obtained from the atomic distribution of the cloud.

In Chapter 5, the first experimental realisation of the atomic HOM was discussed. We retrieved a visibility of $65 \pm 7\%$, that cannot been explained with classical waves, showing the quantumness of our state. We attribute the non-maximal visibility to the average population which lies around 0.8 atoms. In Section 5.5, we showed that the half-width at $1/\sqrt{e}$ of the HOM-dip is equal to 70 (40) μs and compared it to a simple theoretical prediction. An educated guess for the discrepancy between the experimental and theoretical results would rely on the measured transverse angle of the atomic beam-splitter (0.8° along the $x-$axis) leading to a reduction of the spatial overlap between the pairs.

The HOM effect is of fundamental interest in order to study the state describing the atomic pairs. The result is a proof that one can, with this experimental set-up, create a twin particle source for quantum interferometry. The possibility of applying such system to the case of macroscopic atomic beams in momentum space is discussed in Section 5.7. This could open the door to quantum interferometry similar to what is performed in the domain of spin squeezing with the advantage that the particles are not trapped and, so, could be used for inertial measurements.

Perspectives - test of Bell's inequalities

Although historically antecedent to the HOM experiment, the violation of Bell's inequalities is a conceptual more complicated phenomenon [9, 16–18]. The Bell's inequality test based on the *gedanken* experiment of Einstein, Podolsky and Rosen [1], corresponds to the translation of an epistemological problem to the domain of experimental physics. The problem raised by Einstein and co-authors shows the profound abstract nature of quantum mechanics. In their paper, the following question was asked: *Can quantum-mechanical description of physical reality be considered complete?* The question was centred on the fact that "In quantum mechanics in the case of two physical quantities described by non-commuting operators, the knowledge of one precludes the knowledge of the other.".

The situation can be easily explained considering that one creates a pair of entangled particles travelling away from each other. The particles are described by the same quantum state, this means, that one cannot describe each particle independently of the other. Suppose then the situation in which after a certain time t, one of the two particles is read. For the case of photons, for example, the situation is often represented by the measurement of the polarisation after a certain travelling time t [218]. Once the measurement is performed, the answer on one of the two-particles immediately fixes the result on the other particle. The question raised by Einstein, Podolsky and Rosen, is how can information be instantly exchanged between the two particles knowing that nothing can travel faster than the speed of light? One solution would be that a *hidden* information, not described by quantum mechanics, would immediately fix the result of the two particles when they are still close to each other. This would mean that quantum theory is not complete which was exactly the point of view of the Copenhagen interpretation [2]. Quantum mechanics however, would argue that although the measurement of the two particles is 100% dependent of each other, this strong correlation would only appear once we compare the result of the two measurements and, in this sense, no information had travelled

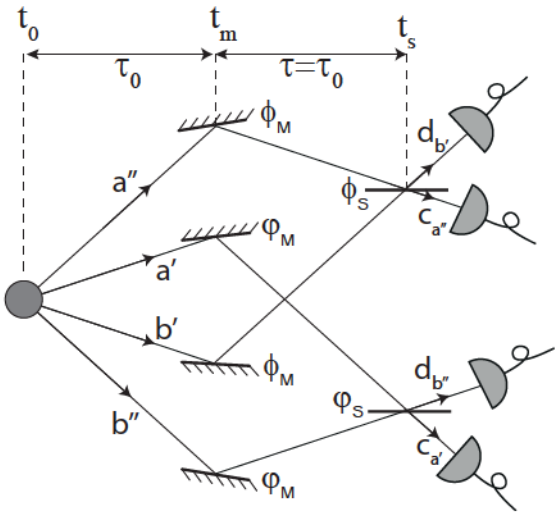

Figure 6.1: *Schematic representation of an experimental realisation of Bell's inequality test. Several modes are outcoming from the initial source, mode a correlated with b, a′ with b′ and a″ with b″. The mirror and beam-splitter are calibrated such that a and b overlap on the beam-splitter. This implies that mode a′ overlap with mode b″ and a″ with b′.*

faster than light.

Bell transformed this question to an algebraic prediction [6]. The local realism defended by Einstein and co-authors, translated then in the verification of a certain inequality, denominated of Bell's inequality. A violation of such inequality would irremediably proof that the description of the system by quantum mechanics is complete and that the particles are entangled. This has been proved to be true in several experiments, since the first Bell's inequality test using polarisation of entangled photons [9, 16, 17] to tests violations based on phase and momentum variables [18].

The main goal in the near future would be test Bell's inequality in our experimental set-up. The steps towards this result would resemble very much to the 1990's Rarity and Tapster experiment [18]. In our case, particles are entangled in momentum space and the inequality can be sorted out by playing with the relative phase of the pairs [219]. The experimental situation of Bell's inequalities violation corresponds, in its simpler form, to the one represented in Fig. 6.1. Two modes described by the momenta $\{k_{a'}, k_{b'}\}$ and $\{k_{a''}, k_{b''}\}$ are created at time $t_0 = 0$. The interferometric scheme is such that the modes are mixed, this meaning that $k_{a'}$ is recombined with $k_{b''}$ and $k_{a''}$ with $k_{b'}$. Furthermore, the mirror for $k_{a'}$ and $k_{b''}$ imprints a phase ϕ_M on the atomic beams while the beams $k_{a''}$ and $k_{b'}$ get a different phase φ_M. The same happens with the 50:50 beam-splitter, with a phase ϕ_S and φ_S, respectively. This is easily performed experimentally by applying the two laser pulses at different times and changing the relative phase between the laser beams meanwhile.

The Bell's inequalities can be written from a parameter S introduced in late 60's, see Ref. [7], and known as the Clauser–Horne–Shimony–Holt (CHSH) parameter such that if

$$|S| > 2\,, \tag{6.1}$$

with S being a function dependent of the correlations between the different output ports, the state is entangled and local hidden-variables cannot explain real measurements, see Appendix E for details calculations.

Let us assume that the state is described by two independent parametric down-conversion

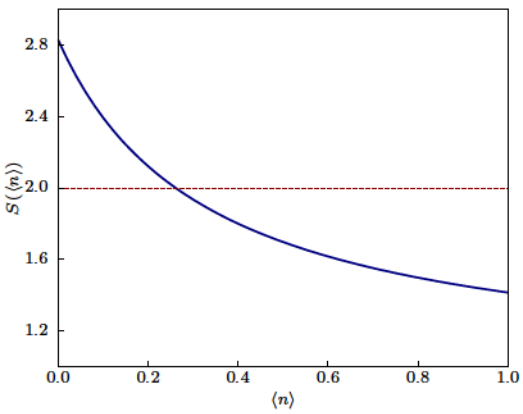

Figure 6.2: Dependence of S as a function of ⟨n⟩. For increasing values of ⟨n⟩, one sees a reduction of S to the value of $\frac{2}{3}\sqrt{2}$. For ⟨n⟩ → 0, S tends to its maximum value of $2\sqrt{2} \approx 2.8$.

states, such that

$$|\psi\rangle = \sum_n \frac{\tanh^n(\lambda)}{\cosh(\lambda)} \sum_m \frac{\tanh^m(\lambda)}{\cosh(\lambda)} |n, n, m, m\rangle ,$$

with $\sinh^2(\lambda) = \langle n\rangle = \langle m\rangle$. The expression of S can, after some calculations, be written as [219]

$$S = 2\sqrt{2}\,\frac{(1+\langle n\rangle)}{(1+3\langle n\rangle)} .$$

For $\langle n\rangle = 0$, S reaches the maximum value of $S = 2\sqrt{2}$ and for increasing average populations, $\langle n\rangle \to \infty$, S decreases to the asymptotic value of $S = \frac{2}{3}\sqrt{2}$. Thus, the Bell's inequality is violate when the number of particles is small. The behaviour of S as a function of $\langle n\rangle$ is represented in Fig. 6.2. One can see that for an average population above 0.26 the CHSH's parameter is smaller than 2 and one does no longer violated the inequality. Once again, the importance of having a low population number in the pairs is essential to increase the degree of violation of the inequality. The reduction of the average population is even stronger than the one needed for the HOM experiment which will lead to even longer acquisition time in order to increase the signal-to-noise ratio.

Other questions, concerning the quantum efficiency, the change in the two mirror or beam-splitter phases timing, can still lead to loopholes where hidden variables could explain the result through local realism. However, in our experiment these questions would probably be rather difficult to address experimentally. This experiment, nonetheless, can explore interesting regimes for theories of gravitational decoherence [219–222] and can therefore be of main interest for the theoretical construction of quantum gravity.

In summary, with the results of the HOM experiment in mind, the realisation of the Bell's inequality test seems rather straightforward to perform. The only experimental difficulty, at the moment, is relative to the control of the phase of both mirror and beam-splitter. This phase determines the value of θ. It is fundamental to guarantee a stability of $\phi_M - \phi_S$ and $\varphi_M - \varphi_S$ well below $\pi/4$. As discussed in Chapter 4, the study of this stability has already been initiated during the presented work and further tests are being carried on. It is also important to have in mind, as a side note, that not only the phase of both mirror and beam-splitter determines the value of θ but also the contribution of both time difference $t_s - 2t_s$ and the energy conservation $k^2_{a''} + k^2_{b''} - k^2_{a'} - k^2_{b'}$ (see more informations in Appendix E). As for the HOM experiment, an integration will be performed in momentum space in order to increase the signal-to-noise ratio and, consequently, the contribution of $k^2_{a''} + k^2_{b''} - k^2_{a'} - k^2_{b'}$ will not be zero. Nevertheless, since

it is associate with $t_s - 2t_m$, by choosing $t_s = 2t_m$ it is possible to cancel out this term. This is ensured, once more, via the results of our HOM experiment discussed in this manuscript.

Appendix A

Speed of sound expression in the case of a quasi-1D Bose–Einstein condensate

We present a continuation of the work presented in Ref. [64] allowing to the determine the speed of sound of the condensate c in the intermediate quasi-1D regime. Although the determination of the speed of sound is well known for both 3D and 1D systems, its determination in the intermediate regime, of interest in our work, is here reported.

Starting from the dispersion relation

$$\mathcal{E}_k(z) = \sqrt{E_k\left(E_k + 2\frac{4\pi\hbar^2 a}{m} n_{0,\bar{A}}(z)\right)}$$

where E_k is the kinetic energy given by

$$E_k = \frac{\hbar^2 k^2}{2m}$$

and $n_{0,\bar{A}}(z)$ is the linear peak density

$$n_{0,\bar{A}}(z) = n_{1D}(z) \int_0^\infty \int_0^{2\pi} d\rho\, d\theta\, \rho\, \left|f_\perp(\rho)\right|^2 = \frac{n_{1D}(z)}{2\pi w_\perp^2[n_{1D}(z)]}.$$

The chemical potential can then be written as

$$2\frac{4\pi\hbar^2 a}{m} n_{0,\bar{A}}(z) = \hbar\omega_\perp\left(\bar{\mu}[n_{1D}(z)] - \frac{1}{\bar{\mu}[n_{1D}(z)]}\right)$$

where $\bar{\mu}[n_{1D}(z)] = \mu_{e.l.}[n_{1D}(z)]/(\hbar\omega_\perp)$, see Subsection 2.2.3.

The speed of sound is usually introduced in the dispersion relation by

$$\mathcal{E}_k = \sqrt{E_k(E_k + 2mc^2)}.$$

By looking at the previous equations, one finds

$$c(z) = \sqrt{\frac{\hbar\omega_\perp}{2m}\left(\bar{\mu}[n_{1D}(z)] - \frac{1}{\bar{\mu}[n_{1D}(z)]}\right)}.$$

The value of c can be obtained by integrating $n(z)$ over z, so one finally retrieves

$$c = \frac{\hbar\omega_\perp}{m}\frac{L}{N_{at}}\int_{-L}^{L} dz \left[\left(1+\frac{\alpha}{2}\left(1-z^2\right)\right) - \frac{1}{\left(1+\frac{\alpha}{2}\left(1-z^2\right)\right)}\right]. \tag{A.1}$$

Table A.1 summarises the different results of the speed of sound as function of the typical trapping frequencies of our experimental set-up.

$\omega_\perp = 2\pi \times 1275\,\mathrm{Hz}$			
	$\omega_z = 2\pi \times 7\,\mathrm{Hz}$ $N_{at} = 3 \times 10^4$	$\omega_z = 2\pi \times 93\,\mathrm{Hz}$ $N_{at} = 5 \times 10^4$	$\omega_z = 2\pi \times 170\,\mathrm{Hz}$ $N_{at} = 7 \times 10^4$
c (cm/s)	1.14	2.28	2.8

Table A.1: *Typical values of the speed of sound c. The typical values of the speed of sound in our set-up are given following Ref. [64].*

Appendix B

Characterisation of the crossed dipole trap

The crossed dipole trap corresponds to one IPG laser, at 1550 nm with maximum power 5 W, split in two independent optical paths with independent acousto-optic modulators (see Fig. B.1). The effective maximum power on the atoms is equal to 2 W. Most of the optical power is distributed on the vertical beam and around 10% to the horizontal beam. Both beams are red shifted with respect to the atomic transition $2^3S_1 \rightarrow 2^3P$ (wavelength of 1083 nm) with their frequency shifted 80 MHz with respect to each other, in other to avoid low frequency modulation of the trap intensity [1]. One beam propagates along the vertical $z-$axis corresponding to the "original" trap described in Ref. [150] and the second on the horizontal plane and forms an angle of 8.6 ° with respect to the $x-$axis, defined by the magnetic trap (see Fig. B.1 and Fig. B.2). The typical power used for the crossed dipole trap is 600 mW for the vertical trap and 30 mW for the horizontal trap.

For the vertical beam, the waist is 43 (1.5) μm. This value was indirectly obtained by parametric excitation of the cloud [168]. However, this measurement does not agree with an independent, geometrical measurement realised on the optical bench. This consisted in measuring the waist of the beam at different positions after the lens. It was then expected a waist on the atoms of 35 μm [150]. This difference is probably due to aberrations introduced either by the window of the science chamber or by accidental modifications of the optical path during the final alignment. For more details in these calculations please see Ref. [150]

For the horizontal beam, the same geometric calibration of the waist has been carried out. Several measurements of the spot size were performed after a lens of focal 400 mm as a function of the relative position to the focal plane as shown in Fig. B.3. The data is fitted by the function

$$w(x) = w_0 \sqrt{1 + \left(\frac{\lambda x}{\pi w_0^2}\right)^2},$$

with $w(x)$ corresponding to the spot size at a position x, w_0 the waist radius of the beam and λ the wavelength. From this fit, it was extracted a value of $w_0 = 58\,(1)$ μm corresponding to the theoretical expected waist of the horizontal trap beam on the focal plane. The lowest experimental measured value of the waist was equal to 65 μm. Since we did not measure the waist at $x = 0$, one can only guarantee, that even in the presence of aberrations, the minimum waist must be, at least, of 65 μm.

[1] If the modulation intensity is close to a trapping frequency, this induces parametric excitation of the cloud. Since the typical frequencies of our trap are on the order of the kHz, a detuning of 80 MHz between both trapping beams guarantees that we avoid the resonance.

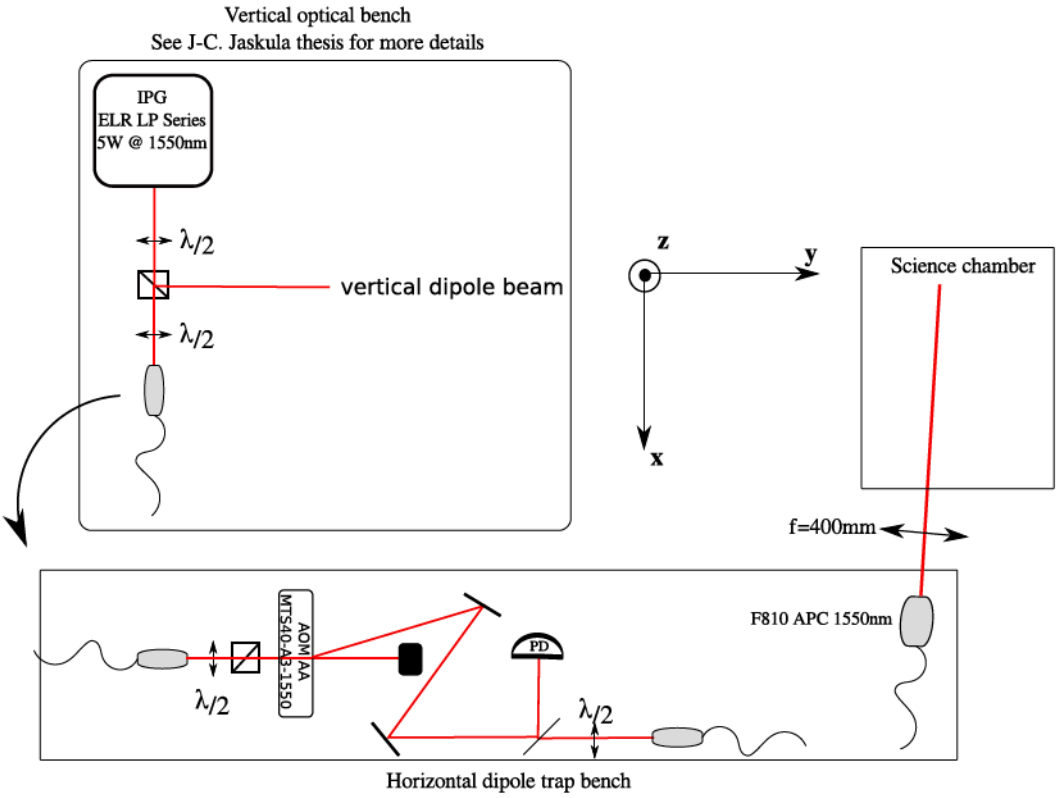

Figure B.1: Schematic representation of the optical bench for the horizontal beam trap. The laser beam is split in two with one part used for the vertical dipole trap described in Ref. [150] and the other injected into a polarisation-maintaining optical fiber taking the beam to another optical bench. There, the beam goes through an acousto-optic modulator where it is diffracted into the +1 order with an efficiency of 90%. The optical power on the order +1 is set by increasing the RF power on the acousto-optic modulator. Order +1 is detuned by 40 MHz with respect to the order 0. The beam is then split with 1% of the power sent to a photodiode in order to lock the horizontal beam intensity. The other part is again injected and the output collimator corresponds to a F810APC from Thorlabs leading to a diameter beam of 7 mm. The beam goes then by a focus lens of 400 mm leading to a waist on the atoms of 82μ m.

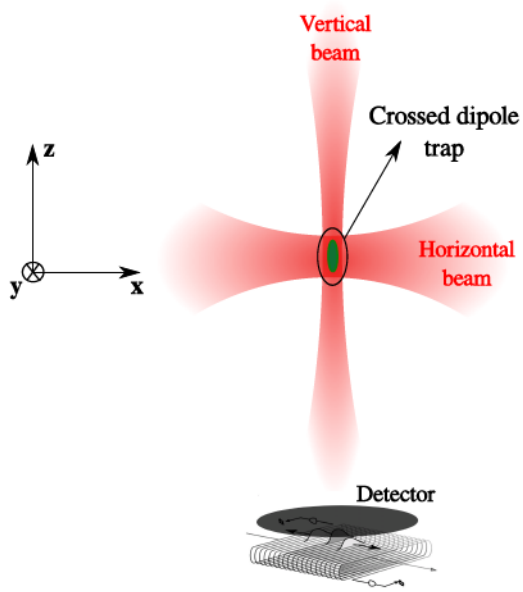

Figure B.2: Schematic representation of the crossed dipole trap.

However, as for the case of the vertical trap, this value does not correspond to the measured value on the atoms. Indeed, one retrieves from parametric excitation a waist of 82 (4) μm [168].

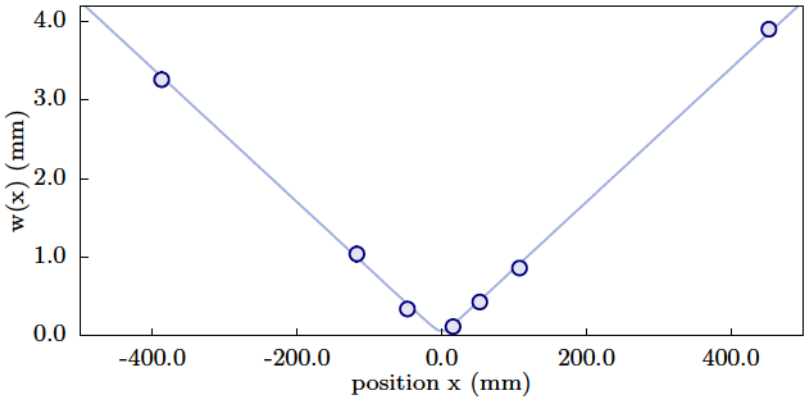

Figure B.3: Waist calibration of the horizontal beam. The spot size is determined at different positions after the focusing lens of focal length f = 400 mm. The minimum value of the waist is 65 μm.

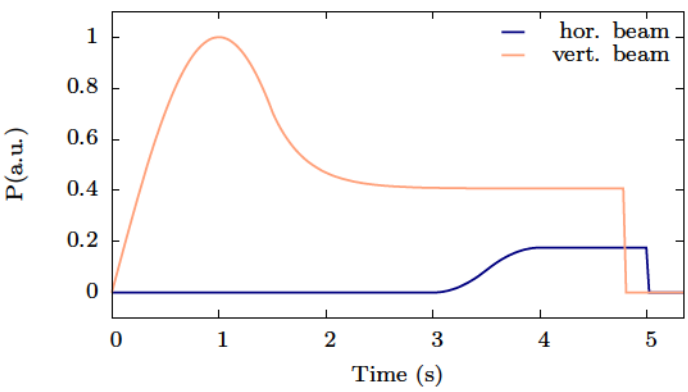

Figure B.4: Loading sequence for the alignment between the vertical and horizontal dipole traps. The vertical dipole trap is turned on and superimposed with the magnetic trap for 1 s. During this time, a small fraction of the atoms are transferred in the vertical dipole trap. The magnetic trap is then switched off and the atoms are kept in the vertical trap for 3 s. The horizontal beam is turned on in 1 s and kept at its maximum intensity. The vertical trap is then switched off and 200 ms later the horizontal trap is also switched off. By looking at the number of atoms remaining inside the horizontal trap one can infer the alignment between the two traps.

This *systematic* difference could point on the direction of the role played by the science chamber window, although, at the moment no concluding test has been performed.

Alignment protocol

In order to overlap the two beams, the experimental sequence represented in Fig. B.4 is applied. The atoms are adiabatically loaded in the vertical dipole trap from the magnetic trap by ramping up the intensity of the vertical beam in 1 s. When the intensity reaches its maximum value, the magnetic trap is switched off and the atoms only remain in the vertical trap. The non transferred atoms fall due to gravity and are lost. The intensity of the beam is then adiabatically ramped down to a given final value. At this moment, the root-mean-square size of the cloud is 200 – 300 μm along the vertical axis and 5 μm transversally, given by the temperature of the cloud and the trapping frequencies. The horizontal beam is then adiabatically turned on and when its maximum value is reached the vertical beam is switched off.

If the horizontal beam overlaps perfectly and if atoms are cold enough to not escape from the horizontal trap, then all of them are transferred to the horizontal trap and no atom is lost. The horizontal beam is then switched off and, after time-of-flight, we record the atoms on the MCP.

The alignment with the horizontal trap is then scanned by moving the vertical position of the horizontal beam. To do so, we move the vertical position of the lens which is fixed on a 3–axis stage. A typical transferred population ratio as a function of the horizontal beam position is plotted in Fig. B.5. The width of the transfer profile is a convolution between the size of the cloud and the waist of the horizontal beam. The fact that the population transfer does not rise up to 1 is due to several reasons. First, the typical temperature of the cloud in the vertical trap

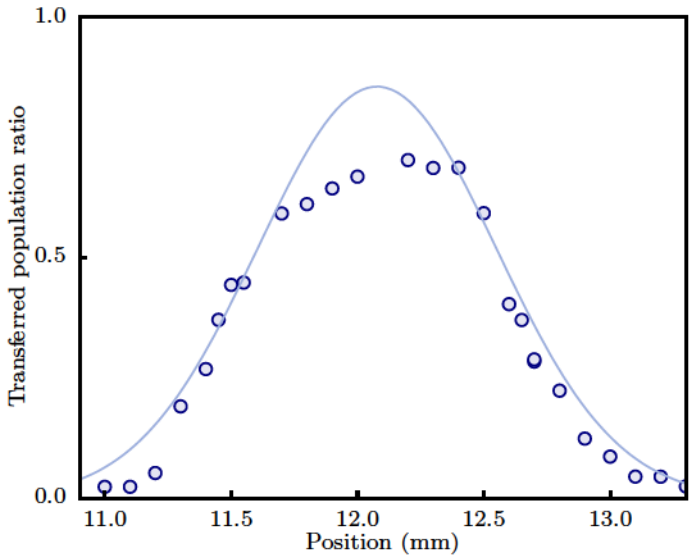

Figure B.5: Typical loading efficiency. Transfer of population between the vertical and horizontal dipole trap. The width of the transfer corresponds to a convolution between the initial cloud size along the vertical direction 300 μm and the horizontal beam waist.

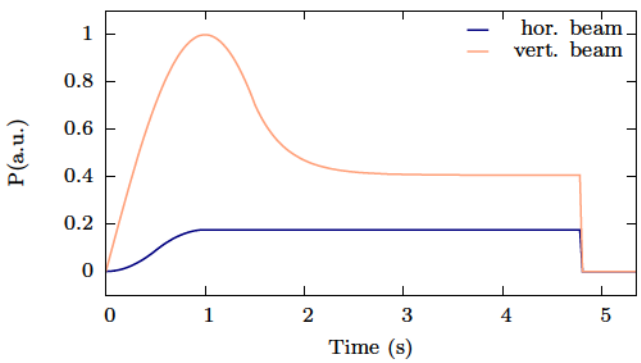

Figure B.6: Usual loading sequence of the atoms in the crossed dipole trap. Both optical beams intensities are turned on adiabatically in 1 s during which they are superposed to the magnetic trap. After this adiabatic loading of the atoms, the magnetic trap is switched off in a few ms. The horizontal beam is kept at its maximum intensity while the vertical undergoes an adiabatic decrease of its intensity leading to evaporative cooling of the thermal cloud. After the evaporation, the vertical trap alone cannot trap the atoms, and, as a consequence, the remaining atoms have to be in the crossed region. The condensate is then created in the potential formed by the two beams with trapping frequencies given by second derivatives of Eq. (B.1).

(500 nK) is comparable to the trap depth of the horizontal trap (1 μK) and, consequently, some atoms escape from the new trap. Second, we observed the presence of residual magnetic fields which induce oscillations along the long axis of the horizontal trap. When the vertical trap is turned off the atoms are only confined by the horizontal beam. If a magnetic gradient induces a force along its propagation axis, where the trapping potential is weaker, then the atoms start to oscillate in the trap. If the perturbations are strong enough to push atoms outside of the trapping potential it can result in losses. When both dipole traps are on, however, the residual magnetic force is completely negligible compared to the vertical confinement created by only the vertical beam.

B.1 Crossed dipole trap potential

In order to create an attractive or repulsive potential via light-matter interaction, one can take advantage of the induced dipole of the electromagnetic field [151].

The final loading sequence corresponds to the scheme of Fig. B.6. Both beams are adiabatically ramped on in 1 s, after which the magnetic trap is switched off. The horizontal beam is maintained at a constant final value while the vertical beam performs an evaporation ramp until it reaches a final value, which is kept constant. The final power of the vertical beam allows

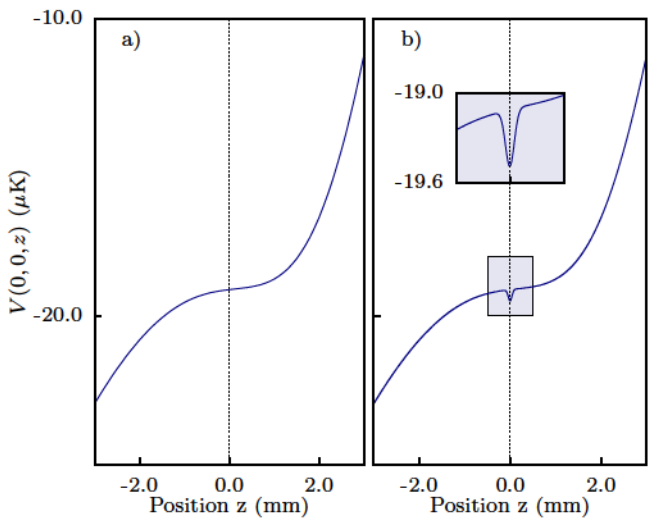

Figure B.7: ***Representation of the dipole potential felt by the atoms.*** *a) Dipole potential as a function of z for the case of the vertical beam. The dipole potential only compensates gravity and no well is visible. b) Dipole potential as a function of z for the case of a crossed beam situation. A well appears at $z = 0$ which corresponds to the crossing of the two beams.*

one to compensate the gravity potential at the position of the horizontal beam but cannot form a trapping potential alone along the longitudinal direction. This corresponds, for a waist of $w_{\text{vert}} = 43.0\,(5)\ \mu\text{m}$, to an optical power of $P_{\text{vert}} = 585\,\text{mW}$ and results in the potential profile displayed in Fig. B.7a). When the horizontal beam is added the potential presents a well centred at $z = 0$ as shown in Fig. B.7b) with

$$V_{\text{opt}}(x,y,z) = V_{\text{vert}} \frac{\text{Exp}\left[-\frac{2(x^2+y^2)}{w_{\text{vert}}^2\left(\left(\frac{z-z_0}{z_{\text{vert}}}\right)^2+1\right)}\right]}{\left(\frac{z-z_0}{z_{\text{vert}}}\right)^2+1} - mgz + V_{\text{hor}} \frac{\text{Exp}\left[-\frac{2(y^2+(z-z_0)^2)}{w_{\text{hor}}^2\left[\left(\frac{x}{x_{\text{hor}}}\right)^2+1\right]}\right]}{\left(\frac{x}{x_{\text{hor}}}\right)^2+1}, \tag{B.1}$$

where

$$V_{\text{vert}} = -\frac{3\pi c^2}{2\omega_0^3}\frac{2P_{\text{vert}}}{\pi w_{\text{vert}}^2}\left(\frac{\Gamma}{\omega_0-\omega_{\text{dip}}}+\frac{\Gamma}{\omega_0+\omega_{\text{dip}}}\right)$$

and

$$V_{\text{hor}} = -\frac{3\pi c^2}{2\omega_0^3}\frac{2P_{\text{hor}}}{\pi w_{\text{hor}}^2}\left(\frac{\Gamma}{\omega_0-\omega_{\text{dip}}}+\frac{\Gamma}{\omega_0+\omega_{\text{dip}}}\right)$$

with $\Gamma = 2\pi \times 1.6\,\text{MHz}$ corresponding to the width of the transition $2^3\text{S}_1 \rightarrow 2^3\text{P}_2$, ω_0 the frequency of the transition, ω_{dip} the frequency of the electromagnetic field, w_{vert} the waist of the vertical beam, $z_{\text{vert}} = \left(\pi w_{\text{vert}}^2\right)/\lambda_{\text{dip}}$ the vertical beam Rayleigh length, $x_{\text{hor}} = \left(\pi w_{\text{hor}}^2\right)/\lambda_{\text{dip}}$ the horizontal beam Rayleigh length, w_{hor} the horizontal beam waist and $z_0 = 2.3$ mm the central position of the vertical waist. The usual approximation where the term $\Gamma/(\omega_0+\omega_{\text{dip}})$ is neglected cannot be performed since the wavelength of the laser $\lambda_{\text{dip}} = 1550\,\text{nm}$ is not close to the resonant wavelength $\lambda_0 = 1083\,\text{nm}$.

As seen previously, $w_{\text{vert.}} = 43\,\mu\text{m}$ while $w_{\text{hor}} = 82\,\mu\text{m}$. In the inset, we can see that the well, for a horizontal beam power of 30 mW, is very shallow, with a depth of only 400 nK. A shallow well has its own advantages since it is very easy for atoms with non zero speed to escape from the trap. It is important to note that the transverse confinement is almost unchanged since

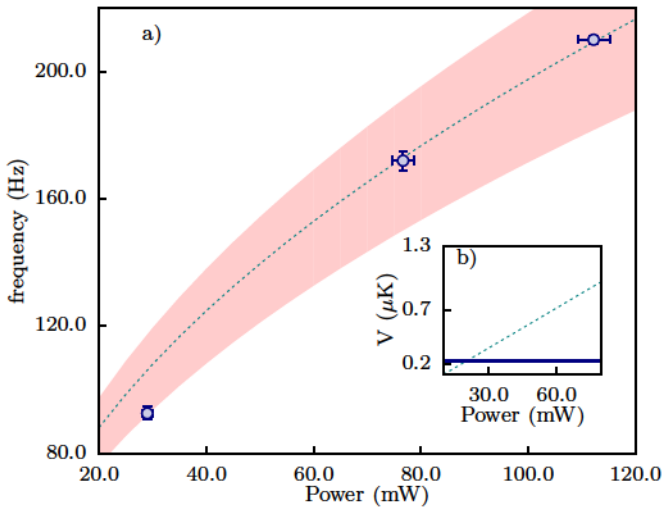

Figure B.8: Determination of the horizontal beam waist. Indirect measurement of the horizontal beam waist via the evolution of the trapping frequency along the vertical z−axis as a function of the horizontal beam power. The red shaded area corresponds to the theoretical estimation of the frequency evolution using Eq. (B.2) for w_{hor} ranging from 78 μm to 88 μm. In inset the dipole trap depth is represented as a function of the horizontal beam power. The horizontal blue line corresponds to the residual thermal cloud temperature.

the contribution of the horizontal beam is negligible when compared to the vertical one. It is the inverse situation along the vertical axis where the horizontal trap defines the confining potential.

Determination of the horizontal beam waist

One can use the produced potential in order to indirectly measure the waist of the horizontal beam. By scanning the longitudinal frequency as a function of the horizontal beam power, through the oscillation of the BEC in the dipole trap (see Subsection 2.2.5), one retrieves a curve which can be fitted by the theoretical value

$$\omega_z = \sqrt{\frac{1}{m}\frac{\partial^2 V_{\text{opt}}(0,0,z)}{\partial z^2}}, \tag{B.2}$$

assuming an harmonic potential and where $V_{\text{opt}}(x, y, z)$ is defined by Eq. (B.1). For steeper potentials, the oscillation frequency increases. Since the waist of the vertical beam has been independently calibrated, the only free parameter is then the value of the horizontal beam waist w_{hor}.

The result is plotted in Fig. B.8. The blue circles correspond to the experimental measurement of the longitudinal frequency for powers $P_{\text{hor}} = 110\,\text{mW}$, 75 mW and 30 mW. The horizontal beam waist is then estimated at $w_{\text{hor}} = 82\,(4)$ μm where the uncertainty is due to the fact that for lower optical power, the atoms reach the edges of the trap, as shown in the inset of Fig. B.8. Consequently, the oscillation is modified by the anharmonicity of the trap and, for low optical powers, the speed given by the atoms start to be equal to the trap depth and the harmonic approximation does not hold any more. This invalidates the *fitting* curve described by Eq. (B.2) and the point at 30 mW lays outside the prediction.

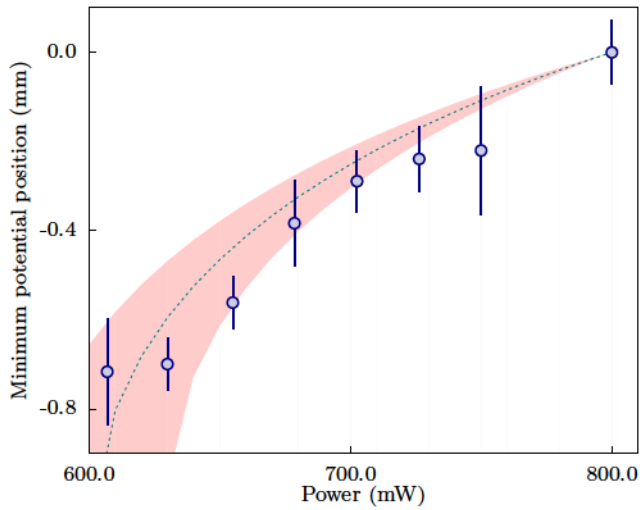

Figure B.9: ***Determination of the vertical dipole trap beam waist.*** *Indirect measurement of the vertical dipole trap beam waist on the atoms via the alignment of the horizontal beam with the vertical one as a function of the vertical beam power. Since, gravity tends to lower the position of the potential minimum, this changes as a function of the beam power. By scanning the power of the vertical beam and retrieving its displacement by the transfer of population with the horizontal trap, one estimates the waist of the vertical beam.*

Determination of the vertical beam waist

As for the horizontal beam waist determination, one can also extract information of the vertical trap via Eq. (B.1). Due to the gravity, the position of the potential well minimum depends on the vertical beam power and, as the power decreases the potential minimum moves to negative positions. By changing the vertical beam power, one induces a shift of the minimum potential position and, consequently, of the vertical position of the cloud. The alignment of the horizontal arm is performed as before, by changing the vertical position of the lens. Now, for each power value of the vertical beam, one retrieves a different optimised alignment between the two beams as shown in Fig. B.9 (blue dots). The experimental results can be fitted by Eq. (B.2) with $w_{\text{vert.}}$ as free parameter. The reference frame origin corresponds to the retrieved experimental value at 800 mW.

In Fig. B.9, the experimental points are compared to the theoretical minimum trap position for different vertical waist. The shaded red area corresponds to the expected theoretical evolution, for a waist varying from 43.5 μm to 42.5 μm and assuming that the measured power corresponds to the value on the atoms. It is possible to see that our experimental points fit well in between this two theoretical predictions giving us an estimation of the waist of 43.0 (5) μm. This value agrees with the previous measurements described in Ref. [142].

Appendix C

Raman transfer set-up for a metastable Helium experiment

In our experimental procedure, after the optical trap has been switched off, transfer to the $m = 0$ state is done. This is necessary due to the presence of stray magnetic fields in the vacuum chamber that otherwise would lead to a severe deformation of the atomic distribution during the long free fall. The transfer is achieved by introducing a two-photon coupling between the $m = 1$ state, in which the atoms are initially, and the $m = 0$ state using two laser beams resultant from a single source emitting at 1083 nm and detuned by 600 MHz from the 2^3S_1 to 2^3P_0 transition as shown in Fig. C.1. The optical polarisation of the first beam is set horizontally in order to perform the π transition and the other beam is vertically polarised guaranteeing the σ^- transition. Because the vertical polarisation beam is decomposed into σ^- and σ^+, the power is two times larger than for the other laser beam.

The frequency difference of the laser beams is chirped across the two-photon resonance so as to realise an adiabatic fast passage transition (the frequency change is 300 kHz in 300 μs). We have measured the fraction of transferred atoms to be 94 %. This is calibrated by looking at the detected number of atoms in state $m_j = 1$ without Raman transfer and by compare it with the remaining population in the $m_j = 1$ state after transfer as shown in Fig. C.2. The transfer efficiency corresponds then simply to the ratio between the populations of both situations. The remaining 6 % stay in the $m = 1$ state and are pushed away from the integration volumes by the stray magnetic field gradients.

Since the relative angle between the two laser beams is non zero, a small velocity vector is given to the transferred atoms. This corresponds to an increase of the speed along the vertical direction of $0.2\,v_{lat}$. This is accounted in the condition of resonance of Bragg diffraction.

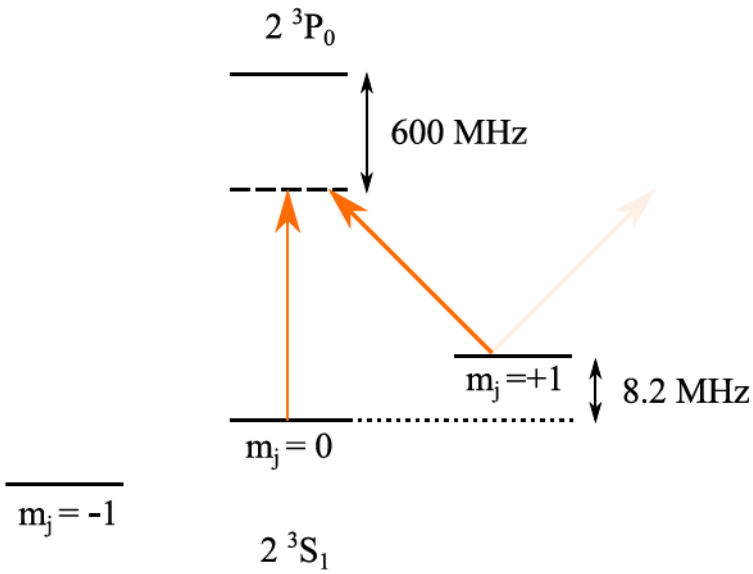

Figure C.1: Representation of the atomic transition $2^3S_1 \rightarrow 2^3P_0$ used for the Raman transfer. The energetic difference between the sublevels $m_j = \pm 1$ is due to a magnetic bias field of 3 G. This corresponds to an energy difference of $2\pi \times \hbar \times 8.2$ MHz.

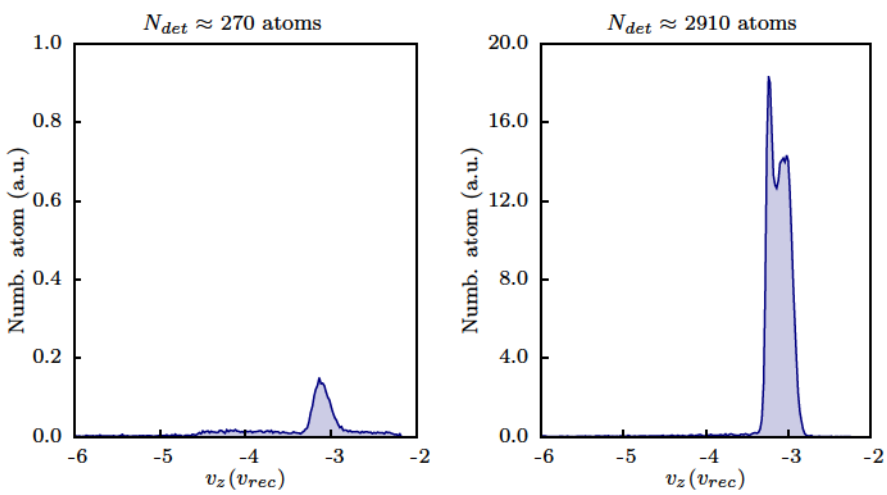

Figure C.2: Raman efficiency calibration. a) Remaining atom number in the state $m_j = 1$ after applying the Raman transfer. The number of detected atoms is 272, averaged over 40 realisations. b) Detected number of atoms in the state $m_j = 1$ without applying a Raman transfer. The number of atoms is, in average, 2910. However, this number is probably a low estimation since the cloud seems to saturate the detector (see Subsection 2.1.2.)

Appendix D

Detailed calculations for the HOM experiment

D.1 Beam-splitter scattering matrix

In order to describe the evolution of the atomic pairs a 2×2 matrix description will be adopted. This corresponds to a Rabi oscillation between two external states via the application of a shallow optical lattice. An optical lattice is created via the interference of two laser beams that give rise to a spatial periodic modulation of light intensity. For an atom shinned by both laser beams this corresponds to a periodic potential as seen in Chapter 3. In the weak depth regime, the periodic potential leads to a coupling between an atom with momentum k_{bms} to an atom with momentum $-k_{\text{bms}}$, where k_{bms} is the periodicity of the beam-splitter lattice in momentum space. This corresponds, effectively, to a two-state interaction Hamiltonian, described in the center of mass frame of reference by

$$\hat{H} = \hbar \begin{pmatrix} 0 & \Omega/2 \\ \bar{\Omega}/2 & 0 \end{pmatrix}. \tag{D.1}$$

where $|\Omega| = \Omega_R$ corresponds to the two-photon Rabi frequency. This frequency corresponds to a complex number and its phase, defined as

$$e^{i\phi} = \Omega/|\Omega|, \tag{D.2}$$

plays an important role. It corresponds to the phase difference between the two interfering laser beams and, in all the manuscript, is randomly chosen.

The Hamiltonian (D.1) gives rise to a coherent transfer of population between the external state k_{bms} and $-k_{\text{bms}}$. This is used in the case of the atomic pairs to realise an atomic 50:50 beam-splitter and mirror. As seen in Chapter 4, the beam-splitter corresponds to a lattice with periodicity in momentum space equal to $0.55\,\text{k}_{\text{lat}}$. The atomic beams a and b are then created with a momentum difference of $0.55\,\text{k}_{\text{lat}}$. The mirror exchanges the two atomic beams in momentum space as represented in Fig. D.1 and the beam-splitter swaps their momenta as schematically described in Fig. D.2.

The eigenvalues and eigenvectors of the Hamiltonian D.1 are defined as

$$E_x = |\Omega|/2, \qquad |x\rangle = \frac{1}{\sqrt{2}}\Big(|a\rangle + e^{-i\phi}|b\rangle\Big), \tag{D.3a}$$

$$E_y = -|\Omega|/2, \quad |y\rangle = \frac{1}{\sqrt{2}}\Big(-e^{i\phi}|a\rangle + |b\rangle\Big), \tag{D.3b}$$

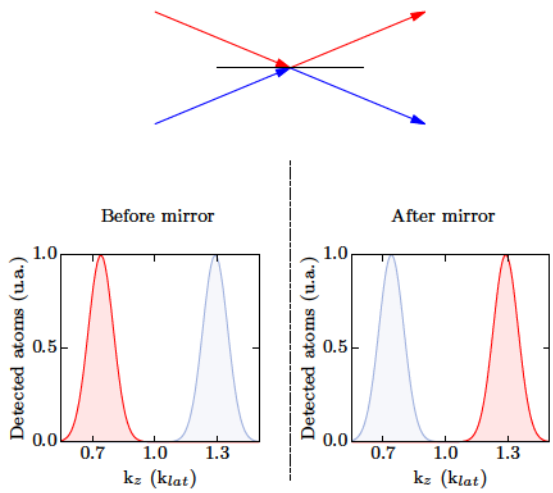

Figure D.1: Schematic representation of the atomic mirror on the atomic beams. The two input arrows in blue and red colour represent respectively beam b with momentum distribution centred on $k_b = 1.29\,q_{lat}$ and beam a with momentum distribution centred on $k_a = 0.74\,q_{lat}$. If the mirror resonance is sufficiently wide, the two beams are entirely exchanged after the atomic mirror. Such that the initial blue atom is now centred on $0.74\,k_{lat}$ and the red one at $1.29\,k_{lat}$. In our notation at the output of the beam-splitter the beam centred at $0.74\,k_{lat}$ is called c and the one at $1.29\,k_{lat}$ d.

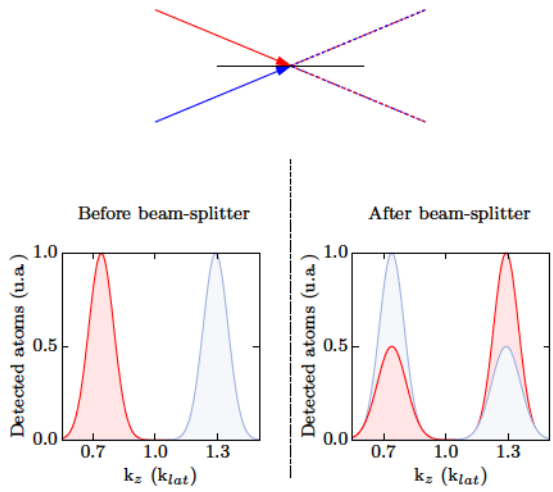

Figure D.2: Schematic representation of the atomic beam-splitter on the atomic beams. The two input arrows in blue and red colour represent respectively beam b with momentum distribution centred on $k_b = 1.29\,q_{lat}$ and beam a with momentum distribution centred on $k_a = 0.74\,q_{lat}$. If the beam-splitter resonance is sufficiently wide the two beams are equally swapped after the atomic beam-splitter. Such that the half the population of blue beam is now centred on $0.74\,k_{lat}$ and the other half stays at $1.29\,k_{lat}$. The same thing happens with red atoms. At the output of the beam-splitter the beam centred at $0.74\,k_{lat}$ is called c and the one at $1.29\,k_{lat}$ d.

and, consequently, the time evolution of field operators $\hat{a}$ and $\hat{b}$, corresponding to the input fields of the beam-splitter can be written as

$$|a\rangle = \frac{1}{\sqrt{2}}\Big(|x\rangle - e^{-i\phi}|y\rangle\Big) \xrightarrow{t} \frac{1}{\sqrt{2}}\Big(e^{-i|\Omega|t/2}|x\rangle - e^{-i\phi}e^{i|\Omega|t/2}|y\rangle\Big), \tag{D.4a}$$

$$|b\rangle = \frac{1}{\sqrt{2}}\Big(e^{i\phi}|x\rangle + |y\rangle\Big) \xrightarrow{t} \frac{1}{\sqrt{2}}\Big(e^{i\phi}e^{-i|\Omega|t/2}|x\rangle + e^{i|\Omega|t/2}|y\rangle\Big). \tag{D.4b}$$

D.1.1 50:50 beam-splitter

For the case of a 50:50 beam-splitter, as seen in Chapter 4, the time interaction corresponds to $\Omega_R t = \pi/2$ which transforms Eq. (D.4b) into

$$|a\rangle \xrightarrow{\pi/2\Omega} \frac{1}{2}\Big((1-i)|x\rangle - e^{-i\phi}(1+i)|y\rangle\Big) = |c\rangle = \frac{1}{\sqrt{2}}\Big(|a\rangle - i\,e^{-i\phi}|b\rangle\Big), \tag{D.5a}$$

$$|b\rangle \xrightarrow{\pi/2\Omega} \frac{1}{2}\Big(e^{i\phi}(1-i)|x\rangle + (1+i)|y\rangle\Big) = |d\rangle = \frac{1}{\sqrt{2}}\Big(-i\,e^{i\phi}|a\rangle + |b\rangle\Big). \tag{D.5b}$$

where $\hat{c}$ and $\hat{d}$ stand for the output field operators of the beam-splitter, such that the transformation is given by

$$\begin{pmatrix}\hat{c}\\ \hat{d}\end{pmatrix} = \frac{1}{\sqrt{2}}\begin{pmatrix}1 & i\,e^{-i\phi_S}\\ i\,e^{i\phi_S} & 1\end{pmatrix}\begin{pmatrix}\hat{a}\\ \hat{b}\end{pmatrix},$$

with $\phi_S = \phi + \pi$, the phase associated to the beam-splitter operation. The scattering matrix $\hat{S}$ is then defined as

$$\hat{S} = \frac{1}{\sqrt{2}} \begin{pmatrix} 1 & ie^{-i\phi_S} \\ ie^{i\phi_S} & 1 \end{pmatrix}. \tag{D.6}$$

D.1.2 Mirror

The time interaction corresponding to a complete exchange of momenta corresponds to $\Omega_R t = \pi$ and matchs the mirror situation. The evolution of the operators a and b can then be written as

$$|a\rangle \xrightarrow{\pi/\Omega} \frac{i}{\sqrt{2}}\Big(-|x\rangle - e^{-i\phi}|y\rangle\Big) = |c\rangle = -i\,e^{-i\phi}|b\rangle\,, \tag{D.7a}$$

$$|b\rangle \xrightarrow{\pi/\Omega} \frac{i}{\sqrt{2}}\Big(-e^{i\phi}|x\rangle + |y\rangle\Big) = |d\rangle = -i\,e^{i\phi}|a\rangle\,. \tag{D.7b}$$

Finally, one obtains the transformation associated to the mirror, such that,

$$\begin{pmatrix} \hat{c} \\ \hat{d} \end{pmatrix} = \begin{pmatrix} 0 & i\,e^{-i\phi_M} \\ i\,e^{i\phi_M} & 0 \end{pmatrix} \begin{pmatrix} \hat{a} \\ \hat{b} \end{pmatrix},$$

leading to the scattering matrix $\hat{M}$,

$$\hat{M} = \begin{pmatrix} 0 & ie^{-i\phi_M} \\ ie^{i\phi_M} & 0 \end{pmatrix}, \tag{D.8}$$

with $\phi_M = \phi + \pi$ the phase associated to the mirror operation. The phase has been named ϕ_M in order to differentiate it from the 50:50 beam-splitter ϕ_S. As seen in Chapter 4, for small time differences between the application of the mirror and the 50:50 beam-splitter, the stability of the phase is sufficient to observe interference fringes after integrating over several experimental realisations. In this sense, one can consider that although the absolute phase is randomly defined, the difference between the phases is stable. For real interferometers, all terms would only depend of this difference and not of the absolute value. Nevertheless, this is untrue in our situation as discussed in the next section.

D.2 Field operator evolution

In order to determine the interference effect, we start by looking at the temporal evolution of the operators $\hat{a}_{k_a}$ and $\hat{a}_{k_b}$ standing for the atoms with momenta k_a and k_b at the output ports of the beam-splitter. This corresponds to changing the previous notation, such that $\hat{a} = \hat{a}_{k_a}$ and $\hat{b} = \hat{a}_{k_b}$.

The two atomic beams move apart from each other since their speed is different. At time t_m the mirror is applied, such that their momenta is exchanged making the two beams recombine on a 50:50 beam-splitter at time t_s as represented in Fig. D.3.

At time t, the operators can simply be written as

$$\hat{a}_{k_a}(t) = \hat{a}_{k_a}(t_{s^+})e^{-i\frac{\hbar k_a^2}{2m}(t-t_s)}\,, \tag{D.9a}$$

$$\hat{a}_{k_b}(t) = \hat{a}_{k_b}(t_{s^+})e^{-i\frac{\hbar k_b^2}{2m}(t-t_s)}\,, \tag{D.9b}$$

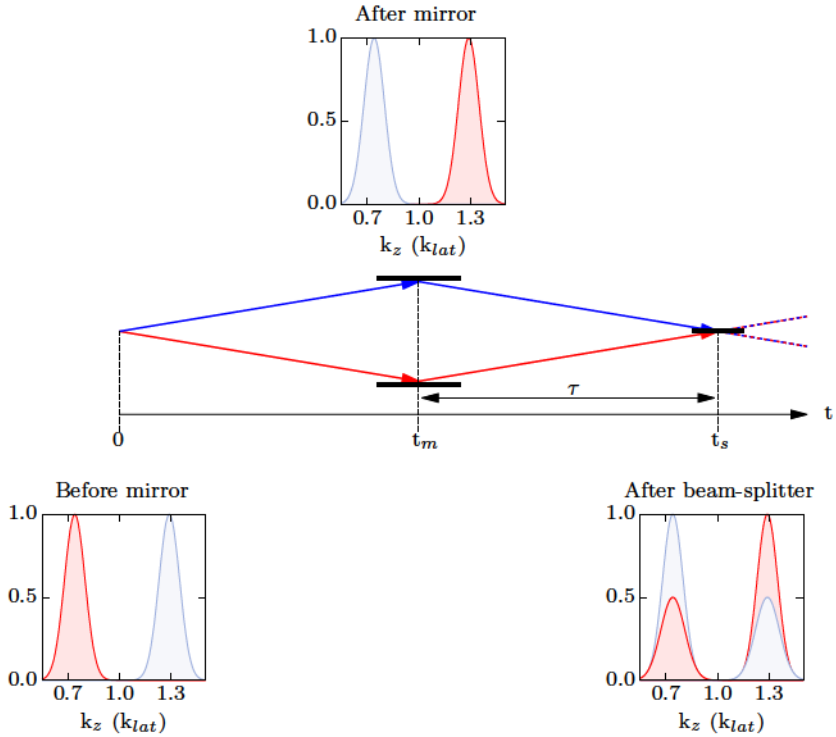

Figure D.3: *Schematic representation of atomic the HOM experiment. The two beams a and b in red and blue respectively, produced at time $t = 0$ move apart from each other. At time $t = t_m$ their momenta are exchanged such that beam a is now blue, and beam b is red. The two atomic beam are then recombined on the 50:50 beam-splitter at time t_s. After the beam-splitter the atoms exit in either beam c with momentum $k_c = k_a$ or beam d with momentum $k_d = k_b$. If $t_s - t_m = \tau = t_m$ then the two beams are indistinguishable after the beam-splitter.*

with t_s corresponding to the application time of the 50:50 beam-splitter. The beam-splitter operation corresponds to the scattering matrix

$$\hat{S} = \frac{1}{\sqrt{2}} \begin{pmatrix} 1 & ie^{-i\phi_S} \\ ie^{i\phi_S} & 1 \end{pmatrix},$$

where we attribute a local phase ϕ_S. In the same manner, the mirror is also associated to a scattering matrix

$$\hat{M} = \begin{pmatrix} 0 & ie^{-i\phi_M} \\ ie^{i\phi_M} & 0 \end{pmatrix},$$

with ϕ_M the phase associated to it. It is important to note that the phase of the mirror or beam-splitter is completely random from one realisation to the other while their relative phase is maintained constant.

The operators can then be written as

$$\hat{a}_{k_a}(t) = \frac{e^{-i\frac{\hbar k_a^2}{2m}(t-t_s)}}{\sqrt{2}} \left[ie^{i\phi_1'} \hat{a}_{k_a+k_{\text{bms}}} - e^{i\phi_1} \hat{a}_{k_a} \right], \tag{D.10a}$$

$$\hat{a}_{k_b}(t) = \frac{e^{-i\frac{\hbar k_b^2}{2m}(t-t_s)}}{\sqrt{2}} \left[ie^{i\phi_2'} \hat{a}_{k_b-k_{\text{bms}}} - e^{i\phi_2} \hat{a}_{k_b} \right], \tag{D.10b}$$

where k_{bms} corresponds to the momentum given by the beam-splitter lattice. The phases

ϕ_1, ϕ_1', ϕ_2 and ϕ_2' correspond to

$$\phi_1 = -(\phi_S - \phi_M) - \frac{\hbar t_s}{2m}(k_a + k_{\text{bms}})^2 - \frac{\hbar t_m}{2m}(k_a^2 - (k_a + k_{\text{bms}})^2)\,, \tag{D.11a}$$

$$\phi_1' = -\phi_M - \frac{\hbar t_s}{2m}k_a^2 + \frac{\hbar t_m}{2m}(k_a^2 - (k_a + k_{\text{bms}})^2)\,, \tag{D.11b}$$

$$\phi_2 = (\phi_S - \phi_M) - \frac{\hbar t_s}{2m}(k_b - k_{\text{bms}})^2 - \frac{\hbar t_m}{2m}(k_b^2 - (k_b - k_{\text{bms}})^2)\,, \tag{D.11c}$$

$$\phi_2' = \phi_M - \frac{\hbar t_s}{2m}k_b^2 + \frac{\hbar t_m}{2m}(k_b^2 - (k_b - k_{\text{bms}})^2)\,. \tag{D.11d}$$

The detection is performed at a time t which as no importance in the calculation of the cross-correlation between the output ports of the beam-splitter as we are going to see.

D.3 Cross-correlation and HOM-dip

The cross-correlation function after application of the 50:50 beam-splitter corresponds to

$$G_{cd}^{(2)} = \langle \hat{a}_{k_a}(t\to\infty)^\dagger \hat{a}_{k_b}(t\to\infty)^\dagger \hat{a}_{k_a}(t\to\infty)\,\hat{a}_{k_b}(t\to\infty)\rangle\,, \tag{D.12}$$

where, experimentally, $\langle\rangle$ corresponds to a statistical average over N experimental realisations with $N\to\infty$. Using Eq. (D.39), one obtains the following expression

$$\begin{aligned} G_{cd}^{(2)} = {} & \frac{1}{2}\Delta + \frac{1}{4}[\langle \hat{a}^\dagger_{k_a+k_{\text{bms}}}\hat{a}^\dagger_{k_b-k_{\text{bms}}}\hat{a}_{k_a+k_{\text{bms}}}\,\hat{a}_{k_b-k_{\text{bms}}}\rangle - \langle e^{i(\phi_1-\phi_1'+\phi_2-\phi_2')}\hat{a}^\dagger_{k_a}\hat{a}^\dagger_{k_b}\hat{a}_{k_a+k_{\text{bms}}}\,\hat{a}_{k_b-k_{\text{bms}}}\rangle \\ & - \langle e^{-i(\phi_1-\phi_1'+\phi_2-\phi_2')}\hat{a}^\dagger_{k_a+k_{\text{bms}}}\hat{a}^\dagger_{k_b-k_{\text{bms}}}\hat{a}_{k_a}\,\hat{a}_{k_b}\rangle + \langle \hat{a}^\dagger_{k_a}\hat{a}^\dagger_{k_b}\hat{a}_{k_a}\,\hat{a}_{k_b}\rangle] \\ & + \frac{1}{4}[\langle \hat{a}^\dagger_{k_a}\hat{a}^\dagger_{k_b-k_{\text{bms}}}\hat{a}_{k_a}\,\hat{a}_{k_b-k_{\text{bms}}}\rangle + \langle \hat{a}^\dagger_{k_b}\hat{a}^\dagger_{k_a+k_{\text{bms}}}\hat{a}_{k_b}\,\hat{a}_{k_a+k_{\text{bms}}}\rangle]\,, \end{aligned} \tag{D.13}$$

where for the resonant situation $k_a + k_{\text{bms}} = k_b$, one can write

$$G_{cd}^{(2)} = \frac{1}{4}\Delta + \frac{G_{ab}^{(2)}}{2}\left[1 - \text{Re}\left[\langle e^{i(\phi_1+\phi_2-\phi_1'-\phi_2')}\rangle\right]\right] + \frac{1}{4}\left[G_{aa}^{(2)} + G_{bb}^{(2)}\right]. \tag{D.14}$$

The first term corresponds to

$$\Delta = \text{Re}\left[\langle e^{i(\phi_1'-\phi_1+\phi_2-\phi_2')}\hat{a}^\dagger_{k_a+k_{\text{bms}}}\hat{a}^\dagger_{k_b}\hat{a}_{k_a}\,\hat{a}_{k_b-k_{\text{bms}}}\rangle\right]\,, \tag{D.15}$$

and depends on the phase

$$\phi_1' - \phi_1 + \phi_2 - \phi_2' = 2(\phi_S - \phi_M) - 2\phi_M - \frac{\hbar}{2m}\left[(k_b - k_{\text{bms}})^2 - (k_a + k_{\text{bms}})^2 - \left(k_b^2 - k_a^2\right)\right](t_s - 2t_m)\,,$$

which depends of the absolute phase ϕ_M. As we said before, this phase is kept random, such that after averaging over the different realisations it washes out.

D.3.1 Visibility without assumption of the incoming state

In order to experimentally verify that this is the case one can re-write the cross-correlation for indistinguishable particles as

$$G_{\text{Ind}}^{(2)} = \frac{1}{4}\left(G_{aa}^{(2)} + G_{bb}^{(2)}\right) + \frac{1}{2}\Delta\,, \tag{D.16}$$

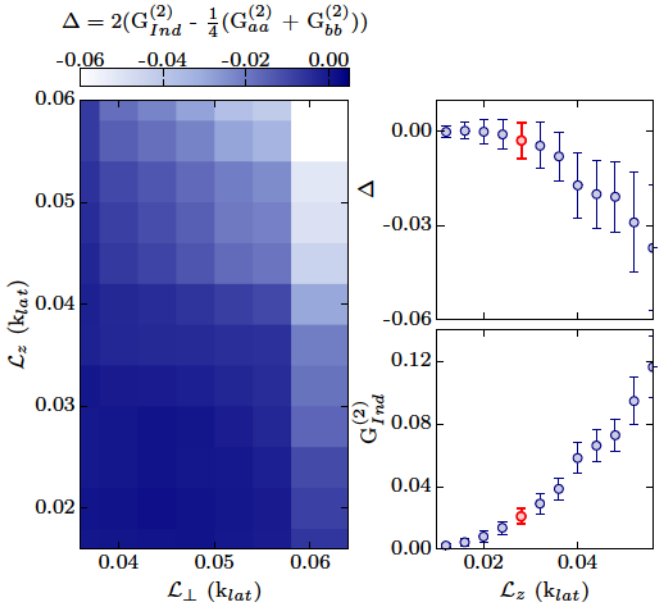

Figure D.4: *Evolution of Δ as a function of the integration volume Ω_V. Left panel: 2D representation of Δ as a function of the integration volume $\Omega_V = [\mathcal{L}_\perp^2 \times \mathcal{L}_z]$. The length of $\mathcal{L}_z$ is increased by values of $0.04\,k_{lat}$ as well as the length $\mathcal{L}_\perp$. Right canvas: top; Evolution of Δ as a function of $\mathcal{L}_z$ for a fixed value of $\mathcal{L}_\perp = 0.048\,k_{lat}$. For short integration length along the z–axis, one finds a value of $\Delta = 0$. One the since of the integration increases Δ decreases towards negative values as a consequence of the mixing between indistinguishable and distinguishable particles. Right canvas: bottom; Evolution of the cross-correlation for the indistinguishable case as a function of $\mathcal{L}_z$. In both cases, the red circles indicates the optimised volume of integration for which Δ is still approximatively null.*

and, consequently, the value of Δ can be extracted from $2\left[G^{(2)}_{\text{Ind}} - \frac{1}{4}\left(G^{(2)}_{aa} + G^{(2)}_{bb}\right)\right]$ with $G^{(2)}_{\text{Ind.}}$ corresponding to the experimental value of $G^{(2)}_{cd}(\tau = 550\,\mu s)$. The value of Δ is then determined as a function of the integration volume Ω_V as shown in Fig. D.4 left panel.

Fig. D.4 shows the evolution of Δ for different integration volumes defined by the integration length on the transverse direction and longitudinal one, $\mathcal{L}_\perp$ and $\mathcal{L}_z$, respectively. A cut along $\mathcal{L}_z$ is performed for both $G^{(2)}_{cd,\text{Ind}}$ and Δ for a fixed integration length on the transverse direction $\mathcal{L}_\perp = 0.048 k_{\text{lat}}$. It is possible to note that for small integration volume, $\Delta \to 0$ and tends to decreases towards negative values when the volume of integration increases. This is related to the fact that with an increased volume of integration different modes start to be taking into account as discussed in Subsection 5.1.2. Thus the value of $G^{(2)}_{cd}(\tau = 550\,\mu s)$ does not correspond any more to the indistinguishable case which invalidate the use of Eq. (D.16). The integration volume corresponding to the optimised volume of integration described in the main text is identified by the red circle ($\mathcal{L}_z = 0.028 k_{\text{lat}}$). For this volume, we can extract a value of $\Delta = -2.8 \times 10^{-3} \pm 6.0 \times 10^{-}3$ which is, taking into account the error bars, negligible.

Although the goal here was to demonstrate that $\Delta \to 0$, one can note that for a well defined phase, the measurement of Δ gives important information on the phase difference between the particles, via $\phi_a - \phi_b$ and on the produced state through the measurement of non symmetric components leading to a quantum state tomography [223].

D.3.2 Indistinguishable and distinguishable cases

Let us consider the two extreme cases corresponding to either perfect indistinguishable paths or distinguishable ones. The two cases can be seen as:

- Indistinguishable case, $k_a + k_{\text{bms}} = k_b$;

- Distinguishable case, $k_a + k_{\text{bms}} \neq k_b$ such that $k_a + k_{\text{bms}}$ and k_b corresponds to different modes.

For the indistinguishable case $G^{(2)}_{cd}$ can be re-written as

$$\begin{aligned} G^{(2)}_{cd} =& \frac{1}{2}\left\{\langle \hat{a}^\dagger_{k_a}\hat{a}^\dagger_{k_b}\hat{a}_{k_a}\hat{a}_{k_b}\rangle - \text{Re}\left[\langle e^{i(\phi_1+\phi_2-\phi_1'-\phi_2')}\hat{a}^\dagger_{k_a}\hat{a}^\dagger_{k_b}\hat{a}_{k_a}\hat{a}_{k_b}\rangle\right]\right\} \\ &+\frac{1}{4}[\langle \hat{a}^\dagger_{k_a}\hat{a}^\dagger_{k_a}\hat{a}_{k_a}\hat{a}_{k_a}\rangle + \langle \hat{a}^\dagger_{k_b}\hat{a}^\dagger_{k_b}\hat{a}_{k_b}\hat{a}_{k_b}\rangle] \end{aligned} \tag{D.17}$$

with $\phi_1 + \phi_2 - \phi_1' - \phi_2' = 0$ and, consequently,

$$G^{(2)}_{cd} = \frac{1}{4}\left(G^{(2)}_{aa} + G^{(2)}_{bb}\right) \tag{D.18}$$

where $G^{(2)}_{aa}$ and $G^{(2)}_{bb}$ stand for the autocorrelation of k_a and k_b, this means, the autocorrelations before the mirror and the 50:50 beam-splitter.

The distinguishable situation corresponds to $k_a + k_{\text{bms}} \neq k_b$ such that the term

$$\phi_1 + \phi_2 - \phi_1' - \phi_2' = \frac{\hbar k_{\text{bms}}}{m}(k_{\text{bms}} + k_a - k_b)(2t_m - t_s) \tag{D.19}$$

oscillates quickly over time. Thus, this term vanishes and one retrieves

$$G^{(2)}_{cd} = \frac{1}{4}\left(G^{(2)}_{aa} + G^{(2)}_{bb}\right) + \frac{1}{2}G^{(2)}_{ab}. \tag{D.20}$$

The HOM-dip visibility corresponds then to

$$\bar{V} = 1 - \frac{G^{(2)}_{cd,\text{Ind.}}}{G^{(2)}_{cd,\text{Dis.}}} = \frac{2G^{(2)}_{ab}}{G^{(2)}_{aa} + G^{(2)}_{bb} + 2G^{(2)}_{ab}}$$

and can be related to the Cauchy-Schwarz inequality coefficient, $C = G^{(2)}_{ab}/\sqrt{G^{(2)}_{aa} + G^{(2)}_{bb}}$, such that

$$\bar{V} = \frac{1}{1 + \delta/C}$$

with the coefficient δ standing for

$$\delta = \frac{G^{(2)}_{aa} + G^{(2)}_{bb}}{2\sqrt{G^{(2)}_{aa}G^{(2)}_{bb}}}.$$

One sees that for the case of an input state $|1_a, 1_b\rangle$, the autocorrelation before the beam-splitter is equal to zero and one finds, after the beam-splitter, a vanishing coincidence count. In this situation, the visibility is equal to one.

D.3.3 HOM-dip width

In the case of a multimode source of atomic pairs, a finite width of the HOM-dip can appear as a consequence of the different modes contributions. Since the measurement corresponds to an integration over a certain volume in momentum space, one can retrieve the theoretical width by integrating $G^{(2)}_{cd}(k_a, k_b)$ over k_a and k_b.

The cross-correlation can, in the general case, be written as

$$G^{(2)}_{cd}(\theta) = \frac{1}{4}\left[G^{(2)}_{aa} + G^{(2)}_{bb}\right] + \frac{1}{2}G^{(2)}_{ab}\left[1 - \cos(\theta)\right] \tag{D.21}$$

with $\theta = \phi_1 + \phi_2 - \phi_1' - \phi_2' = \frac{\hbar}{m}\left(k_{\text{bms}}(k_a + k_{\text{bms}} - k_b)\right)(t_s - 2t_m)$. One can already see that several widths will be at play, in particular,

- the autocorrelation width associated to $G^{(2)}_{aa}$ and $G^{(2)}_{bb}$ (σlc_a and σlc_b, respectively) although, since it does not influence the visibility itself, has negligible influence;
- the cross-correlation width associated to $G^{(2)}_{ab}$ (σCr);
- the density width since the cloud has a finite size in momentum space (σnk_a and σnk_b);
- the stability of the beam-splitter which relates into a width in momentum space of the different possible k_{bms}. This width σ_{bms} has been proved in Chapter 4 to be smaller than the autocorrelation width.

With this in mind, one can writes the most general solution of $G^{(2)}_{cd}$ as

$$\begin{aligned} G^{(2)}_{cd,\,\text{Measured}} = &\left(\frac{\eta}{\mathcal{L}_z}\right)^2 \mathcal{N}_a\mathcal{N}_b \int_{k_{\text{bms},C}-\mathcal{L}_z/2}^{k_{\text{bms},C}+\mathcal{L}_z/2} \frac{dk_{\text{bms}}}{\mathcal{L}_z} \int_{k_{aC}-\mathcal{L}_a}^{k_{aC}+\mathcal{L}_a} dk_a \int_{k_{bC}-\mathcal{L}_b}^{k_{bC}+\mathcal{L}_b} dk_b \\ &\times \exp\left(-\frac{(k_a - k_{aC})^2}{2\sigma n k_a^2}\right)\exp\left(-\frac{(k_b - k_{bC})^2}{2\sigma n k_b^2}\right)\exp\left(-\frac{(k_{\text{bms}} - k_{\text{bms},C})^2}{2\sigma_{\text{bms}}^2}\right) \\ &\times\left[\frac{1}{4}\left(g^{(2)}_{aa}(0)\exp\left(-\frac{(k_a - k_{aC})^2}{2\sigma lc_a^2}\right) + g^{(2)}_{bb}(0)\exp\left(-\frac{(k_b - k_{bC})^2}{2\sigma lc_b^2}\right)\right)\right. \\ &\left.+\frac{1}{2}\left(g^{(2)}_{ab}(0)\exp\left(-\frac{((k_a + k_b)/2 - 1)^2}{2\sigma Cr^2}\right)(1 - \cos\theta)\right)\right] \end{aligned} \tag{D.22}$$

with $\mathcal{L}_a = \mathcal{L}_b = \mathcal{L}_z/2$ standing for the integration length along the z−axis around the central momenta under study k_{aC} and k_{bC}.

Consider the case in which the integration volume ($\mathcal{L}_a = \mathcal{L}_b = \mathcal{L}_z$) is much smaller than all the widths associated to $G^{(2)}_{cd}$. In this case, one can assume that the functions are constant and that the only varying term corresponds to $(1 - \cos\theta)$. $G^{(2)}_{cd,\,\text{Measured}}$ simplifies then into

$$G^{(2)}_{cd}(\tau\,,\text{Measured}) = \eta^2\mathcal{N}_a\mathcal{N}_b\{1 - \alpha\,\text{sinc}^2(\mathcal{L}_z k_{\text{bms}}\frac{\hbar}{2m}[\tau - t_m])\} \tag{D.23}$$

with $\tau = t_s - t_m$ and α a coefficient proportional to k_{bms}. Thus, the width of the measured cross-correlation depends only of the volume of integration. For smaller volumes of integration, the dip will get larger.

D.4 Autocorrelation and coalescence effect

The same treatment can be applied to the coalescence effect. For this purpose, we look at the evolution of $G^{(2)}_{cc}$ or $G^{(2)}_{dd}$ as a function of τ. In this situation, one considers the momenta k_a and k_a' corresponding of two different modes at the output port c. The operator evolution can then

be written as

$$\hat{a}_{k_a}(t) = \frac{e^{-i\frac{\hbar k_a^2}{2m}(t-t_s)}}{\sqrt{2}}\left(ia_{k_a+k_{\text{bms}}}e^{i\phi_1'} - a_{k_a}e^{i\phi_1}\right), \tag{D.24a}$$

$$\hat{a}_{k_a'}(t) = \frac{e^{-i\frac{\hbar k_a'^2}{2m}(t-t_s)}}{\sqrt{2}}\left(ia_{k_a'+k_{\text{bms}}}e^{i\varphi_1'} - a_{k_a'}e^{i\varphi_1}\right), \tag{D.24b}$$

with

$$\phi_1 = -(\phi_S - \phi_M) - \frac{\hbar t_s}{2m}(k_a + k_{\text{bms}})^2 - \frac{\hbar t_m}{2m}(k_a^2 - (k_a + k_{\text{bms}})^2), \tag{D.25a}$$

$$\varphi_1 = -(\phi_S - \phi_M) - \frac{\hbar t_s}{2m}(k_a' + k_{\text{bms}})^2 - \frac{\hbar t_m}{2m}(k_a'^2 - (k_a' + k_{\text{bms}})^2), \tag{D.25b}$$

$$\phi_1' = -\phi_M - \frac{\hbar t_s}{2m}k_a^2 - \frac{\hbar t_m}{2m}\left((k_a + k_{\text{bms}})^2 - k_a^2\right), \tag{D.25c}$$

$$\varphi_1' = -\phi_M - \frac{\hbar t_s}{2m}k_a'^2 - \frac{\hbar t_m}{2m}\left((k_a' + k_{\text{bms}})^2 - k_a'^2\right). \tag{D.25d}$$

The autocorrelation of beam c thus simplifies into

$$G_{cc}^{(2)} = \langle \hat{a}_{k_a}^\dagger \hat{a}_{k_a'}^\dagger \hat{a}_{k_a'} \hat{a}_{k_a} \rangle \tag{D.26}$$

and, with the same argument as before [1], the autocorrelation is given by

$$G_{cc}^{(2)} = \frac{1}{4}\left(G_{aa}^{(2)} + G_{bb}^{(2)}\right) + \frac{1}{2}G_{ab}^{(2)}\left(1 + \cos\left(\frac{\hbar k_{\text{bms}}}{m}(k_a - k_a')(\tau - t_m)\right)\right). \tag{D.27}$$

For the case of distinguishable atoms at the entrance of the 50:50 beam-splitter, meaning $\tau \to \infty$, once integrated over k_a the cosinus term tends to zero and the autocorrelation is equal to

$$G_{cc}^{(2)} = \frac{1}{4}\left(G_{aa}^{(2)} + G_{bb}^{(2)}\right) + \frac{1}{2}G_{ab}^{(2)},$$

which corresponds to the same expression of the cross-correlation between ports c and d for distinguishable particles. One can understand this result through the simple picture of two distinguishable particles entering a beam-splitter. The probability of having one particle on each output port is 1/2 while the probability of having 2 particles on either one of the output ports is also 1/2. Thus, the probability of detecting either 2 or 1 particle in one of the output ports is equal.

For indistinguishable atoms at the entrance of the 50:50 beam-splitter, $(k_a - k_a')(\tau - t_m) = 0$, the situation is rather different. The autocorrelation is then equal to

$$G_{cc}^{(2)} = \frac{1}{4}\left(G_{aa}^{(2)} + G_{bb}^{(2)}\right) + G_{ab}^{(2)}, \tag{D.28}$$

which strongly differs of the cross-correlation result $G_{cd}^{(2)} = \frac{1}{4}\left(G_{aa}^{(2)} + G_{bb}^{(2)}\right)$. This signal corresponds to the increased probability of having 2 particles in either one of the output ports.

[1] We consider that the absolute phase of the mirror or beam-splitter is randomly chosen for each experimental realisation

D.4.1 Width of the autocorrelation measurement

The experimental measurement translates into an integration of the autocorrelation described by

$$\begin{aligned} G^{(2)}_{cc,\text{Measured}} = & \left(\frac{\eta}{\mathcal{L}_z}\right)^2 \mathcal{N}_a \mathcal{N}_b \int_{k_{\text{bms},C}-\mathcal{L}_z/2}^{k_{\text{bms},C}+\mathcal{L}_z/2} \frac{dk_{\text{bms}}}{\mathcal{L}_z} \int_{k_{aC}-\mathcal{L}_a}^{k_{aC}+\mathcal{L}_a} dk_a \int_{k_{bC}-\mathcal{L}_b}^{k_{bC}+\mathcal{L}_b} dk_b \\ & \times e^{-\frac{(k_a-k_{aC})^2}{2\sigma n k_a^2}} \exp\left(-\frac{(k_b-k_{bC})^2}{2\sigma n k_b^2}\right) \exp\left(-\frac{(k_{\text{bms}}-k_{\text{bms},C})^2}{2\sigma_{\text{bms}}^2}\right) \\ & \times \left[\frac{1}{4}\left(G^{(2)}_{aa}(0)\exp\left(-\frac{(k_a-k_{aC})^2}{2\sigma l c_a^2}\right) + G^{(2)}_{bb}(0)\exp\left(-\frac{(k_b-k_{bC})^2}{2\sigma l c_b^2}\right)\right)\right. \\ & \left. + \frac{1}{2}\left(G^{(2)}_{ab}(0)\exp\left(-\frac{(k_a+k_b/2-1)^2}{2\sigma C r^2}\right)(1+\cos\vartheta)\right)\right] \end{aligned} \tag{D.29}$$

with $\vartheta = \frac{\hbar k_{\text{bms}}}{m}(k_a - k_a')\tau$.

One notes that in this situation the width of the dip is going to be determined by the volume of integration and the correlations width.

D.5 Variance of the population difference

Another variable that can help to translate the effect of the destructive interference at play is the evolution of the normalised variance of the difference as a function of τ. The variance of the difference corresponds to

$$V = \frac{\left\langle\left(\hat{a}^\dagger_{k_a}\hat{a}_{k_a} - \hat{a}^\dagger_{k_b}\hat{a}_{k_b}\right)^2\right\rangle - \langle\hat{a}^\dagger_{k_a}\hat{a}_{k_a} - \hat{a}^\dagger_{k_b}\hat{a}_{k_b}\rangle^2}{\langle\hat{a}^\dagger_{k_a}\hat{a}_{k_a}\rangle + \langle\hat{a}^\dagger_{k_b}\hat{a}_{k_b}\rangle} \tag{D.30}$$

which simplifies, for the case of a random phase ϕ_M, into

$$V = 1 + \frac{1}{2\langle n\rangle}\left(G^{(2)}_{cc} + G^{(2)}_{dd} - 2G^{(2)}_{cd}\right) \tag{D.31}$$

with $\langle n\rangle$ the averaged population in both output ports c and d. Thus, the two limiting cases correspond to:

- Distinguishable case, $V = 1$;
- Indistinguishable case , $V = 1 + \frac{2}{2\langle n\rangle}G^{(2)}_{ab}$.

Once again, it is possible to re-write the observable as a function of the distinguishability criterion τ as

$$V = 1 + \alpha G^{(2)}_{ab}\left[\cos\left(\frac{k_{\text{bms}}\hbar}{m}(\tau - t_m)(k_a - k_a' + k_a + k_{\text{bms}} - k_b)\right) \times \cos\left(\frac{k_{\text{bms}}\hbar}{m}(\tau - t_m)(k_a' + k_{\text{bms}} - k_b)\right)\right] \tag{D.32}$$

which, in the limit of $k_a = k_a'$, simplifies into

$$V = 1 + \frac{\alpha}{2}G^{(2)}_{ab}\left[1 + \cos\left(\frac{2k_{\text{bms}}\hbar}{m}(\tau - t_m)(k_a + k_{\text{bms}} - k_b)\right)\right]. \tag{D.33}$$

One can directly see from this result that the oscillation period is twice higher that the one of the cross-correlation. Consequently, the rise of V will be twice larger, after integration along k_a and k_b, than the dip of $G^{(2)}_{cd}$. Thus, the measured value of the normalised variance can be written as

$$V_{\text{Measured}} = V_{\text{Bg.}} + \frac{2}{2\langle n\rangle} G^{(2)}_{ab} \left[4\mathcal{L}^2(1 + 2\alpha' \text{sinc}^2(\mathcal{L}k_{\text{bms}}\tau))\right], \tag{D.34}$$

with $V_{\text{Bg.}}$ standing for the background value of the variance. Since for the case of a parametric amplification $G^{(2)}_{ab} = 2\langle n\rangle^2 + \langle n\rangle$ the rise of V goes up to the value of

$$V = 1 + \frac{(2\langle n\rangle^2 + \langle n\rangle)}{\langle n\rangle} = (2 + 2\langle n\rangle) \tag{D.35}$$

As seen in Section 3.4.2, the detection efficiency affects the measured value of the variance with $V_{\text{Det.}} = \eta V + (1 - \eta)$ which implies that after the beam-splitter for the indistinguishable case

$$V_{\text{Det., Ind.}} = (1 - \eta) + \eta(2(1 + \langle n\rangle)) = 1 + \eta + 2\langle n\rangle\eta\,. \tag{D.36}$$

For the distinguishable case, the variance is still equal to

$$V_{\text{Det., Dis.}} = 1.$$

The visibility for the variance of the difference as a function of τ, corresponding to

$$\bar{V}_V = \frac{V_{\text{Ind.}}}{V_{\text{Dis.}}} - 1\,, \tag{D.37}$$

is then equal to

$$\bar{V}_V = \eta\,(1 + 2\langle n\rangle)\,. \tag{D.38}$$

D.6 Effect of the beam-splitter transmittance

In the last sections, it was assumed that both the mirror and the 50:50 beam-splitter had perfect coefficients of reflectivity and transmittance, this meaning, that the reflectivity was total for the mirror and of 50% for the 50:50 beam-splitter. However, this is not true as it has been shown in Eq. (4) where we showed that the reflectivity of the mirror is equal to 93% and the transmittance of the 50:50 beam-splitter to 49%. What is the impact of these small imperfections on the visibility of the HOM-dip?

Let us model the 50:50 beam-splitter and mirror by the following scattering matrix

$$\hat{S} = \frac{1}{\sqrt{2}} \begin{pmatrix} t & re^{-i\phi_S} \\ -r^* e^{i\phi_S} & t^* \end{pmatrix},$$

and

$$\hat{M} = \frac{1}{\sqrt{2}} \begin{pmatrix} T & Re^{-i\phi_M} \\ -R^* e^{i\phi_M} & T^* \end{pmatrix},$$

with t, r the transmittance and reflectivity coefficients of the 50:50 beam-splitter and R, T the coefficients for the mirror. Two things are to be kept in mind. First, even if the mirror or the 50:50 beam-splitter have imperfections, they are rather small. This implies certain approximations such as $T \ll 1$ or $|r|^2 \approx |t|^2$. Second, it is important to remember that the absolute phase of either the 50:50 beam-splitter or mirror are randomly chosen from one realisation to the other and that cross-correlation corresponds to an average over N realisations. This means that, on average, any oscillatory term depending of the absolute value of either ϕ_S or ϕ_M will vanish. Nevertheless, as we saw in Chapter 4, the relative phase of the beam-splitter $\phi_S - \phi_M$ is rather stable, and thus, only the terms depending on the phase difference are kept.

Applying the new matrices $\hat{M}$ and $\hat{S}$, one recovers the expressions for $\hat{a}_{k_a}$ and $\hat{a}_{k_b}$

$$\hat{a}_{k_a}(t) = e^{-i\frac{\hbar k_a^2}{2m}(t-t_s)}\left[\hat{a}_{k_a}\left(tTe^{-\phi_1} - rR^*e^{-i\varphi_1}\right) + \hat{a}_{k_a+k_{\text{bms}}}\left(tRe^{-i\varphi_1'} + rT^*e^{-i\phi_1'}\right)\right], \tag{D.39a}$$

$$\hat{a}_{k_b}(t) = e^{-i\frac{\hbar k_b^2}{2m}(t-t_s)}\left[\hat{a}_{k_b}\left(t^*T^*e^{-\phi_2} - r^*Re^{-i\varphi_2}\right) - \hat{a}_{k_b-k_{\text{bms}}}\left(t^*R^*e^{-i\varphi_2'} + r^*Te^{-i\phi_2'}\right)\right], \tag{D.39b}$$

with

$$\phi_1 = \frac{\hbar k_a^2}{2m}t_s\,, \tag{D.40a}$$

$$\phi_2 = \frac{\hbar k_b^2}{2m}t_s\,, \tag{D.40b}$$

$$\varphi_1 = \left(\phi_S - \phi_M\right) + \frac{\hbar}{2m}(k_a + k_{\text{bms}})^2(t_s - t_m) + \frac{\hbar k_a^2}{2m}t_m\,, \tag{D.40c}$$

$$\varphi_2 = \left(\phi_M - \phi_S\right) + \frac{\hbar}{2m}(k_b - k_{\text{bms}})^2(t_s - t_m) + \frac{\hbar k_b^2}{2m}t_m\,, \tag{D.40d}$$

$$\phi_1' = \frac{\hbar(k_a + k_{\text{bms}})^2}{2m}t_s + \phi_S\,, \tag{D.40e}$$

$$\phi_2' = \frac{\hbar(k_b - k_{\text{bms}})^2}{2m}t_s - \phi_S\,, \tag{D.40f}$$

$$\varphi_1' = \phi_M + \frac{\hbar}{2m}(k_a + k_{\text{bms}})^2 t_m + \frac{\hbar k_a^2}{2m}(t_s - t_m)\,, \tag{D.40g}$$

$$\varphi_2' = -\phi_M + \frac{\hbar}{2m}(k_b - k_{\text{bms}})^2 t_m + \frac{\hbar k_b^2}{2m}(t_s - t_m)\,. \tag{D.40h}$$

Applying Eqs. (D.39) and Eqs. (D.40) to the cross-correlation $G_{cd}^{(2)} = \langle \hat{a}_{k_a}^\dagger \hat{a}_{k_b}^\dagger \hat{a}_{k_a} \hat{a}_{k_b}(t)\rangle$ one gets, to the first order in T,

$$\begin{aligned} G_{cd}^{(2)} =& G_{ab}^{(2)}\left[\left(|t|^4|R|^4 + |r|^4|R|^4\right) - \left(2|R|^4|r|^2|t|^2\cos\theta_1 - 2(|t|^2 - |r|^2)(\cos\theta_2 + \cos\theta_3)|R|^2 rR^*tT\right)\right] \\ &+ \left[|r|^2|t|^2|R|^4 - |R|^2 tRr^*T\cos\theta_4\left(|t|^2 - |r|^2\right)\right]\left(G_{aa}^{(2)} + G_{bb}^{(2)}\right), \end{aligned} \tag{D.41}$$

with

$$\theta_1 = \frac{\hbar k_{\text{bms}}}{m}(k_b - k_{\text{bms}} - k_a)(\tau - t_m)\,, \tag{D.42a}$$

$$\theta_2 = (\phi_M - \phi_S) + \frac{\hbar k_{\text{bms}}}{2m}\left[(k_b - k_{\text{bms}})(\tau - t_m) - (k_{\text{bms}} + 2k_a)t_m\right], \tag{D.42b}$$

$$\theta_3 = (\phi_S - \phi_M) + \frac{\hbar k_{\text{bms}}}{2m}\left[-(k_{\text{bms}} + k_a)(\tau - t_m) - (k_{\text{bms}} - 2k_b)t_m\right], \tag{D.42c}$$

$$\theta_4 = (\phi_S - \phi_M) + \frac{\hbar k_{\text{bms}}}{2m}\tau(k_{\text{bms}} + 2k_a)\,, \tag{D.42d}$$

$$\tag{D.42e}$$

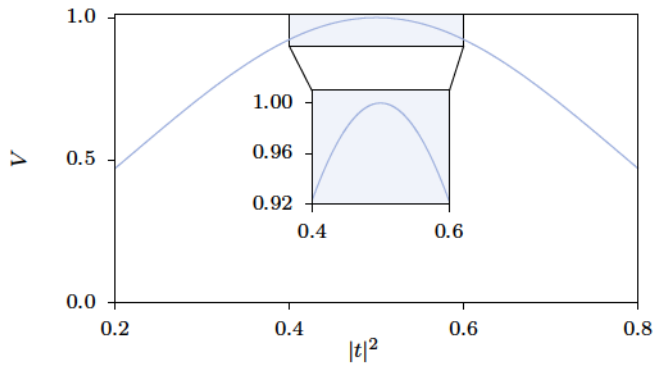

***Figure D.5:** Influence of the beam-splitter transmittance on the HOM-dip visibility. The visibility of the HOM-dip is plotted as a function of the transmittance of the beam-splitter $|t|^2$. One can see that the visibility is rather stable over the possible values of $|t|^2$.*

where $\tau = t_s - t_m$.

One sees that not only the terms associated to T are small since $T \ll 1$, but also that they are inevitably associated to the difference $|t|^2 - |r|^2$ which also tends to be negligible. In good approximation, for our experimental conditions these terms are completely negligible and one retrieves the simpler expression

$$G^{(2)}_{cd} = G^{(2)}_{ab}\left[|t|^4 |R|^4 + |r|^4 |R|^4 - 2|R|^4 |r|^2 |t|^2 \cos\theta_1\right] + |r|^2 |t|^2 |R|^4 \left(G^{(2)}_{aa} + G^{(2)}_{bb}\right), \tag{D.43}$$

which tends to the expected value when $r = t = 1/\sqrt{2}$ and $R = 1$,

$$G^{(2)}_{cd} = \frac{1}{2} G^{(2)}_{ab} (1 - \cos\theta_1) + \frac{1}{4}\left(G^{(2)}_{aa} + G^{(2)}_{bb}\right).$$

The dip visibility $\bar{V}$ can then be written as

$$\bar{V} = 1 - \frac{G^{(2)}_{cd,\text{Ind.}}}{G^{(2)}_{cd,\text{Dis.}}} = \frac{2G^{(2)}_{ab}}{\left(G^{(2)}_{aa} + G^{(2)}_{bb}\right) + G^{(2)}_{ab}\left(\frac{|r|^4+|t|^4}{|r|^2|t|^2}\right)} \tag{D.44}$$

which for the ideal input state $|1_a, 1_b\rangle$ translates into

$$\bar{V} = \frac{2|r|^2 |t|^2}{|r|^4 + |t|^4}. \tag{D.45}$$

Fig. D.5 shows the evolution of $\bar{V}$ with the transmission probability $|t|^2$, assuming that the energy is conserved such that $|r|^2 + |t|^2 = 1$. One can conclude that even if $|t|^2$ vary between 0.4 to 0.6, the visibility varies only between 0.92 and 1.00. In our case, since $|t|^2$ varies between 0.49 and 0.51, the effect on the HOM-visibility is completely negligible.

In this sense, we conclude that, based on the calibration of both the mirror and 50:50 beam-splitter performed in Subsection 4.2, the imperfections of our interferometric scheme do not play any major role on the observed HOM effect.

Appendix E

Detailed calculations for test of Bell's inequality

The situation of Bell's inequalities violation corresponds, in its simpler form, to the one represented in Fig. E.1. Two pairs with momenta $\{k_{a'}, k_{b'}\}$ and $\{k_{a''}, k_{b''}\}$ are created at time $t_1 = 0$. The interferometric scheme is such that the pairs are mixed, this meaning, $k_{a'}$ is recombined with $k_{b''}$ and $k_{a''}$ with $k_{b'}$. The phase difference between the mirror and the beam-splitter is extremely well defined while the absolute phase of both is randomly chosen from one realisation to the other. The mirror pulse for $k_{a'}$ and $k_{b''}$ imprints a phase ϕ_M on the atomic beams while the beams $k_{a''}$ and $k_{b'}$ are imprinted with a phase φ_M. The same thing happens with the 50:50 beam-splitter, with phases ϕ_S and φ_S, respectively. This is easily performed experimentally by applying the two pulses at different times and changing the relative phase between the laser beams in the meanwhile. We also assume that the phase differences $\phi_M - \varphi_M$ and $\phi_S - \varphi_S$ are well defined.

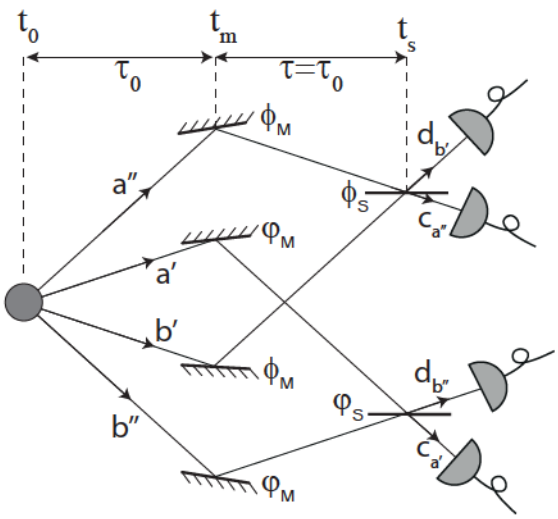

Figure E.1: Schematic representation of an experimental realisation of Bell's inequality test Several modes are out-coming from the initial source, mode a correlated with b, a′ with b′ and a″ with b″. The mirror and beam-splitter are calibrated such that a and b overlap on the beam-splitter. This implies that mode a′ overlap with mode b″ and a″ with b′.

Consider the time evolution of the field operators $\hat{a}_{k_{a'}}$, $\hat{a}_{k_{b'}}$, $\hat{a}_{k_{a''}}$ and $\hat{a}_{k_{b''}}$

$$\hat{a}_{k_{a'}}(t) = \frac{e^{-i\hbar k_{a'}(t-t_s)}}{\sqrt{2}}\left[ie^{i\phi_{1'}}\hat{a}_{k_{a'}+k_{\text{bms}}} - e^{i\phi_1}\hat{a}_{k_{a'}}\right], \tag{E.1a}$$

$$\hat{a}_{k_{a''}}(t) = \frac{e^{-i\hbar k_{a''}(t-t_s)}}{\sqrt{2}}\left[ie^{i\varphi_{1'}}\hat{a}_{k_{a''}+k_{\text{bms}}} - e^{i\varphi_1}\hat{a}_{k_{a''}}\right], \tag{E.1b}$$

$$\hat{a}_{k_{b'}}(t) = \frac{e^{-i\hbar k_{b'}(t-t_s)}}{\sqrt{2}}\left[ie^{i\phi_{2'}}\hat{a}_{k_{b'}-k_{\text{bms}}} - e^{i\phi_2}\hat{a}_{k_{b'}}\right], \tag{E.1c}$$

$$\hat{a}_{k_{b''}}(t) = \frac{e^{-i\hbar k_{b''}(t-t_s)}}{\sqrt{2}}\left[ie^{i\varphi_{2'}}\hat{a}_{k_{b''}-k_{\text{bms}}} - e^{i\varphi_2}\hat{a}_{k_{b''}}\right], \tag{E.1d}$$

with

$$\phi_1 = (\phi_M - \phi_S) - \frac{\hbar t_m}{2m}k_{a'}^2 - \frac{\hbar(t_s - t_m)}{2m}(k_{a'} + k_{\text{bms}})^2, \tag{E.2a}$$

$$\phi_{1'} = -\phi_M - \frac{\hbar t_m}{2m}(k_{a'} + k_{\text{bms}})^2 - \frac{\hbar(t_s - t_m)}{2m}(k_{a'})^2, \tag{E.2b}$$

$$\phi_2 = -(\phi_M - \phi_S) - \frac{\hbar t_m}{2m}k_{b'}^2 - \frac{\hbar(t_s - t_m)}{2m}(k_{b'} - k_{\text{bms}})^2, \tag{E.2c}$$

$$\phi_{2'} = \phi_M - \frac{\hbar t_m}{2m}(k_{b'} - k_{\text{bms}})^2 - \frac{\hbar(t_s - t_m)}{2m}(k_{b'})^2, \tag{E.2d}$$

$$\varphi_1 = (\phi_M - \phi_S) - \frac{\hbar t_m}{2m}k_{a''}^2 - \frac{\hbar(t_s - t_m)}{2m}(k_{a''} + k_{\text{bms}})^2, \tag{E.2e}$$

$$\varphi_{1'} = -\phi_M - \frac{\hbar t_m}{2m}(k_{a''} + k_{\text{bms}})^2 - \frac{\hbar(t_s - t_m)}{2m}(k_{a''})^2, \tag{E.2f}$$

$$\varphi_2 = -(\phi_M - \phi_S) - \frac{\hbar t_m}{2m}k_{b''}^2 - \frac{\hbar(t_s - t_m)}{2m}(k_{b''} - k_{\text{bms}})^2, \tag{E.2g}$$

$$\varphi_{2'} = \phi_M - \frac{\hbar t_m}{2m}(k_{b''} - k_{\text{bms}})^2 - \frac{\hbar(t_s - t_m)}{2m}(k_{b''})^2. \tag{E.2h}$$

The resonant situation for which beam a'' is recombined with beam b' and beam b'' with a', such that,

$$k_{a''} + k_{\text{bms}} = k_{b''},$$
$$k_{a'} + k_{\text{bms}} = k_{b'}.$$

The violation of Bell's inequalities is deduced from the parameter S known as the Clauser–Horne–Shimony–Holt (CHSH) parameter [7]

$$S = |E(\theta_{LR}) - E(\theta_{LR'}) + E(\theta_{L'R}) + E(\theta_{L'R'})|, \tag{E.3}$$

with

$$E(\theta) = \frac{G_{14}^{(2)}(\theta) + G_{23}^{(2)}(\theta) - G_{12}^{(2)}(\theta) - G_{34}^{(2)}(\theta)}{G_{14}^{(2)}(\theta) + G_{23}^{(2)}(\theta) + G_{12}^{(2)}(\theta) + G_{34}^{(2)}(\theta)}, \tag{E.4}$$

where

$$G^{(2)}_{14}(\theta) = \langle \hat{a}_{k_{b''}}(t)^\dagger \hat{a}_{k_{b'}}(t)^\dagger \hat{a}_{k_{b''}}(t)\, \hat{a}_{k_{b'}}(t)\rangle\,, \tag{E.5a}$$

$$G^{(2)}_{23}(\theta) = \langle \hat{a}_{k_{a''}}(t)^\dagger \hat{a}_{k_{a'}}(t)^\dagger \hat{a}_{k_{a''}}(t)\, \hat{a}_{k_{a'}}(t)\rangle\,, \tag{E.5b}$$

$$G^{(2)}_{12}(\theta) = \langle \hat{a}_{k_{a''}}(t)^\dagger \hat{a}_{k_{b''}}(t)^\dagger \hat{a}_{k_{a''}}(t)\, \hat{a}_{k_{b''}}(t)\rangle\,, \tag{E.5c}$$

$$G^{(2)}_{34}(\theta) = \langle \hat{a}_{k_{a'}}(t)^\dagger \hat{a}_{k_{b'}}(t)^\dagger \hat{a}_{k_{a'}}(t)\, \hat{a}_{k_{b'}}(t)\rangle\,, \tag{E.5d}$$

$$\tag{E.5e}$$

and

$$\begin{aligned}
\theta_{LR} &= \pi/4\,,\\
\theta_{LR'} &= 3\pi/4\,,\\
\theta_{L'R} &= -\pi/4\,,\\
\theta_{L'R'} &= \pi/4\,.
\end{aligned}$$

The value of S is bound, for any non-entangled state, between -2 and 2 such that any measurement of $|S| > 2$ indicates the presence of entanglement.

The cross-correlation can be written, assuming that the absolute phase of the each mirror is undefined, as

$$G^{(2)}_{14}(\theta) = \frac{1}{4}\left[G^{(2)}_{k_{a''},k_{a'}} + G^{(2)}_{k_{b''},k_{b'}} + G^{(2)}_{k_{b'},k_{a'}} + G^{(2)}_{k_{b''},k_{a''}} + 2\,\mathrm{Re}\left[e^{i\theta}\langle \hat{a}^\dagger_{k_{a''}}\hat{a}^\dagger_{k_{b''}}\hat{a}_{k_{b'}}\,\hat{a}_{k_{a'}}\rangle\right]\right]\,, \tag{E.6a}$$

$$G^{(2)}_{23}(\theta) = \frac{1}{4}\left[G^{(2)}_{k_{a''},k_{a'}} + G^{(2)}_{k_{b''},k_{b'}} + G^{(2)}_{k_{b'},k_{a'}} + G^{(2)}_{k_{b''},k_{a''}} + 2\,\mathrm{Re}\left[e^{i\theta}\langle \hat{a}^\dagger_{k_{a''}}\hat{a}^\dagger_{k_{b''}}\hat{a}_{k_{b'}}\,\hat{a}_{k_{a'}}\rangle\right]\right]\,, \tag{E.6b}$$

$$G^{(2)}_{12}(\theta) = \frac{1}{4}\left[G^{(2)}_{k_{a''},k_{a'}} + G^{(2)}_{k_{b''},k_{b'}} + G^{(2)}_{k_{b'},k_{a'}} + G^{(2)}_{k_{b''},k_{a''}} - 2\,\mathrm{Re}\left[e^{i\theta}\langle \hat{a}^\dagger_{k_{a''}}\hat{a}^\dagger_{k_{b''}}\hat{a}_{k_{b'}}\,\hat{a}_{k_{a'}}\rangle\right]\right]\,, \tag{E.6c}$$

$$G^{(2)}_{34}(\theta) = \frac{1}{4}\left[G^{(2)}_{k_{a''},k_{a'}} + G^{(2)}_{k_{b''},k_{b'}} + G^{(2)}_{k_{b'},k_{a'}} + G^{(2)}_{k_{b''},k_{a''}} - 2\,\mathrm{Re}\left[e^{i\theta}\langle \hat{a}^\dagger_{k_{a''}}\hat{a}^\dagger_{k_{b''}}\hat{a}_{k_{b'}}\,\hat{a}_{k_{a'}}\rangle\right]\right]\,, \tag{E.6d}$$

$$\tag{E.6e}$$

where

$$\begin{aligned}
\theta &= (\phi_2 + \varphi_{2'} - \phi_{2'} - \varphi_2) = (\phi_1 + \varphi_{1'} - \phi_{1'} - \varphi_1) = (\varphi_{1'} + \varphi_{2'} - \varphi_1 - \varphi_2) = (\phi_{1'} + \phi_{2'} - \phi_1 - \phi_2)\\
&= 2(\phi_M - \varphi_M) + (\varphi_S - \phi_S) + \frac{\hbar}{2m}(t_S - 2t_m)\left(k^2_{a'} + k^2_{b'} - k^2_{a''} - k^2_{b''}\right)\,.
\end{aligned}$$

This leads to the expression

$$E(\theta) = \frac{2\,\mathrm{Re}\left[e^{i\theta}\langle \hat{a}^\dagger_{k_{a''}}\hat{a}^\dagger_{k_{b''}}\hat{a}_{k_{b'}}\,\hat{a}_{k_{a'}}\rangle\right]}{\left(G^{(2)}_{k_{a'},k_{b'}} + G^{(2)}_{k_{a''},k_{b''}}\right) + \left(G^{(2)}_{k_{a''},k_{a'}} + G^{(2)}_{k_{b''},k_{b'}}\right)} \tag{E.7}$$

and to

$$S = 2\sqrt{2}\,\frac{\langle \hat{a}^\dagger_{k_{a''}}\hat{a}^\dagger_{k_{b''}}\hat{a}_{k_{a'}}\,\hat{a}_{k'_b}\rangle}{\frac{1}{2}\left(G^{(2)}_{k_{a''},k_{b''}} + G^{(2)}_{k_{a''},k_{a'}} + G^{(2)}_{k_{b''},k_{b'}} + G^{(2)}_{k_{a'},k_{b'}}\right)}\,. \tag{E.8}$$

If one is able to determine the value of $\langle \hat{a}^\dagger_{k_{a''}}\hat{a}^\dagger_{k_{b''}}\hat{a}_{k_{a'}}\,\hat{a}_{k'_b}\rangle$, corresponding to the probability of creating a pair $(k_{a''}, k_{b''})$ knowing that a pair $(k_{a'}k_{b'})$ exists, S can be easily predicted.

This result is completely free from any assumptions on the produced state. The fact that the absolute phase of both ϕ_M and φ_M is randomly chosen for each experimental realisation guarantees that any asymmetric contribution of $G^{(2)}$ washes out.

Particular solution for a parametric conversion state

Assuming that the state is described by two independent parametric conversion state, such that

$$|\psi\rangle = \sum_n \frac{\tanh^n(\lambda_1)}{\cosh(\lambda_1)} \sum_m \frac{\tanh^m(\lambda_2)}{\cosh(\lambda_2)} |n, n, m, m\rangle ,$$

with $\sinh^2(\lambda_1) = \langle n\rangle$ and $\sinh^2(\lambda_2) = \langle m\rangle$, one finds for the autocorrelation that

$$G^{(2)}_{k_{a''}, k_{a'}} = G^{(2)}_{k_{b''}, k_{b'}} = \langle n\rangle\langle m\rangle ,$$

and the cross-correlation terms can be written as

$$G^{(2)}_{k_{a'}, k_{b'}} + G^{(2)}_{k_{a''}, k_{b''}} = \langle n\rangle (1 + 2\langle n\rangle) + \langle m\rangle (1 + 2\langle m\rangle) .$$

$E(\theta)$ then becomes

$$E(\theta) = \frac{2\,\mathrm{Re}\left[e^{i\theta}\langle \hat{a}^\dagger_{k_{a''}} \hat{a}^\dagger_{k_{b''}} \hat{a}_{k_{b'}} \hat{a}_{k_{a'}}\rangle\right]}{\left(G^{(2)}_{k_{a'}k_{b'}} + G^{(2)}_{k_{a''}k_{b''}}\right) + \left(G^{(2)}_{k_{a'}k_{a'}} + G^{(2)}_{k_{b''}k_{b'}}\right)} = \frac{2\,\mathrm{Re}\left[e^{i\theta}\langle \hat{a}^\dagger_{k_{a''}} \hat{a}^\dagger_{k_{b''}} \hat{a}_{k_{b'}} \hat{a}_{k_{a'}}\rangle\right]}{2\langle n\rangle\langle m\rangle + \langle n\rangle(2\langle n\rangle + 1) + \langle m\rangle(2\langle m\rangle + 1)} ,$$

which simplifies in the case of a symmetric average population $\langle n\rangle = \langle m\rangle$ to

$$E(\theta) = \frac{\mathrm{Re}\left[e^{i\theta}\langle \hat{a}^\dagger_{k_{a''}} \hat{a}^\dagger_{k_{b''}} \hat{a}_{k_{b'}} \hat{a}_{k_{a'}}\rangle\right]}{\langle n\rangle(3\langle n\rangle + 1)} .$$

The unknown term left is then the numerator $\langle \hat{a}^\dagger_{k_{a''}} \hat{a}^\dagger_{k_{b''}} \hat{a}_{k_{b'}} \hat{a}_{k_{a'}}\rangle$. From Ref. [87], it is possible to express this term for the parametric conversion state as

$$\langle \hat{a}^\dagger_{k_{a''}} \hat{a}^\dagger_{k_{b''}} \hat{a}_{k_{b'}} \hat{a}_{k_{a'}}\rangle = \langle n\rangle (1 + \langle n\rangle) .$$

Then the expression of $E(\theta)$ can finally be expressed as

$$E(\theta) = \frac{\cos(\theta)\,(1 + \langle n\rangle)}{(1 + 3\langle n\rangle)} ,$$

leading to

$$S = |E(\pi/4) - E(-3\pi/4) + E(-\pi/4) + E(\pi/4)| = 2\sqrt{2}\,\frac{(1 + \langle n\rangle)}{(1 + 3\langle n\rangle)} ,$$

which reaches a maximum value of $S = 2\sqrt{2} \approx 2.8$ for $\langle n\rangle = 0$ and decreases to $S = \frac{2}{3}\sqrt{2} \approx 0.93$ for $\langle n\rangle \to \infty$. Thus, the CHSH's inequality is violated when the number of particles is reduced and verified for increasing averaged densities. As for the HOM experiment, it is preferable to work with very weak average particle number per input beam. The threshold value, above which the inequality is no longer violated, corresponds to an average population $\langle n\rangle = 0.26$.

Appendix Bibliography

[7] J. F. Clauser, M. A. Horne, A. Shimony, and R. A. Holt, "Proposed Experiment to Test Local Hidden-Variable Theories", Phys. Rev. Lett. **23**, 880–884 (1969) (cit. on pp. 3, 169, 200).

[64] F. Gerbier, "Quasi-1D Bose-Einstein condensates in the dimensional crossover regime", EPL (Europhysics Letters) **66**, 771 (2004) (cit. on pp. 6, 48, 59, 78, 173, 174).

[87] C. M. Savage, P. E. Schwenn, and K. V. Kheruntsyan, "First-principles quantum simulations of dissociation of molecular condensates: Atom correlations in momentum space", Phys. Rev. A **74**, 033620 (2006) (cit. on pp. 21, 202).

[142] M. Bonneau, "Atomic four-wave mixing in an optical lattice", Theses (Université Paris Sud - Paris XI, Dec. 2011) (cit. on pp. 38, 44, 45, 53, 54, 71, 83, 181).

[150] J.-C. Jaskula, "Creation and characterization of non-classical states for quantum atom optics", Theses (Université Paris Sud - Paris XI, Dec. 2010) (cit. on pp. 40–42, 50, 175, 176).

[151] R. Grimm, M. Weidemüller, and Y. B. Ovchinnikov, "Optical Dipole Traps for Neutral Atoms", in , Vol. 42, edited by B. Bederson and H. Walther, Adv. Atom. Mol. Opt. Phy. (Academic Press, 2000), pp. 95–170 (cit. on pp. 40, 66, 71, 178).

[168] M.-O. Mewes, M. R. Andrews, N. J. van Druten, D. M. Kurn, D. S. Durfee, C. G. Townsend, and W. Ketterle, "Collective Excitations of a Bose-Einstein Condensate in a Magnetic Trap", Phys. Rev. Lett. **77**, 988–991 (1996) (cit. on pp. 57, 175, 176).

[223] A. I. Lvovsky and M. G. Raymer, "Continuous-variable optical quantum-state tomography", Rev. Mod. Phys. **81**, 299–332 (2009) (cit. on p. 190).

Bibliography

[1] A. Einstein, B. Podolsky, and N. Rosen, "Can Quantum-Mechanical Description of Physical Reality Be Considered Complete?", Phys. Rev. **47**, 777–780 (1935) (cit. on pp. 3, 168).

[2] J. G. Cramer, "The transactional interpretation of quantum mechanics", Rev. Mod. Phys. **58**, 647–687 (1986) (cit. on pp. 3, 168).

[3] N. Bohr, "Can Quantum-Mechanical Description of Physical Reality be Considered Complete?", Phys. Rev. **48**, 696–702 (1935) (cit. on p. 3).

[4] E. Schrödinger, "Discussion of Probability Relations between Separated Systems", Mathematical Proceedings of the Cambridge Philosophical Society **31**, 555–563 (1935) (cit. on p. 3).

[5] E. Schrödinger, "Probability relations between separated systems", Mathematical Proceedings of the Cambridge Philosophical Society **32**, 446–452 (1936) (cit. on p. 3).

[6] J. S. Bell, "On the Einstein-Podolsky-Rosen paradox", Physics **1**, 195–200 (1964) (cit. on pp. 3, 169).

[7] J. F. Clauser, M. A. Horne, A. Shimony, and R. A. Holt, "Proposed Experiment to Test Local Hidden-Variable Theories", Phys. Rev. Lett. **23**, 880–884 (1969) (cit. on pp. 3, 169, 200).

[8] J. F. Clauser and A. Shimony, "Bell's theorem. Experimental tests and implications", Reports on Progress in Physics **41**, 1881 (1978) (cit. on p. 3).

[9] S. J. Freedman and J. F. Clauser, "Experimental Test of Local Hidden-Variable Theories", Phys. Rev. Lett. **28**, 938–941 (1972) (cit. on pp. 3, 168, 169).

[10] E. S. Fry and R. C. Thompson, "Experimental Test of Local Hidden-Variable Theories", Phys. Rev. Lett. **37**, 465–468 (1976) (cit. on p. 3).

[11] A. Aspect, P. Grangier, and G. Roger, "Experimental Tests of Realistic Local Theories via Bell's Theorem", Phys. Rev. Lett. **47**, 460–463 (1981) (cit. on p. 3).

[12] D. C. Burnham and D. L. Weinberg, "Observation of Simultaneity in Parametric Production of Optical Photon Pairs", Phys. Rev. Lett. **25**, 84–87 (1970) (cit. on pp. 3, 94).

[13] L.-A. Wu, H. J. Kimble, J. L. Hall, and H. Wu, "Generation of Squeezed States by Parametric Down Conversion", Phys. Rev. Lett. **57**, 2520–2523 (1986) (cit. on pp. 3, 14, 21, 72, 91).

[14] A. Aspect, "Proposed experiment to test the nonseparability of quantum mechanics", Phys. Rev. D **14**, 1944–1951 (1976) (cit. on p. 3).

[15] M. Lamehi-Rachti and W. Mittig, "Quantum mechanics and hidden variables: A test of Bell's inequality by the measurement of the spin correlation in low-energy proton-proton scattering", Phys. Rev. D **14**, 2543–2555 (1976) (cit. on p. 3).

[16] A. Aspect, P. Grangier, and G. Roger, "Experimental Realization of Einstein-Podolsky-Rosen-Bohm *Gedankenexperiment* : A New Violation of Bell's Inequalities", Phys. Rev. Lett. **49**, 91–94 (1982) (cit. on pp. 3, 168, 169).

[17] A. Aspect, J. Dalibard, and G. Roger, "Experimental Test of Bell's Inequalities Using Time-Varying Analyzers", Phys. Rev. Lett. **49**, 1804–1807 (1982) (cit. on pp. 3, 168, 169).

[18] J. G. Rarity and P. R. Tapster, "Experimental violation of Bell's inequality based on phase and momentum", Phys. Rev. Lett. **64**, 2495–2498 (1990) (cit. on pp. 3, 168, 169).

[19]G. Weihs, T. Jennewein, C. Simon, H. Weinfurter, and A. Zeilinger, "Violation of Bell's Inequality under Strict Einstein Locality Conditions", Phys. Rev. Lett. **81**, 5039–5043 (1998) (cit. on p. 3).
[20]M. A. Rowe, D. Kielpinski, V. Meyer, C. A. Sackett, W. M. Itano, C. Monroe, and D. J. Wineland, "Experimental violation of a Bell's inequality with efficient detection", Nature **409**, 791–794 (2001) (cit. on p. 3).
[21]M. Giustina, A. Mech, S. Ramelow, B. Wittmann, J. Kofler, J. Beyer, A. Lita, B. Calkins, T. Gerrits, S. W. Nam, R. Ursin, and A. Zeilinger, "Bell violation using entangled photons without the fair-sampling assumption", Nature **497**, 227–230 (2013) (cit. on p. 3).
[22]A. K. Ekert, "Quantum cryptography based on Bell's theorem", Phys. Rev. Lett. **67**, 661–663 (1991) (cit. on p. 3).
[23]J. L. Duligall, M. S. Godfrey, K. A. Harrison, W. J. Munro, and J. G. Rarity, "Low cost and compact quantum key distribution", New Journal of Physics **8**, 249 (2006) (cit. on p. 3).
[24]E. Knill, R. Laflamme, and G. J. Milburn, "A scheme for efficient quantum computation with linear optics", Nature **409**, 46–52 (2001) (cit. on pp. 3, 16).
[25]J. M. Raimond, M. Brune, and S. Haroche, "Manipulating quantum entanglement with atoms and photons in a cavity", Rev. Mod. Phys. **73**, 565–582 (2001) (cit. on p. 3).
[26]H. J. Kimble, "The quantum internet", Nature **453**, 1023–1030 (2008) (cit. on p. 3).
[27]C. H. Bennett, G. Brassard, C. Crépeau, R. Jozsa, A. Peres, and W. K. Wootters, "Teleporting an unknown quantum state via dual classical and Einstein-Podolsky-Rosen channels", Phys. Rev. Lett. **70**, 1895–1899 (1993) (cit. on p. 3).
[28]D. Bouwmeester, J.-W. Pan, K. Mattle, M. Eibl, H. Weinfurter, and A. Zeilinger, "Experimental quantum teleportation", Nature **390**, 575–579 (1997) (cit. on p. 3).
[29]R. Ursin, F. Tiefenbacher, T. Schmitt-Manderbach, H. Weier, T. Scheidl, M. Lindenthal, B. Blauensteiner, T. Jennewein, J. Perdigues, P. Trojek, B. Omer, M. Furst, M. Meyenburg, J. Rarity, Z. Sodnik, et al., "Entanglement-based quantum communication over 144[thinsp]km", Nat Phys **3**, 481–486 (2007) (cit. on p. 4).
[30]T. Scheidl, R. Ursin, A. Fedrizzi, S. Ramelow, X.-S. Ma, T. Herbst, R. Prevedel, L. Ratschbacher, J. Kofler, T. Jennewein, and A. Zeilinger, "Feasibility of 300 km quantum key distribution with entangled states", New. J. Phys. **11**, 085002 (2009) (cit. on p. 4).
[31]X.-S. Ma, T. Herbst, T. Scheidl, D. Wang, S. Kropatschek, W. Naylor, B. Wittmann, A. Mech, J. Kofler, E. Anisimova, V. Makarov, T. Jennewein, R. Ursin, and A. Zeilinger, "Quantum teleportation over 143 kilometres using active feed-forward", Nature **489**, 269–273 (2012) (cit. on pp. 4, 25).
[32]A. Rubenok, J. A. Slater, P. Chan, I. Lucio-Martinez, and W. Tittel, "Real-World Two-Photon Interference and Proof-of-Principle Quantum Key Distribution Immune to Detector Attacks", Phys. Rev. Lett. **111**, 130501 (2013) (cit. on pp. 4, 25).
[33]M. H. Anderson, J. R. Ensher, M. R. Matthews, C. E. Wieman, and E. A. Cornell, "Observation of Bose-Einstein Condensation in a Dilute Atomic Vapor", Science **269**, 198–201 (1995) (cit. on p. 4).
[34]M. Greiner, C. A. Regal, and D. S. Jin, "Emergence of a molecular Bose-Einstein condensate from a Fermi gas", Nature **426**, 537–540 (2003) (cit. on p. 4).
[35]W. S. Bakr, A. Peng, M. E. Tai, R. Ma, J. Simon, J. I. Gillen, S. Fölling, L. Pollet, and M. Greiner, "Probing the Superfluid–to–Mott Insulator Transition at the Single-Atom Level", Science **329**, 547–550 (2010) (cit. on p. 4).
[36]"A Quantum Gas Microscope for Fermionic Atoms", arXiv [1503.02648] (cit. on pp. 4, 27).
[37]J. Steinhauer, "Observation of self-amplifying Hawking radiation in an analogue black-hole laser", Nat Phys **10**, 864–869 (2014) (cit. on p. 4).
[38]O. Lahav, A. Itah, A. Blumkin, C. Gordon, S. Rinott, A. Zayats, and J. Steinhauer, "Realization of a Sonic Black Hole Analog in a Bose-Einstein Condensate", Phys. Rev. Lett. **105**, 240401 (2010) (cit. on p. 4).

[39]J.-C. Jaskula, G. Partridge, M. Bonneau, R. Lopes, J. Ruaudel, D. Boiron, and C. Westbrook, "Acoustic Analog to the Dynamical Casimir Effect in a Bose-Einstein Condensate", Phys. Rev. Lett. **109**, 220401 (2012) (cit. on pp. 4, 7, 34, 44, 46, 167, 217).
[40]M. Endres, T. Fukuhara, D. Pekker, M. Cheneau, P. Schau[bgr], C. Gross, E. Demler, S. Kuhr, and I. Bloch, "The /'Higgs/' amplitude mode at the two-dimensional superfluid/Mott insulator transition", Nature **487**, 454–458 (2012) (cit. on p. 4).
[41]L. Pollet and N. Prokof'ev, "Higgs Mode in a Two-Dimensional Superfluid", Phys. Rev. Lett. **109**, 010401 (2012) (cit. on p. 4).
[42]C. Salomon, N. Dimarcq, M. Abgrall, A. Clairon, P. Laurent, P. Lemonde, G. Santarelli, P. Uhrich, L. Bernier, G. Busca, A. Jornod, P. Thomann, E. Samain, P. Wolf, F. Gonzalez, et al., "Cold atoms in space and atomic clocks:" Comptes Rendus de l'Académie des Sciences - Series {IV} - Physics **2**, 1313–1330 (2001) (cit. on p. 4).
[43]A. D. Cronin, J. Schmiedmayer, and D. E. Pritchard, "Optics and interferometry with atoms and molecules", Rev. Mod. Phys. **81**, 1051–1129 (2009) (cit. on pp. 4, 108).
[44]M. Riebe, H. Haffner, C. F. Roos, W. Hansel, J. Benhelm, G. P. T. Lancaster, T. W. Korber, C. Becher, F. Schmidt-Kaler, D. F. V. James, and R. Blatt, "Deterministic quantum teleportation with atoms", Nature **429**, 734–737 (2004) (cit. on p. 4).
[45]R. Blatt and D. Wineland, "Entangled states of trapped atomic ions", Nature **453**, 1008–1015 (2008) (cit. on p. 4).
[46]C. Gross, H. Strobel, E. Nicklas, T. Zibold, N. Bar-Gill, G. Kurizki, and M. K. Oberthaler, "Atomic homodyne detection of continuous-variable entangled twin-atom states", Nature **480**, 219–223 (2011) (cit. on p. 4).
[47]J. M. Vogels, K. Xu, and W. Ketterle, "Generation of Macroscopic Pair-Correlated Atomic Beams by Four-Wave Mixing in Bose-Einstein Condensates", Phys. Rev. Lett. **89**, 020401 (2002) (cit. on pp. 4, 27).
[48]A. Perrin, H. Chang, V. Krachmalnicoff, M. Schellekens, D. Boiron, A. Aspect, and C. I. Westbrook, "Observation of Atom Pairs in Spontaneous Four-Wave Mixing of Two Colliding Bose-Einstein Condensates", Phys. Rev. Lett. **99**, 150405 (2007) (cit. on pp. 4, 27, 34, 167).
[49]M. Greiner, C. A. Regal, J. T. Stewart, and D. S. Jin, "Probing Pair-Correlated Fermionic Atoms through Correlations in Atom Shot Noise", Phys. Rev. Lett. **94**, 110401 (2005) (cit. on p. 4).
[50]J. Esteve, C. Gross, A. Weller, S. Giovanazzi, and M. K. Oberthaler, "Squeezing and entanglement in a Bose-Einstein condensate", Nature **455**, 1216–1219 (2008) (cit. on p. 4).
[51]J.-C. Jaskula, M. Bonneau, G. B. Partridge, V. Krachmalnicoff, P. Deuar, K. V. Kheruntsyan, A. Aspect, D. Boiron, and C. I. Westbrook, "Sub-Poissonian Number Differences in Four-Wave Mixing of Matter Waves", Phys. Rev. Lett. **105**, 190402 (2010) (cit. on pp. 4, 34, 39, 167).
[52]R. Bucker, J. Grond, S. Manz, T. Berrada, T. Betz, C. Koller, U. Hohenester, T. Schumm, A. Perrin, and J. Schmiedmayer, "Twin-atom beams", Nat Phys **7**, 608–611 (2011) (cit. on pp. 4, 27).
[53]H. Strobel, W. Muessel, D. Linnemann, T. Zibold, D. B. Hume, L. Pezzè, A. Smerzi, and M. K. Oberthaler, "Fisher information and entanglement of non-Gaussian spin states", Science **345**, 424–427 (2014) (cit. on pp. 4, 27, 162, 163).
[54]C. K. Hong, Z. Y. Ou, and L. Mandel, "Measurement of subpicosecond time intervals between two photons by interference", Phys. Rev. Lett. **59**, 2044–2046 (1987) (cit. on pp. 4, 13, 14, 16, 17, 130–132, 134, 143, 152).
[55]M. R. Ray and S. J. van Enk, "Verifying entanglement in the Hong-Ou-Mandel dip", Phys. Rev. A **83**, 042318 (2011) (cit. on p. 4).
[56]C. Lang, C. Eichler, L. Steffen, J. M. Fink, M. J. Woolley, A. Blais, and A. Wallraff, "Correlations, indistinguishability and entanglement in Hong-Ou-Mandel experiments at microwave frequencies", Nat Phys **9**, 345–348 (2013) (cit. on pp. 4, 25).

[57]J. Chen, J. B. Altepeter, M. Medic, K. F. Lee, B. Gokden, R. H. Hadfield, S. W. Nam, and P. Kumar, "Demonstration of a Quantum Controlled-NOT Gate in the Telecommunications Band", Phys. Rev. Lett. **100**, 133603 (2008) (cit. on p. 4).
[58]A. Crespi, R. Ramponi, R. Osellame, L. Sansoni, I. Bongioanni, F. Sciarrino, G. Vallone, and P. Mataloni, "Integrated photonic quantum gates for polarization qubits", Nat Commun **2**, 566 (2011) (cit. on p. 4).
[59]J. Dubois, T. Jullien, F. Portier, P. Roche, A. Cavanna, Y. Jin, W. Wegscheider, P. Roulleau, and D. C. Glattli, "Minimal-excitation states for electron quantum optics using levitons", Nature **502**, 659–663 (2013) (cit. on p. 4).
[60]E. Bocquillon, V. Freulon, J.-M. Berroir, P. Degiovanni, B. Plaçais, A. Cavanna, Y. Jin, and G. Fève, "Coherence and Indistinguishability of Single Electrons Emitted by Independent Sources", Science **339**, 1054–1057 (2013) (cit. on p. 4).
[61]J. S. Fakonas, H. Lee, Y. A. Kelaita, and H. A. Atwater, "Two-plasmon quantum interference", Nat Photon **8**, 317–320 (2014) (cit. on p. 4).
[62]G. Di Martino, Y. Sonnefraud, M. S. Tame, S. Ké na-Cohen, F. Dieleman, S. K. Ozdemir, M. S. Kim, and S. A. Maier, "Observation of Quantum Interference in the Plasmonic Hong-Ou-Mandel Effect", Phys. Rev. Applied **1**, 034004 (2014) (cit. on p. 4).
[63]A. M. Kaufman, B. J. Lester, C. M. Reynolds, M. L. Wall, M. Foss-Feig, K. R. A. Hazzard, A. M. Rey, and C. A. Regal, "Two-particle quantum interference in tunnel-coupled optical tweezers", Science **345**, 306–309 (2014) (cit. on pp. 4, 27).
[64]F. Gerbier, "Quasi-1D Bose-Einstein condensates in the dimensional crossover regime", EPL (Europhysics Letters) **66**, 771 (2004) (cit. on pp. 6, 48, 59, 78, 173, 174).
[65]V. V. Dodonov, "Dynamical Casimir effect: Some theoretical aspects", Journal of Physics: Conference Series **161**, 012027 (2009) (cit. on p. 7).
[66]F. X. Dezael and A. Lambrecht, "Analogue Casimir radiation using an optical parametric oscillator", EPL (Europhysics Letters) **89**, 14001 (2010) (cit. on p. 7).
[67]C. M. Wilson, G. Johansson, A. Pourkabirian, M. Simoen, J. R. Johansson, T. Duty, F. Nori, and P. Delsing, "Observation of the dynamical Casimir effect in a superconducting circuit", Nature **479**, 376–379 (2011) (cit. on p. 7).
[68]R. Lopes, A. Imanaliev, M. Bonneau, J. Ruaudel, M. Cheneau, D. Boiron, and C. I. Westbrook, "Second-order coherence of superradiance from a Bose-Einstein condensate", Phys. Rev. A **90**, 013615 (2014) (cit. on pp. 7, 34, 37, 53, 217).
[69]S. Inouye, A. P. Chikkatur, D. M. Stamper-Kurn, J. Stenger, D. E. Pritchard, and W. Ketterle, "Superradiant Rayleigh Scattering from a Bose-Einstein Condensate", Science **285**, 571–574 (1999) (cit. on p. 7).
[70]M. G. Moore and P. Meystre, "Theory of Superradiant Scattering of Laser Light from Bose-Einstein Condensates", Phys. Rev. Lett. **83**, 5202–5205 (1999) (cit. on p. 7).
[71]D. Schneble, G. K. Campbell, E. W. Streed, M. Boyd, D. E. Pritchard, and W. Ketterle, "Raman amplification of matter waves", Phys. Rev. A **69**, 041601 (2004) (cit. on p. 7).
[72]F. T. ppel, A. Aiello, and G. Leuchs, "All photons are equal but some photons are more equal than others", New. J. Phys. **14**, 093051 (2012) (cit. on pp. 13, 16).
[73]J. Beugnon, M. P. A. Jones, J. Dingjan, B. Darquié, G. Messin, A. Browaeys, and P. Grangier, "Quantum interference between two single photons emitted by independently trapped atoms", Nature **440**, 779–782 (2006) (cit. on p. 14).
[74]S. P. Walborn, A. N. de Oliveira, S. Pádua, and C. H. Monken, "Multimode Hong-Ou-Mandel Interference", Phys. Rev. Lett. **90**, 143601 (2003) (cit. on p. 16).
[75]Y. L. Lim and A. Beige, "Generalized Hong–Ou–Mandel experiments with bosons and fermions", New. J. Phys. **7**, 155–155 (2005) (cit. on p. 16).
[76]Z. Y. Ou, *Multi-Photon Quantum Interference* (Springer, 2007) (cit. on pp. 16, 153).

[77] T. B. Pittman, D. V. Strekalov, A. Migdall, M. H. Rubin, A. V. Sergienko, and Y. H. Shih, "Can Two-Photon Interference be Considered the Interference of Two Photons?", Phys. Rev. Lett. **77**, 1917–1920 (1996) (cit. on pp. 16, 130).
[78] Y. J. Lu, R. L. Campbell, and Z. Y. Ou, "Mode-Locked Two-Photon States", Phys. Rev. Lett. **91**, 163602 (2003) (cit. on p. 16).
[79] Z. Y. Ou, J.-K. Rhee, and L. J. Wang, "Observation of Four-Photon Interference with a Beam Splitter by Pulsed Parametric Down-Conversion", Phys. Rev. Lett. **83**, 959–962 (1999) (cit. on pp. 17, 130, 158).
[80] B. H. Liu, F. W. Sun, Y. X. Gong, Y. F. Huang, G. C. Guo, and Z. Y. Ou, "Four-photon interference with asymmetric beam splitters", Opt. Lett. **32**, 1320–1322 (2007) (cit. on p. 17).
[81] L. Mandel, "Photon interference and correlation effects produced by independent quantum sources", Phys. Rev. A **28**, 929–943 (1983) (cit. on p. 17).
[82] T. S. Iskhakov, K. Y. Spasibko, M. V. Chekhova, and G. Leuchs, "Macroscopic Hong–Ou–Mandel interference", New. J. Phys. **15**, 093036 (2013) (cit. on pp. 17, 18, 162).
[83] K. Y. Spasibko, F. Töppel, T. S. Iskhakov, M. Stobińska, M. V. Chekhova, and G. Leuchs, "Interference of macroscopic beams on a beam splitter: phase uncertainty converted into photon-number uncertainty", New. J. Phys. **16**, 013025 (2014) (cit. on pp. 17–19).
[84] R. Campos, B. Saleh, and M. Teich, "Quantum-mechanical lossless beam splitter: SU(2) symmetry and photon statistics", Physical Review A **40**, 1371–1384 (1989) (cit. on p. 18).
[85] R. J. Lewis-Swan and K. V. Kheruntsyan, "Proposal for demonstrating the Hong–Ou–Mandel effect with matter waves", Nat Commun **5** (2014) (cit. on pp. 20, 135).
[86] W. H. Louisell, A. Yariv, and A. E. Siegman, "Quantum Fluctuations and Noise in Parametric Processes. I.", Phys. Rev. **124**, 1646–1654 (1961) (cit. on pp. 21, 72).
[87] C. M. Savage, P. E. Schwenn, and K. V. Kheruntsyan, "First-principles quantum simulations of dissociation of molecular condensates: Atom correlations in momentum space", Phys. Rev. A **74**, 033620 (2006) (cit. on pp. 21, 202).
[88] G. Grynberg, A. Aspect, and C. Fabre, *Introduction aux lasers et à l'optique quantique* (Ecole polytechnique, Département de physique Paris, Palaiseau, 1997) (cit. on p. 23).
[89] G. Agarwal, *Quantum Optics*, Quantum Optics (Cambridge University Press, 2012) (cit. on p. 23).
[90] H.-A. Bachor and T. C. Ralph, *A Guide to Experiments in Quantum Optics, 2nd, Revised and Enlarged Edition* (Mar. 2004) (cit. on p. 23).
[91] P. Edwards, X. Huang, and Y. Li, "Novel Macroscopic Violation of a Cauchy Schwarz Inequality Using Bunched and Unbunched Twin Beams", in *Coherence and quantum optics vii*, edited by J. Eberly, L. Mandel, and E. Wolf (Springer US, 1996), pp. 713–714 (cit. on p. 24).
[92] H. J. Kimble, M. Dagenais, and L. Mandel, "Photon Antibunching in Resonance Fluorescence", Phys. Rev. Lett. **39**, 691–695 (1977) (cit. on p. 24).
[93] A. M. Marino, V. Boyer, and P. D. Lett, "Violation of the Cauchy-Schwarz Inequality in the Macroscopic Regime", Phys. Rev. Lett. **100**, 233601 (2008) (cit. on p. 24).
[94] J. M. Steele, *The Cauchy-Schwarz Master Class: An Introduction to the Art of Mathematical Inequalities* (Cambridge University Press, Cambridge, 2004) (cit. on p. 24).
[95] R. Glauber, "The Quantum Theory of Optical Coherence", Phys. Rev. **130**, 2529–2539 (1963) (cit. on pp. 25, 123).
[96] K. V. Kheruntsyan, J.-C. Jaskula, P. Deuar, M. Bonneau, G. B. Partridge, J. Ruaudel, R. Lopes, D. Boiron, and C. I. Westbrook, "Violation of the Cauchy-Schwarz Inequality with Matter Waves", Phys. Rev. Lett. **108**, 260401 (2012) (cit. on pp. 25, 28, 97, 98, 167, 217).
[97] T. Wasak, P. Sza ńkowski, P. Zi ń, M. Trippenbach, and J. Chwede ńczuk, "Cauchy-Schwarz inequality and particle entanglement", Phys. Rev. A **90**, 033616 (2014) (cit. on pp. 25, 98).
[98] P. G. Kwiat, K. Mattle, H. Weinfurter, A. Zeilinger, A. V. Sergienko, and Y. Shih, "New High-Intensity Source of Polarization-Entangled Photon Pairs", Phys. Rev. Lett. **75**, 4337–4341 (1995) (cit. on p. 25).

[99]C. Santori, D. Fattal, J. Vuckovic, G. S. Solomon, and Y. Yamamoto, "Indistinguishable photons from a single-photon device", Nature **419**, 594–597 (2002) (cit. on p. 25).
[100]A. Kuhn, M. Hennrich, and G. Rempe, "Deterministic Single-Photon Source for Distributed Quantum Networking", Phys. Rev. Lett. **89**, 067901 (2002) (cit. on p. 25).
[101]L.-M. Duan and C. Monroe, "*COLLOQUIUM* : QUANTUM NETWORKS WITH TRAPPED IONS", Rev. Mod. Phys. **82**, 1209–1224 (2010) (cit. on pp. 25, 27).
[102]P. Michler, A. Kiraz, C. Becher, W. V. Schoenfeld, P. M. Petroff, L. Zhang, E. Hu, and A. Imamoglu, "A Quantum Dot Single-Photon Turnstile Device", Science **290**, 2282–2285 (2000) (cit. on p. 25).
[103]T. Wasak, P. Sza ńkowski, P. Zi ń, M. Trippenbach, and J. Chwede ńczuk, "Cauchy-Schwarz inequality and particle entanglement", Phys. Rev. A **90**, 033616 (2014) (cit. on p. 25).
[104]B. Lücke, J. Peise, G. Vitagliano, J. Arlt, L. Santos, G. Tóth, and C. Klempt, "Detecting Multiparticle Entanglement of Dicke States", Phys. Rev. Lett. **112**, 155304 (2014) (cit. on p. 27).
[105]G. K. Campbell, J. Mun, M. Boyd, E. W. Streed, W. Ketterle, and D. E. Pritchard, "Parametric Amplification of Scattered Atom Pairs", Phys. Rev. Lett. **96**, 020406 (2006) (cit. on pp. 27, 45, 71, 86).
[106]T. Wilk, A. Gaëtan, C. Evellin, J. Wolters, Y. Miroshnychenko, P. Grangier, and A. Browaeys, "Entanglement of Two Individual Neutral Atoms Using Rydberg Blockade", Phys. Rev. Lett. **104**, 010502 (2010) (cit. on p. 27).
[107]A. G. Manning, R. Khakimov, R. G. Dall, and A. G. Truscott, "Single-Atom Source in the Picokelvin Regime", Phys. Rev. Lett. **113**, 130403 (2014) (cit. on p. 27).
[108]M. Bonneau, J. Ruaudel, R. Lopes, J.-C. Jaskula, A. Aspect, D. Boiron, and C. I. Westbrook, "Tunable source of correlated atom beams", Phys. Rev. A **87**, 061603 (2013) (cit. on pp. 27, 34, 44–46, 83, 91, 167, 217).
[109]E. Andersson, M. T. Fontenelle, and S. Stenholm, "Quantum statistics of atoms in microstructures", Phys. Rev. A **59**, 3841–3850 (1999) (cit. on pp. 27, 163, 164).
[110]W. S. Bakr, J. I. Gillen, A. Peng, S. Folling, and M. Greiner, "A quantum gas microscope for detecting single atoms in a Hubbard-regime optical lattice", Nature **462**, 74–77 (2009) (cit. on p. 27).
[111]J. F. Sherson, C. Weitenberg, M. Endres, M. Cheneau, I. Bloch, and S. Kuhr, "Single-atom-resolved fluorescence imaging of an atomic Mott insulator", Nature **467**, 68–72 (2010) (cit. on p. 27).
[112]E. Haller, J. Hudson, A. Kelly, D. Cotta, B. Peaudecerf, G. Bruce, and S. Kuhr, "Single-atom imaging of fermions in a quantum-gas microscope", arXiv [1503.02005v2] (cit. on p. 27).
[113]R. Bücker, A. Perrin, S. Manz, T. Betz, C. Koller, T. Plisson, J. Rottmann, T. Schumm, and J. Schmiedmayer, "Single-particle-sensitive imaging of freely propagating ultracold atoms", New. J. Phys. **11**, 103039 (2009) (cit. on p. 27).
[114]M. Schellekens, R. Hoppeler, A. Perrin, J. V. Gomes, D. Boiron, A. Aspect, and C. I. Westbrook, "Hanbury Brown Twiss Effect for Ultracold Quantum Gases", Science **310**, 648–651 (2005) (cit. on pp. 28, 34).
[115]J. V. Gomes, A. Perrin, M. Schellekens, D. Boiron, C. I. Westbrook, and M. Belsley, "Theory for a Hanbury Brown Twiss experiment with a ballistically expanding cloud of cold atoms", Phys. Rev. A **74**, 053607 (2006) (cit. on pp. 28, 120).
[116]D. M. Giltner, R. W. McGowan, and S. A. Lee, "Atom Interferometer Based on Bragg Scattering from Standing Light Waves", Phys. Rev. Lett. **75**, 2638–2641 (1995) (cit. on pp. 28, 106).
[117]E. M. Rasel, M. K. Oberthaler, H. Batelaan, J. Schmiedmayer, and A. Zeilinger, "Atom Wave Interferometry with Diffraction Gratings of Light", Phys. Rev. Lett. **75**, 2633–2637 (1995) (cit. on p. 28).
[118]M. Kozuma, L. Deng, E. W. Hagley, J. Wen, R. Lutwak, K. Helmerson, S. L. Rolston, and W. D. Phillips, "Coherent Splitting of Bose-Einstein Condensed Atoms with Optically Induced Bragg Diffraction", Phys. Rev. Lett. **82**, 871–875 (1999) (cit. on p. 28).

[119] A. Robert, O. Sirjean, A. Browaeys, J. Poupard, S. Nowak, D. Boiron, C. I. Westbrook, and A. Aspect, "A Bose-Einstein Condensate of Metastable Atoms", Science **292**, 461–464 (2001) (cit. on pp. 34, 40).
[120] R. Hanbury Brown and R. Q. Twiss, "Correlation between Photons in two Coherent Beams of Light", Nature **177**, 27–29 (1956) (cit. on p. 34).
[121] T. Jeltes, J. M. McNamara, W. Hogervorst, W. Vassen, V. Krachmalnicoff, M. Schellekens, A. Perrin, H. Chang, D. Boiron, A. Aspect, and C. I. Westbrook, "Comparison of the Hanbury Brown-Twiss effect for bosons and fermions.", Nature **445**, 402–5 (2007) (cit. on p. 34).
[122] R. Lopes, A. Imanaliev, A. Aspect, M. Cheneau, D. Boiron, and C. I. Westbrook, "Atomic Hong-Ou-Mandel experiment", Nature **520**, 66–68 (2015) (cit. on pp. 34, 37, 217).
[123] C. N. Cohen-Tannoudji, "Nobel Lecture: Manipulating atoms with photons", Rev. Mod. Phys. **70**, 707–719 (1998) (cit. on p. 34).
[124] W. D. Phillips, "Nobel Lecture: Laser cooling and trapping of neutral atoms", Rev. Mod. Phys. **70**, 721–741 (1998) (cit. on pp. 34, 39).
[125] F. Pereira Dos Santos, J. Léonard, J. Wang, C. J. Barrelet, F. Perales, E. Rasel, C. S. Unnikrishnan, M. Leduc, and C. Cohen-Tannoudji, "Bose-Einstein Condensation of Metastable Helium", Phys. Rev. Lett. **86**, 3459–3462 (2001) (cit. on p. 34).
[126] S. V. Nguyen, S. C. Doret, C. B. Connolly, R. A. Michniak, W. Ketterle, and J. M. Doyle, "Evaporative cooling of metastable helium in the multi-partial-wave regime", Phys. Rev. A **72**, 060703 (2005) (cit. on p. 34).
[127] A. S. Tychkov, T. Jeltes, J. M. McNamara, P. J. J. Tol, N. Herschbach, W. Hogervorst, and W. Vassen, "Metastable helium Bose-Einstein condensate with a large number of atoms", Phys. Rev. A **73**, 031603 (2006) (cit. on p. 34).
[128] R. Dall and A. Truscott, "Bose–Einstein condensation of metastable helium in a bi-planar quadrupole Ioffe configuration trap", Optics Communications **270**, 255–261 (2007) (cit. on p. 34).
[129] M. Keller, M. Kotyrba, F. Leupold, M. Singh, M. Ebner, and A. Zeilinger, "Bose-Einstein condensate of metastable helium for quantum correlation experiments", Phys. Rev. A **90**, 063607 (2014) (cit. on p. 34).
[130] Q. Bouton *et al.* (in preparation). (cit. on p. 34).
[131] W. Vassen, C. Cohen-Tannoudji, M. Leduc, D. Boiron, C. I. Westbrook, A. Truscott, K. Baldwin, G. Birkl, P. Cancio, and M. Trippenbach, "Cold and trapped metastable noble gases", Rev. Mod. Phys. **84**, 175–210 (2012) (cit. on p. 34).
[132] J. R. Anglin and W. Ketterle, "Bose-Einstein condensation of atomic gases", Nature **416**, 211–218 (2002) (cit. on p. 34).
[133] S. S. Hodgman, R. G. Dall, L. J. Byron, K. G. H. Baldwin, S. J. Buckman, and A. G. Truscott, "Metastable Helium: A New Determination of the Longest Atomic Excited-State Lifetime", Phys. Rev. Lett. **103**, 053002 (2009) (cit. on p. 37).
[134] S. Moal, M. Portier, J. Kim, J. Dugué, U. D. Rapol, M. Leduc, and C. Cohen-Tannoudji, "Accurate Determination of the Scattering Length of Metastable Helium Atoms Using Dark Resonances between Atoms and Exotic Molecules", Phys. Rev. Lett. **96**, 023203 (2006) (cit. on p. 37).
[135] M. Przybytek and B. Jeziorski, "Bounds for the scattering length of spin-polarized helium from high-accuracy electronic structure calculations", J. Chem. Phys. **123**, 134315 (2005) (cit. on p. 37).
[136] A. Browaeys, "Piégeage magnétique d'un gaz d'hélium métastable : vers la condensation de Bose-Einstein", Theses (Université Paris Sud - Paris XI, Nov. 2000) (cit. on pp. 35, 39, 40).
[137] H. Hoendervanger, Lynn, "A New Metastable Helium Machine : An Investigation into the Attributes of Trapping, Cooling and Detecting Metastable Helium", Theses (Institut d'Optique Graduate School, Oct. 2014) (cit. on p. 35).

[138] A. L. Hoendervanger, D. Clément, A. Aspect, C. I. Westbrook, D. Dowek, Y. J. Picard, and D. Boiron, "Influence of gold coating and interplate voltage on the performance of chevron micro-channel plates for temporally and spatially resolved single particle detection", Rev. Sci. Instrum. **84**, 023307, pages (2013) (cit. on p. 35).
[139] M. Schellekens, "The Hanbury Brown and Twiss Effet for Cold Atoms", Theses (Université Paris Sud - Paris XI, May 2007) (cit. on pp. 37–39).
[140] T. Wasak, J. Chwede ńczuk, P. Zi ń, and M. Trippenbach, "Raman scattering of atoms from a quasicondensate in a perturbative regime", Phys. Rev. A **86**, 043621 (2012) (cit. on p. 37).
[141] J. Ruaudel, "Creation and characterization of a tunable source of correlated atoms pairs", Theses (Institut d'Optique Graduate School, Dec. 2013) (cit. on pp. 38, 44, 45, 74, 77, 83, 86, 87).
[142] M. Bonneau, "Atomic four-wave mixing in an optical lattice", Theses (Université Paris Sud - Paris XI, Dec. 2011) (cit. on pp. 38, 44, 45, 53, 54, 71, 83, 181).
[143] A. J. Palmer, M. Baker, and R. T. Sang, "Quantitative comparison of rare-gas cold cathode discharge metastable atomic beam sources", Rev. Sci. Instrum. **75**, 5056–5058 (2004) (cit. on p. 39).
[144] W. Lu, M. D. Hoogerland, D. Milic, K. G. H. Baldwin, and S. J. Buckman, "A bright metastable atom source at 80 K", Rev. Sci. Instrum. **72**, 2558–2561 (2001) (cit. on p. 39).
[145] A. Aspect, N. Vansteenkiste, R. Kaiser, H. Haberland, and M. Karrais, "Preparation of a pure intense beam of metastable helium by laser cooling", Chemical Physics **145**, 307–315 (1990) (cit. on p. 39).
[146] P. O. Schmidt, S. Hensler, J. Werner, T. Binhammer, A. Görlitz, and T. Pfau, "Doppler cooling of an optically dense cloud of magnetically trapped atoms", J. Opt. Soc. Am. B **20**, 960–967 (2003) (cit. on p. 40).
[147] W. Ketterle, "Nobel lecture: When atoms behave as waves: Bose-Einstein condensation and the atom laser", Rev. Mod. Phys. **74**, 1131–1151 (2002) (cit. on pp. 40, 44).
[148] J. C. Viana Gomes, "THERMOMETRY AND COHERENCE PROPERTIES OF A ULTRA-COLD QUANTUM GAS OF METASTABLE HELIUM", Theses (Université Paris Sud - Paris XI, Feb. 2007) (cit. on p. 40).
[149] G. B. Partridge, J.-C. Jaskula, M. Bonneau, D. Boiron, and C. I. Westbrook, "Bose-Einstein condensation and spin mixtures of optically trapped metastable helium", Phys. Rev. A **81**, 053631 (2010) (cit. on pp. 40, 41).
[150] J.-C. Jaskula, "Creation and characterization of non-classical states for quantum atom optics", Theses (Université Paris Sud - Paris XI, Dec. 2010) (cit. on pp. 40–42, 50, 175, 176).
[151] R. Grimm, M. Weidemüller, and Y. B. Ovchinnikov, "Optical Dipole Traps for Neutral Atoms", in , Vol. 42, edited by B. Bederson and H. Walther, Adv. Atom. Mol. Opt. Phy. (Academic Press, 2000), pp. 95–170 (cit. on pp. 40, 66, 71, 178).
[152] W. Ketterle and N. J. van Druten, "Bose-Einstein condensation of a finite number of particles trapped in one or three dimensions", Phys. Rev. A **54**, 656–660 (1996) (cit. on p. 44).
[153] C. Pethick and H. Smith, *Bose-Einstein Condensation in Dilute Gases* (Cambridge University Press, 2002) (cit. on pp. 44, 75, 111).
[154] B. Wu and Q. Niu, "Landau and dynamical instabilities of the superflow of Bose-Einstein condensates in optical lattices", Phys. Rev. A **64**, 061603 (2001) (cit. on pp. 45, 71, 77–80).
[155] K. M. Hilligsøe and K. Mølmer, "Phase-matched four wave mixing and quantum beam splitting of matter waves in a periodic potential", Phys. Rev. A **71**, 041602 (2005) (cit. on pp. 45, 71).
[156] L. H. Thomas, "The calculation of atomic fields", P Camb. Philos. Soc. **23**, 542 (1927) (cit. on p. 47).
[157] E. Fermi, "Un metodo statistico per la determinazione di alcune proprietà dell'atomo.", Rend. Lincei **6**, 602–607 (1927) (cit. on p. 47).

[158]J. Esteve, J.-B. Trebbia, T. Schumm, A. Aspect, C. Westbrook, and I. Bouchoule, "Observations of Density Fluctuations in an Elongated Bose Gas: Ideal Gas and Quasicondensate Regimes", Phys. Rev. Lett. **96**, 130403 (2006) (cit. on p. 47).

[159]B. Paredes, A. Widera, V. Murg, O. Mandel, S. Folling, I. Cirac, G. V. Shlyapnikov, T. W. Hansch, and I. Bloch, "Tonks-Girardeau gas of ultracold atoms in an optical lattice", Nature **429**, 277–281 (2004) (cit. on p. 47).

[160]T. Kinoshita, T. Wenger, and D. S. Weiss, "Observation of a One-Dimensional Tonks-Girardeau Gas", Science **305**, 1125–1128 (2004) (cit. on p. 47).

[161]C. Menotti and S. Stringari, "Collective oscillations of a one-dimensional trapped Bose-Einstein gas", Phys. Rev. A **66**, 043610 (2002) (cit. on pp. 47, 48).

[162]D. S. Petrov, G. V. Shlyapnikov, and J. T. M. Walraven, "Phase-Fluctuating 3D Bose-Einstein Condensates in Elongated Traps", Phys. Rev. Lett. **87**, 050404 (2001) (cit. on p. 49).

[163]S. Dettmer, D. Hellweg, P. Ryytty, J. J. Arlt, W. Ertmer, K. Sengstock, D. S. Petrov, G. V. Shlyapnikov, H. Kreutzmann, L. Santos, and M. Lewenstein, "Observation of Phase Fluctuations in Elongated Bose-Einstein Condensates", Phys. Rev. Lett. **87**, 160406 (2001) (cit. on p. 53).

[164]S. Hofferberth, I. Lesanovsky, B. Fischer, T. Schumm, and J. Schmiedmayer, "Non-equilibrium coherence dynamics in one-dimensional Bose gases.", Nature **449**, 324–7 (2007) (cit. on p. 53).

[165]S. Manz, R. Bücker, T. Betz, C. Koller, S. Hofferberth, I. E. Mazets, A. Imambekov, E. Demler, A. Perrin, J. Schmiedmayer, and T. Schumm, "Two-point density correlations of quasicondensates in free expansion", Phys. Rev. A **81**, 031610 (2010) (cit. on p. 53).

[166]I. Bouchoule, M. Arzamasovs, K. V. Kheruntsyan, and D. M. Gangardt, "Two-body momentum correlations in a weakly interacting one-dimensional Bose gas", Phys. Rev. A **86**, 033626 (2012) (cit. on p. 53).

[167]Y. Castin and R. Dum, "Bose-Einstein Condensates in Time Dependent Traps", Phys. Rev. Lett. **77**, 5315–5319 (1996) (cit. on pp. 54, 55).

[168]M.-O. Mewes, M. R. Andrews, N. J. van Druten, D. M. Kurn, D. S. Durfee, C. G. Townsend, and W. Ketterle, "Collective Excitations of a Bose-Einstein Condensate in a Magnetic Trap", Phys. Rev. Lett. **77**, 988–991 (1996) (cit. on pp. 57, 175, 176).

[169]L. Landau and E. Lifshitz, *Mechanics, Course of Theoretical Physics, Volume 1*, Butterworth Heinemann (Butterworth-Heinemann, 1976), pp. 80–84 (cit. on p. 57).

[170]N. Ashcroft and N. Mermin, *Solid State Physics* (Saunders College, Philadelphia, 1976) (cit. on pp. 66, 68).

[171]C. Kittel, *Introduction to Solid State Physics*, 6th (John Wiley & Sons, Inc., New York, 1986) (cit. on pp. 66, 68).

[172]M. Greiner, "Ultracold quantum gases in three-dimensional optical lattice", PhD thesis (Ludwig-Maximilians-Universität München, 2003) (cit. on pp. 66, 68).

[173]J. H. Denschlag, J. E. Simsarian, H. Häffner, C. McKenzie, A. Browaeys, D. Cho, K. Helmerson, S. L. Rolston, and W. D. Phillips, "A Bose-Einstein condensate in an optical lattice", J. Phys. B-At. Mol. Opt. **35**, 3095 (2002) (cit. on pp. 68, 69, 106).

[174]A. Ferris, M. Davis, R. Geursen, P. Blakie, and A. Wilson, "Dynamical instabilities of Bose-Einstein condensates at the band edge in one-dimensional optical lattices", Phys. Rev. A **77**, 012712 (2008) (cit. on p. 68).

[175]N. Katz, E. Rowen, R. Ozeri, and N. Davidson, "Collisional Decay of a Strongly Driven Bose-Einstein Condensate", Phys. Rev. Lett. **95**, 220403 (2005) (cit. on p. 68).

[176]A. Messiah, *Quantum mechanics*, Quantum Mechanics vol. 1 (North-Holland, 1965) (cit. on p. 69).

[177]J. Dalibard, *Cours du collège de France* (2014) (cit. on pp. 69, 107).

[178]T. Gericke, F. Gerbier, A. Widera, S. Fölling, O. Mandel, and I. Bloch, "Adiabatic loading of a Bose–Einstein condensate in a 3D optical lattice", J. Mod. Optic **54**, 735–743 (2007) (cit. on pp. 69, 71, 83).

[179]M. Greiner, I. Bloch, O. Mandel, T. Hänsch, and T. Esslinger, "Exploring Phase Coherence in a 2D Lattice of Bose-Einstein Condensates", Phys. Rev. Lett. **87**, 160405 (2001) (cit. on pp. 69, 85, 106).
[180]M. Greiner, O. Mandel, T. Esslinger, T. W. Hansch, and I. Bloch, "Quantum phase transition from a superfluid to a Mott insulator in a gas of ultracold atoms", Nature **415**, 39–44 (2002) (cit. on p. 71).
[181]S. R. Clark and D. Jaksch, "Dynamics of the superfluid to Mott-insulator transition in one dimension", Phys. Rev. A **70**, 043612 (2004) (cit. on p. 71).
[182]H. Metcalf and P. Van der Straten, *Laser Cooling and Trapping*, Graduate texts in contemporary physics (Springer, 1999) (cit. on p. 71).
[183]F. Gerbier and Y. Castin, "Heating rates for an atom in a far-detuned optical lattice", Phys. Rev. A **82**, 013615 (2010) (cit. on p. 71).
[184]M. Modugno, C. Tozzo, and F. Dalfovo, "Role of transverse excitations in the instability of Bose-Einstein condensates moving in optical lattices", Phys. Rev. A **70**, 043625 (2004) (cit. on p. 71).
[185]O. Morsch and M. Oberthaler, "Dynamics of Bose-Einstein condensates in optical lattices", Rev. Mod. Phys. **78**, 179–215 (2006) (cit. on p. 71).
[186]L. Fallani, "Bose-Einstein condensates in optical lattices", Theses (Universitá degli Studi di Firenze Facoltà di Scienze Matematiche Fisiche e Naturali) (cit. on pp. 71, 88).
[187]K. Berg-Sørensen and K. Mølmer, "Bose-Einstein condensates in spatially periodic potentials", Phys. Rev. A **58**, 1480–1484 (1998) (cit. on p. 71).
[188]B. Wu and Q. Niu, "Superfluidity of Bose–Einstein condensate in an optical lattice: Landau–Zener tunnelling and dynamical instability", New. J. Phys. **5**, 104 (2003) (cit. on pp. 71, 72).
[189]L. De Sarlo, L. Fallani, J. Lye, M. Modugno, R. Saers, C. Fort, and M. Inguscio, "Unstable regimes for a Bose-Einstein condensate in an optical lattice", Phys. Rev. A **72**, 013603 (2005) (cit. on pp. 71, 85).
[190]N. Fabbri, D. Clément, L. Fallani, C. Fort, M. Modugno, K. van der Stam, and M. Inguscio, "Excitations of Bose-Einstein condensates in a one-dimensional periodic potential", Phys. Rev. A **79**, 043623 (2009) (cit. on p. 71).
[191]L. Fallani, L. De Sarlo, J. Lye, M. Modugno, R. Saers, C. Fort, and M. Inguscio, "Observation of Dynamical Instability for a Bose-Einstein Condensate in a Moving 1D Optical Lattice", Phys. Rev. Lett. **93**, 140406 (2004) (cit. on p. 71).
[192]J. Ruostekoski and L. Isella, "Dissipative Quantum Dynamics of Bosonic Atoms in a Shallow 1D Optical Lattice", Phys. Rev. Lett. **95**, 110403 (2005) (cit. on p. 71).
[193]M. Machholm, C. Pethick, and H. Smith, "Band structure, elementary excitations, and stability of a Bose-Einstein condensate in a periodic potential", Phys. Rev. A **67**, 053613 (2003) (cit. on pp. 72, 85).
[194]S. Burger, F. S. Cataliotti, C. Fort, P. Maddaloni, F. Minardi, and M. Inguscio, "Quasi-2D Bose-Einstein condensation in an optical lattice", EPL (Europhysics Letters) **57**, 1 (2002) (cit. on p. 72).
[195]L. Deng, E. W. Hagley, J. Wen, M. Trippenbach, Y. Band, P. S. Julienne, J. E. Simsarian, K. Helmerson, S. L. Rolston, and W. D. Phillips, "Four-wave mixing with matter waves", Nature **398**, 218–220 (1999) (cit. on p. 73).
[196]J. Ruostekoski and Z. Dutton, "Dynamical and energetic instabilities in multicomponent Bose-Einstein condensates in optical lattices", Phys. Rev. A **76**, 063607 (2007) (cit. on p. 85).
[197]P. L. Kapitza and P. A. M. Dirac, "The reflection of electrons from standing light waves", Math. Proc. Cambridge **29**, 297–300 (1933) (cit. on p. 111).
[198]M. R. Andrews, C. G. Townsend, H.-J. Miesner, D. S. Durfee, D. M. Kurn, and W. Ketterle, "Observation of Interference Between Two Bose Condensates", Science **275**, 637–641 (1997) (cit. on p. 119).

[199] A. J. Ferris, M. K. Olsen, and M. J. Davis, "Atomic entanglement generation and detection via degenerate four-wave mixing of a Bose-Einstein condensate in an optical lattice", Phys. Rev. A **79**, 043634 (2009) (cit. on p. 123).
[200] C. Cohen-Tannoudji, J. Dupont-Roc, and G. Grynberg, *Photons et atomes : introduction à l'électrodynamique quantique*, Savoirs actuels, Précédemment publié en co-édition par InterÉditions et CNRS Éditions (Paris, 1987), dans la collection Savoirs actuels, ISSN 0989-3334, avec un avant-propos différent (EDP sciences Paris, Les Ulis, 2001) (cit. on p. 123).
[201] R. Glauber, "Coherent and Incoherent States of the Radiation Field", Phys. Rev. **131**, 2766–2788 (1963) (cit. on p. 123).
[202] R. Glauber, "The Quantum Theory of Optical Coherence", Physical Review **130**, 2529–2539 (1963) (cit. on p. 123).
[203] M. A. Bernstein, K. F. King, and X. J. Zhou, *Handbook of MRI Pulse Sequences*, 1st ed. (Academic Press, Sept. 21, 2004) (cit. on p. 125).
[204] A. Tannús and M. Garwood, "Adiabatic pulses", NMR in Biomedicine **10**, 423–434 (1997) (cit. on p. 125).
[205] T. Esslinger, F. Sander, M. Weidemüller, A. Hemmerich, and T. Hänsch, "Subrecoil Laser Cooling with Adiabatic Transfer", Phys. Rev. Lett. **76**, 2432–2435 (1996) (cit. on p. 125).
[206] J. G. Rarity and P. R. Tapster, "Fourth-order interference in parametric downconversion", J. Opt. Soc. Am. B **6**, 1221–1226 (1989) (cit. on pp. 130, 134, 140, 158).
[207] J.-F. Morizur, S. Armstrong, N. Treps, J. Janousek, and H.-A. Bachor, "Spatial reshaping of a squeezed state of light", The European Physical Journal D **61**, 237–239 (2011) (cit. on pp. 134, 142).
[208] N. Treps, V. Delaubert, A. Maître, J. M. Courty, and C. Fabre, "Quantum noise in multipixel image processing", Phys. Rev. A **71**, 013820 (2005) (cit. on pp. 134, 142).
[209] M. Martinelli, N. Treps, S. Ducci, S. Gigan, A. Maître, and C. Fabre, "Experimental study of the spatial distribution of quantum correlations in a confocal optical parametric oscillator", Phys. Rev. A **67**, 023808 (2003) (cit. on pp. 134, 142).
[210] B. Lucke, M. Scherer, J. Kruse, L. Pezze, F. Deuretzbacher, P. Hyllus, O. Topic, J. Peise, W. Ertmer, J. Arlt, L. Santos, A. Smerzi, and C. Klempt, "Twin Matter Waves for Interferometry Beyond the Classical Limit", Science **334**, 773–6 (2011) (cit. on pp. 162, 163).
[211] L. Gil, R. Mukherjee, E. Bridge, M. Jones, and T. Pohl, "Spin Squeezing in a Rydberg Lattice Clock", Phys. Rev. Lett. **112**, 103601 (2014) (cit. on p. 163).
[212] N. Behbood, F. Martin Ciurana, G. Colangelo, M. Napolitano, G. z. Tó th, R. J. Sewell, and M. W. Mitchell, "Generation of Macroscopic Singlet States in a Cold Atomic Ensemble", Phys. Rev. Lett. **113**, 093601 (2014) (cit. on p. 163).
[213] M. F. Riedel, P. Böhi, Y. Li, T. W. Hänsch, A. Sinatra, and P. Treutlein, "Atom-chip-based generation of entanglement for quantum metrology", Nature **464**, 1170–1173 (2010) (cit. on p. 163).
[214] C. Gross, T. Zibold, E. Nicklas, J. Estève, and M. K. Oberthaler, "Nonlinear atom interferometer surpasses classical precision limit", Nature **464**, 1165–1169 (2010) (cit. on p. 163).
[215] T. Berrada, S. van Frank, R. Bücker, T. Schumm, J.-F. Schaff, and J. Schmiedmayer, "Integrated Mach–Zehnder interferometer for Bose–Einstein condensates", Nat Commun **4** (2013) (cit. on p. 163).
[216] C. F. Ockeloen, R. Schmied, M. F. Riedel, and P. Treutlein, "Quantum Metrology with a Scanning Probe Atom Interferometer", Phys. Rev. Lett. **111**, 143001 (2013) (cit. on p. 163).
[217] W. Muessel, H. Strobel, D. Linnemann, D. B. Hume, and M. K. Oberthaler, "Scalable Spin Squeezing for Quantum-Enhanced Magnetometry with Bose-Einstein Condensates", Phys. Rev. Lett. **113**, 103004 (2014) (cit. on p. 163).
[218] A. Aspect, "Bell's inequality test: more ideal than ever", Nature **398**, 189–190 (1999) (cit. on p. 168).

[219] R. J. Lewis-Swan and K. V. Kheruntsyan, "Proposal for a motional-state Bell inequality test with ultracold atoms", Phys. Rev. A **91**, 052114 (2015) (cit. on pp. 169, 170).
[220] R. Penrose, "On Gravity's role in Quantum State Reduction", English, General Relativity and Gravitation **28**, 581–600 (1996) (cit. on p. 170).
[221] R. Penrose, "Quantum computation, entanglement and state reduction", Philosophical Transactions of the Royal Society of London. Series A: Mathematical, Physical and Engineering Sciences **356**, 1927–1939 (1998) (cit. on p. 170).
[222] M. Czachor, "Einstein-Podolsky-Rosen-Bohm experiment with relativistic massive particles", Phys. Rev. A **55**, 72–77 (1997) (cit. on p. 170).
[223] A. I. Lvovsky and M. G. Raymer, "Continuous-variable optical quantum-state tomography", Rev. Mod. Phys. **81**, 299–332 (2009) (cit. on p. 190).

List of publications

Violation of the Cauchy-Schwarz Inequality with Matter Waves

K. V. Kheruntsyan, J.-C. Jaskula, P. Deuar, M. Bonneau, G. B. Partridge, J. Ruaudel, R. Lopes, D. Boiron, and C. I. Westbrook

Phys. Rev. Lett. **108**, 260401 (2012)

Cited as [96]

Acoustic Analog to the Dynamical Casimir Effect in a Bose-Einstein Condensate

J.-C. Jaskula, G. B. Partridge, M. Bonneau, R. Lopes, J. Ruaudel, D. Boiron, and C. I. Westbrook

Phys. Rev. Lett. **109**, 220401 (2012)

Cited as [39]

Tunable source of correlated atom beams

M. Bonneau, J. Ruaudel, R. Lopes, J.-C. Jaskula, A. Aspect, D. Boiron, and C. I. Westbrook

Phys. Rev. A **87** 061603(R) (2013)

Cited as [108]

Second-order coherence of superradiance from a Bose-Einstein condensate

R. Lopes, A. Imanaliev, M. Bonneau, J. Ruaudel, M. Cheneau, D. Boiron, and C. I. Westbrook

Phys. Rev. A **90**, 013615 (2014)

Cited as [68]

Atomic Hong-Ou-Mandel experiment

R.Lopes, A. Imanaliev, A. Aspect, M. Cheneau, D. Boiron, C-I. Westbrook

Nature **520**, 66-68 (2015).

Cited as [122]

Violation of the Cauchy-Schwarz Inequality with Matter Waves

K. V. Kheruntsyan,[1] J.-C. Jaskula,[2,*] P. Deuar,[3] M. Bonneau,[2] G. B. Partridge,[2,†] J. Ruaudel,[2] R. Lopes,[2] D. Boiron,[2] and C. I. Westbrook[2]

[1]*The University of Queensland, School of Mathematics and Physics, Brisbane, Queensland 4072, Australia*
[2]*Laboratoire Charles Fabry de l'Institut d'Optique, CNRS, Université Paris-Sud, Campus Polytechnique RD128, 91127 Palaiseau, France*
[3]*Institute of Physics, Polish Academy of Sciences, Al. Lotników 32/46, 02-668 Warsaw, Poland*
(Received 30 March 2012; published 25 June 2012)

The Cauchy-Schwarz (CS) inequality—one of the most widely used and important inequalities in mathematics—can be formulated as an upper bound to the strength of correlations between classically fluctuating quantities. Quantum-mechanical correlations can, however, exceed classical bounds. Here we realize four-wave mixing of atomic matter waves using colliding Bose-Einstein condensates, and demonstrate the violation of a multimode CS inequality for atom number correlations in opposite zones of the collision halo. The correlated atoms have large spatial separations and therefore open new opportunities for extending fundamental quantum-nonlocality tests to ensembles of massive particles.

DOI: 10.1103/PhysRevLett.108.260401 PACS numbers: 03.75.Be, 03.75.Gg, 34.50.Cx, 42.50.Dv

The Cauchy-Schwarz (CS) inequality is ubiquitous in mathematics and physics [1]. Its utility ranges from proofs of basic theorems in linear algebra to the derivation of the Heisenberg uncertainty principle. In its basic form, the CS inequality simply states that the absolute value of the inner product of two vectors cannot be larger than the product of their lengths. In probability theory and classical physics, the CS inequality can be applied to fluctuating quantities and states that the expectation value of the cross correlation $\langle I_1 I_2 \rangle$ between two quantities I_1 and I_2 is bounded from above by the autocorrelations in each quantity,

$$|\langle I_1 I_2 \rangle| \leq \sqrt{\langle I_1^2 \rangle \langle I_2^2 \rangle}. \tag{1}$$

This inequality is satisfied, for example, by two classical currents emanating from a common source.

In quantum mechanics, correlations can, however, be stronger than those allowed by the CS inequality [2–4]. Such correlations have been demonstrated in quantum optics using, for example, antibunched photons produced via spontaneous emission [5], or twin photon beams generated in a radiative cascade [6], parametric down conversion [7], and optical four-wave mixing [8]. Here the discrete nature of the light and the strong correlation (or anticorrelation in antibunching) between photons is responsible for the violation of the CS inequality. The violation has even been demonstrated for two light beams detected as continuous variables [8].

In this work we demonstrate a violation of the CS inequality in matter-wave optics using pair-correlated atoms formed in a collision of two Bose-Einstein condensates (BECs) of metastable helium [9–12] (see Fig. 1). The CS inequality which we study is a *multimode* inequality, involving integrated atomic densities, and therefore is different from the typical two-mode situation studied in quantum optics. Our results demonstrate the potential of atom optics experiments to extend the fundamental tests of quantum mechanics to ensembles of massive particles. Indeed, violation of the CS inequality implies the possibility of (but is not equivalent to) formation of quantum states that exhibit the Einstein-Podolsky-Rosen (EPR) correlations or violate a Bell's inequality [3]. The EPR and Bell-state correlations are of course of wider significance

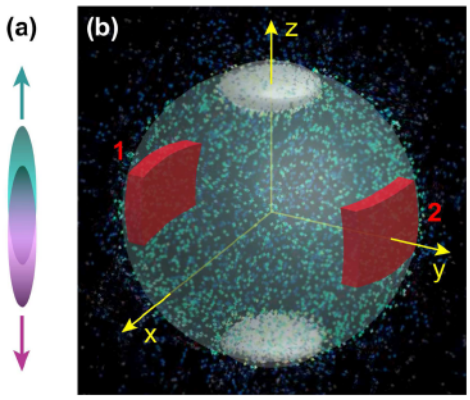

FIG. 1 (color online). Diagram of the collision geometry. (a) Two cigar-shaped condensates moving in opposite directions along the axial direction z shortly after their creation by a Bragg laser pulse (the anisotropy and spatial separation are not to scale). (b) Spherical halo of scattered atoms produced by four-wave mixing after the cloud expands and the atoms fall to the detector 46 cm below. During the flight to the detector, the unscattered condensates acquire a disk shape shown in white on the north and south poles of the halo. The (red) boxes 1 and 2 illustrate a pair of diametrically symmetric counting zones (integration volumes) for the average cross-correlation and autocorrelation functions, $\tilde{\mathcal{G}}_{12}^{(2)}$ and $\tilde{\mathcal{G}}_{ii}^{(2)}$ ($i = 1, 2$) (see text), used in the analysis of the Cauchy-Schwarz inequality.

 © 2012 American Physical Society

to foundational principles of quantum mechanics than those that violate a CS inequality. Nevertheless, the importance of understanding the CS inequality in new physical regimes lies in the fact that: (i) they are the simplest possible tests of stronger-than-classical correlations, and (ii) they can be viewed as precursors, or necessary conditions, for the stricter tests of quantum mechanics.

The atom-atom correlations resulting from the collision and violating the CS inequality are measured after long time-of-flight expansion using time- and position-resolved atom detection techniques unique to metastable atoms [13]. The 307 ms long expansion time combined with a large collision and hence scattering velocity results in a ~6 cm spatial separation between the scattered, correlated atoms. This separation is quite large compared to what has been achieved in recent related BEC experiments based on double-well or two-component systems [14–16], trap modulation techniques [17], or spin-changing interactions [18,19]. This makes the BEC collisions ideally suited to quantum-nonlocality tests using ultracold atomic gases and the intrinsic interatomic interactions.

In a simple two-mode quantum problem, described by boson creation and annihilation operators $\hat{a}_i^\dagger$ and $\hat{a}_i$ ($i = 1, 2$), the Cauchy-Schwarz inequality of the form of Eq. (1) can be formulated in terms of the second-order correlation functions, $G_{ij}^{(2)} = \langle :\hat{n}_i \hat{n}_j: \rangle = \langle \hat{a}_i^\dagger \hat{a}_j^\dagger \hat{a}_j \hat{a}_i \rangle$, and reads [2–4]

$$G_{12}^{(2)} \leq [G_{11}^{(2)} G_{22}^{(2)}]^{1/2}, \tag{2}$$

or simply $G_{12}^{(2)} \leq G_{11}^{(2)}$ in the symmetric case of $G_{11}^{(2)} = G_{22}^{(2)}$. Here, $G_{12}^{(2)} = G_{21}^{(2)}$, $\hat{n}_i = \hat{a}_i^\dagger \hat{a}_i$ is the particle number operator, and the double colons indicate normal ordering of the creation and annihilation operators, which ensures the correct quantum-mechanical interpretation of the process of detection of pairs of particles that contribute to the measurement of the second-order correlation function [2]. Stronger-than-classical correlation violating this inequality would require $G_{12}^{(2)} > [G_{11}^{(2)} G_{22}^{(2)}]^{1/2}$, or $G_{12}^{(2)} > G_{11}^{(2)}$ in the symmetric case.

The situation we analyze here is counterintuitive in that we observe a peak cross correlation (for pairs of atoms scattered in opposite directions) that is smaller than the peak autocorrelation (for pairs of atoms propagating in the same direction). In a simple two-mode model such a ratio of the cross correlation and autocorrelation satisfies the classical CS inequality. However, in order to adequately treat the atom-atom correlations in the BEC collision problem, one must generalize the CS inequality to a multimode situation, which takes into account the fact that the cross correlations and autocorrelations in matter-wave optics are usually *functions* (in our case of momentum). The various correlation functions can have different widths and peak heights, and one must define an appropriate integration domain over multiple momentum modes to recover an inequality that plays the same role as that in the two-mode case and *is* actually violated, as we show below.

The experimental setup was described in Refs. [11,12]. Briefly, a cigar-shaped BEC of metastable helium, containing approximately $\sim 10^5$ atoms, trapped initially in a harmonic trapping potential with frequencies $(\omega_x, \omega_y, \omega_z)/2\pi = (1500, 1500, 7.5)$ Hz, was split by Bragg diffraction into two parts along the axial (z-) direction [see Fig. 1(a)], with velocities differing by twice the single photon recoil velocity $v_{\rm rec} = 9.2$ cm/s. Atoms interact via binary, momentum conserving s-wave collisions and scatter onto a nearly spherical halo [see Fig. 1(b)] whose radius in velocity space is about the recoil velocity [11,20]. The scattered atoms fall onto a detector that records the arrival times and positions of individual atoms [13] with a quantum efficiency of ~10%. The halo diameter in position space at the detector is ~6 cm. We use the arrival times and positions to reconstruct three-dimensional velocity vectors $\mathbf{v}$ for each atom. The unscattered BECs locally saturate the detector. To quantify the strength of correlations corresponding only to spontaneously scattered atoms, we exclude from the analysis the data points containing the BECs and their immediate vicinity ($|v_z| < 0.5 v_{\rm rec}$) and further restrict ourselves to a spherical shell of radial thickness $0.9 < v_r/v_{\rm rec} < 1.1$ (where the signal to noise is large enough), defining the total volume of the analyzed region as $\mathcal{V}_{\rm data}$.

Using the atom arrival and position data, we can measure the second-order correlation functions between the atom number densities $\hat{n}(\mathbf{k})$ at two points in momentum space, $\mathcal{G}^{(2)}(\mathbf{k}, \mathbf{k}') = \langle :\hat{n}(\mathbf{k})\hat{n}(\mathbf{k}'): \rangle$ (see Supplementary Material [21]), with $\mathbf{k}$ denoting the wave vector $\mathbf{k} = m\mathbf{v}/\hbar$ and $\hbar\mathbf{k}$ the momentum. The correlation measurements are averaged over a certain counting zone (integration volume $\mathcal{V}$) on the scattering sphere in order to get statistically significant results. By choosing $\mathbf{k}'$ to be nearly opposite or nearly collinear to $\mathbf{k}$, we can define the averaged back-to-back (BB) or collinear (CL) correlation functions,

$$\mathcal{G}_{\rm BB}^{(2)}(\Delta\mathbf{k}) = \int_{\mathcal{V}} d^3\mathbf{k}\, \mathcal{G}^{(2)}(\mathbf{k}, -\mathbf{k} + \Delta\mathbf{k}), \tag{3}$$

$$\mathcal{G}_{\rm CL}^{(2)}(\Delta\mathbf{k}) = \int_{\mathcal{V}} d^3\mathbf{k}\, \mathcal{G}^{(2)}(\mathbf{k}, \mathbf{k} + \Delta\mathbf{k}), \tag{4}$$

which play a role analogous to the cross-correlation and autocorrelation functions, $G_{12}^{(2)}$ and $G_{ii}^{(2)}$, in the simple two-mode problem discussed above. The BB and CL correlations are defined as functions of the relative displacement $\Delta\mathbf{k}$, while the dependence on $\mathbf{k}$ is lost due to the averaging.

The normalized BB and CL correlations functions, $g_{\rm BB}^{(2)}(\Delta\mathbf{k})$ and $g_{\rm CL}^{(2)}(\Delta\mathbf{k})$, averaged over the unexcised part of the scattering sphere $\mathcal{V}_{\rm data}$ are shown in Fig. 2. The BB correlation peak results from binary, elastic collisions between atoms, whereas the CL correlation peak is a variant

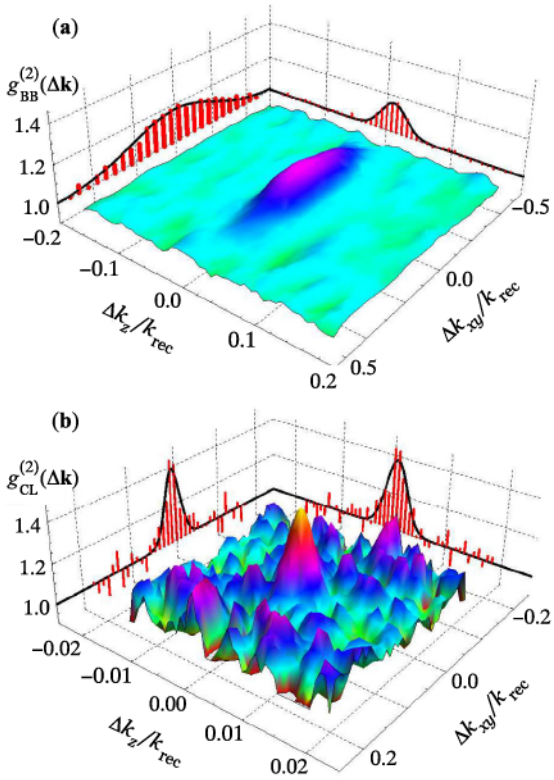

FIG. 2 (color online). Normalized back-to-back (a) and collinear (b) correlation functions, $g^{(2)}_{BB}(\Delta\mathbf{k})$ and $g^{(2)}_{CL}(\Delta\mathbf{k})$, in momentum space integrated over $\mathcal{V}_{data}$ corresponding to $|k_z| < 0.5k_{rec}$ and $0.9 < k_r/k_{rec} < 1.1$, where $k_{rec} = mv_{rec}/\hbar$ is the recoil momentum. The data are averaged over 3600 experimental runs. Because of the cylindrical symmetry of the initial condensate and of the overall geometry of the collision, the dependence on the k_x and k_y components should physically be identical and therefore can be combined (averaged); the correlation functions can then be presented as two-dimensional surface plots on the (k_z, k_{xy}) plane. The two-dimensional plots were smoothed with a nearest neighbor running average. The data points along the k_z and k_{xy} projections (corresponding to thin slices centered at $k_{xy} = 0$ and $k_z = 0$, respectively) are not smoothed. The solid lines show the Gaussian fits to these projections. The peak height of the back-to-back correlation function is ~1.2 while that of the collinear correlation function is ~1.4, apparently confirming the Cauchy-Schwarz inequality. The widths of the two distributions are, however, very different ($\sigma_{BB,x} \simeq \sigma_{BB,y} \simeq 0.21k_{rec}$, $\sigma_{BB,z} \simeq 0.019k_{rec}$, whereas $\sigma_{CL,x} \simeq \sigma_{CL,y} \simeq 0.036k_{rec}$, $\sigma_{CL,z} \simeq 0.002k_{rec}$) and a multimode formulation of the Cauchy-Schwarz inequality, which relates the relative volumes of the correlation functions, *is* violated.

of the Hanbury Brown and Twiss effect [22,23]—a two-particle interference involving members of two different atom pairs [9,10,24,25]. Both correlation functions are anisotropic because of the anisotropy of the initial colliding condensates.

An important difference with the experiment of Ref. [9] is that the geometry in the present experiment (with vertically elongated condensates) is such that the observed widths of the correlation functions are not limited by the detector resolution. Here we now observe that the BB and CL correlations have very different widths, with the BB width being significantly larger than the CL width. This broadening is largely due to the size of the condensate in the vertical direction (~ 1 mm). The elongated nature of the cloud and the estimated temperature of ~200 nK also means that the condensates correspond in fact to *quasicondensates* [26] whose phase coherence length is smaller than the size of the atomic cloud. The broadening of the BB correlation due to the presence of quasicondensates will be discussed in another paper [27], but we emphasize that the CS inequality analyzed here is insensitive to the detailed broadening mechanism as it relies on integrals over correlation functions. This is one of the key points in considering the multimode CS inequality.

Since the peak of the CL correlation function corresponds to a situation in which the two atoms follow the same path, we can associate it with the autocorrelation of the momentum of the particles on the collision sphere. Similarly, the peak of the BB correlation function corresponds to two atoms following two distinct paths and therefore can be associated with the cross-correlation function between the respective momenta. Hence we realize a situation in which one is tempted to apply the CS inequality to the peak values of these correlation functions. As we see from Fig. 2, if one naively uses only the peak heights, the CS inequality is *not* violated since $g^{(2)}_{BB}(0) < g^{(2)}_{CL}(0)$ and hence $\mathcal{G}^{(2)}_{BB}(0) < \mathcal{G}^{(2)}_{CL}(0)$ due to the nearly identical normalization factors (see Supplementary Material [21]).

We can, however, construct a CS inequality that *is* violated if we use integrated correlation functions, $\bar{\mathcal{G}}^{(2)}_{ij}$, that correspond to atom numbers $\hat{N}_i = \int_{\mathcal{V}_i} d^3\mathbf{k}\,\hat{a}^\dagger(\mathbf{k})\hat{a}(\mathbf{k})$ $(i = 1, 2)$ in two distinct zones on the collision halo [21],

$$\bar{\mathcal{G}}^{(2)}_{ij} = \langle :\hat{N}_i\hat{N}_j: \rangle = \int_{\mathcal{V}_i} d^3\mathbf{k} \int_{\mathcal{V}_j} d^3\mathbf{k}'\,\mathcal{G}^{(2)}(\mathbf{k}, \mathbf{k}'). \quad (5)$$

The choice of the two integration (zone) volumes $\mathcal{V}_i$ and $\mathcal{V}_j$ determines whether the $\bar{\mathcal{G}}^{(2)}_{ij}$-function corresponds to the BB $(i \neq j)$ or CL $(i = j)$ correlation functions, Eqs. (3) and (4).

The CS inequality that we can now analyze for violation reads $\bar{\mathcal{G}}^{(2)}_{12} \leq [\bar{\mathcal{G}}^{(2)}_{11}\bar{\mathcal{G}}^{(2)}_{22}]^{1/2}$. To quantify the degree of violation, we introduce a correlation coefficient,

$$C = \bar{\mathcal{G}}^{(2)}_{12}/[\bar{\mathcal{G}}^{(2)}_{11}\bar{\mathcal{G}}^{(2)}_{22}]^{1/2}, \quad (6)$$

which is smaller than unity classically, but can be larger than unity for states with stronger-than-classical correlations.

In Fig. 3 we plot the correlation coefficient C determined from the data for different integration zones $\mathcal{V}_1$ and $\mathcal{V}_2$, but always keeping the two volumes equal. When $\mathcal{V}_1$ and $\mathcal{V}_2$ correspond to diametrically opposed, correlated pairs

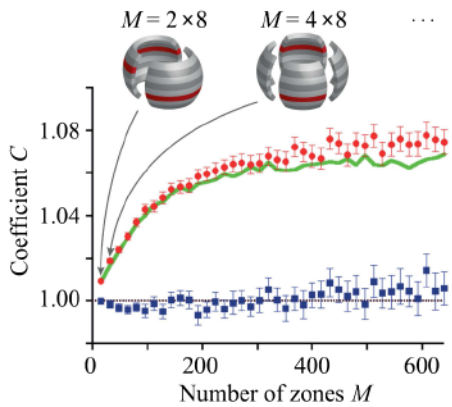

FIG. 3 (color online). Correlation coefficient C as a function of the number of zones $M = \mathcal{V}_{\rm data}/\mathcal{V}_1$ into which we cut the scattering sphere. $C > 1$ corresponds to violation of the Cauchy-Schwarz inequality. The scattering sphere was cut into 8 polar and from 2 to 80 azimuthal zones; the resulting arrangement of zones for $M = 16$ and 32 is illustrated in the upper panel. The observed values of C for pairs of correlated diametrically opposite zones (shown as darker red stripes in the upper panel as an example) were averaged to get one data point for a given M; the data points for such zones are shown as red circles, for uncorrelated (neighboring) zones—as blue squares. The error bars show the standard deviation of the mean over the number of zone pairs. The (green) thick solid curve is the theoretical prediction (see Supplementary Material [21]) calculated using the experimental parameters and a stochastic Bogoliubov approach [20,28].

of zones (red circles), C is greater than unity, violating the CS inequality, while for neighboring, uncorrelated pairs (blue squares) the CS inequality is not violated. The figure also shows the results of a quantum-mechanical calculation of C using a stochastic Bogoliubov approach (green thick solid curve) [20,21,28]. The calculation is for the initial total number of atoms $N = 85\,000$ and is in good agreement with the observations. The choice of large integration volumes (small number of zones M) results in only weak violations, while using smaller volumes (large M) increases the violation. This behavior is to be expected (see Supplementary Material [21]) because large integration zones include many, uncorrelated events which dilute the computed correlation. The saturation of C, in the current arrangement of integration zones—with a fixed number of polar cuts and hence a fixed zone size along z which always remains larger than the longitudinal correlation width—occurs when the tangential size of the zone begins to approach the transverse width of the CL correlation function. If the zone sizes were made smaller in all directions, we would recover the situation applicable to the peak values of the correlation functions (and hence no CS violation) as soon as the sizes become smaller than the respective correlation widths (see Eq. (S11) in the Supplementary Material [21]).

We have shown the violation of the CS inequality using the experimental data of Ref. [11] in which a sub-Poissonian variance in the atom number difference between opposite zones was observed. Although the two effects are linked mathematically in simple cases, they are not equivalent in general [8,21]. Because of the multimode nature of the four-wave mixing process, we observe stronger (weaker) suppression of the variance below the shot-noise level for the larger (smaller) zones (see Fig. 3 of [11]), whereas the degree of violation of the CS inequality follows the opposite trend. This difference can be of importance for other experimental tests of stronger-than-classical correlations in inherently multimode situations in matter-wave optics.

The nonclassical character of the observed correlations implies that the scattered atoms cannot be described by classical stochastic random variables [29]. Our experiment is an important step toward the demonstrations of increasingly restrictive types of nonlocal quantum correlations with matter waves, which we hope will one day culminate in the violation of a Bell inequality as well. In this case, the nonclassical character of correlations will also defy a description via a local hidden variable theory [4,29]. Nonoptical violations of Bell's inequalities have so far only been demonstrated for *pairs* of massive particles (such as two trapped ions [30] or proton-proton pairs in the decay of ^{2}He [31]), but never in the multiparticle regime. The BEC collision scheme used here is particularly well-suited for demonstrating a Bell inequality violation [32] using an atom optics analog of the Rarity-Tapster setup [33].

We thank P. Ziń and T. Wasak for useful discussions. K. V. K. is supported by the ARC FT100100285 grant, P. D. by Polish Government research grants for the years 2010–2013 and the EU contract PERG06-GA-2009-256291, J. R. by the DGA, R. L. by the FCT SFRH/BD/74352/2010, and support for the experimental work comes from the IFRAF program, the Triangle de la Physique, and the ANR grants DESINA and ProQuP.

*Current address: Harvard-Smithsonian Center for Astrophysics, Cambridge, MA 02138, USA.
†Current address: Agilent Laboratories, Santa Clara, CA 95051, USA.

[1] J. M. Steele, *The Cauchy-Schwarz Master Class: An Introduction to the Art of Mathematical Inequalities* (Cambridge University Press, Cambridge, England, 2004).
[2] R. J. Glauber, Phys. Rev. **130**, 2529 (1963).
[3] M. D. Reid and D. F. Walls, Phys. Rev. A **34**, 1260 (1986).
[4] D. F. Walls and G. J. Milburn, *Quantum Optics* (Springer-Verlag, Berlin, 2008), 2nd ed.
[5] H. J. Kimble, M. Dagenais, and L. Mandel, Phys. Rev. Lett. **39**, 691 (1977).
[6] J. F. Clauser, Phys. Rev. D **9**, 853 (1974).

[7] X. Zou, L. J. Wang, and L. Mandel, Opt. Commun. **84**, 351 (1991).
[8] A. M. Marino, V. Boyer, and P. D. Lett, Phys. Rev. Lett. **100**, 233601 (2008).
[9] A. Perrin, H. Chang, V. Krachmalnicoff, M. Schellekens, D. Boiron, A. Aspect, and C. I. Westbrook, Phys. Rev. Lett. **99**, 150405 (2007).
[10] A. Perrin, C. M. Savage, D. Boiron, V. Krachmalnicoff, C. I. Westbrook, and K. V. Kheruntsyan, New J. Phys. **10**, 045021 (2008).
[11] J.-C. Jaskula, M. Bonneau, G. B. Partridge, V. Krachmalnicoff, P. Deuar, K. V. Kheruntsyan, A. Aspect, D. Boiron, and C. I. Westbrook, Phys. Rev. Lett. **105**, 190402 (2010).
[12] G. B. Partridge, J.-C. Jaskula, M. Bonneau, D. Boiron, and C. I. Westbrook, Phys. Rev. A **81**, 053631 (2010).
[13] W. Vassen, C. Cohen-Tannoudji, M. Leduc, D. Boiron, C. I. Westbrook, A. Truscott, K. Baldwin, G. Birkl, P. Cancio, and M. Trippenbach, Rev. Mod. Phys. **84**, 175 (2012).
[14] J. Estève, C. Gross, A. Weller, S. Giovanazzi, and M. K. Oberthaler, Nature (London) **455**, 1216 (2008).
[15] C. Gross, T. Zibold, E. Nicklas, J. Estève, and M. K. Oberthaler, Nature (London) **464**, 1165 (2010).
[16] M. F. Riedel, P. Böhi, Y. Li, T. W. Hänsch, A. Sinatra, and P. Treutlein, Nature (London) **464**, 1170 (2010).
[17] R. Bücker, J. Grond, S. Manz, T. Berrada, T. Betz, C. Koller, U. Hohenester, T. Schumm, A. Perrin, and J. Schmiedmayer, Nature Phys. **7**, 608 (2011).
[18] B. Lücke, M. Scherer, J. Kruse, L. Pezzé, F. Deuretzbacher, P. Hyllus, O. Topic, J. Peise, W. Ertmer, J. Arlt, L. Santos, A. Smerzi, and C. Klempt, Science **334**, 773 (2011).
[19] E. M. Bookjans, C. D. Hamley, and M. S. Chapman, Phys. Rev. Lett. **107**, 210406 (2011).
[20] V. Krachmalnicoff, J.-C. Jaskula, M. Bonneau, V. Leung, G. B. Partridge, D. Boiron, C. I. Westbrook, P. Deuar, P. Ziń, M. Trippenbach, and K. V. Kheruntsyan, Phys. Rev. Lett. **104**, 150402 (2010).
[21] See Supplementary Material at http://link.aps.org/supplemental/10.1103/PhysRevLett.108.260401 for a more detailed discussion of correlation functions, the correlation coefficient C, and simulation methods.
[22] M. Schellekens, R. Hoppeler, A. Perrin, J. Viana Gomes, D. Boiron, A. Aspect, and C. I. Westbrook, Science **310**, 648 (2005).
[23] S. S. Hodgman, R. G. Dall, A. G. Manning, K. G. H. Baldwin, and A. G. Truscott, Science **331**, 1046 (2011).
[24] K. Mølmer, A. Perrin, V. Krachmalnicoff, V. Leung, D. Boiron, A. Aspect, and C. I. Westbrook, Phys. Rev. A **77**, 033601 (2008).
[25] M. Ögren and K. V. Kheruntsyan, Phys. Rev. A **79**, 021606 (2009).
[26] D. S. Petrov, G. V. Shlyapnikov, and J. T. M. Walraven, Phys. Rev. Lett. **87**, 050404 (2001).
[27] P. Deuar *et al.* (to be published).
[28] P. Deuar, J. Chwedeńczuk, M. Trippenbach, and P. Ziń, Phys. Rev. A **83**, 063625 (2011).
[29] C. Su and K. Wódkiewicz, Phys. Rev. A **44**, 6097 (1991).
[30] M. A. Rowe, D. Kielpinski, V. Meyer, C. A. Sackett, W. M. Itano, C. Monroe, and D. J. Wineland, Nature (London) **409**, 791 (2001).
[31] H. Sakai *et al.*, Phys. Rev. Lett. **97**, 150405 (2006).
[32] R. Lewis-Swan and K. V. Kheruntsyan (to be published).
[33] J. G. Rarity and P. R. Tapster, Phys. Rev. Lett. **64**, 2495 (1990).

Acoustic Analog to the Dynamical Casimir Effect in a Bose-Einstein Condensate

J.-C. Jaskula,* G. B. Partridge,† M. Bonneau, R. Lopes, J. Ruaudel, D. Boiron, and C. I. Westbrook

Laboratoire Charles Fabry, Institut d'Optique, CNRS, Université Paris-Sud, 2 avenue Augustin Fresnel, 91127 Palaiseau, France

(Received 5 July 2012; published 26 November 2012)

We have modulated the density of a trapped Bose-Einstein condensate by changing the trap stiffness, thereby modulating the speed of sound. We observe the creation of correlated excitations with equal and opposite momenta, and show that for a well-defined modulation frequency, the frequency of the excitations is half that of the trap modulation frequency.

DOI: 10.1103/PhysRevLett.109.220401 PACS numbers: 03.75.Kk, 42.50.Lc, 67.10.Jn

Although we often picture the quantum vacuum as containing virtual quanta whose observable effects are only indirect, it is a remarkable prediction of quantum field theory that the vacuum can generate real particles when boundary conditions are suddenly changed [1–4]. Known as the dynamical Casimir effect, a cavity with accelerating boundaries generates photon pairs. Recent experiments have demonstrated this effect in the microwave regime using superconducting circuits [5,6]. Hawking radiation [7] is another situation characterized by spontaneous pair creation and work on sonic analogs to the Hawking problem [8] has led to the realization that Bose-Einstein condensates (BEC) are attractive candidates to study such analog models [9–11], because their low temperatures promise to reveal quantum effects. Here we exhibit an acoustic analog to the dynamical Casimir effect by modulating the speed of sound in a BEC. We show that correlated pairs of elementary excitations, both phononlike and particlelike, are produced, in a process that formally resembles parametric down-conversion [4,12].

The first analyses of the dynamical Casimir effect considered moving mirrors, but it has been suggested that a changing index of refraction could mimic the effect [13,14]. Our experiment is motivated by a suggestion in Ref. [12] that one can realize an acoustic analog to the dynamical Casimir effect by changing the scattering length in an interacting Bose gas. The change in the interaction strength is analogous to an optical index change: the speed of sound (or light) changes. Seen in a more microscopic way, the ground state of such a gas is the vacuum of Bogoliubov quasiparticles whose makeup is interaction dependent. Changing the interaction strength projects this old vacuum onto a new state containing pairs of the new quasiparticles [12], which appear as pairwise excitations. Instead of changing the interaction strength, we have simply modified the confining potential, which in turn changes the density. Sudden changes such as these have also been suggested as analogs to cosmological phenomena [15–17].

We study two situations, in the first the confining potential is suddenly increased and in the second the potential is modulated sinusoidally. The sinusoidal modulation of the trapping potential was studied in Refs. [18–20] in the context of the observation of Faraday waves. Our results on sinusoidal modulation are similar to this work and we have extended it to observe correlated pairs of Bogoliubov excitations. We produce these excitations in both the phonon and particle regimes, and observe correlations in momentum space. Parametric excitation of a quantum gas was also studied in optical lattices in which the optical lattice depth was modulated [21,22], although in that experiment, the excitation was observed as a broadening of a momentum distribution.

The experimental apparatus is the same as that described in Refs. [23,24] and is shown schematically in Fig. 1(a). We start from a BEC of approximately 10^5 metastable helium (He^*) atoms evaporatively cooled in a vertical optical trap to a temperature of about 200 nK. The trapped cloud is cigar shaped with axial and radial frequencies of 7 and 1500 Hz. In the first experiment we raise the trapping laser intensity by a factor of 2 with a time constant of 50 μs using an acousto-optic modulator [see inset to Fig. 1(b)]. The trap frequencies thus increase by $\sqrt{2}$. The compressed BEC is held for 30 ms before the trap laser is switched off (in less than 10 μs). The cloud falls onto a position sensitive, single atom detector which allows us to measure the atom velocities [25]. After compression, the gas is excited principally in the vertical direction: transversely we only observe a slight heating (about 100 nK). Figure 1(b) shows a single shot distribution of vertical atom velocities relative to the center of mass and integrated horizontally, while Fig. 1(c) shows the same distribution averaged over 50 shots. These distributions are more than 1 order of magnitude wider than that of an unaffected BEC. The individual shots show a complex structure which is not reproduced from shot to shot, as is seen from the washing out of the peaks upon averaging.

We consider the correlations between atoms with vertical velocities v_z and v_z', by constructing a normalized second-order correlation function, $g^{(2)}(v_z, v_z')$ [25], averaged over the x-y plane and shown in Fig. 2(a). The plot exhibits two noticeable features along the $v_z' = v_z$ and $v_z' = -v_z$ diagonals. The former reflects the fluctuations in the momentum distribution, as in the Hanbury Brown–Twiss effect [26], except that this cloud is far from thermal

 © 2012 American Physical Society

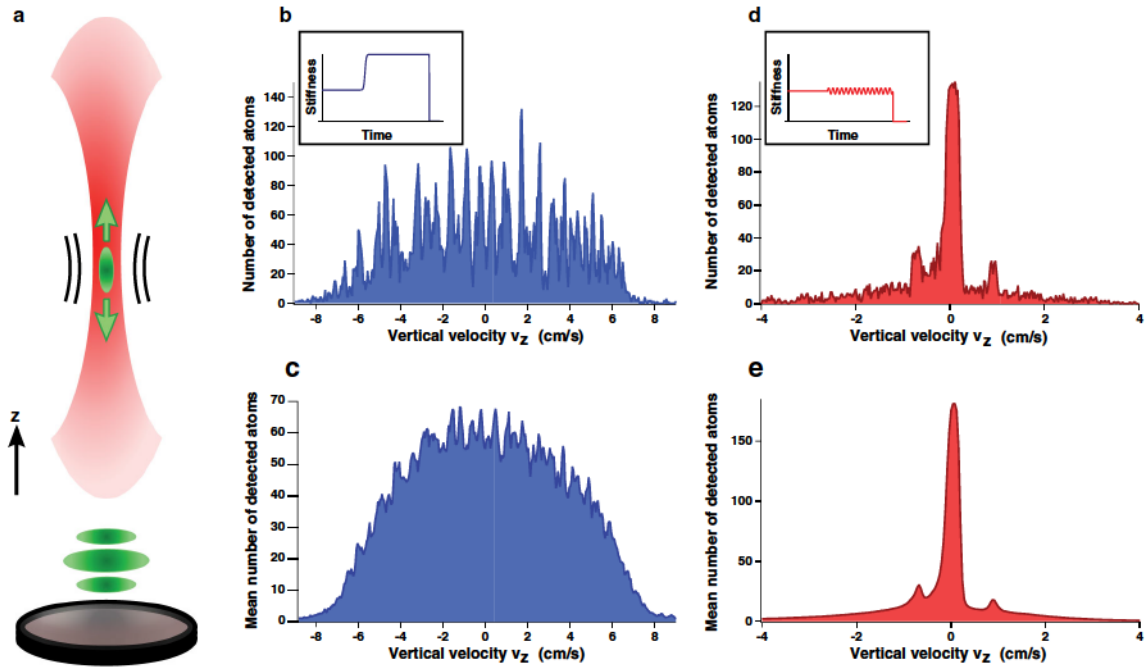

FIG. 1 (color online). Effects of time-varying potentials. (a) Schematic view of the experiment. Pairs of Bogoliubov quasiparticles are created by varying the trap stiffness. After the flight to the detector these excitations appear as a broadening or sidebands on the atom cloud in the vertical (z) direction. In the following plots we convert arrival times to relative velocities and average over the transverse dimensions. (b) Single shot velocity distribution for a cloud which was subjected to a sudden increase in the trap stiffness. The inset shows the time evolution of the trap stiffness. (c) As in (b) but averaged over 50 shots. (d) Single shot velocity distribution for a cloud which was subjected to a weak, sinusoidal modulation of the trap stiffness at 2.17 kHz. The inset shows the time evolution of the trap stiffness. (e) As in (d) but averaged over 780 shots.

equilibrium. The $v_z' = -v_z$ correlation is a clear signature of a correlation between quasiparticles of opposite velocities. A projection of this off-diagonal correlation is shown in Fig. 2(b). At low momentum, the excitations created by the perturbation are density waves (phonons) which in general consist of superpositions of several atoms traveling in opposite directions. In the conditions of our clouds, a phonon is adiabatically converted into a single atom of the same momentum during the release by a process referred to as "phonon evaporation" [27]. Therefore in the phonon regime as well as in the particle regime, we interpret the back-to-back correlation in Fig. 2(a) as the production of pairs of Bogoliubov excitations with oppositely directed momenta as predicted in the acoustic dynamical Casimir effect analysis [12].

To further study this process, we replace the compression by a sinusoidal modulation of the laser intensity $I(t) = I_0(1 + \delta \cos \omega_m t)$ [inset of Fig. 1(d)]. We choose δ such that the trap frequencies are modulated peak to peak by about 10%. The modulation is applied for 25 ms before releasing the condensate. Figures 1(d) and 1(e) show, respectively, single shot and averaged momentum distributions resulting from the modulation. One sees that the momentum distribution develops sidebands, approximately symmetrically placed about the center. Figure 3(a) shows the normalized correlation function, plotted in the same way as in Fig. 2(a), for a modulation frequency $\omega_m/2\pi = 2170$ Hz. We again observe antidiagonal correlations as for a sudden excitation except that the correlations now appear at a well-defined velocity, which coincides with that of the sidebands [see Fig. 3(b)].

We have examined sinusoidal modulation for frequencies $\omega_m/2\pi$ between 900 and 5000 Hz and observed excitations similar to those in Fig. 3. We summarize our observations in Fig. 4(a) in which we plot the excitation frequency as a function of the sideband velocity. We also plot the locations of the peaks in the correlation functions on the same graph. For modulation frequencies much above 2 kHz, the antidiagonal correlation functions are quite noisy preventing us from clearly identifying correlation peaks. This noise may have to do with the proximity of the parametric resonance with the transverse trap frequency (~ 3 kHz) [19].

A weakly interacting quantum gas obeys the well-known Bogoliubov–de Gennes dispersion relation between the frequency $\omega_{\mathbf{k}}$ and wave vector k:

$$\omega_{\mathbf{k}} = \alpha\sqrt{c^2k^2 + \left(\frac{\hbar k^2}{2m}\right)^2}, \tag{1}$$

with $\alpha = 1$ and c, the sound velocity. This relation describes both phonons (long wavelength excitations)

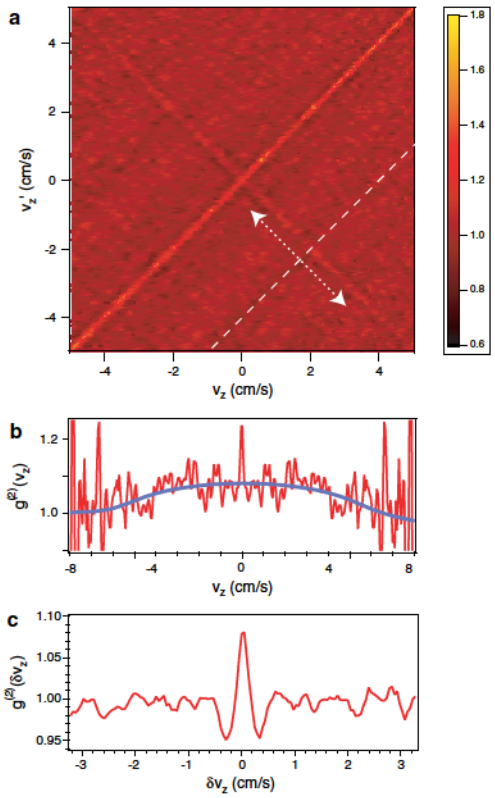

FIG. 2 (color online). Density correlations after a sudden compression. (a) Normalized correlation function $g^{(2)}(v_z, v_z')$ of the data in Fig. 1(c) (50 shot average). The signal on the diagonal results from the density fluctuations in the cloud. The antidiagonal line indicates the creation of correlated quasiparticles with opposite momenta, and is the signature of the dynamical Casimir effect. (b) Antidiagonal correlation function $g^{(2)}(v_z, v_z' = -v_z)$. The smooth line shows the result of smoothing the data over a window of about 1 cm/s. The correlations apparently persist over a scale comparable to that of the density distribution. (c) Correlation function along the dashed line and integrated over a region indicated by the dotted arrows, as a function of $\delta v_z = v_z' - v_z$. The dips on either side of the peak may be related to the effect reported in [32].

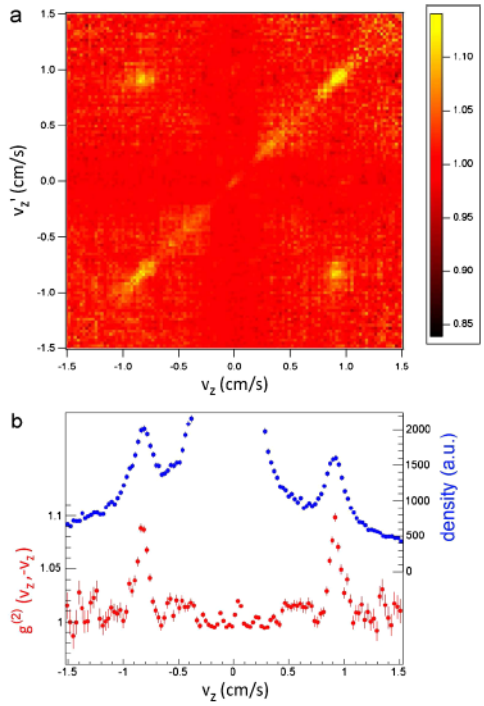

FIG. 3 (color online). Density correlations after a periodic modulation. (a) Normalized correlation function $g^{(2)}(v_z, v_z')$ measured after sinusoidal modulation of the trap frequency at a frequency $\omega_m/2\pi = 2.17$ kHz, averaging over 243 experimental shots. We observe a strong correlation between well-defined, oppositely directed velocities. (b) Plot of the density distribution (blue) and of the antidiagonal velocity correlation function, $g^{(2)}(v_z, v_z' = -v_z)$ (red).

whose dispersion is linear and free particles, whose dispersion is quadratic. If our observation indeed corresponds to the creation of pairs, we expect the total excitation energy to be shared between the two excitations. Momentum conservation, on the other hand, requires that the two energies be equal, implying $\omega_m = 2\omega_{\mathbf{k}}$. Therefore the relation between the modulation frequency and the sideband velocity should also be given by Eq. (1) but with $\alpha = 2$ and $k = mv_z/\hbar$. Fitting the points in Fig. 4(a) to (1) with α and c as free parameters, we obtain $\alpha = 2.2 \pm 0.3$. The fitted sound velocity, 8 ± 3 mm/s, is consistent with the value one can calculate from the trap parameters and the estimated number of atoms [25].

We can further corroborate our interpretation of pairwise excitations by a method more direct and robust than the 2 parameter fit to the data in Fig. 4(a). In Fig. 4(b), we compare the dispersion relation resulting from modulation with that obtained by Bragg scattering. Bragg scattering produces single excitations of quasiparticles at a definite energy and momentum [28]. We excited the BEC with two lasers in the Bragg configuration to determine the frequency for a given k vector [25]. Then, under the same experimental conditions, using sinusoidal trap laser modulation, we excited the BEC at various frequencies and found the corresponding velocities. The lower curve in Fig. 4(b) is a fit to the Bragg data in which we fix $\alpha = 1$ and fit the speed of sound. The upper curve is a fit to the trap modulation data in which we set the speed of sound to that found in the first fit and we allowed α to vary. This second fit yields $\alpha = 2.07 \pm 0.2$. The fitted speed of sound for this data set (about 13 mm/s) is higher than in the data of Fig. 4(a), because during these runs the number of atoms in the condensate was larger.

An even more dramatic confirmation of our interpretation would be the observation of sub-Poissonian intensity differences in the two sidebands, as was observed in the experiment of Ref. [5], as well as in Refs. [29]. The latter experiment modulated the center of a trapped, one dimensional gas producing transverse excitations which in turn

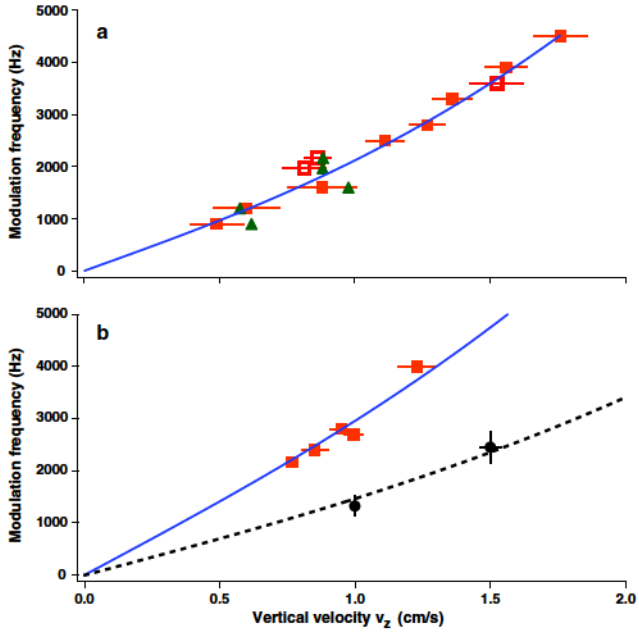

FIG. 4 (color online). Dispersion relation observed by modulating the trap depth. (a) The orange squares show the sideband velocity determined from the density distributions. The green triangles are derived from the correlation functions of the same data. The curve is a fit to the dispersion relation (1) as described in the text. Only the solid squares were included in the fit: these points were all taken on the same day, whereas the open squares were taken under slightly different trap conditions, with possibly different density. The error bars are statistical estimates based on the fits to the velocity distributions such as in Fig. 3(b). (b) Comparison between trap modulation and Bragg scattering. The black circles are observations of the dispersion relation by Bragg spectroscopy. The orange squares are found as in (a), and clearly show that the corresponding frequency is about a factor of 2 higher than in the Bragg data at a given velocity. The curves show the two fits discussed in the text. The vertical error bars on the Bragg data are determined by fits to the Bragg resonances.

produced twin beams. Equivalently, one could ask whether the Cauchy-Schwarz inequality is violated [30], indicating a nonclassical correlation. Comparing intensity differences in the sidebands we observe a reduction of the fluctuations compared to uncorrelated regions of the distribution. However, we observe no sub-Poissonian fluctuations or Cauchy-Schwarz violation, probably because of a background under the sidebands [see Fig. 1(d)]. The background is due to atoms spilling out of the trap before release.

Another difference between our experiment and an ideal realization of the dynamical Casimir effect is that the temperature is not negligible. This means that the pair generation did not arise from the vacuum but rather from thermal noise. For our temperature of 200 nK, the thermal occupation of the mode of frequency 2 kHz is 1.6. In the absence of a thermal background, the normalized correlation function would show an even higher peak. Using the perturbative approach of Ref. [12], one can show that $g^{(2)}(v_z, v_z' = -v_z)$ is a decreasing function of the temperature, since thermal quasiparticles are uncorrelated and only dilute the correlation.

Many authors have discussed the relationship of the dynamical Casimir effect to Hawking and Unruh radiation (see [4] for a recent review). It has also been pointed out that the two-particle correlations arising in the sonic Hawking problem constitute an important potential detection strategy [10,31], although the above authors discussed correlations in position space. The present study has confirmed the power of correlation techniques, and shown in addition that *momentum space* is a good place to look for them. We expect that a similar approach can be applied to Hawking radiation analogs as well as the general problem of studying the physics of curved spacetime by laboratory analogies.

This work was supported by the IFRAF institute, the Triangle de la Physique, the ANR-ProQuP project, J. R. by the DGA, R. L. by the FCT scholarship SFRH/BD/74352/2010, and G. B. P. by the Marie Curie program of the European Union. We acknowledge fruitful discussions with D. Clément, I. Carusotto, A. Recati, R. Balbinot, A. Fabbri, N. Pavloff, and P.-E. Larré.

*Present address: Harvard-Smithsonian Center for Astrophysics, Cambridge, MA 02138, USA.
†Present address: Agilent Laboratories, Santa Clara, CA 95051, USA.

[1] G. T. Moore, J. Math. Phys. (N.Y.) **11**, 2679 (1970).
[2] S. A. Fulling and P. C. W. Davies, Proc. R. Soc. A **348**, 393 (1976).
[3] V. V. Dodonov, Phys. Scr. **82**, 038105 (2010).
[4] P. D. Nation, J. R. Johansson, M. P. Blencowe, and F. Nori, Rev. Mod. Phys. **84**, 1 (2012).
[5] C. M. Wilson, G. Johansson, A. Pourkabirian, M. Simoen, J. R. Johansson, T. Duty, F. Nori, and P. Delsing, Nature (London) **479**, 376 (2011).
[6] P. Lähteenmäki, G. S. Paraoanu, J. Hassel, and P. J. Hakonen, arXiv:1111.5608.
[7] S. W. Hawking, Nature (London) **248**, 30 (1974).
[8] W. G. Unruh, Phys. Rev. Lett. **46**, 1351 (1981).
[9] L. J. Garay, J. R. Anglin, J. I. Cirac, and P. Zoller, Phys. Rev. Lett. **85**, 4643 (2000).
[10] R. Balbinot, A. Fabbri, S. Fagnocchi, A. Recati, and I. Carusotto, Phys. Rev. A **78**, 021603 (2008).
[11] O. Lahav, A. Itah, A. Blumkin, C. Gordon, S. Rinott, A. Zayats, and J. Steinhauer, Phys. Rev. Lett. **105**, 240401 (2010).
[12] I. Carusotto, R. Balbinot, A. Fabbri, and A. Recati, Eur. Phys. J. D **56**, 391 (2009).
[13] E. Yablonovitch, Phys. Rev. Lett. **62**, 1742 (1989).
[14] F. X. Dezael and A. Lambrecht, Europhys. Lett. **89**, 14001 (2010).

[15] P. O. Fedichev and U. R. Fischer, Phys. Rev. A **69**, 033602 (2004).
[16] P. Jain, S. Weinfurtner, M. Visser, and C. W. Gardiner, Phys. Rev. A **76**, 033616 (2007).
[17] C.-L. Hung, V. Guarie, and C. Chin, arXiv:1209.0011.
[18] P. Engels, C. Atherton, and M. A. Hoefer, Phys. Rev. Lett. **98**, 095301 (2007).
[19] K. Staliunas, S. Longhi, and G. J. de Valcárcel, Phys. Rev. A **70**, 011601 (2004).
[20] Y. Kagan and L. A. Manakova, Phys. Rev. A **76**, 023601 (2007).
[21] C. Schori, T. Stöferle, H. Moritz, M. Köhl, and T. Esslinger, Phys. Rev. Lett. **93**, 240402 (2004).
[22] C. Tozzo, M. Krämer, and F. Dalfovo, Phys. Rev. A **72**, 023613 (2005).
[23] G. B. Partridge, J.-C. Jaskula, M. Bonneau, D. Boiron, and C. I. Westbrook, Phys. Rev. A **81**, 053631 (2010).
[24] J.-C. Jaskula, M. Bonneau, G. B. Partridge, V. Krachmalnicoff, P. Deuar, K. V. Kheruntsyan, A. Aspect, D. Boiron, and C. I. Westbrook, Phys. Rev. Lett. **105**, 190402 (2010).
[25] See Supplemental Material at http://link.aps.org/supplemental/10.1103/PhysRevLett.109.220401 for a description of our data analysis, Bragg spectroscopy, and calculations of the speed of sound.
[26] M. Schellekens, R. Hoppeler, A. Perrin, J. V. Gomes, D. Boiron, A. Aspect, and C. I. Westbrook, Science **310**, 648 (2005).
[27] C. Tozzo and F. Dalfovo, Phys. Rev. A **69**, 053606 (2004).
[28] R. Ozeri, N. Katz, J. Steinhauer, and N. Davidson, Rev. Mod. Phys. **77**, 187 (2005).
[29] R. Bücker, J. Grond, S. Manz, T. Berrada, T. Betz, C. Koller, U. Hohenester, T. Schumm, A. Perrin, and J. Schmiedmayer, Nat. Phys. **7**, 608 (2011).
[30] K. V. Kheruntsyan, J.-C. Jaskula, P. Deuar, M. Bonneau, G. B. Partridge, J. Ruaudel, R. Lopes, D. Boiron, and C. I. Westbrook, Phys. Rev. Lett. **108**, 260401 (2012).
[31] P.-E. Larré, A. Recati, I. Carusotto, and N. Pavloff, Phys. Rev. A **85**, 013621 (2012).
[32] A. Imambekov, I. E. Mazets, D. S. Petrov, V. Gritsev, S. Manz, S. Hofferberth, T. Schumm, E. Demler, and J. Schmiedmayer, Phys. Rev. A **80**, 033604 (2009).

PHYSICAL REVIEW A **87**, 061603(R) (2013)

Tunable source of correlated atom beams

M. Bonneau,* J. Ruaudel, R. Lopes, J.-C. Jaskula,† A. Aspect, D. Boiron, and C. I. Westbrook
Laboratoire Charles Fabry, Institut d'Optique, CNRS, Univ Paris Sud, 2 avenue Augustin Fresnel, 91127 Palaiseau, France
(Received 21 December 2012; published 17 June 2013)

We use a one-dimensional optical lattice to modify the dispersion relation of atomic matter waves. Four-wave mixing in this situation produces atom pairs in two well-define beams. We show that these beams present a narrow momentum correlation, that their momenta are precisely tunable, and that this pair source can be operated in the regimes of low mode occupancy and of high mode occupancy.

DOI: 10.1103/PhysRevA.87.061603 PACS number(s): 03.75.Lm, 34.50.Cx, 42.50.Dv, 67.85.Hj

In quantum optics, the existence of mechanisms to produce photon pairs, such as parametric down-conversion, enabled the realization of several fundamental experiments on quantum mechanics. For example, the violation of Bell's inequalities [1] or the Hong-Ou-Mandel effect [2] reveal the surprising properties of quantum correlations in entangled photon pairs. These fascinating properties have found applications in quantum information and communications [3]. In analogy to photon pairs, there have been several recent demonstrations of correlated atom-pair production [4–10]. In particular, momentum correlations of spatially separated samples is an important requirement for the demonstration of an atomic Einstein-Podolsky-Rosen state [11,12] and the violation of Bell's inequalities. Such momentum correlations were demonstrated for atom pairs produced by molecule dissociation [4] or by spontaneous four-wave mixing in free space through the collision of two Bose-Einstein condensates (BECs) [5,13]. In these experiments the pairs which were produced lay on a spherical shell. This geometry is disadvantageous because many spatial modes are populated, and if one wishes to use Bragg diffraction to manipulate and recombine the pairs on a beam splitter [11,14], the vast majority of the pairs are unusable.

On the other hand, if pair production is concentrated in a small number of modes, experimenters can make more efficien use of the generated pairs. One can then choose to work either with low mode occupation, the well-separated pair regime, or with high mode occupation, referred to as the squeezing regime in Ref. [15]. An example of twin beams generated in the latter regime is described in Ref. [6]. The squeezing regime is well suited to the study of highly entangled multiparticle systems and for investigations of atom interferometry below the standard quantum limit [16,17]. The source we study in this Rapid Communication can be operated in both regimes. We use atomic four-wave mixing in a one-dimensional (1D) optical lattice, which results in production of atom pairs in two well-define beams, as proposed in Ref. [18] and demonstrated in Ref. [19]. We show that these beams present a narrow momentum correlation, that their momenta are precisely tunable, and that we can control their intensities.

*bonneau@lens.unifi.it Present address: INO-CNR, via G. Sansone 1, 50019 Sesto Fiorentino - Firenze, Italy.
†Present address: Harvard-Smithsonian Center for Astrophysics, Cambridge, Massachusetts 02138, USA.

In atom optics, four-wave mixing corresponds to scattering into new momentum classes subject to energy and momentum conservation. In a wave picture, the conservation requirements can be thought of as phase-matching conditions. The presence of an optical lattice modifie the free-space atomic dispersion relation and therefore, for a range of initial quasimomenta k_0 [20], the 1D scattering event $2k_0 \rightarrow k_1 + k_2$ is allowed, as shown in Fig. 1(a). Thus, beginning from a BEC at k_0, atom pairs are spontaneously generated along the lattice axis with well-define quasimomenta k_1 and k_2. We refer to this process as four-wave mixing, but it can also be viewed as a special case of a dynamical instability [21,22], which was studied in the

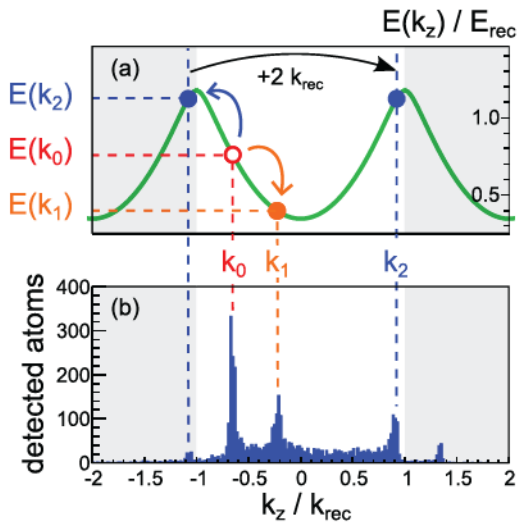

FIG. 1. (Color online) (a) 1D pair creation process in an optical lattice with period $\lambda_{\text{latt.}}/2$: The dispersion relation in the firs Bloch band (green solid curve) allows scattering of atoms from a BEC with quasimomentum k_0 (open red circle) in the lattice frame into pairs with quasimomenta k_1 (fille orange circle) and k_2 (fille blue circle), so that phase-matching conditions given by energy and momentum conservations are fulfilled The example here is for a lattice depth $V_0 = 0.725E_{\text{rec}}$ and $k_0 = -0.65k_{\text{rec}}$, with $k_{\text{rec}} = 2\pi/\lambda_{\text{latt.}}$ the recoil momentum and $E_{\text{rec}} = \hbar^2 k_{\text{rec}}^2/2m = h \times 44$ kHz the recoil energy. (b) Vertical single-shot momentum distribution (integrated over the total transverse distribution) measured for these conditions. The three main peaks correspond to the initial BEC and to the macroscopically populated beams centered at k_1 and k_2, which are mainly projected in the f rst Brillouin zone (in white) when the lattice is switched off. As expected, small diffraction peaks at $k_0 + 2k_{\text{rec}}$ and $k_2 - 2k_{\text{rec}}$ are also visible, due to the proximity of k_0 and k_2 to the band edge.

 ©2013 American Physical Society

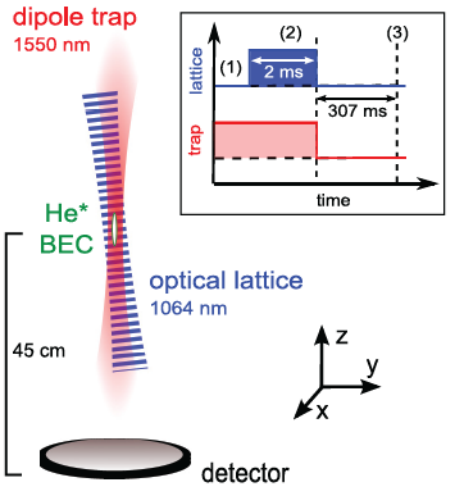

FIG. 2. (Color online) Experimental setup and sequence: (1) Initially, a BEC of metastable helium is trapped in a vertical optical potential with a 43 μm waist. (2) An optical lattice is suddenly applied in the presence of the trap. It is tilted by 7° with respect to the trap axis, and is focused on the BEC with a 200 μm waist. (3) After the dipole trap and optical lattice switch off, the cloud expands and falls on the 3D resolved single atom detector. Given the values of the vertical and transverse Thomas-Fermi radii (0.5 mm and 3 μm), the arrival time and position reflec the 3D momentum distribution, provided the momenta are well above $3 \times 10^{-2} k_{\rm rec}$ along z and $2 \times 10^{-4} k_{\rm rec}$ transversely.

context of coherence [23,24] and atomic [25] losses appearing for a BEC moving in a lattice.

The experiment is performed on ^{4}He atoms in the $m_x = 1$ sublevel of the $2\,^3S_1$ metastable state. The experimental setup and sequence are shown in Fig. 2. After evaporative cooling in an elongated, vertical dipole trap with frequencies $\nu_\perp = 1.5$ kHz and $\nu_z = 6.5$ Hz [26], we produce a BEC (or more precisely a quasi-BEC [27]) with about 10^5 atoms. We then apply a 1D optical lattice with a depth $V_0 = 0.725 E_{\rm rec}$. This lattice is tuned 19 nm to the blue of the 1083 nm $2\,^3S_1$–$2\,^3P$ transition of helium. It is formed by two counterpropagating 17 mW beams with 200 μm waists and whose relative detuning $\delta\nu$ can be varied using acousto-optic modulators. We thus control the value of $k_0/k_{\rm rec} = h\,\delta\nu/4E_{\rm rec}$, the BEC's momentum in the lattice frame. The lattice is held on for a duration $T_L = 2$ ms, and suddenly switched off, simultaneously with the optical trap. To avoid magnetic perturbation of the cloud during free fall, we apply an rf pulse that transfers 50% of the atoms to the fiel insensitive $m_x = 0$ sublevel [26]. The atoms remaining in $m_x = 1$ are subsequently removed by a strong magnetic gradient. After a 307 ms mean time of f ight, the $m_x = 0$ atoms fall on a microchannel plate detector, which permits 3D reconstruction of the atomic cloud [28].

As shown in Fig. 1(b), we observe three main density peaks after the time of f ight. The tallest is the initial BEC. The two others are formed by atoms scattered into momentum classes centered in k_1 and k_2, whose values are consistent with those expected from the phase-matching conditions illustrated in Fig. 1(a). Since the optical lattice is switched off abruptly, the Bloch states of momenta k_0, k_1, and k_2 are projected onto plane waves, mainly in the f rst Brillouin zone due to the low lattice depth. Each of the beams at k_1 and k_2 contains about 10^2 detected atoms, which we estimate to correspond to about 2×10^3 atoms per beam. We also detect some atoms between the beams, which result from scattering into excited transverse modes [29]. Due to the low overlap between the transversely excited states and the initial wave function, this transverse excitation is far less efficien than the previously described 1D process. In addition, scattered atoms can also undergo secondary scattering contributing to the background between the beams.

In the following, we focus on the two beams. Using them for quantum atom optics experiments or for interferometry will require recombining them. It is therefore crucial to know the width of their correlation. From the 3D-momentum distribution $n(\mathbf{k})$, we computed the normalized second-order cross-correlation function,

$$g_C^{(2)}(\mathbf{k},\mathbf{k}') = \frac{\langle n(\mathbf{k})\, n(\mathbf{k}')\rangle}{\langle n(\mathbf{k})\rangle\, \langle n(\mathbf{k}')\rangle}, \tag{1}$$

where $\mathbf{k}$ belongs to beam 1 and $\mathbf{k}'$ to beam 2. The BEC is not exactly at rest in the optical trap, but exhibits shot-to-shot momentum fluctuation on the order of $10^{-2}\, k_{\rm rec}$. We correct for these fluctuation by recentering separately the single shot momentum distributions $n(\mathbf{k})$ around k_1 and k_2, using the shift obtained from Gaussian fit to the peak at k_1 and to the diffraction peak at $k_0 + 2k_{\rm rec}$. This correlation function exhibits a peak for $k_z \simeq k_1$ and $k'_z \simeq k_2$ [Figs. 3(a) and 3(b)]. The presence of this peak indicates that the two atomic beams are indeed correlated.

We wish to determine the number of modes present in each beam, and how many of these modes are correlated. We therefore examine the *local* second-order correlation function of a single beam, $g_L^{(2)}(\mathbf{k},\mathbf{k}')$, which is obtained as in Eq. (1) but with both $\mathbf{k}$ and $\mathbf{k}'$ belonging to beam 1. This correlation function, plotted in Figs. 3(c) and 3(d), exhibits bunching for $k'_z \simeq k_z \simeq k_1$, due to density fluctuation [as in the Hanbury-Brown–Twiss (HBT) effect [30]]. Similar bunching is observed at k_2. If we suppose that the widths of the local correlation defin the size of a single mode, we can compare them to those of the density (longitudinal rms: $4 \times 10^{-2} k_{\rm rec}$; transverse rms: $4 \times 10^{-1} k_{\rm rec}$). We see that about 10 longitudinal and 3 transverse modes are populated. Thus the mode population is, roughly, 70 atoms/mode. For comparison, in the case of free-space four-wave mixing [31], starting from a similar initial BEC, 10^5 modes were populated, with only about 0.02 atoms/mode.

It appears in Fig. 3 that, while in the transverse direction, the cross and local correlations have similar widths [Figs. 3(a) and 3(c)], the cross correlation is 5 times broader than the local one along the vertical axis [Figs. 3(b) and 3(d)]: each mode is correlated with several modes of the other beam. If one uses two such beams as inputs to a beam splitter, this broadening amounts to a loss of coherence, and the interference contrast would be reduced. We emphasize that the observed widths may be broadened by other effects, and so their numerical ratio is not exactly equal to the number of correlated modes. For the local correlation, we estimate that the finit vertical resolution of the microchannel plate detector contributes notably to the observed width. This resolution comes about because the surface which define the atom arrival

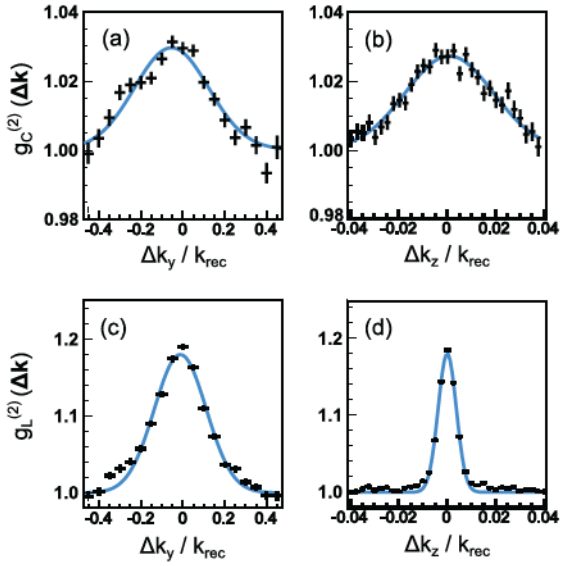

FIG. 3. (Color online) (a) and (b) Cuts along y and z of the integrated, normalized cross-correlation function of the two beams, $g_C^{(2)}(\Delta\mathbf{k}) = \int d\mathbf{k_i}\, g_C^{(2)}(\mathbf{k_i},\mathbf{k_j}+\Delta\mathbf{k})$. The integration over the momentum distribution $\mathbf{k_i}$ is performed on a box with dimensions $L_{k_x} = L_{k_y} = 0.4k_{\rm rec}$ and $L_{k_z} = 5\times10^{-2}k_{\rm rec}$ centered on beam 1, $\mathbf{k_i}+\mathbf{k_j} = (k_1+k_2)\,\hat{\mathbf{e}}_z$, and the cuts have a thickness $10^{-2}k_{\rm rec}$ ($1.5\times10^{-1}k_{\rm rec}$) along z (x and y). The bunching, due to the correlation between the two beams, has a longitudinal (transverse) width $\sigma_{c,z} = 1.8\times10^{-2}k_{\rm rec}$ ($\sigma_{c,y} = 1.6\times10^{-1}k_{\rm rec}$). (c) and (d) Cuts along y and z of the integrated, normalized local correlation function of beam 1, $g_L^{(2)}(\Delta\mathbf{k}) = \int d\mathbf{k_i}\, g_L^{(2)}(\mathbf{k_i},\mathbf{k_i}+\Delta\mathbf{k})$. The integration region is the same as for the cross correlation, and the cuts have a thickness $2.5\times10^{-3}k_{\rm rec}$ ($0.1k_{\rm rec}$) along z (x and y). The bunching, due to the HBT effect, has a longitudinal (transverse) width $\sigma_{l,z} = 3.7\times10^{-3}k_{\rm rec}$ ($\sigma_{l,y} = 1.3\times10^{-1}k_{\rm rec}$). Cuts along x (not shown here) have the same widths and amplitudes as cuts along y. These correlation functions are calculated using 850 experimental realizations, with $k_0 = -0.65k_{\rm rec}$, a lattice depth $V_0 = 0.725E_{\rm rec}$, and a lattice duration $T_L = 2$ ms. In all plots, the horizontal error bars indicate the bin size and the vertical ones correspond to the statistical 1σ uncertainties. The solid lines are Gaussian fit to the data from which we extract the correlation widths.

time is not fla but consists of tilted channels which intercept the atoms at different heights. The width shown in Fig. 3(d) is consistent with this interpretation. For the cross correlation, the observed width is broadened by the fact that the vertical source size is not negligible [32]. Note also that the limited coherence of the initial quasi-BEC plays a role in the cross correlation width [32].

The use of an optical lattice permits control over the output beam momenta. Changing the detuning $\delta\nu$ between the lattice beams results in varying the value of k_0. In Fig. 4, we plot the mean vertical momenta k_1 and k_2 of both beams, measured for different k_0, as well as the expectation (solid line) based on the phase-matching conditions illustrated in Fig. 1(a). We obtain a fair agreement over a large range, even though the solid line presents a small shift in comparison to the data points and does not reproduce the observed shape for high values of k_0. However, as already observed for four-wave mixing in free space [33], phase-matching conditions can be influence by

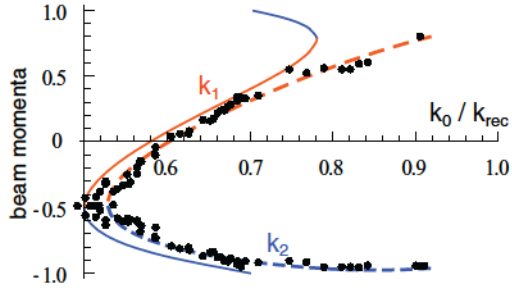

FIG. 4. (Color online) Measured mean momenta k_1 and k_2 of the beams (black dots, in units of $k_{\rm rec}$) as a function of k_0 (initial BEC momentum in the lattice frame) for a depth $V_0 = 1.05E_{\rm rec}$ and a duration $T_L = 1.5$ ms of the lattice. The solid line shows the phase-matching curve expected without interactions, while the dashed line includes the mean fiel [see Eq. (2)].

mean-fiel effects. A simple correction to the phase-matching curve is found just by adding the mean fiel to the energy conservation condition: Since the two atoms of a scattered pair are distinguishable from the atoms of the initial BEC, the mean-fiel energy experienced by each of them is not gn_0 (with $g = 4\pi\hbar^2 a/m$, a and m the scattering length and the mass of He* and $n_0 \simeq 10^{13}$ atoms/cm^3 the BEC density), but $2gn_0$, so that the energy conservation condition reads:

$$2E(k_0) + 2gn_0 = E(k_1) + E(k_2) + 4gn_0, \qquad (2)$$

where the energy $E(k)$ is given by the dispersion relation in the f rst Bloch band of the lattice without interaction. As seen in Fig. 4 (dashed line), this correction leads to very good agreement with the experimental data, and accounts for the shift of the phase-matching curve and the change of its shape. A more exact calculation of the phase-matching conditions, inspired by Ref. [21], confirm the accuracy of Eq. (2) in our experimental conditions and will be given in Ref. [34].

Another degree of freedom results from the fact that pair creation only takes place while the lattice is on. We can thus tune the beam populations with the lattice duration T_L. In the example of Fig. 5 these populations increase exponentially with T_L during a few hundred μs, and then reach a plateau. This saturation could be explained by several mechanisms such as the decrease of spatial overlap between condensate and scattered beams [19], multimode effects [35], and secondary scatterings from the beams. Condensate depletion is at most about 20% and should be of little importance in the saturation. For small T_L, there is no discernible population difference between both beams. By contrast, we observe that at large T_L the population of beam 1 is almost twice that of beam 2, a phenomenon also noticed in Ref. [19]. This may be due to k_2 being in a dynamically unstable region while atoms with quasimomentum k_1 can only undergo secondary scattering to excited transverse modes.

At intermediate T_L, we observe negligible losses due to secondary scattering *and* high mode population (around 60 atoms per mode at $T_L = 0.2$ ms in the example of Fig. 5). The resulting beams should contain strongly correlated pairs. In an attempt to verify a nonclassical correlation, we examined atom number difference between the two beams. By selecting two regions around the centers of the two beams, we do indeed

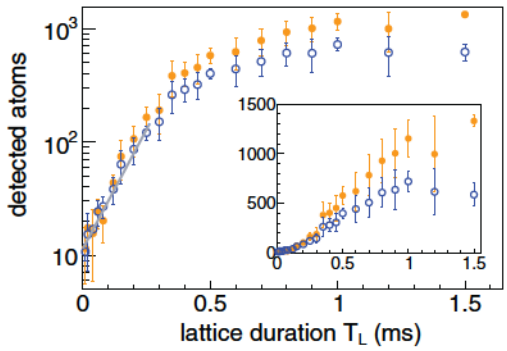

FIG. 5. (Color online) Dependence of the population of beam 1 (orange fille circles) and beam 2 (blue open circles) on the lattice duration T_L for $k_0 = -0.67k_{\rm rec}$ and for a lattice depth $V_0 = 1.05E_{\rm rec}$. The gray line is an exponential f t of the detected population in beam 2 for $T_L < 0.3$ ms, which gives a time constant of 0.1 ms and an offset of 11.5 detected atoms. This offset is due to the small thermal part of the source cloud with quasimomenta k_1 and k_2. For a lower lattice depth, as for the data of Fig. 3, the temporal evolution is a few times slower [21]. Inset: same data with linear scale.

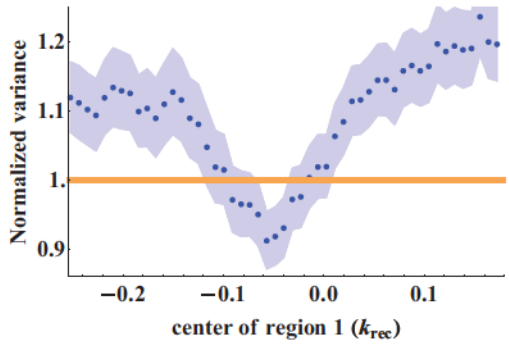

FIG. 6. (Color online) Normalized variance of atom number difference between two regions selected close to beams 1 and 2. The data are the same as those of Fig. 3. Regions are vertical cylinders of radius $2.5 \times 10^{-2}k_{\rm rec}$ and height $8.5 \times 10^{-2}k_{\rm rec}$. They are centered on the two beams in the transverse plane. Along the vertical axis, the center momentum (in the lattice frame) of region 1 is scanned, whereas region 2 is f xed. A variance below unity indicates sub-Poissonian fluctuations

observe a sub-Poissonian number difference [6,31], as shown in Fig. 6. The observed variance is consistent with that observed in Ref. [31], and is limited in large part by the quantum efficien y of the detector. Other features of the variance are puzzling, however. First the minimum of the dip in the variance occurs when the center of region 1 is shifted by $0.1k_{\rm rec}$ with respect to the center of the density distribution in beam 1. Second, in the transverse plane, the size of the regions over which the variance is reduced is nearly an order of magnitude smaller than the transverse width of the correlation function. We plan to investigate these effects in future experiments.

To conclude, we have demonstrated an efficien process for the production of correlated atom pairs. We have control over both the fina momenta and the intensity of the correlated beams. We characterize the width of the correlation in momentum and fin evidence of sub-Poissonian fluctuation of population difference. This source should be useful in multiple particle interference experiments both in the regime of well-isolated pairs [12] and in the regime of large occupation numbers [11].

We thank K. Mølmer, M. Ebner, J. Schmiedmayer. and P. Zin for useful discussions. J.R. is supported by the DGA, R.L. by the FCT scholarship SFRH/BD/74352/2010, and support for the experimental work comes from the IFRAF program, the Triangle de la Physique, the ANR Grant ProQuP, and ERC Grant 267 775 Quantatop.

[1] A. Aspect, Nature **398**, 189 (1999).
[2] C. K. Hong, Z. Y. Ou, and L. Mandel, Phys. Rev. Lett. **59**, 2044 (1987).
[3] J.-W. Pan, Z.-B. Chen, C.-Y. Lu, H. Weinfurter, A. Zeilinger, and M. Zukowski, Rev. Mod. Phys. **84**, 777 (2012).
[4] M. Greiner, C. A. Regal, J. T. Stewart, and D. S. Jin, Phys. Rev. Lett. **94**, 110401 (2005).
[5] A. Perrin, H. Chang, V. Krachmalnicoff, M. Schellekens, D. Boiron, A. Aspect, and C. I. Westbrook, Phys. Rev. Lett. **99**, 150405 (2007).
[6] R. Bücker, J. Grond, S. Manz, T. Berrada, T. Betz, C. Koller, U. Hohenester, T. Schumm, A. Perrin, and J. Schmiedmayer, Nat. Phys. **7**, 608 (2011).
[7] B. Lücke, M. Scherer, J. Kruse, L. Pezzé, F. Deuretzbacher, P. Hyllus, O. Topic, J. Peise, W. Ertmer, J. Arlt *et al.*, Science **334**, 773 (2011).
[8] W. RuGway, S. S. Hodgman, R. G. Dall, M. T. Johnsson, and A. G. Truscott, Phys. Rev. Lett. **107**, 075301 (2011).
[9] C. Gross, H. Strobel, E. Nicklas, T. Zibold, N. Bar-Gill, G. Kurizki, and M. K. Oberthaler, Nature **480**, 219 (2012).
[10] C. D. Hamley, C. S. Gerving, T. M. Hoang, E. M. Bookjans, and M. S. Chapman, Nat. Phys. **8**, 305 (2012).
[11] A. J. Ferris, M. K. Olsen, and M. J. Davis, Phys. Rev. A **79**, 043634 (2009).
[12] J. Kofler M. Singh, M. Ebner, M. Keller, M. Kotyrba, and A. Zeilinger, Phys. Rev. A **86**, 032115 (2012).
[13] K. V. Kheruntsyan, J.-C. Jaskula, P. Deuar, M. Bonneau, G. B. Partridge, J. Ruaudel, R. Lopes, D. Boiron, and C. I. Westbrook, Phys. Rev. Lett. **108**, 260401 (2012).
[14] T. Kitagawa, A. Aspect, M. Greiner, and E. Demler, Phys. Rev. Lett. **106**, 115302 (2011).
[15] L.-M. Duan, A. Sørensen, J. I. Cirac, and P. Zoller, Phys. Rev. Lett. **85**, 3991 (2000).
[16] P. Bouyer and M. A. Kasevich, Phys. Rev. A **56**, R1083 (1997).
[17] J. A. Dunningham, K. Burnett, and S. M. Barnett, Phys. Rev. Lett. **89**, 150401 (2002).
[18] K. M. Hilligsøe and K. Mølmer, Phys. Rev. A **71**, 041602 (2005).
[19] G. K. Campbell, J. Mun, M. Boyd, E. W. Streed, W. Ketterle, and D. E. Pritchard, Phys. Rev. Lett. **96**, 020406 (2006).

[20] Throughout this paper we denote momenta by their value divided by $\hbar$.
[21] B. Wu and Q. Niu, Phys. Rev. A **64**, 061603 (2001).
[22] A. Smerzi, A. Trombettoni, P. G. Kevrekidis, and A. R. Bishop, Phys. Rev. Lett. **89**, 170402 (2002).
[23] F. S. Cataliotti, L. Fallani, F. Ferlaino, C. Fort, P. Maddaloni, and M. Inguscio, New J. Phys **5**, 71 (2003).
[24] M. Cristiani, O. Morsch, N. Malossi, M. Jona-Lasinio, M. Anderlini, E. Courtade, and E. Arimondo, Opt. Express **12**, 4 (2004).
[25] L. Fallani, L. De Sarlo, J. E. Lye, M. Modugno, R. Saers, C. Fort, and M. Inguscio, Phys. Rev. Lett. **93**, 140406 (2004).
[26] G. B. Partridge, J.-C. Jaskula, M. Bonneau, D. Boiron, and C. I. Westbrook, Phys. Rev. A **81**, 053631 (2010).
[27] D. S. Petrov, G. V. Shlyapnikov, and J. T. M. Walraven, Phys. Rev. Lett. **87**, 050404 (2001).
[28] M. Schellekens, R. Hoppeler, A. Perrin, J. V. Gomes, D. Boiron, A. Aspect, and C. I. Westbrook, Science **310**, 648 (2005).
[29] M. Modugno, C. Tozzo, and F. Dalfovo, Phys. Rev. A **70**, 043625 (2004).
[30] K. Mølmer, A. Perrin, V. Krachmalnicoff, V. Leung, D. Boiron, A. Aspect, and C. I. Westbrook, Phys. Rev. A **77**, 033601 (2008).
[31] J.-C. Jaskula, M. Bonneau, G. B. Partridge, V. Krachmalnicoff, P. Deuar, K. V. Kheruntsyan, A. Aspect, D. Boiron, and C. I. Westbrook, Phys. Rev. Lett. **105**, 190402 (2010).
[32] P. Ziń *et al.* (unpublished).
[33] V. Krachmalnicoff, J.-C. Jaskula, M. Bonneau, V. Leung, G. B. Partridge, D. Boiron, C. I. Westbrook, P. Deuar, P. Ziń, M. Trippenbach *et al.*, Phys. Rev. Lett. **104**, 150402 (2010).
[34] J. Ruaudel *et al.* (unpublished).
[35] R. Bücker, U. Hohenester, T. Berrada, S. van Frank, A. Perrin, S. Manz, T. Betz, J. Grond, T. Schumm, and J. Schmiedmayer, Phys. Rev. A **86**, 013638 (2012).

Second-order coherence of superradiance from a Bose-Einstein condensate

R. Lopes, A. Imanaliev, M. Bonneau,* J. Ruaudel,† M. Cheneau, D. Boiron, and C. I. Westbrook‡
Laboratoire Charles Fabry, Institut d'Optique–CNRS–Université Paris-Sud, 2 avenue Augustin Fresnel, 91127 Palaiseau, France
(Received 23 December 2013; published 16 July 2014)

We have measured the two-particle correlation function of atoms from a Bose-Einstein condensate participating in a superradiance process, which directly reflect the second-order coherence of the emitted light. We compare this correlation function with that of atoms undergoing stimulated emission. Whereas the stimulated process produces correlations resembling those of a coherent state, we fin that superradiance, even in the presence of strong gain, shows a correlation function close to that of a thermal state, just as for ordinary spontaneous emission.

DOI: 10.1103/PhysRevA.90.013615 PACS number(s): 03.75.Kk, 42.50.Lc, 67.10.Jn

Ever since the publication of Dicke's 1954 paper [1], the problem of the collective emission of radiation has occupied many researchers in the field of light scattering, lasers, and quantum optics. Collective emission is characterized by a rate of emission which is strongly modifie compared to that of individual atoms [2]. It occurs in many different contexts: hot gases, cold gases, solids and even planetary and astrophysical environments [3]. The case of an enhanced rate of emission, originally dubbed superradiance, is closely connected to stimulated emission and gain and, as such, resembles laser emission [4]. Lasers are typically characterized by high phase coherence but also by a stable intensity, corresponding to a Poissonian noise, or a fla second-order correlation function [5]. Here we present measurements showing that the coherence properties of superradiance, when it occurs in an ultracold gas and despite strong amplifie emission, are much closer to those of a thermal state, with super-Poissonian-intensity noise.

Research has shown that the details of collective emission depend on many parameters such as the pumping configura tion, dephasing and relaxation processes, sample geometry, presence of a cavity, etc., and, as a result, a complex nomenclature has evolved including the terms superradiance, superfluorescence amplifie spontaneous emission, mirrorless lasing, and random lasing [2,4,6–9], the distinctions among which we do not attempt to summarize here. The problem has recently seen renewed interest in the fiel of cold atoms [10–25]. This is partly because cold atoms provide a reproducible, easily characterized ensemble in which Doppler broadening effects are small and relaxation is generally limited to spontaneous emission. Most cold-atom experiments differ in an important way from the archetypal situation f rst envisioned by Dicke: instead of creating an ensemble of excited atoms at a well-define time and then allowing this ensemble to evolve freely, the sample is typically pumped during a period long compared to the relaxation time and emission lasts essentially only as long as the pumping. The authors of Ref. [10], however, have argued that there is a close analogy to the Dicke problem, and we follow them in designating this process superradiance.

In the literature on superradiance there has been relatively little discussion about the coherence and correlation properties of the light. The theoretical treatments we are aware of show that the coherence of collective emission can be quite complicated but does not resemble that of a laser [2,13,20,26–28]. These results, however, were obtained for simple models that do not include all parameters relevant to laboratory experiments. Experimentally, a study performed on Rydberg atoms coupled to a millimeter-wave cavity [29] showed a thermal mode occupation, and an experiment in a cold atomic vapor in free space [24] observed a nonfla second-order correlation function. In the present work, we show that even if the initial atomic state is a Bose-Einstein condensate (BEC), the second-order correlation function looks thermal rather than coherent.

Such behavior, which may seem counterintuitive, can be understood by describing superradiance as a four-wave mixing process between two matter waves and two electromagnetic waves. The initial state consists of a condensate, a coherent optical pump beam, and empty modes for the scattered atoms and the scattered photons. If we make the approximation that the condensate and the pump beam are not depleted and can be treated as classical fields the matter-radiation interaction Hamiltonian is given by

$$\hat{H} = \sum_i [\chi_i \, \hat{a}^\dagger_{\mathrm{at},i} \, \hat{a}^\dagger_{\mathrm{ph},i} + \chi_i^* \, \hat{a}_{\mathrm{at},i} \, \hat{a}_{\mathrm{ph},i}], \tag{1}$$

where $\hat{a}^\dagger_{\mathrm{at},i}$ ($\hat{a}_{\mathrm{at},i}$) and $\hat{a}^\dagger_{\mathrm{ph},i}$ ($\hat{a}_{\mathrm{ph},i}$) denote atom and photon creation (annihilation) operators for a specifi pair of momenta i fi ed by energy and momentum conservation and χ_i is a coupling constant. Textbooks [30] show that, starting from an input vacuum state, this Hamiltonian leads to a product of two-mode squeezed states. When one traces over one of the two modes, $\alpha = \{\mathrm{at}, i\}$ or $\{\mathrm{ph}, i\}$, the remaining mode β has a thermal occupation with a normalized two-particle or second-order correlator

$$\frac{\langle \hat{a}^\dagger_\beta \, \hat{a}^\dagger_\beta \, \hat{a}_\beta \, \hat{a}_\beta \rangle}{\langle \hat{a}^\dagger_\beta \, \hat{a}_\beta \rangle^2} = 2, \tag{2}$$

whereas it is unity for a laser. The problem has also been treated for four-wave mixing of matter waves [31]. We emphasize

*Current address: Vienna Center for Quantum Science and Technology, Atominstitut, TU Wien, Stadionallee 2, 1020 Vienna, Austria.
†Current address: Laboratoire Kastler Brossel, Université Pierre et Marie Curie–École normale supérieure–CNRS, 4 place Jussieu, 75005 Paris, France.
‡christoph.westbrook@institutoptique.fr

 ©2014 American Physical Society

that, when starting from initially empty modes, the occupation remains thermal *regardless* of the gain.

In the experiment, we start from initially nearly motionless atoms of a BEC and observe their recoil upon photon emission. To the extent that each recoil corresponds to the emission of a single photon, we can obtain essentially the same information about the radiation from such measurements as by observing it directly. In doing this, we are following the approach pioneered in experiments such as [10] and [29] and followed by many others, which uses highly developed atom detection and imaging techniques to glean most of the experimental information about the process. We are able to make time-integrated measurements of the emission, resolved in transverse and longitudinal momentum as well as in polarization, and reconstruct the two-particle correlation function of the recoiling atoms or, equivalently, the second-order correlation function of the scattered light. We show that in the configuratio of our experiment, the second-order correlation is close to that of a thermal sample and very different from the correlation properties of the initial, condensed atomic state.

We use helium in the $2\,^3S_1$, $m = 1$ state confine in a crossed dipole trap [see Fig. 1(a)] with frequencies of 1300 Hz in the x and y directions and 130 Hz in the (vertical) z direction. The dipole trap wavelength is 1.5 μm. The atom number is approximately 50 000, and the temperature of the remaining thermal cloud 140 nK. A 9-G magnetic fiel along the y axis define a quantization axis. After producing the condensate, we irradiate it with a laser pulse of 2.4 W/cm^2 tuned 600 MHz to the red of the $2\,^3S_1 \rightarrow 2\,^3P_0$ transition at $\lambda = 1083$ nm and with natural linewidth 1.6 MHz. The excitation beam propagates

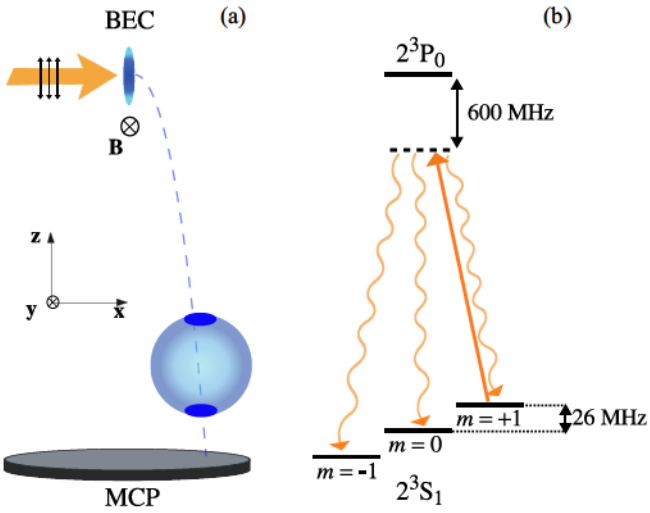

FIG. 1. (Color online) (a) Sketch of the experiment. A 9-G magnetic fiel **B** applied along the y axis define the quantization axis. The excitation beam propagates with an angle of 10° (not shown) relative to the x axis and its polarization is linear, with the same angle relative to the z axis. After emission, the atoms fall 46 cm to a position-sensitive microchannel plate (MCP). The atom cloud forms a sphere with enhanced occupation of the endfir modes. (b) Atomic level scheme. The atoms, initially in the $2\,^3S_1$, $m = +1$ state, are excited to the $2\,^3P_0$ state. From there, they can decay with equal branching ratios to the three sublevels of the ground state. We detect only the atoms which scatter into the $m = 0$ state.

with an angle of 10° relative to the x axis and its polarization is linear, with the same angle relative to the z axis [see Fig. 1(a)]. The pulse length is 5 μs and it is applied with a delay τ after switching off the trap. The expansion of the cloud during this delay is a convenient way to vary both the optical density and the anisotropy of the sample at constant atom number. The absorption dipole matrix element is of the σ^- form and thus one-half of the laser intensity is coupled to the atomic transition corresponding to a Rabi frequency of 56 MHz. The excited atoms decay with equal branching ratios to the three ground states. During the pulse, less than 10% of the atoms are pumped into each of these states. Because of the polarization selection rules, the atoms which are pumped into the $m = 0$ state cannot reabsorb light from the excitation laser. By focusing on these atoms, we study the regime of "Raman superradiance" [15,32], by which we mean that an absorption and emission cycle is accompanied by a change in the internal state of the atom. When the trap is switched off, the atoms fall toward a microchannel plate detector which detects individual atoms with three-dimensional imaging capability and a 10% to 20% quantum efficien y [33]. A magnetic-fiel gradient is applied to sweep away all atoms except those scattered into the $m = 0$ magnetic sublevel. The average time of f ight to the detector is 310 ms and is long enough that the atoms' positions at the detector reflec the atomic momenta after interaction with the excitation laser. Conservation of momentum then requires that these atoms lie on a sphere with a radius equal to the recoil momentum $k_{\rm rec} = 2\pi/\lambda$. Any additional scattering of light, whether from imperfect polarization of the excitation laser or from multiple scattering by the atoms, will result in the atoms lying outside the sphere. We see no significan signal from such events, but in order to completely eliminate the possibility of multiple scattering we restrict our analysis of the data to the spherical shell with inner radius 0.8 $k_{\rm rec}$ and outer radius 1.2 $k_{\rm rec}$.

We excite atoms in an elongated BEC in such a way that an allowed emission dipole can radiate along the long axis. In an anisotropic source, collective emission builds up more efficientl in the directions of highest optical thickness. Superradiance is therefore expected to occur along the long axis of the BEC, in so-called "endfire modes [10,34]. An important parameter, then, is the Fresnel number of the sample [2], $F = 2R_\perp^2/\lambda R_z$, where $R_\perp$ and R_z are the horizontal and vertical Thomas-Fermi radii of the condensate. The Fresnel number distinguishes between the diffraction limited ($F < 1$) and the multimode superradiance regimes ($F > 1$). In our case, $R_\perp \approx 5$ μm and $R_z \approx 50$ μm, yielding a Fresnel number of about unity.

Typical cuts through the atomic momentum distribution in the yz plane are shown in Fig. 2, for $\tau = 500$ μs (left) and $\tau \approx 0$ (right). In both cases, the spherical shell with radius 1 $k_{\rm rec}$ appears clearly. For the short delay, when the atomic sample remains dense and anisotropic, we observe strong scattering in the endfir modes at the top and bottom poles of the sphere. In addition to this change in the profil of the distribution, we measure an increase in the *total number* of atoms on the sphere by a factor of ~5 from $\tau = 500$ μs to $\tau \approx 0$. Because each atom has scattered a single photon, this increase directly reflect an increase in the rate of emission in the sample and therefore demonstrates the collective nature

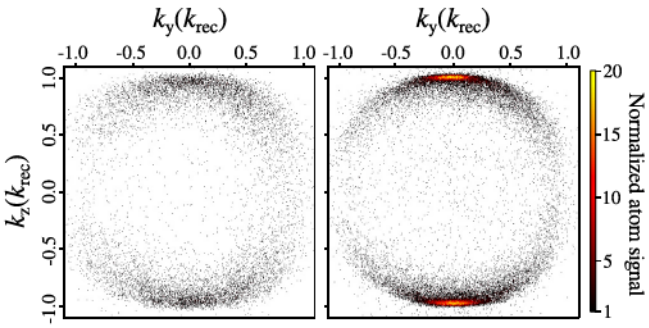

FIG. 2. (Color online) Momentum distribution of scattered atoms in the yz plane (containing the emission dipole). Both panels show the distribution in the yz plane, integrated between $k_x = \pm 0.1\,k_{rec}$ and summed over 100 shots. See the Supplemental Information for a cut in the xz plane [35]. Left: Excitation laser applied 500 μs after the trap switch-off. Only the radiation pattern for a y-polarized dipole is visible. Right: Excitation laser applied immediately after the trap switch-off. Strong superradiance is visible in the vertical, endfir modes.

of the scattering process. At long delays, the condensate has expanded sufficientl that the optical thickness and anisotropy have fallen dramatically, suppressing the collective scattering. By looking at the number of scattered atoms in the x direction (perpendicular to the plane in Fig. 2), we have verifie that, away from the endfir modes, the rate of emission varies by less than 10% for different delays [35].

To see the distribution in a more quantitative way, we show in Fig. 3 an angular plot of the atom distribution in the yz plane. Data are shown for three delays τ before application of the

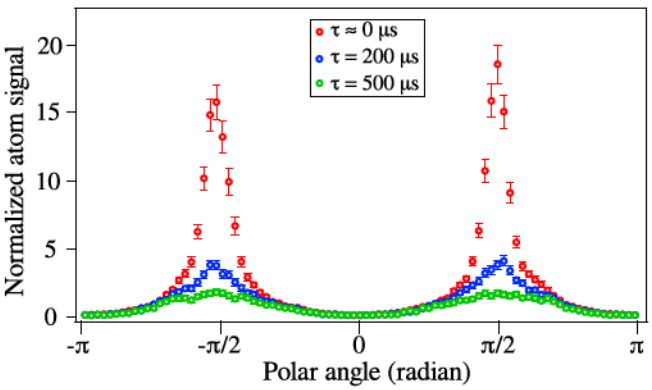

FIG. 3. (Color online) Angular distribution of scattered atoms in the yz plane (containing the emission dipole) for different values of the delay τ before the excitation pulse. From bottom to top: light-gray (green) circles correspond to $\tau = 500\ \mu$s; dark-gray (blue) circles, to $\tau = 200\ \mu$s; and light-gray (red) circles, to $\tau = 0\ \mu$s. Data for $\tau = 0$ and 500 μs are the same as those shown in Fig. 2. Images were integrated along the x axis between $\pm 0.1\,k_{rec}$, and only atoms lying inside a shell with inner radius $0.8\,k_{rec}$ and outer radius $1.2\,k_{rec}$ were taken into account. The delays $\tau = 0$, 200, and 500 μs correspond to peak densities of $\approx$8, 2, and 0.4×10^{18} m^{-3} and to aspect ratios of 10, 5, and 2.5, respectively. The endfir modes are located at $\pm\pi/2$. The half-width at half-maximum of the highest peak is 0.14 rad. Error bars are shown, denoting the 68% confidenc interval.

excitation pulse. For the 500-μs delay, the angular distribution follows the well-known "$\sin^2\theta$" linear dipole emission pattern, with the angles $\theta = 0$ and π corresponding to the orientation of the dipole along the y axis [35]. For the 200-μs delay, the superradiant peaks are already visible at the top of the dipole emission profile For the shortest delay, the half-width of the superradiant peaks is $0.14\,k_{rec}$, or 0.14 rad, consistent with the diffraction angle and the aspect ratio of the source. In the vertical direction, the superradiant peaks are 10 times narrower than in the horizontal direction [35].

In the strongly superradiant case, we observe large and uncorrelated fluctuation of the heights of the two superradiant peaks on a shot-to-shot basis. These fluctuation directly reflec the fluctuation of the population of the superradiant modes. We investigate these fluctuation further by measuring the normalized two-particle correlation function of the scattered atoms, define as

$$g^{(2)}(\Delta\mathbf{k}) = \frac{\langle : \hat{n}(\mathbf{k})\hat{n}(\mathbf{k}+\Delta\mathbf{k}) : \rangle}{\langle \hat{n}(\mathbf{k})\rangle\ \langle \hat{n}(\mathbf{k}+\Delta\mathbf{k})\rangle}. \tag{3}$$

Here, $\hat{n}$ is the atomic density and : : denotes normal ordering. In practice, this function is obtained from a histogram of pair separations $\Delta\mathbf{k}$ normalized to the autoconvolution of the average particle momentum distribution [36,37]. Figure 4 shows the experimentally measured correlation functions integrated over the momentum along two of three axes, both

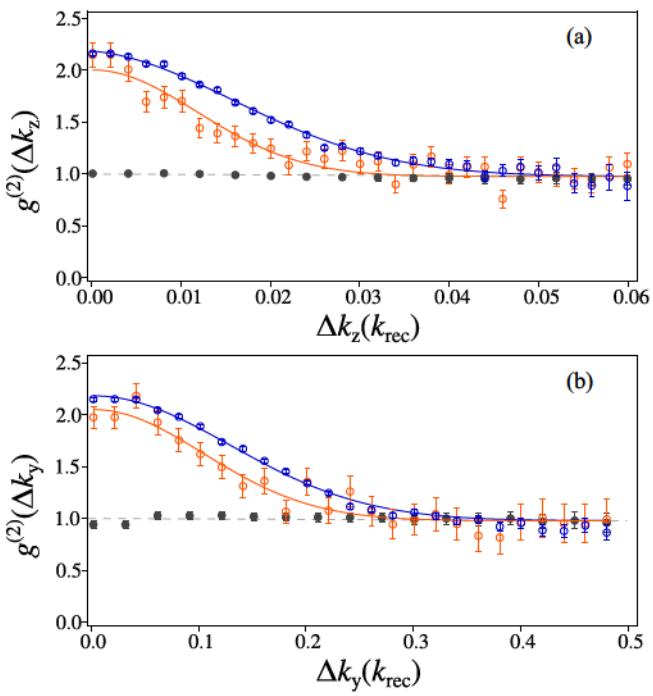

FIG. 4. (Color online) Correlation functions along the (a) z and (b) y axis for $\tau \approx 0$. Darker (blue) circles correspond to superradiant peaks (define by $|k_z| > 0.95\,k_{rec}$). Lighter (orange) circles correspond to atoms from the scattering sphere away from the superradiant peaks (define by $|k_z| < 0.92\,k_{rec}$). Solid lines are Gaussian fit constrained to approach unity at large separation. Filled gray circles correspond to a fraction of the initial condensate transferred to the $m = 0$ state via a stimulated Raman transfer. The dashed gray line shows unity. Error bars denote the 68% confidenc interval.

for the superradiant peaks and on the scattering sphere away from the peaks [35].

We see that in both cases the correlation function at zero separation reaches a value close to 2. This shows clearly that, despite strong amplifie emission in the endfir modes, the atoms undergoing a superradiant process have statistics comparable to that of a thermal sample. As emphasized in the introductory section, these large fluctuation can be simply understood by modeling the superradiant emission as a four-wave mixing process; they arise from the fact that the emission is triggered by spontaneous emission. For the superradiant peaks, the correlation actually is slightly larger than 2. Similar behavior has appeared in some models [20,38], but these models may not be directly applicable to our situation.

Figure 4 also shows that the correlation widths of the superradiant modes are somewhat broader than those of the atoms scattered in other modes. The effect is a factor of about 1.5 in the vertical direction and about 1.25 in the horizontal direction [35]. The broadening indicates that the effective source size for superradiance is slightly smaller than that for spontaneous scattering. A decreased vertical source size for superradiance is consistent with the observations in Refs. [39] and [40], which showed that the superradiant emission is concentrated near the ends of the sample. In the horizontal direction, one also expects a slightly reduced source size relative to the atom cloud since the gain is higher in the center, where the density is higher. The fact that the correlation widths are close to the widths of the momentum distribution [35] indicates that the superradiant peaks are almost single mode as expected for samples with a Fresnel number close to unity [2].

The spontaneous superradiant scattering process should be contrasted with stimulated Raman scattering. In terms of the model described by Hamiltonian (1), stimulated Raman scattering corresponds to seeding one of the photon modes with a coherent state. In this case, vacuum fluctuation do not initiate the scattering process, and the resulting mode occupation is not thermal but coherent. To study stimulated scattering, we applied the excitation beam together with another beam polarized parallel to the magnetic fiel and detuned by the Zeeman shift (25 MHz) with respect to the σ-polarized beam, inducing a stimulated Raman transition. The laser intensities were adjusted to transfer a similar number of atoms to the $m = 0$ state as in the superradiance experiment. The normalized correlation functions in this situation, shown in Fig. 4, are very nearly fla and equal to unity as we expect for a BEC [36,41,42]. The complementary experiment, seeding the *atomic* mode with a coherent state has also been observed to produce a coherent amplifie matter wave [43,44]. As a side remark, we have also observed that the superradiant atom peaks are 2.8 times narrower in the vertical direction than the vertical width of the transferred condensate [35]. We attribute this to a longitudinal gain narrowing effect [27].

We also investigated the influenc of several other experimental parameters on the second-order coherence of the superradiant emission: We have excited the atomic sample with a longer and stronger pulse (10 μs, 3.2 W/cm^2), so that the initial condensate was entirely depleted. We have explored the Rayleigh scattering regime, in which the atoms scatter back to their initial internal state. We also changed the longitudinal confinemen frequency of the BEC to 7 Hz, leading to a much higher aspect ratio. These different configuration led to two-particle correlation functions which were very similar to the one discussed above. We believe that similar fluctuation will occur in superradiance from a thermal cloud provided that the gain in the medium is large enough. We were unable to confir this experimentally in our system, precisely because of the vastly reduced optical density. However, noncoherent intensity fluctuation have been observed using magneto-optically trapped atoms [24]. This seems to confir our interpretation that the large fluctuation of the superradiant mode occupation is an intrinsic property of superradiant emission, reflectin the seeding by spontaneous emission. The only way to suppress these fluctuation would be to restrict the number of scattering modes to one by means of a cavity and to saturate the gain by completely depleting the atomic cloud. The occupation of the superradiant mode would then simply reflec that of the initial atomic sample.

An interesting extension of the techniques used here is to examine superradiant Rayleigh scattering of a light pulse short enough and strong enough to populate oppositely directed modes [45]. It has been predicted [13,14,46] that the modes propagating in opposite directions are entangled, similar to those produced in atomic four-wave mixing [47–49]. A similar measurement technique should be able to reveal them.

We acknowledge fruitful discussions with A. Browaeys, J.-J. Greffet, and P. Pillet. This work was supported by the IFRAF institute, the Triangle de la Physique, the LABEX PALM, the ANR-ProQuP project, and the ERC Quantatop (Grant No. 267 775). J.R. was supported by the DGA; R.L., by FCT scholarship SFRH/BD/74352/2010.

[1] R. H. Dicke, Phys. Rev. **93**, 99 (1954).
[2] M. Gross and S. Haroche, Phys. Rep. **93**, 301 (1982).
[3] V. Letokhov and S. Johansson, *Astrophysical Lasers* (Oxford University Press, New York, 2008).
[4] A. E. Siegman, *Lasers* (University Science Books, Mill Valley, CA, 1986).
[5] R. Loudon, *The Quantum Theory of Light* (Oxford University Press, Oxford, 2000).
[6] N. Rehler and J. Eberly, Phys. Rev. A **3**, 1735 (1971).
[7] L. Allen and G. Peters, Phys. Rev. A **8**, 2031 (1973).
[8] R. Bonifacio and L. Lugiato, Phys. Rev. A **11**, 1507 (1975).
[9] J. MacGillivray and M. Feld, Phys. Rev. A **14**, 1169 (1976).
[10] S. Inouye, A. P. Chikkatur, D. M. Stamper-Kurn, J. Stenger, D. E. Pritchard, and W. Ketterle, Science **285**, 571 (1999).
[11] M. G. Moore, O. Zobay, and P. Meystre, Phys. Rev. A **60**, 1491 (1999).
[12] Ö. E. Müstecaplioglu and L. You, Phys. Rev. A **62**, 063615 (2000).
[13] N. Piovella, M. Cola, and R. Bonifacio, Phys. Rev. A **67**, 013817 (2003).

[14] H. Pu, W. Zhang, and P. Meystre, Phys. Rev. Lett. **91**, 150407 (2003).
[15] Y. Yoshikawa, T. Sugiura, Y. Torii, and T. Kuga, Phys. Rev. A **69**, 041603 (2004).
[16] N. Bar-Gill, E. E. Rowen, and N. Davidson, Phys. Rev. A **76**, 043603 (2007).
[17] T. Wang, S. F. Yelin, R. Côté, E. E. Eyler, S. M. Farooqi, P. L. Gould, M. Koštrun, D. Tong, and D. Vrinceanu, Phys. Rev. A **75**, 033802 (2007).
[18] E. Paradis, B. Barrett, A. Kumarakrishnan, R. Zhang, and G. Raithel, Phys. Rev. A **77**, 043419 (2008).
[19] A. Hilliard, F. Kaminski, R. le Targat, C. Olausson, E. S. Polzik, and J. H. Müller, Phys. Rev. A **78**, 051403 (2008).
[20] D. Meiser and M. J. Holland, Phys. Rev. A **81**, 063827 (2010).
[21] L. Deng, E. W. Hagley, Q. Cao, X. Wang, X. Luo, R. Wang, M. G. Payne, F. Yang, X. Zhou, X. Chen *et al.*, Phys. Rev. Lett. **105**, 220404 (2010).
[22] T. Vogt, B. Lu, X. X. Liu, X. Xu, X. Zhou, and X. Chen, Phys. Rev. A **83**, 053603 (2011).
[23] J. G. Bohnet, Z. Chen, J. M. Weiner, D. Meiser, M. J. Holland, and J. K. Thompson, Nature **484**, 78 (2012).
[24] J. A. Greenberg and D. J. Gauthier, Phys. Rev. A **86**, 013823 (2012).
[25] Q. Baudouin, N. Mercadier, V. Guarrera, W. Guerin, and R. Kaiser, Nat. Phys. **9**, 357 (2013).
[26] F. Haake and R. J. Glauber, Phys. Rev. A **5**, 1457 (1972).
[27] M. G. Moore and P. Meystre, Phys. Rev. Lett. **83**, 5202 (1999).
[28] V. V. Temnov and U. Woggon, Opt. Express **17**, 5774 (2009).
[29] J.-M. Raimond, P. Goy, M. Gross, C. Fabre, and S. Haroche, Phys. Rev. Lett. **49**, 1924 (1982).
[30] C. C. Gerry and P. Knight, *Introductory Quantum Optics* (Cambridge University Press, Cambridge, 2005).
[31] K. Mølmer, A. Perrin, V. Krachmalnicoff, V. Leung, D. Boiron, A. Aspect, and C. I. Westbrook, Phys. Rev. A **77**, 033601 (2008).
[32] D. Schneble, G. K. Campbell, E. W. Streed, M. Boyd, D. E. Pritchard, and W. Ketterle, Phys. Rev. A **69**, 041601 (2004).
[33] J.-C. Jaskula, M. Bonneau, G. B. Partridge, V. Krachmalnicoff, P. Deuar, K. V. Kheruntsyan, A. Aspect, D. Boiron, and C. I. Westbrook, Phys. Rev. Lett. **105**, 190402 (2010).
[34] R. H. Dicke, in *Quantum Electronics; Proceedings of the Third International Congress, Paris.*, edited by P. Grivet and N. Bloembergen (Columbia University Press, New York, 1964).
[35] See Supplemental Material at http://link.aps.org/supplemental/10.1103/PhysRevA.90.013615 for the atomic distribution in the xz plane, details on the calculation of the correlation functions, and a table summarizing the widths of the momentum distributions and correlation functions.
[36] M. Schellekens, R. Hoppeler, A. Perrin, J. V. Gomes, D. Boiron, A. Aspect, and C. I. Westbrook, Science **310**, 648 (2005).
[37] K. V. Kheruntsyan, J.-C. Jaskula, P. Deuar, M. Bonneau, G. B. Partridge, J. Ruaudel, R. Lopes, D. Boiron, and C. I. Westbrook, Phys. Rev. Lett. **108**, 260401 (2012).
[38] T. Wasak, J. Chwedeńczuk, P. Ziń, and M. Trippenbach, Phys. Rev. A **86**, 043621 (2012).
[39] O. Zobay and G. M. Nikolopoulos, Phys. Rev. A **73**, 013620 (2006).
[40] L. E. Sadler, J. M. Higbie, S. R. Leslie, M. Vengalattore, and D. M. Stamper-Kurn, Phys. Rev. Lett. **98**, 110401 (2007).
[41] A. Öttl, S. Ritter, M. Köhl, and T. Esslinger, Phys. Rev. Lett. **95**, 090404 (2005).
[42] S. S. Hodgman, R. G. Dall, A. G. Manning, K. G. H. Baldwin, and A. G. Truscott, Science **331**, 1046 (2011).
[43] S. Inouye, T. Pfau, S. Gupta, A. P. Chikkatur, A. Gorlitz, D. E. Pritchard, and W. Ketterle, Nature **402**, 641 (1999).
[44] M. Kozuma, Y. Suzuki, Y. Torii, T. Sugiura, T. Kuga, E. Hagley, and L. Deng, Science **286**, 2309 (1999).
[45] D. Schneble, Y. Torii, M. Boyd, E. W. Streed, D. E. Pritchard, and W. Ketterle, Science **300**, 475 (2003).
[46] L. F. Buchmann, G. M. Nikolopoulos, O. Zobay, and P. Lambropoulos, Phys. Rev. A **81**, 031606 (2010).
[47] W. RuGway, S. S. Hodgman, R. G. Dall, M. T. Johnsson, and A. G. Truscott, Phys. Rev. Lett. **107**, 075301 (2011).
[48] R. Bucker, J. Grond, S. Manz, T. Berrada, T. Betz, C. Koller, U. Hohenester, T. Schumm, A. Perrin, and J. Schmiedmayer, Nat. Phys. **7**, 608 (2011).
[49] M. Bonneau, J. Ruaudel, R. Lopes, J.-C. Jaskula, A. Aspect, D. Boiron, and C. I. Westbrook, Phys. Rev. A **87**, 061603 (2013).

An atomic Hong–Ou–Mandel experiment

R. Lopes, A. Imanaliev, A. Aspect, M. Cheneau, D. Boiron, C. I. Westbrook

Laboratoire Charles Fabry
Institut d'Optique Graduate School – CNRS – Université Paris Sud,
2 avenue Augustin Fresnel, 91127 Palaiseau, France

16th January 2015

arXiv:1501.03065v2 [quant-ph] 15 Jan 2015

Quantum mechanics is a very successful and still intriguing theory, introducing two major counter-intuitive concepts. *Wave-particle duality* means that objects normally described as particles, such as electrons, can also behave as waves, while entities primarily described as waves, such as light, can also behave as particles. This revolutionary idea nevertheless relies on notions borrowed from classical physics, either waves or particles evolving in our ordinary space-time. By contrast, *entanglement* leads to interferences between the amplitudes of multi-particle states, which happen in an abstract mathematical space and have no classical counterpart. This fundamental feature has been strikingly demonstrated by the violation of Bell's inequalities[1–4]. There is, however, a conceptually simpler situation in which the interference between two-particle amplitudes entails a behaviour impossible to describe by any classical model. It was realised in the Hong, Ou and Mandel (HOM) experiment[5], in which two photons arriving simultaneously in the input channels of a beam-splitter always emerge together in one of the output channels. In this letter, we report on the realisation, with atoms, of a HOM experiment closely following the original protocol. This opens the prospect of testing Bell's inequalities involving mechanical observables of massive particles, such as momentum, using methods inspired by quantum optics[6,7], with an eye on theories of the quantum-to-classical transition[8–11]. Our work also demonstrates a new way to produce and benchmark twin-atom pairs[12,13] that may be of interest for quantum information processing[14] and quantum simulation[15].

A pair of entangled particles is described by a state vector that cannot be factored as a product of two state vectors associated with each particle. Although entanglement does not require that the two particles be identical[2], it arises naturally in systems of indistinguishable particles due to the symmetrisation of the state. A remarkable illustration is the HOM experiment, in which two photons enter in the two input channels of a beam-splitter and one measures the correlation between the signals produced by photon counters placed at the two output channels. A joint detection at these detectors arises from two possible processes: either both photons are transmitted by the beam-splitter or both are reflected (Fig. 1c). If the two photons are indistinguishable, both processes lead to the same final quantum state and the probability of joint detection results from the addition of their amplitudes. Because of elementary properties of the beam-splitter, these amplitudes have same modulus but opposite signs, thus their sum vanishes and so also the probability of joint detection (Refs. [16, 17] and Methods). In fact, to be fully indistinguishable, not only must the photons have the same energy and polarisation, but their final spatio-temporal modes must be identical. In the HOM experiment, it means that the two photons enter the beam-splitter in modes that are the exact images of each other. As a result, when measured as a function of the delay between the arrival times of the photons on the beam-splitter, the correlation exhibits the celebrated 'HOM dip', ideally going to zero at null delay.

In this letter, we describe an experiment equivalent in all important respects to the HOM experiment, but performed with bosonic atoms instead of photons. We produce freely propagating twin beams of metastable Helium 4 atoms[18], which we then reflect and overlap on a beam-splitter using Bragg scattering on an optical lattice (Ref. [19] and Fig. 1). The photon counters after the beam-splitter are replaced by a time-resolved, multi-pixel atom-counting detector[20], which enables the measurement of intensity correlations between the atom beams in well defined spatial and spectral regions. The temporal overlap between the atoms can be continuously tuned by changing the moment when the atomic beam-splitter is applied. We observe the HOM dip when the atoms simultaneously pass through the beam-splitter. Such a correlation has no explanation in terms of classical particles. In addition, a quantitative analysis of the visibility of the dip also rules out any interpretation in terms of single-particle matter waves. Our observation must instead result from a quantum interference between multi-particle amplitudes.

Our experiment starts by producing a Bose–Einstein condensate (BEC) of metastable Helium 4 atoms in the $2\,^3\mathrm{S}_1, m = 1$ internal state. The BEC contains 5 to 6×10^4 atoms and is confined in an elliptical optical trap with its long axis along the vertical (z) direction (Fig. 1a). The atomic cloud has radii of 58 and 5 µm along the longitudinal and transverse ($\perp$) directions, respectively. A moving optical lattice, superimposed on the BEC for 300 µs, induces the scattering of atom pairs (hereafter referred to as twin atoms) in the longitudinal direction through a process analogous to spontaneous four wave mixing (Refs. [18, 21, 22] and Methods). One beam, labelled a, has a free-space velocity $v_z \simeq 12.1\,\mathrm{cm\,s^{-1}}$ in the laboratory frame of reference and the other beam, labelled b, has a velocity $v_z \simeq 7.0\,\mathrm{cm\,s^{-1}}$ (Fig. 1b,c). The twin atom beams clearly appear in the velocity distribution of the atoms, which is displayed in Fig. 2. The visible difference in population between the beams probably results from secondary scattering processes in the optical lattice, leading to the decay over time of the quasi-momentum states[18]. After the optical lattice has been switched off (time t_1), the twin atoms propagate in the optical trap for 200 µs. At this moment, the trap itself is switched off and the atoms are transferred to the magnetically insensitive $m = 0$ internal state by a two-photon Raman transition (Methods).

From here on, the atoms evolve under the influence of gravity and continue to move apart (Fig. 1b). At time $t_2 = t_1 + 500\,\mu\mathrm{s}$, we deflect the beams using Bragg diffraction on a second optical lattice, so as to make them converge. In the centre-of-mass frame of reference, this deflection reduces to a simple specular reflection (Fig. 1c and Methods). At time $t_3 \simeq 2t_2 - t_1$, we apply the same diffraction lattice for half the amount of time in order to realise a beam-splitting operation on the crossing atom beams. Changing the time t_3 allows us to tune the degree of temporal overlap between the twin atoms. Fig. 1c shows the atomic trajectories in the centre-of-mass frame of reference and reveals the close analogy with a photonic HOM experiment. The atoms end their fall on a micro-channel plate detector located 45 cm below the position of the initial BEC and we record the time and transverse position of each atomic impact with a detection efficiency $\eta \sim 25\,\%$ (Methods). The time of flight to the detector is approximately 300 ms, long enough that the recorded signal yields the three components of the atomic velocity. By collecting data from several hundred repetitions of the experiment under the same conditions, we are able to reconstruct all desired atom number correlations within

variable integration volumes of extent $\Delta v_z \times \Delta v_\perp^2$. These volumes play a similar role to that of the spatial and spectral filters in the HOM experiment and can be adjusted to erase the information that could allow tracing back the origin of a detected particle to one of the input channels.

The HOM dip should appear in the cross-correlation between the detection signals in the output channels of the beam-splitter (Ref. [16] and Methods):

$$G_{cd}^{(2)} = \left(\frac{\eta}{\Delta v_z \Delta v_\perp^2}\right)^2 \iint_{\mathcal{V}_c \times \mathcal{V}_d} \langle \hat{a}_{\mathbf{v}_c}^\dagger \hat{a}_{\mathbf{v}_d}^\dagger \hat{a}_{\mathbf{v}_d} \hat{a}_{\mathbf{v}_c} \rangle \, \mathrm{d}^{(3)}\mathbf{v}_c \, \mathrm{d}^{(3)}\mathbf{v}_d \, . \tag{1}$$

Here, $\hat{a}_{\mathbf{v}}$ and $\hat{a}_{\mathbf{v}}^\dagger$ denote the annihilation and creation operators of an atom with three-dimensional velocity $\mathbf{v}$, respectively, $\langle \cdot \rangle$ stands for the quantum and statistical average and $\mathcal{V}_{c,d}$ designate the integration volumes centred on the output atom beams c and d (Fig. 1c). We have measured this correlation as a function of the duration of propagation $\tau = t_3 - t_2$ between the mirror and the beam-splitter (Fig. 3) and for various integration volumes (see supplementary material). We observe a marked reduction of the correlation when τ is equal to the duration of propagation from the source to the mirror ($t_3 - t_2 \simeq t_2 - t_1$) and for small enough integration volumes, corresponding to a full overlap of the atomic wave-packets on the beam-splitter. Fitting the data with an empirical Gaussian profile yields a visibility:

$$V = \frac{\max_\tau G_{cd}^{(2)}(\tau) - \min_\tau G_{cd}^{(2)}(\tau)}{\max_\tau G_{cd}^{(2)}(\tau)} = 0.65(7) \, , \tag{2}$$

where the number in parenthesis stands for the 68 % confidence interval. As we shrink the integration volumes, we observe that the dip visibility first increases and then reaches a saturation value, as is expected when the integration volumes become smaller than the elementary atomic modes. The data displayed in Fig. 3 were obtained for $\Delta v_z = 0.3\,\mathrm{cm\,s^{-1}}$ and $\Delta v_\perp = 0.5\,\mathrm{cm\,s^{-1}}$, which maximises the reduction of the correlation while preserving a statistically significant number of detection events (see supplementary material).

The dip in the cross-correlation function cannot be explained in terms of classical particles, for which we would have no correlation at all between the detections in the output channels. When the atoms are viewed as waves however, demonstrating the quantum origin of the dip

necessitates a deeper analysis. The reason is that two waves can interfere at a beam-splitter and give rise to an intensity imbalance between the output ports. If, in addition, the coherence time of the waves is finite, the cross-correlation can display a dip similar to the one observed in our experiment. But once averaged over the phase difference between the beams, the visibility is bounded from above and cannot exceed 0.5 (Refs. [23, 24] and Methods). In our experiment, this phase difference is randomised by the shot-to-shot fluctuations of the relative phase between the laser beams used for Bragg diffraction (Methods). Since our measured visibility exceeds the limit for waves by two standard deviations, we can safely rule out any interpretation of our observation in terms of interference between two 'classical' matter waves or, in other words, between two ordinary wave functions describing each of the two particles separately.

Two contributions may be responsible for the non-zero value of the correlation function at the centre of the dip: the detected particles may not be fully indistinguishable and the number of particles contained in the integration volume may exceed unity for each beam (Refs. [23, 25] and Methods). The effect of the atom number distribution can be quantified by measuring the intensity correlations of the twin atom beams upstream of the beam-splitter (Fig. 1c), which bound the visibility of the dip through the relation:

$$V_{\max} = 1 - \frac{G^{(2)}_{aa} + G^{(2)}_{bb}}{G^{(2)}_{aa} + G^{(2)}_{bb} + 2G^{(2)}_{ab}} \,, \tag{3}$$

where $G^{(2)}_{aa}$, $G^{(2)}_{bb}$ and $G^{(2)}_{ab}$ are defined according to Eq. 1 (Ref. [24] and Methods). Here, one immediately sees that the finite probability of having more than one atom in the input channels will lead to finite values of the auto-correlations $G^{(2)}_{aa}$, $G^{(2)}_{bb}$ and therefore to a reduced visibility. We have performed the measurement of these correlations following the same experimental procedure as before, except that we did not apply the mirror and beam-splitter. We find non-zero values $G^{(2)}_{aa} = 0.016(5)$, $G^{(2)}_{bb} = 0.047(9)$, and $G^{(2)}_{ab} = 0.048(7)$, yielding $V_{\max} = 0.60(10)$, where the uncertainty is the standard deviation of the statistical ensemble. Because of the good agreement with the measured value, we conclude that the atom number distribution in the input channels entirely accounts for the visibility of the HOM dip. For the present experiment we estimate the average number of incident atoms to be 0.5(1) in $\mathcal{V}_a$ and 0.8(2) in $\mathcal{V}_b$, corresponding to a ratio of the probability for having two atoms to that for having one atom of 0.25(5) and

0.40(10), respectively (Methods). Achieving much smaller values is possible, for instance by reducing the pair production rate, but at the cost of much lower counting statistics.

Although multi-particle interferences can be observed with particles emitted or prepared independently[13,26–29], twin particle sources are at the heart of many protocols for quantum information processing[14] and quantum simulation[15]. The good visibility of the HOM dip in our experiment demonstrates that our twin atom source produces beams which have highly correlated populations and are well mode matched. This is an important achievement in itself, which may have the same impact for quantum atom optics as the development of twin photon sources using non-linear crystals had for quantum optics (see for instance Ref. [30]).

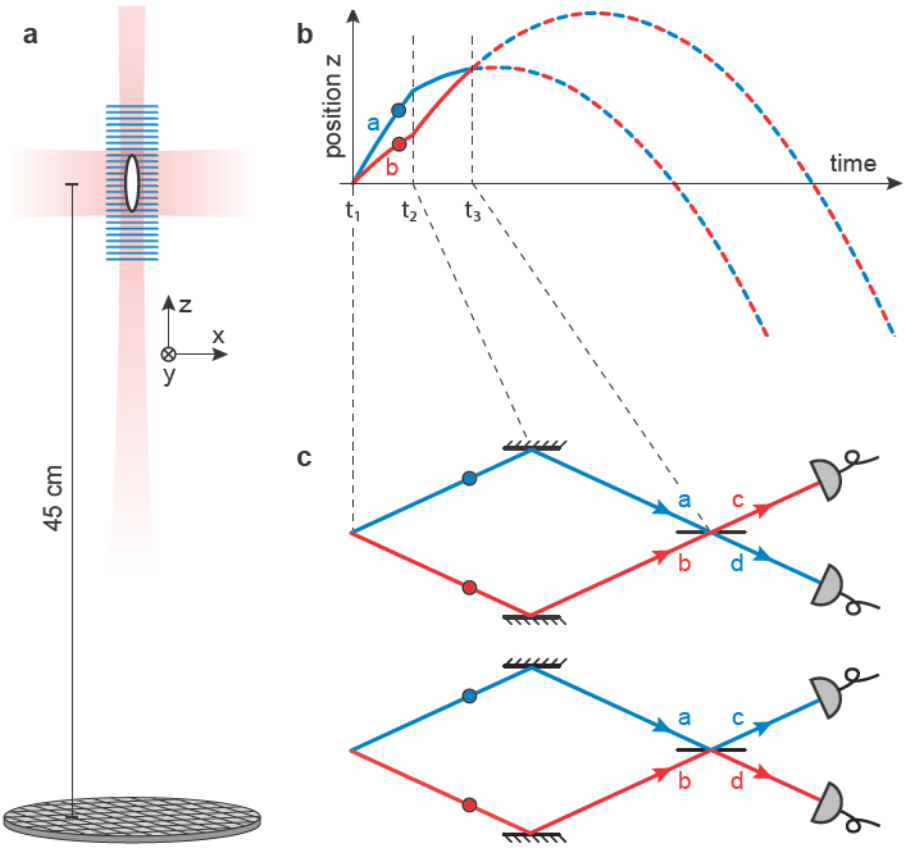

Figure 1 | Schematic of the experiment. a, A Bose–Einstein condensate (BEC, white oval) of metastable Helium 4 atoms is trapped in an elongated optical trap (red shaded area). A moving optical lattice, here depicted in blue, is superimposed on the BEC and triggers the scattering of atom pairs along the z-axis. When this lattice and the trap are switched off, the atoms fall towards a micro-channel plate detector located 45 cm below the initial position of the BEC (drawing not to scale). **b,** The time diagram shows the evolution of the twin atom vertical coordinates (blue and red lines). Between t_1 and t_2, t_2 and t_3, and after t_3, the atoms move under the sole influence of gravity (drawing not to scale). At t_2, the twin atom velocities are swapped using Bragg diffraction on an optical lattice. At time t_3, when the atomic trajectories cross again, the same lattice is applied for half the amount of time in order to realise a beam-splitter. **c,** In the centre-of-mass frame of reference, the trajectories of the atoms resemble those of the photons in the Hong–Ou–Mandel experiment. A joint detection arises either when both atoms are transmitted through the beam-slitter (upper panel) or when both are reflected (lower panel). If the two particles are indistinguishable, these processes end in the same final quantum state and the probability of joint detection results from the addition of their amplitudes. For bosons these amplitudes have same modulus but opposite signs, thus their sum vanishes and so also the probability of joint detection.

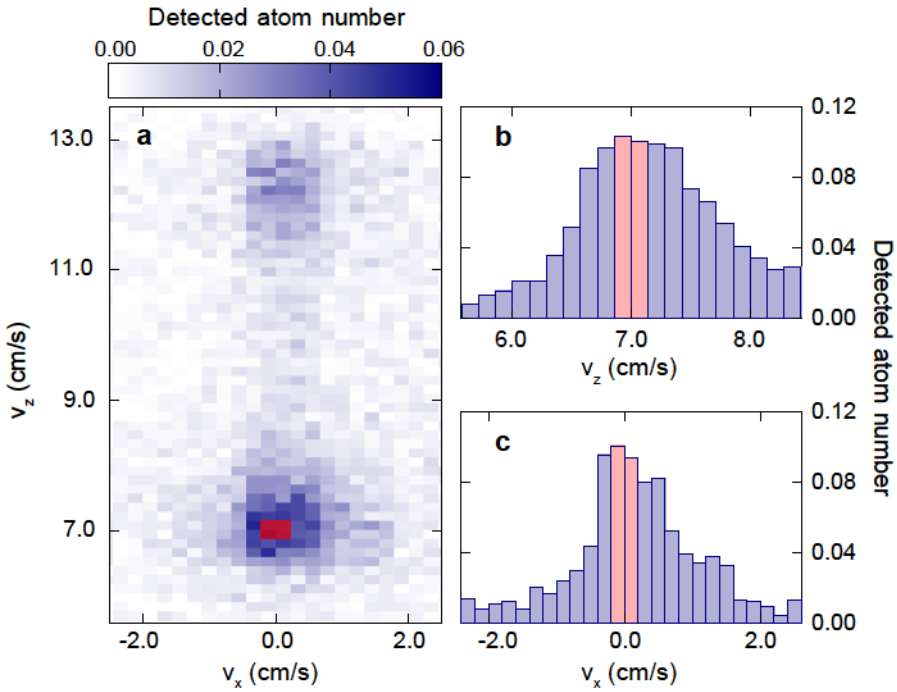

Figure 2 | Velocity distribution of the twin atoms. a, Two-dimensional velocity distribution of the twin atom beams emitted by the source. The red shaded area, drawn here only for the lower beam, labelled *b* in Fig. 1b and c, shows the integration volume used for computing the correlation function displayed in Fig. 3. The distribution corresponds to an average over about 1,100 measurements and is not corrected for the limited detection efficiency. The velocities are given relative to the laboratory frame of reference. The size of each pixel is $0.25\,\mathrm{cm\,s^{-1}}$ in the transverse directions (x and y) and $0.15\,\mathrm{cm\,s^{-1}}$ in the longitudinal (z) direction and an integration over 2 pixels is performed along the y direction. **b,c,** Cuts of the two-dimensional velocity distribution through the centre of the lower beam along the longitudinal (**b**) and transverse (**c**) directions. The data points result from the average over 2 pixels along the direction perpendicular to the cut. The full width at half-maximum of the distribution, obtained from a Gaussian fit, is about $1.4\,\mathrm{cm\,s^{-1}}$ along both the longitudinal and transverse directions. The red shaded area again shows the integration volume.

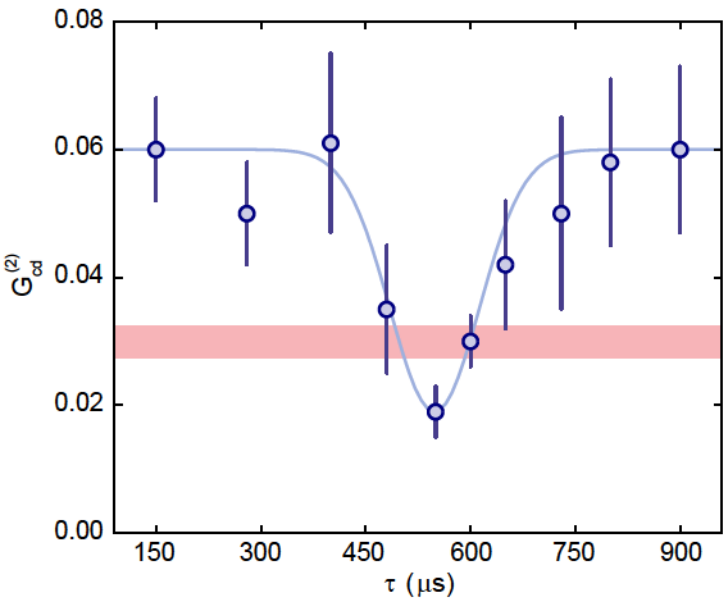

Figure 3 | HOM dip in the cross-correlation function. The correlation $G^{(2)}_{cd}$ between the output ports of the beam-splitter, defined in Eq. 1, was measured as a function of the duration of propagation $\tau = t_3 - t_2$ between the mirror and the beam splitter. The HOM dip is directly visible as a marked reduction of the correlation when τ equals the duration of propagation $t_2 - t_1 \simeq 500\,\mu\text{s}$ between the source and the mirror, corresponding to symmetric paths between the source and the beam-splitter, i.e. when one cannot distinguish between the two diagrams of Fig. 1c. A Gaussian fit (blue line) precisely locates the dip at $\tau = 550(50)\,\mu\text{s}$, with a full-width at half-maximum of $150(40)\,\mu\text{s}$, where the uncertainty corresponds to the 68 % confidence interval. The measured visibility is $V = 0.65(7)$. It is two standard deviations beyond the classical-to-quantum threshold represented by the red shaded area, which takes into account the experimental uncertainty over the background correlation value. Each data point was obtained from an average over about 500 to 1,400 repetitions of the experiment. Error bars denote the standard deviation of the statistical ensemble. The mean detected atom number was constant over the range of values of τ displayed here (see supplementary material).

Acknowledgements We thank Josselin Ruaudel and Marie Bonneau for their contribution to the early steps of the experiment. We also thank Karen Kheruntsyan, Jan Chwedeńczuk and Piotr Deuar for discussions. We acknowledge funding by IFRAF, Triangle de la Physique, Labex PALM, ANR (PROQUP), FCT (scholarship SFRH/BD/74352/2010 to R.L.) and EU (ERC Grant 267775 – QUANTATOP and Marie Curie CIG 618760 – CORENT).

Author Information Correspondence and requests for materials should be addressed to R.L. (raphael.lopes@institutoptique.fr) or M.C. (marc.cheneau@institutoptique.fr).

Methods

Twin atom source

The twin atom beams result from a scattering process between pairs of atoms from the BEC occurring when the gas is placed in a moving one-dimensional optical lattice. The experimental set-up has been described in Ref. [18]. The lattice is formed by two laser beams derived from the same source emitting at the wavelength $\lambda = 1{,}064\,\mathrm{nm}$. In contrast to our previous work, the axis of the optical lattice was now precisely aligned with the long axis of the optical trap confining the atoms. The laser beams intersect with an angle of $\theta = 166°$, their frequency difference is set to 100.5 kHz and the lattice depth to $0.4\,E_{\mathrm{rec}}$. This constrains the longitudinal wave-vector of the twin atoms to the values $k_{z,a} = 0.75\,k_{\mathrm{rec}}$ and $k_{z,b} = 1.30\,k_{\mathrm{rec}}$ in order to fulfil the conservation of quasi-momentum and energy in the frame co-propagating with the lattice. Here, $k_{\mathrm{rec}} = 2\pi\sin(\theta/2)/\lambda$ is the recoil wave-vector along the longitudinal axis gained upon absorption of a photon from a lattice laser and $E_{\mathrm{rec}} = \hbar^2 k_{\mathrm{rec}}^2/2m$ is the associated kinetic energy, with $\hbar$ the reduced Planck constant and $m = 6.64 \times 10^{-27}\,\mathrm{kg}$ the mass of an Helium 4 atom. The observed velocities of the twin atom beams coincide with the expected values above, using the relation $v = \hbar k/m$. The optical lattice is turned on and off adiabatically so as to avoid diffraction of the atoms during this phase of the experiment.

Transfer to the magnetically insensitive internal state

Transfer to the $m = 0$ state after the optical trap has been switched off is made necessary by the presence of stray magnetic fields in the vacuum chamber that otherwise would lead to a severe deformation of the atomic distribution during the long free fall. The transfer is achieved by introducing a two-photon coupling between the $m = 1$ state, in which the atoms are initially, and the $m = 0$ state using two laser beams derived from a single source emitting at 1,083 nm and detuned by 600 MHz from the $2\,^3\mathrm{S}_1$ to $2\,^3\mathrm{P}_0$ transition. The frequency difference of the laser beams is chirped across the two-photon resonance so as to realise an adiabatic fast passage transition (the frequency change is 300 kHz in 300 µs). We have measured the fraction of transferred atoms to be 94 %. The remaining 6 % stay in the $m = 1$ state and are pushed

away from the integration volumes by the stray magnetic field gradients.

Atomic mirror and beam-splitter

The mirror and beam-splitter are both implemented using Bragg scattering on a second optical lattice. This effect can be seen as a momentum exchange between the atoms and the laser beams forming the lattice, a photon being coherently absorbed from one beam and emitted into the other. In our experiment, the laser beams forming the lattice have a waist of 1 mm and are detuned by 600 MHz from the $2\,^3\mathrm{S}_1$ to $2\,^3\mathrm{P}_0$ transition (they are derived from the same source as the beams used for the Raman transfer). In order to fulfil the Bragg resonance condition for the atom beams, the laser beams are made to intersect at an angle of 32° and the frequency of one of the beams is shifted by 53.4 kHz. In addition to this fixed frequency difference, a frequency chirp is performed to compensate for the acceleration of the atoms during their free fall. The interaction time between the atoms and the optical lattice was 100 µs for the mirror operation (π-pulse) and 50 µs for the beam-splitter operation ($\pi/2$-pulse). The resonance condition for the momentum state transfer is satisfied by all atoms in the twin beams but only pairs of states with a well defined momentum difference are coupled with each other. We measured the reflectivity of the mirror and the transmittance of the beam-splitter to be 0.95(2) and 0.49(2), respectively. Spontaneous scattering of photons by the atoms was negligible.

Detection efficiency

Our experiment relies on the ability to detect the atoms individually. The detection efficiency is an essential parameter for achieving good signal to noise ratios, although it does not directly influence the visibility of the HOM dip. Our most recent estimate of the detection efficiency relies on the measurement of the variance of the atom number difference between the twin beams. For this we use the same procedure as described in Ref. [18], but with an integration volume that includes the entire velocity distribution of each beam. We find a normalised variance of 0.75(5), well below the Poissonian floor. Since for perfectly correlated twin beams the measured variance would be $1-\eta$, we attribute the lower limit of 25(5) % to our detection efficiency. This value for η is a factor of about 2 larger than the lower bound quoted in Ref. [31].

The difference is due to the change of method employed for transferring the atoms from the $m = 1$ to the $m = 0$ state after the optical trap has been switched off. We previously used a radio-frequency transfer with roughly 50 % efficiency whereas the current optical Raman transfer has close to 100 % efficiency.

Distribution of the number of incident atoms

We have estimated the average number of incident atoms in each input channel of the beam-splitter, n_a and n_b, by analysing the distribution of detected atoms in the integration volumes $\mathcal{V}_a$ and $\mathcal{V}_b$. We fitted these distributions by assuming an empirical Poissonian law for the distribution of incident atoms and taking into account the independently calibrated detection efficiency. The values of n_a and n_b given in the main text are the mean values of the Poissonian distributions that best fit the data. The probabilities for having one or two atoms in each of the input channels of the beam splitter was obtained from the same analysis. The uncertainty on these numbers mostly stems from the uncertainty on the detection efficiency.

The HOM effect

The HOM effect appears in the correlator $\langle \hat{a}^\dagger_{\mathbf{v}_c} \hat{a}^\dagger_{\mathbf{v}_d} \hat{a}_{\mathbf{v}_d} \hat{a}_{\mathbf{v}_c} \rangle$ of Eq. 1. The simplest way to calculate such a correlator is to transform the operators and the state vector back in the input space before the beam-splitter and to use the Heisenberg picture. The transformation matrix between the operators $\hat{a}_{\mathbf{v}_c}(t_3)$, $\hat{a}_{\mathbf{v}_d}(t_3)$ and $\hat{a}_{\mathbf{v}_a}(t_3)$, $\hat{a}_{\mathbf{v}_b}(t_3)$ can be worked out from first principles. For the Bragg beam-splitter, and using a Rabi two-state formalism, we find:

$$\begin{cases} \hat{a}_{\mathbf{v}_c} = \dfrac{1}{\sqrt{2}} \left(i\, e^{i\phi}\, \hat{a}_{\mathbf{v}_a} + \hat{a}_{\mathbf{v}_b} \right) \ , \\ \hat{a}_{\mathbf{v}_d} = \dfrac{1}{\sqrt{2}} \left(\hat{a}_{\mathbf{v}_a} + i\, e^{-i\phi}\, \hat{a}_{\mathbf{v}_b} \right) \ , \end{cases} \tag{4}$$

where ϕ is the relative phase between the laser beams forming the optical lattice. In the ideal case of an input state with exactly one atom in each channel, $|1_{\mathbf{v}_a}, 1_{\mathbf{v}_b}\rangle$, we therefore obtain:

$$\begin{aligned}
\left\| \hat{a}_{\mathbf{v}_d}\hat{a}_{\mathbf{v}_c} |1_{\mathbf{v}_a}, 1_{\mathbf{v}_b}\rangle \right\|^2 &= \frac{1}{4} \left\| \left(i\, e^{i\phi}\, \hat{a}^2_{\mathbf{v}_a} + i\, e^{-i\phi}\, \hat{a}^2_{\mathbf{v}_b} + \hat{a}_{\mathbf{v}_a}\hat{a}_{\mathbf{v}_b} + i^2\, \hat{a}_{\mathbf{v}_b}\hat{a}_{\mathbf{v}_a} \right) |1_{\mathbf{v}_a}, 1_{\mathbf{v}_b}\rangle \right\|^2 && (5)\\
&= \frac{1}{4} \left\| 0 + \left(1 + i^2\right) |0_{\mathbf{v}_a}, 0_{\mathbf{v}_b}\rangle \right\|^2 && (6)\\
&= 0\,. && (7)
\end{aligned}$$

meaning that the probability of joint detection is strictly zero. The detailed calculation above makes clear that the perfect destructive interference between the two-particle state amplitudes associated with the two diagrams of Fig. 1c is at the heart of the HOM effect. By contrast, input states containing more than one atom per channel are transformed into a sum of orthogonal states and the interference can only be partial. Taking $|2_{\mathbf{v}_a}, 2_{\mathbf{v}_b}\rangle$, for instance, yields:

$$\begin{aligned}
\left\| \hat{a}_{\mathbf{v}_d}\hat{a}_{\mathbf{v}_c} |2_{\mathbf{v}_a}, 2_{\mathbf{v}_b}\rangle \right\|^2 &= \frac{1}{4} \left\| \left(i\, e^{i\phi}\, \hat{a}^2_{\mathbf{v}_a} + i\, e^{-i\phi}\, \hat{a}^2_{\mathbf{v}_b} + \hat{a}_{\mathbf{v}_a}\hat{a}_{\mathbf{v}_b} + i^2\, \hat{a}_{\mathbf{v}_b}\hat{a}_{\mathbf{v}_a} \right) |2_{\mathbf{v}_a}, 2_{\mathbf{v}_b}\rangle \right\|^2 && (8)\\
&= \frac{1}{2} \left\| i\, e^{i\phi}\, |0_{\mathbf{v}_a}, 2_{\mathbf{v}_b}\rangle + i\, e^{-i\phi}\, |2_{\mathbf{v}_a}, 0_{\mathbf{v}_b}\rangle + \sqrt{2}\left(1 + i^2\right) |1_{\mathbf{v}_a}, 1_{\mathbf{v}_b}\rangle \right\|^2 && (9)\\
&= \frac{1}{2} \left\| e^{i\phi}\, |0_{\mathbf{v}_a}, 2_{\mathbf{v}_b}\rangle + e^{-i\phi}\, |2_{\mathbf{v}_a}, 0_{\mathbf{v}_b}\rangle \right\|^2 && (10)\\
&= 1\,. && (11)
\end{aligned}$$

Finally, we note that losses in one of the incident beams, for instance beam a, can be modelled by a fictitious beam-splitter with a transmission coefficient T. In the above calculation, these losses would therefore only manifest by an additional factor $\sqrt{T}$ in front of every operator $\hat{a}_{\mathbf{v}_a}$, leaving unaffected the destructive interference that gives rise to the HOM effect.

Visibility of the HOM dip

A slightly less general form of Eq. 3 has been derived in Ref. [24] assuming a two-mode squeezed state as an input state. The same calculation can be performed for an arbitrary input state. Leaving aside the integration over the velocity distribution, we find that the cross-correlation

for indistinguishable particles can be expressed as:

$$G^{(2)}_{cd}\big|_{\text{indisc.}} = \frac{1}{4}\left(G^{(2)}_{aa} + G^{(2)}_{bb} + \Delta\right) \ , \quad \Delta = 2\eta^2\,\mathrm{Re}\big[e^{2i\phi}\langle \hat{a}^\dagger_{\mathbf{v}_a}\hat{a}^\dagger_{\mathbf{v}_a}\hat{a}_{\mathbf{v}_b}\hat{a}_{\mathbf{v}_b}\rangle\big] \ , \tag{12}$$

whereas that of distinguishable particles reads

$$G^{(2)}_{cd}\big|_{\text{disc.}} = \frac{1}{4}\left(G^{(2)}_{aa} + G^{(2)}_{bb} + 2G^{(2)}_{ab}\right) \ . \tag{13}$$

Here, the correlators appearing in the right-hand side are taken at time t_1, that is immediately after the the atom beams have been produced. The term Δ corresponds to an interference between single-particle matter waves. It depends on both the relative phase between the atom beams and the relative phase between the laser beams used for Bragg diffraction. The latter is counted once for the atomic mirror and once for the atomic beam-splitter. Twin beams with perfect correlations in their population would have a fully random relative phase. In our experiment however, the population imbalance between the atom beams could entail a residual phase coherence. Instead, the relative phase between the laser beams was left uncontrolled and its value was randomly distributed between two repetitions of the experiment. As a result, the term Δ must average to zero and the visibility of the HOM dip be given by Eq. 3, as observed in the experiment. Following Ref. [24], we also note that Eq. 3 entails the ultimate bound for waves interfering on the beam-splitter: because waves must fulfil the Cauchy–Schwarz inequality, $G^{(2)}_{ab} < \sqrt{G^{(2)}_{aa}G^{(2)}_{bb}}$, the visibility of the classical dip cannot exceed 0.5.

The above results holds true for a finite integration over the atomic velocity distribution if two conditions are met: (i) It must remain impossible to distinguish the atoms entering the beam-splitter through channel a from the atoms entering through channel b once they have exited the beam-splitter; (ii) The transformation matrix of the beam-splitter must keep the same form after integration. In our experiment, the second condition is naturally satisfied because the Bragg diffraction only couples atomic states with a well defined momentum difference and we fulfil the first condition by reducing the integration volume as much as it is necessary.

Supplementary material

Optimization of the Hong-Ou-Mandel dip

The visibility of the Hong-Ou-Mandel dip is plotted in Fig. S1 as a function of the longitudinal (a) and transverse (b) integration volume. The red dots identify the integration volume used in Fig. 3 of the main text and correspond to a compromise between signal to noise ratio and visibility amplitude. As we shrink the integration volumes, the dip visibility first increases and then reaches a saturation value, meaning that the integration volume becomes smaller than the elementary atomic modes[32–34]. Reducing further the integration volume only leads to an increase of the statistical uncertainty.

The visibility V is obtained by fitting the cross-correlation function $G^{(2)}_{cd}(\tau)$ measured in the experiment with the empirical function:

$$f(\tau) = G^{(2)}_{\mathrm{bg}}\Big(1 - V\exp\big(-(\tau-\tau_0)^2/2\sigma^2\big)\Big)\ ,$$

where the background correlation $G^{(2)}_{\mathrm{bg}}$, the center of the dip τ_0 and the width of the dip σ are all left as free parameters.

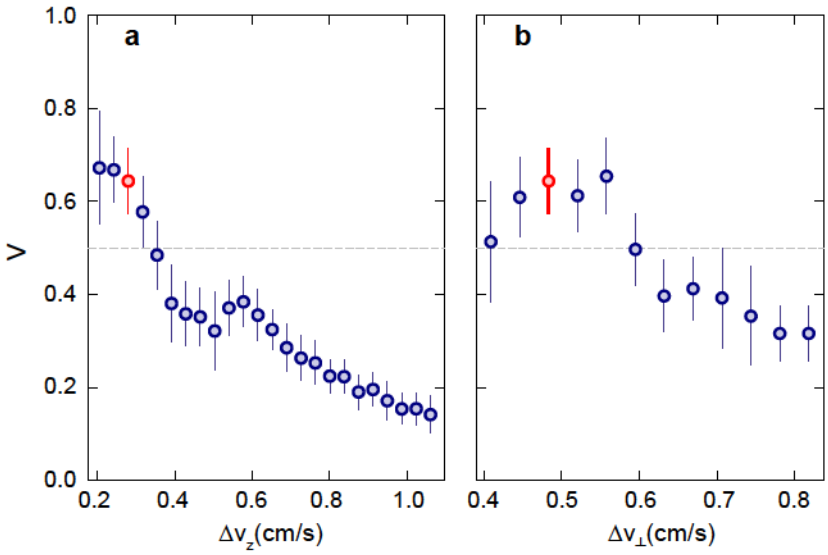

Figure S1 | Visibility as a function of the integration volume. a, Visibility as a function of the longitudinal integration interval Δv_z. The transverse integration interval is kept constant at $\Delta v_\perp = 0.48\,\mathrm{cm\,s^{-1}}$. **b,** Visibility as a function of the transverse integration interval $\Delta v_\perp$. The longitudinal integration interval is kept constant at $\Delta v_z = 0.28\,\mathrm{cm\,s^{-1}}$. The red points mark the values discussed in the main text.

Stability of the atom number in the output ports

The mean detected atom number in the output ports c and d is plotted as function of τ in Fig. S2. The mean atom number is constant as function of τ within the statistical uncertainty. To easily compare the atom number fluctuations to the variation of the cross-correlation across the HOM dip, the product of the averaged populations $\langle n_c \rangle \cdot \langle n_d \rangle$ and the cross-correlation $G^{(2)}_{cd}$ are displayed together as a function of τ in Fig. S2c. In contrast to the cross-correlation, it is impossible to identify a marked reduction of $\langle n_c \rangle \cdot \langle n_d \rangle$ around $\tau = 550\,\mu\mathrm{s}$. This confirms our interpretation of the dip as a destructive two-particle interference.

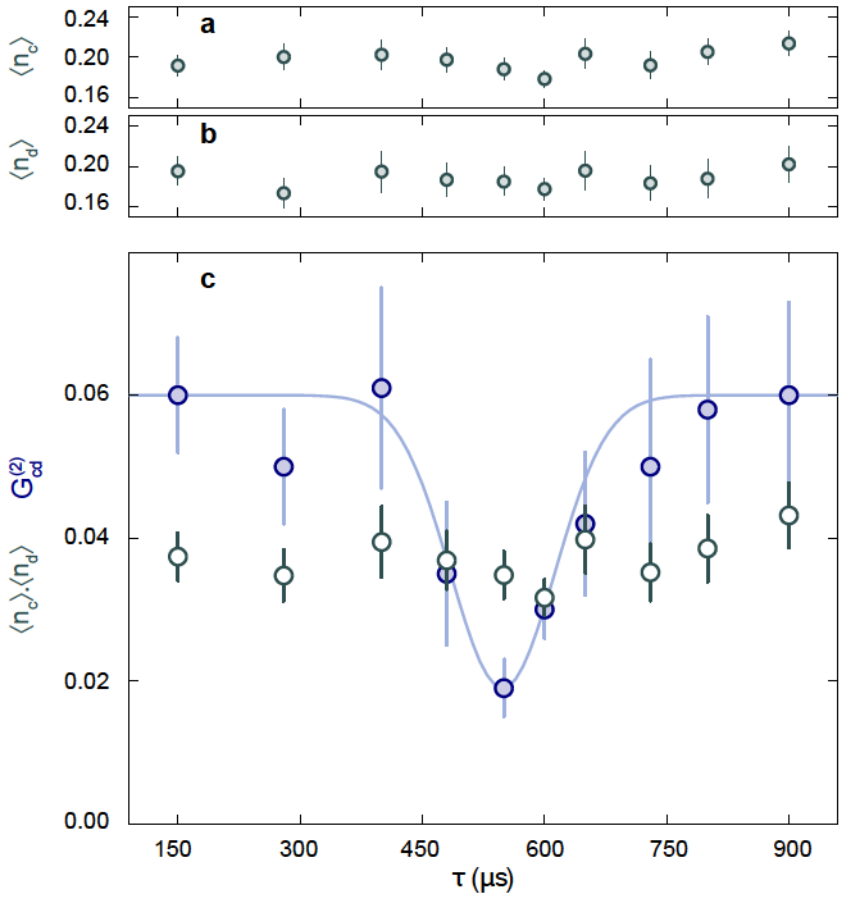

Figure S2 | Stability of the output population over propagation duration. a, Averaged atom number detected in $\mathcal{V}_c$ as a function of the propagation time τ. The mean value of n_c is 0.20 with a standard deviation of 0.01. **b,** Averaged atom number detected in $\mathcal{V}_d$ as a function of the propagation time τ. The mean value of n_d is 0.19 with a standard deviation of 0.01. **c,** The cross-correlation between the output ports c and d (solid blue circles), corresponding to the HOM dip, is compared to the product of the average density populations $\langle n_c \rangle \cdot \langle n_d \rangle$ (open gray circles). The product of the averaged population is constant while the cross correlation exhibits a dip around $\tau = 550\,\mu\text{s}$.

References

1. Bell, J. S. On the Einstein-Podolsky-Rosen paradox. *Physics* **1,** 195–200 (1964).
2. Aspect, A. Bell's inequality test: more ideal than ever. *Nature* **398,** 189–190 (1999).
3. Giustina, M. *et al.* Bell violation using entangled photons without the fair-sampling assumption. *Nature* **497,** 227–230 (2013).
4. Christensen, B. G. *et al.* Detection-Loophole-Free Test of Quantum Nonlocality, and Applications. *Physical Review Letters* **111,** 130406 (2013).
5. Hong, C. K., Ou, Z. Y. & Mandel, L. Measurement of Subpicosecond Time Intervals between Two Photons by Interference. *Physical Review Letters* **59,** 2044–2046 (1987).
6. Rarity, J. G. & Tapster, P. R. Experimental violation of Bell's inequality based on phase and momentum. *Physical Review Letters* **64,** 2495–2498 (1990).
7. Lewis-Swan, R. J. & Kheruntsyan, K. V. Motional-state Bell inequality test with ultracold atoms, arXiv:1411.0191 (2014).
8. Penrose, R. Quantum computation, entanglement and state reduction. *Philosophical Transactions of the Royal Society of London. Series A: Mathematical, Physical and Engineering Sciences* **356,** 1927–1939 (1998).
9. Zurek, W. H. Decoherence, einselection, and the quantum origins of the classical. *Reviews of Modern Physics* **75,** 715–775 (2003).
10. Schlosshauer, M. Decoherence, the measurement problem, and interpretations of quantum mechanics. *Reviews of Modern Physics* **76,** 1267–1305 (2005).
11. Leggett, A. J. How far do EPR-Bell experiments constrain physical collapse theories? *Journal of Physics A: Mathematical and Theoretical* **40,** 3141–3149 (2007).
12. Bücker, R. *et al.* Twin-atom beams. *Nature Physics* **7,** 608–611 (2011).
13. Kaufman, A. M. *et al.* Two-particle quantum interference in tunnel-coupled optical tweezers. *Science* **345,** 306–309 (2014).
14. Nielsen, M. A. & Chuang, I. L. *Quantum Computation and Quantum Information* (Cambridge University Press, 2000).

15. Kitagawa, T., Aspect, A., Greiner, M. & Demler, E. Phase-Sensitive Measurements of Order Parameters for Ultracold Atoms through Two-Particle Interferometry. *Physical Review Letters* **106,** 115302 (2011).

16. Ou, Z. Y. *Multi-Photon Quantum Interference* (Springer, 2007).

17. Grynberg, G., Aspect, A. & Fabre, C. *Introduction to Quantum Optics: From the Semi classical Approach to Quantized Light* (Cambridge University Press, 2010).

18. Bonneau, M. *et al.* Tunable source of correlated atom beams. *Physical Review A* **87,** 061603 (2013).

19. Cronin, A. D., Schmiedmayer, J. & Pritchard, D. E. Optics and interferometry with atoms and molecules. *Reviews of Modern Physics* **81,** 1051–1129 (2009).

20. Schellekens, M. *et al.* Hanbury Brown Twiss Effect for Ultracold Quantum Gases. *Science* **310,** 648–651 (2005).

21. Hilligsøe, K. M. & Mølmer, K. Phase-matched four-wave mixing and quantum beam splitting of matter waves in a periodic potential. *Physical Review A* **71,** 041602 (2005).

22. Campbell, G. K. *et al.* Parametric Amplification of Scattered Atom Pairs. *Physical Review Letters* **96,** 020406 (2006).

23. Ou, Z. Y. Quantum theory of fourth-order interference. *Physical Review A* **37,** 1607–1619 (1988).

24. Lewis-Swan, R. J. & Kheruntsyan, K. V. Proposal for demonstrating the Hong–Ou–Mandel effect with matter waves. *Nature Communications* **5,** 3752 (2014).

25. Ou, Z. Y., Rhee, J.-K. & Wang, L. J. Observation of Four-Photon Interference with a Beam Splitter by Pulsed Parametric Down-Conversion. *Physical Review Letters* **83,** 959–962 (1999).

26. Beugnon, J. *et al.* Quantum interference between two single photons emitted by independently trapped atoms. *Nature* **440,** 779–782 (2006).

27. Bocquillon, E. *et al.* Coherence and Indistinguishability of Single Electrons Emitted by Independent Sources. *Science* **339,** 1054–1057 (2013).

28. Lang, C. *et al.* Correlations, indistinguishability and entanglement in Hong–Ou–Mandel experiments at microwave frequencies. *Nature Physics* **9,** 345–348 (2013).

29. Dubois, J. *et al.* Minimal-excitation states for electron quantum optics using levitons. *Nature* **502,** 659–663 (2013).

30. Ghosh, R. & Mandel, L. Observation Of Nonclassical Effects In The Interference Of 2 Photons. *Physical Review Letters* **59,** 1903–1905 (1987).

31. Jaskula, J.-C. *et al.* Sub-Poissonian Number Differences in Four-Wave Mixing of Matter Waves. *Physical Review Letters* **105,** 190402 (2010).

32. Rarity, J. G. & Tapster, P. R. Fourth-order interference in parametric downconversion. *Journal of the Optical Society of America B* **6,** 1221–1226 (1989).

33. Treps, N., Delaubert, V., Maître, A., Courty, J. M. & Fabre, C. Quantum noise in multipixel image processing. *Physical Review A* **71,** 013820 (2005).

34. Morizur, J.-F., Armstrong, S., Treps, N., Janousek, J. & Bachor, H.-A. Spatial reshaping of a squeezed state of light. *The European Physical Journal D* **61,** 237–239 (2011).